ADVANCES IN MONITORING, MODELING AND MANAGING INDUCED SEISMICITY

EDITED BY: Francesco Grigoli, Antonio Pio Rinaldi, Marco Maria Scuderi and Rebecca M. Harrington

PUBLISHED IN: Frontiers in Earth Science

frontiers Research Topics

ISSN 1664-8714
ISBN 978-2-88974-433-6
DOI 10.3389/978-2-88974-433-6

About Frontiers

Frontiers is more than just an open-access publisher of scholarly articles: it is a pioneering approach to the world of academia, radically improving the way scholarly research is managed. The grand vision of Frontiers is a world where all people have an equal opportunity to seek, share and generate knowledge. Frontiers provides immediate and permanent online open access to all its publications, but this alone is not enough to realize our grand goals.

Frontiers Journal Series

The Frontiers Journal Series is a multi-tier and interdisciplinary set of open-access, online journals, promising a paradigm shift from the current review, selection and dissemination processes in academic publishing. All Frontiers journals are driven by researchers for researchers; therefore, they constitute a service to the scholarly community. At the same time, the Frontiers Journal Series operates on a revolutionary invention, the tiered publishing system, initially addressing specific communities of scholars, and gradually climbing up to broader public understanding, thus serving the interests of the lay society, too.

Dedication to Quality

Each Frontiers article is a landmark of the highest quality, thanks to genuinely collaborative interactions between authors and review editors, who include some of the world's best academicians. Research must be certified by peers before entering a stream of knowledge that may eventually reach the public - and shape society; therefore, Frontiers only applies the most rigorous and unbiased reviews.
Frontiers revolutionizes research publishing by freely delivering the most outstanding research, evaluated with no bias from both the academic and social point of view. By applying the most advanced information technologies, Frontiers is catapulting scholarly publishing into a new generation.

What are Frontiers Research Topics?

Frontiers Research Topics are very popular trademarks of the Frontiers Journals Series: they are collections of at least ten articles, all centered on a particular subject. With their unique mix of varied contributions from Original Research to Review Articles, Frontiers Research Topics unify the most influential researchers, the latest key findings and historical advances in a hot research area! Find out more on how to host your own Frontiers Research Topic or contribute to one as an author by contacting the Frontiers Editorial Office: frontiersin.org/about/contact

ADVANCES IN MONITORING, MODELING AND MANAGING INDUCED SEISMICITY

Topic Editors:
Francesco Grigoli, ETH Zürich, Switzerland
Antonio Pio Rinaldi, ETH Zurich, Switzerland
Marco Maria Scuderi, Sapienza University of Rome, Italy
Rebecca M. Harrington, Ruhr University Bochum, Germany

Citation: Grigoli, F., Rinaldi, A. P., Scuderi, M. M., Harrington, R. M., eds. (2022). Advances in Monitoring, Modeling and Managing Induced Seismicity. Lausanne: Frontiers Media SA. doi: 10.3389/978-2-88974-433-6

Table of Contents

frontiers in Earth Science

ORIGINAL RESEARCH
published: 29 March 2021
doi: 10.3389/feart.2021.635193

Induced Seismicity Completeness Analysis for Improved Data Mining

Arnaud Mignan[1,2]*

[1]Institute of Risk Analysis, Prediction and Management (Risks-X), Academy for Advanced Interdisciplinary Studies, Southern University of Science and Technology (SUSTech), Shenzhen, China, [2]Department of Earth and Space Sciences, Southern University of Science and Technology (SUSTech), Shenzhen, China

The study of induced seismicity at sites of fluid injection is paramount to assess the seismic response of the earth's crust and to mitigate the potential seismic risk. However statistical analysis is limited to events above the completeness magnitude m_c, which estimation may significantly vary depending on the employed method. To avoid potential biases and optimize the data exploitable for analysis, a better understanding of completeness, detection capacity and censored data characteristics is needed. We apply various methods previously developed for natural seismicity on 16 underground stimulation experiments. We verify that different techniques yield different m_c values and we suggest using the 90% quantile of the m_c distribution obtained from high-resolution mapping, with m_c defined from the mode of local magnitude frequency distributions (MFD). We show that this distribution can be described by an asymmetrical Laplace distribution and the bulk MFD by an asymmetric Laplace mixture model. We obtain an averaged Gutenberg-Richter parameter $b = 1.03 \pm 0.48$ and a detection parameter $k = 3.18 \pm 1.97$ from mapping, with values subject to high uncertainties across stimulations. We transfer Bayesian m_c mapping developed for natural seismicity to the context of induced seismicity, here adapted to local three-dimensional seismicity clouds. We obtain the new prior parameterization $m_{c,pred} = 1.64log_{10}(d_3) - 1.83$, with d_3 the distance to the 3rd nearest seismic station. The potential use of censored data and of m_c prediction is finally discussed in terms of data mining to improve the monitoring, modeling and managing of induced seismicity.

Keywords: enhanced geothermal system, earthquake detection, earthquake monitoring, completeness magnitude, magnitude frequency distribution, bayesian inference, mixture modeling

OPEN ACCESS

Edited by:
Rebecca M. Harrington, Ruhr University Bochum, Germany

Reviewed by:
Qi Yao, China Earthquake Networks Center, China
Joern Lauterjung, German Research Centre for Geosciences, Germany

***Correspondence:**
Arnaud Mignan
mignana@sustech.edu.cn

Specialty section:
This article was submitted to Geohazards and Georisks, a section of the journal Frontiers in Earth Science

Received: *30 November 2020*
Accepted: *10 February 2021*
Published: *29 March 2021*

Citation:
Mignan A (2021) Induced Seismicity Completeness Analysis for Improved Data Mining. Front. Earth Sci. 9:635193. doi: 10.3389/feart.2021.635193

INTRODUCTION

The evaluation of the completeness magnitude m_c, above which the Gutenberg-Richter law is verified as all the data is by definition observed, is a prerequisite to virtually all statistical analyses of seismicity. This includes the study of induced seismicity at sites of underground stimulation by fluid injection. Underestimating m_c yields to biased estimates of the slope of the Gutenberg-Richter law, the b-value, and overestimating it may lead to unnecessary under-sampling. Selection of m_c has therefore indirect consequences on seismic hazard assessment. Most published works provide an estimate of m_c but rarely explain how it has been calculated and rarely, if ever, provide a sensitivity analysis.

The present study aims at filling this gap by an in-depth analysis of the magnitude frequency distribution (MFD) at multiple sites. To the best of our knowledge, this is the first study dedicated to completeness magnitude analysis in the induced seismicity context. We will test different m_c

TABLE 1 | Available public data for induced seismicity completeness analysis.

Site	Catalog		Stations (N_{sta})	Source
	N_{tot}	Coord		
S93. Soultz-sous-forêts, 1993	10,742	✓	✓	EOST and GEIEEMC (2017)
KTB94. KTB, 1994	182	✗	✗	Jost et al. (1998)
PV94. Paradox Valley, 1994–2008	4,569	✓	✗	Bureau of Reclamation (2017)
S00. Soultz-sous-forêts, 2000	7,215	✓	✓	EOST and GEIEEMC (2018a)
S03. Soultz-sous-forêts, 2003	4,728	✓	✓	EOST and GEIEEMC (2018b)
S04. Soultz-sous-forêts, 2004	5,861	✓	✓	EOST and GEIEEMC (2018c)
S05. Soultz-sous-forêts, 2005	3,709	✓	✓	EOST and GEIEEMC (2018d)
B06. Basel, 2006	1,980	✓	✗	Kraft and Deichmann (2014)
G07. Geisers, 2007–2014	1,606	✓	✗	IS EPOS (2017a)
GS08. Groß Schönebeck, 2008	29	✓	✓	IS EPOS (2017b)
CB12. Cooper Basin, 2012	20,735	✓	✓	IS EPOS (2020)
NB12. Newberry, 2012–14	494	✓	✗	U.S. Dept. Energy (2020)
SG13. St Gallen, 2013	347	✓	✓	IS EPOS (2018)
A15. Äspö, 2015	196	✓	✗	Kwiatek et al. (2018)
P16. Pohang, 2016–2017	98	✓	✓	Woo et al. (2019)
E18. Espoo, 2018	1,977	✓	✗	Kwiatek (2019)

techniques (e.g., Wiemer and Wyss, 2000; Amorèse, 2007) and transfer two recent models originally developed by the author for natural seismicity: The Asymmetric Laplace MFD model to describe the incomplete part of seismicity (Mignan, 2012; Mignan, 2019), and the Bayesian Magnitude of Completeness (BMC) method for robust m_c mapping (Mignan et al., 2011), based on m_c being the mode of local MFDs, in agreement with the Asymmetric Laplace formulation.

The BMC method has been successfully applied in various regions of the world, but so far only in the context of natural seismicity: Taiwan (Mignan et al., 2011), Mainland China (Mignan et al., 2013), Switzerland (Kraft et al., 2013), Lesser Antilles arc (Vorobieva et al., 2013), California (Tormann et al., 2014), Greece (Mignan and Chouliaras, 2014), Iceland (Panzera et al., 2017), South Africa (Brandt, 2019) and Venezuela (Vásquez and Bravo de Guenni, n.d.)[1]. It becomes urgent to apply it to induced seismicity, which requires a reformulation of the model. Based on the new parameterization and additional information on incomplete (so-called censored) data, we will discuss how such information could improve induced seismicity data mining, or in other words, how it could improve knowledge on the underground feedback activation and the management of the associated risk.

MATERIALS AND METHODS

Induced Seismicity Data

We consider 16 underground stimulations by deep fluid injection (**Table 1**), all of which are publicly available and often available from dedicated data portals (e.g., EOST and GEIE EMC, IS EPOS): the Soultz-sous-Forêts stimulations at the GPK1 well in 1993 [S93] (Cornet et al., 1997), GPK2 well in 2000 [S00] (Cuenot et al., 2008), GPK3 well in 2003 [S03] (Calò and Dorbath, 2013) and GPK4 well in both 2004 [S04] and 2005 [S05] (Charléty et al., 2007), the KTB deep drilling site [KTB94] (Jost et al., 1998), the Paradox Valley continuous injection from 1994 to 2008 [PV94] (Ake et al., 2005), the 2006 Basel 1 well stimulation [B06] (Häring et al., 2008; Kraft and Deichmann, 2014), the 2007–2014 Geysers [G07] Prati-9 and Prati-29 well injections (Kwiatek et al., 2015), the 2008 Groß Schönebeck injection [GS07] (Kwiatek et al., 2010), the Cooper Basin Habanero 4 well stimulation of 2012 [CB12] (Baisch et al., 2015). the Newberry Volcano EGS demonstration 2012 stimulation and 2014 restimulation [NB12] (Cladouhos et al., 2013; Cladouhos et al., 2015), the 2013 St Gallen reservoir simulation [SG13] (Diehl et al., 2017), the 2015 Äspö Hard Rock Laboratory experiment [A15] (Kwiatek et al., 2018), the 2016–2017 Pohang stimulation experiment [P16] (Woo et al., 2019), and the 2018 Espoo stimulation [E18] near Helsinki (Kwiatek, 2019). Most stimulations considered took place at EGS sites.

Depending on the parameters provided (see **Table 1**), different completeness analysis levels are achievable. When earthquake coordinates are not included, the study is limited to the bulk MFD analysis (Woessner and Wiemer, 2005; Mignan and Woessner, 2012) and to the application of the Asymmetric Laplace distribution (Mignan, 2019); when earthquake coordinates are included, observed completeness magnitude $m_{c,obs}$ mapping is performed (e.g., Wiemer and Wyss, 2000). In the ideal situation in which the coordinates of the seismic stations are also given, posterior completeness magnitude $m_{c,post}$ maps are also generated using the BMC method (Mignan et al., 2011).

Since this study is solely dedicated to seismicity completeness, data such as total volume injected, flow rate profile, or injection/post-injection windows are not considered (only mentioned in the discussion, *Discussion and Perspectives on Data Mining*). For statistical analyses related to the fluid injection process at different sites, the reader can refer to, e.g., Dinske and Shapiro (2013), van der Elst et al. (2016), Mignan et al. (2017) or Bentz et al. (2020).

[1]Vásquez, R., and Bravo de Guenni, L. n. d. Bayesian estimation of the spatial variation of the completeness magnitude for the Venezuelan seismic catalogue. Available at: https://www.statistics.gov.hk/wsc/CPS204-P47-S.pdf. (Accessed Aug 2014)

Standard Magnitude Frequency Distribution Analysis

The bulk magnitude frequency distribution (MFD) of an earthquake catalog can be described by a probability density function that takes the form:

$$p(m) = cq(m)f_{GR}(m) = cq(m)e^{-\beta m}$$

where m is the earthquake magnitude, $f_{GR}(m)$ the Gutenberg-Richter law (Gutenberg and Richter, 1944), $q(m)$ a detection function that controls the shape of the MFD and c a normalization constant so that $\int p(x)dx = 1$. The non-cumulative MFD, defined as the number of earthquakes per magnitude bin m, is simply $n(m) = \Delta m N_{tot} p(m)$ with N_{tot} the total number of events and $\Delta m = 0.1$ the magnitude bin. The cumulative MFD is more commonly formulated as $N(\geq m) = 10^{a-bm}$ where $b = \beta/log10$ and a is the overall seismicity activity.

We should have the condition $q(\geq m_c) = 1$ by definition, although it may only tend to 1 if q is unbounded, for example if defined as a cumulative Normal distribution (Ringdal, 1975; Ogata and Katsura, 1993), a log-normal distribution (Martinsson and Jonsson, 2018), or a power-law (so that p can be represented by a gamma distribution; Kijko and Smith, 2017). Mignan (2012), Mignan (2019), in contrast, consider the gradual curvature of the MFD to be due to the sum of "angular" MFDs, each of constant m_c, with q a bounded exponential function and p an asymmetric Laplace distribution (see below). "Curved" q functions would then be fitting proxies not representative of the spatially varying and scale-variant detection process (Mignan and Chen, 2016).

Various methods have been proposed to estimate m_c from the bulk MFD, independently of the function $q(m)$ (see reviews by Woessner and Wiemer, 2005; Mignan and Woessner, 2012). We here consider two non-parametric techniques, the mode of the MFD (also known as "maximum curvature" method; Wiemer and Wyss, 2000) and the Median-Based Analysis of the Segment Slope (MBASS) method (Amorèse, 2007). The b-value of the Gutenberg-Richter law can then be estimated with the maximum likelihood estimation (MLE) method (Aki, 1965) for the complete magnitude range $(m_c - \Delta m/2, +\infty)$. It is important to note that m_c values obtained from the bulk MFD can vary significantly across methods, which hampers the evaluation of b. A spatial analysis can limit the potential ambiguity (Mignan and Chouliaras, 2014).

Spatial heterogeneities in m_c, due at first order to the seismic network spatial configuration (*Bayesian Magnitude of Completeness Mapping Method*), can be evaluated by a simple mapping procedure. We perform a three-dimensional mapping of $m_{c,obs}(x, y, z)$ in cubic cells 100-m wide. No smoothing kernel (e.g., Wiemer and Wyss, 2000) is used in order to minimize m_c heterogeneities in individual cells. The parameter is estimated by using the mode of the distribution of magnitudes m in each cell (x, y, z). The mode is a reasonable choice for localized data where no significant spatial variations in m_c is expected (Mignan, 2012; Mignan and Chen, 2016). It also yields robust results for sample sizes as low as $n_{min} = 4$ earthquakes (Mignan et al., 2011), the threshold used in the present mapping procedure. The set of m_c estimates for all cells is then represented by the vector $m_{c,obs}$, which distribution explains the curvature characteristics of the bulk MFD. Different quantiles of $m_{c,obs}$ can be tested to evaluate b. The map of $m_{c,obs}(x, y, z)$ is also used as input for the BMC method described in *Bayesian Magnitude of Completeness Mapping Method*.

Local MFDs of cells (x, y, z) can be used to estimate both b and the parameter k of the detection function q. We consider the asymmetric Laplace probability density function:

$$p_{AL}(m) = \frac{1}{\frac{1}{\kappa-\beta} + \frac{1}{\beta}} \begin{cases} e^{(\kappa-\beta)(m-m_c)}, & m < m_c \\ e^{-\beta(m-m_c)}, & m \geq m_c \end{cases}$$

with mode m_c and the detection parameter $k = \kappa/log(10)$ also estimated using the MLE method (Mignan, 2012; see also equation *Asymmetric Laplace Mixture Model*). This parameter has been shown to be relatively stable with $k \approx 3$ for natural seismicity in Southern California and Nevada (Mignan, 2012). We apply the same approach to test how this parameter behaves in the context of induced seismicity. We only consider cells with $n_{min} = 50$ for those calculations. The asymmetric Laplace distribution is the basic component of the mixture model presented below (*Asymmetric Laplace Mixture Model*). It also explains why the mode is used to compute m_c in the BMC method (*Bayesian Magnitude of Completeness Mapping Method*).

Asymmetric Laplace Mixture Model

The sum of local "angular" MFDs of different m_c which forms the bulk "curved" MFD can be approximated by mixture modeling instead of a mapping procedure. This is particularly practical if earthquake coordinates are unavailable with only access to a magnitude vector. The Asymmetric Laplace Mixture Model (ALMM) (Mignan, 2019) is defined as:

$$p_{ALMM}(m; w_i, m_{c,i}, \kappa, \beta) = \sum_{i=1}^{K} w_i p_{AL}(m; m_{c,i}, \kappa, \beta)$$

with K the number of Asymmetric Laplace mixture components ordered by m_c value $(m_{c,1} < m_{c,2} < \cdots < m_{c,i} < \cdots < m_{c,K})$ and w_i the mixing weight of the i^{th} component such that $\sum_{i=1}^{K} w_i = 1$. Parameters κ and β are assumed constant across components.

Any MFD shape can be fitted by the flexible ALMM based on the Expectation-Maximization (EM) algorithm (Dempster et al., 1977). The initial parameter values are estimated by applying K-means (MacQueen, 1967), with w_i the normalized number of events per cluster and $m_{c,i}$ the cluster centroid. Each component is formed of the magnitude vector $\boldsymbol{M}_i = (m_1, m_2, \cdots)$. The completeness magnitude $m_{c,i}$ is estimated from the mode of the component. Parameter κ is estimated from the incomplete part of the first component $\boldsymbol{M}_{left} = \{m \in \boldsymbol{M}_1 : m \leq m_{c,1} - \Delta m/2\}$ while parameter β is estimated from the complete part of the last component $\boldsymbol{M}_{right} = \{m \in \boldsymbol{M}_K : m > m_{c,K} - \Delta m/2\}$. The maximum likelihood estimates are respectively:

$$\begin{cases} \chi = \dfrac{1}{\left(m_{c,1} - \dfrac{\Delta m}{2}\right) - \overline{\boldsymbol{M}}_{left}} \\ \beta = \dfrac{1}{\overline{\boldsymbol{M}}_{right} - \left(m_{c,K} - \dfrac{\Delta m}{2}\right)} \end{cases}$$

with $\chi = \kappa - \beta$ the slope of the incomplete part of the asymmetric Laplace distribution in a log-linear plot.

At each EM iteration j, a deterministic version of the expectation step (E-step) attributes a hard label i to each event magnitude from the parameter set $\theta_i^{(j-1)} = \{m_{c,i}, \kappa, \beta\}$ defined in the previous iteration $j-1$ ($j = 0$ corresponding to the K-means estimate). Hard labels are assigned as:

$$i = argmax_i p_{AL}\left(m, \theta_i^{(j-1)}\right)$$

The maximization step (M-step) then updates the component parameters. The best number of components K is finally selected from the lowest Bayesian Information Criterion estimate $BIC = -LL + 1/2\,(2+K)ln(N_{tot})$ (Schwarz, 1978) where LL is the log-likelihood of the ALMM. Details of the full method are given in Mignan (2019). For MFD mixture modeling based on a log-normal component, the reader may refer to Martinsson and Jonsson (2018).

Bayesian Magnitude of Completeness Mapping Method

The last method to be tested in the present study is the Bayesian Magnitude of Completeness (BMC) method that consists in using Bayesian inference to estimate m_c based on incomplete information and prior belief. The incomplete information is the $m_{c,obs}$ map (see *Standard Magnitude Frequency Distribution Analysis*), which presents gaps in cells of low seismicity and is highly uncertain when estimated from a limited number of earthquake magnitudes. BMC is constrained by a prior model $m_{c,pred} = f(d_k)$ relating the spatial heterogeneities in m_c to the density of seismic stations, approximated by the distance d_k to the k^{th} nearest station (Mignan et al., 2011). Priors were defined so far in the literature for two-dimensional m_c mapping. We here define a new prior based on three-dimensional distance, which is a requirement for fluid injections characterized by a three-dimensional seismicity cloud centered at the borehole depth and detected by a combination of surface stations and downhole stations. The distance between a cell and a station of coordinates $(x_{sta}, y_{sta}, z_{sta})$ is thus $d = \sqrt{(x-x_{sta})^2 + (y-y_{sta})^2 + (z-z_{sta})^2}$. We additionally improve the functional form of the prior, moving from $m_{c,pred} = c_1 d_k^{c_2} + c_3$ (Mignan et al., 2011) to the form $m_{c,pred} = c_1 log_{10}(d_k) + c_2$, a simpler attenuation function reduced to two free parameters.

Following Bayes' Theorem, we obtain the posterior completeness magnitude $m_{c,post}$ and standard deviation σ_{post}:

$$\begin{cases} m_{c,post} = \dfrac{m_{c,pred}\sigma_{obs}^2 + m_{c,obs}\sigma_{pred}^2}{\sigma_{pred}^2 + \sigma_{obs}^2} \\ \sigma_{post} = \sqrt{\dfrac{\sigma_{pred}^2\sigma_{obs}^2}{\sigma_{pred}^2 + \sigma_{obs}^2}} \end{cases}$$

where σ_{obs} and σ_{pred} are the standard deviations of m_c observations (based on 100 bootstraps) and of the prior model, respectively. Note that all the aforementioned parameters depend on location (x, y, z), except for σ_{pred} which is constant.

RESULTS

Results of a Standard m_c Analysis

We first apply the standard methods of m_c evaluation, based on bulk MFD analysis and m_c mapping. This is the first systematic comparison of completeness level for different induced seismicity sequences.

Figure 1 shows the cumulative bulk MFD for the 16 fluid injections and the matching $m_{c,obs}$ distribution. **Figure 1** also shows the estimates $m_{c,mode}$ (dotted vertical line) and $m_{c,MBASS}$ (dashed vertical line) which are often close to the $m_{c,obs}$ median. More conservative estimates of m_c, such as the 75% or 90% quantiles of $m_{c,obs}$ seem to provide reasonable b-values. We use $q_{90}(m_{c,obs})$ to estimate the Gutenberg-Richter slope b in **Figure 1**. Note that the $m_{c,obs}$ distribution shape matches the curvature of the bulk MFD, which verifies that it is due at first order to spatial heterogeneities. **Table 2** lists $m_{c,bulk}$ estimates obtained from different approaches with their respective b-values for comparison. For most cases, the m_c range for induced seismicity is comprised between -2 and 1. It goes down to -4 for the Äspö Hard Rock Laboratory experiment where pico-seismicity is detected. Such low m_c values have been reached at other underground laboratories (e.g., Villiger et al., 2020). The range of b-values is consistent with the ones obtained by Dinske and Shapiro (2013) for the 5 datasets common to both studies. The authors however only provided one estimate while our **Table 2** shows its sensitivity to the minimum magnitude cutoff.

Figure 2 shows $m_{c,obs}$ maps at selected depths z for the two stimulations the richest in induced seismicity ($N_{tot} > 10,000$): S93 and CB12. Other maps will be shown in *Bayesian Magnitude of Completeness Prior & Posterior m_c Maps when used as input for BMC mapping. Local MFDs for cells that include more than 400 earthquakes are also displayed with their asymmetric Laplace distribution fit. Considering all cells of all sites together, assuming that k and b variations in space are random (Mignan, 2012; Kamer and Hiemer, 2015), we obtain for induced seismicity $k = 3.18 \pm 1.97$ and $b = 1.03 \pm 0.48$, which is consistent with natural seismicity regimes but here with significantly larger uncertainties. The plots of **Figures 2B,D** confirm that the mode of the local MFD is a reasonable choice to estimate m_c.*

This so-called standard m_c analysis highlights the importance to test several techniques to minimize possible biases in the b-value. Mapping remains the best approach to evaluate the m_c range. Reasonable b-values are obtained when using conservative $m_{c,obs}$ quantiles (e.g., 75% or 90%).

Asymmetric Laplace Mixture Model Fits

We then apply the ALMM to the 16 magnitude vectors but only get reasonable fits for 9 of them. We find that the ALMM requires

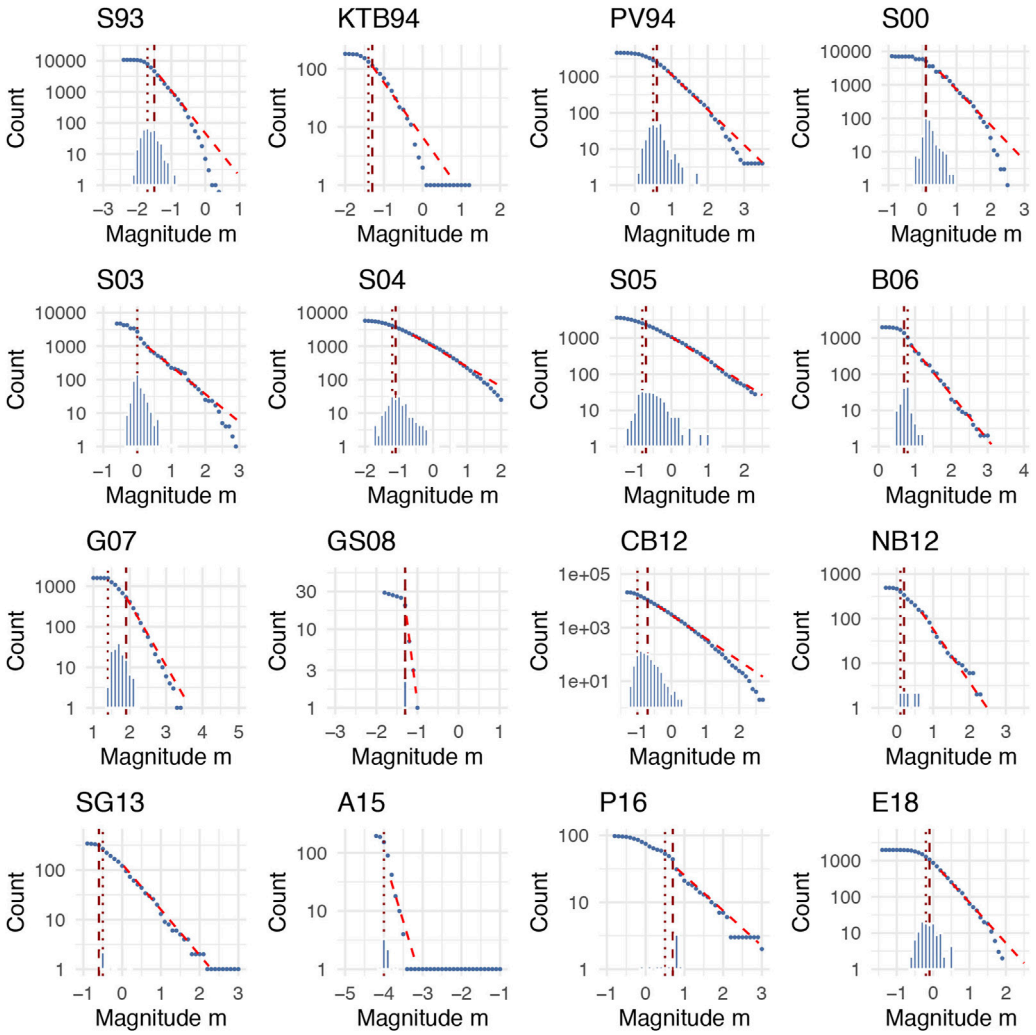

FIGURE 1 | Cumulative magnitude frequency distribution (MFD) of 16 underground stimulations. The histogram shows the $m_{c,obs}$ distribution derived from three-dimensional m_c mapping (except for KTB94 for which case coordinates are unavailable). Parameter b (dashed red line) is estimated for $m_c = q_{90}(m_{c,obs})$ (for $m_c = m_{c,MBASS}$ in the KTB94 case). The vertical dotted and dashed dark-red lines represent $m_{c,mode}$ and $m_{c,MBASS}$, respectively. See **Table 2** for values.

$n_{min} > 300$ for statistically significant component modeling. It means that the ALMM is not applicable for KTB94, GS08, A15 and P17. It fails for 3 other cases, S00, S03, B06, due to anomalous fluctuations in the observed non-cumulative MFD, which will be discussed in another paragraph.

Figure 3 shows the 9 ALMM fits (for S93, PV94, S04, S05, G07, CB12, NB12, SG13 and E18). Parameters $max(m_{c,i})$ and b are listed in **Table 2** for comparison with the techniques tested in *Results of a Standard m_c Analysis*. Those values range between estimates obtained with the MBASS method and $q_{75}(m_{c,obs})$ *so the method does not seem to provide any new insight into which method to prefer. We observe that the number of K* components reflects the gradual curvature of the bulk MFD. For instance, only 2 components suffice to fit the almost angular SG13 MFD while 13 components are needed for the wide S05 MFD, proving the flexibility of the ALMM to fit different MFD shapes. It also verifies that bulk MFDs can be described by the sum of angular MFDs with m_c as modes. We obtain $k = \{7.6, 3.3, 2.1, 2.8, 6.5, 9.1, 4.5, 3.7, 3.1\}$, respectively, with median 3.7 and mean 4.7.

The ALMM is highly sensible to abnormal fluctuations in the non-cumulative MFD, which are often not visible from the cumulative MFD. In the case of Soultz-sous-Fôrets, the S00 non-cumulative MFD shows significant drops in the number of events inconsistent with any model monotonously increasing up to m_c and monotonously decreasing above m_c. In the latter, we observe $n_i = \{0, 7, 7\}$ for bins $m_i = \{0.2, 0.4, 0.6\}$; for comparison, $n_i = \{1468, 1114, 717, 430\}$ for $m_i = \{0.1, 0.3, 0.5, 0.7\}$. Such anomaly is smoothed out in the cumulative MFD and does not hamper b-value fitting. However, the ALMM anchors at those anomalies, failing to develop into the proper curved MFD. The S03 case shows numerous fluctuations also visible on the cumulative MFD and on the non-trivial evolution of b estimates as the minimum magnitude cutoff increases (**Table 2**). In regards of the Basel catalog, a zig-zag pattern is observed on the non-cumulative MFD, suggesting an

TABLE 2 | Parameters m_c and $b(m_c)$ for different m_c estimation methods applied to the bulk MFD.

Site		$m_{c,mode}$ [a]	$m_{c,MBASS}$ [a]	$q_{75}(m_{c,obs})$ [b]	$q_{90}(m_{c,obs})$	$max(m_{c,obs})$	ALMM [c]
S93	m_c	−1.7	−1.6	−1.5	−1.4	−0.9	−1.5
	b	1.24	1.34	1.35	1.36	1.73	1.39
KTB94	m_c	−1.4	−1.3	N/A	N/A	N/A	N/A
	b	0.89	0.94	N/A	N/A	N/A	N/A
PV94	m_c	0.5	0.6	0.7	0.9	1.7	0.7
	b	0.83	0.88	0.92	0.97	1.16	0.89
S00	m_c	0.1	0.1	0.3	0.5	0.9	N/A
	b	0.94	0.94	1.00	1.06	1.20	N/A
S03	m_c	0.0	2.2	0.1	0.3	1.1	N/A
	b	1.22	1.77	0.98	0.83	0.85	N/A
S04	m_c	−1.2	−1.1	−0.8	−0.6	0.6	-0.7
	b	0.52	0.53	0.57	0.59	0.81	0.56
S05	m_c	−0.8	−0.8	−0.3	0.0	1.3	−0.2
	b	0.52	0.52	0.60	0.64	0.89	0.60
B06	m_c	0.8	0.7	0.8	0.9	1.4	N/A
	b	1.48	1.42	1.48	1.24	1.38	N/A
G07	m_c	1.4	1.7	1.8	1.9	2.4	1.6
	b	1.06	1.26	1.36	1.54	1.83	1.28
GS08	m_c	−1.3	−1.3	−1.3	−1.3	−1.3	N/A
	b	4.14	4.14	4.14	4.14	4.14	N/A
CB12	m_c	−1.0	−0.7	−0.6	−0.4	0.4	−0.8
	b	0.74	0.81	0.83	0.85	1.01	0.78
NB12	m_c	0.1	0.2	0.6	0.7	0.8	0.2
	b	0.89	0.92	1.07	1.22	1.33	0.81
SG13	m_c	−0.5	−0.5	−0.2	0.0	0.2	−0.5
	b	0.77	0.77	0.84	0.91	0.83	0.77
A15	m_c	−4.0	−3.9	−3.9	−3.8	−3.7	N/A
	b	2.40	2.55	2.55	2.09	1.35	N/A
P16	m_c	0.5	1.0	0.8	0.8	0.9	N/A
	b	0.61	0.47	0.55	0.55	0.52	N/A
E18	m_c	−0.2	−0.1	0.0	0.2	0.5	−0.2
	b	0.98	1.06	1.07	1.12	1.17	0.96

[a] *Mean value of 200 bootstrap estimates.*
[b] $m_{c,obs}$ *the vector of* m_c *values in cells* (x,y,z).
[c] *Only max* $(m_{c,i})$ *of the ALMM* m_c *distribution given.*

error in rounding between odd and even magnitude digits, which confuses the ALMM algorithm. Those cases indicate more problems with the magnitude vectors than with the ALMM. This suggests that seismologists preparing earthquake catalogs should analyze the non-cumulative distribution of magnitudes to check for potential errors and/or explain the origin of those anomalies incompatible with the Gutenberg-Richter law.

Bayesian Magnitude of Completeness Prior and Posterior m_c Mmaps

We define a BMC prior model for induced seismicity by combining the relation between m_c and the distance d_3 to the 3rd nearest seismic station, observed for the earthquake catalogs that come with seismic network information (**Table 1**). We choose d_3 (over e.g. d_4 or d_5) since this metric shows the minimal residual error (see σ_{pred} below). We assume that $m = M_L = M_w$ so that seismicity clouds from different depth levels can be combined to fit one model constrained on a relatively wide d_3 range.

Figure 4 represents the BMC prior derived from 7 datasets: S93, S04, S05, GS08, CB12, SG13, and P16. The model, represented by the solid curve, is defined as

$$m_{c,pred} = f_{prior}(d_3) = 1.64log_{10}(d_3) - 1.83;\ \sigma_{pred} = 0.37$$

with distance d_3 in km. Note that the uncertainty σ_{pred} is greater than the ones obtained from natural seismicity ($\sigma_{pred} \lesssim 0.25$; e.g., Mignan et al., 2011; Mignan et al., 2013; Kraft et al., 2013; Mignan and Chouliaras, 2014; Tormann et al., 2014). Several reasons may be advanced: different sites are here combined, representative of different soil conditions and thus potentially of different seismic attenuation functions; considering the depth component may add uncertainty on distance measures; finally, the model is constrained on far shorter distance ($d_3 < 10$ km) compared to up to hundreds of kilometers in regional catalogs. It is interesting to compare the model prediction to the pico-seismicity completeness level $m_c \approx -4$ observed at Äspö (A15). We learn from Kwiatek et al. (2018) that sensors were located between a few meters and 100 m from the injection borehole. We independently predict $m_{c,pred}(10m) = -5.1$ and $m_{c,pred}(100m) = -3.5$, which is a reasonable approximation. Adding further datasets to the model will help better constraining it.

Two datasets, S00 and S03, were not included in this analysis as event declaration depended in those cases on two triggering conditions from both the downhole and surface networks

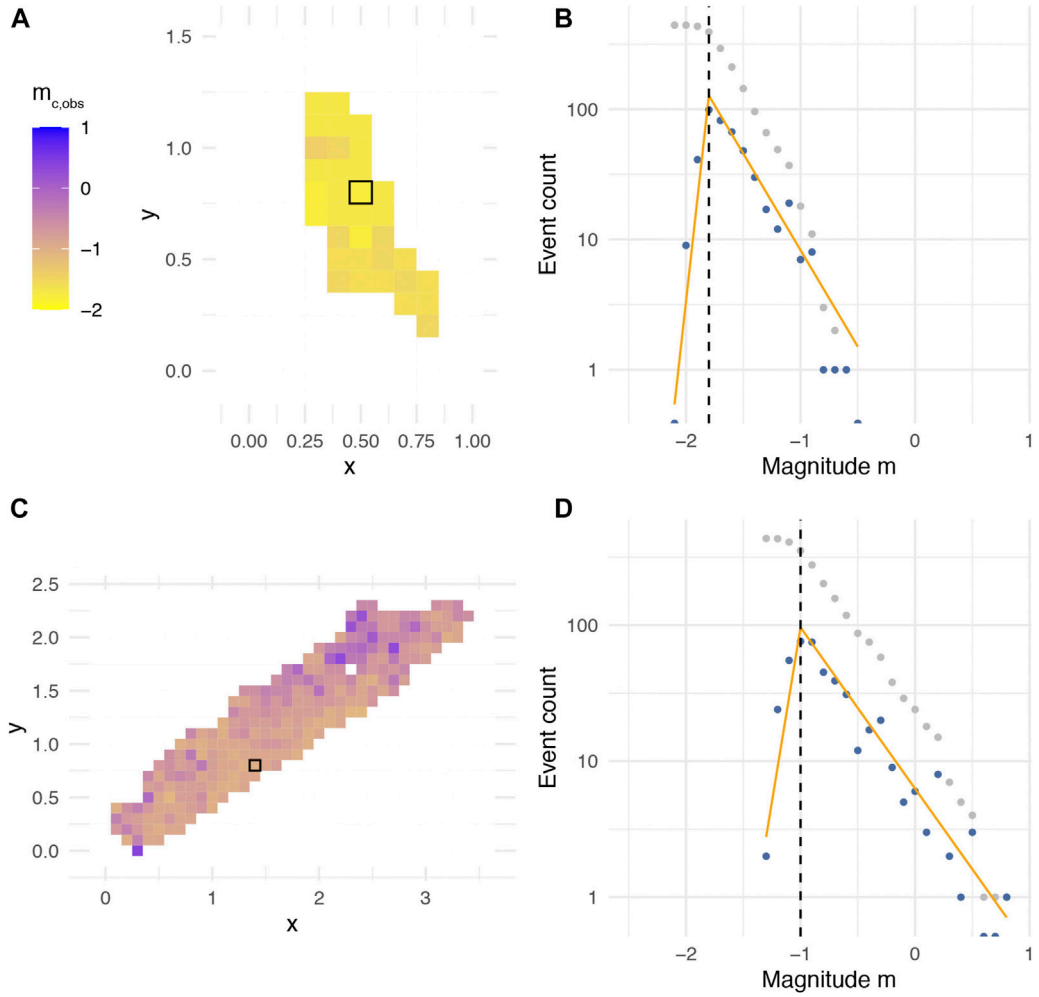

FIGURE 2 | Examples of 100 m-resolution $m_{c,obs}$ maps and of local MFDs. **(A)** $m_{c,obs}$ map at depth $z = -2.7$ km for the 1993 Soultz-sous-Forêts stimulation (S93) **(B)** local MFD observed in the cell highlighted on the S93 map, with Asymmetric Laplace distribution fit **(C)** $m_{c,obs}$ map at depth $z = -4.1$ km for the 2012 Cooper Basin stimulation (CB12) **(D)** local MFD observed in the cell highlighted on the CB12 map, with Asymmetric Laplace distribution fit.

(EOST and GEIEEMC, 2018a; EOST and GEIEEMC, 2018b), which is likely inconsistent with the simple d_3 metric. Testing with d_3 leads to a systematic bias requiring a correction $f_{prior}(d_3) + 1$. Use of such formula would however be inadequate. It remains unclear if the magnitude scale used for S00 and S03, duration magnitude m_D, could also play a role in the observed m_c shift upward.

We then combine the $m_{c,obs}$ with the prior model to derive the posterior $m_{c,post}$ maps. We show some examples taken from S93 and CB12 in **Figure 5**. The BMC methods fills all the gaps in $m_{c,obs}$, and provides completeness levels expected for future seismicity, e.g., during cloud development as more fluids get injected, which can be of use to the injection operators. The BMC method also decreases m_c uncertainties, as can be observed when comparing σ_{post} to σ_{obs}. Note finally that the BMC method is consistent with the Asymmetric Laplace detection model previously described. It makes use of the mode of local MFDs so that the number of cells with $m_{c,obs}$ values is maximized while f_{prior} explains how m_c evolves in space, from which the bulk FMD, approximated by the ALMM, emerges.

DISCUSSION AND PERSPECTIVES ON DATA MINING

We reviewed some standard approaches to estimate the completeness magnitude m_c and ported the recent ALMM mixture and BMC mapping methods to the induced seismicity context. We provided various estimates of m_c, b (**Table 2**) and detection parameter k so that better informed choices could be made in future statistical analyses of induced seismicity. We observed that the k-value for induced seismicity is compatible with the one obtained for natural seismicity, suggesting a common detection process although uncertainties are high. We also provided the first parameterization of the BMC prior for three-dimensional seismicity clouds.

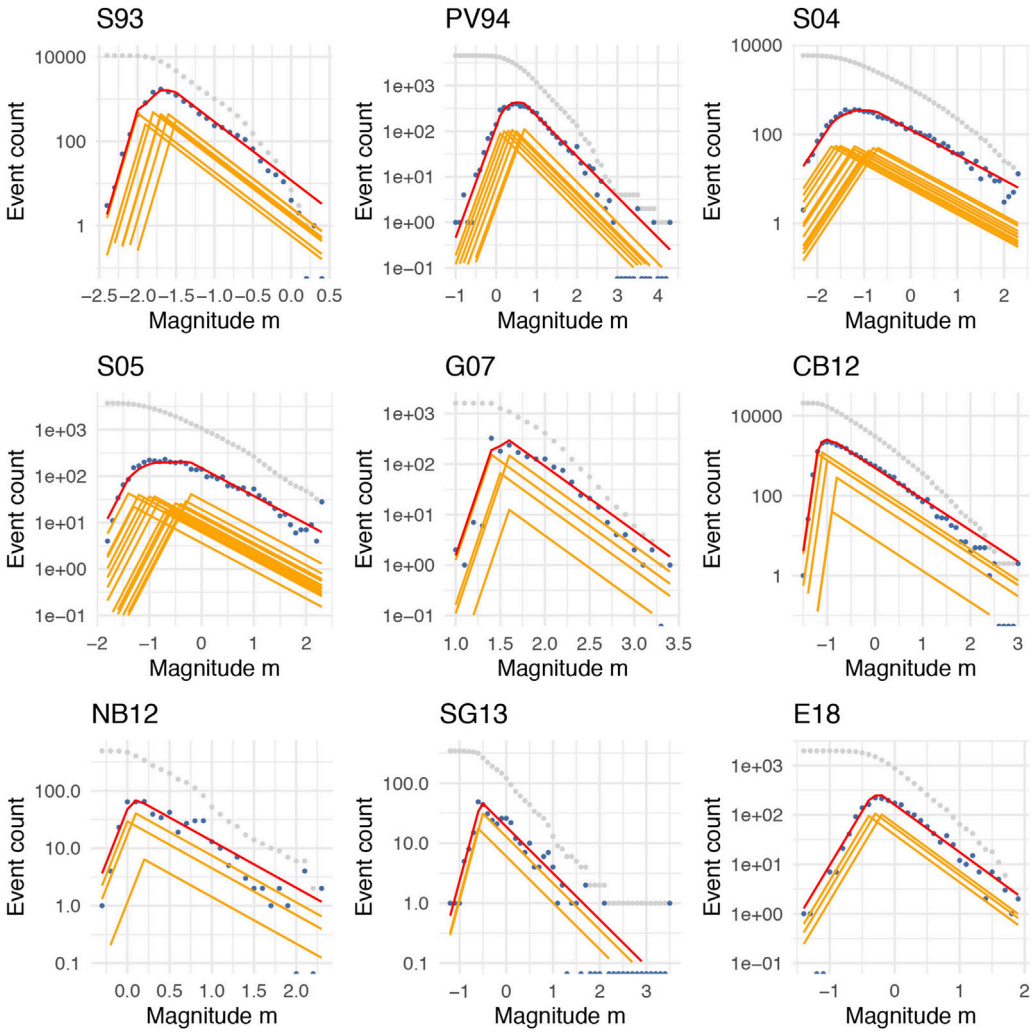

FIGURE 3 | Non-cumulative MFD (in blue) of 9 underground stimulations for which an Asymmetric Laplace Mixture Model (ALMM) fit is available, shown in red, with the mixture components shown in orange. See **Table 2** for some values.

The present study could help refine future seismic hazard analyses, since the parameter m_c is a prerequisite to the estimation of the hazard inputs: the a- and b-values of the Gutenberg-Richter law. In contrast to the tectonic regime, the a-value is normalized to the total injected volume V for comparisons across stimulations, so that $N(\geq m) = V10^{a_{fb}-bm}$ with a_{fb} the normalized a-value, called underground feedback parameter in Mignan et al. (2017) and seismogenic index in poroelasticity parlance (e.g., Dinske and Shapiro, 2013). The term a_{fb} is agnostic, while alternatives to poroelasticity exist (e.g., Mignan, 2016). *A priori* knowledge of the Gutenberg-Richter parameters is required in pre-stimulation risk assessment (e.g., Mignan et al., 2015; Broccardo et al., 2020), and the parameterization may be updated during stimulations via a dynamic traffic light system (e.g., Broccardo et al., 2017; Mignan et al., 2017). Note also that the maximum magnitude m_{mas} relates directly to b (e.g., van der Elst et al., 2016; Broccardo et al., 2017).

We first showed the impact of m_c values on b and selected q_{90} ($m_{c,obs}$) as conservative estimates. We also found that the ALMM does not provide any new insight to the problem and is hampered by fluctuations in the non-cumulative MFD observed in some experiments. As a consequence, m_c mapping remains the best alternative and is simple enough to implement.

While m_c also alters a_{fb} via b, we can consider another aspect that may improve our knowledge of the underground feedback. It has been observed that a_{fb} significantly varies across sites and across stimulations at a same site (e.g., Dinske and Shapiro, 2013; Mignan et al., 2017) which may lead to risk aversion of potential investors in geo-energy for instance (Mignan et al., 2019). One may difficultly infer a_{fb} from the literature when no information about completeness is given, which is especially true for early articles. However, we can now estimate a_{fb} despite the total number of events induced $N(\geq m_?)$ being potentially ambiguous. To illustrate the problem posed, let us consider the 1988 stimulation at Hijiori, Japan. We learn from Sasaki (1998) that $N(\geq m_?) = 65$

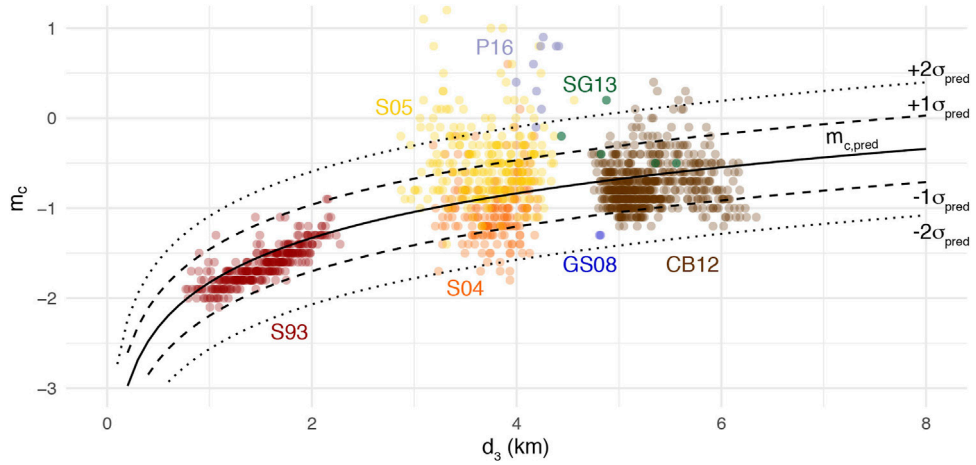

FIGURE 4 | Prior model $m_{c,pred} = f(d_3)$ of the Bayesian Magnitude of Completeness (BMC) method for the three-dimensional induced seismicity case with distance d_3 to the third nearest seismic station.

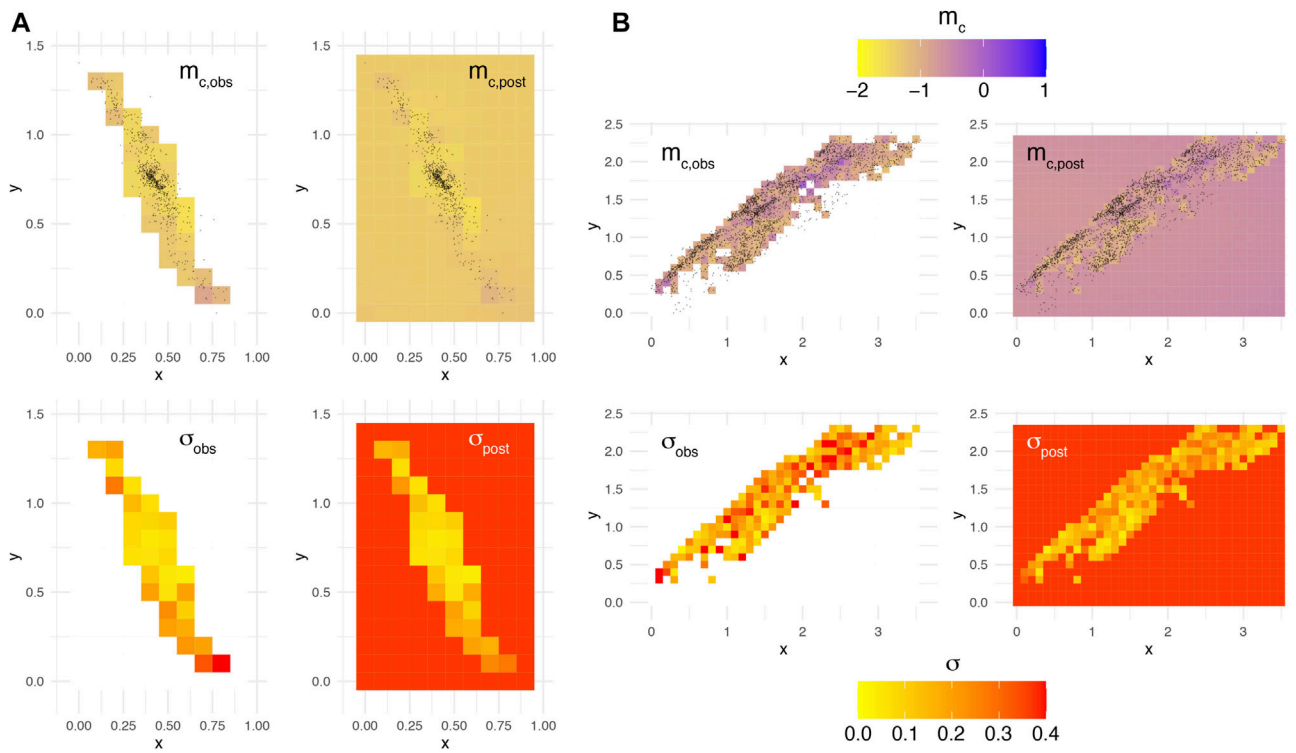

FIGURE 5 | Observed $m_{c,obs}$ vs. posterior $m_{c,post}$ maps derived from the BMC prior model. **(A)** S93 at depth $z = -3.1$ km **(B)** CB12 at depth $z = -4.2$ km.

micro-earthquakes were observed above $m_? = -4$ (their **Figure 6**) for an injected volume $V = 2,000$ m^3. The equation $a_{fb} = log_{10}(N(\geq m_?)/V) + bm_?$ is valid only if $m_? \geq m_c$. Information in Sasaki (1998) is however ambiguous, and we may have $m_? = min(m) < m_c$ instead, which would underestimate the underground feedback activation since the data would then be incomplete. Considering all datasets of **Table 1** with $N_{tot} > 200$, we can estimate from their censored data the metrics $\delta m = m_c - min(m)$ and $\gamma = N(\geq m_c)/N(\geq min(m))$ which range on the intervals [0.8, 1.9] and [0.20, 0.37], respectively (with no trend observed). The distributions are shown in **Figure 6A** alongside the corrected underground feedback parameter $a_{fb,corrected} = log_{10}(\gamma N(\geq min(m))/V) + b(min(m) + \delta m)$. Assuming δm and γ representative (and $b = 1$, see *Results of a*

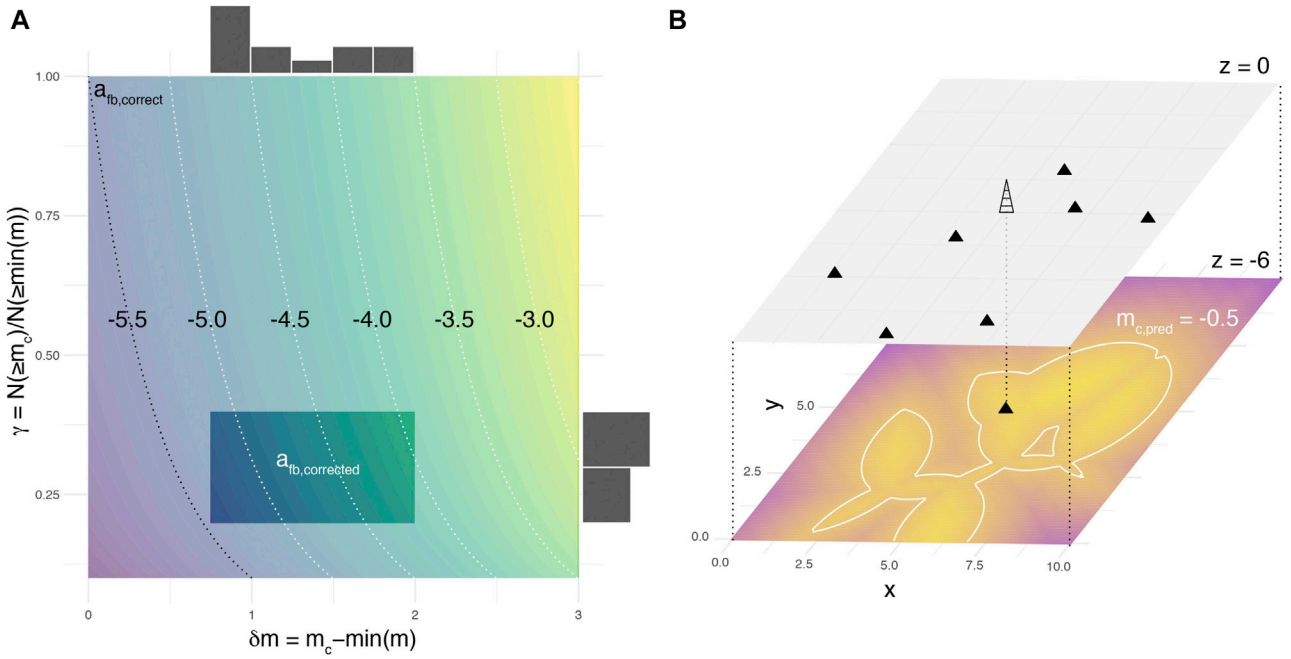

FIGURE 6 | Induced seismicity data mining potential from completeness analysis. **(A)** Estimating the underground feedback parameter a_{fb} despite potential ambiguity on the minimum magnitude cutoff mentioned in the literature, by using information on $\delta m = m_c - min(m)$ and $\gamma = N(\geq m_c)/N(\geq min(m))$ obtained for the sites considered in the present study (histograms) – a_{fb} estimates given for $b = 1, N(\geq m_?) = 65$ and $V = 2,000$ m^3 (1988 Hijiori case) **(B)** Predicting the completeness level of a planned seismic network configuration using the prior model $f_{prior}(d_3)$ of the BMC method (here with 8 stations, 7 randomly distributed at the surface and 1 located at the ad-hoc borehole with coordinates (5, 5, –6) km).

Standard m_c Analysis), the 1988 Hijiori underground feedback activation may be $a_{fb,correct} = -5.5$ if $m_? = m_c$, or $a_{fb,corrected} = [-5.4, -3.9]$ if $m_? = min(m)$. Despite the ambiguity, an estimate may therefore still be provided. A review of the literature could provide additional values from other fluid injections to better constrain the range of a_{fb} to be considered as *a priori* information in risk assessment, which is so far potentially biased toward high a_{fb} values (e.g., Mignan et al., 2017).

Finally, if the BMC method allows defining robust m_c maps (no spatial gap, uncertainty constrained by the seismic network configuration), BMC may be even more useful for seismic network planification (e.g., Kraft et al., 2013) prior to new stimulations. Seismic safety criteria can be mapped into magnitude thresholds not to be crossed (Mignan et al., 2017), which tell us the completeness magnitude level required for sound statistical analysis. One can then use the BMC prior $f_{prior}(d_3)$ to test how a completeness level can be achieved given a seismic network configuration. **Figure 6B** illustrates such an application. The two approaches presented in **Figure 6** demonstrate how induced seismicity data mining can be done from completeness magnitude knowledge, which in turn can improve induced seismicity monitoring, modeling and managing.

DATA AVAILABILITY STATEMENT

Publicly available datasets were analyzed in this study. This data can be found here See **Table 1** and reference list.

AUTHOR CONTRIBUTIONS

AM did all the research and writing.

REFERENCES

Ake, J., Mahrer, K., O'Connell, D., and Block, L. (2005). Deep-injection and closely monitored induced seismicity at Paradox Valley, Colorado. *Bull. Seismol. Soc. Am.* 95, 664–683. doi:10.1785/0120040072

Aki, K. (1965). Maximum likelihood estimate of b in the formula Log N = a-bM and its confidence limits. *Bull. Earthq. Res. Inst. Univ. Tokyo* 43, 237–239.

Amorèse, D. (2007). Applying a change-point detection method on frequency-magnitude distributions. *Bull. Seismol. Soc. Am.* 97 (1), 742–751. doi:10.1785/0120060181

Baisch, S., Rothert, E., Stang, H., Vörös, R., Koch, C., and McMahon, A. (2015). Continued geothermal reservoir stimulation experiments in the Cooper Basin (Australia). *Bull. Seismol. Soc. Am.* 105, 198–209. doi:10.1785/0120140208

Bentz, S., Kwiatek, G., Martínez-Garzón, P., Bohnhoff, M., and Dresen, G. (2020). Seismic moment evolution during hydraulic stimulations. *Geophys. Res. Lett.* 47, e2019GL086185. doi:10.1029/2019gl086185

Brandt, M. B. C. (2019). Performance of the South African national seismograph network from october 2012 to february 2017: spatially varying magnitude completeness. *S. Afr. J. Geol.* 122, 57–68. doi:10.25131/sajg.122.0004

Broccardo, M., Mignan, A., Grigoli, F., Karvounis, D., and Rinaldi, A. P (2020). Induced seismicity risk analysis of the hydraulic stimulation of a geothermal

well on Geldinganes, Iceland. *Nat. Hazards Earth Syst. Sci.* 20 (1573-1), 593. doi:10.5194/nhess-20-1573-2020

Broccardo, M., Mignan, A., Wiemer, S., Stojadinovic, B., and Giardini, D. (2017). Hierarchical bayesian modeling of fluid-induced seismicity. *Geophys. Res. Lett.* 44 (11), 357–411. doi:10.1002/2017gl075251

Bureau of Reclamation (2017). Paradox Valley earthquake catalogue. Available at: https://www.usbr.gov/uc/wcao/progact/paradox/RI.html. (Accessed June 2017)

Calò, M., and Dorbath, C. (2013). Different behaviours of the seismic velocity field at Soultz-sous-Fôrets revealed by 4-D seismic tomography: case study of GPK3 and GPK2 injection tests. *Geophys. J. Int.* 194 (1), 119–121. doi:10.1093/gji/ggt153

Charléty, J., Cuenot, N., Dorbath, L., Dorbath, C., Haessler, H., and Frogneux, M. (2007). Large earthquakes during hydraulic stimulations at the geothermal site of Soultz-sous-Forêts. *Int. J. Rock Mech. Mining Sci.* 44 (1), 105–111. doi:10.1016/j.ijrmms.2007.06.003

Cladouhos, T. T., Petty, S., Nordin, Y., Moore, M., Grasso, K., and Uddenberg, M. (2013). "Microseismic monitoring of Newberry Volcano EGS demonstration," in Proc. 38th workshop geotherm. Reservoir. Engineering, February 11-13, 2013 (Stanford, CA: Stanford University).

Cladouhos, T. T., Petty, S., Swyer, M., Uddenberg, M., and Nordin, Y. (2015). "Results from Newberry Volcano EGS demonstration," in Proc. 40th workshop geotherm. Reserv. Eng, January 26–28, 2015 (Stanford, CA: Stanford University).

Cornet, F. H., Helm, J., Poitrenaud, H., and Etchecopar, A. (1997). Seismic and aseismic slips induced by large-scale fluid injections. *Pure Appl. Geophys.* 150, 563–583. doi:10.1007/s000240050093

Cuenot, N., Dorbath, C., and Dorbath, L. (2008). Analysis of the microseismicity induced by fluid injections at the EGS site of soultz-sous-forêts (alsace, France): implications for the characterization of the geothermal reservoir properties. *Pure Appl. Geophys.* 165, 797–828. doi:10.1007/s00024-008-0335-7

Dempster, A. P., Laird, N. M., and Rubin, D. B. (1977). Maximum likelihood from incomplete data via theEMAlgorithm. *J. R. Stat. Soc. Ser. B* 39, 1–22. doi:10.1111/j.2517-6161.1977.tb01600.x

Diehl, T., Kraft, T., Kissling, E., and Wiemer, S. (2017). The induced earthquake sequence related to the St. Gallen deep geothermal project (Switzerland): fault reactivation and fluid interactions imaged by microseismicity. *J. Geophys. Res. Solid Earth* 122 (7), 272–277. doi:10.1002/2017jb014473

Dinske, C., and Shapiro, S. A. (2013). Seismotectonic state of reservoirs inferred from magnitude distributions of fluid-induced seismicity. *J. Seismol.* 17, 13–25. doi:10.1007/s10950-012-9292-9

EOST and GEIEEMS (2017). Episode: 1993 stimulation soultz-sous-forêts [collection]. *EOST CDGP* 107, 2247–2257. doi:10.25566/SSFS1993

EOST and GEIEEMS (2018a). Episode: 2000 stimulation soultz-sous-forêts [collection]. *EOST CDGP* [Epub ahead of print]. doi:10.25577/SSFS2000

EOST and GEIEEMS (2018b). Episode: 2003 stimulation soultz-sous-forêts [collection]. *EOST CDGP* [Epub ahead of print]. doi:10.25577/SSFS2003

EOST and GEIEEMS (2018c). Episode: 2004 stimulation soultz-sous-forêts [collection]. *EOST CDGP* [Epub ahead of print]. doi:10.25577/SSFS2004

EOST and GEIEEMS (2018d). Episode: 2005 stimulation soultz-sous-forêts [collection]. *EOST CDGP* [Epub ahead of print]. doi:10.25577/SSFS2005

Gutenberg, B., and Richter, C. F. (1944). Frequency of earthquakes in California. *Bull. Seismol. Soc. Am.* 34, 184–188.

Häring, M. O., Schanz, U., Ladner, F., and Dyer, B. C. (2008). Characterisation of the Basel 1 enhanced geothermal system. *Geothermics* 37, 469–495. doi:10.1016/j.geothermics.2008.06.002

IS EPOS (2017a). Episode: THE geysers Prati 9 and Prati 29 cluster. Available at: https://tcs.ah-epos.eu/#episode. (Accessed November 2020)

IS EPOS (2017b). Episode: gross schoenebeck. Available at: https://tcs.ah-epos.eu/#episode. (Accessed November 2020)

IS EPOS (2018). Episode THE GEYSERS Prati 9 and Prati 29 cluster. Available at: https://tcs.ah-epos.eu/#episode. (Accessed November 2020)

IS EPOS (2020). Episode: cooper BASIN. Available at: https://tcs.ah-epos.eu/#episode. (Accessed November 2020)

Jost, M. L., Büsselberg, T., Jost, Ö., and Harjes, H. P. (1998). Source parameters of injection-induced microearthquakes at 9 km depth at the KTB deep drilling site, Germany. *Bull. Seismol. Soc. Am.* 88, 815–832.

Kamer, Y., and Hiemer, S. (2015). Data-driven spatial *b* value estimation with applications to California seismicity: to *b* or not to *b*. *J. Geophys. Res. Solid Earth* 120 (5), 191–195. doi:10.1002/2014jb011510

Kijko, A., and Smit, A. (2017). Estimation of the frequency-magnitude gutenberg-richterb-value without making assumptions on levels of completeness. *Seismol. Res. Lett.* 88, 311–318. doi:10.1785/0220160177

Kraft, T., and Deichmann, N. (2014). High-precision relocation and focal mechanism of the injection-induced seismicity at the Basel EGS. *Geothermics* 52, 59–73. doi:10.1016/j.geothermics.2014.05.014

Kraft, T., Mignan, A., and Giardini, D. (2013). Optimization of a large-scale microseismic monitoring network in northern Switzerland. *Geophys. J. Int.* 195, 474–490. doi:10.1093/gji/ggt225

Kwiatek, G., Bohnhoff, M., Dresen, G., Schulze, A., Schulte, T., and Zimmermann, G. (2010). Microseismicity induced during fluid-injection: a case study from the geothermal site at Groß Schönebeck, North German Basin. *Acta Geophys.* 58, 995–1020. doi:10.2478/s11600-010-0032-7

Kwiatek, G. (2019). Controlling fluid-induced seismicity during a 6.1-km-deep geothermal stimulation in Finland. *Sci. Adv.* 5, eaav7224. doi:10.1126/sciadv.aav7224

Kwiatek, G., Martínez-Garzón, P., Dresen, G., Bohnhoff, M., Sone, H., and Hartline, C. (2015). Effects of long-term fluid injection on induced seismicity parameters and maximum magnitude in northwestern part of the Geysers geothermal field. *J. Geophys. Res. Solid Earth* 120 (7), 101–107. doi:10.1002/2015jb012362

Kwiatek, G., Martínez-Garzón, P., Plenkers, K., Leonhardt, M., Zang, A., and von Specht, S. (2018). Insights into complex subdecimeter fracturing processes occurring during a water injection experiment at depth in Äspö Hard Rock Laboratory, Sweden. *J. Geophys. Res. Solid Earth* 123, 6616–6635. doi:10.1029/2017JB014715

MacQueen, J. (1967). "Some methods for classification and analysis of multivariate observations," in Proc. 5th berkeley symposium on mathematics, statistics and probability Editors M. L. M. Le Cam and J. Neyman (Univ. California Press), vol. 5.1, 281–297.

Martinsson, J., and Jonsson, A. (2018). A new model for the distribution of observable earthquake magnitudes and applications to b -value estimation. *IEEE Geosci. Rem. Sens. Lett.* 15, 833–837. doi:10.1109/lgrs.2018.2812770

Mignan, A., Broccardo, M., Wiemer, S., and Giardini, D. (2017). Induced seismicity closed-form traffic light system for actuarial decision-making during deep fluid injections. *Sci. Rep.* 7, 13607. doi:10.1038/s41598-017-13585-9

Mignan, A., and Chen, C.-C. (2016). The spatial scale of detected seismicity. *Pure Appl. Geophys.* 173, 117–124. doi:10.1007/s00024-015-1133-7

Mignan, A., and Chouliaras, G. (2014). Fifty years of seismic network performance in Greece (1964-2013): spatiotemporal evolution of the completeness magnitude. *Seismol. Res. Lett.* 85, 657–667. doi:10.1785/0220130209

Mignan, A. (2012). Functional shape of the earthquake frequency-magnitude distribution and completeness magnitude. *J. Geophys. Res.* 117, B08302. doi:10.1029/2012jb009347

Mignan, A. (2019). Generalized earthquake frequency-magnitude distribution described by asymmetric Laplace mixture modelling. *Geophys. J. Int.* 219 (1), 348–351. doi:10.1093/gji/ggz373

Mignan, A., Jiang, C., Zechar, J. D., Wiemer, S., Wu, Z., and Huang, Z. (2013). Completeness of the Mainland China earthquake catalog and implications for the setup of the China earthquake forecast testing center. *Bull. Seismol. Soc. Am.* 103, 845–859. doi:10.1785/0120120052

Mignan, A., Landtwing, D., Kästli, P., Mena, B., and Wiemer, S. (2015). Induced seismicity risk analysis of the 2006 Basel, Switzerland, Enhanced Geothermal System project: influence of uncertainties on risk mitigation. *Geothermics* 53, 133–146. doi:10.1016/j.geothermics.2014.05.007

Mignan, A., Karvounis, D., Broccardo, M., Wiemer, S., and Giardini, D. (2019). Including seismic risk mitigation measures into the Levelized Cost of Electricity in enhanced geothermal systems for optimal siting. *Appl. Energ.* 238, 831–850. doi:10.1016/j.apenergy.2019.01.109

Mignan, A. (2016). Static behaviour of induced seismicity. *Nonlin. Process. Geophys.* 23, 107–113. doi:10.5194/npg-23-107-2016

Mignan, A., Werner, M. J., Wiemer, S., Chen, C. C., and Wu, Y. M. (2011). Bayesian estimation of the spatially varying completeness magnitude of earthquake catalogs. *Bull. Seismol. Soc. Am.* 101, 1371–1385. doi:10.1785/0120100223

Mignan, A., and Woessner, J. (2012). Estimating the magnitude of completeness for earthquake catalogs. Available at: http://www.corssa.org: Community Online Resource for Statistical Seismicity Analysis. (Accessed November 2020)

Ogata, Y., and Katsura, K. (1993). Analysis of temporal and spatial heterogeneity of magnitude frequency distribution inferred from earthquake catalogues. *Geophys. J. Int.* 113, 727–738. doi:10.1111/j.1365-246x.1993.tb04663.x

Panzera, F., Mignan, A., and Vogfjörð, K. S. (2017). Spatiotemporal evolution of the completeness magnitude of the Icelandic earthquake catalogue from 1991 to 2013. *J. Seismol.* 21, 615–630. doi:10.1007/s10950-016-9623-3

Ringdal, F. (1975). On the estimation of seismic detection thresholds. *Bull. Seismol. Soc. Am.* 65 (1), 631.

Sasaki, S. (1998). Characteristics of microseismic events induced during hydraulic fracturing experiments at the Hijiori hot dry rock geothermal energy site, Yamagata, Japan. *Tectonophysics* 289, 171–188. doi:10.1016/s0040-1951(97)00314-4

Tormann, T., Wiemer, S., and Mignan, A. (2014). Systematic survey of high-resolution *b* value imaging along Californian faults: inference on asperities. *J. Geophys. Res. Solid Earth* 119 (2), 029–32. doi:10.1002/2013jb010867

U.S. Department of Energy (2020). Newberry. Available at: http://fracture.lbl.gov/cgi-bin/Web_CatalogSearch.py. (Accessed November 2020)

van der Elst, N. J., Page, M. T., Weiser, D. A., Goebel, T. H. W., and Hosseini, S. M. (2016). Induced earthquake magnitudes are as large as (statistically) expected. *J. Geophys. Res. Solid Earth* 121 (4), 575–584. doi:10.1002/2016jb012818

Villiger, L., Gischig, V. S., Doetsch, J., Krietsch, H., and Dutler, N. O. (2020). Influence of reservoir geology on seismic response during decameter-scale hydraulic stimulations in crystalline rock. *Solid Earth* 11, 627–655. doi:10.5194/se-11-627-2020

Vorobieva, I., Narteau, C., Shebalin, P., Beauducel, F., Nercessian, A., and Clouard, V. (2013). Multiscale mapping of completeness magnitude of earthquake catalogs. *Bull. Seismol. Soc. Am.* 103 (2), 188–192. doi:10.1785/0120120132

Wiemer, S., and Wyss, M. (2000). Minimum magnitude of completeness in earthquake catalogs: examples from Alaska, the western United States, and Japan. *Bull. Seismol. Soc. Am.* 90, 859–869. doi:10.1785/0119990114

Woessner, J., and Wiemer, S. (2005). Assessing the quality of earthquake catalogues: estimating the magnitude of completeness and its uncertainty. *Bull. Seismol. Soc. Am.* 95, 684–698. doi:10.1785/0120040007

Woo, J.-U., Kim, M., Sheen, D.-H., Kang, T.-S., Rhie, J., and Grigoli, F. (2019). An in-depth seismological analysis revealing a causal link between the 2017 M_w 5.5 Pohang earthquake and EGS project. *J. Geophys. Res. Solid Earth* 124 (13), 060–113. doi:10.1029/2019jb018368

Conflict of Interest: The author declares that the research was conducted in the absence of any commercial or financial relationships that could be construed as a potential conflict of interest.

frontiers in Earth Science

ORIGINAL RESEARCH
published: 01 April 2021
doi: 10.3389/feart.2021.626720

Effect of Groundwater on Noise-Based Monitoring of Crustal Velocity Changes Near a Produced Water Injection Well in Val d'Agri (Italy)

Andrea Berbellini[1]*, *Lucia Zaccarelli*[1], *Licia Faenza*[1], *Alexander Garcia*[1], *Luigi Improta*[2], *Pasquale De Gori*[2] *and Andrea Morelli*[1]

[1] *Istituto Nazionale di Geofisica e Vulcanologia, Sezione di Bologna, Bologna, Italy,* [2] *Istituto Nazionale di Geofisica e Vulcanologia, Osservatorio Nazionale Terremoti, Rome, Italy*

We study the crustal velocity changes occurred at the restart of produced water injection at a well in the Val d'Agri oil field in January–February 2015 using seismic noise cross-correlation analysis. We observe that the relative velocity variations fit well with the hydrometric level of the nearby Agri river, which may be interpreted as a proxy of the total water storage in the shallow aquifers of the Val d'Agri valley. We then remove from the relative velocity trend the contribution of hydrological variations and observe a decrease in relative velocity of $\approx 0.08\%$ starting seven days after the injection restart. In order to investigate if this decreasing could be due to the water injection restart, we compute the medium diffusivity from its delay time and average station-well distance. We found diffusivity values in the range 1–5 m^2/s, compatible with the observed delay time of the small-magnitude ($M_L \leq 1.8$) induced seismicity occurrences, triggered by the first injection tests in June 2006 and with the hydraulic properties of the hydrocarbon reservoir. Our results show that water storage variations can not be neglected in noise-based monitoring, and they can hide the smaller effects due to produced water injection.

Keywords: seismic noise, induced seismicity, seismic velocity changes, groundwater, produced water injection

OPEN ACCESS

Edited by:
Antonio Pio Rinaldi,
ETH Zurich, Switzerland

Reviewed by:
Piero Poli,
Université Grenoble Alpes, France
Pilar Sánchez-Pastor,
ETH Zurich, Switzerland

***Correspondence:**
Andrea Berbellini
andrea.berbellini@ingv.it

Specialty section:
This article was submitted to Solid Earth Geophysics, a section of the journal Frontiers in Earth Science

Received: *06 November 2020*
Accepted: *04 March 2021*
Published: *01 April 2021*

Citation:
Berbellini A, Zaccarelli L, Faenza L, Garcia A, Improta L, De Gori P and Morelli A (2021) Effect of Groundwater on Noise-Based Monitoring of Crustal Velocity Changes Near a Produced Water Injection Well in Val d'Agri (Italy). Front. Earth Sci. 9:626720. doi: 10.3389/feart.2021.626720

1. INTRODUCTION

The Val d'Agri oil field in the Southern Apennines range of Italy is the largest onshore reservoir in Europe (**Figure 1**). Co-produced saltwater is re-injected back through the high-rate disposal well Costa Molina 2 (CM2), into a marginal portion of the fractured carbonate reservoir. Injection started in June 1st 2006 and was accompanied by the occurrence of a low energy seismic swarm ($M_L \leq 1.8$; Improta et al., 2015). Low-magnitude induced seismicity ($M_L \leq 2.0$) continued to be recorded in the following 6 years by the monitoring network of the local operator ENI. Induced seismicity showed hypocentral distance ranging between 0.8 and 2.4 km from the well bottom within the injection reservoir (Improta et al., 2017; **Figure 1**). Since 2012 the seismicity rate in the area slowed down and remained at low levels, while disposal operations continued at almost constant pressure (around 110 bar until 2017, then 80 bar) and rate (around 2,500 m^3/d until 2017, 2,000 m^3/d later; Improta et al., 2017). On January 26th 2015 the disposal activity began to be halted for technical operations and restarted on February 18th after 23 days. As soon as

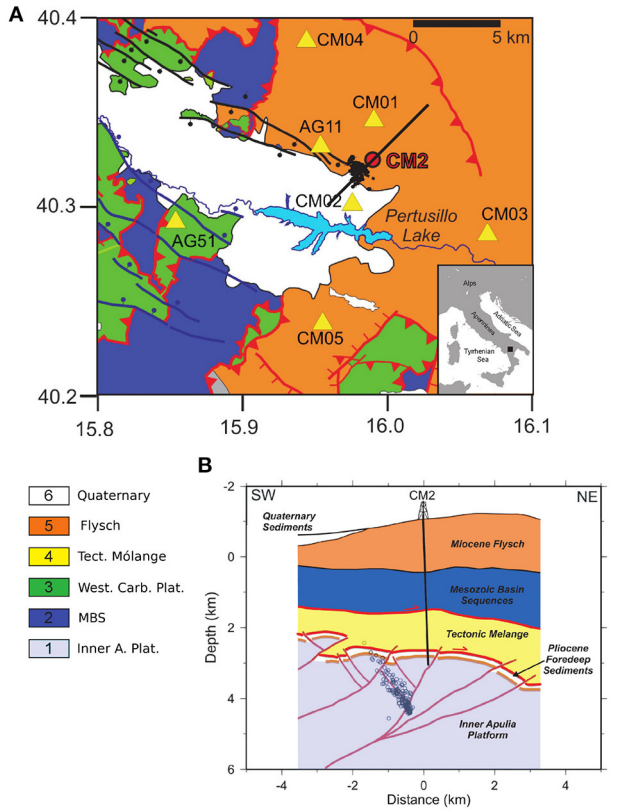

FIGURE 1 | (A) Geologic map of the southern sector of the Val d'Agri (modified after; Improta et al., 2017). 1—Inner Apulia platform (Mesozoic–Miocene); 2—deep basin pelagic sequences (Mesozoic); 3—Western carbonate platform (Mesozoic); 4—Tectonic mólange (Late Miocene–Lower Pliocene); 5—Flysch deposits, pelagic-slope successions (Miocene); 6—Quaternary continental deposits. Red lines denote main reverse faults; blue and black thick lines denote Quaternary normal-fault systems; yellow triangles are seismic stations used in this study; the red circle is the injection well CM2. The black dots denote the epicenters of the 2006–2014 fluid injection induced earthquakes analyzed by Improta et al. (2017). **(B)** Schematic geologic cross-section across the CM2 well injection site. The trace of the section is reported in map with a thick line. The black circles denote the 2006–2014 fluid injection induced earthquakes located through the double-difference method by Improta et al. (2017). The schematic geologic model is modified after Buttinelli et al. (2016) and Improta et al. (2017).

we obtain information about the stop, a temporary network of five stations was installed by Istituto Nazionale di Geofisica e Vulcanologia (INGV) around CM2 to monitor in detail the restarting phase. These temporary stations operated since January 26th and during the following three months recorded 25 microearthquakes ($-0.1 < M_L < 0.8$) located in an area of 5 km radius centered on CM2 (black dots in **Figures 2**, **3**). Those events mostly cluster in the same zone that experienced intense microseismicity between 2006 and 2011 resembling previous activity (Improta et al., 2017), but the rapid resumption of the injection activity was not accompanied by an evident increase in earthquake rate (**Figure 3**). Due to the small number of seismic events in the records and to their sparse occurrence in time, a classical analysis of earthquake signals cannot be used to study possible variations of crustal velocity from injection restart. Hence we focus here on a noise-based monitoring technique (Brenguier et al., 2008a), which do not need any earthquake signal, and allows the reconstruction of the relative velocity temporal variations in the crust.

It is now common ground that Green's function between two seismic station can be extracted from cross-correlations (hereafter CCs) of ambient seismic noise (Lobkis and Weaver, 2001; Larose, 2006; Gouédard et al., 2008). Green's functions can then be used to retrieve a tomographic image of the crust and uppermost mantle under the region where the seismic network is deployed (Shapiro et al., 2005). This approach allows computing a static image of the seismic velocities of the subsurface with the only requirements that the noise sources are homogeneously distributed and stable in time. In practice, even though the noise sources are not homogeneously distributed, the Green's function may be achieved thanks to CCs of longer time recordings and scattering in the medium (Larose, 2006). Besides that, a temporal monitoring of the seismic velocities in the Earth crust can be performed even with an inhomogeneous noise source distribution, i.e., without a optimal reconstruction of the Green function of the medium (Hadziioannou et al., 2009), by analysing the coda of the cross-correlation functions. Coda waves are detected in the latter part of the seismogram and they can last much longer than the direct waves before reaching the background noise level (up to 10 times according to Aki, 1969). They are excited by direct waves, repeatedly scattered by small-scale heterogeneities fractures and cracks in the medium. Hence they sample the medium much more densely than direct waves, so they are more sensitive to small variations in the medium. For these reasons coda waves are also less sensitive to possible noise source changing positions (Froment et al., 2010). Noise-based monitoring has recently become an important tool to track local changes in crustal velocities and it has been successfully used in various settings: from active faults (Brenguier et al., 2008a; Zaccarelli et al., 2011), to volcanic areas (Brenguier et al., 2008b; Zaccarelli and Bianco, 2017); and geothermal reservoirs such as the St. Gallen site in Switzerland (Obermann et al., 2015), Valhall overburden in the North Sea (Mordret et al., 2014), the Reykjanes geothermal system in Iceland (Sànchez-Pastor et al., 2019).

In this study we apply the noise-based monitoring technique to detect relative variations of crustal seismic velocity in the Val d'Agri oil field using the Moving-Window Cross-Spectral analysis (Poupinet et al., 1984; Brenguier et al., 2008a; Clarke et al., 2011; Zaccarelli and Bianco, 2017). To check whether the seismic noise sources are stable in time we analyze data using the DOP-E approach (Berbellini et al., 2019). We locate our results in depth thanks to the sensitivity kernels computed from the velocity model of this region (Valoroso et al., 2009) using a modal summation approach by Herrmann (2013). Interestingly, we find a strong correlation of the velocity trend to the hydrological level of the Agri river. Hence, we remove the contribution of hydrological parameter changes to the crustal velocity changes and we interpret the residual results in terms of local diffusivity of the medium.

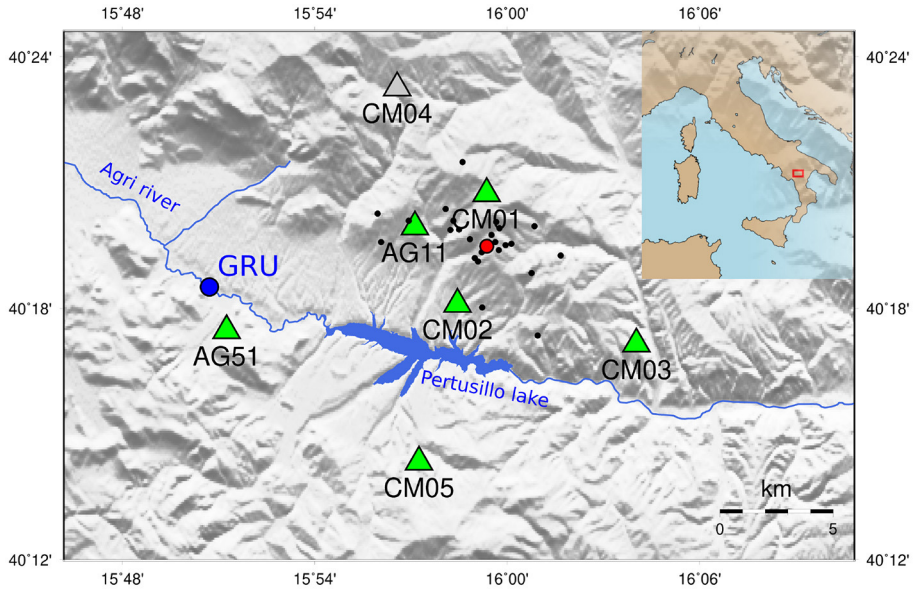

FIGURE 2 | Seismic network (green) around the Val d'Agri oil field and Costa Molina re-injection well (red). Black dots indicate the 2015 recorded seismicity (25 events with $-0.1 < M_L < 0.8$.). Seismic station CM04 (gray) has not be used due to irrecoverable technical problems with the clock. Blue dot indicate the Ponte Grumento meteorological station.

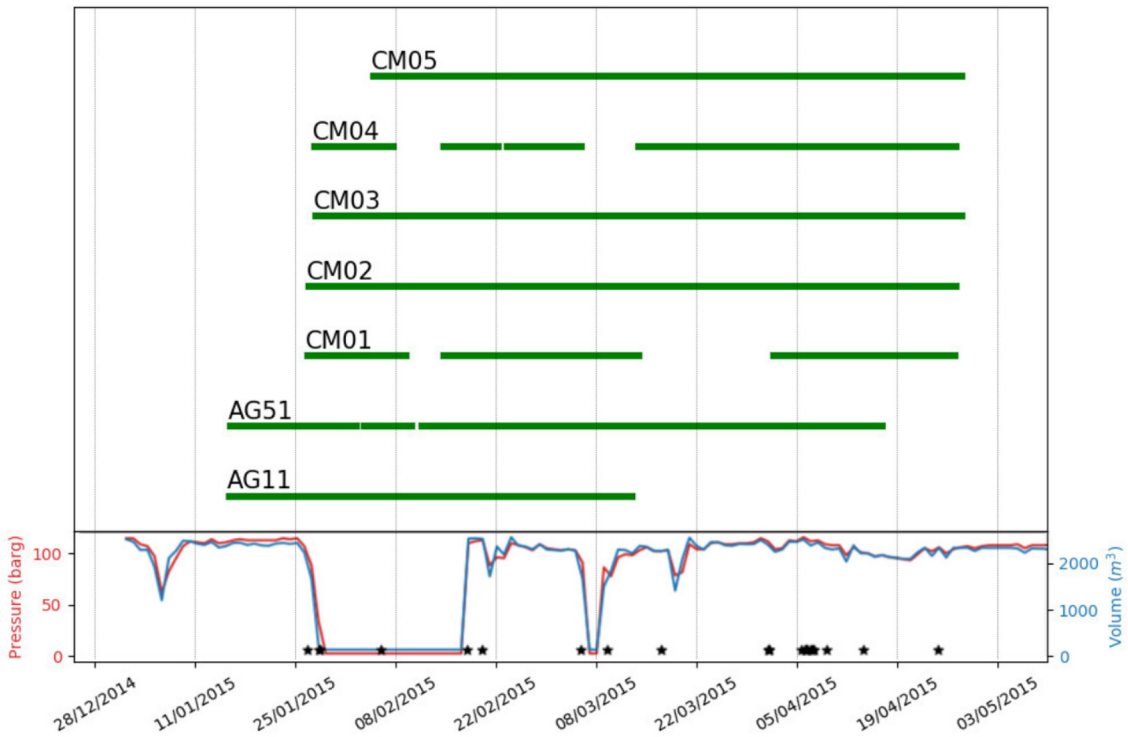

FIGURE 3 | Data availability for each station (top panel) and daily injection data (blue: injection rate; red: maximum wellhead pressure). Black stars indicate the recorded seismicity (25 events with $-0.1 < M_L < 0.8$).

2. GEOLOGICAL SETTING

The study area is located in the Lucania arc of the NE-verging southern Apennines thrust-and-fold belt. The upper crust includes NW-trending Mio-Pliocene thrusts and related folds deforming Meso-Cenozoic shelf carbonate and basin sequences (Mazzoli et al., 2001). The subsurface is structured into two main units: (i) an upper pile of rootless thrust sheets formed by carbonate platform, deep pelagic, and flysch sequences 2–4 km thick, (ii) the 5–7 km thick Inner Apulia carbonate Platform (IAP) deformed during Late Pliocene—Early Pleistocene by deeply rooted, steep reverse faults (**Figure 1**; Mazzoli et al., 2001). The IAP hosts the reservoir of the Val d'Agri oil field with hydrocarbon and brines trapped into thrust-related anticlines formed by low-porosity, strongly fractured limestone (**Figure 1**). The cap rocks consist of low-permeability mudstones and siltstones that form a Pliocene tectonic mèlange up to 1 km thick and tectonically sandwiched between the upper rootless nappes and the IAP (**Figure 1**; Shiner et al., 2004).

In the survey area, several oil wells reached the Apulian carbonate reservoir at 2–3 km depth b.s.l. (Improta et al., 2017). The geologic units drilled by the injection well CM2 include from top to bottom (Buttinelli et al., 2016): (i) clay-sandstone alternances and marly-calcareous strata referable to Miocene flysch (from 1,045 to 468 m b.s.l.), (ii) deep basin Mesozoic sequences also including Cretaceous shales (468–1,490 m b.s.l.), (iii) mudstones and siltstones sequences of the Pliocene tectonic mèlange (1,490–2,712 m b.s.l.), (iv) foredeep Pliocene clays and sandstones (2,712–2,821 m b.s.l.), and (v) fractured high permeability Miocene-Cretaceous limestone of the IAP (2,821–3,071 m b.s.l.). The presence of very thick and very-low permeability clayey sequences at the top of the IAP hinders the hydraulic communication between the rootless nappes and the carbonate reservoir (Improta et al., 2017).

Co-produced salt water has been re-injected in the high permeability Cretaceous limestone of the Apulian reservoir through the CM2 wellbore. Due to the alternance of low permeability clays with medium permeability sandstones and marly-limestones, the underground water circulation in the injection area is characterized by a near-surface, thin aquifer developed in the weathered flysch deposits and fed by rainfall and by deeper, compartmentalized, and overlapping aquifers developed in the medium-porosity and/or fractured sandy and calcareous beds. The quasi-instantaneous onset of microseismicity located under the well was explained in terms of rapid propagation of pore-pressure perturbation from the wellbore to an inherited Pliocene reverse fault that is confined within the reservoir (**Figure 1**; Buttinelli et al., 2016; Improta et al., 2017). The fault is located to the SW of the well CM2 and optimally oriented to slip in the present extensional stress field. Permeability of the Apulian carbonate reservoir has been estimated in the order of $k = 10^{-13} m^2$ from hydraulic well tests, production data and diffusivity analysis on the injection induced seismicity (Chelini et al., 1997; Improta et al., 2015).

3. DATA

The 2015 passive seismic survey was carried out from January 26th to April 27th. During this experiment five stations (**Figure 2**) were installed within 10 km from the CM2 well (named CM01–CM05). Two additional INGV temporary stations, AG11 and AG51, that were operating in the injection area before the suspension of disposal operations, complete the 7-stations network that we use here to monitor possible changes in relative crustal velocities. The stations were equipped with Reftek130 acquisition systems coupled with Lennartz 3-D 5 s sensors, and recorded at a sampling rate of 125 Hz. We discard station CM04 because of irrecoverable technical problems with the clock. Apart from CM02 and AG11, the seismic stations used in this study and surrounding the well CM2 were installed on Miocene flysch deposits (**Figure 1**). Seismic station CM02 was installed in the valley on Quaternary continental sediments about 100 m thick that overlay the Miocene flysch. The seismic station AG51 was deployed on Mesozoic fractured limestone belonging to the uppermost rootless nappe. Due to the strong fracturing, these terrains are characterized by a poorly known carbonate basal aquifer. While seismic stations are missing in the NE region from CM2, the azimuthal coverage of the station couples is quite complete. Five out of seven stations (CM01-05) have been installed the same day the injection was halted (see **Figure 3**; injection data from De Gori et al., 2015), therefore recorded data do not allow investigating the status of the system before the injection stop. This would have been very important to better interpret the velocity variations after the injection re-start.

4. METHOD

4.1. Polarization Analysis

The CCs temporal analysis is based on the assumption that the ambient noise sources are stable in time (Hadziioannou et al., 2009). In order to verify this assumption we perform a polarization analysis using the DOP-E method (Berbellini et al., 2019). This method filters the portion of ambient noise containing the most polarized signals and extract different observables such as the ellipticity of Rayleigh waves. Moreover, it is able to measure the back azimuth of the incoming signal, a useful tool to study the ambient noise sources. We apply this scheme to our data and we show in **Figure 4** the overall polarization for four sample stations. We observe here that for the majority of the stations the noise sources are located on a direction coming from the south-west. This is more evident in the frequency band 0.5–1.0 Hz, while in the frequency band 0.1–0.5 Hz the signals are more diffuse, but still in the south-west direction. Only station CM03 shows a different incoming azimuth, with a peak at around 315^o. This can be due to the particular local geology in the area surrounding the station. Pischiutta et al. (2014) measured polarization of signals from the analysis of local microseismicity. They observed an overall NE-SW distribution and an anomalous polarization in the CM03 area (they used records from temporary station AG10 located 300 m far from CM03). Our results are then in good agreement with previous findings. The presence of a non homogeneous

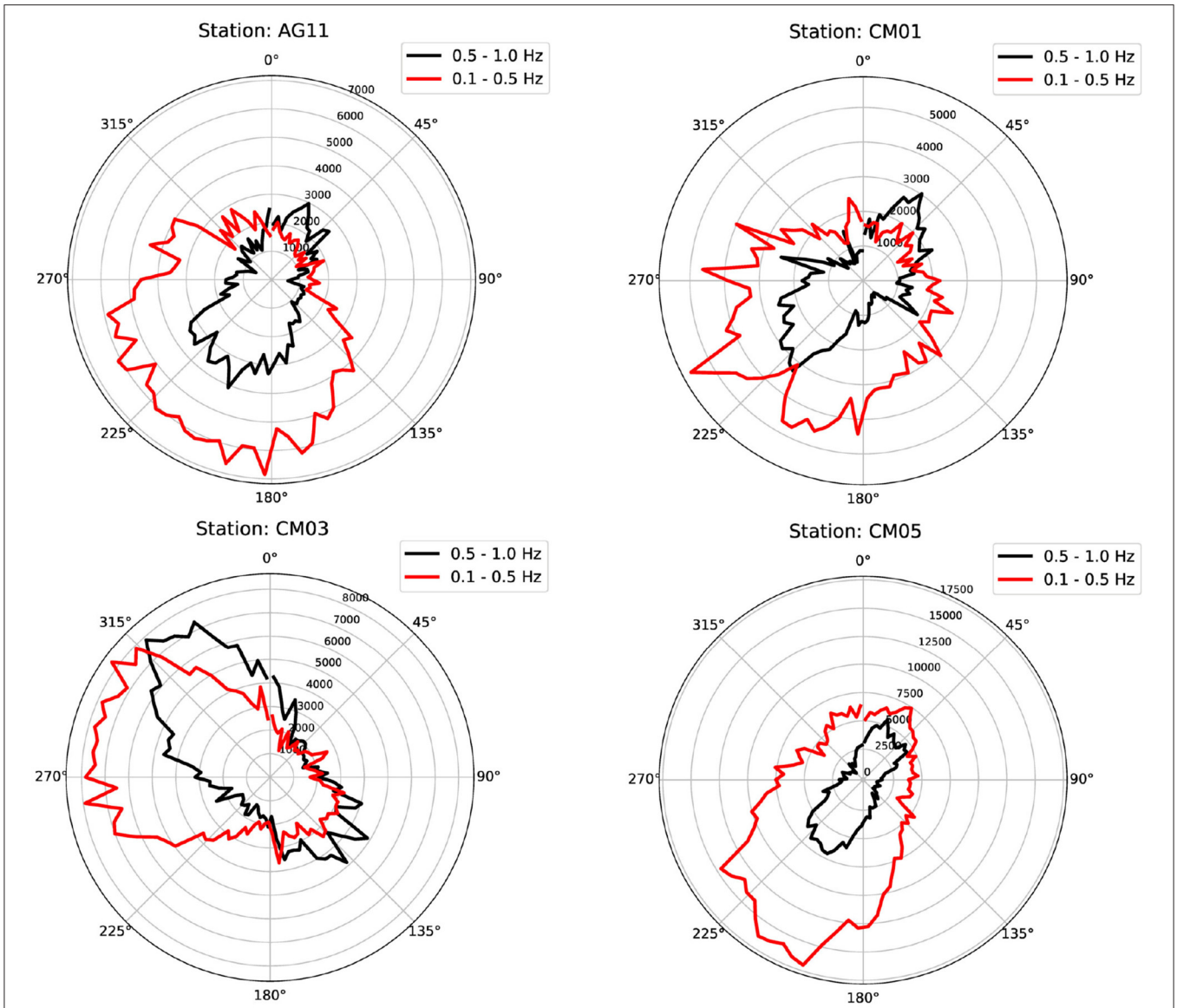

FIGURE 4 | Azimuthal source distribution in all the period for 4 sample stations measured using the DOP-E approach (Berbellini et al., 2019) in two different frequency bands, 0.5–1.0 Hz (black line) and 0.1–0.5 Hz (red line).

spatial distribution of the noise sources cause asymmetrical CC functions, as we can observe in **Figure 5**, but such an uneven distribution of the sources does not prevent us from using our approach, as long as the noise source distribution is stable in time. We verify its stability by repeating the DOP-E analysis on data stacked every 15 days. Station AG51 showed problems on one of the horizontal components, so the polarization analysis was not possible on this station. Since the vertical component shows good quality data and in the followings we perform CC analysis only on this component, we keep the station for the main analysis. All the other stations (see **Supplementary Figures 1–5**) showed a main direction for the incoming noise sources which is quite stable in time during the recording period. Moreover, it is noteworthy that, as already mentioned, we take into account only the coda of the cross-correlation functions, thus avoiding its central part, which is more sensitive to the changing position of the noise sources (Froment et al., 2010).

4.2. Pre-processing

We compute the relative variations of crustal velocities using the Moving-Window Cross-Spectral analysis (Poupinet et al., 1984; Brenguier et al., 2008a):

we fill the data gaps through a linear interpolation. We apply the filling if the gaps last <20% of the 1 h length used as quantum of data. Then we apply a signal whitening in the frequency domain in the frequency band 0.1–1.0 Hz, as proposed by Zaccarelli et al. (2011) and a 1-bit normalization in the time

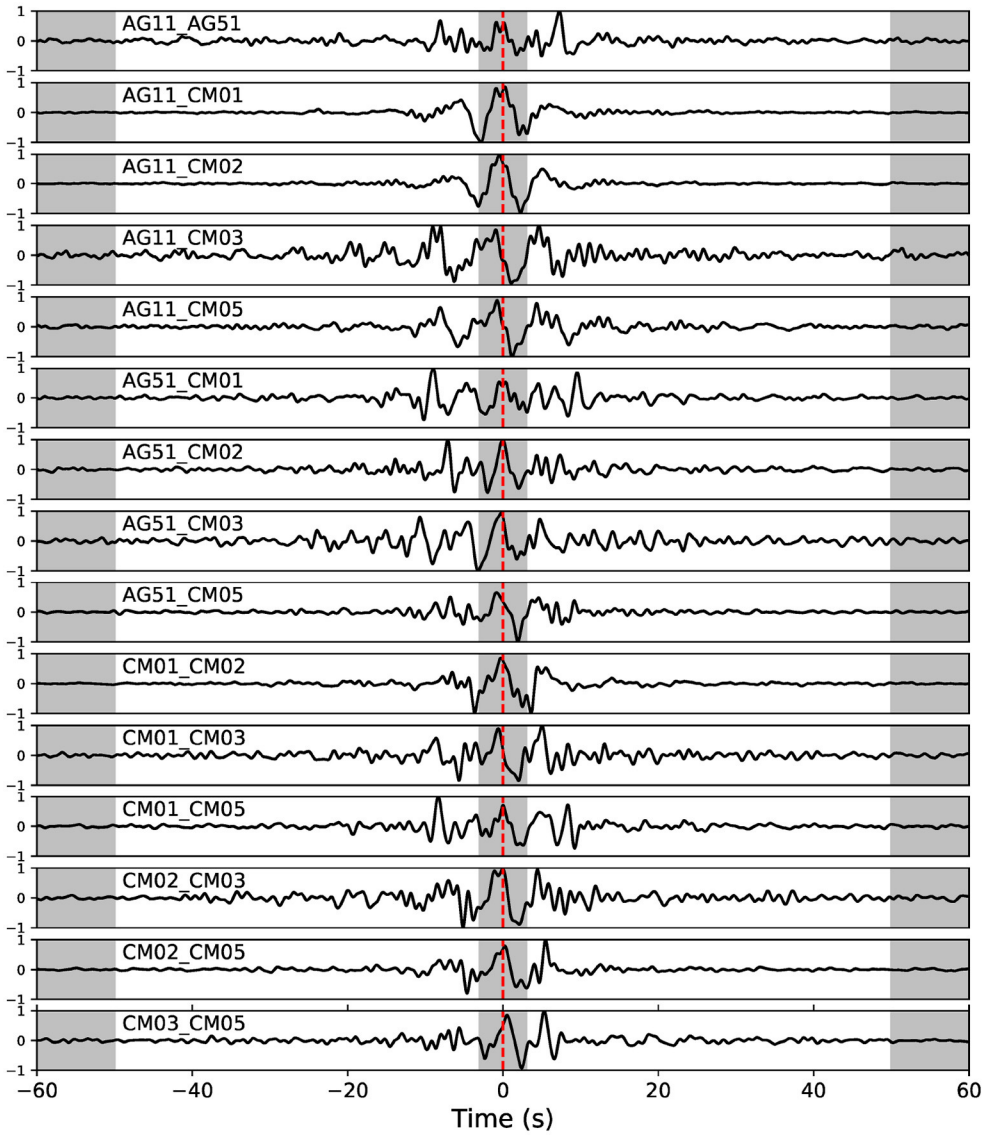

FIGURE 5 | Reference cross-correlations for all the station pairs available. Gray areas are the part of the signal excluded from the analysis.

domain. Finally we compare a reference cross-correlation (CC-ref) of ambient noise with the cross-correlations measured for each time interval (CC-cur). The whole analysis is performed in the frequency band 0.1–1.0 Hz.

4.3. Reference and Current Cross-Correlations

As a first step after this pre-processing we define the reference CC for each station pair by computing the cross-correlation for the whole available recordings by stacking all 1 h CCs computed on the entire recordings in the frequency band 0.1–1.0 Hz. In **Figure 5**, we show all the reference cross correlations used in this study.

Hence we compute the current cross-correlation over subsequent time intervals along the whole dataset, stacked over a certain number of days. The number of days that we are using for the stacking is quite important, since if the time interval is too short, then the CC-cur will be too different from the reference CC and the measurement will be unstable. On the opposite, if the stacking time is too long, the current CC will be very similar to the reference but the variations will loose time resolution. In order to select the optimal time interval we compute the mean correlation coefficients between the reference and current CC for 4 sample station pairs using different number of stacking days (see Zaccarelli et al., 2011). We choose a convergence test which is quantitative compared to the qualitative method chosen by D'Hour et al. (2015) (visual inspection). Our test is actually equivalent to Nuez et al. (2020) that looks at the similarity evolution between CCref and CCcur with the increasing stacking length. Results are shown in **Figure 6**. Here we notice that the

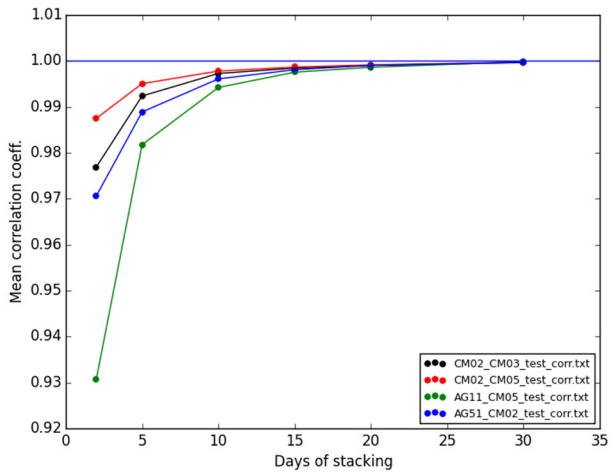

FIGURE 6 | Test to select the optimal number of days of stacking. Mean correlation coefficient between CC current and reference for four sample couples as a function of the number of stacking days.

mean correlation coefficient increases with the number of days and, as expected, tends asymptotically to 1. On the basis of this plot we choose 15 days as a good compromise between similarity of the CC and time resolution Our CC-cur's are then computed every day and they are computed as the stacking of the previous 15 days.

4.4. Moving Window Cross-Spectral Method

In order to measure the relative crustal velocity variation in time, we apply the Moving Window Cross-Spectral approach described by Clarke et al. (2011). This approach estimates the time-shift between the CC-cur (relative to 15 days of stacking) and the CC-ref (relative to all the period) waveforms. Time shift is directly related to the relative velocity variation following the relationship:

$$\frac{\tau}{t} = -\frac{\Delta v}{v} \tag{1}$$

where τ is the time-shift, t is the time, v is the crustal velocity and Δv its variation. We discard a time interval of 3 s around 0 (gray areas in **Figure 5**), estimated as an average propagation time of surface waves between each station in the region (Improta et al., 2017). We also exclude cross-correlations after 50 s, since after this interval the signal is lost in the background noise. In order to stabilize the measurements we include in the computation only the CC-cur with a correlation coefficient relative to the CC-ref larger than 0.85. We merge together all time-shifts estimated for each couple by computing their median values before estimating the final $\Delta v/v$, in order to get a picture of the mean time evolution of relative velocities variations in the whole medium included in the network. The velocity variations are defined in depth by the penetration of surface waves in the frequency band considered, estimated by the sensitivity kernels described in the following.

5. RESULTS

5.1. Description of the Results

Results are shown in **Figure 7**. Here we plot the relative velocity variation (top), the correlation coefficient between currents and reference for all the station pairs (central), and the daily injected volume and maximum well-head pressure (bottom panel; De Gori et al., 2015). We can observe a clear increase in relative velocity in the second half of February, followed by a decrease between the end of February and the beginning of March. After this, $\Delta v/v$ tends to a slightly larger value that remains more stable afterwards, with variations of about $\pm 0.02\%$. Observing the correlation coefficient plot (central panel) we notice a general low correlation in the very first part of the period, followed by a strong increase in correlation corresponding to the injection restart. Then, the correlation coefficient does not vary substantially. We observe a decrease for couples containing AG11 at the end of the recording period, at the same time of occurrence of some local earthquakes nearby. These two factors do not find any correspondence in $\Delta v/v$ variations. To complete the analysis we split the frequency band into two segments, 0.1–0.5 and 0.5–1.0 Hz. With this test we want to verify if the high frequency waves, sensitive to shallower depths show different trends compared to lower frequencies, sensitive to deeper structures. Results are shown in **Supplementary Figure 6**. Here we observe that both the frequency bands show the same trend observed using the whole band, but the lower frequencies show much larger errors and an overall larger instability. Higher frequency at the contrary show very similar behavior to the results based on the whole frequency range.

5.2. Sensitivity Kernels

In order to better constrain the results in depth we compute the sensitivity kernels for phase and group velocities using the 1D, flat layered model for the Val D'Agri region by Valoroso et al. (2009). Kernels show the sensitivity of the observable at the surface (i.e., phase velocity) to variations of a crustal parameter (v_S, v_P, and density) with depth. We compute the sensitivity kernels numerically using a modal summation approach (Herrmann, 2013): we divide each flat layer into 0.1 km thick sub-layers. We increment and decrement v_S at each depth by 10% and for the two models we compute the phase velocity using the modal summation approach. For each sub-layer we compute the derivative using the finite differences approach.

Results are shown at **Figure 8**. We notice that at the higher frequencies (0.5–1 Hz), that mainly contribute to our results, the sensitivity is stronger and confined in the top 5 km, while it decreases and becomes deeper at lower frequencies. At $1Hz$ the sensitivity is an order of magnitude bigger than $0.1Hz$, but it does not extend below 3 km depth. Co-produced saltwater is re-injected between 2.8 and 3.0 km depth b.s.l. within the liquid-bearing saturated reservoir. In the southern sector of the oil field, the IAP culminations are at 1.8–2.8 km depth b.s.l. and the reservoir thickness is 3–4 km (Improta et al., 2017). Therefore, the relative velocity changes resolved by the high frequency data (0.5–1.0 Hz) may be confined in

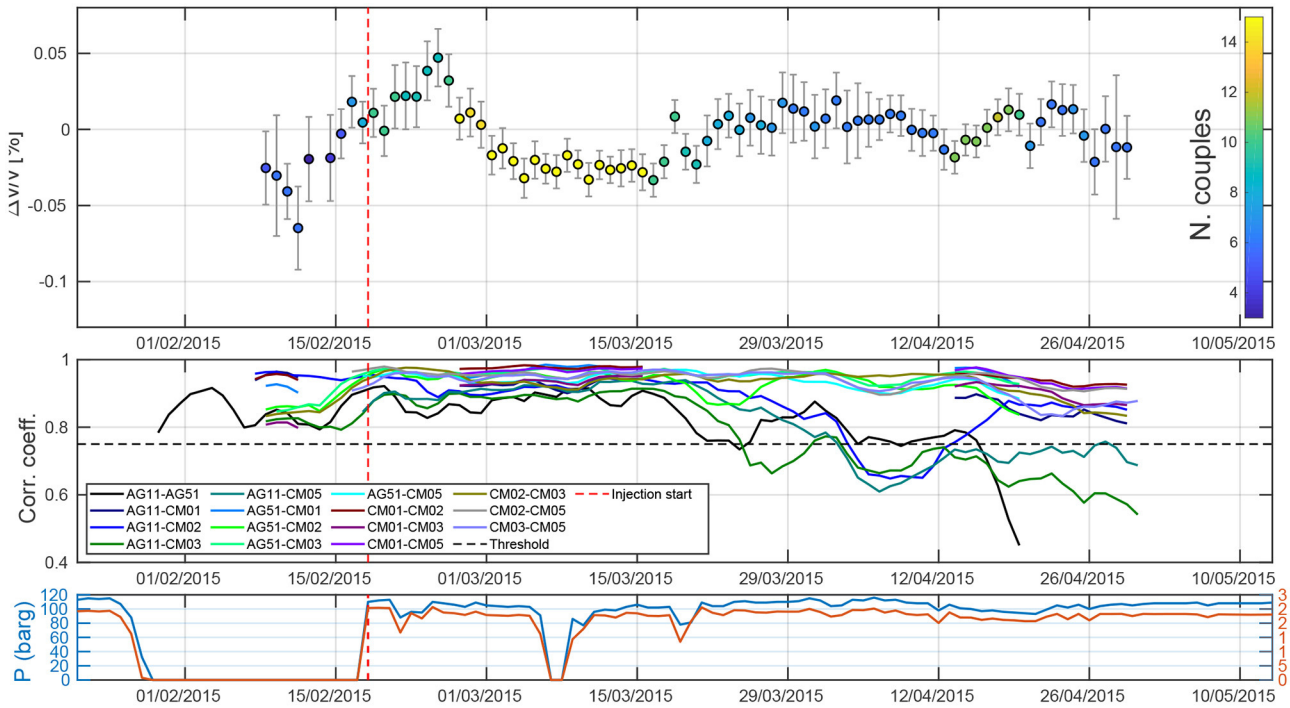

FIGURE 7 | (Top) Percentual crustal velocities variations as a function of time in the frequency band 0.1–1.0 Hz. Colors represent the number of station couples available at each time. **(Middle)** Correlation coefficient between currents and reference for each couple as a function of time. We exclude from the computation the data with a correlation coefficient lower than 0.75 (black dotted line). **(Bottom)** Injection daily pressure (red) and rate (blue) from De Gori et al. (2015).

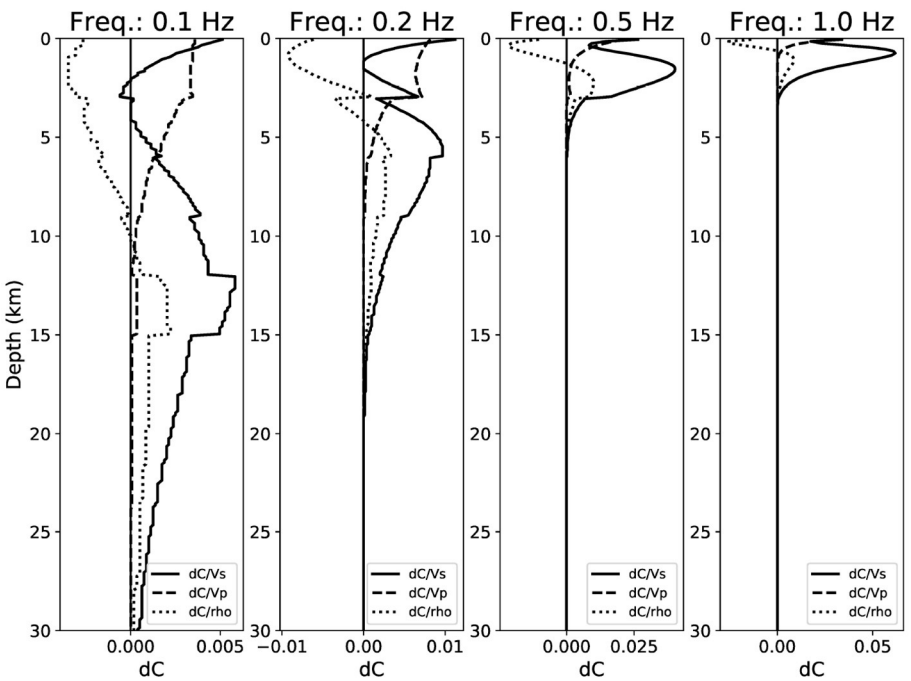

FIGURE 8 | Sensitivity kernels for the phase velocity as a function of v_S, v_P, and density computed using a modal summation approach (Herrmann, 2013) using the 1D model of the Val d'Agri area by Valoroso et al. (2009).

the top 5 km of the crust and can be reasonably associated to the fractured carbonate reservoir and to the overlying thrust sheets.

6. RAINFALL AND HYDROMETRIC COMPARISON

Recent studies showed that water table fluctuations in the top hundreds meters can cause variations in the crustal velocities that can be successfully detected by ambient noise monitoring (Sens-Schönfelder and Wegler, 2006; Rivet et al., 2015 and more recently Lecocq et al., 2017; Wang et al., 2017; Clements and Denolle, 2018; Liu et al., 2020; Poli et al., 2020). They observed that these variations can be large enough to cover other minor fluctuations due to secondary mechanisms. For this reason we first want to verify if the relative velocity variations shown in **Figure 7** are due to hydrological effects. We compare the observed velocity trend with three datasets from the regional civil protection office (downloaded from http://centrofunzionalebasilicata.it; see **Supplementary Figure 7**): daily rainfall (that we have cumulated by 15 days before comparison to our measurements) recorded at the nearest meteorological station (Ponte Grumento, GRU in **Figure 2**), river Agri hydrometric level, recorded at the same location and the water level of the Pertusillo artificial Lake (**Figure 2**). The first two (sign-reversed) time series are very similar to the dv/v trend, while the Pertusillo charge/discharge rate is definitely acting at longer period compared to the previous observables. We try to remove the contribution of precipitation to the observed velocity variations. Following the method proposed by Wang et al. (2017), we firstly compute the pore pressure variations induced by precipitations. Then we use it to compute the synthetic velocity variation due to rainfall. We observe that predicted synthetic velocity variations are much smaller than the observed ones, so we conclude that this method is not suitable to remove the contribution of rainfall to crustal velocity variations. Furthermore, we observe that the parameter that best fits the velocity variations is the hydrometric level of the Agri river (**Supplementary Figure 7**). We observe that the main dv/v maximum peak around the 24th of February fits well with the minimum of the hydrometric level (sign-reversed in the plot). The fit is quite good until the 8th of April, then the two trends do not fit well. The anti-correlation is quite clear: higher hydrometric levels correspond to slower crustal velocities. In fact, the CC codas at the frequencies 0.1–1.0 Hz are mainly composed by surface waves, meaning that we measure dv/v of multiple scattered coda waves, which decrease their velocity in the presence of fluids. The Agri river hydrometric level can be considered as a proxy of the total water storage in the valley, as it depends not only on the rainfalls but also on the total underground water amount. Consequently, the observed variation of shear-wave velocity can be interpreted in terms of variations in the aquifers hosted in the medium-permeability intervals (i.e., fractured sandstone and marly-limestones) of the thick Miocene flysch deposits outcropping in the survey area.

7. DISCUSSION

The velocity variations that we observe are mainly due to hydrological effects (rainfall, snow melting...) hiding any possible velocity variations due to the water injection restart.

In order to verify if it is still possible to observe a velocity change due to the produced water injection restart, we remove the hydrometric trend from the velocity time-series. We de-mean and normalize both the dv/v and hydrometric trends to make them comparable. Finally we deconvolve the velocity time-series with the hydrometric level and plot the deconvolution reminder (**Figure 9**). Here we observe that the deconvolved velocity trend still shows a velocity peak in 24th February 2015, which is smaller than the original one. This could be possibly due to water injection restart, which happened 7 days before (18 February 2015). Other minor peaks are observed around the 8th of March and the 17th of March (**Figure 9** bottom panel) which could be possibly linked to minor injection reductions (see **Figure 7**). Since the injection reductions are very small and the two peaks are quite isolated, we prefer not to over-interpret them as effect of injection variations.

We evaluate if the observed peak has some statistical significance with respect to the other peaks observed in the dv/v time series. With this aim we use a z-test to assess, for each dv/v point in the time series, if a random sample generated from a Normal distribution with mean dv/v and standard deviation the double of the respective formal error can be drawn from a reference Normal distribution characterized by the mean and the standard deviation (considering the double standard error of that point as well) of the maximum peak. It is worth noting that assuming the double of the formal error to set the standard deviation is a conservative choice justified by the fact that the MWCS analysis tends to underestimate the errors (Clarke et al., 2011). In practice, we take the peak value (i.e., the one on 24th February 2015) and the related uncertainty as a reference set of parameters, and use the z-test to compare this reference distribution with samples drawn from the distributions defined for each of the other points. We find that the probability that any of the generated samples is drawn from the peak distribution is very low (p-values $<<$ 1% in all the cases), indicating that the observed peak is significantly higher respect to all the other points. Similar results are obtained using non parametric tests (as e.g., the Kolmogorov-Smirnov test).

Knowing that the 24th February 2015 peak in dv/v is statistically significant, we intend to investigate on its possible relationship with the water injection restart. We start by computing the medium diffusivity, assuming that the observed velocity decrease is due to the propagation of produced water from the Costa Molina injection, restarted on 18th February 2015. Then we want to verify if the obtained diffusivity is compatible with the value computed from independent studies based on the seismicity induced by the first injection tests in 2006 and on hydraulic well tests in the hydrocarbon reservoir (Chelini et al., 1997; Improta et al., 2015). Hence we measure the delay time from the injection start (7 ± 1 days) and the average distance between the stations and the injection well (6.40 km). We then compute the medium diffusivity, using the

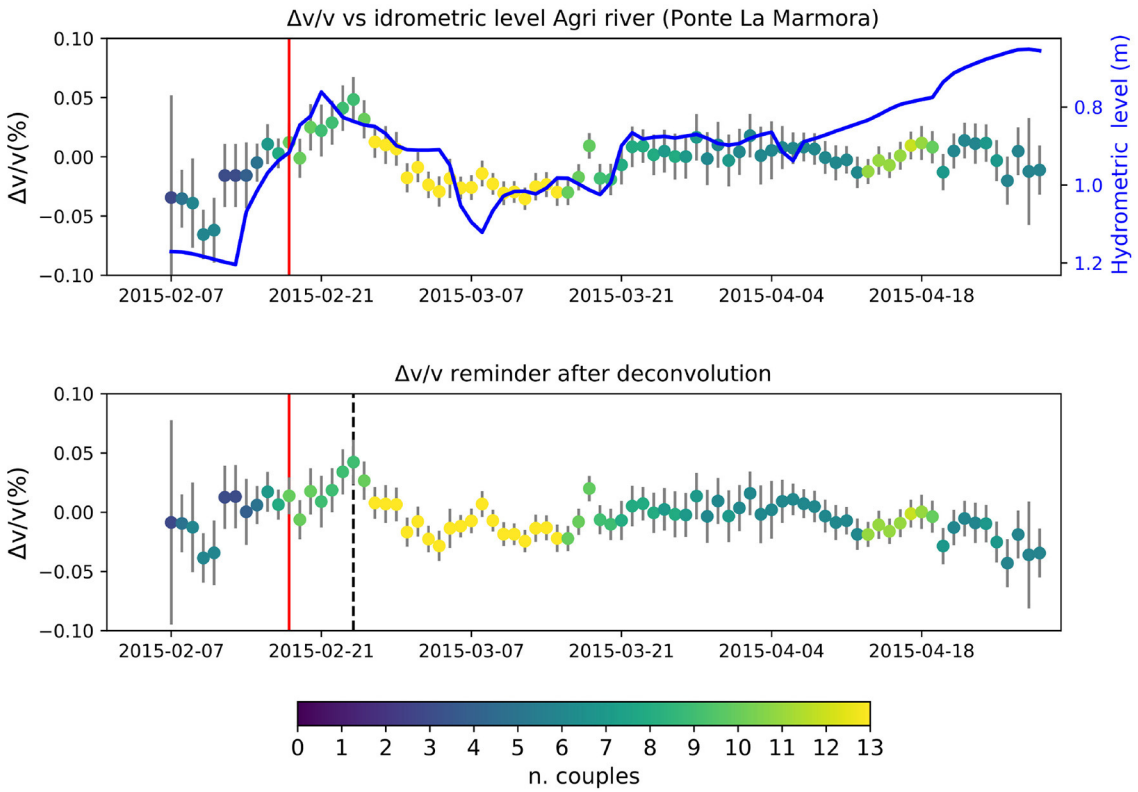

FIGURE 9 | (Top) Percentual crustal velocities variations as a function of time (dots) compared to the idrometric level of the Agri river (blue line, reversed y axes). **(Bottom)** Percentual crustal velocities variations after removing the Agri river idrometric level. Red line: produced water injection restart. Black dotted line: dv/v maximum.

equation (Shapiro, 2015):

$$D = \frac{R_T^2}{4\pi t} \tag{2}$$

where R_T is radius of the triggering front (in this case the average station-well distance) and t is the delay time from the injection start to the time when $\Delta v/v$ curves reach their maxima. We compute a diffusivity value of $5m^2/s$. We repeat the calculation using for R_T the average station-well distance for the three closest stations (2.82 km for stations AG11, CM01, and CM02) obtaining a diffusivity value of $1m^2/s$.

We compute both values aiming at a diffusivity range definition, since we do not have the spatial resolution to precisely locate dv/v in the map. The peak in dv/v means that a crustal variation has occurred in the medium included in the seismic network, and either it is very localized but big enough to be visible (not canceled) from all the stations, or it is small but spread out over all station locations. We then estimate the time evolution of the triggering front R_T given the observed diffusivity values (**Table 1**) using the Equation (2). Results are shown in **Figure 10**. Here we also plot the seismicity observed in June 2006 during the first injection tests (Improta et al., 2017), plotted as a function of distance from the CM2 well and time after the first injection test initiated the 1st June. The 2006 seismicity has been demonstrated to be induced by the first injection tests (Improta et al., 2017). Here we focus on the first events only to verify if the delay times observed in the 2006 induced sequence are compatible with the two triggering fronts obtained from the two diffusivity values. We observe that the first events triggered in 2006 fall in the range between the two triggering fronts estimated from the diffusivity range based on our observations. The first injection tests in 2006 activated a fault $\approx$ 1.7km far from the well bottom (Improta et al., 2015), with a delay time in the range expected from the diffusivity values we obtained here. No other faults slip seismically during the injection tests in 2006 (Improta et al., 2015), so it is not possible to compare our results to other seismic swarms. From this experiment we can conclude that the peak observed in 24th February 2015 could possibly be due to the produced water injection re-start, since the diffusivity estimated from its delay time is in the same order of magnitude of what we observe from other independent measurements, such as 2006 induced seismicity, but other studies should be done to confirm this hypothesis.

The obtained diffusivity values are compatible with the expected ones in such a geological setting. For instance, diffusivity values in the range 0.3–2 m^2/s has been observed in many different regions (Costain et al., 1987; Rothert et al., 2003; Costain, 2008; Costain and Bollinger, 2010). Also, Christiansen et al. (2007) estimated a diffusivity value of $\approx$ $2m^2/s$ for the Parkfield area at 5 km depth. Finally, Hainzl et al. (2006) found a diffusivity equals to 3.3 $\pm$ 0.8m^2/s for rain-induced events in Bavaria, Germany.

TABLE 1 | Average inter-station distance, observed peak delay time and diffusivity computed from Improta et al. (2017).

Stations	Av. distance (km)	Delay time (days)	Diffusivity (m^2/s)
All	6.40	7 ± 1	5.4 (4.7–6.3)
AG11,CM01,CM02	2.82	7 ± 1	1.0 (0.9–1.2)

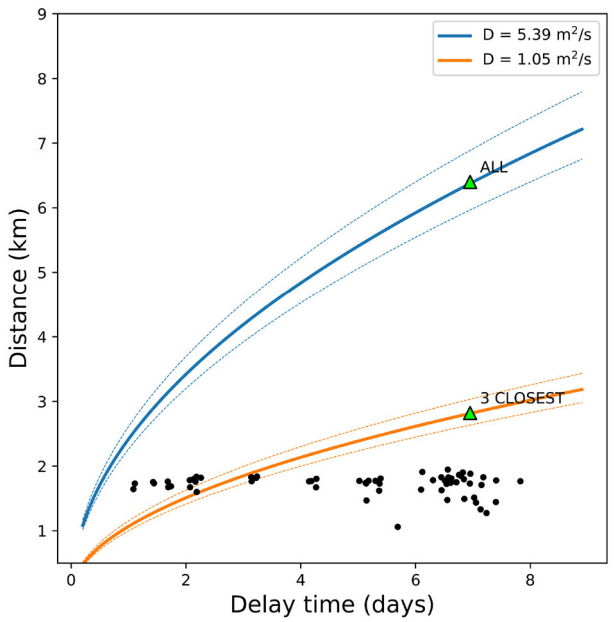

FIGURE 10 | Colored lines: triggering front computed from diffusivity values estimated from Equation (2) for station AG11 and CM02 (green triangles). Diffusivity values are reported in the legend. Black dots: seismicity recorded in June 2006 during the first injection tests (Improta et al., 2017), plotted as a function of delay time and distance from the injection well.

8. CONCLUSIONS

We monitored crustal velocity changes in a time period including the restart of produced water re-injection at the CM2 well in the Val d'Agri oil field (southern Italy) from noise-based monitoring. We used continuous recordings from a temporary seismic array deployed during the first out of 22 days pause of the injection in January–February 2015.

We observed that the relative velocity time-series match well with the hydrometric level of the Agri river. Hence we hypothesize that the observed velocity changes are mainly due to variations of water storage in the shallow aquifers developed in the thick, Miocene flysch deposits that crop out in the survey area. This effect can hide smaller variations due to the produced water injection restart in the Costa Molina 2 well.

We removed by deconvolution the hydrometric level time-series of the Agri river from the relative velocity change and we noticed that the peak observed 7 days after injection restart is lower but still visible.

Using this time delay we compute the medium diffusivity to verify if the observed peak can be related to the water injection re-start and finding values in the range 1–5 $m^{2/s}$, which are compatible with the delay time of the induced seismicity measured in 2006 after the first injection tests (Improta et al., 2015) and with hydraulic properties of similar geological settings.

Our results demonstrate that observed crustal velocity changes are often mainly due to changes in the total underground water storage. This can totally hide the weaker effects due to produced water injection and can not be neglected when monitoring with ambient noise cross-correlations.

DATA AVAILABILITY STATEMENT

Seismic data from stations CM01-05 are from a temporary deployment and they are available upon request by emailing to: luigi.improta@ingv.it. Data from stations AG11 and AG51 are provided by INGV and are available from ORFEUS-EIDA data center (http://www.orfeus-eu.org/data/eida).

AUTHOR CONTRIBUTIONS

AB carried out the measurements, wrote the manuscript, and coordinated the co-authors. LZ provided the original scripts, supervised the measurement process, and contributed with the interpretation of the results. LF provided the original codes and supervised their setting. LI wrote the geological setting section, interpreted the results from a geological point of view, and planned the seismic survey and contributed to the stations deployment. PD carried out the instrument installation and provided data. AG carried out the diffusivity computation and helped with the statistical assessment of the results. AM coordinated the whole project, supervised the interpretation of the results, and raised funds. All authors contributed to the article and approved the submitted version.

FUNDING

This study benefitted from support by Clypea, the Innovation Network for Future Energy financed by the Italian Ministry of Economic Development, Direzione Generale per le Infrastrutture e la Sicurezza dei Sistemi Energetici e Geominerari (DG ISSEG); and by Regione Basilicata (Italy) in the framework of the Protocollo d'Intesa: Accordo per la sperimentazione delle Linee Guida in Val d'Agri.

ACKNOWLEDGMENTS

Well injection data are collected by ENI and archived and made accessible upon request by the regional regulatory agency (Basilicata Region). We also thank the two reviewers for their helpful suggestions and comments that greatly improved this manuscript.

SUPPLEMENTARY MATERIAL

The Supplementary Material for this article can be found online at: https://www.frontiersin.org/articles/10.3389/feart.2021.626720/full#supplementary-material

REFERENCES

Aki, K. (1969). Analysis of the seismic coda of local earthquakes as scattered waves. *J. Geophys. Res*. 74, 615–631. doi: 10.1029/JB074i002p00615

Berbellini, A., Schimmel, M., Ferreira, A. M., and Morelli, A. (2019). Constraining S -wave velocity using Rayleigh wave ellipticity from polarization analysis of seismic noise. *Geophys. J. Int*. 216, 1817–1830. doi: 10.1093/gji/ggy512

Brenguier, F., Campillo, M., Hadziioannou, C., Shapiro, N. M., Nadeau, R. M., and Larose, E. (2008a). Postseismic relaxation along the San Andreas fault at Parkfield from continuous seismological observations. *Science* 321, 1478–1481. doi: 10.1126/science.1160943

Brenguier, F., Shapiro, N., Campillo, M., Ferrazzini, V., Duputel, Z., Coutant, O., et al. (2008b). Toward forecasting volcanic eruptions using seismic noise. *Nat. Geosci*. 1, 126–130. doi: 10.1038/ngeo104

Buttinelli, M., Improta, L., Bagh, S., and Chiarabba, C. (2016). Inversion of inherited thrusts by wastewater injection induced seismicity at the Val d'Agri oilfield (Italy). *Sci. Rep*. 6:37165. doi: 10.1038/srep37165

Chelini, V., Sartori, G., Ciammetti, G., Giorgioni, M., and Pelliccia, A. (1997). "Enhancing the image of the Southern Apennines," in *Reservoir Optimization Conference* (Milan: Schlumberger).

Christiansen, L. B., Hurwitz, S., and Ingebritsen, S. E. (2007). Annual modulation of seismicity along the san andreas fault near parkfield, ca. *Geophys. Res. Lett*. 34:L04306. doi: 10.1029/2006GL028634

Clarke, D., Zaccarelli, L., Shapiro, N. M., and Brenguier, F. (2011). Assessment of resolution and accuracy of the Moving Window Cross Spectral technique for monitoring crustal temporal variations using ambient seismic noise. *Geophys. J. Int*. 186, 867–882. doi: 10.1111/j.1365-246X.2011.05074.x

Clements, T., and Denolle, M. A. (2018). Tracking groundwater levels using the ambient seismic field. *Geophys. Res. Lett*. 45, 6459–6465. doi: 10.1029/2018GL077706

Costain, J. K. (2008). Intraplate seismicity, hydroseismicity, and predictions in hindsight. *Seismol. Res. Lett*. 79, 578–589. doi: 10.1785/gssrl.79.4.578

Costain, J. K., and Bollinger, G. A. (2010). Review: research results in hydroseismicity from 1987 to 2009. *Bull. Seismol. Soc. Am*. 100, 1841–1858. doi: 10.1785/0120090288

Costain, J. K., Bollinger, G. A., and Speer, J. A. (1987). Hydroseismicity: a hypothesis for the role of water in the generation of intraplate seismicity. *Geology* 15, 618–621. doi: 10.1130/0091-7613(1987)15<618:HHFTRO>2.0.CO;2

De Gori, P., Improta, L., Moretti, M., Colasanti, G., and Criscuoli, F. (2015). "Monitoring the restart of a high-rate wastewater disposal well in the Val d'Agri oilfield (Italy)," in *AGU Fall Meeting Abstracts*, (Cambridge), S13B–2802.

D'Hour, V., Schimmel, M., Nascimento, A., Ferreira, J., and Neto, H. (2015). Detection of subtle hydromechanical medium changes caused by a small-magnitude earthquake swarm in ne Brazil. *Pure Appl. Geophys*. 173, 1097–1113. doi: 10.1007/s00024-015-1156-0

Froment, B., Campillo, M., Roux, P., Gouédard, P., Verdel, A., and Weaver, R. L. (2010). Estimation of the effect of nonisotropically distributed energy on the apparent arrival time in correlations. *Geophysics* 75, SA85–SA93. doi: 10.1190/1.3483102

Gouédard, P., Stehly, L., Brenguier, F., Campillo, M., Colin de Verdiére, Y., Larose, E., et al. (2008). Cross-correlation of random fields: mathematical approach and applications. *Geophys. Prospect*. 56, 375–393. doi: 10.1111/j.1365-2478.2007.00684.x

Hadziioannou, C., Larose, E., Coutant, O., Roux, P., and Campillo, M. (2009). Stability of monitoring weak changes in multiply scattering media with ambient noise correlation: laboratory experiments. *J. Acoust. Soc. Am*. 125:2654. doi: 10.1121/1.3125345

Hainzl, S., Kraft, T., Wassermann, J., Igel, H., and Schmedes, E. (2006). Evidence for rainfall-triggered earthquake activity. *Geophys. Res. Lett*. 33:L19303. doi: 10.1029/2006GL027642

Herrmann, R. B. (2013). Computer programs in seismology: an evolving tool for instruction and research. *Seismol. Res. Lett*. 84, 1081–1088. doi: 10.1785/0220110096

Improta, L., Bagh, S., De Gori, P., Valoroso, L., Pastori, M., Piccinini, D., et al. (2017). Reservoir structure and wastewater-induced seismicity at the Val d'Agri oilfield (Italy) shown by three-dimensional V p and V p /V s local earthquake tomography. *J. Geophys. Res*. 122, 9050–9082. doi: 10.1002/2017JB014725

Improta, L., Valoroso, L., Piccinini, D., and Chiarabba, C. (2015). A detailed analysis of wastewater-induced seismicity in the Val d'Agri oil field (Italy). *Geophys. Res. Lett*. 42, 2682–2690. doi: 10.1002/2015GL063369

Larose, E. (2006). Mesoscopics of ultrasound and seismic waves: application to passive imaging. *Ann. Phys*. 31, 1–126. doi: 10.1051/anphys:2007001

Lecocq, T., Longuevergne, L., Pedersen, H. A., Brenguier, F., and Stammler, K. (2017). Monitoring ground water storage at mesoscale using seismic noise: 30 years of continuous observation and thermo-elastic and hydrological modeling. *Sci. Rep*. 7:14241. doi: 10.1038/s41598-017-14468-9

Liu, C., Aslam, K., and Daub, E. (2020). Seismic velocity changes caused by water table fluctuation in the new Madrid seismic zone and Mississippi embayment. *J. Geophys. Res*. 125:e2020JB019524. doi: 10.1029/2020JB019524

Lobkis, O. I., and Weaver, R. L. (2001). On the emergence of the green's function in the correlations of a diffuse field. *J. Acoust. Soc. Am*. 110, 3011–3017. doi: 10.1121/1.1417528

Mazzoli, S., Barkham, S., Cello, G., Gambini, R., Mattioni, L., Shiner, P., et al. (2001). Reconstruction of continental margin architecture deformed by the contraction of the lagonegro basin, Southern Apennines, Italy. *J. Geol. Soc*. 158, 309–319. doi: 10.1144/jgs.158.2.309

Mordret, A., Shapiro, N. M., and Singh, S. (2014). Seismic noise-based time-lapse monitoring of the valhall overburden. *Geophys. Res. Lett*. 41, 4945–4952. doi: 10.1002/2014GL060602

Nuez, E., Schimmel, M., Stich, D., and Iglesias, A. (2020). Crustal velocity anomalies in Costa Rica from ambient noise tomography. *Pure Appl. Geophys*. 177, 941–960. doi: 10.1007/s00024-019-02315-z

Obermann, A., Kraft, T., Larose, E., and Wiemer, S. (2015). Potential of ambient seismic noise techniques to monitor the St. Gallen geothermal site (Switzerland). *J. Geophys. Res. B* 120, 4301–4316. doi: 10.1002/2014JB011817

Pischiutta, M., Pastori, M., Improta, L., Salvini, F., and Rovelli, A. (2014). Orthogonal relation between wavefield polarization and fast S wave direction in the val d'agri region: An integrating method to investigate rock anisotropy. *J. Geophys. Res*. 119, 396–408. doi: 10.1002/2013JB010077

Poli, P., Marguin, V., Wang, Q., D'Agostino, N., and Johnson, P. (2020). Seasonal and coseismic velocity variation in the region of l'aquila from single station measurements and implications for crustal rheology. *J. Geophys. Res*. 125:e2019JB019316. doi: 10.1029/2019JB019316

Poupinet, G., Ellsworth, W. L., and Frechet, J. (1984). Monitoring velocity variations in the crust using earthquake doublets: an application to the Calaveras fault, California (USA). *J. Geophys. Res*. 89, 5719–5731. doi: 10.1029/JB089iB07p05719

Rivet, D., Brenguier, F., and Cappa, F. (2015). Improved detection of preeruptive seismic velocity drops at the piton de la fournaise volcano. *J. Geophys. Res*. 42, 6332–6339. doi: 10.1002/2015GL064835

Rothert, E., Shapiro, S. A., Buske, S., and Bohnhoff, M. (2003). Mutual relationship between microseismicity and seismic reflectivity: case study at the German continental deep drilling site (KTB). *Geophys. Res. Lett*. 30:1893. doi: 10.1029/2003GL017848

Sánchez-Pastor, P., Obermann, A., Schimmel, M., Weemstra, C., Verdel, A., and Jousset, P. (2019). Short- and long-term variations in the reykjanes geothermal reservoir from seismic noise interferometry. *Geophys. Res. Lett*. 46, 5788–5798. doi: 10.1029/2019GL082352

Sens-Schönfelder, C. and Wegler, U. (2006). Passive image interferometry and seasonal variations of seismic velocities at Merapi Volcano, Indonesia. *Geophys. Res. Lett*. 33:L21302. doi: 10.1029/2006GL027797

Shapiro, N. M., Campillo, M., Stehly, L., and Ritzwoller, M. H. (2005). High-resolution surface-wave tomography from ambient seismic noise. *Science* 307, 1615–1618. doi: 10.1126/science.1108339

Shapiro, S. A. (2015). *Fluid-Induced Seismicity*. Cambridge: Cambridge University Press. doi: 10.1017/CBO9781139051132

Shiner, P., Beccacini, A., and Mazzoli, S. (2004). Thin-skinned versus thick-skinned structural models for apulian carbonate reservoirs: constraints from the Val d'agri fields, Southern Apennines, Italy. *Mar. Petrol. Geol*. 21, 805–827. doi: 10.1016/j.marpetgeo.2003.11.020

Valoroso, L., Improta, L., Chiaraluce, L., Di Stefano, R., Ferranti, L., Govoni, A., et al. (2009). Active faults and induced seismicity in the Val d'Agri area (Southern Apennines, Italy). *Geophys. J. Int.* 178, 488–502. doi: 10.1111/j.1365-246X.2009.04166.x

Wang, Q.-Y., Brenguier, F., Campillo, M., Lecointre, A., Takeda, T., and Aoki, Y. (2017). Seasonal crustal seismic velocity changes throughout Japan. *J. Geophys. Res.* 122, 7987–8002. doi: 10.1002/2017JB014307

Zaccarelli, L., and Bianco, F. (2017). Noise-based seismic monitoring of the Campi Flegrei caldera. *Geophys. Res. Lett.* 44, 2237–2244. doi: 10.1002/2016GL072477

Zaccarelli, L., Shapiro, N. M., Faenza, L., Soldati, G., and Michelini, A. (2011). Variations of crustal elastic properties during the 2009 L'Aquila earthquake inferred from cross-correlations of ambient seismic noise. *Geophys. Res. Lett.* 38, 1–6. doi: 10.1029/2011GL049750

Conflict of Interest: The authors declare that the research was conducted in the absence of any commercial or financial relationships that could be construed as a potential conflict of interest.

The handling Editor APR declared a past co-authorship with one of the authors LI.

frontiers in Earth Science

ORIGINAL RESEARCH
published: 13 April 2021
doi: 10.3389/feart.2021.638723

Sensitivity of the Seismic Moment Released During Fluid Injection to Fault Hydromechanical Properties and Background Stress

Nicolas Wynants-Morel[1], Louis De Barros[1]* and Frédéric Cappa[1,2]*

[1] Université Côte d'Azur, CNRS, Observatoire de la Côte d'Azur, IRD, Géoazur, Valbonne, France, [2] Institut Universitaire de France, Paris, France

Fluid pressure perturbations in subsurface rocks affect the fault stability and can induce both seismicity and aseismic slip. Nonetheless, observations show that the partitioning between aseismic and seismic fault slip during fluid injection may strongly vary among reservoirs. The processes and the main fault properties controlling this partitioning are poorly constrained. Here we examine, through 3D hydromechanical modeling, the influence of fault physical properties on the seismic and aseismic response of a permeable fault governed by a slip-weakening friction law. We perform a series of high-rate, short-duration injection simulations to evaluate the influence of five fault parameters, namely the initial permeability, the dilation angle, the friction drop, the critical slip distance, and the initial proximity of stress to failure. For sake of comparison between tests, all the simulations are stopped for a fixed rupture distance relative to the injection point. We find that while the fault hydraulic behavior is mainly affected by the change in initial permeability and the dilation angle, the mechanical and seismic response of the fault strongly depends on the friction drop and the initial proximity of stress to failure. Additionally, both parameters, and to a lesser extent the initial fault permeability and the critical slip distance, impact the spatiotemporal evolution of seismic events and the partitioning between seismic and aseismic moment. Moreover, this study shows that a modification of such parameters does not lead to a usual seismic moment-injected fluid volume relationship, and provides insights into why the fault hydromechanical properties and background stress should be carefully taken into account to better anticipate the seismic moment from the injected fluid volume.

Keywords: induced seismicity, fluid injection, fault mechanics, hydromechanical modeling, aseismic slip

OPEN ACCESS

Edited by:
Rebecca M. Harrington, Ruhr University Bochum, Germany

Reviewed by:
William B. Frank, Massachusetts Institute of Technology, United States
David Eaton, University of Calgary, Canada

****Correspondence:***
Nicolas Wynants-Morel
nicolas.wm@orange.fr
Louis De Barros
debarros@geoazur.unice.fr

Specialty section:
This article was submitted to Solid Earth Geophysics, a section of the journal Frontiers in Earth Science

Received: *07 December 2020*
Accepted: *25 March 2021*
Published: *13 April 2021*

Citation:
Wynants-Morel N, De Barros L and Cappa F (2021) Sensitivity of the Seismic Moment Released During Fluid Injection to Fault Hydromechanical Properties and Background Stress. Front. Earth Sci. 9:638723. doi: 10.3389/feart.2021.638723

HIGHLIGHTS

- During fluid injection, the friction drop, dilation angle, and initial proximity of stress to failure of a fault influence its mechanical behavior.
- Friction, initial permeability, and initial proximity of stress to failure of a fault act on the spatiotemporal evolution of injection-induced seismic events.
- Relationship between seismic moment and injected fluid volume strongly depends on fault hydromechanical properties and background stress.

INTRODUCTION

Fluid injection in the upper crust induces earthquakes (Keranen and Weingarten, 2018). Over the past 20 years, the question of injection-induced seismicity became more prominent as the rate of such events strongly increased worldwide (Ellsworth, 2013; Grigoli et al., 2017). This category of earthquakes includes large events such as the 2011 M_w 5.7 and 2016 M_w 5.8 wastewater-induced shocks in Oklahoma (Keranen et al., 2013; Yeck et al., 2017), and the 2017 M_w 5.5 earthquake close to a geothermal plant in Pohang, South Korea (Grigoli et al., 2018; Kim et al., 2018; Lee et al., 2019). Even though injection-induced seismicity is frequently associated with wastewater disposal or geothermal activities, hydraulic fracturing also induces seismic events with moment magnitudes up to 4.6 in the Western Canada sedimentary basin (WCSB) (Schultz et al., 2015; Atkinson et al., 2016; Bao and Eaton, 2016). Thus, understanding how fluid injection induces seismicity, or not, is important to reduce human-induced seismic risk and build a safer energy future.

Nonetheless, observations have shown that fluid injections do not always trigger seismic events. They can also induce aseismic slip related to a slow propagation of the rupture in and outside the injection zone (Guglielmi et al., 2015a; Bhattacharya and Viesca, 2019; Cappa et al., 2019; Eyre et al., 2019). Indeed, some studies show that the deformation induced by the injection is dominantly aseismic, with an area totally devoid of seismicity around the injection. These observations were made at reservoir scale (Cornet et al., 1997; Calò et al., 2011; Cornet, 2012, 2016; Zoback et al., 2012; Schmittbuhl et al., 2014; Wei et al., 2015; Lengliné et al., 2017; Eyre et al., 2019; Hopp et al., 2019), in laboratory (Goodfellow et al., 2015; Wang et al., 2020) and from meter-scale *in-situ* experiments (Guglielmi et al., 2015a; De Barros et al., 2016; Duboeuf et al., 2017). The aseismic deformation estimated in these small-scale experiments represents more than 95% of the total deformation released during injection (Goodfellow et al., 2015; De Barros et al., 2016, 2018, 2019; Duboeuf et al., 2017).

In the conventional model used to explain injection-induced seismicity, the fault ruptures when the Mohr-Coulomb failure criterion is reached through an increase of fluid pressure, which causes the decrease of effective normal stress and frictional resistance (Hubbert and Rubey, 1959). Within this framework, the ruptures are only driven by fluid pressure diffusion and are contained inside the pressurized zone (Shapiro et al., 1997, 2002, 2011; McGarr, 2014). Poroelastic stress changes and earthquake nucleation effects have been added later to this model (Segall, 1989; Segall and Lu, 2015). The triggering of the rupture therefore depends on the distance to injection: at short distances, fluid pressure dominates, while stress perturbations dominate at larger distances (Goebel et al., 2017). Recently, the role of aseismic deformation on injection-induced earthquakes was considered. Models proposed by Guglielmi et al. (2015a), Cappa et al. (2018, 2019), De Barros et al. (2018), Bhattacharya and Viesca (2019), and Wynants-Morel et al. (2020), show that fluid pressure primarily induces aseismic deformation. Then, the seismicity is triggered by the elastic stress perturbations transferred from aseismic slip. As the deformation may occur outside the pressurized zone, seismicity may outpace the pressure front, as observed at different scales (De Barros et al., 2018; Cappa et al., 2019; Eyre et al., 2019).

At the same time, the estimation of the maximum seismic moment that can be released during a fluid injection is crucial in seismic hazard and risk analysis (McClure and Horne, 2011; Eaton and Igonin, 2018; Norbeck and Horne, 2018). The most common method to evaluate the maximum seismic moment released during fluid injection is based on the injected fluid volume (McGarr, 1976, 2014; van der Elst et al., 2016; Galis et al., 2017; McGarr and Barbour, 2018). However, such models do not consider the contribution of the aseismic component of the deformation in the moment determination (De Barros et al., 2019). Moreover, the theoretical limit in the relationship between moment and volume is sometimes exceeded, as for the M_w 5.5 mainshock near Pohang, South Korea (Grigoli et al., 2018; Kim et al., 2018; Lee et al., 2019) or the M_w 3.3 mainshock that occurred during the test of the St-Gallen geothermal project (Zbinden et al., 2020). Therefore, seismic moment does not depend only on the fluid injected volume. Indeed, other authors showed that the seismic moment is also related to injection parameters (Weingarten et al., 2015; Almakari et al., 2019; De Barros et al., 2019) and fault properties (Weingarten et al., 2015; Schoenball and Ellsworth, 2017; De Barros et al., 2018; Hearn et al., 2018; Pei et al., 2018).

Several fault physical parameters are recognized to act on the released seismic moment and on the seismic or aseismic nature of the rupture on the fault (e.g., Chang and Segall, 2016; Fan et al., 2016; Kroll et al., 2017; Pei et al., 2018; Dublanchet, 2019b). In this study, we focus on five main independent parameters. The permeability is known to influence the spatio-temporal repartition of induced seismicity (Shapiro et al., 1997; Zhang et al., 2013; McNamara et al., 2015; Chang and Segall, 2016; Norbeck and Horne, 2016; Yeck et al., 2016) and is thought to influence the rupture mode of the fault (Guglielmi et al., 2015a,b; Wei et al., 2015; Cappa et al., 2018). The initial proximity of background stress to rupture of the fault also acts on the seismic-to-total moment ratio released during fluid injection (Garagash and Germanovich, 2012; Gischig, 2015; Bhattacharya and Viesca, 2019; Wynants-Morel et al., 2020). Similarly, the critical slip distance D_c influences this moment ratio (Cueto-Felgueroso et al., 2017). The effect of shear-induced dilation is known to induce a damping of the seismicity (Segall et al., 2010; McClure and Horne, 2011), while the moment magnitude of the induced seismicity gets higher with increasing friction drop (Rutqvist et al., 2015). Therefore, it is important to investigate the following key question: how do fault physical parameters influence the released seismic moment and the seismicity repartition in time and space during fluid injection?

In the following, we numerically explore the influence of these five fault parameters (namely, the initial permeability, the dilation angle, the initial state of stress, the friction drop and the critical slip distance) on the spatiotemporal distribution of seismicity and on the seismic and aseismic moment released during a fluid injection. The response of a permeable, slip-weakening fault to a short-duration injection is computed using a three-dimensional fully coupled hydromechanical model capable of simulating seismic and aseismic slip. We then analyze and

discuss the seismic, hydrological and mechanical behaviors of the fault with varying properties. We show that shear stress perturbations over the fault are impacted by the friction drop, the initial stress state and the dilation angle. We also find, as expected, that the initial permeability and the dilation angle affect the hydrological behavior of the fault. Finally, we observe that the seismic moment released during injection is mostly influenced by the friction drop and the initial stress criticality, while the permeability and the critical slip distance have less influence. Therefore, such fault parameters should be considered in protocols and methods used to estimate the maximum seismic moment that can be released during a fluid injection.

NUMERICAL METHOD AND MODEL SETUP

Numerical Method

We use a 3D Distinct Element Code (3DEC, Itasca Consulting Group, Inc, 2016) to model a fluid injection in a permeable, slip-weakening fault separating two three-dimensional (3D) elastic, impervious blocks (**Figure 1**). We consider the distinct element method (Cundall, 1988) to simulate the hydromechanical interactions and slip along the fault. The blocks are meshed in tetrahedral zones linked by nodes. The fault is discretized in 0.7 m-sized cells. Using an explicit

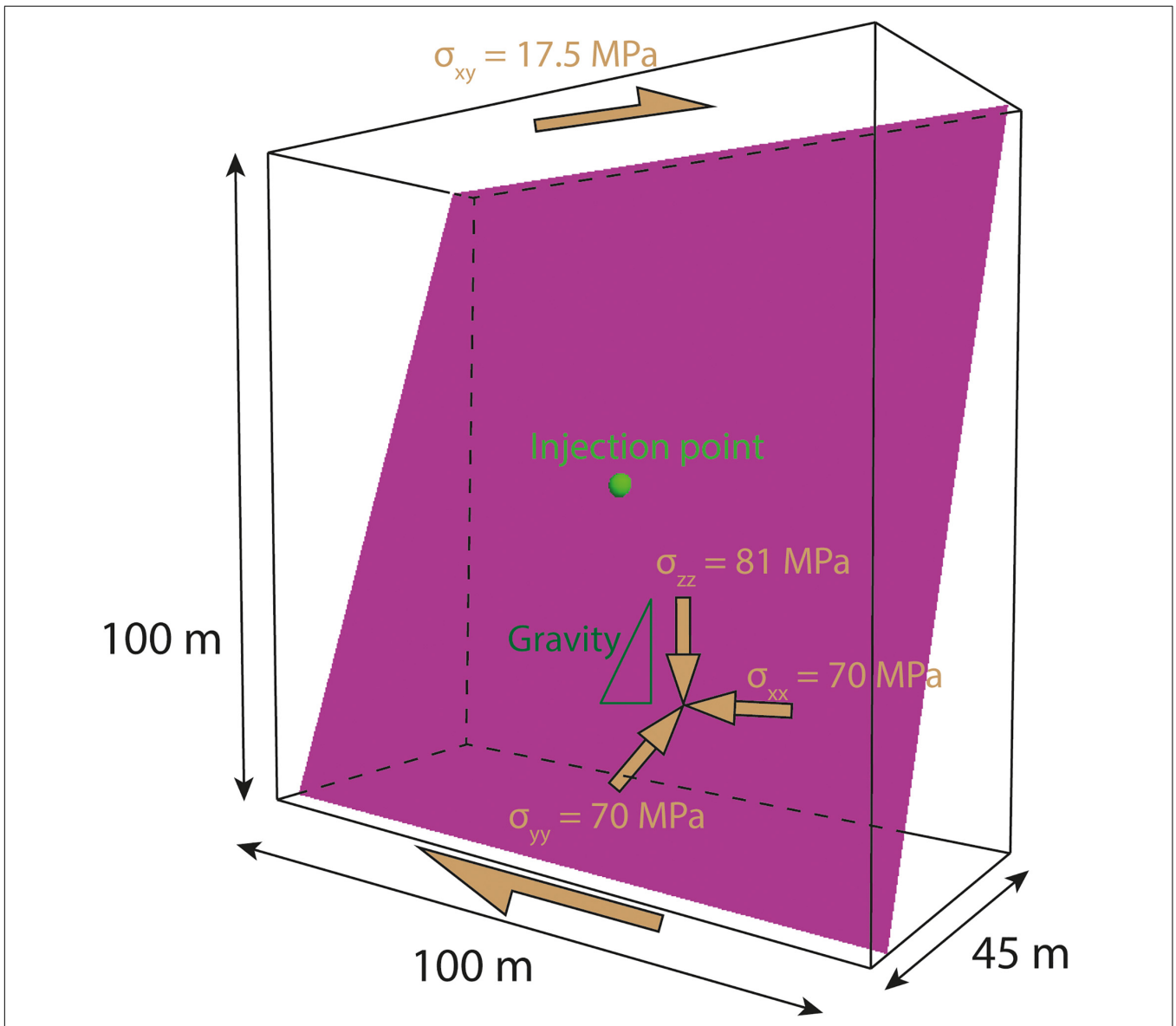

FIGURE 1 | 3D model geometry of the 70° dipping fault represented in purple and the injection point in light green at the center of the fault. The initial state of stress has a vertical (σ_{zz}) and horizontal (σ_{xx} and σ_{yy}) stresses, plus a deviatoric component (σ_{xy}) to simulate dominantly strike-slip stress regime. The gradient of stress with depth and gravity is indicated as a dark green triangle that gets larger downwards.

time-marching procedure, the distinct element method considers force-displacement relations updated at each time step to describe the interaction between the blocks. Newton's laws (i.e., the differential equations of motion) and constitutive relations are used to calculate the translation and rotation of the blocks at each time step, and thus their position, velocity, displacement and applied nodal forces. The discontinuities forces are updated through constitutive laws before next time step.

The model is hydromechanically fully coupled, with hydraulic and frictional parameters that vary during injection. This affects the normal and shear displacement on the fault as well as the seismic and aseismic deformation during rupture. Seismicity is generated using an inherently discrete rupture model (Wynants-Morel et al., 2020). Given the values adopted in our model, the nucleation size of earthquakes for a slip-weakening fault (Uenishi and Rice, 2003) varies between 0.01 and 0.32 m, depending on the effective normal stress at rupture and the frictional fault properties (**Tables 1**, **2**). It means that the nucleation phase of the earthquakes is smaller than the cell size, which prevents to compute it accurately, but the model allows to generate seismic events with rupture size of a m^2 up to few tens of m^2. We use an adaptive time step to be able to simulate both fast ruptures (i.e., seismic) and slow deformations (i.e., aseismic). The time step can decrease down to 10^{-6} second during co-seismic ruptures and increase to 1 s during aseismic periods. We then estimate earthquake source properties using classical seismological assumptions detailed in Wynants-Morel et al. (2020).

TABLE 1 | Model parameters for the reference case.

Rock mechanical properties	Shear modulus (G)	15 GPa
	Bulk modulus (K)	25 GPa
	Density (ρ)	2,750 kg/m^3
Elastic stiffness of the fault	Normal stiffness (k_n)	300 GPa/m
	Shear stiffness (k_s)	300 GPa/m
Slip-weakening frictional properties of the fault	Static friction (μ_S)	0.6
	Dynamic friction (μ_D)	**0.4**
	Critical slip distance (D_c)	**10 μm**
Hydraulic properties of the fault	**Initial aperture (b_{h0})**	**200 μm**
	Initial fluid pressure (P_0)	30 MPa
	Dilation angle (ψ)	**0°**
Fluid properties	Fluid bulk modulus (K_w)	2 GPa
	Fluid density (ρ_w)	1,000 kg/m^3
	Fluid viscosity (μ_f)	10^{-3} Pa.s
Stress state	Initial effective normal stress (σ_{N0})	41.3 MPa
	Initial shear stress (τ_0)	16.8 MPa
	SCU = $\tau_0/\mu_S(\sigma_{N0}$-$P_0)$	**68%**

Bold cases correspond to fault parameters that are modified during the parametric study.

Fluid Flow and Hydromechanical Coupling

During fluid injection into a fault, the pressure and fluid flow are related to the hydraulic aperture through the cubic law (Witherspoon et al., 1980). Before the injection, an initial hydraulic aperture (b_{ho}) is assigned to the fault within the initial background stress and pressure conditions. Variations of hydraulic aperture (Δb_h) from initial aperture come from two main processes: (1) variations of effective normal stress and (2) dilations while the fracture slips. Thus, they can be expressed as:

$$\Delta b_h = \frac{\Delta \sigma_n'}{k_n} + \Delta u_s \cdot \tan \psi \quad (1)$$

where $\Delta\sigma_n$' is the increment in effective normal stress (total normal stress minus fluid pressure) (Pa), k_n is the normal stiffness (Pa/m), Δu_s (m) is the shear slip increment, and ψ is the dilation angle (°).

The permeability (k) is related to the square of the hydraulic aperture (Jaeger and Cook, 1984). Modeling studies show that the permeability on a fault affects the fault slip behavior (Cappa and Rutqvist, 2011; Yeo et al., 2020) but also the spatio-temporal distribution of seismic events (Shapiro et al., 1997). In addition, as the permeability increases with increasing pressure and fault slip, the evolution of permeability during injection can affect aseismic deformation developing outside the pressurized zone

TABLE 2 | Varying fault parameters (initial permeability, dilation angle, friction drop, critical slip distance, SCU) for the reference case and the other 20 simulations considered in this study.

	Initial permeability (m^2)
Test 1	5.62×10^{-9}
Test 2	1.78×10^{-9}
Test 3	1×10^{-9}
Test 4	5.62×10^{-10}
	Dilation angle (°)
Test 5	1
Test 6	2
Test 7	4
Test 8	8
	Friction drop
Test 9	0.125
Test 10	0.15
Test 11	0.175
Test 12	0.225
	Critical slip distance (m)
Test 13	5×10^{-6}
Test 14	2×10^{-5}
Test 15	4×10^{-5}
Test 16	8×10^{-5}
	SCU = $\tau_0/[\mu_S(\sigma_{N0}$-$P_0)]$
Test 17	0.53
Test 18	0.59
Test 19	0.64
Test 20	0.71

Five values of each of these parameters have been considered.

(Cappa et al., 2018) as well as induced seismicity at short and long distances from injection (Rinaldi and Nespoli, 2017). Thus, the study of the permeability and its variations are fundamental to understand the relationship between injection parameters and the seismic and aseismic slip released during fluid injection.

The existence of a strong coupling between permeability and shear failure is frequently observed in natural reservoirs and *in-situ* experiments (e.g., Guglielmi et al., 2015a,b; Zhang and Li, 2016). Previous studies showed that the dilation angle is adequate to model this coupling, that occurs during deep underground CO_2 injection (Cappa and Rutqvist, 2011), the stimulation of a geothermal reservoir (Fomin et al., 2004) or *in-situ* injections (Guglielmi et al., 2015b; Tsopela et al., 2019). This parameter is commonly used to model the simulation of the geomechanical and hydraulic response of natural fracture systems (Latham et al., 2013; Lei et al., 2014, 2016). It is thus a critical parameter to understand hydromechanical coupling during fault deformation.

Rupture Initiation and Slip-Weakening Friction Law

The Mohr-Coulomb failure criterion (Jaeger and Cook, 1984) is given by:

$$\tau_f = c + \mu_S(\sigma_n - P) = c + \mu_S\sigma_n^{'} \quad (2)$$

where τ_f is the shear strength of the fault (Pa), σ_n is the normal stress (Pa), and P is the fluid pressure (Pa) acting on the fault. μ_S is the friction coefficient before failure. The fault is reactivated when the Mohr-Coulomb criterion is reached (i.e., when the shear stress and the shear strength of the faults are equal). Thus, slip begins and the slip velocity may increase. We assume here a null cohesive strength of the fault ($c = 0$).

The Shear Capacity Utilization (SCU), proposed in Buijze et al. (2019a), is a parameter that allows us to quantify the initial closeness to failure of the fault. It is defined as the ratio between initial shear stress (τ_0) and initial strength on the fault (τ_{f0}), before the injection starts:

$$SCU = \frac{\tau_0}{\tau_{f_0}} = \frac{\tau_0}{\mu_S(\sigma_{n_0} - P_0)} \quad (3)$$

with σ_{n_0} and P_0 the initial normal stress and pressure acting on the fault. A maximal SCU (100%) corresponds to a fault at failure that can slip without any perturbation.

The Mohr-Coulomb criterion can be reached by increasing either the fluid pressure (and, thus decreasing the effective stress and the shear strength) or the shear stress. We use the Shear Stress Contribution (SSC) to quantify the respective role of the fluid pressure and the shear stress in the rupture:

$$SSC = \frac{\Delta\tau(\bar{x})}{\mu_S\left(\sigma_{n_0}(\bar{x}) - P_0(\bar{x})\right) - \tau_0(\bar{x})} \quad (4)$$

where $\tau_0(\bar{x})$, $\sigma_{n_0}(\bar{x})$, and $P_0(\bar{x})$ are, respectively, the shear stress, the normal stress and the fluid pressure measured at position $\bar{x}$ before injection. $\Delta\tau(\bar{x})$ is the shear stress variation between the initial state and the state for which rupture occurs at the location $\bar{x}$. The SSC varies between 0 and 100%, respectively between a failure only triggered by fluid pressure changes and a failure only induced by shear stress perturbations.

During the slip periods, we consider that the friction coefficient only evolves with the shear slip, assuming a conventional linear slip-weakening model (Ida, 1972). In this law, a friction drop occurs as the friction coefficient decreases linearly over a critical slip distance (D_c) from a peak static value (μ_S) to a residual dynamic value (μ_D) (**Figure 2A** and **Table 1**). Both the friction drop ($\mu_S - \mu_D$) and D_c control the slip behavior (e.g., Ampuero et al., 2002; Mikumo et al., 2003; Uenishi and Rice, 2003; Dunham, 2007), and thus the seismic or aseismic nature of the fault response.

In our modeling, the use of a linear slip-weakening friction law reflects of a simplified approach of fault slip and earthquake rupture modeling. However, for simplicity, the slip-weakening friction is here preferred to the more sophisticated rate-and-state friction law as our model is used to show a series of few seismic events in a large aseismic rupture (Wynants-Morel et al., 2020).

Model Set-Up: Geometry, Physical Properties, and Boundary Conditions

Our objective is to study the effect of fault physical properties on the distribution of seismic events and the seismic-to-total partitioning during fluid injection in a single fault, at a typical depth of storage reservoirs (3 km). This fault, with a dip angle of 70°, is 106 m long and 100 m large, along dip and strike, respectively. Around the fault, the rock medium is elastic and impervious (**Figure 1**). In the parametric analysis, we consider a reference case from which the other simulations differ by varying one parameter (**Table 2**).

We apply constant principal stresses to the model (σ_{zz} = 81 MPa, $\sigma_{xx} = \sigma_{yy}$ = 70 MPa), which vary with depth through a lithostatic gradient due to gravity (g = 9.81 m/s^2). We then test different initial stress state, varying the SCU of the fault between 53 and 71%. In order to do so, we add a deviatoric stress component σ_{xy} that varies between 13.5 and 18.5 MPa. It allows us to keep the normal stress constant among the tests and change the shear stress only. Before injection, we apply an initial fluid pressure (P_0) of 30 MPa, which varies with depth with a hydrostatic gradient.

To activate the fault, we consider a fluid injection at the center of the fault (**Figure 1**). The applied flowrate linearly increases during the first hundred seconds of injection and it is then kept constant at a value of 0.09 m^3/s (**Figure 2B**). This short-duration, high-rate injection leads to a fast pressurization of the fault at the injection point. Nonetheless, considering a single small injection point may not be pertinent in certain operational injection scenarios such as saltwater disposal where multiple wells are generally used. The simulations are stopped when the rupture over the fault reached a fixed distance from injection point (corresponding to 38 m and 76% of the length of the fault). Therefore, the simulation duration differs among tests, and lasts 190 s in our reference case (**Figure 2B**). However, considering an imposed rupture size implies that the behavior of the seismicity

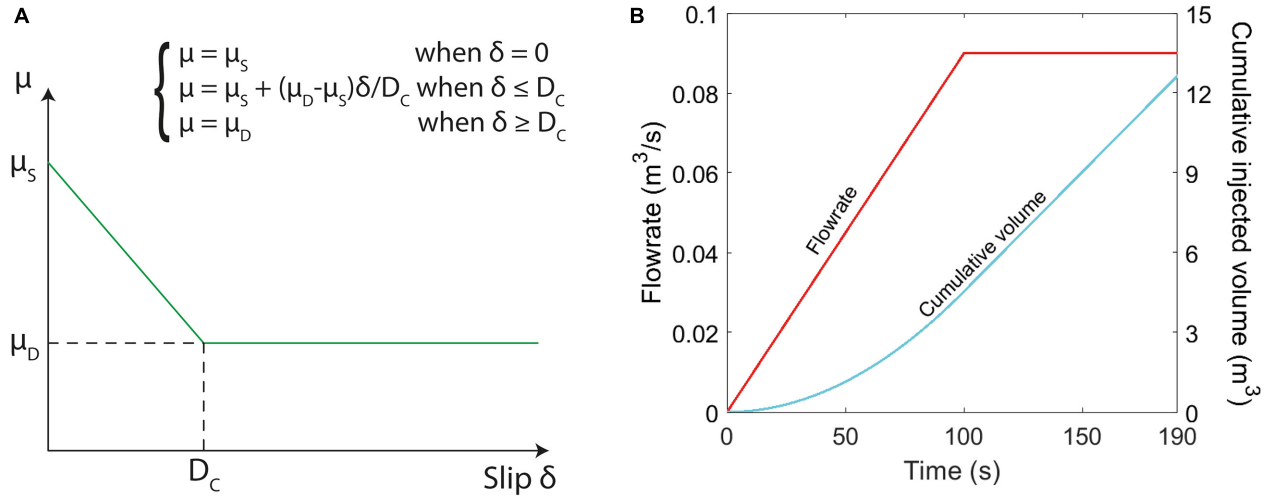

FIGURE 2 | (A) Linear slip-weakening friction with slip (δ), static friction coefficient (μ_S), dynamic friction coefficient (μ_D), and critical slip distance (D_c). **(B)** Cumulative injected fluid volume and flowrate vs. time applied at injection in the fault.

is well-represented at short distances from the injection, and therefore for very short duration lengths.

We set elastic properties for rocks to typical constant values for sedimentary material (**Table 1**). These values are standard in crustal reservoirs, as for instance in Oklahoma, a region of pronounced injection-induced seismicity (Barbour et al., 2017). We test different values of dilation angle (**Table 2**), which are consistent with previous simulations (Segall et al., 2010; McClure and Horne, 2011; Guglielmi et al., 2015b). Several values of fault initial permeability are also tested. Nonetheless, the considered values are very high, to explore the behavior of highly conductive channels that can be observed in subsurface reservoirs (Jeanne et al., 2012).

We consider a classical static friction coefficient for faults at crustal conditions (μ_S = 0.6; Byerlee, 1978). We then test different values of the dynamic friction coefficient μ_D in the range 0.375–0.475. The critical slip distance D_c also varies between 5 and 80 μm. Such values are consistent with laboratory observations (Marone, 1998; Rubino et al., 2017). No fault healing is considered as test durations are small in this study, and also because healing is not well-known during fluid injection.

In a simulation, the evolution of fluid pressure, fault opening, fault slip, stress, friction, and hydraulic aperture are monitored. Seismic ruptures are detected using a typical threshold on the slip velocity from Cochard and Madariaga (1994):

$$v_{thres} = \frac{\sigma_n^{'}(\mu_S - \mu_D)}{G} 2c_S \quad (5)$$

where c_S is the shear wave speed (m/s) and G is the rock shear modulus (Pa). Usual velocity threshold values from literature go from 0.1 mm/s to 0.1 m/s (McClure and Horne, 2011; Gischig, 2015; McClure, 2015). We adopt here a 1 mm/s threshold.

Neighboring grid cells that show subsequent seismic slip velocities during an overlapping period of time are then grouped to form seismic events when at least seven cells are regrouped (Wynants-Morel et al., 2020). The seismic event stops when the slip velocity of the last cell drops under the threshold. Non-seismic ruptures are considered aseismic. At the end of a simulation, the location, timing and moment magnitude of seismic events are estimated using the criteria described in Wynants-Morel et al. (2020).

RESULTS OF THE PARAMETRIC STUDY

This section presents the modeling results of the spatiotemporal evolution of injection-induced seismicity for different levels of five fault parameters.

Generalities in the Spatiotemporal Repartition of Seismic Events

First, we examine the common set of hydromechanical and seismological features between the 21 injection tests considered in our study. The first rupture occurred at the injection point, then the rupture starts expanding radially on the fault (Wynants-Morel et al., 2020). The resulting fault slip patch has an elliptic shape elongated in the maximal shear stress direction (**Figure 3**). Oppositely, the fluid diffuses with a circular shape in all cases (Wynants-Morel et al., 2020). The induced deformation is a combination of aseismic slip and seismic events. The maximum aseismic slip is located at the injection point (4.1–18.0 mm, depending on the simulation), and decreases progressively when getting closer to the rupture edge. Induced by the fluid injections, some seismic events occurred. In the simulations, a minimum threshold for the moment magnitude of seismic events has been fixed to −1.6 to have rupture on patches greater than 6 grid cells. This limit is equivalent to a detection threshold for induced seismicity recorded at reservoir-scale (e.g., Kwiatek et al., 2019). Thus, the distribution of seismic slip on the fault is sparse (**Figure 4**). We observe 7–73 events, depending on the test,

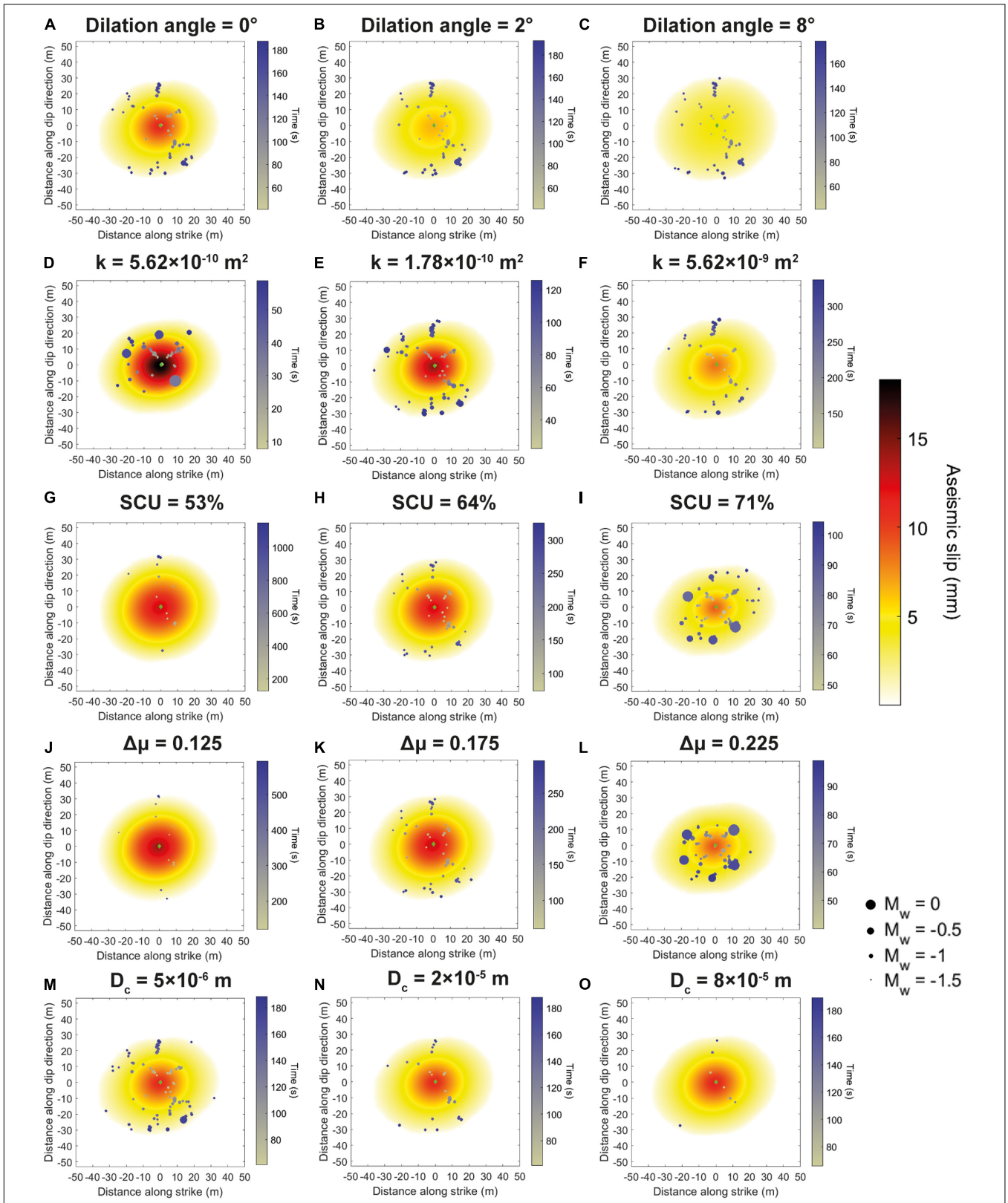

FIGURE 3 | Aseismic slip on the fault at the end of the simulations for various dilation angles (**A:** 0°; **B:** 2°; **C:** 8°), permeabilities (**D:** 5.6×10^{-10} m^2; **E:** 1.8×10^{-9} m^2; **F:** 5.6×10^{-9} m^2), stress criticalities (**G:** 53%; **H:** 64%; **I:** 71%), friction drops (**J:** 0.125; **K:** 0.175; **L:** 0.225), and critical slip distances (**M:** 5×10^{-6} m; **N:** 2×10^{-5} m; **O:** 8×10^{-5} m). The seismic events generated during the test are represented by black disks whose size is function of their magnitude.

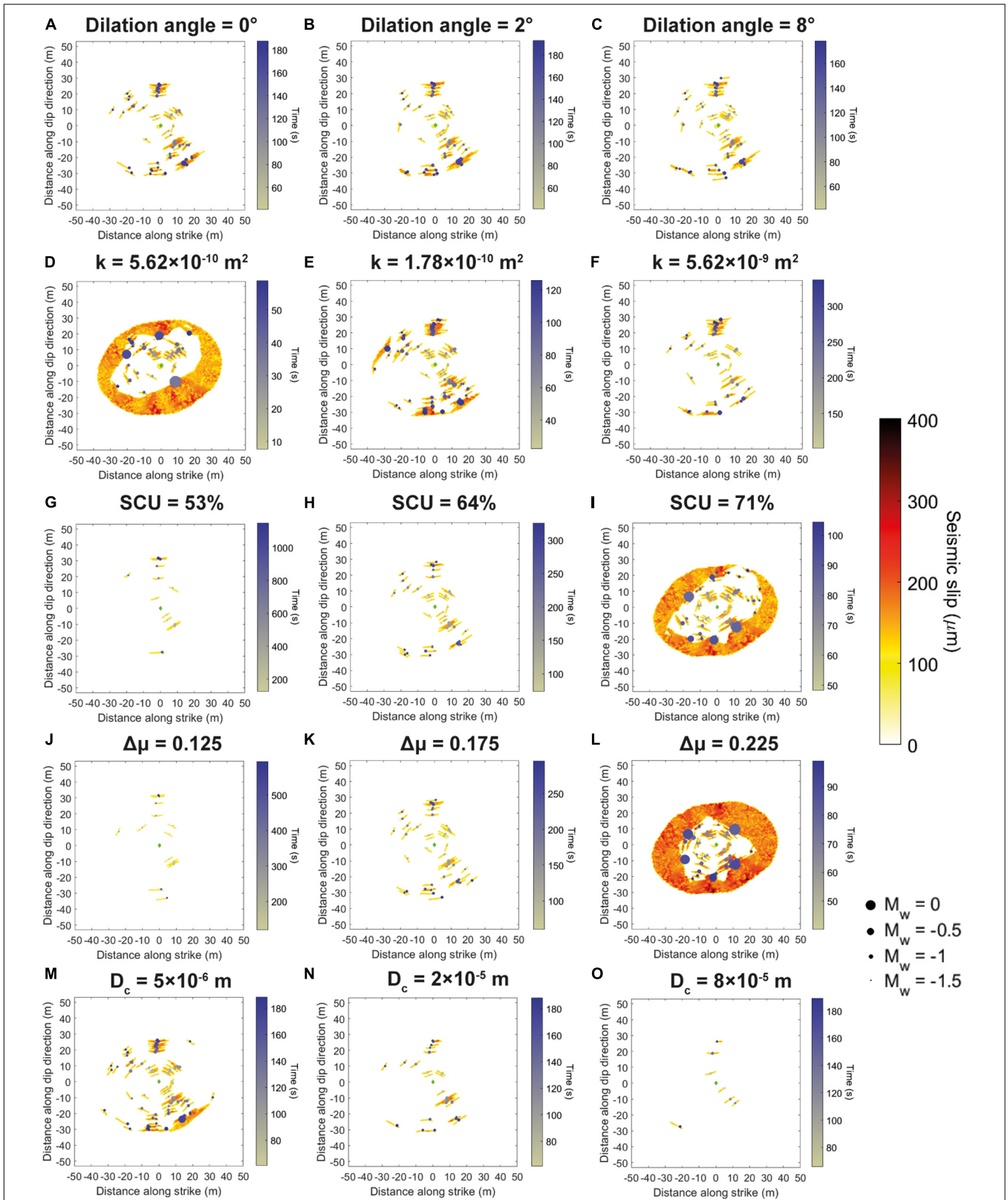

FIGURE 4 | Seismic slip on the fault at the end of the simulations for various dilation angles (**A:** 0°; **B:** 2°; **C:** 8°), permeabilities (**D:** 5.6×10^{-10} m^2; **E:** 1.8×10^{-9} m^2; **F:** 5.6×10^{-9} m^2), stress criticalities (**G:** 53%; **H:** 64%; **I:** 71%), friction drops (**J:** 0.125; **K:** 0.175; **L:** 0.225), and critical slip distances (**M:** 5×10^{-6} m; **N:** 2×10^{-5} m; **O:** 8×10^{-5} m). The seismic events generated during the test are represented by black disks whose size is function of their magnitude.

with magnitude ranging from −1.6 to 0.3. Cumulated seismic slip is smaller than a few tens of microns (0.114–0.383 mm, depending on the simulation). It is 20–128 times smaller than the maximum aseismic slip (0.413–1,800 mm). Therefore, the calculated deformation is mostly aseismic, with at most 4% of the total moment that is seismic. This result is consistent with independent seismological observations in both *in-situ* decametric-scale and small-scale laboratory experiments (e.g., Goodfellow et al., 2015; De Barros et al., 2018). As the rupture is stopped at a fixed distance from injection, the ruptured area and final aseismic moment are very similar for all simulations.

To better understand the relationship between seismicity, fluid pressure and shear stress, we represent the seismicity in a distance-time diagram (or r-t plot) (**Figure 5**). The pressure front, defined by an overpressure of 5% compared to the hydrostatic level, follows a diffusion curve of the form $r = \sqrt{4\pi Dt}$ (Shapiro et al., 1997) where D is a diffusivity coefficient (m^2/s). As the fault friction reduces with slip (i.e., slip-weakening), when the rupture occurs, the slipping patch has a residual shear stress lower than the initial one, and is surrounded by an area with increased stress. We therefore define the shear stress front as the peak of stress at the edge of the slipping area. Since the rupture zone has an elliptical shape, the distance from the shear stress front to the injection varies with the angles on the fault. Therefore, in a r-t plot, the shear stress front varies within a band that gets wider as the rupture grows with time (**Figure 5**). The rupture front is defined as the largest distance of the shear stress front. We observe that the seismicity always occurs on the shear stress front and does not follow the pressure front (**Figure 5**). The shear stress front may or may not outpace the pressure front. When it does, the seismic front accelerates, and tends to have a constant or increasing migration velocity. This migration velocity corresponds to the propagation velocity of the aseismic rupture. A pronounced acceleration of the seismic moment rate is observed at the same time. This feature is observed for large SCU and friction drop tests (**Figures 5I,L**). On the contrary, when the shear stress front stays behind the pressure front, the seismic migration velocity slows down, and shows a diffusive shape.

In this study, injection is flowrate-controlled. Thus, time and injected volume are interdependent (**Figure 2B**). Since the test duration evolves with the initial permeability, the friction drop and the SCU (**Figures 5D–L**), the injected volume needed to reach a same rupture size depends on these three fault properties. Moreover, since the rupture front at the end of the simulation is fixed, an increase in the test duration implies a decrease in the migration velocity of the shear stress and seismicity fronts.

The shear stress contribution required to induce failure (SSC, Eq. 4) is calculated to quantify the respective contribution of shear stress and fluid pressure in the triggering of seismic events. It increases with time and distance to injection (**Figure 5**). In 10 out of 21 simulations, the first 1–to–3 seismic events have a SSC under 50% during each test, which means they are mostly triggered by fluid overpressure. In the other simulations, the SSC is always between 50 and 99%, which corresponds to seismic events dominantly triggered by shear stress variations.

Influence of Fault Physical Properties on the Fault Sismo-Hydromechanical Responses

Variations in the SCU and friction drop lead to very similar behaviors (**Figures 5G–L**). First, increasing SCU or friction drops, leads to smaller fluid injected volume, and smaller test durations, without any changes in the pressure front shape (**Table 3**). For small SCU or friction drop, the shear stress front and thus the seismicity stay behind the pressure front. The seismicity migrates with small velocities (less than 0.1 m/s) which slow down with time (**Figure 6F**). For larger values, the shear stress front is first behind the pressure front, before accelerating and outpacing it. Therefore, the seismic migration velocity increases with increasing SCU or friction drop. The shear stress contribution (SSC, Eq. 4), the number of seismic events and the cumulative seismic moment at the end of injection also increase with increasing SCU and friction drop (**Figures 6D–E**, **7**). Therefore, the seismic-to-total moment ratio also increases with increasing SCU (from 0.040 to 3.2%) and friction drop (from 0.034 to 4.2%).

Variations among tests with different dilation angle (**Figures 5A–C**, **6C–E**, **7** and **Table 2**) are not observed in the spatio-temporal distribution of the seismicity, the shear stress front, the seismic moment, the seismic-to-total moment ratio, nor in the number of events. The main differences when varying the dilation angles concern the amplitude of the fluid pressure at the injection, and the shape of the pressure front. With a null dilation angle (i.e., no shear-induced dilation), the diffusive-like pressure front reaches 29 m at the end of injection (**Figure 5A**), while with a 8° dilation angle, it stops following a diffusion curve near 100 s and accelerates to reach 39 m (**Figure 5C**). Therefore, while the stress front outpaces the pressure front for low dilation angles, it stays behind for high dilation angles.

While an increase of initial fault permeability allows a faster diffusion of the fluid, it also reduces the migration velocity of the rupture (**Figure 6F**) and the seismicity (**Table 3**). Therefore, an increase of the initial permeability leads to an increase of the injected fluid volume and test duration to reach the same rupture size (**Figures 5D–F**). Moreover, permeability increases in the pressurized zone during the simulation. As shown in **Figure 8A**, the permeability variations increase at injection point with decreasing initial permeability (from 53 to 2,500% of its initial value) and increasing dilation angle (from 108 to 1,700%). Nonetheless, the seismicity and shear stress fronts still accelerate and outpace the pressure front during the injection simulation. Increasing initial permeability also induces a decrease in the final cumulative seismic moment released during the simulation (from 47.0×10^8 N.m to 5.8×10^8 N.m), as well as in the seismic-to-total moment ratio (from 1.8 to 0.38%). The initial permeability mainly acts on the fluid pressure at the injection, with a change of behavior that can be observed for $k = 1.78 \times 10^{-9}$ m^2. For smaller values, the increase of pressure at the injection leads to a null effective normal stress before the end of the simulation (**Figure 6B**). Therefore, a maximum number of events is reached for this value (**Figure 6E**).

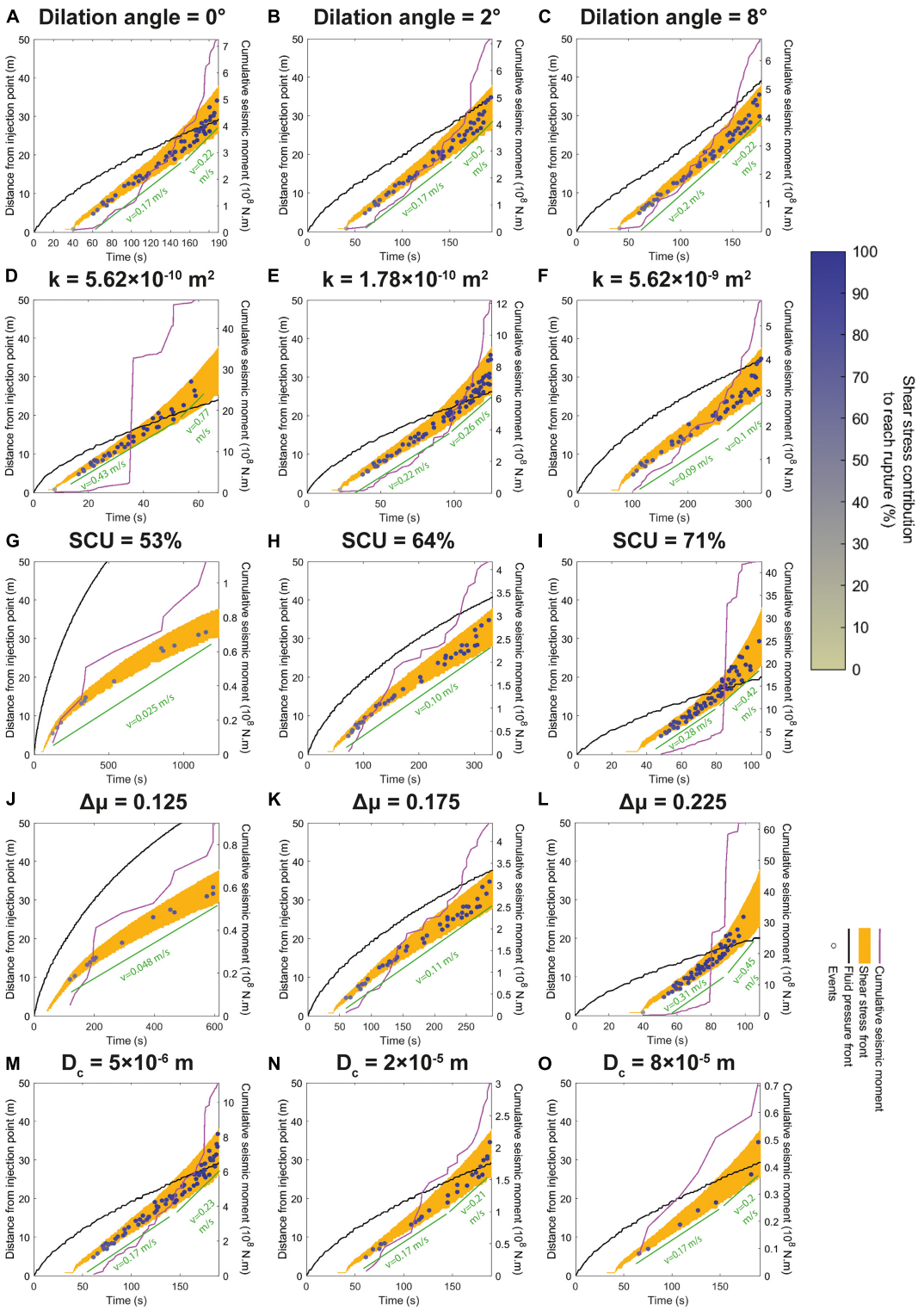

FIGURE 5 | Distance between seismic events and injection point as a function of their time of occurrence for various dilation angles (**A:** 0°; **B:** 2°; **C:** 8°), initial permeabilities (**D:** 5.6 × 10^{-10} m^2; **E:** 1.8 × 10^{-9} m^2; **F:** 5.6 × 10^{-9} m^2), stress criticalities (**G:** 53%; **H:** 64%; **I:** 71%), friction drops (**J:** 0.125; **K:** 0.175; **L:** 0.225) and critical slip distances (**M:** 5 × 10^{-6} m; **N:** 2 × 10^{-5} m; **O:** 8 × 10^{-5} m). The seismic events are represented by disks whose color is function of the shear stress transfer contribution (SSC) to reach rupture for each event. The cumulative seismic moment during the simulation is shown in magenta. The pressure front is defined as a black line, the shear stress front is represented in orange. The green straight line below seismicity indicates the mean migration velocity of seismic events. Note that time and moment scales differ among panels.

TABLE 3 | Summary of the main modeling results of the sensitivity analysis.

	SCU	Dilation angle	Initial permeability	Friction drop	Critical slip distance
Injected fluid volume	◄	0	►	◄	0
Maximal fluid overpressure	◄	◄	◄	◄	0
Diffusivity of the fluid pressure front	0	►	◄	0	0
SSC	►	◄	0	►	0
Migration velocity of the seismicity	►	0	◄	►	0
Number of seismic events	►	0	0	►	◄
Seismic moment	►	0	◄	►	◄
Seismic-to-total moment ratio	►	0	◄	►	◄

►, ◄, *and 0 indicate an increase, a decrease or no change, respectively, in the monitoring parameters in response to increase of one of the fault parameters.*

A factor of 10 increase in the critical slip distance D_c only affects the number of seismic events and the cumulative seismic moment which are, respectively, divided by 10 and 16 (**Figures 6E**, **7**). Therefore, the seismic-to-total moment ratio is also strongly reduced when increasing critical slip distance. Neither the spatiotemporal repartition of the seismicity, the shear stress front nor the fluid pressure front are influenced by this parameter (**Table 3**).

Monitoring Parameters and Fault Properties

Here we examine how the operational parameters that can be monitored (i.e., injected fluid volume, seismicity) during reservoir stimulations depend on the fault properties.

First, for a same rupture size, the injected fluid volume is strongly modified by the friction drop, the SCU and the initial permeability (**Figure 6**), highlighting the importance of the hydromechanical coupling on the fault ruptured area. It is divided by 21.4 for a SCU multiplied by 1.3 and by 10.2 for a friction drop multiplied by 1.8. It is also multiplied by 12.75 for a 10-fold increase of the initial permeability. No significant injection volume variations are observed with dilation angle and critical slip distance simulations.

The pressure front at the end of the injections can be modeled using a single hydraulic diffusivity (D) equals to 0.37 m^2/s for the simulations with varying friction drop, SCU and critical slip distance (**Figure 6A**). Therefore, these three fault properties do not influence the hydrological behavior of the fault. A saturation of the pressure front is nonetheless observed for the smallest SCU test (SCU = 53%), as the pressure front reaches the edges of the model. On the contrary, the diffusivity measured on the pressure front obviously varies with the initial permeability, from 0.28 to 0.68 m^2/s. A non-null dilation angle also changes the shape of the pressure front, which cannot be modeled by a linear diffusion law anymore (see section "Influence of Fault Physical Properties on the Fault Sismo-Hydromechanical Responses"). Besides, both initial permeability and dilation angles strongly modify fluid pressure at the injection (**Figure 6B**). Indeed, after a sharp increase of the injection pressure leading to the first rupture, the pressure at the injection slowly increases when no dilation is considered, but it decreases with dilation angles larger than 2° (**Figure 8B**). For smaller dilation angles, the pressure at injection point decreases later, after the rupture of a larger zone around injection. Moreover, the maximum overpressure reached during the simulations decreases with an increasing dilation angle (38.4–17.2 MPa for a dilation angle rising from 0° to 8°) and with an increasing initial permeability (46.3–25.9 MPa from $k = 5.62 \times 10^{-10}$ m^2 to $k = 5.62 \times 10^{-9}$ m^2). The SCU and friction drop also influence the fluid pressure at the injection, but to a lesser extent.

A population of seismic events is induced during each simulation. The number of events is mostly impacted by the critical slip distance, the SCU and the friction drop (**Figure 6E**). It is divided by 10.4 for an 8-fold increase of the critical slip distance. This number is also multiplied by 5 and 3.7 for a SCU and friction drop, respectively, multiplied by 1.3 and 1.8. The initial permeability also acts on the number of events, but due to the pressure threshold reached in high permeability tests, no particular evolution can be shown regarding this fault property (see section "Influence of Fault Physical Properties on the Fault Sismo-Hydromechanical Responses"). No noticeable variations of the number of events are observed with dilation angle simulations.

The cumulative seismic moment is mostly influenced by the friction drop and the SCU, and, to a lesser extent, by the initial permeability and the critical slip distance (**Figure 7**). It is multiplied by 41.6 and 76.2 for a SCU and friction drop multiplied, respectively, by 1.3 and 1.8. It is also divided by 8.3 and 15.6 for an 8-fold increase of the critical slip distance and a 10-fold increase of the initial permeability, respectively. No significant seismic moment variations are observed with dilation angle simulations. As the total deformation is similar for all simulations, the seismic-to-total moment partitioning has the same sensitivity as the seismic moment, and is mainly modified by the friction drop and the SCU. The seismic-to-total moment ratio is indeed divided by 80 and 120 within the explored range of these two parameters. The critical slip distance and the initial permeability have a smaller influence (factor 16 and factor 5, respectively).

The shear stress contribution (SSC, Eq. 4) quantifies how much the shear stress (and conversely, the fluid pressure) contributes to the seismic rupture. Friction drop and SCU strongly influence the SSC. SSC decreases quickly for most events when friction drop and SCU decreases, meaning that the fluid pressure is playing a larger role in inducing seismic slips over the course of injection (**Figure 6D**). Besides, we also note an influence

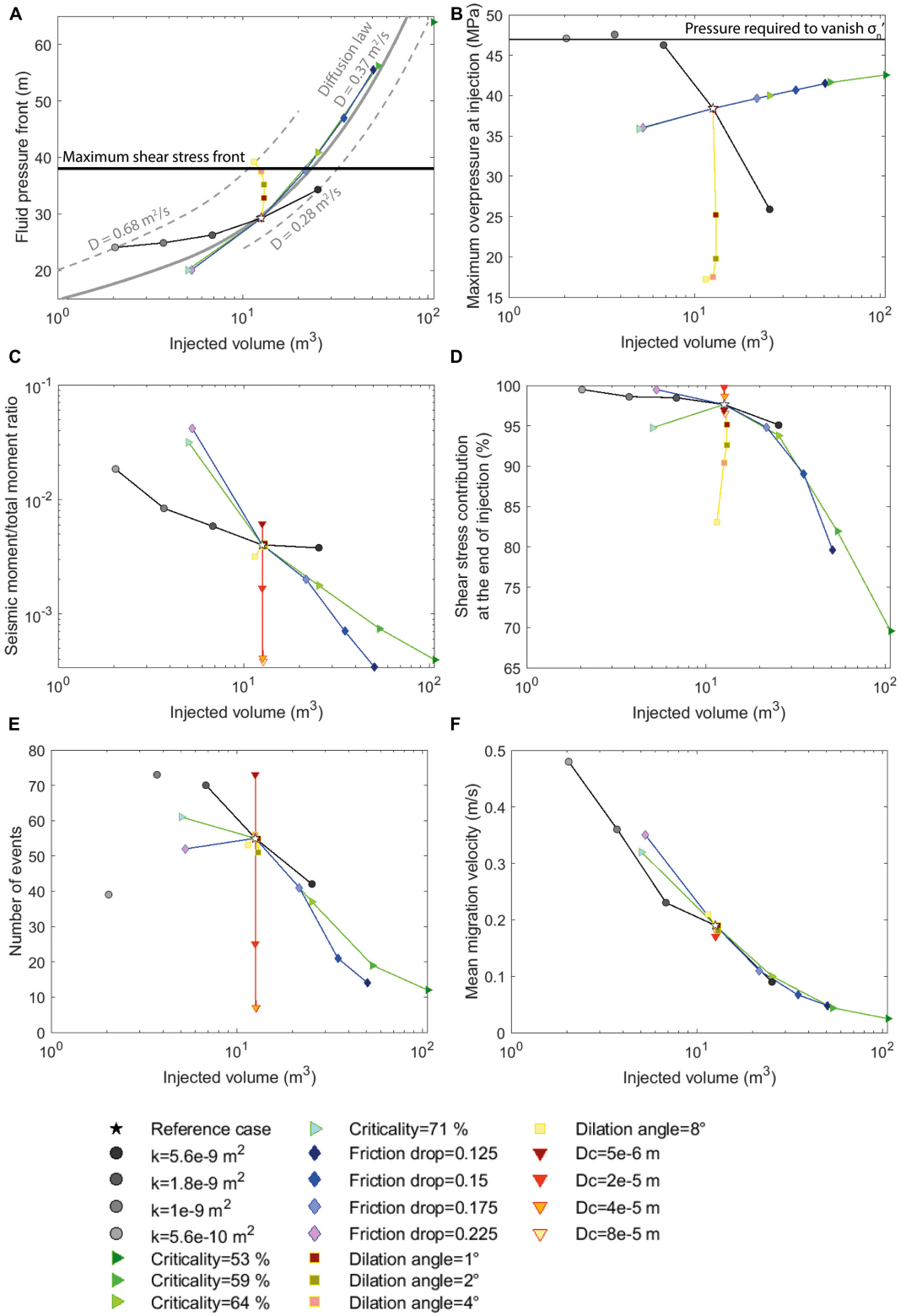

FIGURE 6 | (A) Fluid pressure front, **(B)** maximum overpressure at injection, **(C)** seismic-to-total moment ratio, **(D)** shear stress contribution, **(E)** number of seismic events, and **(F)** mean migration velocity as a function of total injected fluid volume for the 21 simulations. Each simulation is defined by a color and a symbol. The reference case is represented by a star. Injection tests with a same varying parameter are linked by a single-colored line. In panel **(A)**, the black horizontal line shows the position of the maximum shear stress front (fixed for all tests at 38 m from injection point) and the gray curves show theoretical diffusion profiles where D is the hydraulic diffusivity.

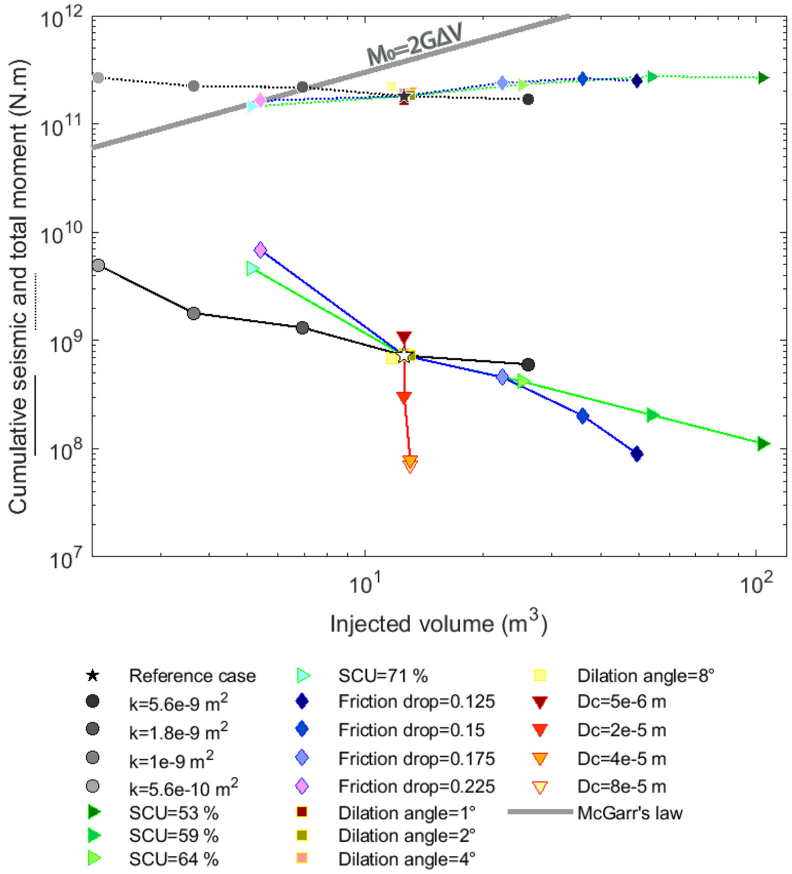

FIGURE 7 | Cumulative seismic (solid line) and total moment (dashed line) as a function of total injected fluid volume for the 21 simulations (**Table 2**). Injection tests with a same varying parameter are linked by a single-colored line. Each test is defined by a color and a symbol. The reference case is represented by a white (for the seismic moment) or black (for the total moment) star. The gray thick diagonal line shows the upper bound given by Eq. (5) of McGarr and Barbour (2018).

of the dilation angle on the SSC, which varies from 98 to 83% for dilation angles between 0° and 8°.

Therefore, the spatiotemporal distribution of induced seismicity as well as the partitioning between seismic and aseismic moment released during injection are deeply influenced by the initial proximity of stress to failure of the fault and by its friction drop with slip, and, to a lesser extent, by the initial permeability of the fault and the critical slip distance D_c. These behaviors are consistent with independent field observations (De Barros et al., 2016, 2018; Lund Snee and Zoback, 2016; Hearn et al., 2018).

During a fluid injection, the released seismic moment is usually related to the injected fluid volume (McGarr, 2014; Galis et al., 2017; McGarr and Barbour, 2018). The 21 simulations we have performed can be seen as the response of 21 different reservoirs. We showed that the volume depends on three fault parameters (i.e., the SCU, the friction drop, the initial permeability; **Figure 7**). The seismic moment also depends on these three parameters, as well as on the critical slip distance. In a moment-volume diagram (**Figure 7**), the dependence we observed between these two parameters is counter-intuitive, and not in agreement with classical laws. The seismic moment decreases with the injected volume when three parameters (the initial permeability, the SCU and the friction drop) are modified. Therefore, the effect of the considered parameters on the fault hydraulic, mechanical and seismic responses has to be considered in order to anticipate the released seismic moment from the injected fluid volume.

DISCUSSION

This study presents a series of numerical simulations of the coupled seismo-hydro-mechanical response of a permeable, slip-weakening fault in which fluid is injected at high-rate over a short duration in a local point source. We investigate the influence of fault physical parameters on the induced seismicity sequences. Based on a range of five important fault parameters, which are the initial permeability, dilation angle, SCU, friction drop and critical slip distance D_c, we identified that:

(1) the seismic, mechanical and hydraulic responses of the fault are deeply influenced by these fault parameters;
(2) the observed relationship between the injected fluid volume and the cumulative seismic moment appear much

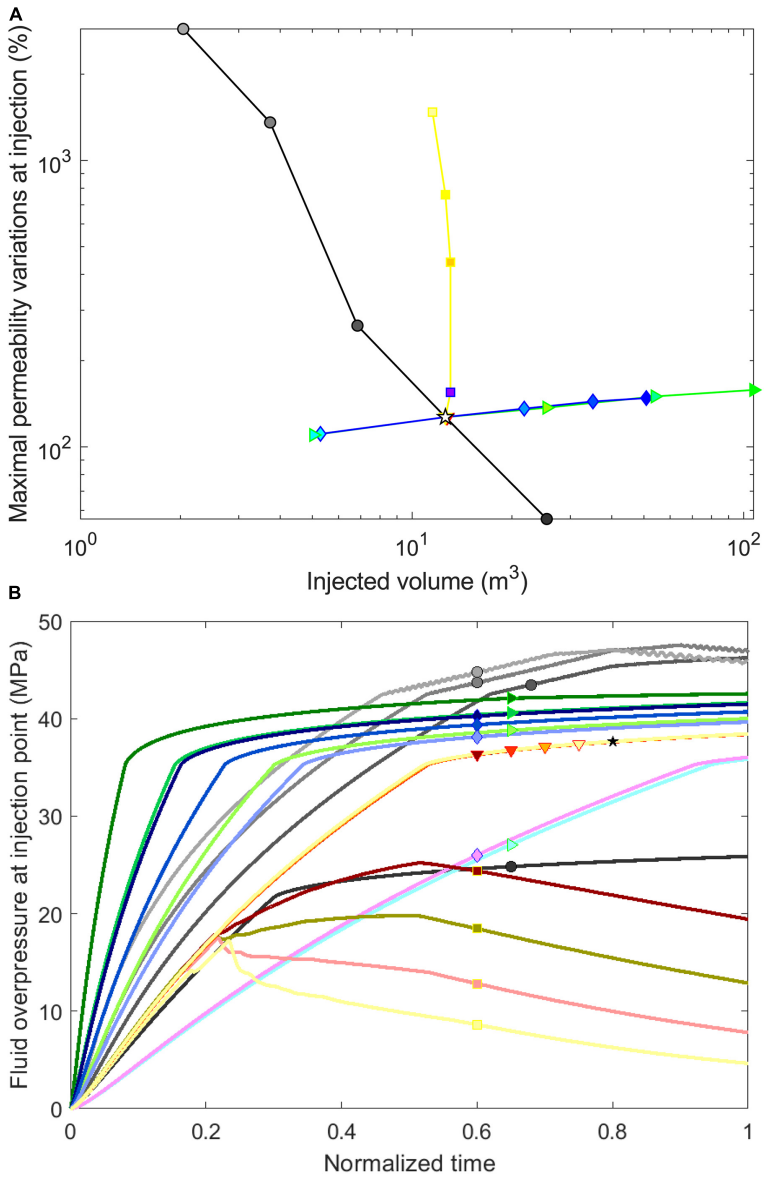

FIGURE 8 | (A) Maximal permeability variations at the injection point as a function of total injected fluid volume for the 21 simulations (**Table 2**). Injection tests with a same varying parameter are linked by a single-colored line. Each test is defined by a color and a symbol. The reference case is represented by a star. **(B)** Fluid overpressure at injection point as a function of normalized time for the 21 simulations (**Table 2**). Each test is defined by a color and a symbol. The curves for the reference case, represented by a black star, and the critical slip test (down-pointing triangle symbol) are the same.

more complex than the classical predictive analytical solutions (Galis et al., 2017; McGarr and Barbour, 2018).

We have to notice that these fault parameters and stress state may nonetheless be difficult to obtain in practice in the field, especially for deep faults that cannot be accessed or sampled easily.

Processes for the Different Fault Parameters

We find in our models that an increase in the friction drop or the SCU leads to a faster migration of the rupture and of the seismicity (**Figures 5J–L**) and to an increase of both the magnitude and the number of seismic events (**Figure 7**). These fault properties act on the background stress drop, defined as the difference between the initial stress state and the residual shear stress $\mu_d \times \sigma_n$ after an aseismic or seismic rupture (e.g., Galis et al., 2017). The background stress drop represents the shear stress exceeding the dynamic strength of the fault before injection. It corresponds to an excess or a lack of stress, which can either lead or slow down the rupture, depending of the sign of the background stress drop. If the friction drop or the SCU are high, the background stress drop is positive. Therefore, the aseismic

rupture, as well as the shear stress front, accelerates. The increase of the seismicity migration velocity with the SCU is observed in previous modeling studies considering a pressurized fault driven by a slip-weakening (Bhattacharya and Viesca, 2019; Wynants-Morel et al., 2020) or a rate-and-state friction (Gischig, 2015; Dublanchet, 2019a). Moreover, the acceleration of the seismicity migration in high SCU cases is also mentioned in previous studies (Dublanchet, 2019a; Wynants-Morel et al., 2020).

Both the number and magnitudes of induced earthquakes are larger with higher SCU and friction drop. This increase of the seismic moment with SCU and friction drop was observed in previous works (Gischig, 2015; Rutqvist et al., 2015; Dublanchet, 2019a; Wynants-Morel et al., 2020). Moreover, the SCU acts on the triggering of seismic events and on their spatial distribution (Keranen et al., 2014; Lund Snee and Zoback, 2016; Jin and Zoback, 2018a,b; Buijze et al., 2019b). Indeed, for instance in Oklahoma (US), earthquakes are triggered even for stress and fluid pressure perturbations less than 3 MPa, because of the near-critical stress state of the faults (Lund Snee and Zoback, 2016; Schoenball and Ellsworth, 2017).

The initial permeability and the dilation angle both modify the hydraulic response of the fault. As shown by Eq. (1), while the evolution of permeability is related to the initial opening of the fault and the change in effective stress, the dilation angle only acts on the opening of the fault during the slip episodes. The initial permeability mainly acts on the migration velocity of seismic events, but oppositely to what is expected from poroelastic diffusion (Shapiro et al., 1997). An increase of initial permeability indeed decreases the seismic migration velocity (**Figure 6F**). It can be explained by the lower level of fluid pressure reached on the fault at a given time for higher initial permeability. As the injection is flowrate-controlled in this study (**Figure 2B**), the fluid pressure increases more slowly in a higher permeability simulation. Moreover, the SSC, and thus the pressure contribution, is not impacted by the initial permeability (**Figure 6D**). Consequently, the duration needed to reach a fixed level of fluid pressure at the maximum rupture distance increases with the permeability, which means a slower rupture migration velocity. This is in contradiction with Chang and Segall (2016) and Norbeck and Horne (2016), who showed that the rupture is faster with a higher permeability. Nonetheless, shear stress variations from aseismic slip is not considered in their studies, while it contributes to the majority of the rupture propagation in our model (**Figure 6D**; Wynants-Morel et al., 2020). It also supports the importance of full hydromechanical coupling, which is not taken into account in Chang and Segall (2016). Our study also shows that the cumulative seismic moment, and therefore the seismic-to-total ratio, increases with decreasing fault permeability (**Figure 7**). Such behavior has been observed in reservoir injection sites, for instance in Oklahoma (Shah and Keller, 2017; Hearn et al., 2018).

We observe that the Shear Stress Contribution to reach rupture (SSC) decreases with an increase of the dilation angle. This is due to a higher opening of the fault before rupture due to the slipping of close regions; therefore, fluid pressure can diffuse more easily and reaches higher values just before rupture. Thus, the pressure contribution to reach rupture is higher, which means a smaller SSC. Moreover, as the dilation angle does not influence the rupture itself, dilation angles have no effect on the seismic moment and the spatio-temporal evolution of the seismic front (**Figure 7**). This does not agree to what has been found in previous models (Segall et al., 2010; McClure and Horne, 2011; Ciardo and Lecampion, 2019), in which a damping of the seismicity is observed. However, these models do not consider shear stress variations from previous rupture as a mechanism to reach rupture. This highlights the importance of shear stress variations in the seismic triggering mechanism.

The cumulated seismic moment decreases with increasing critical slip distance D_c (**Figure 7**). Moreover, a high value of this frictional parameter means that the friction drops on a larger slip distance (**Figure 2A**). Therefore, the friction weakening rate (i.e., the ratio between the friction drop and the critical slip distance) is small, which impedes slip acceleration and reduces the possibilities of unstable, seismic slip (Hillers et al., 2009). Thus, a sparse seismicity is observed, leading to a small released seismic moment. A similar result is shown in Cueto-Felgueroso et al. (2017) for an injection in a rate-and-state fault. Rutqvist et al. (2015) observed a decrease of the maximal seismic moment for an increasing D_c, but also an increase of the number of events. Nonetheless, they do not consider aseismic rupture in their model; most of the events observed by Rutqvist et al. (2015) for high critical slip distance may be considered aseismic in our model.

Seismic Moment and Injected Fluid Volume Relationship

We now investigate the contribution and consequences of our modeling results on the seismic moment vs. injected fluid volume relationship (**Figure 7**) commonly used to estimate the maximum earthquake magnitude induced by a fluid injection (Galis et al., 2017; McGarr and Barbour, 2018).

McGarr (1976) first considered the seismic moment (M_0^{seis}) released during a fluid injection to be related at first order to the injected fluid volume (V) through the shear modulus (G) of the surrounding rock. Then, this relationship has been updated in McGarr and Barbour (2018) to incorporate the aseismic moment (M_0^{aseis}) occurring during the injection:

$$M_0^{tot} = M_0^{seis} + M_0^{aseis} = 2GV \tag{6}$$

This relationship stands for an upper bound that cannot be exceeded during a fluid injection.

Our results show that four fault parameters (i.e., the initial permeability, the SCU, the friction drop and the critical slip distance) modify the moment-volume relationship. Indeed, the seismic moment decreases with the injected volume when three parameters (the initial permeability, the SCU and the friction drop) are modified. The sensitivity to the critical slip distance of the fault leads to similar injected volume but different seismic moment (**Figure 7**). Assuming that these 21 tests are responses from different and independent reservoirs, the mean trend that shows up from this test is that the released moment decreases with injected volume. This is in total disagreement with the McGarr's relations. Because our simulations are stopped for

similar total moment, the latter does not follow either the eq. 6. However, even if the total moment was corrected to fit such a law, the seismic moment would not show an increasing dependency with the volume. Indeed, we here observed that seismic and total moment do not follow the same trend, i.e., that the seismic-to-total ratio globally decreases here with increasing injected fluid volume. It means that the fault physical properties have a significant impact on the moment-volume relationships by modifying the seismic-to-total ratio, at least within the small range of volume and seismic moment we have here explored. To better anticipate the released seismicity, the aseismic component of the deformation should be considered (De Barros et al., 2019). This motivates a reformulation of the available moment-volume models since most of them do not include the aseismic deformation that occurs during fluid injection. Nonetheless, we want to precise that the seismic moment does follow a power law with the injected volume in each individual test, as observed in the literature (Buijze et al., 2015; Bentz et al., 2020).

The relationship given by McGarr and Barbour (2018) (Eq. 6) is considering the total moment, that is the seismic plus aseismic deformation. However, it is exceeded for small values of initial permeability and it will probably be exceeded for values of SCU and friction drop larger than those adopted in this study (**Figure 7**). This is in agreement with reservoir stimulation cases in which the observed moment is far above the expected value obtained from Eq. (6) (Atkinson et al., 2016; Ellsworth et al., 2019). For instance, Chang et al. (2020) consider that the low permeability of the basement near the geothermal field of Pohang, South Korea, favored the triggering of the 2017 post-injection M_w 5.4 event. According to Atkinson et al. (2016), the diffusion of fluids from previous near injections brought a large zone in a critical state of stress close to the location of hydraulic fracturing exploitations in the WCSB. This may explain that 6 $M_w > 3.5$ events induced by these exploitations do not follow the prevision of the McGarr's law (Atkinson et al., 2016). Therefore, seismic moment that largely exceeds prediction from

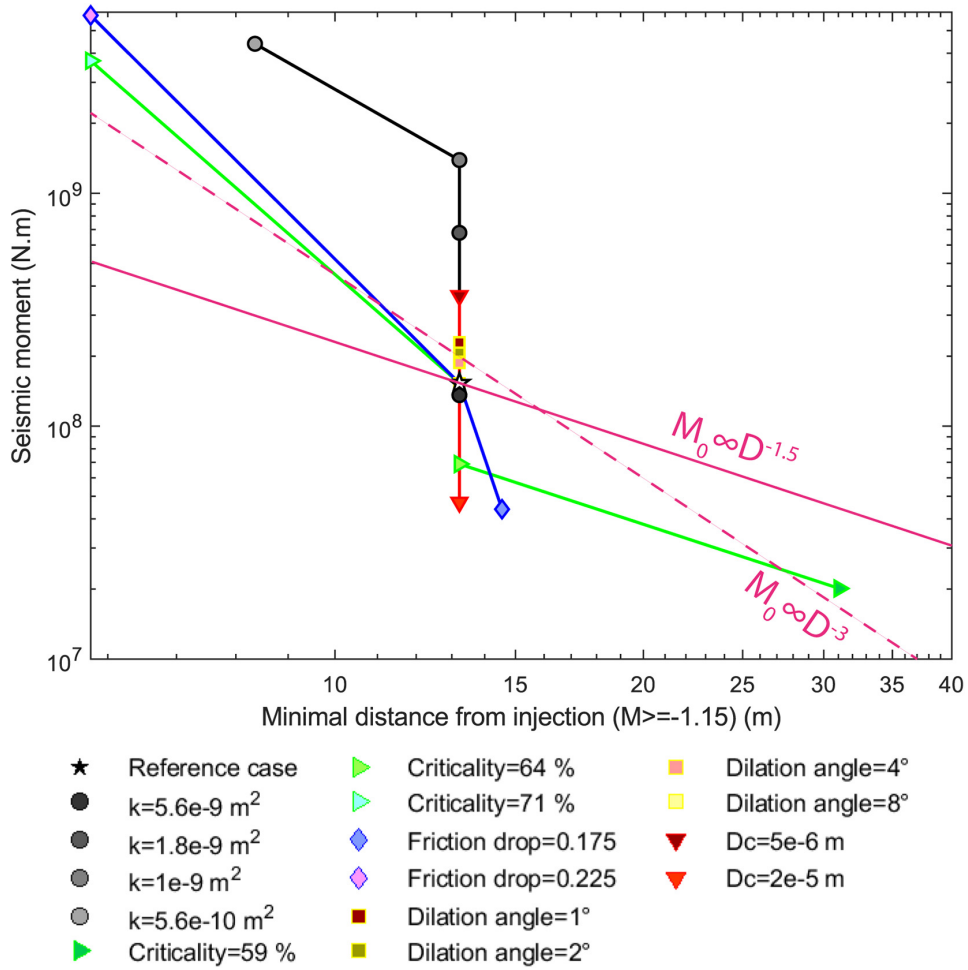

FIGURE 9 | Seismic moment as a function of the minimal distance from injection to seismic events whose magnitude exceeds –1.15 for the 16 simulations having at least one event with a moment magnitude above this threshold. Injection tests with a same varying parameter are linked by a single-colored line. Each test is defined by a color and a symbol. The reference case is represented by a star. The pink diagonal line represents the relation between seismic moment and distance from injection of the first detectable seismic event found by De Barros et al. (2019).

the fluid volume may exist in case of low permeability or highly critical stress state.

As neither the seismic nor the total moment released during injection can be directly anticipated from the injected fluid volume only, we look for another measurable parameter that can be considered as a proxy of the released seismic moment. We observe that no detectable seismic event is observed close to injection point (**Figure 5**), which is consistent with De Barros et al. (2016) and Duboeuf et al. (2017) observations in *in-situ* controlled decametric scale experiments. We approximate the size of the aseismic slip patch around injection point as the distance between the injection point and the first seismic event with a magnitude above a magnitude threshold $M_t = -1.15$. Following the approach of De Barros et al. (2019), we observe that the induced moment of events with magnitude $M_w \geq M_t$ decreases with the distance to first seismic event for the 16 simulations (**Figure 9**) with seismic events with magnitude above −1.15. A scaling relating the seismic moment to the power −3 of the size of the aseismic patch around injection give a poor fit with the data at first order. Therefore, this parameter seems to be a possible probe to estimate the amount of aseismic deformation. Nonetheless, the power coefficient is lower to the coefficient proposed by De Barros et al. (2019), equal to −1.5. This difference can be explained by pressure or stress effects, as De Barros et al. (2019) find a different coefficient (equal to −1) by including the critical fluid pressure into the moment/distance relation. Therefore, such parameter, in combination with other parameters, might be useful to correct the moment-volume relationship for the fault properties and the aseismic deformation. Nonetheless, this parameter stays dependent to the knowing of the injection location, which may not be available in many deep injection cases.

CONCLUSION

This study focuses on the influence of fault physical properties during a fluid injection on the spatiotemporal distribution of the induced seismicity and on the moment partitioning between seismic and aseismic slip. Using a series of numerical simulations with a three-dimensional hydromechanical code, we considered an inherently discrete earthquake rupture model with a slip-weakening friction law. We carried out simulations testing a range of values for different fault hydraulic and mechanical properties. We obtained synthetic seismicity catalogs for each of these simulations.

Our observations showed that the mechanical behavior of the fault is impacted by the friction drop, initial proximity of stress to failure and dilation angle. These parameters influence the shear stress and fluid pressure perturbations that contribute to rupture. We found, as expected, that the hydrological behavior of the fault depends on the initial permeability and the dilation angle. Moreover, the spatiotemporal distribution of induced seismicity as well as the partitioning between seismic and aseismic moment released during injection are deeply influenced by the initial proximity of stress to failure of the fault and by its friction drop, and, to a lesser extent, by the initial permeability of the fault and the critical slip distance D_c. Moreover, the moment-volume relationship inferred from the fault sismo-hydromechanical responses when modifying these four parameters do not follow the classical relationship defined in McGarr and Barbour (2018). It means that the fault properties are important parameters to consider in order to anticipate the released seismic moment associated with injection. In particular, they are strongly modifying the seismic-to-total ratio, which impact on the relation between the seismic moment and the injected volume. This motivates the question to reformulate such models, considering other monitoring parameters, in order to improve the estimation of the maximum expected earthquake magnitude associated with a given injected fluid volume. We found that the distance between the injection point and the first detectable seismic event is a simple yet effective parameter to estimate the released seismic moment, as proposed by De Barros et al. (2019). Nonetheless, relationships between the seismic moment and other measurable parameters, such as the mineralogy of the surrounding rock (De Barros et al., 2016), the proximity to the crystalline basement (Hincks et al., 2018), or operational injection parameters (Kim, 2013; Weingarten et al., 2015; Almakari et al., 2019; De Barros et al., 2019), should be explored in future studies.

DATA AVAILABILITY STATEMENT

The original contributions presented in the study are included in the article/supplementary material, further inquiries can be directed to the corresponding author/s.

AUTHOR CONTRIBUTIONS

LD and FC designed the study. NW-M performed the numerical simulations. All authors contributed to the analysis of the data and simulations, and preparation of the manuscript.

FUNDING

This work was supported by the French Government, through the HYDROSEIS project under contract ANR-13-JS06-0004-01 and through the UCAJEDI Investments in the Future project managed by the National Research Agency (ANR) with the reference number ANR-15-IDEX-01. NW-M benefits from a financial support of the Université Côte d'Azur (UCA).

ACKNOWLEDGMENTS

We thank the associate editor, RH, and two reviewers for their constructive comments that improve our manuscript during the review process.

REFERENCES

Almakari, M., Dublanchet, P., Chauris, H., and Pellet, F. (2019). Effect of the injection scenario on the rate and magnitude content of injection-induced seismicity: case of a heterogeneous fault. *J. Geophys. Res. Solid Earth* 124, 8426–8448. doi: 10.1029/2019JB017898

Ampuero, J.-P., Vilotte, J.-P., and Sánchez-Sesma, F. J. (2002). Nucleation of rupture under slip dependent friction law: simple models of fault zone. *J. Geophys. Res. Solid Earth* 107, ESE 2-1–ESE 2-19. doi: 10.1029/2001JB000452

Atkinson, G. M., Eaton, D. W., Ghofrani, H., Walker, D., Cheadle, B., Schultz, R., et al. (2016). hydraulic fracturing and seismicity in the Western Canada sedimentary basin. *Seismol. Res. Lett.* 87, 631–647. doi: 10.1785/0220150263

Bao, X., and Eaton, D. W. (2016). Fault activation by hydraulic fracturing in western Canada. *Science* 354, 1406–1409. doi: 10.1126/science.aag2583

Barbour, A. J., Norbeck, J. H., and Rubinstein, J. L. (2017). The effects of varying injection rates in Osage County, Oklahoma, on the 2016 M_w 5.8 Pawnee Earthquake. *Seismol. Res. Lett.* 88, 1040–1053. doi: 10.1785/0220170003

Bentz, S., Kwiatek, G., Martínez-Garzón, P., Bohnhoff, M., and Dresen, G. (2020). Seismic moment evolution during hydraulic stimulations. *Geophys. Res. Lett* 47:e2019GL086185. doi: 10.1029/2019GL086185

Bhattacharya, P., and Viesca, R. C. (2019). Fluid-induced aseismic fault slip outpaces pore-fluid migration. *Science* 364, 464–468. doi: 10.1126/science.aaw7354

Buijze, L., van Bijsterveldt, L., Cremer, H., Jaarsma, B., Paap, B., Veldkamp, H., et al. (2019b). Induced seismicity in geothermal systems: occurrences worldwide and implications for the Netherlands. *Paper Presented at the European Geothermal Congress 2019, The Hague, Netherlands*, The Hague.

Buijze, L., van den Bogert, P., Wassing, B. B. T., and Orlic, B. (2019a). Nucleation and arrest of dynamic rupture induced by reservoir depletion. *J. Geophys. Res. Solid Earth* 124, 3620–3645. doi: 10.1029/2018JB016941

Buijze, L., Wassing, B. B. T., Fokker, P. A., and van Wees, J. D. (2015). Moment partitioning for injection-induced seismicity: case studies and insights from numerical modeling. *Paper Presented at the Proceedings World Geothermal Congress 2015, Melbourne, Australia*, Melbourne, Vic.

Byerlee, J. (1978). Friction of rocks. *Pure Appl. Geophys.* 116, 615–626. doi: 10.1007/BF0087652

Calò, M., Dorbath, C., Cornet, F. H., and Cuenot, N. (2011). Large-scale aseismic motion identified through 4-D P-wave tomography: temporal subsetting of the stimulation period. *Geophys. J. Int.* 186, 1295–1314. doi: 10.1111/j.1365-246X.2011.05108.x

Cappa, F., and Rutqvist, J. (2011). Impact of CO_2 geological sequestration on the nucleation of earthquakes. *Geophys. Res. Lett.* 38:L17313. doi: 10.1029/2011GL048487

Cappa, F., Guglielmi, Y., Nussbaum, C., and Birkholzer, J. (2018). On the relationship between fault permeability increases, induced stress perturbation, and the growth of aseismic slip during fluid injection. *Geophys. Res. Lett* 45, 11,012–11,020. doi: 10.1029/2018GL080233

Cappa, F., Scuderi, M. M., Collettini, C., Guglielmi, Y., and Avouac, J.-P. (2019). Stabilization of fault slip by fluid injection in the laboratory and in situ. *Sci. Adv.* 5:eaau4065. doi: 10.1126/sciadv.aau4065

Chang, K. W., and Segall, P. (2016). Injection-induced seismicity on basement faults including poroelastic stressing. *J. Geophys. Res. Solid Earth* 121, 2708–2726. doi: 10.1002/2015JB012561

Chang, K. W., Yoon, H., Kim, Y., and Lee, M. Y. (2020). Operational and geological controls of coupled poroelastic stressing and pore-pressure accumulation along faults: induced earthquakes in Pohang, South Korea. *Sci. Rep* 10:2073. doi: 10.1038/s41598-020-58881-z

Ciardo, F., and Lecampion, B. (2019). Effect of dilatancy on the transition from aseismic to seismic slip due to fluid injection in a fault. *J. Geophys. Res. Solid Earth* 124, 3724–3743. doi: 10.1029/2018JB016636

Cochard, A., and Madariaga, R. (1994). Dynamic faulting under rate-dependent friction. *Pure Appl. Geophys. Pageoph.* 142, 419–445. doi: 10.1007/BF00876049

Cornet, F. H. (2012). The relationship between seismic and aseismic motions induced by forced fluid injections. *Hydrogeol. J.* 20, 1463–1466. doi: 10.1007/s10040-012-0901-z

Cornet, F. H. (2016). Seismic and aseismic motions generated by fluid injections. *Geomech. Energy Environ.* 5, 42–54. doi: 10.1016/j.gete.2015.12.003

Cornet, F. H., Helm, J., Poitrenaud, H., and Etchecopar, A. (1997). Seismic and aseismic slips induced by large-scale fluid injections. *Pure Appl. Geophys.* 150, 563–583. doi: 10.1007/s000240050093

Cueto-Felgueroso, L., Santillán, D., and Mosquera, J. C. (2017). Stick-slip dynamics of flow-induced seismicity on rate and state faults. *Geophys. Res. Lett.* 44, 4098–4106. doi: 10.1002/2016GL072045

Cundall, P. A. (1988). Formulation of a three-dimensional distinct element model—Part I. A scheme to detect and represent contacts in a system composed of many polyhedral blocks. *Int. J. Rock Mech. Min. Sci. Geomech. Abstr.* 25, 107–116. doi: 10.1016/0148-9062(88)92293-0

De Barros, L., Cappa, F., Guglielmi, Y., Duboeuf, L., and Grasso, J.-R. (2019). Energy of injection-induced seismicity predicted from in-situ experiments. *Sci. Rep.* 9:4999. doi: 10.1038/s41598-019-41306-x

De Barros, L., Daniel, G., Guglielmi, Y., Rivet, D., Caron, H., Payre, X., et al. (2016). Fault structure, stress, or pressure control of the seismicity in shale? Insights from a controlled experiment of fluid-induced fault reactivation. *J. Geophys. Res. Solid Earth* 121, 4506–4522. doi: 10.1002/2015JB012633

De Barros, L., Guglielmi, Y., Rivet, D., Cappa, F., and Duboeuf, L. (2018). Seismicity and fault aseismic deformation caused by fluid injection in decametric in-situ experiments. *Comptes Rendus Geosci.* 350, 464–475. doi: 10.1016/j.crte.2018.08.002

Dublanchet, P. (2019a). Fluid driven shear cracks on a strengthening rate-and-state frictional fault. *J. Mech. Phys. Solids* 132:103672. doi: 10.1016/j.jmps.2019.07.015

Dublanchet, P. (2019b). Scaling and variability of interacting repeating earthquake sequences controlled by asperity density. *Geophys. Res. Lett.* 46, 11950–11958. doi: 10.1029/2019GL084614

Duboeuf, L., De Barros, L., Cappa, F., Guglielmi, Y., Deschamps, A., and Seguy, S. (2017). aseismic motions drive a sparse seismicity during fluid injections into a fractured zone in a carbonate reservoir. *J. Geophys. Res. Solid Earth* 122, 8285–8304. doi: 10.1002/2017JB014535

Dunham, E. M. (2007). Conditions governing the occurrence of supershear ruptures under slip-weakening friction. *J. Geophys. Res.* 112:B07302. doi: 10.1029/2006JB004717

Eaton, D. W., and Igonin, N. (2018). What controls the maximum magnitude of injection-induced earthquakes? *Lead. Edge* 37, 135–140. doi: 10.1190/tle37020135.1

Ellsworth, W. L. (2013). Injection-induced earthquakes. *Science* 341, 1225942–1225942. doi: 10.1126/science.1225942

Ellsworth, W. L., Giardini, D., Townend, J., Ge, S., and Shimamoto, T. (2019). Triggering of the Pohang, Korea, earthquake (Mw 5.5) by enhanced geothermal system stimulation. *Seismol. Res. Lett.* 90, 1844–1858. doi: 10.1785/0220190102

Eyre, T. S., Eaton, D. W., Garagash, D. I., Zecevic, M., Venieri, M., Weir, R., et al. (2019). The role of aseismic slip in hydraulic fracturing–induced seismicity. *Sci. Adv.* 5:eaav7172. doi: 10.1126/sciadv.aav7172

Fan, Z., Eichhubl, P., and Gale, J. F. W. (2016). Geomechanical analysis of fluid injection and seismic fault slip for the M w 4.8 Timpson, Texas, earthquake sequence. *J. Geophys. Res. Solid Earth* 121, 2798–2812. doi: 10.1002/2016JB012821

Fomin, S., Jing, Z., and Hashida, T. (2004). "The Effect of Thermal, Chemical, Hydrological, and Mechanical Factors on Water/Rock Interaction in HDR Geothermal Systems," in *Elsevier Geo-Engineering Book Series*, ed. O. Stephanson (Amsterdam: Elsevier), 649–654. doi: 10.1016/S1571-9960(04)80113-7

Galis, M., Ampuero, J. P., Mai, P. M., and Cappa, F. (2017). Induced seismicity provides insight into why earthquake ruptures stop. *Sci. Adv.* 3:eaa7528. doi: 10.1126/sciadv.aap7528

Garagash, D. I., and Germanovich, L. N. (2012). Nucleation and arrest of dynamic slip on a pressurized fault. *J. Geophys. Res. Solid Earth* 117:B10310. doi: 10.1029/2012JB009209

Gischig, V. S. (2015). Rupture propagation behavior and the largest possible earthquake induced by fluid injection into deep reservoirs. *Geophys. Res. Lett.* 42, 7420–7428. doi: 10.1002/2015GL065072

Goebel, T. H. W., Weingarten, M., Chen, X., Haffener, J., and Brodsky, E. E. (2017). The 2016 Mw5.1 fairview, Oklahoma earthquakes: evidence for long-range poroelastic triggering at >40 km from fluid disposal wells. *Earth Planet. Sci. Lett.* 472, 50–61. doi: 10.1016/j.epsl.2017.05.011

Goodfellow, S. D., Nasseri, M. H. B., Maxwell, S. C., and Young, R. P. (2015). Hydraulic fracture energy budget: insights from the laboratory. *Geophys. Res. Lett.* 42, 3179–3187. doi: 10.1002/2015GL063093

Grigoli, F., Cesca, S., Priolo, E., Rinaldi, A. P., Clinton, J. F., Stabile, T. A., et al. (2017). Current challenges in monitoring, discrimination, and management of induced seismicity related to underground industrial activities: a European perspective. *Rev. Geophys.* 55, 310–340. doi: 10.1002/2016RG000542

Grigoli, F., Cesca, S., Rinaldi, A. P., Manconi, A., López-Comino, J. A., Clinton, J. F., et al. (2018). The november 2017 M_w 5.5 Pohang earthquake: a possible case of induced seismicity in South Korea. *Science* 360, 1003–1006. doi: 10.1126/science.aat2010

Guglielmi, Y., Cappa, F., Avouac, J.-P., Henry, P., and Elsworth, D. (2015a). Seismicity triggered by fluid injection-induced aseismic slip. *Science* 348, 1224–1226. doi: 10.1126/science.aab0476

Guglielmi, Y., Elsworth, D., Cappa, F., Henry, P., Gout, C., Dick, P., et al. (2015b). In situ observations on the coupling between hydraulic diffusivity and displacements during fault reactivation in shales. *J. Geophys. Res. Solid Earth* 120, 7729–7748. doi: 10.1002/2015JB012158

Hearn, E. H., Koltermann, C., and Rubinstein, J. L. (2018). Numerical models of pore pressure and stress changes along basement faults due to wastewater injection: applications to the 2014 Milan, Kansas earthquake. *Geochem. Geophys. Geosyst.* 19, 1178–1198. doi: 10.1002/2017GC007194

Hillers, G., Carlson, J. M., and Archuleta, R. J. (2009). Seismicity in a model governed by competing frictional weakening and healing mechanisms. *Geophys. J. Int.* 178, 1363–1383. doi: 10.1111/j.1365-246X.2009.04217.x

Hincks, T., Aspinall, W., Cooke, R., and Gernon, T. (2018). Oklahoma's induced seismicity strongly linked to wastewater injection depth. *Science* 359, 1251–1255. doi: 10.1126/science.aap7911

Hopp, C., Sewell, S., Mroczek, S., Savage, M., and Townend, J. (2019). Seismic response to injection well stimulation in a high-temperature, high-permeability reservoir. *Geochem. Geophys. Geosyst.* 20, 2848–2871. doi: 10.1029/2019GC008243

Ida, Y. (1972). Cohesive force across the tip of a longitudinal-shear crack and Griffith's specific surface energy. *J. Geophys. Res.* 77, 3796–3805. doi: 10.1029/JB077i020p03796

Itasca Consulting Group, Inc. (2016). *3DEC — Three-Dimensional Distinct Element Code*. Minneapolis: Itasca.

Jaeger, J. C., and Cook, N. G. (1984). *Fundamentals of rock Mechanics, repr. ed, Science Paperbacks*, 3. Edn. London: Chapman and Hall.

Jeanne, P., Guglielmi, Y., Lamarche, J., Cappa, F., and Marié, L. (2012). Architectural characteristics and petrophysical properties evolution of a strike-slip fault zone in a fractured porous carbonate reservoir. *J. Struct. Geol.* 44, 93–109. doi: 10.1016/j.jsg.2012.08.016

Jin, L., and Zoback, M. D. (2018a). Modeling induced seismicity: co-seismic fully dynamic spontaneous rupture considering fault poroelastic stress. *Paper Presented at the 52th US Rock Mechanics/Geomechanics Symposium, American Rock Mechanics Association (ARMA)*, Seattle, WA.

Jin, L., and Zoback, M. D. (2018b). Hydromechanical–stochastic modeling of fluid-induced seismicity in fractured poroelastic media. *EarthArXiv* [Preprint]. doi: 10.31223/osf.io/8ynm7

Keranen, K. M., and Weingarten, M. (2018). Induced seismicity. *Annu. Rev. Earth Planet. Sci.* 46, 149–174. doi: 10.1146/annurev-earth-082517-010054

Keranen, K. M., Savage, H. M., Abers, G. A., and Cochran, E. S. (2013). Potentially induced earthquakes in Oklahoma, USA: links between wastewater injection and the 2011 Mw 5.7 earthquake sequence. *Geology* 41, 699–702. doi: 10.1130/G34045.1

Keranen, K. M., Weingarten, M., Abers, G. A., Bekins, B. A., and Ge, S. (2014). Sharp increase in central Oklahoma seismicity since 2008 induced by massive wastewater injection. *Science* 345, 448–451. doi: 10.1126/science.1255802

Kim, K.-H., Ree, J.-H., Kim, Y., Kim, S., Kang, S. Y., and Seo, W. (2018). Assessing whether the 2017 M_w 5.4 Pohang earthquake in South Korea was an induced event. *Science* 360, 1007–1009. doi: 10.1126/science.aat6081

Kim, W.-Y. (2013). Induced seismicity associated with fluid injection into a deep well in Youngstown, Ohio. *J. Geophys. Res. Solid Earth* 118, 3506–3518. doi: 10.1002/jgrb.50247

Hubbert, M., and Rubey, W. W. (1959). Role of fluid pressure in mechanics of overthrust faulting. *Geol. Soc. Am. Bull.* 70:115.

Kroll, K. A., Cochran, E. S., and Murray, K. E. (2017). Poroelastic properties of the Arbuckle group in Oklahoma derived from well fluid level response to the 3 september 2016 M w 5.8 Pawnee and 7 november 2016 M w 5.0 cushing earthquakes. *Seismol. Res. Lett.* 88, 963–970. doi: 10.1785/0220160228

Kwiatek, G., Saarno, T., Ader, T., Bluemle, F., Bohnhoff, M., Chendorain, M., et al. (2019). Controlling fluid-induced seismicity during a 6.1-km-deep geothermal stimulation in Finland. *Sci. Adv.* 5:eaav7224. doi: 10.1126/sciadv.aav7224

Latham, J.-P., Xiang, J., Belayneh, M., Nick, H. M., Tsang, C.-F., and Blunt, M. J. (2013). Modelling stress-dependent permeability in fractured rock including effects of propagating and bending fractures. *Int. J. Rock Mech. Min. Sci.* 57, 100–112. doi: 10.1016/j.ijrmms.2012.08.002

Lee, K.-K., Ellsworth, W. L., Giardini, D., Townend, J., Ge, S., Shimamoto, T., et al. (2019). Managing injection-induced seismic risks. *Science* 364, 730–732. doi: 10.1126/science.aax1878

Lei, Q., Latham, J.-P., and Xiang, J. (2016). Implementation of an empirical joint constitutive model into finite-discrete element analysis of the geomechanical behaviour of fractured rocks. *Rock Mech. Rock Eng.* 49, 4799–4816. doi: 10.1007/s00603-016-1064-3

Lei, Q., Latham, J.-P., Xiang, J., Tsang, C.-F., Lang, P., and Guo, L. (2014). Effects of geomechanical changes on the validity of a discrete fracture network representation of a realistic two-dimensional fractured rock. *Int. J. Rock Mech. Min. Sci.* 70, 507–523. doi: 10.1016/j.ijrmms.2014.06.001

Lengliné, O., Boubacar, M., and Schmittbuhl, J. (2017). Seismicity related to the hydraulic stimulation of GRT1, Rittershoffen, France. *Geophys. J. Int* 208, 1704–1715. doi: 10.1093/gji/ggw490

Lund Snee, J.-E., and Zoback, M. D. (2016). State of stress in Texas: implications for induced seismicity. *Geophys. Res. Lett* 43, 208–210. doi: 10.1002/2016GL070974

Marone, C. (1998). Laboratory-derived friction laws and their application to seismic faulting. *Annu. Rev. Earth Planet. Sci.* 26, 643–696. doi: 10.1146/annurev.earth.26.1.643

McClure, M. W. (2015). Generation of large postinjection-induced seismic events by backflow from dead-end faults and fractures. *Geophys. Res. Lett.* 42, 6647–6654. doi: 10.1002/2015GL065028

McClure, M. W., and Horne, R. N. (2011). Investigation of injection-induced seismicity using a coupled fluid flow and rate/state friction model. *Geophysics* 76, WC181–WC198. doi: 10.1190/geo2011-0064.1

McGarr, A. (1976). Seismic moments and volume changes. *J. Geophys. Res.* 81, 1487–1494. doi: 10.1029/JB081i008p01487

McGarr, A. (2014). Maximum magnitude earthquakes induced by fluid injection. *J. Geophys. Res. Solid Earth* 119, 1008–1019. doi: 10.1002/2013JB010597

McGarr, A., and Barbour, A. J. (2018). Injection-induced moment release can also be aseismic. *Geophys. Res. Lett.* 45, 5344–5351. doi: 10.1029/2018GL078422

McNamara, D. E., Benz, H. M., Herrmann, R. B., Bergman, E. A., Earle, P., Holland, A., et al. (2015). Earthquake hypocenters and focal mechanisms in central Oklahoma reveal a complex system of reactivated subsurface strike-slip faulting. *Geophys. Res. Lett.* 42, 2742–2749. doi: 10.1002/2014GL062730

Mikumo, T., Olsen, K., Fukuyama, E., and Yagi, Y. (2003). Stress-breakdown time and slip-weakening distance inferred from slip-velocity functions on earthquake faults. *Bull. Seismol. Soc. Am.* 93, 264–282. doi: 10.1785/0120020082

Norbeck, J. H., and Horne, R. N. (2016). Evidence for a transient hydromechanical and frictional faulting response during the 2011 M_w 5.6 Prague, Oklahoma earthquake sequence. *J. Geophys. Res. Solid Earth* 121, 8688–8705. doi: 10.1002/2016JB013148

Norbeck, J. H., and Horne, R. N. (2018). Maximum magnitude of injection-induced earthquakes: a criterion to assess the influence of pressure migration along faults. *Tectonophysics* 733, 108–118. doi: 10.1016/j.tecto.2018.01.028

Pei, S., Peng, Z., and Chen, X. (2018). Locations of injection-induced earthquakes in Oklahoma controlled by crustal structures. *J. Geophys. Res. Solid Earth* 123, 2332–2344. doi: 10.1002/2017JB014983

Rinaldi, A. P., and Nespoli, M. (2017). TOUGH2-seed: a coupled fluid flow and mechanical-stochastic approach to model injection-induced seismicity. *Comput. Geosci.* 108, 86–97. doi: 10.1016/j.cageo.2016.12.003

Rubino, V., Rosakis, A. J., and Lapusta, N. (2017). Understanding dynamic friction through spontaneously evolving laboratory earthquakes. *Nat. Commun* 8:15991. doi: 10.1038/ncomms15991

Rutqvist, J., Rinaldi, A. P., Cappa, F., and Moridis, G. J. (2015). Modeling of fault activation and seismicity by injection directly into a fault zone associated with hydraulic fracturing of shale-gas reservoirs. *J. Pet. Sci. Eng.* 127, 377–386. doi: 10.1016/j.petrol.2015.01.019

Schmittbuhl, J., Lengliné, O., Cornet, F., Cuenot, N., and Genter, A. (2014). Induced seismicity in EGS reservoir: the creep route. *Geotherm. Energy* 2:14. doi: 10.1186/s40517-014-0014-0

Schoenball, M., and Ellsworth, W. L. (2017). A systematic assessment of the spatiotemporal evolution of fault activation through induced seismicity in Oklahoma and Southern Kansas. *J. Geophys. Res. Solid Earth* 122, 10,189–10,206. doi: 10.1002/2017JB014850

Schultz, R., Stern, V., Novakovic, M., Atkinson, G., and Gu, Y. J. (2015). Hydraulic fracturing and the crooked lake sequences: insights gleaned from regional seismic networks. *Geophys. Res. Lett.* 42, 2750–2758. doi: 10.1002/2015GL063455

Segall, P. (1989). . Earthquakes triggered by fluid extraction. *Geology* 17:942. doi: 10.1130/0091-76131989017<0942:ETBFE<2.3.CO;2

Segall, P., and Lu, S. (2015). Injection-induced seismicity: poroelastic and earthquake nucleation effects. *J. Geophys. Res. Solid Earth* 120, 5082–5103. doi: 10.1002/2015JB012060

Segall, P., Rubin, A. M., Bradley, A. M., and Rice, J. R. (2010). Dilatant strengthening as a mechanism for slow slip events. *J. Geophys. Res* 115:B12305. doi: 10.1029/2010JB007449

Shah, A. K., and Keller, G. R. (2017). Geologic influence on induced seismicity: constraints from potential field data in Oklahoma. *Geophys. Res. Lett.* 44, 152–161. doi: 10.1002/2016GL071808

Shapiro, S. A., Huenges, E., and Borm, G. (1997). Estimating the crust permeability from fluid-injection-induced seismic emission at the KTB site. *Geophys. J. Int.* 131, F15–F18. doi: 10.1111/j.1365-246X.1997.tb01215.x

Shapiro, S. A., Krüger, O. S., Dinske, C., and Langenbruch, C. (2011). Magnitudes of induced earthquakes and geometric scales of fluid-stimulated rock volumes. *Geophysics* 76, WC55–WC63. doi: 10.1190/geo2010-0349.1

Shapiro, S. A., Rothert, E., Rath, V., and Rindschwentner, J. (2002). Characterization of fluid transport properties of reservoirs using induced microseismicity. *Geophysics* 67, 212–220. doi: 10.1190/1.1451597

Tsopela, A., Donzé, F.-V., Guglielmi, Y., Castilla, R., and Gout, C. (2019). Hydromechanical reactivation of natural discontinuities: mesoscale experimental observations and DEM modeling. *Acta Geotech.* 14, 1585–1603. doi: 10.1007/s11440-019-00791-0

Uenishi, K., and Rice, J. R. (2003). Universal nucleation length for slip-weakening rupture instability under nonuniform fault loading. *J. Geophys. Res. Solid Earth* 108, ESE17.1–ESE17.14. doi: 10.1029/2001JB001681

van der Elst, N. J., Page, M. T., Weiser, D. A., Goebel, T. H. W., and Hosseini, S. M. (2016). Induced earthquake magnitudes are as large as (statistically) expected. *J. Geophys. Res. Solid Earth* 121, 4575–4590. doi: 10.1002/2016JB012818

Wang, L., Kwiatek, G., Rybacki, E., Bonnelye, A., Bohnhoff, M., and Dresen, G. (2020). Laboratory study on fluid-induced fault slip behavior: the role of fluid pressurization rate. *Geophys. Res. Lett* 47:e2019GL086627. doi: 10.1029/2019GL086627

Wei, S., Avouac, J.-P., Hudnut, K. W., Donnellan, A., Parker, J. W., Graves, R. W., et al. (2015). The 2012 Brawley swarm triggered by injection-induced aseismic slip. *Earth Planet. Sci. Lett.* 422, 115–125. doi: 10.1016/j.epsl.2015.03.054

Weingarten, M., Ge, S., Godt, J. W., Bekins, B. A., and Rubinstein, J. L. (2015). High-rate injection is associated with the increase in U.S. mid-continent seismicity. *Science* 348, 1336–1340. doi: 10.1126/science.aab1345

Witherspoon, P. A., Wang, J. S. Y., Iwai, K., and Gale, J. E. (1980). Validity of cubic law for fluid flow in a deformable rock fracture. *Water Resour. Res.* 16, 1016–1024. doi: 10.1029/WR016i006p01016

Wynants-Morel, N., Cappa, F., De Barros, L., and Ampuero, J. (2020). Stress perturbation from aseismic slip drives the seismic front during fluid injection in a permeable fault. *J. Geophys. Res. Solid Earth* 125:e2019JB019179. doi: 10.1029/2019JB019179

Yeck, W. L., Hayes, G. P., McNamara, D. E., Rubinstein, J. L., Barnhart, W. D., Earle, P. S., et al. (2017). Oklahoma experiences largest earthquake during ongoing regional wastewater injection hazard mitigation efforts. *Geophys. Res. Lett.* 44, 711–717. doi: 10.1002/2016GL071685

Yeck, W. L., Weingarten, M., Benz, H. M., McNamara, D. E., Bergman, E. A., Herrmann, R. B., et al. (2016). Far-field pressurization likely caused one of the largest injection induced earthquakes by reactivating a large preexisting basement fault structure. *Geophys. Res. Lett.*43, 10,198–10,207. doi: 10.1002/2016GL070861

Yeo, I. W., Brown, M. R. M., Ge, S., and Lee, K. K. (2020). Causal mechanism of injection-induced earthquakes through the Mw 5.5 Pohang earthquake case study. *Nat. Commun.* 11:2614. doi: 10.1038/s41467-020-16408-0

Zbinden, D., Rinaldi, A. P., Diehl, T., and Wiemer, S. (2020). Hydromechanical modeling of fault reactivation in the St. Gallen Deep geothermal project (Switzerland): poroelasticity or hydraulic connection? *Geophys. Res. Lett.* 47:e2019GL085201. doi: 10.1029/2019GL085201

Zhang, F., Damjanac, B., and Huang, H. (2013). Coupled discrete element modeling of fluid injection into dense granular media. *J. Geophys. Res. Solid Earth* 118, 2703–2722. doi: 10.1002/jgrb.50204

Zhang, Z., and Li, X. (2016). The shear mechanisms of natural fractures during the hydraulic stimulation of shale gas reservoirs. *Materials* 9:713. doi: 10.3390/ma9090713

Zoback, M. D., Kohli, A., Das, I., and Mcclure, M. W. (2012). The importance of slow slip on faults during hydraulic fracturing stimulation of shale gas reservoirs. *Paper Presented at the SPE Americas Unconventional Resources Conference: SPE Americas Unconventional Resources Conference*, (Pittsburgh, PA: Society of Petroleum Engineers). doi: 10.2118/155476-MS

Conflict of Interest: The authors declare that the research was conducted in the absence of any commercial or financial relationships that could be construed as a potential conflict of interest.

frontiers in Earth Science

BRIEF RESEARCH REPORT
published: 17 May 2021
doi: 10.3389/feart.2021.670757

Rupture Directivity in 3D Inferred From Acoustic Emissions Events in a Mine-Scale Hydraulic Fracturing Experiment

José Ángel López-Comino[1,2,3]*, *Simone Cesca*[4], *Peter Niemz*[3,4], *Torsten Dahm*[3,4] and *Arno Zang*[3,4]

[1]Instituto Andaluz de Geofísica, Universidad de Granada, Granada, Spain, [2]Departamento de Física Teórica y del Cosmos, Universidad de Granada, Granada, Spain, [3]Institute of Geosciences, University of Potsdam, Potsdam, Germany, [4]GFZ German Research Centre for Geosciences, Potsdam, Germany

Rupture directivity, implying a predominant earthquake rupture propagation direction, is typically inferred upon the identification of 2D azimuthal patterns of seismic observations for weak to large earthquakes using surface-monitoring networks. However, the recent increase of 3D monitoring networks deployed in the shallow subsurface and underground laboratories toward the monitoring of microseismicity allows to extend the directivity analysis to 3D modeling, beyond the usual range of magnitudes. The high-quality full waveforms recorded for the largest, decimeter-scale acoustic emission (AE) events during a meter-scale hydraulic fracturing experiment in granites at ~410 m depth allow us to resolve the apparent durations observed at each AE sensor to analyze 3D-directivity effects. Unilateral and (asymmetric) bilateral ruptures are then characterized by the introduction of a parameter κ, representing the angle between the directivity vector and the station vector. While the cloud of AE activity indicates the planes of the hydrofractures, the resolved directivity vectors show off-plane orientations, indicating that rupture planes of microfractures on a scale of centimeters have different geometries. Our results reveal a general alignment of the rupture directivity with the orientation of the minimum horizontal stress, implying that not only the slip direction but also the fracture growth produced by the fluid injections is controlled by the local stress conditions.

Keywords: directivity, earthquake source, induced seismicity, hydraulic fracturing, acoustic emissions

OPEN ACCESS

Edited by:
Antonio Pio Rinaldi, ETH Zurich, Switzerland

Reviewed by:
Linus Villiger, ETH Zürich, Switzerland
Chet Hopp, Lawrence Berkeley National Laboratory, United States

***Correspondence:**
José Ángel López-Comino
jalopezcomino@ugr.es

Specialty section:
This article was submitted to Solid Earth Geophysics, a section of the journal Frontiers in Earth Science

Received: *22 February 2021*
Accepted: *05 May 2021*
Published: *17 May 2021*

Citation:
López-Comino JÁ, Cesca S, Niemz P, Dahm T and Zang A (2021) Rupture Directivity in 3D Inferred From Acoustic Emissions Events in a Mine-Scale Hydraulic Fracturing Experiment. Front. Earth Sci. 9:670757. doi: 10.3389/feart.2021.670757

INTRODUCTION

Rupture directivity defines preferred earthquake rupture propagation directions through the identification of azimuthal patterns in the apparent seismic source features (e.g., apparent durations, scaled amplitudes), as recorded at a network of stations (Haskell, 1964). Earthquake ruptures can be classified in pure unilateral or pure bilateral (symmetric) ruptures, as well as asymmetric bilateral ruptures, describing an intermediate case between the two previous models. It is well know that a predominance of unilateral ruptures is observed for large earthquakes (McGuire et al., 2002); however, recent studies demonstrated that directivity might be also a common feature of small to moderate events (e.g., Kane et al., 2013; Kurzon et al., 2014; Calderoni et al., 2015; Meng

et al., 2020; Ross et al., 2020). So far, rupture directivity has also been identified for a few cases of weak fluid-injection induced earthquakes (Folesky et al., 2016; López-Comino and Cesca, 2018; Király Proag et al., 2019; Wu et al., 2019) and fluid-induced microcracks or acoustic emission (AE) events in mine-scale hydraulic fracturing (HF) experiments (Dahm, 2001), suggesting that such properties could persist at smaller magnitudes. In fact, a recent work has been able to identify directivity effects even at laboratory scale (Kolár et al., 2020).

The most commonly used approach to estimate rupture directivity for small earthquakes is based on empirical Green's functions (EGFs) techniques, using the waveform recordings of fore- or aftershocks with 1–2 magnitude units less than the target event or mainshock (Hartzell, 1978). EGFs are used to account for the poorly know propagation and site effects, which similarly affect EGF and mainshock waveforms, by applying a time-domain or frequency-domain deconvolution process (e.g., Ammon et al., 2006; López-Comino et al., 2012; Abercrombie et al., 2017; Stich et al., 2020). As a result, apparent source time functions (ASTFs) are obtained for each receiver, showing different apparent durations, depending on their relative location to the source and the direction of rupture propagation. Directivity effects and source complexities are typically revealed by the azimuthal patterns of ASTFs in a 2D approach, simplifying the intrinsic 3D rupture propagation problem. Directivity effects in 3D can be also studied applying different approaches, for instance, through stretching techniques (e.g., Warren and Shearer, 2006; Abercrombie et al., 2017; Huang et al., 2017) or using the second order seismic moment (e.g., McGuire, 2004; McGuire, 2017; Fan and McGuire, 2018). The importance of directivity along the dip or vertical direction has been generally evidenced for the analysis of deep-focus earthquakes, by considering the differences among rupture propagation and take off vectors (Warren and Shearer, 2006; Park and Ishii, 2015), as well as for subduction earthquakes (Tilmann et al., 2016; An et al., 2017), using finite source modeling and back projection techniques. For these large scale applications, the directivity analysis is done using surface monitoring networks, i.e. well above the earthquake source, and thus with a poor 3D coverage of the foci. Nevertheless, 3D seismic monitoring configurations deployed recently in deep underground laboratories bear us new opportunities to extend the directivity analysis to microseismicity with moment magnitude (Mw) well below 0 in a 3D environment.

In the last years, decameter-scale *in-situ* hydraulic stimulation experiments have been carried out in deep underground laboratories with the purpose to improve our understanding about the nucleation and rupture growth processes linked with fluid-injection induced seismicity (Zang et al., 2017; Gischig et al., 2018; Kneafsey et al., 2018; Dresen et al., 2019; Schoenball et al., 2020; Villiger et al., 2020; Villiger et al., 2021). These experiments have been promoted in recent years by the development of enhanced geothermal systems and unconventional resources driven by HF operations (Schultz et al., 2020). Mine-scale *in-situ* experiments serve as a bridge between laboratory experiments and deep reservoir stimulations, offering improved control and more realistic boundary conditions. AE piezoelectric sensors are deployed at different borehole locations around the fluid-injection intervals providing complex 3D seismic monitoring networks. Microfractures generated during HF stimulations are then characterized by AE signals involving, for instance, M_w between −4.2 and −3.5 and rupture sizes of decimeter scale (Kwiatek et al., 2018).

In this framework, on June 2015 a mine-scale underground HF experiment at 410 m depth was carried out in the Äspö Hard Rock Laboratory (HRL), Sweden (Zang et al., 2017). Six HF stimulations with three different injection schemes were tested to assess the fatigue HF (FHF) concept in order to reduce the number and magnitude of fluid-injection induced seismicity. Each HF stimulation composed by the initial fracture phase (F) and up to five refracturing phases (RF) was performed at selected injection intervals free of pre-existing fractures along a subhorizontal 28 m-long borehole (**Figure 1**). This injection borehole was drilled in the orientation of the minimum horizontal stress magnitude (S_h) with a strike of ~N210 W. The 3D AE monitoring network consists of 11 AE uniaxial side view sensors, recording in the frequency range of 1–100 kHz, oriented toward the stimulated volume of 30 × 30 × 30 m and deployed in different boreholes and along existing experimental tunnels of Äspö HRL. These AE sensors are entirely based on the piezoelectric effect, which means that the seismic wave is guided directly into the sensor where it generates an electric output signal proportional to stress changes introduced. The data acquisition system was improved to operate with 1 MHz sampling rate, obtaining high-quality full waveforms. The AE activity generated during each HF stage has been well-studied and characterized using both triggered mode (Zang et al., 2017; Kwiatek et al., 2018) and continuous recordings (López-Comino et al., 2017; Niemz et al., 2020). **Figure 1** shows the largest AE events with magnitudes (relative magnitude, M_{AE}) exceeding 2.8, according to the last updated catalog, which contains 4,302 events with M_{AE} between ~2.0 and ~4.0 (Niemz et al., 2020). This enhanced catalogue incorporating weaker events allowed for the identification of planar seismogenic regions associated to each HF stimulation (Niemz et al., 2020). On the other hand, the M_w range has been estimated between −4.2 and −3.5 for the 196 AE events recorded in the triggered mode; furthermore, 21 moment tensor inversions were performed, identifying heterogeneous focal mechanisms and suggesting a complex microfracture network generated for the hydraulic stimulations (Kwiatek et al., 2018). Interestingly, for the large majority of the retrieved focal mechanisms, none of the potential fault planes matches the orientation of the larger scale planar seismogenic regions.

Typically, the source finiteness of small magnitude earthquakes, as well as AE events, is neglected under a point source approximation. Seismic source properties are then reduced to earthquake location, magnitude, and, in few cases, to a moment tensor, which analysis has been based on P wave first-motion polarities (Kwiatek et al., 2016). Relevant rupture features, such as rupture size, duration and directivity are not discussed and still represent a challenge at the scale of microseismicity and AEs. Here, we characterize the source

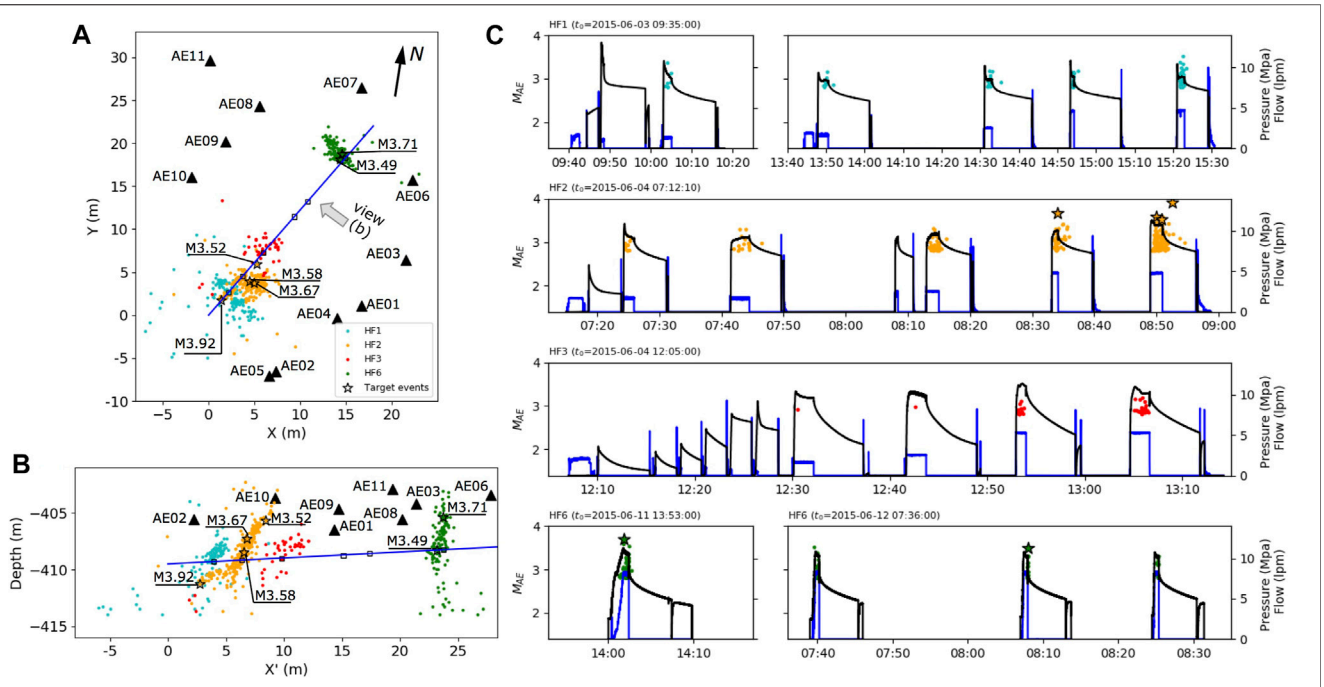

FIGURE 1 | (A) and **(B)** AE hypocenters with M_{AE} >2.8 located in the hydraulic fracturing experiments in the Äspö HRL from the last updated catalogue of Niemz et al. (2020). Stars denote the largest AE events analyzed in this study, indicating the corresponding M_{AE}. The AE sensors (triangles) and injection intervals (squares) along the 28-m-long injection borehole (blue line) are also shown. The direction of view in **(B)** is indicated in **(A)**. **(C)** Temporal evolution of the AE events of each HF experiment shown in **(A)** is plotted together with the injection pressures (black lines) and flow rates (blue lines). Initial time (t_0) is indicated for each plot. HF1, HF2 and HF6 were performed with a conventional continuous injection scheme, while a cyclic progressive injection scheme is followed in HF3 showing less AE activity and lower M_{AE}.

finiteness for the largest AE events recorded during the HF experiments in the Äspö HRL, through a novel 3D-directivity analysis applied to 3D seismic monitoring networks. Unilateral ruptures, as well as, symmetric and asymmetric bilateral ruptures are tested to find the best fitting model for the 3D pattern of ASTFs. Such advanced characterization of the rupture processes can be used to discriminate the rupture and auxiliary plane and to better understand the geometry of induced fractures.

METHODS

Apparent Durations in Mine-Scale Experiments

The high resolution AE seismicity recorded during the different HF stimulations in combination with the 3D geometry of the monitoring network and the high sampling of recordings at the Äspö HRL provide us a great opportunity to obtain apparent durations for AE events, which is a challenging step, considering their extremely low magnitudes and short durations. For some cases of global seismological applications, for instance in the case of deep-focus earthquakes, the initial portion of P-wave displacement is isolated from most other phases and represents well the source time function with a scalar correction for the seismic moment (Fukao, 1972; Kikuchi and Ishida, 1993; Beck et al., 1995; Tibi et al., 1999). Similar conditions are found for the first arrivals of the P-waves recorded in the AE network of this small-scale experiment. The average distance from the source to the borehole sensors is only about 18 m, and the wave propagation is well described by a homogeneous full-space (Niemz et al., 2020). Therefore, the effects of local structure are minimal and secondary arrivals, for instance from reflections at the gallery walls, are expected to be either weak or not significantly overlapping with the fairly short duration of the direct P wave. In such circumstances, we can assume the duration of the first pulse observed in the P-wave as a rough estimation of the apparent duration. Although the amplitudes and polarities of these waveforms are affected by the source radiation pattern of the moment tensor and eventually by the sensor orientation and coupling (Manthei et al., 2001; Maghsoudi et al., 2013), such effects do not alter the apparent durations, which are only considered for the rupture directivity modeling.

We manually select six AE events, four from HF2 and two from HF6 (**Figure 1**), where the first P-wave pulses of unfiltered waveforms are well identified in at least nine out of 11 AE sensors (**Figure 2**, **Supplementary Figure S1**). Normalized square amplitudes of the first P-wave pulses are plotted to improve the visualization of the apparent duration measurements. The M_{AE} of these selected AE events range from 3.49 to 3.92 (i.e., $M_w \sim -3.5$, according to Kwiatek et al., 2018) corresponding with the largest and high-quality AE events. Note that few AE signals are discarded from our analysis, because the first P-wave pulse is not well-constrained, in presence of noisy records, low P amplitudes (e.g., for nodal stations affected by the radiation pattern near the

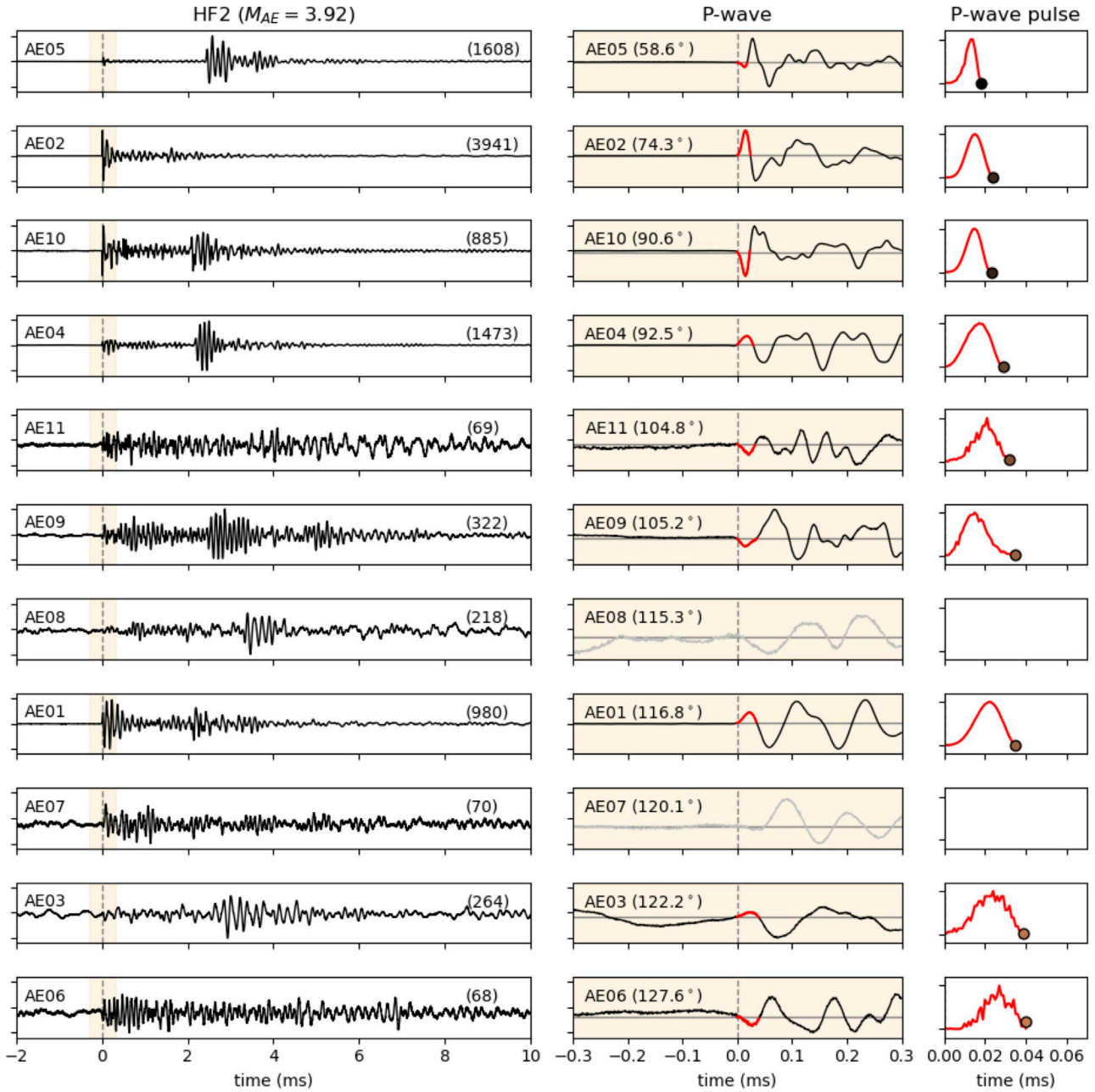

FIGURE 2 | Apparent durations for the largest AE event recorded during HF2 in the Äspö HRL. We plot the unfiltered waveforms (black lines), P-wave window (orange band), the first P-wave pulses (red lines) and the apparent durations (dots according to the colorbar in **Figure 3A**). Manual picking and the baseline are indicated in the second column with vertical dashed gray lines and horizontal gray lines respectively. Waveforms are normalized according to the maximum amplitude (see labels in each trace of the first column) and sorted by the parameter κ (see labels of the second column). Some AE signals are discarded from the rupture directivity analysis because the first P-wave pulse is not well constrained and does not allow a clear estimate of the apparent durations (grey traces in second column for AE07 and AE08). The third column shows the normalized square amplitude of the P-wave pulse shown in the second column to improve the visualization of the apparent duration measurements.

intersection between the compressional and dilation quadrants) or anomalous long pulses, compared to the remaining stations (**Figure 2**). P-wave arrivals are manually picked and we calculate automatically the end of the apparent duration at the intersection of the first P-wave pulse with the baseline. Some variations in the apparent durations are observed in our target AE events ranging from 0.016 to 0.053 ms. This implies apparent corner frequencies in the range of 18–62 kHz and magnitudes as small as $M_W \sim -3.5$ (Kwiatek et al., 2018). On the other hand, the frequency dependent sensitivity of the AE sensors is known to affect

recordings especially above 100 kHz (Ono 2018) and include low frequency noise below 3 kHz (Niemz et al., 2020), which could potentially affect our estimate of the apparent durations. To confirm the robustness of our results, we compared our apparent duration estimates, as retrieved from data filters in the frequency bands 0.5–500 kHz, 0.5–100 kHz, and 3–50 kHz (**Supplementary Figure S2**), and only find out negligible differences yielding the same apparent duration measurements. The lowest possible upper bound of the previous applied bandpass filter can be defined in 31 kHz because the first P-wave pulse cannot contain lower frequencies than the inverse of its period (about two times the minimum apparent duration). The resolution of finite source patterns, such as the directivity, formally requires the inclusion of higher frequencies (e.g., above 50 kHz). While apparent duration results from 2D directivity analysis are typically shown sorting based on the station azimuth, here we introduce other sorting strategy to visualize the 3D directivity effects based on the parameter κ described in the next section.

Rupture Directivity Analysis in 3D

The source parameters associated to a line source (Haskell, 1964) are commonly inferred through the apparent duration fitting (e.g., Cesca et al., 2011; López-Comino et al., 2016). For unilateral ruptures, the apparent durations, $\Delta t(\phi)$, show the longest duration in the forward direction of the rupture propagation (α) and the shortest duration in the backward direction, which can be written as:

$$\Delta t(\phi) = t_r + \frac{L}{v_r} - \frac{L}{v_{P,S}}\cos(\phi - \alpha) \quad (1)$$

depending on the azimuth (ϕ) between the source and each receiver, and involving different variables: rise time (t_r), rupture length (L), rupture velocity (v_r), and P (or S) wave velocities ($v_{P,S}$). In this manner, the rupture directivity is constrained along a horizontal plane and defined by a single angle, α.

For our 3D mine-scale case, we will consider spherical coordinates involving two angles (ϕ, θ): the azimuth ϕ, previously described in **Eq. 1**, and a polar angle θ, describing the deviation from the vertical axis (**Supplementary Figure S3**). We define the 3D rupture directivity vector, $\vec{d}(\phi, \theta)$, applied at the source location, defined by these two angles, and, in the same way, the station vector, $\vec{s}(\phi_i, \theta_i)$, from the source location to each station (i). Thus, we introduce the parameter κ by:

$$\kappa = \angle\left[\vec{d}(\phi, \theta), \vec{s}(\phi_i, \theta_i)\right] \quad (2)$$

representing the angle between the directivity vector and the station vector, ranging from 0° to 180° (**Supplementary Figure S3**). For κ values near 0°, indicating an alignment among station and rupture vectors, and thus observations ahead of the rupture direction, we expect to observe the shortest apparent durations. Conversely, we expect the opposite behavior, showing the largest apparent durations, for κ-values of ~180°.

Replacing the angle ϕ-α in **Eq. 1** with the new parameter κ, we can model the apparent durations Δt in 3D as a function of two angles, i.e., $\Delta t(\phi, \theta)$, assuming a unilateral rupture. Consequently, the general 3D case for unilateral and (asymmetric) bilateral ruptures can be defined combining κ and the parameterization of Cesca et al. (2011), by the equation:

$$\Delta t(\phi, \theta) = \max\left[t_r + (1-\chi)\left(\frac{L}{v_r} - \frac{L}{v_{P,S}}\cos(\kappa)\right), t_r + \chi\left(\frac{L}{v_r} + \frac{L}{v_{P,S}}\cos(\kappa)\right)\right] \quad (3)$$

where the asymmetry of the rupture (χ) ranges from 0 for pure unilateral rupture to 0.5 for pure (symmetric) bilateral rupture. Theoretical radiation patterns of apparent durations for three significant cases (pure unilateral, pure bilateral and asymmetric bilateral) are shown in **Supplementary Figure S4** for one specific directivity vector and considering reasonable values for the involved parameters according to the results obtained in the next section. Average apparent durations increase with decreasing rupture velocities, increasing rupture length and increasing rise time.

Theoretical curves of apparent durations *vs.* κ values following **Eq. 3** can then be tested for all directions, applying a full grid search for ϕ in [0°, 360°] and θ in [0°, 180°]. L1-misfit for each tested direction is then obtained by comparing theoretical and observed apparent durations at each station, showing the uncertainties associated to the best solution (minimum L1-misfit) of the directivity vector. The inversion is solved through a full grid search approach including reasonable intervals and increments for the involved parameters. The χ-parameter varies between 0 (pure unilateral rupture) to 0.5 (pure bilateral rupture). Average P-wave and S-wave velocities were measured *in-situ* (v_p = 5,800 m/s and v_s = 3,200 m/s, Zang et al., 2017), thus we can consider a rupture velocity interval between 0.7 v_s and 1.0 v_s. The rise time is not expected to be larger than 1/3 of the true duration (e.g., Stein and Wysession, 2003), thereby we test below 1/3 of the average apparent duration. Despite our knowledge about the rupture length is limited for this magnitude range, some reasonable values of 10–30 cm can be estimated for such range of magnitudes (e.g., Eshelby, 1957; Kwiatek et al., 2018); then, a broader interval from 1 to 30 cm is tested. A jackknife test is also applied to assess the uncertainties of each parameter, which are quantified by the mean and standard deviation calculated from the different iterations (see **Supplementary Table S1**).

DIRECTIVITY OF DECIMETER-SCALE ACOUSTIC EMISSION EVENTS

Theoretical predictions assuming unilateral and asymmetric bilateral rupture models are considered to adjust the 3D radiation pattern defined by the apparent durations previously identified at each AE sensor (**Figure 3A**). Such predictions are also compared using the 2D approach yielding similar results and azimuthal directivity directions (**Supplementary Figure S5**). We scan all possible directions in 3D by increments of 5° for both

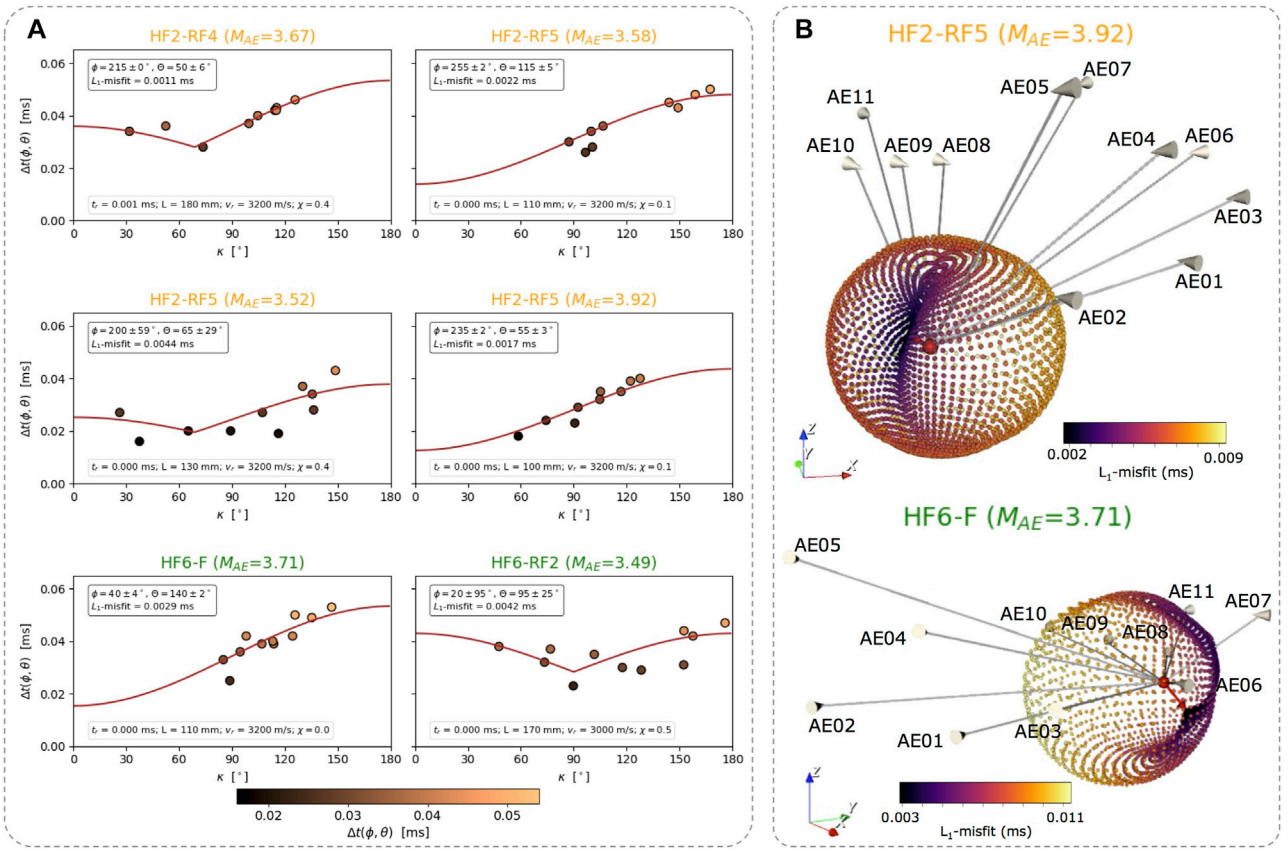

FIGURE 3 | Rupture directivity analysis in 3D for the target AE events recorded during HF2 and HF6 in the Äspö HRL. **(A)** For each target AE event, we show the apparent durations measurements (dots) along with the theoretical prediction (brown line) for the inverted model using a full grid search approach (labels indicate the solution of each parameter). **(B)** L1-misfit for each tested direction (dots) for the largest AE events recorded during HF2 **(top)** and HF6 **(bottom)**. The directivity vector solution with minimum L1-misfit (red arrow) and the station vectors (gray lines) for each AE sensor are also shown. Red dots indicate the origin of the coordinate system. The radius for each tested direction is also scaled according to the L1-misfit values as in the colorbar.

vector angles (ϕ, θ) and the L1-misfit is calculated for each tested direction (**Figure 3B**, **Supplementary Movies S1** and **S2**). The resulting rupture directivity vector is then defined by the minimum L1-misfit. **Figures 3**, **4** summarize the resulting inverted parameters from our 3D rupture directivity analysis (see also **Supplementary Table S1** and **Supplementary Movie S3**).

Despite our monitoring network configuration includes only AE sensors located above the injection borehole, robust results are inferred for four out of six target AE events ($M_{AE} > 3.52$), showing the best adjustments for L1-misfits < 0.003 ms and small uncertainties of <10° associated to the 3D-directivity directions defined by the ϕ and θ angles. These results reveal a slightly predominance of unilateral ruptures for three out of four AE events. Similar azimuthal directivity directions are observed for the AE events belonging to the same HF stimulations, being 200°–255° for HF2 and 20°–40° for HF6 (**Figures 3A**, **4A**). A predominant pattern along the vertical direction cannot be determined. Beside some intrinsic trade-offs among the involved parameters (Stich et al., 2020; López-Comino et al., 2021), we clearly identify high rupture velocities (3.14–3.20 km/s), very short rise times (<0.002 ms), and rupture lengths ranging 10–18 cm.

DISCUSSION AND CONCLUSIONS

Rupture directivity analysis is extended at mine-scale and can be recovered for microearthquakes recorded by 3D complex seismic monitoring configurations. The high-quality full waveforms recorded for the largest AE events during the HF2 and HF6 stimulations in the Äspö HRL has allowed us to estimate the apparent durations through the first pulses observed in the P-wave of the AE signals. We described a 3D-directivity approach where theoretical radiation patterns of apparent durations for unilateral and (asymmetric) bilateral ruptures are characterized by the introduction of a parameter κ, representing the angle between the directivity vector and the station vector. A full grid search is proposed to solve the inversion problem assessing the model performance through the L1-misfit in all plausible rupture directions and quantifying the associated uncertainties by a jackknife approach.

We recognize, for the first time, directivity effects for microfractures within granitic rock with magnitude as small as $M_w \sim -3.5$ and rupture length of ~13 cm lengths. Given the small number and narrow band of target magnitudes, no empirical

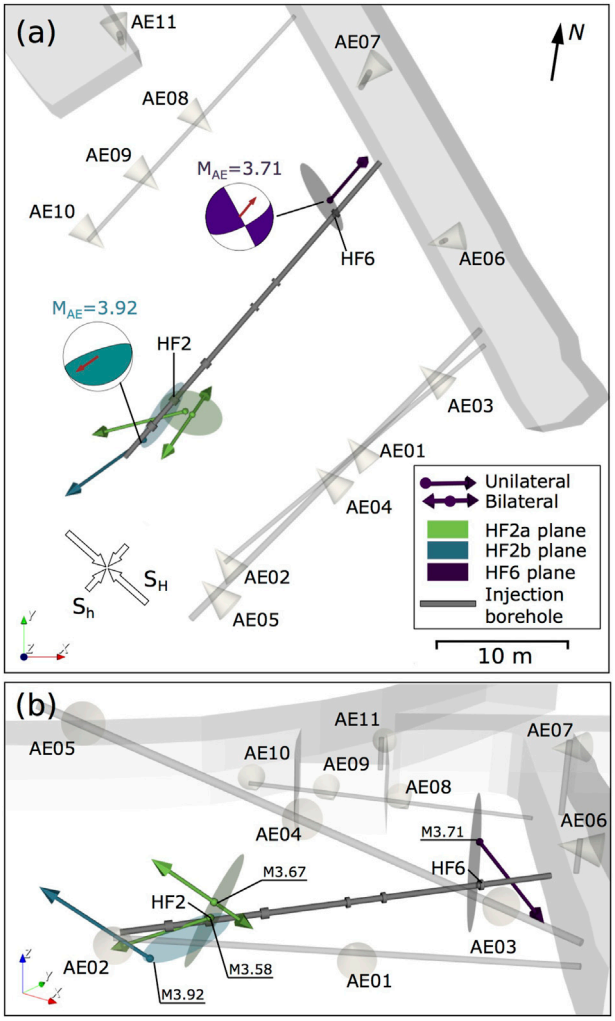

FIGURE 4 | 3D views of the resulting rupture directivity vectors for the four largest target AE events in the Äspö HRL: **(A)** top view and **(B)** perspective view. Planar seismogenic regions identified by the AE activity (Niemz et al., 2020) are shown considering the hypocentral locations of our target events. The AE sensors are located in nearby boreholes and tunnel; they are oriented toward the stimulated volume along the 28-m-long injection borehole. Focal mechanisms obtained by Kwiatek et al. (2018) for the largest AE event in HF2 and HF6 are shown with their rupture directivity vectors (brown arrows) in **(A)**. M_{AE} is indicated for the target events in **(B)**.

relationships between magnitude and rupture length can be derived from our results (**Supplementary Figure S6**). Similar average apparent durations ($\bar{t}$) are observed for all target AE events. Thereby, in these cases the rupture length is mostly controlled by the rupture propagation mode, being larger for (asymmetric) bilateral ruptures and shorter for unilateral ruptures. Accordingly, when considering fixed values of rupture length, rise time and rupture velocity, the apparent durations decrease from unilateral to pure bilateral ruptures (**Supplementary Figure S4**).

Our results can resolve the fault plane ambiguities for the largest AE events in HF2 and HF6, when taking into account the moment tensor solutions reported in Kwiatek et al. (2018). Indeed, rupture vectors are always coplanar to one of the potential fault planes (see **Figure 4A** and the indicated rupture directivity vectors in the moment tensor solutions). Similar conclusions were drawn from a moment tensor study of hydrofrac-induced AE events in salt (Dahm et al., 1999). On the other hand, multiple fractures planes were inferry a 2D approximation of the ellipsoidal AE clusters revealing some strike variations and steep dipping angles (Niemz et al., 2020). Rupture directivity vectors can be discussed with respect to these main planes, considering the hypocentral locations of target AE events (**Figure 4**). For example, a secondary fracture zone mapped in HF2–RF4 and HF2–RF5, with a predominantly grew during the shut-in phase, is roughly aligned with the rupture vector of the largest AE event, which is controlled by the interaction with the previously fractured zone of HF1. For the remaining studied AEs, however, the rupture planes that we identify are inclined, when not perpendicular, to the larger scale (few meters) planar seismogenic regions(**Figure 4B**). Co-seismic rupture planes out of the plane of the hydrofracture were also found by a directivity analysis of AE in salt rock (Dahm, 2001). This confirms a clear difference among the orientation of the large scale extension of the fractured region, and the small scale orientation of single fracture planes. Indeed, single focal mechanisms already indicated a significant variability (Kwiatek et al., 2018), except for their pressure axes being consistently oriented according to a common stress field (i.e., σ_H oriented NE-SW to NNE-SSW).

The discussed mine-scale HF experiments in deep underground laboratories bear us also the chance to discuss rupture directivity patterns, which have been proposed for larger scale seismicity. Fluid-induced seismic processes have been observed over a broad range of spatial scales (Davies et al., 2013; Schultz et al., 2020), and very often with dense dedicated networks, which allow to resolve the rupture propagation for small to moderate earthquakes (e.g., $1.0 < M_w < 5.8$). Lui and Huang (2019) calculated the directivity effects of the largest induced Oklahoma earthquakes and attributed the difference in rupture directions to expected pressurization of the fault zone, which relates to the distance away from injection zones and total injected volume. Folesky et al. (2016) analyzed the rupture directivity of the largest seismic events associated with the stimulation of geothermal reservoir in Basel (Switzerland) and found that the preferred rupture propagation depends on magnitude; events with local magnitude larger than two propagated backward into the perturbed volume while smaller events propagated away from the well. These studies suggest that the fluid injection has an effect on directional properties of the earthquake rupture processes. In this sense, our analysis evidences a predominant pattern of rupture directivity directions, as they are in general well aligned with the orientation of the minimum horizontal stress (e.g., Nolen-Hoeksema and Ruff 2001; Zang and Stephansson 2010); a preferred rupture directivity toward or away from the injection point is, however, not identified.

While based on a limited dataset, our findings suggest that the local stress condition may control the predominant direction of the rupture growth, beside the large scale distribution of AE locations and the pressure axis of the focal mechanism. This study confirms that directivity effects persist even at decimeter-scale ruptures and extends our knowledge to better understand the triggering processes of fluid-injection-induced earthquakes.

DATA AVAILABILITY STATEMENT

Publicly available datasets were analyzed in this study. This data can be found here: The datasets selected for this study are available via request to the authors. Catalogue of induced AEs from Niemz et al. (2020). Moment tensor solutions were extracted from Kwiatek et al. (2018).

AUTHOR CONTRIBUTIONS

JL-C and SC planned the research. JL-C has realized the rupture directivity analysis, supervised by SC; PN compiled the data and realized the movies of the results. JL-C prepared the initial draft and figures, with contributions and editing from all authors. AZ was the principal investigator of the 2015 mine-scale Äspö HRL underground experiments. All authors have contributed to the interpretation and discussion.

FUNDING

This research has been funded by the European Union's Horizon 2020 research and innovation programme under the Marie Skłodowska-Curie grant agreement N° 754446 and UGR Research and Knowledge Transfer Found – Athenea3i; and by the Deutsche Forschungsgemeinschaft (DFG, German Research Foundation) – Projektnummer (407141557). SC and PN received funding from the EU project PostMinQuake, RFCS (899192). AZ was supported by funding received from the European Union's Horizon 2020 research and innovation programme, Grant Agreement No. 691728 (Destress).

ACKNOWLEDGMENTS

The *in situ* experiment at Äspö Hard Rock Laboratory (HRL) was supported by the GFZ German Research Center for Geosciences (75%), the KIT Karlsruhe Institute of Technology (15%) and the Nova Center for University Studies, Research and Development Oskarshamn (10%). An additional in-kind contribution of the Swedish Nuclear Fuel and Waste Management Co. (SKB) for using Äspö HRL as test site for geothermal research is greatly acknowledged.

SUPPLEMENTARY MATERIAL

The Supplementary Material for this article can be found online at: https://www.frontiersin.org/articles/10.3389/feart.2021.670757/full#supplementary-material

REFERENCES

Abercrombie, R. E., Poli, P., and Bannister, S. (2017). Earthquake Directivity, Orientation, and Stress Drop within the Subducting Plate at the Hikurangi Margin, New Zealand. *J. Geophys. Res. Solid Earth* 122 (10), 188. doi:10.1002/2017JB014935

Ammon, C. J., Kanamori, H., Lay, T., and Velasco, A. A. (2006). The 17 July 2006 Java Tsunami Earthquake. *Geophys. Res. Lett.* 33. doi:10.1029/2006GL028005

An, C., Yue, H., Sun, J., Meng, L., and Báez, J. C. (2017). The 2015 Mw 8.3 Illapel, Chile, Earthquake: Direction-Reversed Along-Dip Rupture with Localized Water Reverberation. *Bull. Seismological Soc. America* 107 (5), 2416–2426. doi:10.1785/0120160393

Beck, S. L., Silver, P., Wallace, T. C., and James, D. (1995). Directivity Analysis of the Deep Bolivian Earthquake of June 9, 1994. *Geophys. Res. Lett.* 22, 2257–2260. doi:10.1029/95gl01089

Calderoni, G., Rovelli, A., Ben-Zion, Y., and Di Giovambattista, R. (2015). Along-strike Rupture Directivity of Earthquakes of the 2009 L'Aquila, Central Italy, Seismic Sequence. *Geophys. J. Int.* 203 (1), 399–415. doi:10.1093/gji/ggv275

Cesca, S., Heimann, S., and Dahm, T. (2011). Rapid directivity detection by azimuthal amplitude spectra inversion. *J. Seismol.* 15, 147–164. doi:10.1007/s10950-010-9217-4

Dahm, T., Manthei, G., and Eisenblätter, J. (1999). Automated Moment Tensor Inversion to Estimate Source Mechanisms of Hydraulically Induced Microseismicity in Salt Rock. *Tectonophysics* 306, 1–17. doi:10.1016/s0040-1951(99)00041-4

Dahm, T. (2001). Rupture Dimensions and Rupture Processes of Fluid-Induced Microcracks in Salt Rock. *J. Volcanology Geothermal Res.* 109, 149–162. doi:10.1016/s0377-0273(00)00309-7

Davies, R., Foulger, G., Bindley, A., and Styles, P. (2013). Induced Seismicity and Hydraulic Fracturing for the Recovery of Hydrocarbons. *Mar. Pet. Geology.* 45, 171–185. doi:10.1016/j.marpetgeo.2013.03.016

Dresen, G., Renner, J., Bohnhoff, M., Konietzki, H., Kwiatek, G., Klee, G., et al. (2019). STIMTEC—a Mine-Back Experiment in the Reiche Zeche Underground Laboratory. *Geophys. Res. Abstr.* 21, EGU2019–9357.

Eshelby, J. D. (1957). The Determination of the Elastic Field of an Ellipsoidal Inclusion, and Related Problems. *Proc. R. Soc. A: Math. Phys. Sci.* 241 (1226), 376–396. doi:10.1098/rspa.1957.0133

Fan, W., and McGuire, J. J. (2018). Investigating Microearthquake Finite Source Attributes with IRIS Community Wavefield Demonstration Experiment in Oklahoma. *Geophys. J. Int.* 214 (2), 1072–1087. doi:10.1093/gji/ggy203

Folesky, J., Kummerow, J., Shapiro, S. A., Häring, M., and Asanuma, H. (2016). Rupture Directivity of Fluid-Induced Microseismic Events: Observations from an Enhanced Geothermal System. *J. Geophys. Res.* 121 (11), 8034–8047. doi:10.1002/2016jb013078

Fukao, Y. (1972). Source Process of a Large Deep-Focus Earthquake and its Tectonic Implications - the Western Brazil Earthquake of 1963. *Phys. Earth Planet. Interiors* 5, 61–76. doi:10.1016/0031-9201(72)90074-x

Gischig, V. S., Doetsch, J., Maurer, H., Krietsch, H., Amann, F., Evans, K. F., et al. (2018). On the Link between Stress Field and Small-Scale Hydraulic Fracture Growth in Anisotropic Rock Derived from Microseismicity. *Solid Earth* 9 (1), 39–61. doi:10.5194/se-9-39-2018

Hartzell, S. H. (1978). Earthquake Aftershocks as Green's Functions. *Geophys. Res. Lett.* 5, 1–4. doi:10.1029/gl005i001p00001

Haskell, N. (1964). Total Energy and Energy Spectral Density of Elastic Wave Radiation from Propagating Faults. *Bull. Seismological Soc. America* 54 (6A), 1811–1841.

Huang, H.-H., Aso, N., and Tsai, V. (2017). Toward Automated Directivity Estimates in Earthquake Moment Tensor Inversion. *Geophys. J. Int.* 211, 1084–1098. doi:10.1093/gji/ggx354

Kane, D. L., Shearer, P. M., Goertz-Allmann, B. P., and Vernon, F. L. (2013). Rupture Directivity of Small Earthquakes at Parkfield. *J. Geophys. Res. Solid Earth* 118, 212–221. doi:10.1029/2012JB009675

Kikuchi, M., and Ishida, M. (1993). Source Retrieval for Deep Local Earthquakes with Broadband Records. *Bull. Seismol. Soc. Am.* 83, 1855–1870.

Király-Proag, E., Satriano, C., Bernard, P., and Wiemer, S. (2019). Rupture Process of the Mw 3.3 Earthquake in the St. Gallen 2013 Geothermal Reservoir, Switzerland. *Geophys. Res. Lett.* 46, 7990–7999. doi:10.1029/2019GL082911

Kneafsey, T. J., Dobson, P., Blankenship, D., Morris, J., Knox, H., Schwering, P., et al. (2018). An Overview of the EGS Collab Project: Field Validation of Coupled Process Modeling of Fracturing and Fluid Flow at the Sanford Underground Research Facility, Lead, SD, *Proceedings of the 43rdWorkshop on Geothermal Reservoir Engineering*. Stanford, CA: SGP-TR-213Stanford University.

Kolár, P., Petruzálek, M., Lokajícek, T., Síleny, J., Jechumtálova, Z., Adamová, P., et al. (2020). Acoustic Emission Events Interpreted in Terms of Source Directivity. *Pure Appl. Geophys*. 177, 4271–4288doi:10.1007/s00024-020-02517-w

Kurzon, I., Vernon, F. L., Ben-Zion, Y., and Atkinson, G. (2014). Ground Motion Prediction Equations in the San Jacinto Fault Zone: Significant Effects of Rupture Directivity and Fault Zone Amplification. *Pure Appl. Geophys.* 171 (11), 3045–3081. doi:10.1007/s00024-014-0855-2

Kwiatek, G., Martínez-Garzón, P., and Bohnhoff, M. (2016). HybridMT: A MATLAB/Shell Environment Package for Seismic Moment Tensor Inversion and Refinement. *Seismological Res. Lett.* 87 (4), 964–976. doi:10.1785/0220150251

Kwiatek, G., Martínez-Garzón, P., Plenkers, K., Leonhardt, M., Zang, A., von Specht, S., et al. (2018). Insights into Complex Subdecimeter Fracturing Processes Occurring during a Water Injection Experiment at Depth in Äspö Hard Rock Laboratory, Sweden. *J. Geophys. Res. Solid Earth* 123, 6616–6635. doi:10.1029/2017JB014715

López-Comino, J.-Á., Mancilla, F. d. L., Morales, J., and Stich, D. (2012). Rupture Directivity of the 2011, Mw 5.2 Lorca Earthquake (Spain). *Geophys. Res. Lett.* 39, a–n. doi:10.1029/2011GL050498

López-Comino, J. A., Braun, T., Dahm, T., Cesca, S., and Danesi, S. (2021). On the Source Parameters and Genesis of the 2017, Mw 4 Montesano Earthquake in the Outer Border of the Val d'Agri Oilfield (Italy). *Front. Earth Sci.* doi:10.3389/feart.2020.617794

López-Comino, J. A., Cesca, S., Heimann, S., Grigoli, F., Milkereit, C., Dahm, T., et al. (2017). Characterization of Hydraulic Fractures Growth during the Äspö Hard Rock Laboratory Experiment (Sweden). *Rock Mech. Rock Eng.* 50 (11), 2985–3001. doi:10.1007/s00603-017-1285-0

López-Comino, J. A., and Cesca, S. (2018). Source Complexity of an Injection Induced Event: The 2016 Mw 5.1 Fairview, Oklahoma Earthquake. *Geophys. Res. Lett.* 45, 4025–4032. doi:10.1029/2018GL077631

López-Comino, J. A., Stich, D., Morales, J., and Ferreira, A. M. G. (2016). Resolution of Rupture Directivity in Weak Events: 1-D versus 2-D Source Parameterizations for the 2011, Mw 4.6 and 5.2 Lorca Earthquakes, Spain. *J. Geophys. Res. Solid Earth* 121, 6608–6626. doi:10.1002/2016JB013227

Lui, S. K., and Huang, Y. (2019). Do injection-induced earthquakes rupture away from injection wells due to fluid pressure change? *Bull. Seismol. Soc. Am.* 109 (1), 358–371.

Maghsoudi, S., Cesca, S., Hainzl, S., Kaiser, D., Becker, D., and Dahm, T. (2013). Improving the Estimation of Detection Probability and Magnitude of Completeness in Strongly Heterogeneous Media, an Application to Acoustic Emission (AE). *Geophys. J. Int.* 193, 1556–1569.

Manthei, G., Eisenblätter, J., and Dahm, T. (2001). Moment Tensor Evaluation of Acoustic Emission Sources in Salt Rock. *Constr. Build. Mater.* 193, 297–309. doi:10.1093/gji/ggt049

McGuire, J. J. (2017). A Matlab Toolbox for Estimating the Second Moments of Earthquake Ruptures. *Seismological Res. Lett.* 88 (2A), 371–378. doi:10.1785/0220160170

McGuire, J. J. (2004). Estimating Finite Source Properties of Small Earthquake Ruptures. *Bull. Seismological Soc. America* 94 (2), 377–393. doi:10.1785/0120030091

McGuire, J. J., Zhao, L., and Jordan, T. H. (2002). Predominance of Unilateral Rupture for a Global Catalog of Large Earthquakes. *Bull. Seismological Soc. America* 92 (8), 3309–3317. doi:10.1093/gji/ggt04910.1785/0120010293

Meng, H., McGuire, J. J., and Ben-Zion, Y. (2020). Semiautomated Estimates of Directivity and Related Source Properties of Small to Moderate Southern California Earthquakes Using Second Seismic Moments. *J. Geophys. Res. Solid Earth* 125, e2019JB018566. doi:10.1029/2019JB018566

Niemz, P., Cesca, S., Heimann, S., Grigoli, F., von Specht, S., Hammer, C., et al. (2020). Full-waveform-based Characterization of Acoustic Emission Activity in a Mine-Scale Experiment: a Comparison of Conventional and Advanced Hydraulic Fracturing Schemes. *Geophys. J. Int.* 222 (1), 189–206. doi:10.1093/gji/ggaa127

Nolen-Hoeksema, R. C., and Ruff, L. J. (2001). Moment Tensor Inversion of Microseisms from the B-Sand Propped Hydrofracture, M-Site, Colorado. *Tectonophysics* 336, 163–181. doi:10.1016/s0040-1951(01)00100-7

Ono, K. (2018). Frequency Dependence of Receiving Sensitivity of Ultrasonic Transducers and Acoustic Emission Sensors. *Sensors* 18, 3861. doi:10.3390/s18113861

Park, S., and Ishii, M. (2015). Inversion for Rupture Properties Based upon 3-D Directivity Effect and Application to Deep Earthquakes in the Sea of Okhotsk Region. *Geophys. J. Int.* 203, 1011–1025. doi:10.1093/gji/ggv352

Ross, Z. E., Trugman, D. T., Azizzadenesheli, K., and Anandkumar, A. (2020). Directivity Modes of Earthquake Populations with Unsupervised Learning. *J. Geophys. Res. Solid Earth* 125, e2019JB018299. doi:10.1029/2019JB018299

Schoenball, M., Ajo-Franklin, J. B., Blankenship, D., Chai, C., Chakravarty, A., Dobson, P., et al.The EGS Collab Team (2020). Creation of a Mixed-Mode Fracture Network at Meso-Scale through Hydraulic Fracturing and Shear Stimulation. *J. Geophys. Res. Solid Earth* 125, e2020JB019807. doi:10.1029/2020jb019807

Schultz, R., Skoumal, R. J., Brudzinski, M. R., Eaton, D., Baptie, B., and Ellsworth, W. (2020). Hydraulic Fracturing-Induced Seismicity. *Rev. Geophys.* 58, e2019RG000695. doi:10.1029/2019RG000695

Stein, W., and Wysession, M. (2003). *An Introduction to Seismology, Earthquakes, and Earth Structure*. Malden, Mass: Blackwell, 498.

Stich, D., Martín, R., Morales, J., López-Comino, J. Á., and Mancilla, F. d. L. (2020). Slip Partitioning in the 2016 Alboran Sea Earthquake Sequence (Western Mediterranean). *Front. Earth Sci.* 8, 587356. doi:10.3389/feart.2020.587356

Tibi, R., Estabrook, C. H., and Bock, G. (1999). The 1996 June 17 Flores Sea and 1994 March 9 Fiji-Tonga Earthquakes: Source Processes and Deep Earthquake Mechanisms. *Geophys. J. Int.* 138, 625–642. doi:10.1046/j.1365-246x.1999.00879.x

Tilmann, F., Zhang, Y., Moreno, M., Saul, J., Eckelmann, F., Palo, M., et al. (2016). The 2015 Illapel Earthquake, Central Chile: a Type Case for a Characteristic Earthquake?. *Geophys. Res. Lett.* 43 (2), 574–583. doi:10.1002/2015gl066963

Villiger, L., Gischig, V. S., Doetsch, J., Krietsch, H., Dutler, N. O., Jalali, M., et al. (2020). Influence of Reservoir Geology on Seismic Response during Decameter-Scale Hydraulic Stimulations in Crystalline Rock. *Solid Earth* 11 (2), 627–655. doi:10.5194/se-11-627-2020

Villiger, L., Gischig, V. S., Kwiatek, G., Krietsch, H., Doetsch, J., Jalali, M., et al. (2021). Metre-scale Stress Heterogeneities and Stress Redistribution Drive Complex Fracture Slip and Fracture Growth during a Hydraulic Stimulation Experiment. *Geophys. J. Int.* 225, 1689–1703. doi:10.1093/gji/ggab057

Warren, L. M., and Shearer, P. M. (2006). Systematic Determination of Earthquake Rupture Directivity and Fault Planes from Analysis of Long-periodP-Wave Spectra. *Geophys. J. Int.* 164 (1), 46–62. doi:10.1111/j.1365-246X.2005.02769.x

Wu, Q., Chen, X., and Abercrombie, R. E. (2019). Source Complexity of the 2015 Mw 4.0 Guthrie, Oklahoma Earthquake. *Geophys. Res. Lett.* 46, 4674–4684. doi:10.1029/2019GL082690

Zang, A., Stephansson, O., Stenberg, L., Plenkers, K., Specht, S., Milkereit, C., et al. (2017). Hydraulic Fracture Monitoring in Hard Rock at 410 M Depth with an Advanced Fluid-Injection Protocol and Extensive Sensor Array. *Geophys. J. Int.* 208 (2), 790–813. doi:10.1093/gji/ggw430

Zang, A., and Stephansson, O. (2010). *Stress Field of the Earth's Crust*. Dordrecht: Springer, 322. doi:10.1007/978-1-4020-8444-7

Conflict of Interest: The authors declare that the research was conducted in the absence of any commercial or financial relationships that could be construed as a potential conflict of interest.

The handling editor (APR) declared a past co-authorship with one of the authors (TD).

frontiers in Earth Science

ORIGINAL RESEARCH
published: 17 May 2021
doi: 10.3389/feart.2021.670771

Fault Triggering Mechanisms for Hydraulic Fracturing-Induced Seismicity From the Preston New Road, UK Case Study

Tom Kettley[1*†] *and James P. Verdon*[2†]

[1]*Department of Earth Sciences, University of Oxford, Oxford, United Kingdom,* [2]*School of Earth Sciences, University of Bristol, Bristol, United Kingdom*

We investigate the physical mechanisms governing the activation of faults during hydraulic fracturing. Recent studies have debated the varying importance of different fault reactivation mechanisms in different settings. Pore pressure increase caused by injection is generally considered to be the primary driver of induced seismicity. However, in very tight reservoir rocks, unless a fracture network exists to act as a hydraulic conduit, the rate of diffusion may be too low to explain the spatio-temporal evolution of some microseismic sequences. Thus, elastic and poroelastic stress transfer and aseismic slip have been invoked to explain observations of events occurring beyond the expected distance of a reasonable diffusive front. In this study we use the high quality microseismic data acquired during hydraulic fracturing at the Preston New Road (PNR) wells, Lancashire, UK, to examine fault triggering mechanisms. Injection through both wells generated felt induced seismicity—an M_L 1.6 during PNR-1z injection in 2018 and an M_L 2.9 during PNR-2 in 2019—and the microseismic observations show that each operation activated different faults with different orientations. Previous studies have already shown that PNR-1z seismicity was triggered by a combination of both direct hydraulic effects and elastic stress transfer generated by hydraulic fracture opening. Here we perform a similar analysis of the PNR-2 seismicity, finding that the PNR-2 fault triggering was mostly likely dominated by the diffusion of increased fluid pressure through a secondary zone of hydraulic fractures. However, elastic stress transfer caused by hydraulic fracture opening would have also acted to promote slip. It is significant that no microseismicity was observed on the previously activated fault during PNR-2 operations. This dataset therefore provides a unique opportunity to estimate the minimum perturbation required to activate the fault. As it appears that there was no hydraulic connection between them during each stimulation, any perturbation caused to the PNR-1z fault by PNR-2 stimulation must be through elastic or poroelastic stress transfer. As such, by computing the stress transfer created by PNR-2 stimulation onto the PNR-1z fault, we are able to approximate the minimum bound for the required stress perturbation: in excess of 0.1 MPa, orders of magnitude larger than stated estimates of a generalized triggering threshold.

Keywords: induced seismicity, geomechanics, stress modeling, microseismicity, hydraulic fracturing

OPEN ACCESS

Edited by:
Francesco Grigoli,
ETH Zürich, Switzerland

Reviewed by:
Louis De Barros,
UMR7329 Géoazur (GEOAZUR), France
Ryan Schultz,
Stanford University, United States

****Correspondence:***
Tom Kettley
tom.kettley@earth.ox.ac.uk

†These authors have contributed equally to this work and share first authorship

Specialty section:
This article was submitted to Solid Earth Geophysics, a section of the journal Frontiers in Earth Science

Received: *22 February 2021*
Accepted: *04 May 2021*
Published: *17 May 2021*

Citation:
Kettley T and Verdon JP (2021) Fault Triggering Mechanisms for Hydraulic Fracturing-Induced Seismicity From the Preston New Road, UK Case Study. Front. Earth Sci. 9:670771. doi: 10.3389/feart.2021.670771

INTRODUCTION

Felt induced seismicity occurs when industrial activities create stress changes in the subsurface that reactivate faults. This phenomenon has affected a wide range of industries, including hydroelectric reservoir impoundment (e.g., Gupta, 1992); mining (e.g., Verdon et al., 2018); waste-water disposal (e.g., Keranen et al., 2014); deep geothermal energy extraction (e.g., Grigoli et al., 2018); depletion of conventional hydrocarbon reservoirs (e.g., Bourne et al., 2014); hydraulic fracturing in shale gas reservoirs (e.g., Bao and Eaton, 2016; Lei et al., 2019; Kettley et al., 2019; Verdon and Bommer, 2020; Schultz et al., 2020); natural gas storage (e.g., Cesca et al., 2014); and carbon capture and storage (e.g., Stork et al., 2015).

In some cases, induced seismic events have been of sufficient magnitude to cause significant amounts of damage to nearby buildings and infrastructure. Even where events have not been of sufficient size to cause damage, cases where events are of sufficient magnitude to be felt by the nearby public have caused concern that has, in a number of cases, led to the shut-down of the causative activities (e.g., Deichmann and Giardini, 2009; Cesca et al., 2014; Kettley et al., 2021). As such, it is of great importance to better understand what physical processes underpin the activation of faults by injection, and determine the geologic factors which most strongly affect the likelihood for a particular operation to trigger felt seismicity.

In the UK, 3 wells have been hydraulically fractured in the Fylde Peninsula, Lancashire, targeting the gas-bearing Carboniferous Bowland Shale Formation, and all three have caused induced seismicity (see Clarke et al., 2014; Clarke et al., 2019a; Kettley et al., 2021). In 2011, stimulation of the Preese Hall well was halted after triggering a M_L 2.3 event (Clarke et al., 2014). This led to a moratorium on shale gas hydraulic fracturing imposed by the UK government lasting several years, during which Traffic Light System (TLS) regulations were imposed, with a "red light" magnitude of M_L 0.5. In 2018, the Preston New Road PNR-1z well was stimulated. Stimulation of this well was paused on several occasions as $M_L > 0.5$ events were triggered, with the largest reaching M_L 1.5 (Clarke et al., 2019a). In 2019, the adjacent PNR-2 well was stimulated. On the 26th August, the operations triggered an M_L 2.9 earthquake (Kettley et al., 2021), in response to which the UK government has imposed a further moratorium on shale gas hydraulic fracturing.

Processes that lead to fault reactivation during subsurface fluid injection are typically considered with respect to their impact on the stress conditions in the rock mass. For a given fault, the *in situ* stress field can be resolved into normal (σ_n) and shear (τ) stresses. The Mohr–Coulomb failure envelope describes the conditions at which fault slip will begin to occur:

$$\tau > \mu_{fric}(\sigma_n - P) + C \quad (1)$$

where P is the pore pressure, μ_{fric} is the friction coefficient and C is the fault cohesion. The proximity of the *in situ* stress state to the Mohr–Coulomb threshold can be re-written in terms of the Coulomb failure stress, CFS:

$$CFS = \tau - \mu_{fric}(\sigma_n - P) \quad (2)$$

If a process causes a perturbation that increases CFS (with a change in CFS noted hereafter as ΔCFS) then it will move the fault toward the failure threshold, increasing the likelihood of seismicity occurring. In discussing triggering stress changes (i.e., a ΔCFS), cohesion C is often assumed to be negligible, which may be the case for faults which are very close to failure, or "critically stressed". As will be discussed, the accuracy of this assumption is still a matter of debate in determining the magnitudes of stress required to trigger fault slip.

Subsurface injection will always cause an increase in pore pressure, since additional fluid is added into the system. **Equation 1** shows that this will increase CFS, promoting faults to slip. Hence pore pressure increases associated with injection are typically considered to be the driving mechanism for injection-induced seismicity (e.g., Holland, 2013; Schultz et al., 2015; Verdon et al., 2019).

Subsurface fluid injection can also create geomechanical deformation, especially if injection pressures exceed the minimum pressure required to generate fracturing. Both fracturing and the poroelastic expansion of the rock frame associated with the increase of pressure within the rock pore spaces (e.g., Rice and Cleary, 1976) will perturb the stress field in the surrounding rocks. The impact this deformation has on σ_n or τ acting on a nearby fault will depend on the relative orientations and positions of both the fault in question and the deformation. If the deformation either decreases σ_n or increases τ (or does both) then it will promote slip, and potentially cause induced seismicity (e.g., Bao and Eaton, 2016; Deng et al., 2016; Kettley et al., 2020).

Elastic stress transfer effects from dislocations in the subsurface have been shown to control the positions of aftershock events after a large earthquake (e.g., Stein, 1999; Steacy et al., 2004), and of earthquakes associated with magma movement in volcanic settings (e.g., Toda et al., 2002; Green et al., 2015). Here, the process of deforming the rock matrix, through fault slip, fracture opening, or the intrusion of a dike, elastically changes the state of stress, inducing a ΔCFS which can act to trigger a nearby fault to slip.

Transfer of pore pressure perturbations through the rock pore space, from the injection point to the reactivated fault, requires time (often hours or days); whereas transfer of stress through the rock frame takes place instantaneously (or at least at the speed of a compressional wave, i.e. thousands of meters per second). Hence, event occurrences at a range of distances from an injection point within a short space of time might indicate events triggered by stress transfer, whereas a progression of events at increasing distances with time might indicate a process dominated by pore pressure diffusion (e.g., Shapiro et al., 1997; Shapiro, 2008; Shapiro and Dinske, 2009). Alternatively, the presence of pre-existing permeable fracture corridors, within otherwise low-permeability formations, may provide an alternative mechanism by which events could be induced at relatively large distances from an injection well within a short time period (e.g., Igonin et al., 2021). Aseismic slip has also been shown to induce stress changes and trigger felt seismicity, and has been invoked when the spatiotemporal evolution of seismicity outpaces fluid

diffusion but still is delayed with respect to elastic stress triggering (e.g., Bhattacharya and Viesca, 2019; Eyre et al., 2019). However, modeling of aseismic slip is a challenging process, depending heavily on rheological properties of the host shales and the stress history of the, often small, unmapped faults, both of which are frequently unavailable or generally poorly constrained, as is the case for PNR.

While a positive change in CFS is clearly required to produce fault reactivation, the necessary size of perturbation has remained a matter of debate. In some cases, very small perturbations (<0.01 MPa) have been proposed as being sufficient to have caused fault reactivation (e.g., Kilb et al., 2002; Shapiro et al., 2006; Westwood et al., 2017). In reality, fault criticality is a poorly constrained parameter, which calls into question the use of a general triggering threshold, and the implication that such small magnitude stress changes can induce fault slip in any given locale.

In the following work, we examine the spatiotemporal evolution of microseismicity during the Preston New Road hydraulic fracturing operations in 2019, and use it to characterize the dominant triggering mechanism, whether that be pore pressure diffusion or elastic stress transfer. We then, following the elastostatic modeling approach of Kettley et al. (2020) for PNR operations in 2018, model the elastostatic stress changes produced by the opening of hydraulic fractures. Using this method we show how stress was transferred onto the fault identified in the microseismic data, and assess whether the stress changes would have promoted slip.

One of the most interesting aspects of the PNR microseismicity is that the two wells (PNR-1z and PNR-2), despite being only 200 m apart, reactivated entirely different fault structures. There is no overlap in the microseismic events or induced seismicity generated by the two wells (Kettley et al., 2021). The PNR-1z well did not reactivate the PNR-2 fault, and the PNR-1z well did not reactivate the PNR-2 fault. As such, the perturbations created by stimulation of the PNR-2 well were insufficient to reactivate the PNR-1z fault, despite this fault already having been reactivated during stimulation of PNR-1z. Hence, by computing the perturbations created by PNR-2 injection on the PNR-1z fault, we are able to approximate a minimum bound for the magnitude of perturbation required to reactivate the fault.

PRESTON NEW ROAD HYDRAULIC FRACTURING

The hydraulic fracturing at the Preston New Road wells, and the resulting microseismicity and induced seismicity, has been described in detail by Clarke et al. (2019a) and Kettley et al. (2021). We recap key features here as they pertain to the analysis we present in this study.

In 2018 Cuadrilla Resources Limited (CRL) drilled two horizontal wells into the Upper and Lower Bowland Shale at the Preston New Road site, around 5 km east of the town of Blackpool in Lancashire, UK. The two wells targeted the two reservoir units, with 41 sliding sleeve stages planned on each well, evenly spaced along their ~1 km lateral sections. The first well was hydraulically fractured in October to December 2018, whilst the second was stimulated in August 2019. Microseismicity was monitored by a surface array, which administered the TLS and measured ground motions, and a downhole array, situated in the adjacent well. The downhole arrays were used to track fracture growth, and interaction with any faults, through the observation of microseismic events with magnitudes down to $M_W < -2.0$ [see Clarke et al. (2019a) and Kettley et al. (2021) for discussion of location and magnitude uncertainties].

The deeper well (PNR-1z), drilled to 2.3 km depth, was the first to be fracked: injection started on October 16th, 2018. Stages were frequently ended early due to seismicity concerns. $M_L > 0.0$ seismicity occurred during and after injection of several stages, exceeding the amber ($M_L > 0$) and red light ($M_L > 0.5$) TLS thresholds (Clarke et al., 2019a). Many of the injection sleeves were skipped in an effort to avoid particularly seismogenic areas around the well identified during operations. This can be seen in **Figure 1** by the gaps between worked sleeves for PNR-1z. Toward the end of October, an M_L 1.1 event occurred, and injection was paused throughout November in order to allow seismicity rates to subside. During this hiatus, microseismic observations illuminated a particularly seismogenic planar feature, the trend of which aligned closely to the focal mechanisms of the largest events. Low magnitude seismicity on this NE-SW trending feature (shown as a gray plane in **Figure 1** continued throughout the hiatus, whilst the other areas around the well became quiescent. This "fault zone" was termed "PNR-1zii" by the operator (Cuadrilla Resources Ltd., CRL, 2019). As discussed in Clarke et al. (2019a) and Kettley et al. (2021), it is not clear whether this feature is truly a single fault or a collection of similarly aligned pre-existing fractures, however, from here we will refer to it as the "PNR-1z NE fault", as the major structure responsible for felt seismicity during stimulation of PNR-1z.

PNR-1z operations recommenced in December 2018 and 5 further stages at the heel of the well were injected. During this time, the largest event of the 2018 operations (an M_L 1.6) occurred, within the PNR-1z NE fault zone. This event was felt on the pad, and by a few nearby members of the public.

The second well, PNR-2, targeting the Upper Bowland Shale, is situated ~250 m to the north and ~200 m above PNR-1z. Operations started at the toe of the well (Stage 1) on the August 15, 2019, and continued sequentially through to the 7th stage. The first 5 stages proceeded with full volumes of fluid and proppant injected, and no induced seismicity exceeding the TLS thresholds. The majority of microseismic events occurred on a NS trending feature extending roughly 300 m in either direction from the well (shown in blue in **Figure 1**). The structure delineated by these events is aligned closely to the maximum stress direction (~170°; Fellgett et al., 2017; Clarke et al., 2019b) and thus the events are assumed to track the growth of hydraulic fractures from the well. A smaller, more diffuse cluster of microseismic events developed around 100 m west of the main NS zone during Stages 2 and 3. This is shown in green in **Figure 1** and labeled the "Westward cluster". Hours after the end of Stage 4, another cluster developed 100 m east of the injected interval. This "Eastern cluster" (shown in yellow in **Figure 1**) grew during Stage 5, to reveal another cluster

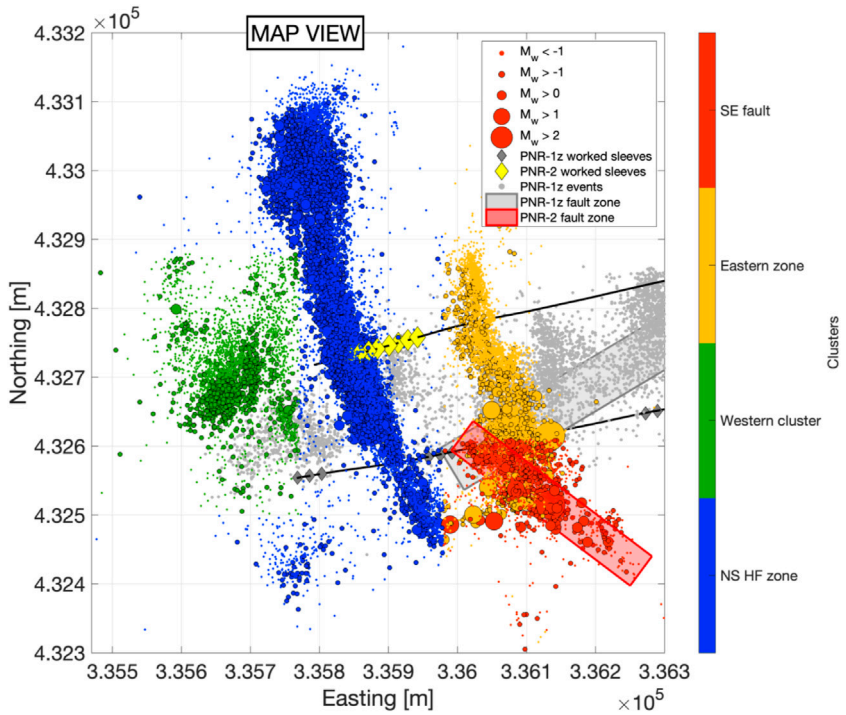

FIGURE 1 | Map view of PNR microseismic event locations, sized by magnitude and colored by cluster, focused on the PNR-2 events. The well paths are shown by the black lines, and sleeve locations (the points from which each stage was injected) are shown as yellow diamonds. Coordinates shown here use the Ordnance Survey United Kingdom grid system, which continues throughout, with the background grid showing 100 m increments.

trending parallel with the maximum stress direction, seemingly another zone of HF growth spatially separated from the main NS zone. As discussed in Kettley et al. (2021), the separation of this area of inferred HF growth could be attributed to a stress shadow effect, with increased breakdown pressure either side of the main NS zone due to the large increase in normal stress. The exact mechanism underpinning this separation is under investigation.

Hours after Stage 6, on the August 21, 2019, activity increased at the southern tip of this eastern zone of suspected HF growth, and several $M_L > 0.5$ events occurred, including an M_L 1.5 event. Seismicity was paused for one day, with Stage 7 conducted on the 23rd August, using a reduced injected volume and higher viscosity injected fluid in an effort to lessen the likelihood of further seismicity. Hours after Stage 7 was completed, activity in the Eastern Zone increased and larger magnitude events began to occur at its southern tip. One day after the end of injection of Stage 7, an M_L 2.1 event occurred in this SE zone, followed on the 26th August by the largest event of the 2019 seismicity, with M_L 2.9. The NW-SE-trending fault zone that hosted these events was referred to by the operator and in Kettley et al. (2020) as "PNR-2i", but here we will refer to it as the "PNR-2 SE fault (SEF)", since it is the key structure responsible for the larger-magnitude events during PNR-2 stimulation. **Figure 2** shows the locations and orientations of PNR-1z and PNR-2 faults in detail.

The focal mechanisms of the large events hosted on the two faults are also shown in **Figure 2A**. Whilst they appear similar (steeply dipping strike-slip, with nodal planes ~45° from N), the structures in microseismic reveal the fault plane from the auxiliary plane. As shown in Kettley et al. (2021), there was very little overlap in the location of microseismic events between the 2018 and 2019 periods of activity, and the largest events are clearly located on two different structures. The edges of the fault activated in 2019 during PNR-2 operations were delineated by the microseismic aftershocks that occurred in the hours after the ML 2.9 event, clearly showing its NW-SE trend (Kettley et al., 2021). With the maximum stress direction at PNR being ~170° (Fellgett et al., 2017; Clarke et al., 2019) both faults are relatively well-oriented for failure (Kettley et al., 2021), with the PNR-2 fault being slightly closer to the optimal orientation. These closely spaced conjugate fault zones exemplify the heavily faulted nature of the Bowland Basin and Fylde peninsula (as described in Corfield et al., 1996; Guion et al., 2000; Anderson and Underhill, 2020).

Kettley et al. (2020) showed that the spatial distribution of the PNR-1z microseismicity was consistent with being triggered by static stress transfer from the opening of hydraulic fractures. Events preferentially occurred in areas where, for NE-SW trending structures (i.e., the PNR-1z NEF or fracture zone), shear stress increased or normal stress decreased such that ΔCFS was positive. Kettley et al. (2020) identified further evidence for the role of stress triggering in the spatio-temporal evolution of the PNR-1z microseismicity: events were observed

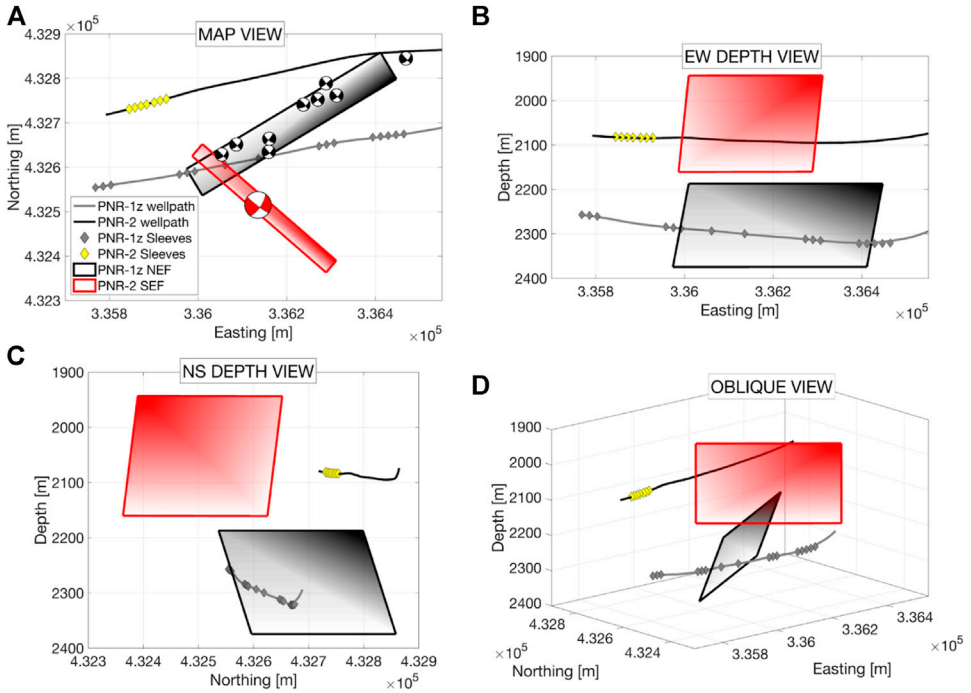

FIGURE 2 | Locations and orientations of the two fault zones activated during hydraulic fracturing operations at Preston New Road. The PNR-1z NE fault, shown by the black plane, was identifed from the locations and FMs of the largest events to occur during PNR-1z operations in 2018 (Clarke et al., 2019a), which are shown as black lower hemisphere beach balls in **(A)**, a map view. The PNR-2 SE fault (shown by the red plane) was constrained from the FM of the ML 2.9 event, shown as a red beach ball in **(A)**, as well as the hypocenters of its microseismic aftershocks (see Kettley et al., 2021, Figure 6). Shading across the planes shown here attempts to aid visualization of the fault orientations in 3-dimensions **(B)** and **(C)**.

to occur at a range of positions near instantaneously, rather than with increasing distance as a function of time, which might be expected if pore pressure diffusion was playing a dominant role.

In the following section, we will use similar methods to assess the triggering mechanisms at play during PNR-2 operations.

SPATIOTEMPORAL EVOLUTION

The evolution of microseismic event distances from the injection point with time can reveal the underlying physical mechanisms that are driving the events (e.g., Shapiro and Dinske, 2009). Shapiro et al. (1997) show that, if microseismicity is driven by pore pressure diffusion from the injection point, then for constant-rate injection a triggering front should develop that extends in distance, r, from the injection point as a function of time t:

$$r = \sqrt{4\pi D t} \tag{3}$$

where D is the hydraulic diffusivity. The diffusive case can be contrasted with the case of hydraulic fracture propagation where, assuming minimal leak-off of fracturing fluid, the length of hydraulic fracture propagation might be expected to show a linear time-distance relationship, since the length of a hydraulic fracture L scales with the injection rate Q, the height h_f and width w_f of the hydraulic fracture (Economides and Nolte, 2003; Shapiro and Dinske., 2009):

$$L = \frac{Qt}{2h_f w_f} \tag{4}$$

It is clear that this is a simplified model, and represents the upper bound in the distance a single hydraulic fracture could extend with minimal leak off. In **Figure 3**, we show the spatio-temporal evolution of the PNR-2 microseismicity within the western event clusters (see **Figure 1**) for Stages 1–6. In **Figure 4**, we show the spatio-temporal evolution of the microseismicity within the eastern clusters (Eastern Zone and the PNR-2 fault zone, see **Figure 1**) for the stages that produced events within this cluster (Stages 4–7).

For the PNR-1z microseismicity, we did not observe any patterns in r vs t behavior, with events occurring near-instantaneously at a range of distances from the well (Kettley et al., 2020). This motivated us to study the effects of stress transfer through the rock frame, since elastic stress transfer through the rock frame occurs at the speed of a compressive wave (thousands of m/s), which is far quicker than the timescales considered here.

For the PNR-2 microseismicity, the envelopes of event distances as a function of time appear to evolve with a dependence of $r \propto t^{0.5}$ (curved lines in **Figures 3**, **4**). This is indicative of a triggering process driven by pore pressure

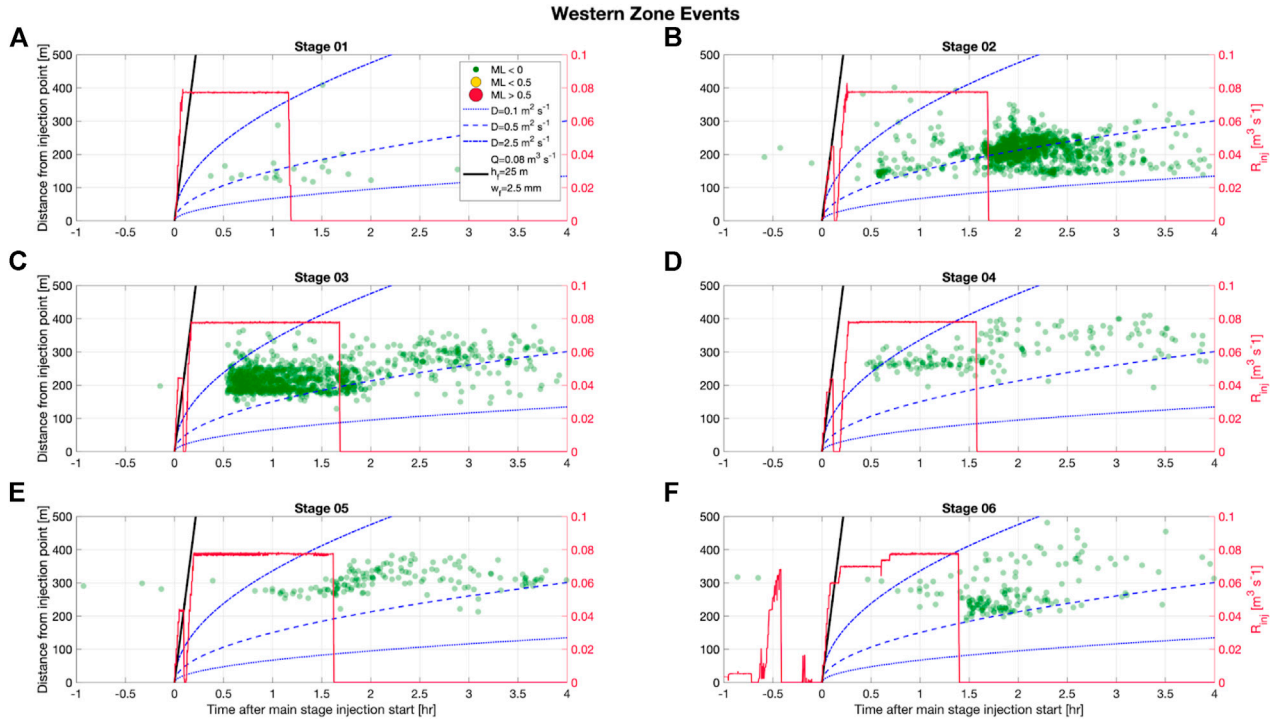

FIGURE 3 | Spatiotemporal evolution of microseismicity (dots, colored and sized by magnitude) within the western clusters for each injection stage. We also show the injection rate (R_{inj}, red line), and the expected time-distance behavior produced by diffusion models with D = 0.1, 1 and 2.5 m^2/s (blue dashed lines), and a simple hydraulic fracture model (black line) assuming h_f = 25 m, w_f = 2.5 mm and no fluid loss.

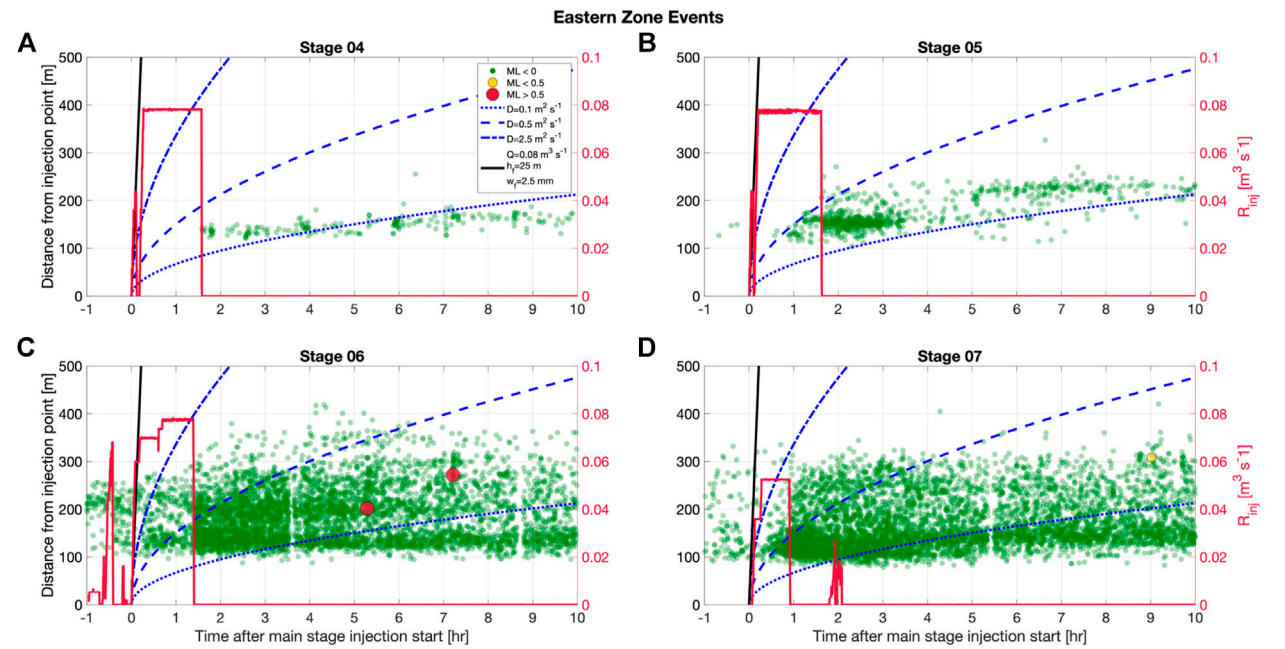

FIGURE 4 | Spatiotemporal evolution of microseismicity within the eastern clusters for each stage. The figure is formatted as in **Figure 3** above. The delay in the onset of seismicity after injection in the eastern zone decreases with subsequent stages, indicative of permeability enhancement in the reservoir. Unlike during PNR-1z (Kettley et al., 2020), the pattern of seismicity is more consistent with a $r \propto t^{0.5}$ relationship i.e., diffusion of increased pore pressure.

diffusion. For the western clusters, the events are best approximated by a diffusivity of $D \approx 2.5$ m^2/s, while the eastern clusters are best approximated by a diffusivity of $D \approx 1$ m^2/s. Also visible in **Figures 3**, **4** is an increase of best fit diffusivity with subsequent stages, which could be illustrative of permeability enhancement in the reservoir.

The system permeability κ can be estimated using the Biot (1962) equations describing the linear dynamics of poroelastic deformation (Shapiro et al., 1997):

$$\kappa = \frac{D\eta}{n} \tag{5}$$

where

$$n = \frac{h\left(K_d + \frac{4}{3}\mu\right)}{K_d + \frac{4}{3}\mu + \alpha^2 h} \tag{6}$$

$$h = \left(\frac{\phi}{K_f} + \frac{\alpha - \phi}{K_g}\right)^{-1} \tag{7}$$

$$\alpha = 1 - \frac{K_d}{K_g} \tag{8}$$

with K as the bulk modulus, with subscripts d, g and f corresponding to the dry rock frame, grain material, and fluid; μ as the rock shear modulus; ϕ is the rock porosity; and η is the fluid viscosity. Using generic values for these properties of $K_d = 20$ GPa, $K_g = 40$ GPa; $K_f = 3$ GPa; $\mu = 10$ GPa; $\phi = 0.1$; and $\eta = 0.001$ Pa s, a diffusivity of $D = 2.5$ m^2/s corresponds to a permeability of $\kappa \approx 125$ mD, and a diffusivity of $D = 1$ m^2/s corresponds to a permeability of $\kappa \approx 50$ mD. Note that with the generic values used to populate these equations, these values should be taken as "order-of-magnitude" estimates, rather than precise values. Estimates for the matrix permeability of the Bowland Shale are typically less than 1×10^{-4} mD (Clarke et al., 2018), so the values estimated above clearly do not correspond to the matrix permeability of the rock.

Instead, we surmise that the permeabilities estimated from the microseismic event spatio-temporal distributions correspond to the permeabilities of the fracture networks created during hydraulic stimulation. In the previous section, we observe that, for most stages, microseismicity occurs along the same zones as reactivated during previous stages (e.g., the NS Zone, and the Eastern Zone). Therefore, the spatial growth of microseismic events will be determined by diffusion of pressure along these features. A permeability of $\kappa \approx 100$ mD is a reasonable value for a stimulated hydraulic fracturing zone (e.g., Carey et al., 2015; Liu et al., 2019).

Overall, the consistency of the microseismic event distributions with a $r \propto t^{0.5}$ relationship leads us to conclude that the seismicity is being driven by propagation of elevated pore pressures from the well to the fault via the hydraulic fracture networks. The Eastern Zone of inferred hydraulic fractures appears to act as a hydraulic conduit for the pressure increase near the injection point. After injection that increased pressure propagates through the Eastern Zone, and at its southernmost tip this pressure front reaches the SE fault zone, and triggers events many tens of hours after injection ceases. This behavior contrasts with that observed at PNR-1z, where elastic stress transfer effects from opening hydraulic fractures appeared to be playing more of a role in controlling the spatiotemporal evolution of seismicity (Kettley et al., 2020). This serves to highlight that fault reactivation during hydraulic stimulation can occur through a variety of different mechanisms, and that multiple mechanisms can drive seismicity even at the same site. This also raises the question as to what is geomechanically different about PNR-2 compared to PNR-1z.

ELASTOSTATIC STRESS MODELLING

In order to examine the effects of elastostatic stress triggering on the PNR faults by opening fractures, we follow the approach developed in Kettley et al. (2020). In this method, we generate model hydraulic fracture sets stochastically, with dimensions scaled to the observed size of the microseismic event clusters, and the number of fractures scaled to the total injected volume during each stage. The hydraulic fractures are used as sources of stress perturbation in the PSCMP code of Wang et al. (2006), which analytically computes the changes in the stress tensor within a homogeneous elastic medium. The Coulomb stress change can then be resolved onto a particular receiver geometry—in this case, the faults activated by the injection at PNR—to assess whether the opening of hydraulic fractures promotes or inhibits failure on the fault surfaces.

In this stochastic modeling approach, many thousands of model instantiations are produced for each zone of hydraulic fracturing, such that the average stressing effect of a zone of opening hydraulic fractures can be assessed, without being tied to a particular model instantiation. As an input to the stochastic model, statistical distributions are defined to parameterize the source hydraulic fractures. We tailor the shapes of the populations to mimic the observed microseismicity, which we use as a proxy for the properties of the hydraulic fractures. The parameters used to characterize the model fractures are given in **Table 1**. We produce two distinct populations: the larger NS zone; and the Eastern zone of HFs. We define the point along the well from which fractures originate, the standard deviations of the normal distributions used to define the location of the fracture initiation point relative to the sleeve, the proportion of fractures trending north or south, the mean strike, the maximum length of the uniform distribution of fracture length, the fracture width, and the fracture aspect ratio (the ratio of length to height). The fixed widths of fractures used in the model is naturally a simplification. However, from the equations for an idealized Griffith crack, and given the injection rate and range of fracture lengths, a fracture width of 2 mm is a reasonable approximation (see Kettley et al., 2020). In order to simulate the natural variation in the orientation of the fractures, we apply a Von-Mises perturbation to the strike and dip, with $\sigma = 5^{\circ}$.

We determine the number of fractures in each instantiation using the volume of fluid pumped into each stage: we generate model fractures until the volume contained within the

TABLE 1 | Summary of the parameters used to characterize the model hydraulic fractures.

HF zone	Initiation point	Distribution parameters	Proportion N and S	Strike	Max length (m)	Width (mm)	Aspect ratio (L/h_f)
NS zone	Sleeve 1	σ = 15 m along well	66% N	350° N	375 m N	2	0.2
		σ = 10 m well perpendicular	33% S	155° S	300 m S		
East zone	Sleeve 15	σ = 10 m	20% N	345 N	100 m N	2	0.2
			80% S	165 S	200 m S		

TABLE 2 | Injection volumes for each stage, and our apportionment of their volumes into the NS and Eastern hydraulic fracturing zones.

Stage	Volume (m^3)	% into NS zone	% into East zone
1	339	100	0
2	436	100	0
3	450	100	0
4	402	90	10
5	428	75	25
6	510	60	40
7	263	40	60
Total volume (with 50% leak off) (m^3)		1,160	255

fractures equals some fraction of the injected volume. Here, we use a leak off factor of 50%, as this is a reasonable approximation given laboratory measurements of leak off rates (REF). This does require an estimate of the relative proportions of each stage volume that might have contributed to each fracture zone. This can't be easily quantified with the available data, though we make assumptions shown in **Table 2**, based on the relative proportions of microseismic observed on each feature during each stage. We model all of the sources as producing strain perpendicular to the fracture face (purely tensional, mode 1 slip), with no component of slip parallel to the fracture face. Example fracture models are shown in **Figure 5**.

We produce 1,000 sets of fractures for both the NS Zone and the Eastern Zone, and then resolve the modeled stress changes from every set onto the geometry of both the PNR-2 SEF plane (with a strike of 130°, dip of 80°, and a rake of 180°) and the PNR-1z NEF plane (with a strike of 240°, dip of 70°, and rake of 0°). These geometries are derived from the orientations of the planes mapped out by the microseismic events, as well as the focal mechanism measured for the largest events on the faults (Clarke et al., 2019b; Kettley et al., 2021). We calculate the Coulomb stress change (ΔCFS) for each geometry for every instantiation, and then take the median ΔCFS at each point in the volume in order to assess the average stressing effect of the opening hydraulic fractures. To calculate ΔCFS, we use a friction coefficient of μ_{fric} = 0.6, a Skempton's ratio of 0.3, a shear modulus μ = 20 GPa, and a Poisson's ratio of 0.25. These values provide a reasonable representation of shales (Ortega et al., 2007; Kohli and Zoback, 2013; Orellana et al., 2019), and in particular the Bowland Shale (Herrmann et al., 2018). The shear modulus and Poisson's ratio are also consistent with the values derived from the velocity model in the reservoir units (CRL, 2019).

Results

Figure 6 shows maps of ΔCFS changes at the well depth produced by both the NS Zone and Eastern Zone sources. In both cases, ΔCFS values decrease in the regions either side of the fractures, and increase in zones ahead of the fracture tips. In **Figures 7**, **8** we show the median ΔCFS values across the PNR-2 SEF and PNR-1z NEF planes respectively. We find that the lowermost corner of the SEF nearest to the fracture zones experiences large negative ΔCFS changes, as expected from the large normal stress increase compressing the fault zone. However, across most of the PNR-2 fault plane, including the region defined as the rupture area by the ML 2.9 event aftershocks (see Figure 6 of Kettley et al., 2021) experiences positive ΔCFS changes from the tensile opening of fractures in both the NS and Eastern zones, due to the increase in the shear stress on the fault beyond the fracture tips. These observations indicate that static stress transfer could have played a role in facilitating slip on a pre-existing fault, as was the case for the PNR-1z stimulation (Kettley et al., 2020).

However, as described in the previous section, the spatiotemporal evolution of the microseismicity shows a clear relationship between time and distance that is indicative of a diffusion-driven process. If static stress transfer were the dominant process, then we would expect a near-instantaneous response with events occurring at a range of distances with little dependence on time. Therefore, while these stress transfer effects may be partly acting to promote slip on the SE fault, overall the microseismicity is driven by the diffusion of elevated pore pressures from the well. Nevertheless, these results show that establishing the causative processes for induced seismicity can be challenging, and that multiple physical processes can act in tandem to reactivate faults during hydraulic stimulation.

Figure 8 shows the median ΔCFS resolved onto the PNR-1z NE-trending fault geometry. The NS zone HFs to the west of the fault zone mostly act to inhibit slip, with around 0.1 MPa of negative ΔCFS across the faults surface. This can be understood intuitively as due to the large normal stress change that extends a significant distance from the zone of HFs opposing the preferred, left-lateral, slip direction of the fault. The East Zone HFs, which are located above the PNR-1z NEF, impart both positive and negative ΔCFS on the order of 0.1 MPa, with the area to the east of the fractures being clamped, and the area to the west being promoted to fail. This due to a similar mechanism as in the NS Zone case, with the large normal stress change acting parallel the preferred slip direction to the west of the HF zone. Despite this triggering effect, no seismicity was located near or on the PNR-1z NEF.

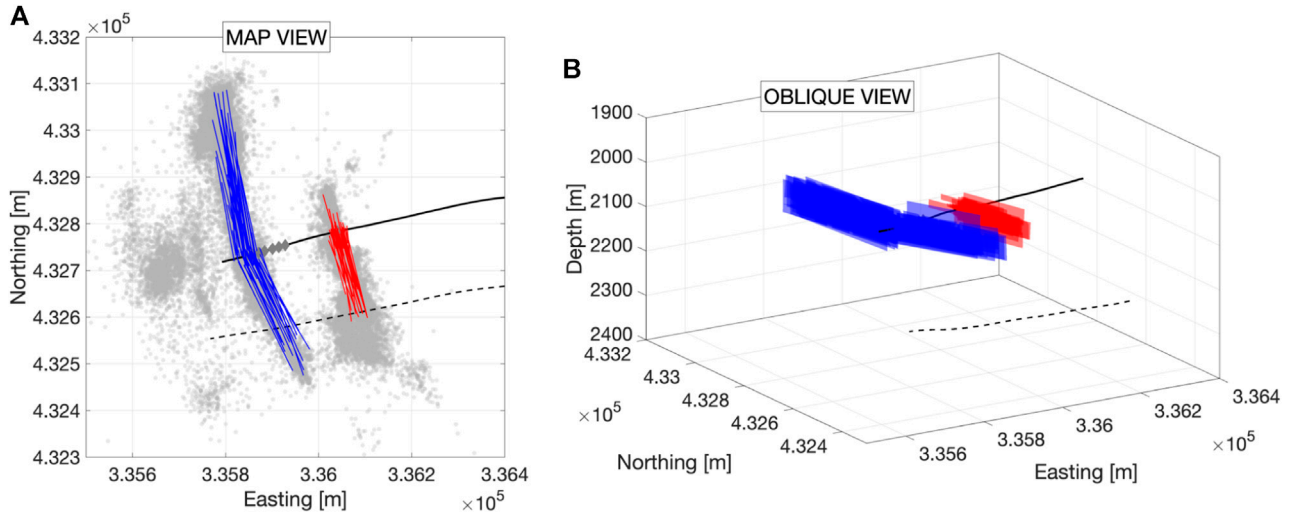

FIGURE 5 | Examples of the stochastically generated hydraulic fracture "sources" used to simulate stress changes in the surrounding rocks. In **(A)** we show a map view of the sources for the NS Zone (blue lines) and the Eastern Zone (red lines) with the observed microseismicity overlain (grey dots). The well paths are shown by the solid black line for PNR-2, and the dashed black line for PNR-1z. The locations of the injection points during PNR-2 operations are shown by the grey diamonds. In **(B)** we show a 3D view of the model hydraulic fracture sources.

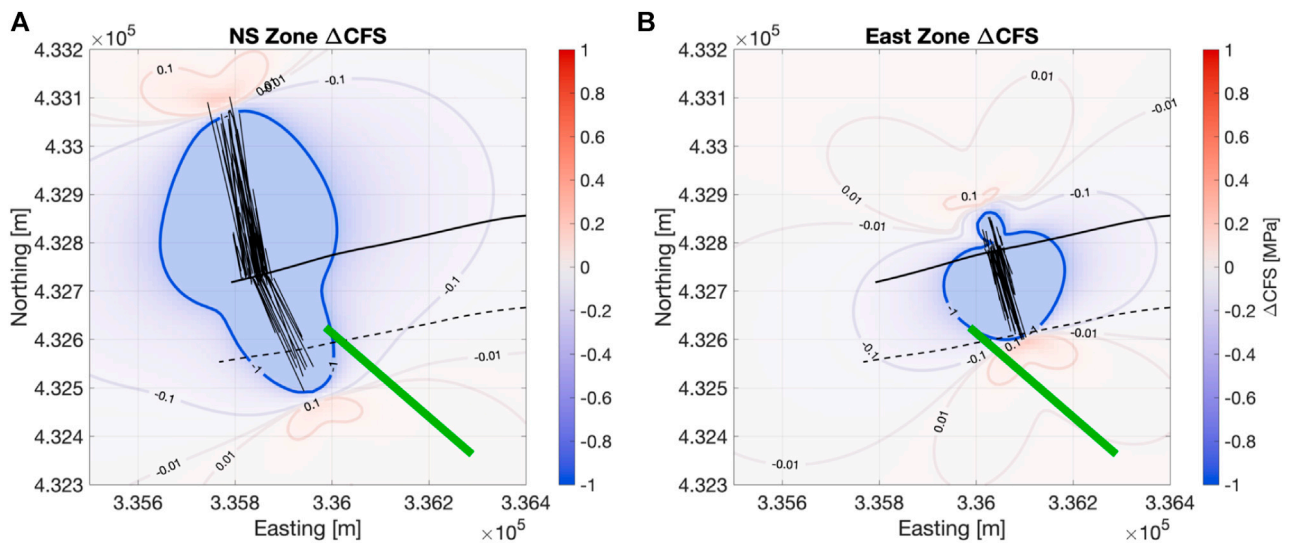

FIGURE 6 | Maps of ΔCFS produced by the NS Zone **(A)** and the Eastern Zone **(B)** at the depth of the PNR-2 injection. In each case an example set of the fracture sources is shown by a population of black lines, the SEF zone by the green line, and the PNR-2 and PNR-1z well paths by the solid and dash lines respectively (as in **Figure 5**). Outside of the portion of large normal stress increase (with negative ΔCFS in blue) there is a region on the SE fault beyond the fracture tips where shear stress increases and positive ΔCFS is promoting failure.

Stress Triggering Thresholds

The observation that no seismicity was triggered on the PNR-1z NEF during PNR-2 operations means that we can assume that whatever triggering effect was provided by the opening fractures was not large enough to initiate slip on the fault. Also, because there was no seismicity near the NEF during PNR-2 stimulation, it is unlikely there is a direct hydraulic connection. From **Figure 8B**, we can see that the East Zone HFs would have induced a ΔCFS of approximately 0.1 MPa across a significant fraction of the fault's surface, meaning to successfully trigger the fault more than 0.1 MPa of stress change would have to be imparted. However, this elastic stress transfer is but one mechanism imparting stress on the NEF. To determine the minimum triggering threshold for the fault, the contributions from other mechanisms should be considered.

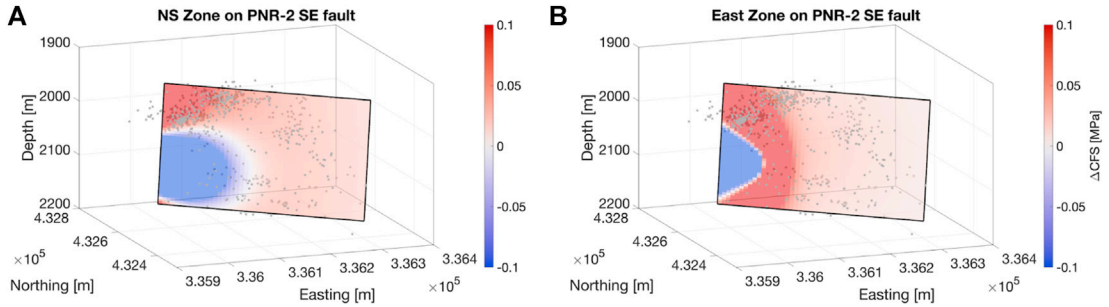

FIGURE 7 | Median ΔCFS values on the SEF fault plane (as defined by the ML 2.9 event aftershocks, shown as grey dots) produced by the NS Zone **(A)** and the Eastern Zone **(B)** of model HFs. The change in the ΔCFS color scale from **Figure 6** should be noted. Outside of the zone of normal stress increase immediately perpendicular to the surfaces of the fractures, ΔCFS is positive due to increases in shear stress. This will act in part to promote failure on the fault's surface.

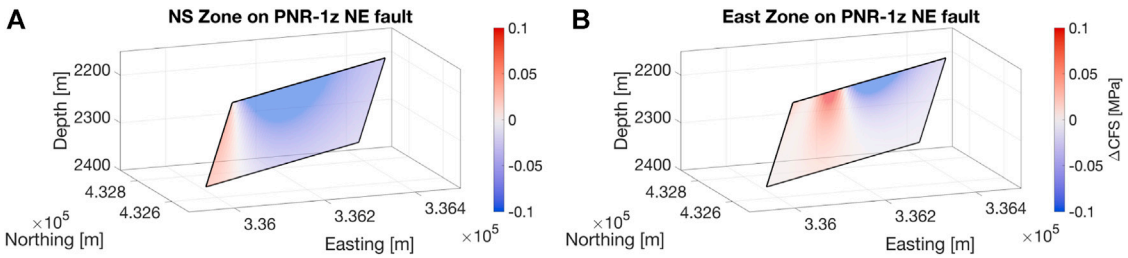

FIGURE 8 | ΔCFS values on the PNR-1z NEF plane (as defined by the largest induced events and seismic activity, see Clarke et al., 2019a) produced by the NS Zone of hydraulic fracturing **(A)** and the Eastern Zone **(B)**.

As fluid is injected into the formation, pore pressures around the injection point increase substantially, by many tens of MPa. This increased pressure will diffuse out into the surrounding rock mass slowly, and preferentially along higher permeability conduits such as natural or newly created fractures. If the formation is more permeable, the zone of increased pore pressure will propagate to larger distances in a shorter time and the magnitude of the change in pressure will be lower. For less permeable rocks, the pressure front will extend to a shorter distance, but the magnitude of pressure increase will be higher (see Rice and Cleary, 1976).

Alongside this simple increase in pore pressure is the poroelastic expansion of the rock frame, whereby a change in pressure within the rock pore space deforms the matrix itself and elastically deforms the surrounding rock. This mechanism can induce stress changes out to a significant distance (Segall and Lu, 2015). The exact magnitude of the stress in three dimensions around the injection point is dependent on the hydraulic structure of the reservoir. To calculate this magnitude using complex multiphase hydromechanical models requires calibration based on a large number of geomechanical and hydraulic parameters, such a drained and undrained elastic moduli, the Biot–Willis coefficients, and the fluid viscosity, each of which vary considerably both in space and time during a hydraulic fracturing operation into a shale gas reservoir. As with most reservoirs, these parameters for PNR are not well constrained.

Without using these underconstrained modeling approaches, we can calculate an order of magnitude estimate for the stress change induced by poroelastic effects using the equations of poroelastic theory (Biot, 1962; explicitly defined for a series of injection intervals in Rudnicki, 1986), which give pore pressure and change in the stress tensor in a 3D homogeneous poroelastic medium. This will allow us to compare order of magnitude estimates of the stress changes induced through fracture-opening elastic stress transfer, poroelastic expansion, and pore pressure increase.

In applying these analytical solutions, we use a series of injection intervals that match the duration and flow rates of those used during PNR-2 (**Figures 3**, **4**). We model the pore pressure and poroelastic stress changes for the duration of the injection operations, and continue up to the time the largest event in the 2019 sequence occurred, the M_L 2.9 event on the SEF.

We use a shear modulus of 20 GPa and a drained Lame parameter of 20 GPa, values that are derived from the velocity model for the reservoir (for acquisition details, see CRL, 2019; Kettley et al., 2020, Kettley et al., 2021). We use an undrained first Lame parameter of 30 GPa, using an appropriate ratio of drained to undrained first Lame parameters for shales (e.g, Islam and Skalle, 2013; Segall and Lu, 2015). With these drained and undrained elastic parameters, poroelastic theory (see Segall and Lu, 2015, Eq. 15) gives a Biot coefficient of 0.77, consistent with laboratory measurements and model estimates (Muller and Sahay, 2016). We use a dynamic viscosity of 1 mPa s, as that

was the stated viscosity in the hydraulic fracture plan for the slickwater used in all but the final stage (CRL, 2019). We examine several permeabilities (0.5 mD, 5 mD, and 50 mD) that cover the range of values appropriate for the enhanced permeability of the hydraulic fractures within the low permeability shale.

From the temporal delay observed between injection and seismic activity near the fault (**Figures 3**, **4**), fracture permeability was estimated to reach on the order of 100 mD, however this is most likely reflective of the maximum permeability of the fractures immediately after injection, which will dominated the permeability structure in comparison to the very low permeability shale matrix (~0.0001 mD). As we are attempting to model the stress changes throughout the medium, some intermediate value is deemed most appropriate. Naturally, the permeability structure in reality will be quite heterogeneous, and a hydraulic pathway could extend the ranges of the stress changes, though this is not apparent for the NEF. The homogeneous model case, however, allows us to similarly compare the order of magnitude stress changes between the pore pressure, the fracture opening stress transfer, and the poroelastic effect.

From **Figure 2** we can see that the injection points during PNR-2 operations were around 200–250 m from the nearest point of PNR-1z NE fault zone. **Figure 9** shows the pore pressure ΔP and the poroelastic ΔCFS change across the top of the NEF plane due to poroelastic expansion during PNR-2 operations. The stress changes at the end of the modeled time would be reflective of those when the SEF fault slipped and the ML 2.9 event occurred.

Figure 9A shows that the pore pressure is estimated to be on the order of 0.1 MPa or less at a distance of ~200 m (i.e., near the NEF), except in the "high" permeability case, where it would be an order of magnitude lower. This is comparable in magnitude to the stress change received by the elastic stress transfer from the opening of hydraulic fractures. However, it appears there was no hydraulic connection between the PNR-2 injection and the NEF. Thus, the permeability approaching the NEF would be significantly lower than those modeled here, and much closer to the matrix. In this case, it is unlikely that any significant (>0.1 MPa) ΔP would extend as far as the NEF during PNR-2 operations, as the increased fluid pressure would take far too long to diffuse that distance. If there was a direct hydraulic connection to the NEF, the ΔP would be somewhere.

The model also produces a maximum poroelastic ΔCFS at the top of the NEF of around 0.01 MPa, significantly smaller than both the ΔP and the ΔCFS created by tensile hydraulic fracture opening. This demonstrates that pore pressure increase and elastic stress transfer from opening HFs have an order of magnitude larger stress perturbations than poroelastic stress transfer from the expansion of the rock frame, and thus the latter mechanism is unlikely to be a dominant contributing mechanism. Whilst in the "low" permeability case the poroelastic ΔCFS near the NEF is slightly larger, it reaches a maximum value (0.07 MPa) just after the pumping of the final stage (around model day 8). At that permeability and model time, the magnitude of ΔP has already far exceeded that of the poroelastic ΔCFS, by around a factor of 4. Thus, even within the variation of permeability, elastic stress transfer from opening fractures would be a more significant triggering mechanism.

DISCUSSION AND CONCLUSION

Microseismic monitoring at the Preston New Road hydraulic fracturing operations in 2018 and 2019 provided an extensive dataset (Clarke et al., 2019b; Kettley et al., 2021), allowing for

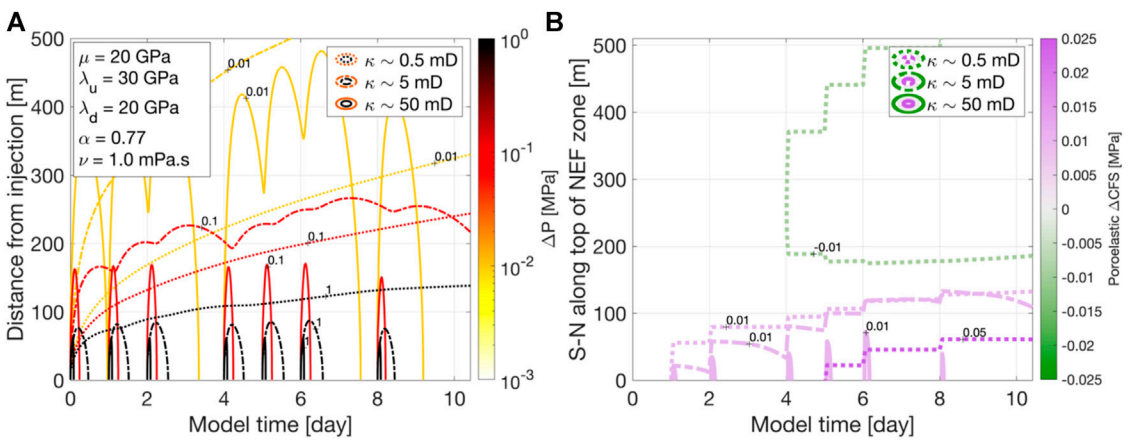

FIGURE 9 | Results of the poroelastic modeling for the PNR-2 operations, using the analytical solutions of Rudnicki (1986) for fluid injection into a homogeneous poroelastic medium. **(A)** shows the change in the pore pressure ΔP with time and distance from the injection points at the end of the PNR-2 well. The poroelastic parameters used are shown inset and described in the text. The colors denote the magnitude of the ΔP contour, and the line styles show the three different permeabilities used. With the PNR-1z NEF being around 250 m away from the injection, this simple model estimates a ΔP on the order of 0.1 MPa. **(B)** shows the poroelastic Coulomb stress change (ΔCFS) resolved onto the geometry of the PNR-1z NEF. This shows how the ΔCFS value evolves with time for the line along the top of the fault zone, going south to north (see **Figure 2** for the orientation of the inferred fault zone in 3D). The maximum poroelastic ΔCFS on the NEF is limited to around 0.01 MPa throughout PNR-2 operations. Poroelastic ΔCFS naturally increases markedly at the start of each injection period, and decays with time.

detailed study of the physical mechanisms underpinning an influential case of hydraulic fracturing-induced fault activation. We use the event hypocentres and their evolution with time (**Figures 3**, **4**) to demonstrate that the most likely fault activation mechanism during PNR-2 seismicity was the diffusion of increased pore pressure along the newly created hydraulic fractures in the Eastern Zone. Whilst this spatiotemporal evolution method relies on a simplified model of fluid pressure propagation (Shapiro et al., 1997), it is substantiated by the relatively small contribution of elastic stress transfer from opening hydraulic fractures (**Figure 6**). Pore pressure modeling (**Figure 9**) also shows possible pore pressure change ΔP of 0.1 MPa or more near the SE-trending fault.

The diffusion of increased pore pressure is a mechanism that has been invoked in many induced seismicity cases (Schultz et al., 2020). It is somewhat surprising that this appears to contrast with the mechanism controlling the spatial distribution of seismicity during the first phase of operations at PNR in 2018, where elastic stress transfer from the opening of hydraulic fractures appeared to control the location of microseismicity along the activated NE-trending fault zone (Kettley et al., 2020). The primary difference appears to be that the NE zone of enhanced seismicity activated during PNR-1z directly intersected the injection well, with multiple stages creating hydraulic fractures through this suspected fault. During PNR-2 operations, the SEF fault that hosted the widely felt M_L 2.9 event was offset entirely from the well, by over 200 m. There was a delay between injection and the onset of activity on fault, most likely due to the finite time required for increased fluid pressure to diffuse along the newly created hydraulic fractures and reach the fault zone. The Preston New Road case study clearly highlights that fault position relative to the injection point is a control on which physical mechanism will contribute to fault triggering.

Using the method developed for the PNR-1z case of fault activation (Kettley et al., 2020), we use an elastic stress transfer model of hydraulic fracture opening to determine if this mechanism promoted slip on the SEF and NEF during PNR-2 operations. We show that a portion of the SEF would receive a positive ΔCFS (~0.1 MPa) due to tensile opening hydraulic fractures, promoting slip on the fault. However, part of the fault would also receive a large negative ΔCFS due to the large normal stress increase of opening fractures clamping the fault. Thus, whilst fracture open stress transfer could have contributed to the triggering of the SEF, we conclude that it was mostly induced by increased fluid pressure diffusing through fractures in the Eastern Zone.

The NEF would receive a mostly negative elastic ΔCFS, inhibiting slip, from the large NS Zone of hydraulic fractures identified during PNR-2 injection, however, over half of its surface would receive a positive ΔCFS of around 0.1 MPa from the Eastern Zone of HFs. Still, this was not enough to trigger activity on the fault, as no events were detected near the NEF. Simplified models of poroelastic stress transfer (**Figure 9**) show the approximate magnitude of stress change from this mechanism would be an order of magnitude less than that expected from this HF opening modeling. This means that if stress transfer were to trigger the NEF, it would require in excess of ~0.1 MPa of ΔCFS.

The fracture-opening stress modeling requires parameterization of the inferred hydraulic fractures, which naturally simplifies the reality of the properties of the hydraulic fractures. The aim of this modeling is to determine the polarity and approximate magnitude of stress change that the faults at PNR would experience as a result of opening fractures. The model parameters which would substantively change the results given in **Figures 6–8** are position and orientation of the fractures, their width, and their number. The location and orientations used in the model are constrained by the trends and extent of the microseismic event clusters. This relies on the interpretation that these clusters are imaging the hydraulic fracture growth, which their evolution (growing outward from the stages), orientation (with respect to the local S_{Hmax}), and location (centered on the injection point) all suggest are the case. The modeled widths are reasonable given the Griffith crack model for fractures of this length and the injection rate (Nordgren, 1972; Kettley et al., 2020), and generally match those found with complex finite element models of fracture growth undertaken by the operator (CRL, 2019). Their number is constrained by their size (see above discussion) and the total volume of fluid which, with some apportionment between HF zones, is well constrained by the rates of injection (**Figures 3**, **4**). Increasing or decreasing the apportionment or leak off rate may change the approximate magnitude by a small amount, but not the polarity of the stress changes. The smoothing introduced by using the median ΔCFS from the Monte Carlo simulation of fractures also decreases the effect of style of failure and the edge effects of the model fractures (Kettley et al., 2020). Deviations outside the constraint placed by the microseismic events to the fracture lengths and orientations would be required in order to significantly shift the patterns in the stress changes observed.

The models used are homogeneous and isotropic, and naturally simplify a complex reservoir structure. However, anisotropic, heterogeneous models of the hydromechanical response of a reservoir to injection require dozens of poorly constrained parameters, as described previously. Despite their lack of complexity, the models used here require significantly fewer parameters, all of which can be estimated from available data about the PNR shales (e.g., shear modulus, Poisson's ratio), measurements from the microseismic (e.g., fault/fracture length, orientation, permeability), and appropriate laboratory analogues (e.g., effective coefficient of friction, Biot coefficient, fluid viscosity). Comparisons between these models allow us to study the relative contributions of the underlying triggering mechanisms, and approximate the magnitudes of the stress changes during this case of fault activation.

This magnitude of stress change expected on PNR-1z NEF is an order of magnitude larger than previously stated triggering thresholds, 0.01 MPa or less (e.g., Shapiro et al., 1997; Westwood et al., 2017). Generally speaking, the calculation of ΔCFS assumes a negligible fault cohesion C, which provides inherent strength to overcome in the Mohr–Coulomb failure criterion (**Equation 2**), and ignores the dynamic friction behavior of the fault rocks (i.e., velocity strengthening or weakening behavior, as in Faulkner et al., 2010). The variability of these properties between faults will naturally in part control the magnitude of the triggering threshold. As laboratory experimentation on the reservoir or fault rocks themselves is required, these properties are more difficult to constrain.

Fault orientation in the regional stress will also be a controlling parameter on the threshold, as well as the most likely triggering mechanism. Whilst the PNR-1z NEF is not as well aligned for failure as the PNR-2 SEF, it is still relatively near the expected optimal orientation for left-lateral faults in this strike-slip regime (Kettley et al., 2021). The assumptions for the determination of the minimum triggering threshold will then also rely on the fault being critically stressed, where a relatively small increase of ~0.1 MPa in ΔCFS could be able to trigger fault slip. With the NEF fault being further from the failure envelope, and potentially having fault cohesion and friction behavior not favourable to fault reactivation, the minimum triggering threshold may be greater than 0.1 MPa.

This work shows that both spatiotemporal analysis and geomechanical modeling can be used to assess the relative importance of triggering mechanisms, and highlights that the magnitude of stress change required to trigger a fault may be significantly larger than previously assumed. Our estimation of a minimum triggering threshold is an order of magnitude larger than some minimum bounds used in hazard assessment (e.g., Westwood et al., 2017), and would only be increased when fault cohesion, orientation, and heterogeneity are considered. Using generalized triggering thresholds with low magnitudes (<0.01 MPa) may significantly overestimate the potential hazard associated with injection operations, and their use in this type of hazard analysis needs to be reevaluated. To accurately assess the seismic risk of a particular injection site, these spatiotemporal and geomechanical analyses need to be linked with studies of rock mechanics, petrophysics, and frictional stability measurements. This will be a key in assessing the risk of induced seismicity for increasingly vital technologies, such as geologic CO_2 or hydrogen storage, and geothermal energy.

DATA AVAILABILITY STATEMENT

Publicly available datasets were analyzed in this study. This data can be found here: https://www.ogauthority.co.uk/exploration-production/onshore/onshore-reports-and-data/preston-new-road-pnr-1z-hydraulic-fracturing-operations-data/, https://consult.environment-agency.gov.uk/onshore-oil-and-gas/information-on-cuadrillas-preston-new-road-site/user_uploads/pnr-2-hfp-v3.0.pdf, https://www.ogauthority.co.uk/media/6970/oga-summary-of-pnr2-studies-final.pdf.

AUTHOR CONTRIBUTIONS

TK and JV both contributed equally to the writing of the manuscript, the development of the research, and conducting the modeling.

FUNDING

TK is supported by the NERC UKUH Challenge Grants SHAPE-UK project (Grant Number NE/R018006/1). JV contribution to this work is supported by NERC (Grant Number NE/R018162/1). The authors would also like to thank the UK Oil and Gas Authority for partial funding of this research.

ACKNOWLEDGMENTS

We would like to acknowledge Cuadrilla Resources Limited, the operator of the PNR site, and Schlumberger Ltd., who conducted the processing of the microseismic data that are presented in this work, and Nanometrics Ltd., who conducted the processing of the surface derived data acquired by Nanometrics Ltd. and the British Geological Survey. We would like to thank Michael Kendall for insightful discussion of the results, as well as Ryan Schultz and Louis De Barros for their constructive feedback. This work was a product of the Bristol University Microseismicity Projects (BUMPs)—a research consortium whose sponsors include several hydrocarbon operators and service providers.

REFERENCES

Anderson, I., and Underhill, J. R. (2020). Structural Constraints on Lower Carboniferous Shale Gas Exploration in the Craven Basin, NW England. *Pet. Geosci.* 26 (2), 303–324. doi:10.1144/petgeo2019-125

Bao, X., and Eaton, D. W. (2016). Fault Activation by Hydraulic Fracturing in Western Canada. *Science* 354, 1406–1409. doi:10.1126/science.aag2583

Bhattacharya, P., and Viesca, R. C. (2019). Fluid-induced Aseismic Fault Slip Outpaces Pore-Fluid Migration. *Science* 364 (6439), 464–468. doi:10.1126/science.aaw7354

Biot, M. A. (1962). Mechanics of Deformation and Acoustic Propagation in Porous Media. *J. Appl. Phys.* 33 (4), 1482–1498. doi:10.1063/1.1728759

Bourne, S. J., Oates, S. J., Van Elk, J., and Doornhof, D. (2014). A Seismological Model for Earthquakes Induced by Fluid Extraction from a Subsurface Reservoir. *J. Geophys. Res. Solid Earth* 119 (12), 8991–9015. doi:10.1002/2014JB011663

Carey, J. W., Lei, Z., Rougier, E., Mori, H., and Viswanathan, H. (2015). Fracture-permeability Behavior of Shale. *J. Unconventional Oil Gas Resour.* 11, 27–43. doi:10.1016/j.juogr.2015.04.003

Cesca, S., Grigoli, F., Heimann, S., González, Á., Buforn, E., Maghsoudi, S., et al. (2014). The 2013 September-October Seismic Sequence Offshore Spain: A Case of Seismicity Triggered by Gas Injection?. *Geophys. J. Int.* 198 (2), 941–953. doi:10.1093/gji/ggu172

Clarke, H., Eisner, L., Styles, P., and Turner, P. (2014). Felt Seismicity Associated with Shale Gas Hydraulic Fracturing: The First Documented Example in Europe. *Geophys. Res. Lett.* 41 (23), 8308–8314. doi:10.1002/2014GL062047

Clarke, H., Soroush, H., and Wood, T. (2019b). Preston New Road: the Role of Geomechanics in Successful Drilling of the UK's First Horizontal Shale Gas Well, Society of Petroleum Engineers EUROPEC at the 81st EAGE Annual Conference SPE-195563, London, June 3, 2019 (. EAGE). doi:10.2118/195563-ms

Clarke, H., Turner, P., Bustin, R. M., Riley, N., and Besly, B. (2018). Shale Gas Resources of the Bowland Basin, NW England: a Holistic Study. *Pet. Geosci.* 24 (3), 287–322. doi:10.1144/petgeo2017-066

Clarke, H., Verdon, J. P., Kettley, T., Baird, A. F., and Kendall, J. M. (2019a). Real-Time Imaging, Forecasting, and Management of Human-Induced Seismicity at Preston New Road, Lancashire, England. *Seismological Res. Lett.* 90 (5), 1902–1915. doi:10.1785/0220190110

Corfield, S. M., Gawthorpe, R. L., Gage, M., Fraser, A. J., and Besly, B. M. (1996). Inversion Tectonics of the Variscan Foreland of the British Isles. *J. Geol. Soc.* 153, 17–32. doi:10.1144/gsjgs.153.1.0017

Cuadrilla Resources Ltd. (CRL) (2019). Hydraulic Fracture Plan: PNR 2. Available at: https://consult.environment-agency.gov.uk/onshore-oil-and-gas/information-on-cuadrillas-preston-new-road-site/user_uploads/pnr-2-hfp-v3.0.pdf (Accessed May 2021).

Deichmann, N., and Giardini, D. (2009). Earthquakes Induced by the Stimulation of an Enhanced Geothermal System below Basel (Switzerland). *Seismological Res. Lett.* 80 (5), 784–798. doi:10.1785/gssrl.80.5.784

Deng, K., Liu, Y., and Harrington, R. M. (2016). Poroelastic Stress Triggering of the December 2013 Crooked Lake, Alberta, Induced Seismicity Sequence. *Geophys. Res. Lett.* 43 (16), 8482–8491. doi:10.1002/2016GL070421

Economides, M. J., and Nolte, K. G. (2003). *Reservoir Stimulation*. 3rd ed. Hoboken, N.J: John Wiley, 5-1–5–14.

Eyre, T. S., Eaton, D. W., Garagash, D. I., Zecevic, M., Venieri, M., Weir, R., et al. (2019). The Role of Aseismic Slip in Hydraulic Fracturing-Induced Seismicity. *Sci. Adv.* 5 (8), eaav7172. doi:10.1126/sciadv.aav7172

Faulkner, D. R., Jackson, C. A. L., Lunn, R. J., Schlische, R. W., Shipton, Z. K., Wibberley, C. A. J., et al. (2010). A Review of Recent Developments Concerning the Structure, Mechanics and Fluid Flow Properties of Fault Zones. *J. Struct. Geology.* 32 (11), 1557–1575. doi:10.1016/j.jsg.2010.06.009

Fellgett, M. W., Kingdon, A., Williams, J. D. O., and Gent, C. M. A. (2017). "State of Stress across UK Regions," in *British Geological Survey Open Report*, Vol. OR/17/048.

Green, R. G., Greenfield, T., and White, R. S. (2015). Triggered Earthquakes Suppressed by an Evolving Stress Shadow from a Propagating Dyke. *Nat. Geosci* 8 (8), 629–632. doi:10.1038/ngeo2491

Grigoli, F., Cesca, S., Rinaldi, A. P., Manconi, A., López-Comino, J. A., Clinton, J. F., et al. (2018). The November 2017Mw5.5 Pohang Earthquake: A Possible Case of Induced Seismicity in South Korea. *Science* 360 (6392), 1003–1006. doi:10.1126/science.aat2010

Guion, P. D., Gutteridge, P., and Davies, S. J. (2000). "Carboniferous Sedimentation and Volcanism on the Laurussian Margin," in *Geological History of Britain and Ireland*. Editors N. H. Woodcock and R. A. Strachan (Oxford, United Kingdom: Blackwell Science), 227–271.

Gupta, H. K. (1992). *Reservoir Induced Earthquakes*. New York: Elsevier.

Herrmann, J., Rybacki, E., Sone, H., and Dresen, G. (2018). Deformation Experiments on Bowland and Posidonia Shale-Part I: Strength and Young's Modulus at Ambient and *In Situ* Pc-T Conditions. *Rock Mech. Rock Eng.* 51 (12), 3645–3666. doi:10.1007/s00603-018-1572-4

Holland, A. A. (2013). Earthquakes Triggered by Hydraulic Fracturing in South-Central Oklahoma. *Bull. Seismological Soc. America* 103 (3), 1784–1792. doi:10.1785/0120120109

Igonin, N., Verdon, J. P., Kendall, J. M., and Eaton, D. W. (2021). Large-Scale Fracture Systems Are Permeable Pathways for Fault Activation during Hydraulic Fracturing. *J. Geophys. Res. Solid Earth* 126. doi:10.1029/2020JB020311

Islam, M. A., and Skalle, P. (2013). An Experimental Investigation of Shale Mechanical Properties through Drained and Undrained Test Mechanisms. *Rock Mech. Rock Eng.* 46 (6), 1391–1413. doi:10.1007/s00603-013-0377-8

Keranen, K. M., Weingarten, M., Abers, G. A., Bekins, B. A., and Ge, S. (2014). Sharp Increase in Central Oklahoma Seismicity since 2008 Induced by Massive Wastewater Injection. *Science* 345 (6195), 448–451. doi:10.1126/science.1255802

Kettley, T., Verdon, J. P., Butcher, A., Hampson, M., and Craddock, L. (2021). High-Resolution Imaging of the ML 2.9 August 2019 Earthquake in Lancashire, United Kingdom, Induced by Hydraulic Fracturing during Preston New Road PNR-2 Operations. *Seismological Res. Lett.* 92, 151–169. doi:10.1785/0220200187

Kettley, T., Verdon, J. P., Werner, M. J., Kendall, J. M., and Budge, J. (2019). Investigating the Role of Elastostatic Stress Transfer during Hydraulic Fracturing-Induced Fault Activation. *Geophys. J. Int.* 217, 1200–1216. doi:10.1093/gji/ggz080

Kettley, T., Verdon, J. P., Werner, M. J., and Kendall, J. M. (2020). Stress Transfer from Opening Hydraulic Fractures Controls the Distribution of Induced Seismicity. *J. Geophys. Res. Solid Earth* 125. doi:10.1029/2019jb018794

Kilb, D., Gomberg, J., and Bodin, P. (2002). Aftershock Triggering by Complete Coulomb Stress Changes. *J. Geophys. Res.* 107 (B4), ESE 2–1. doi:10.1029/2001jb000202),

Kohli, A. H., and Zoback, M. D. (2013). Frictional Properties of Shale Reservoir Rocks. *J. Geophys. Res. Solid Earth* 118 (9), 5109–5125. doi:10.1002/jgrb.50346

Lei, X., Wang, Z., and Su, J. (2019). The December 2018 ML 5.7 and January 2019 ML 5.3 Earthquakes in South Sichuan Basin Induced by Shale Gas Hydraulic Fracturing. *Seismological Res. Lett.* 90 (3), 1099–1110. doi:10.1785/0220190029

Liu, H., Hu, X., Guo, Y., Ma, X., Wang, F., and Chen, Q. (2019). Fracture Characterization Using Flowback Water Transients from Hydraulically Fractured Shale Gas Wells. *ACS Omega* 4, 14688–14698. doi:10.1021/acsomega.9b01117

Müller, T. M., and Sahay, P. N. (2016). Biot Coefficient Is Distinct from Effective Pressure Coefficient. *Geophysics* 81 (4), L27–L33. doi:10.1190/GEO2015-0625.1

Nordgren, R. P. (1972). Propagation of a Vertical Hydraulic Fracture. *Soc. Pet. Eng. J.* 12 (04), 306–314. doi:10.2118/3009-PA

Orellana, L. F., Giorgetti, C., and Violay, M. (2019). Contrasting Mechanical and Hydraulic Properties of Wet and Dry Fault Zones in a Proposed Shale-Hosted Nuclear Waste Repository. *Geophys. Res. Lett.* 46, 1357–1366. doi:10.1029/2018GL080384

Ortega, J. A., Ulm, F.-J., and Abousleiman, Y. (2007). The Effect of the Nanogranular Nature of Shale on Their Poroelastic Behavior. *Acta Geotech.* 2 (3), 155–182. doi:10.1007/s11440-007-0038-8

Rice, J. R., and Cleary, M. P. (1976). Some Basic Stress Diffusion Solutions for Fluid-Saturated Elastic Porous Media with Compressible Constituents. *Rev. Geophys.* 14 (2), 227. doi:10.1029/RG014i002p00227

Rudnicki, J. W. (1986). Fluid Mass Sources and Point Forces in Linear Elastic Diffusive Solids. *Mech. Mater.* 5 (4), 383–393. doi:10.1016/0167-6636(86)90042-6

Schultz, R., Skoumal, R. J., Brudzinski, M. R., Eaton, D., Baptie, B., and Ellsworth, W. (2020). Hydraulic Fracturing-Induced Seismicity. *Rev. Geophys.* 58 (3), 1–43. doi:10.1029/2019RG000695

Schultz, R., Stern, V., Novakovic, M., Atkinson, G., and Gu, Y. J. (2015). Hydraulic Fracturing and the Crooked Lake Sequences: Insights Gleaned from Regional Seismic Networks. *Geophys. Res. Lett.* 42, 2750–2758. doi:10.1002/2015GL063455.Received

Segall, P., and Lu, S. (2015). Injection-induced Seismicity: Poroelastic and Earthquake Nucleation Effects. *J. Geophys. Res. Solid Earth* 120, 5082–5103. doi:10.1002/2015JB012060

Shapiro, S. A. (2008). *Microseismicity: A Tool for Reservoir Characterization*. Amsterdam, The Netherlands: EAGE Publications. doi:10.3997/9789073781702

Shapiro, S. A., and Dinske, C. (2009). Fluid-induced Seismicity: Pressure Diffusion and Hydraulic Fracturing. *Geophys. Prospecting* 57 (2), 301–310. doi:10.1111/j.1365-2478.2008.00770.x

Shapiro, S. A., Huenges, E., and Borm, G. (1997). Estimating the Crust Permeability from Fluid-Injection-Induced Seismic Emission at the KTB Site. *Geophys. J. Int.* 131 (2), F15–F18. doi:10.1111/j.1365-246x.1997.tb01215.x

Shapiro, S. A., Kummerow, J., Dinske, C., Asch, G., Rothert, E., Erzinger, J., et al. (2006). Fluid Induced Seismicity Guided by a Continental Fault: Injection Experiment of 2004/2005 at the German Deep Drilling Site (KTB). *Geophys. Res. Lett.* 33 (1), a–n. doi:10.1029/2005GL024659

Steacy, S., Marsan, D., Nalbant, S. S., and McCloskey, J. (2004). Sensitivity of Static Stress Calculations to the Earthquake Slip Distribution. *J. Geophys. Res.* 109, 16. doi:10.1029/2002JB002365

Stein, R. S. (1999). The Role of Stress Transfer in Earthquake Occurrence. *Nature* 402, 605–609. doi:10.1038/45144

Stork, A. L., Verdon, J. P., and Kendall, J.-M. (2015). The Microseismic Response at the in Salah Carbon Capture and Storage (CCS) Site. *Int. J. Greenhouse Gas Control.* 32, 159–171. doi:10.1016/j.ijggc.2014.11.014

Toda, S., Stein, R. S., and Sagiya, T. (2002). Evidence from the AD 2000 Izu Islands Earthquake Swarm that Stressing Rate Governs Seismicity. *Nature* 419 (6902), 58–61. doi:10.1038/nature00997

Verdon, J. P., Baptie, B. J., and Bommer, J. J. (2019). An Improved Framework for Discriminating Seismicity Induced by Industrial Activities from Natural Earthquakes. *Seismological Res. Lett.* 90 (4), 1592–1611. doi:10.1785/0220190030

Verdon, J. P., Kendall, J.-M., Butcher, A., Luckett, R., and Baptie, B. J. (2018). Seismicity Induced by Longwall Coal Mining at the Thoresby Colliery, Nottinghamshire, U.K. *Geophys. J. Int.* 212 (2), 942–954. doi:10.1093/gji/ggx465

Wang, R., Lorenzo-Martín, F., and Roth, F. (2006). PSGRN/PSCMP-a New Code for Calculating Co- and Post-seismic Deformation, Geoid and Gravity Changes Based on the Viscoelastic-Gravitational Dislocation Theory. *Comput. Geosciences* 32 (4), 527–541. doi:10.1016/j.cageo.2005.08.006

Westwood, R. F., Toon, S. M., Styles, P., and Cassidy, N. J. (2017). Horizontal Respect Distance for Hydraulic Fracturing in the Vicinity of Existing Faults in Deep Geological Reservoirs: a Review and Modelling Study. *Geomech. Geophys. Geo-energ. Geo-resour.* 3 (4), 379–391. doi:10.1007/s40948-017-0065-3

Conflict of Interest: The authors declare that the research was conducted in the absence of any commercial or financial relationships that could be construed as a potential conflict of interest.

frontiers in Earth Science

ORIGINAL RESEARCH
published: 28 May 2021
doi: 10.3389/feart.2021.634688

Accounting for Natural Uncertainty Within Monitoring Systems for Induced Seismicity Based on Earthquake Magnitudes

Corinna Roy[1]*, *Andy Nowacki*[1], *Xin Zhang*[2], *Andrew Curtis*[2,3] and *Brian Baptie*[4]

[1] School of Earth and Environment, University of Leeds, Leeds, United Kingdom, [2] School of GeoSciences, University of Edinburgh, Edinburgh, United Kingdom, [3] Department of Earth Sciences, ETH Zurich, Zurich, Switzerland, [4] British Geological Survey, Edinburgh, United Kingdom

To reduce the probability of future large earthquakes, traffic light systems (TLSs) define appropriate reactions to observed induced seismicity depending on each event's range of local earthquake magnitude (M_L). The impact of velocity uncertainties and station site effects may be greater than a whole magnitude unit of M_L, which can make the difference between a decision to continue ("green" TLS zone) and an immediate stop of operations ("red" zone). We show how to include these uncertainties in thresholds such that events only exceed a threshold with a fixed probability. This probability can be set by regulators to reflect their tolerance to risk. We demonstrate that with the new TLS, a red-light threshold would have been encountered earlier in the hydraulic fracturing operation at Preston New Road, UK, halting operations and potentially avoiding the later large magnitude events. It is therefore critical to establish systems which permit regulators to account for uncertainties when managing risk.

Keywords: induced seismicily, local magnitude, uncertainties, traffic light system, hydraulic fracture, mining, Monte - Carlo method

OPEN ACCESS

Edited by:
Francesco Grigoli, ETH Zurich, Switzerland

Reviewed by:
Arnaud Mignan, Southern University of Science and Technology, China
Marco Broccardo, University of Trento, Italy

***Correspondence:**
Corinna Roy
earcroy@leeds.ac.uk

Specialty section:
This article was submitted to Solid Earth Geophysics, a section of the journal Frontiers in Earth Science

Received: *28 November 2020*
Accepted: *16 April 2021*
Published: *28 May 2021*

Citation:
Roy C, Nowacki A, Zhang X, Curtis A and Baptie B (2021) Accounting for Natural Uncertainty Within Monitoring Systems for Induced Seismicity Based on Earthquake Magnitudes. Front. Earth Sci. 9:634688. doi: 10.3389/feart.2021.634688

1. INTRODUCTION

The increasing number of industrial operations related to hydrocarbon extraction, geothermal power production, hydraulic fracturing for shale gas exploitation, wastewater injection, water impoundment, hydrocarbon storage, and mining operations in recent years, and the potential for large-scale subsurface CO_2 storage in future, has increased the importance of understanding and de-risking induced seismicity both to the scientific community and to the public who live near such operations (Grigoli et al., 2017). The potential to induce seismicity by human activities is well-known (McGarr et al., 2002; Elsworth et al., 2016; Foulger et al., 2018; Keranen and Weingarten, 2018; Schultz et al., 2020). Military waste fluid injected in the Rocky Mountain Arsenal in the 1960's near Denver, Colorado (Healy et al., 1968), induced the so-called "Denver earthquakes." Since then induced earthquakes related to mining (Arabasz et al., 2005; Fritschen, 2010), oil and gas field depletion (Bardainne et al., 2008; Van Thienen-Visser and Breunese, 2015) shale gas exploitation (Bao and Eaton, 2016; Clarke et al., 2019; Lei et al., 2019), geothermal exploitation (Häring et al., 2008; Deichmann and Giardini, 2009), and waste water disposal (Ellsworth, 2013) have been documented around the world (Baisch et al., 2019). In the UK, induced earthquakes related to hydraulic fracturing at Preese Hall (Clarke et al., 2014), and Preston New Road

(Clarke et al., 2019) have been observed, and the latter led to an indefinitely imposed UK government moratorium on fracking.

Traffic light systems (TLS; Bommer et al., 2006; Majer et al., 2012; Mignan et al., 2017; Baisch et al., 2019) are used widely to manage hazard and risk due to induced seismicity in geothermal and hydrocarbon industries, whereby operations are continued ("green"), amended ("amber"), or stopped ("red") based on the local event magnitude. In the original TLS developed by Bommer et al. (2006), the TLS thresholds are based on peak ground velocity, but other TLSs have been implemented based on earthquake magnitude or other ground motion parameters, such as peak ground acceleration (Ader et al., 2020). Depending on the industrial activities, criteria for a TLS may be very different. Baisch et al. (2019) and He et al. (2020) summarized some examples of existing TLSs that correspond to different industrial activities. In the UK the "amber" and "red" thresholds for induced seismicity related to unconventional oil and gas operations are set to local earthquake magnitudes $M_L = 0$ and $M_L = 0.5$, respectively, and this has led to multiple halts of hydraulic fracturing operations during the past few years (Clarke et al., 2019) and finally to an immediate moratorium of operations in November 2019.

The thresholds between zones in TLS are often defined based on limited case studies and on *a priori* assumptions in a best effort to provide simple schemes (Grigoli et al., 2017; Baisch et al., 2019). Consequently, they do not necessarily take into account the range of possible scenarios, nor uncertainties in event magnitudes, and hence some operations will incorrectly continue, increasing the risk of larger triggered earthquakes, while others will be wrongly halted. To ensure actions taken are robust, it is therefore necessary to estimate local magnitudes with uncertainties, and to consider them in the choice of M_L thresholds in TLSs.

Assessing accurate magnitudes for human-induced earthquakes such as shale gas stimulation, waste water storage, or enhanced geothermal systems is difficult, because they are affected by lack of knowledge about the Earth's subsurface between the source and receivers and by the magnitude scale used (Kendall et al., 2019). A standard approach to determine M_L is to first locate the earthquake and then apply an empirical scaling relation to the source-to-receiver distance (Gutenberg and Richter, 1942; Gutenberg, 2013). Source location-related uncertainties in M_L can then be evaluated using the location confidence ellipses. Unfortunately, estimating errors on M_L due to velocity model uncertainties, energy attenuation during propagation or site effects such as wavefield focusing is difficult.

It is well-known that the accuracy of hypocenter locations depends largely on the velocity model accuracy (Husen and Hardebeck, 2010). Various efforts have been made to estimate velocity model uncertainties, by including a correction term to traveltime curve predictions (Myers et al., 2007), making random perturbations around a given velocity model (Poliannikov et al., 2013) and by locating seismic events in an ensemble of velocity models obtained by a Bayesian analysis of independent data (Gesret et al., 2011; Hauser et al., 2011). Recently, Garcia-Aristizabal et al. (2020) analyzed different sources of uncertainty that can be relevant for the determination of earthquake source locations, and introduced a logic-tree-based ensemble modeling approach for framing the problem in a decision-making context. Their approach, however, is not fully probabilistic, but limited to a finite set of explored models.

Here we propose a way to calculate local magnitudes with uncertainties for microseismic events, and to include the uncertainties in the design of TLS. We use a 3D Monte Carlo non-linear traveltime tomography method to jointly invert for hypocenter locations and velocity model. This allows us to obtain posterior distributions for local magnitude M_L, which cover both velocity and source location uncertainties. Results clearly show that velocity uncertainties and station site effects are significant and change the zones of the TLS to which events are assigned, hence they directly affect safety related decisions. We then apply our method to the hydraulic fracturing induced seismicity at Preston New Road, UK and a mining site, and demonstrate that a red-light would have been encountered earlier if uncertainties would have been accounted for in the TLS thresholds.

2. METHODS AND DATA

Usually, local magnitudes M_L are calculated by first locating the earthquake using standard linearized earthquake location methods (e.g., Klein, 2002), which require simple assumptions about the unknown underlying subsurface seismic velocity structure, and then applying an empirical scaling relation to the source-receiver distance to determine M_L (Gutenberg and Richter, 1942; Gutenberg, 2013). The solution found by such location methods depends on the *a priori* best guess velocity model, and so it is not guaranteed to find a location near that of the true earthquake. They also cannot represent uncertainties on M_L related to velocity model uncertainties, energy attenuation during propagation, or site effects such as wavefield focusing.

2.1. Non-linear Joint Hypocenter-Velocity Travel-Time Tomography

We use a probabilistic approach to jointly invert for hypocenter locations and 3D subsurface velocity. Our approach is based on a reversible jump Markov chain Monte Carlo algorithm (Green, 1995), which is an iterative stochastic method to generate samples from a target probability density. In a Bayesian approach all information is described in probabilistic terms. The goal is to calculate the posterior probability distribution function (pdf) which describes the probability of model $\mathbf{m}$ being true given observed data $\mathbf{d}$ and other relevant, *a priori* information. The posterior pdf is defined using Bayes' theorem (Jaynes, 2003): this combines prior knowledge about the model the prior probability $p(\mathbf{m})$ with a likelihood function $p(\mathbf{d}|\mathbf{m})$ that describes the probability of observing the data if the particular given model $\mathbf{m}$ was true. In our approach, the posterior probability is a trans-dimensional function: the number of parameters is not fixed, and hence the posterior pdf is defined across a number of spaces with different dimensionalities.

We use the approach and code of Zhang et al. (2020) and use arrival times of *P* and *S* body waves from local earthquakes as data, and include the velocity model, the average arrival time

uncertainties, source locations and original time as parameters. The 3D subsurface velocity model is defined in terms of a Voronoi tessellation of constant velocity cells, where both the position of Voronoi cells and their number can change during sampling, guided by the data and prior information. However, due to the parsimony of Bayesian inference, complicated models (models with many cells) tend to be rejected in favor of simpler models, if they fit the data equally well. The full model vector $\mathbf{m}$ is given by

$$\mathbf{m} = \left(\boldsymbol{\sigma}, n, \mathbf{s}, \mathbf{V}_s, \mathbf{V}_p, \mathbf{e}\right), \tag{1}$$

where n is the number of Voronoi cells, $\mathbf{s}$ describes their positions, and $\mathbf{V}_s$ and $\mathbf{V}_p$ describe the S- and P wave velocity within each Voronoi cell. The vector $\mathbf{e} = \left(e_x^1, e_y^1, e_z^1, e_t^1, \ldots e_x^N, e_y^N, e_z^N, e_t^N\right)$ contains source locations and origin times of N events, and $\boldsymbol{\sigma}$ is the arrival time data uncertainty. The travel time uncertainties for event i are defined as Zhang et al. (2018):

$$\sigma_i = \sigma_0 t_i + \sigma_1, \tag{2}$$

where σ_0 and σ_1 are noise hyperparameters and t the P or S travel time.

We initialize 20 Markov chains with randomly generated starting models drawn from the prior distribution so that each chain starts from a different point in model space. To minimize dependence on this initial model, chains progress through a large number of samples called the burn-in phase from which all models are discarded. To reduce dependence of each sample on the next, after burn-in we only store every 200th model to use as samples of the posterior distribution. Each chain sampled 1.88 million models. At each step of the Markov chain a new model $\mathbf{m}'$ is generated by perturbing the current model. In our approach we have seven types of possible perturbation: adding, removing or moving a Voronoi cell (i.e., changing $\mathbf{s}$), changing the P or S velocity of a randomly chosen Voronoi cell ($\mathbf{V}_p$, $\mathbf{V}_s$), changing the noise hyperparameter $\boldsymbol{\sigma}$, or changing the source coordinates of one randomly chosen source ($\mathbf{e}$). The type of perturbation is selected randomly at each iteration, and the candidate model $\mathbf{m}'$ is accepted with a probability α (Green, 1995) given by:

$$\alpha\left(\mathbf{m}'|\mathbf{m}\right) = \min\left[1, \frac{\mathrm{p}\left(\mathbf{m}'\right)}{\mathrm{p}\left(\mathbf{m}\right)} \frac{\mathrm{q}\left(\mathbf{m}|\mathbf{m}'\right)}{\mathrm{q}\left(\mathbf{m}'|\mathbf{m}\right)} \frac{\mathrm{p}\left(\mathbf{d}_{obs}|\mathbf{m}'\right)}{\mathrm{p}\left(\mathbf{d}_{obs}|\mathbf{m}\right)} |\mathbf{J}|\right] \tag{3}$$

where $\mathbf{J}$ is the Jacobian matrix of the transformation from $\mathbf{m}$ to $\mathbf{m}'$ and is used to account for the volume changes of parameter space during jumps between dimensions, and $\mathrm{q}(\mathbf{m}|\mathbf{m}')$ are proposal distributions that we use to propose new models $\mathbf{m}'$ at each step. In our case, it can be shown that the Jacobian is an identity matrix (Zhang et al., 2018).

A key function in the acceptance probability is the likelihood $\mathrm{p}(\mathbf{d}|\mathbf{m})$ which quantifies the misfit between the observed data $\mathbf{d}_{\mathrm{obs}}$ and estimated data $\mathbf{d}_{\mathrm{est}}$ obtained by an eikonal solver using the fast marching method (Rawlinson and Sambridge, 2004) in model $\mathbf{m}$. The likelihood is defined as:

$$\mathrm{p}\left(\mathbf{d}|\mathbf{m}\right) \propto \exp\left(\frac{-\phi(\mathbf{m})}{2}\right) \tag{4}$$

where

$$\phi\left(\mathbf{m}\right) = \sum_i \frac{\left(d_{obs}^i - d_{est}^i\right)^2}{\sigma_i} \tag{5}$$

and σ_i is the P or S wave travel time uncertainty for event i given by Equation (2). The likelihood function contains both the effect of the errors in the source locations and the velocity model uncertainties on the travel times. We choose uniform priors for the source location coordinates and the number of Voronoi cells, and Gaussian priors for all other parameters. A full and more detailed description of the methodology can be found in Zhang et al. (2018, 2020).

2.2. M_L Scaling Relations

A general local magnitude scaling relation is described by

$$M_L = \log_{10}(A) + a\log_{10}(r) + br + c + d\exp\left(fr\right), \tag{6}$$

where r is the hypocentral distance in km, and A is the zero-to-peak amplitude in nm on the horizontal components filtered with a Wood-Anderson response (Ottemöller and Sargeant, 2013; Butcher et al., 2017; Luckett et al., 2018). Parameters a, b, c, d, and f are region dependent constants which describe the geometrical spreading (a), attenuation (b), the base level (c), and distance dependent correction terms (d and f), respectively.

The original BGS scaling relation given by Ottemöller and Sargeant (2013) is

$$M_L^{OS} = \log_{10}(A) + 1.11\log_{10}(r) + 0.00189r - 2.09\,. \tag{7}$$

This was updated by Butcher et al. (2017) to account for short source-receiver distances, giving

$$M_L^{B} = \log_{10}(A) + 1.17\log_{10}(r) + 0.0514r - 3\,. \tag{8}$$

The M_L scaling relation now used by the BGS (Luckett et al., 2018) is:

$$M_L^{L} = \log_{10}(A) + 1.11\log_{10}(r) + 0.00189r - 1.16\exp\left(-0.2r\right) - 2.09\,. \tag{9}$$

The latter scale was used for the BGS locations throughout this paper.

2.3. Data

We use data from surface seismic monitoring arrays at two sites in the United Kingdom: (1) Preston New Road, where hydraulic fracturing took place in the Bowland Shale tight gas reservoir, and (2) Thoresby Colliery, a deep coal mine in Nottinghamshire.

At Preston New Road, hydraulic fracturing started on 15 October 2018 at the PNR-1z well in Lancashire, UK under the guidance of Cuadrilla Resources Ltd. and targeted the Bowland shale at a depth of ∼2,300 m (Clarke et al., 2019). During operations, the British Geological Survey (BGS) detected 172 local seismic events with local magnitudes M_L between −1.8 and 1.6. The M_L = 0 threshold ("amber") was exceeded by nine events, six of which had local magnitudes larger than 0.5 ("red" zone). In late October 2018, five events occurred that exceeded

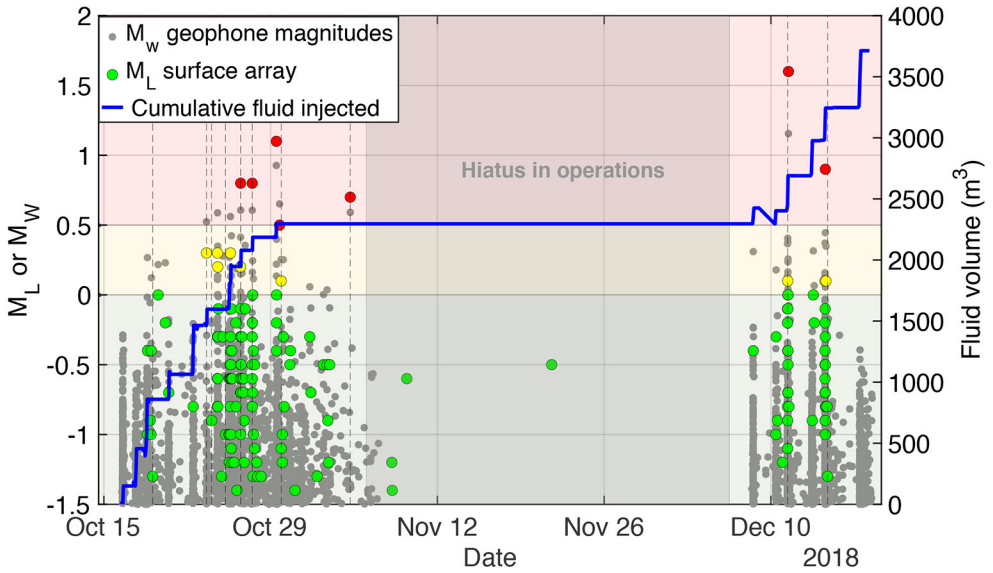

FIGURE 1 | Induced seismicity at hydraulic fracturing site at Preston New Road, UK. Background colors indicate the three zones of the UK TLS. Smaller gray dots show the moment magnitude (M_w) for events observed on the dowhole geophone array. Larger dots show the local magnitude (M_L) for events observed by the surface seismometer array, and are color-coded by the TLS zone into which they fall. The blue line shows the cumulative volume of fluid injected into the well.

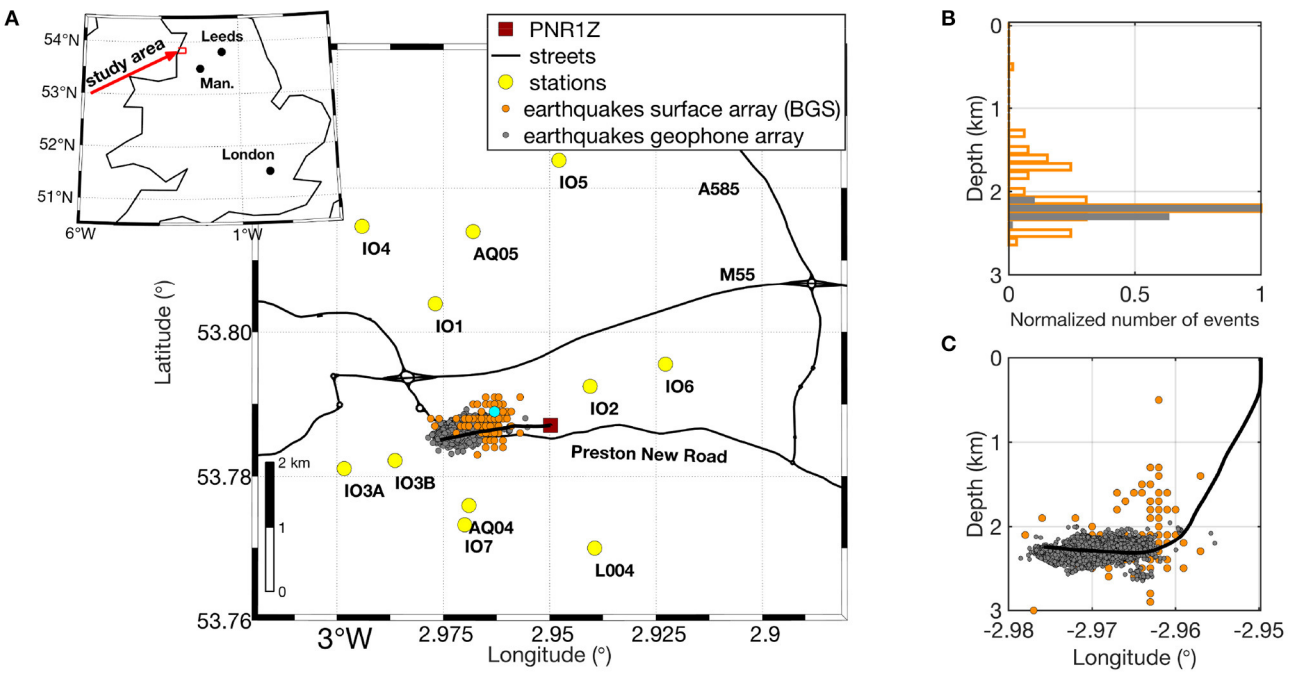

FIGURE 2 | Seismicity at Preston New Road. **(A)** Seismic stations (yellow dots) near the Preston New Road hydraulic fracturing site near Blackpool (location shown in inset) and seismic events used in this study (orange dots). The injection well is shown by a black line. The cyan dot marks an earthquake discussed in **Figure 5**. **(B)** Histogram of depth distribution of the seismic events recorded at the surface array (orange) and the downhole geophone array (gray). **(C)** Distribution of seismic events.

the red light TLS thresholds after which operations were paused for a month, but microseismicity still occurred during the hiatus (**Figure 1**). The largest event with $M_L = 1.6$, which was felt by some local residents, occurred on 11 December 11:21:15 UTC after operations resumed on 8 December. Hydraulic fracturing operations of the well ended on 17 December 2018. Over the course of 3 months more than 38,000 microseismic events were detected in real-time with the geophone array, with moment

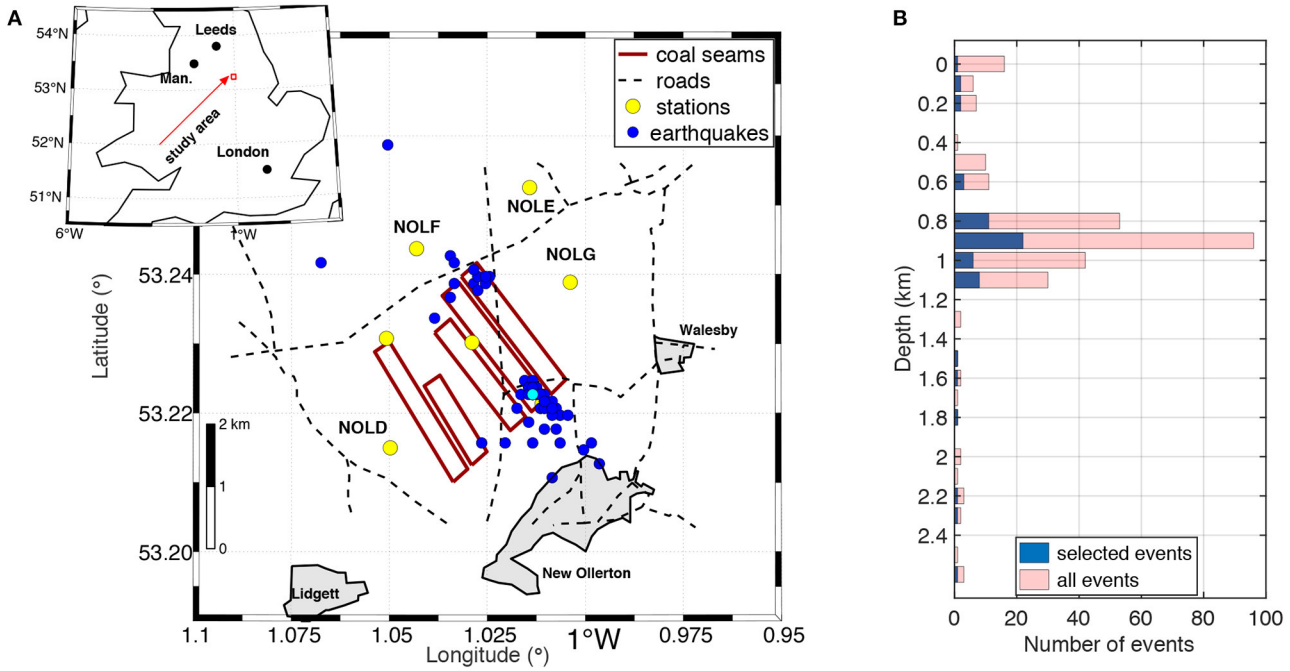

FIGURE 3 | Seismicity at the Thoresby Colliery mining site. **(A)** Seismic stations (yellow dots) near the UK's last deep coal mine in New Ollerton (location shown in inset) and seismic events used in this study (blue dots). The coal seam mine galleries are outlined by red rectangles. **(B)** Depth distribution of the seismic events as determined by the British Geological Survey. Depths for all events in the catalog are shown in pink; the blue bars correspond to the subset of the catalog used in this study.

magnitudes M_w between −3.1 and 1.6 (Clarke et al., 2019). We analyzed the *P*- and *S*-wave travel time data for the 172 largest earthquakes which were recorded at 11 seismic stations by the BGS (**Figure 2**). The majority of these events occurred between 2 and 2.5 km depth and occur in the vicinity of the well.

2.3.1. Thoresby Colliery

Thoresby Colliery in New Ollerton has a history of seismicity related to mining (Bishop et al., 1993), and in response to felt earthquakes between December 2013 and January 2014, the British Geological Survey (BGS) installed a temporary seismic network with seven seismometer stations, four of which are three-component broadband stations (**Figure 3**). Mining-induced earthquakes are some of the most widely studied and their magnitude and depth range is similar to fracking induced earthquake magnitudes (Davies et al., 2013), hence provide an excellent analog for the study of hydrofracturing induced seismicity.

Most of the seismic events used in this study are located north and south of the coal seams (**Figure 3**), and the majority of the events occurs at 800 m depth, which coincides with the depth of the coal seams (Butcher et al., 2017). The northern cluster occurred later in 2014 than the southern one. To reduce the computational costs we only use 61 seismic events out of the 305 recorded, giving 769 *P*- and *S* travel times to invert.

3. RESULTS

The McMC joint inversion provides us 3D posterior distributions of seismic velocities (V_p and V_s), and of the earthquake hypocenter locations (**Figures 4A,B**). Therefore, we can calculate hypocentral distance posterior distributions (**Figure 4C**), which in turn allows us to estimate station-average local magnitudes M_L posterior distributions (**Figure 4D**) using a scaling relation (e.g., one of Equations 6–8). These distributions include the effects of velocity and source location uncertainties as well as the source radiation pattern on the pdf for event magnitudes. The station-averaged M_L posterior distribution for one source may have a width that spans more than one zone of the traffic light system (e.g., cyan distribution in **Figure 4D**) which indicates that velocity model uncertainties alone can change the TLS zone to which the earthquake is attributed. Thus, uncertainties affect real operational decisions.

3.1. Scaling Relation and Station Site Effects on M_L

Figure 5 summarizes uncertainties in M_L due to scaling relation and station site effects at one station at Preston New Road. We observe that the particular choice of M_L scaling relation affects the local magnitude and is itself large enough to change the TLS zone. Local magnitudes are more than half a magnitude unit larger using the original BGS scaling relation (M_L^{OS}, Equation 6) compared to the most recent scale (M_L^L, Equation

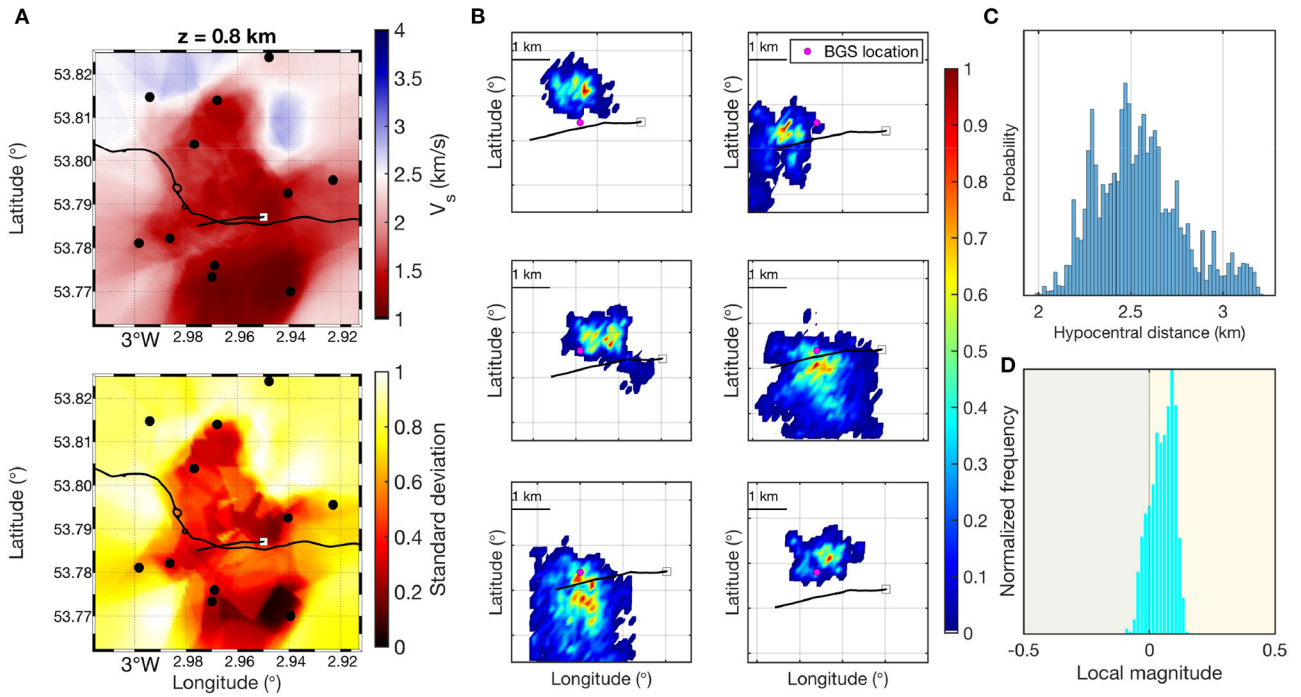

FIGURE 4 | Results of the McMC joint hypocenter-velocity tomography at Preston New Road. **(A)** Shear wave velocity V_s at 0.8 km depth and its standard deviation. **(B)** Posterior probability distribution of hypocenter locations in longitude-latitude for six different sources. **(C)** Posterior probability distribution of hypocentral distance of one source to one station. **(D)** Posterior probability distribution of local magnitude of the same event as in **(C)**, calculated from the hypocentral distance using the scaling relation in Equation (8).

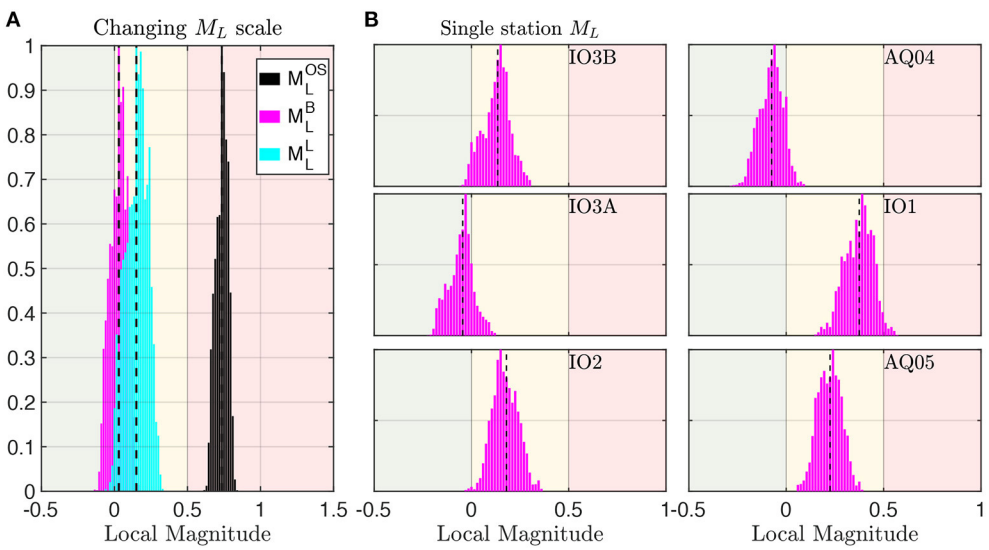

FIGURE 5 | Effect of scaling relation and station site effects on M_L for Preston New Road stations. Local earthquake magnitude M_L posterior probability distributions for the cyan colored earthquake in **Figure 1**. **(A)** Effect of the local magnitude scaling relation (Ottemöller and Sargeant, 2013; Butcher et al., 2017; Luckett et al., 2018) (Equations 6–8). **(B)** Single-station magnitudes at 6 stations using Equation (7). Background colors indicate the zones of the UK traffic light system (Department of Energy and Climate Change, 2013). Dashed lines indicate the mean.

8) (**Figure 5A**; **Supplementary Figure 1**) and therefore make a difference between a continuation ("green") and an immediate stop ("red"). Note, however, that the original BGS scaling relation was not used by the BGS to calculate M_L for these events; we include it here to show the effect of magnitude scale choices. The difference in M_L between the M_L^B scale (Equation 7) and the most

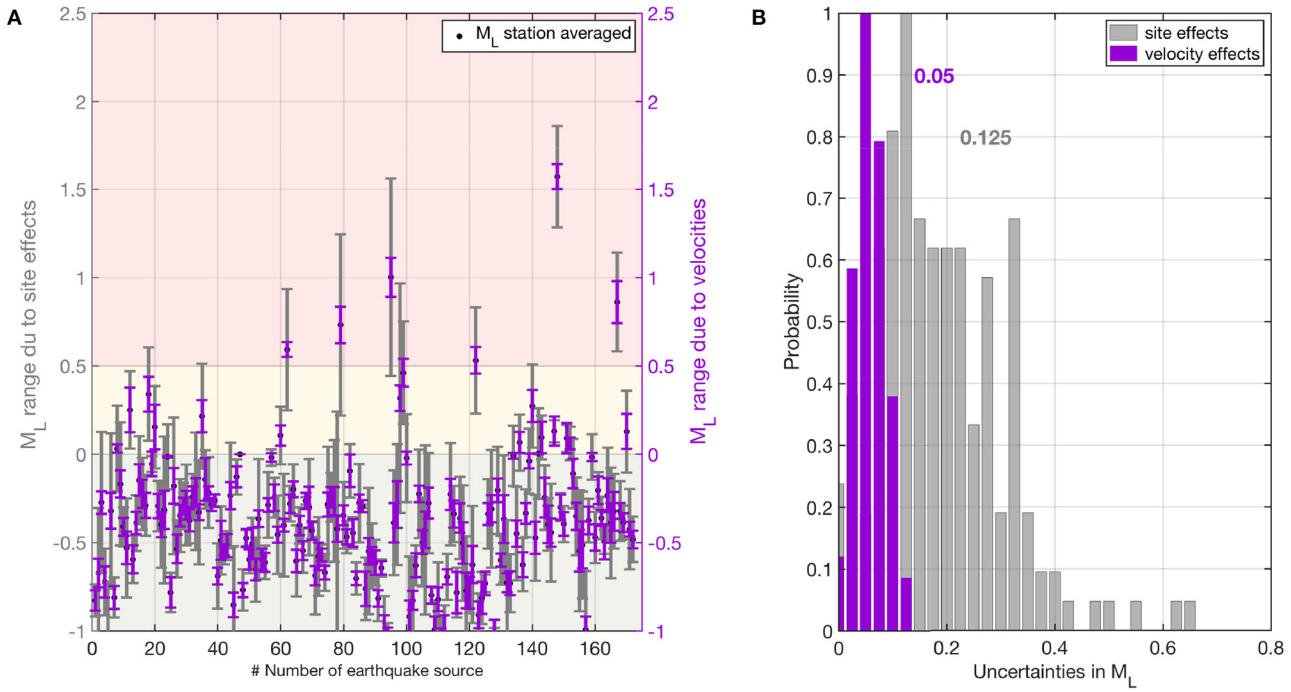

FIGURE 6 | Comparison of velocity and station site effect uncertainties on local magnitudes at Preston New Road. **(A)** Uncertainties on the station-averaged magnitude calculated with the amended BGS scale (Equation 8) due to velocity uncertainties (purple error bars) and station site effects (gray bars). Black dots mark the maximum of the station-averaged M_L distribution for each seismic event. Background colors indicate the three zones of the UK traffic light system, "green," "amber," and "red." **(B)** Normalized histograms of the magnitude uncertainties displayed in **(A)**. Numbers display the velocity and station-site effect uncertainties at which the histograms take maximum values.

recent UK scaling relation M_L^L (Equation, 8) are smaller, but peaks of distributions can lie in different zones of the TLS (**Figure 5A**).

Station site effects such as attenuation, focusing, and radiation pattern become evident by comparing M_L distributions at individual stations. These uncertainties can shift the M_L posterior distribution for one source by half a magnitude unit, sometimes more, easily sufficient to move the source into another zone of the TLS (**Figure 5B**; **Supplementary Figure 2**). We compare velocity and station site effect uncertainties on local magnitudes in **Figure 6** for the hydraulic fracturing induced earthquakes at Preston New Road. The site effect uncertainties are estimated by calculating the mean local magnitude for each seismic source at all 4 stations (using the amended BGS scaling relation, Equation, 8), and then taking the difference between the smallest and largest mean station magnitude as a measure of site-related uncertainties. The velocity-related uncertainties are defined as the width of the interval between the 5–95% percentile of the station-averaged local magnitudes distributions. Their effects each average around ±0.125 and ±0.05 magnitude units, respectively, in our case study, but they vary and can have a combined effect that alters magnitude estimates by up to a whole magnitude unit (**Figure 6**). We observe that uncertainties are also roughly equally important for the mining induced seismicity at New Ollerton—their effects average around ±0.3 and ±0.05 magnitude units for site and velocity-related effects, respectively—with a combined effect that again can alter magnitude estimates by up to a whole magnitude unit, and potentially move events from "green" to "red" zones (**Figure 7**).

4. A PROBABILISTIC TRAFFIC LIGHT SYSTEM

We can now include the velocity and station site effect uncertainties in M_L in a traffic light system (TLS). To do this, we first calculate M_L threshold probability curves using the station-averaged M_L posterior distributions of the microseismic events at Preston New Road. Threshold probability curves describe the probability that an earthquake of a given magnitude is in any one zone of the TLS. They take into account velocity and station-site effect uncertainties, as well as attenuation and geometrical spreading in M_L. Furthermore, the threshold probability curves allow us to draw conclusions about the range of observed M_L for which the probability of any earthquake being in a zone drops below a given confidence level α. The last point is particularly interesting for regulators and operators because it enables them to define the thresholds between zones in such a way that the probability of an earthquake being in each zone of the TLS is always above a chosen confidence level α.

M_L threshold probability curves are obtained by shifting each of the 172 station-averaged event M_L pdfs along the local magnitude axis and estimating the percentage of the distribution lying in each of the three zones of the TLS

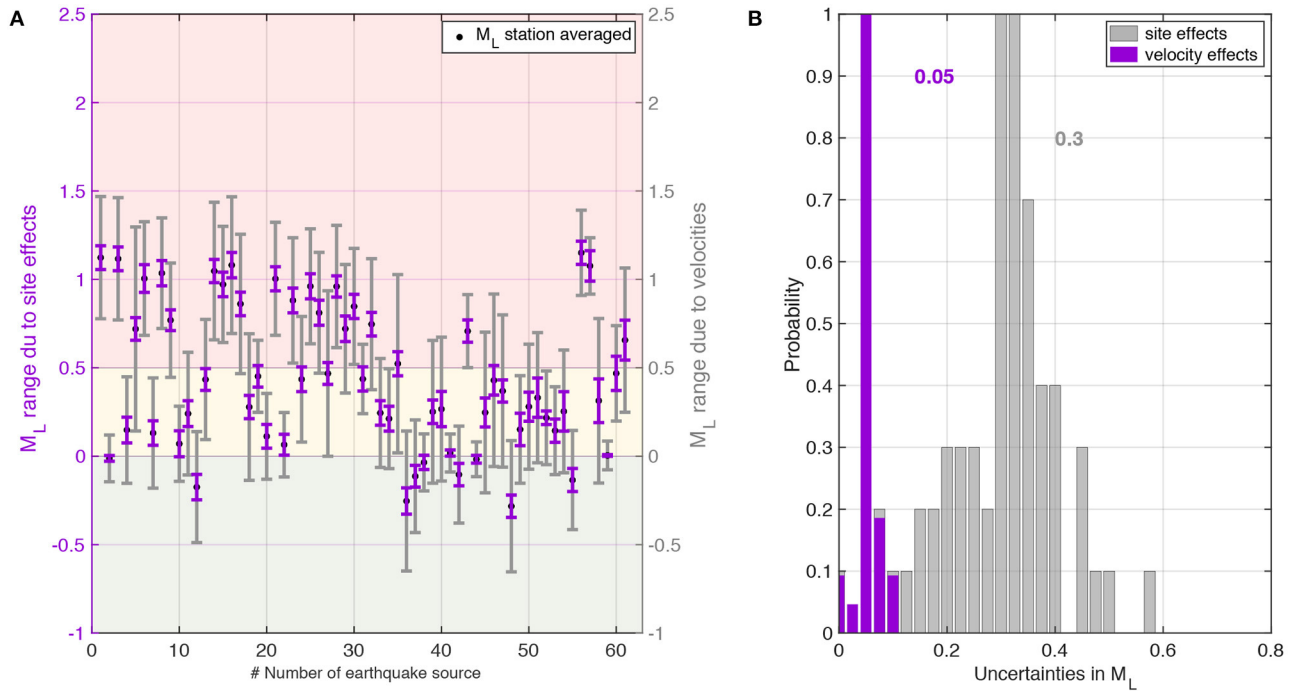

FIGURE 7 | Comparison of velocity and station site effect uncertainties on local magnitudes at New Ollerton mining site. **(A)** Uncertainties on the station-averaged magnitude calculated with the amended BGS scale (Equation 8) due to velocity uncertainties (purple error bars) and station site effects (gray bars). Black dots mark the maximum of the station-averaged ML distribution for each seismic event. Background colors indicate the three zones of the UK traffic light system, "green," "amber," and "red." **(B)** Normalized histograms of the magnitude uncertainties displayed in **(A)**. Numbers display the velocity and station-site effect uncertainties at which the histograms take maximum values.

(**Supplementary Figure 3**). By averaging over all threshold probabilities curves, we obtain one curve that describes the probability of an earthquake with a given magnitude being in any zone of the TLS. This can then be used to draw conclusions about (1) probabilities of earthquakes of a certain event magnitude M_L being in any one of the TLS zones, and (2) the M_L range for which the probability of any earthquake being in a zone drops below a given confidence level α.

Our approach here is approximate, but once the first inversion if performed, subsequent assignment of a new event's M_L to the correct zone of an adjusted TLS is trivial and can be done in real time, as explained below. In theory, however, the most rigorous approach to incorporating uncertainty into the calculation of M_L for any one event is to retrieve its full posterior M_L distribution, which is the averaged pdf across all stations for that one event. Although at this point we can do this for any existing event in our dataset, in practice we want to be able to do this for each new event that occurs, in real time. This presents a large challenge, however, since formally we must add the travel times from this new event to our dataset and re-run the whole sampling procedure again. We have added one new earthquake to the dataset and sampled 140,000 new models. This took 14,880 CPU-hours on the ARCHER HPC machine, and so remains practically impossible for real time monitoring. Furthermore, the M_L pdf of the new event is still sparsely sampled, and hence does not allow for a robust M_L uncertainty quantification.

4.1. TLS With Realistic Uncertainties

A regulator or operator can choose whether they wish to minimize the probability of any such event exceeding a TLS threshold undetected, or to maximize the certainty that an event truly has exceeded the legal magnitude limits in order to avoid unnecessary, costly halt of operations. We term the first TLS^-, where the M_L thresholds are shifted toward smaller apparent-magnitude thresholds. In this way, the risk of smaller-magnitude events leading to large earthquakes is reduced because operations are both halted and put "on caution" earlier. In the latter, the TLS thresholds would effectively be increased to higher values (TLS^+), so that operations could still continue up to larger apparent earthquake magnitudes. The choice of the risk system by the operator (TLS^+ or TLS^-) is, however, subjective and depends on the country's governmental policies. The choice of the confidence level defines the TLS thresholds, but these as well as the risk strategy can be changed at any time.

For example, say a regulator or operator chooses that the confidence level with which each event is assigned to the correct zone must be at least 80% for decisions to be made. The range of estimated M_L values that would have less than $\alpha = 0.8$ probability is $-0.036 < M_L < 0.035$ (zone A) and $0.46 < M_L < 0.53$ (zone B) (gray zones in **Figure 8A**) using the current UK TLS thresholds. Then, in a TLS^-, all of zone A would be attributed to "amber," and zone B to "red," effectively moving the TLS

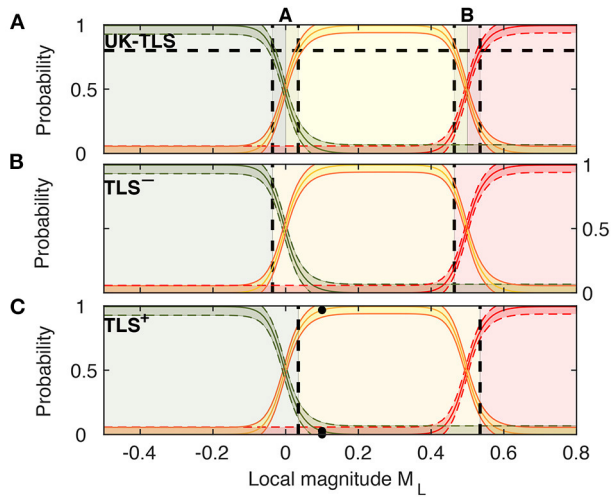

FIGURE 8 | Developing TLS systems where the risk of larger triggered earthquakes is potentially reduced (TLS^{-}), and a TLS where the risk of unnecessary, costly stop of operations is reduced (TLS^{+}). The threshold probability curves describe the probability of an event of local magnitude M_L being in any one of the TLS zones (color coded red/amber/green for each zone). **(A)** Earthquakes that have M_L estimates in zones A and B cannot be assigned to "red/amber/green" with 80% confidence. **(B)** For a 20% risk of an event exceeding a TLS threshold undetected, zones A and B are attributed to "amber" and "red," respectively (TLS^{-}). **(C)** For 80% certainty that any event has exceeded a threshold, zones A and B are attributed to "green" and "amber," respectively (TLS^{+}). Black dots in **(C)** mark probabilities for example earthquakes of different M_L.

thresholds to lower values (**Figure 8B**). Alternatively, in a TLS^{+}, zone A would be assigned to "green" and zone B to "amber," so the TLS thresholds would effectively be increased to higher values (**Figure 8C**).

The uncertainties in M_L discussed here are site specific so need to be determined for each geographical area or industrial operation individually. However, our approach can be applied to any site and to any form of induced seismicity. We have also demonstrated that for the Thoresby Colliery mining site in the UK the velocity model and station site effect uncertainties in M_L are non-negligible (**Figure 7**), and can be accounted for in the choice of TLS thresholds (**Supplementary Figure 4**).

5. APPLICATION OF A PROBABILISTIC TLS TO PRESTON NEW ROAD SEISMICITY

We can use the three TLSs (**Figure 8**) to analyze retrospectively how decisions would have changed at Preston New Road under a TLS^{+} or TLS^{-} (**Figure 9**). We compare here the classification in the UK-TLS, a TLS^{-} and TLS^{+} for a 80% confidence level (**Figure 5**). That means, the risk of exceeding a TLS threshold in TLS^{-} is 20%, while in the TLS^{+}, the certainty that a threshold was exceeded is 80%. The earthquake on October 19th would have been classified as "amber" in all three TLSs using the maximum probability magnitude, whereas it was classified as "green" by the operator. Hence, action would have been taken earlier and the probability of subsequent larger events would have been reduced. The same is true for the seismicity on October 24th (**Figure 9B**), where operations would have stopped immediately with a safety prioritizing system (TLS^{-}), and also in the UK TLS with a M_L that accounts for uncertainties. This demonstrates the importance of accounting for uncertainties in local magnitudes M_L in the decision-making process.

We acknowledge that the occurrence of induced seismicity is a multi-parameter phenomenon, depending on details of subsurface structures as well as on the complete history of operational measures and therefore cannot be predicted. Deformation processes may continue and can still induce seismicity after injections stop. The delay time between hydraulic fracturing completion and the cessation of the observed seismicity can be up to several years (Baisch et al., 2019). It is therefore speculative that an earlier stop would have prevented large magnitude post-injection seismicity at PNR. Nevertheless, it has been shown that lower M_L threshold values in the TLS used for the geothermal stimulation in Basel, Switzerland could have prevented larger magnitude post-injection seismicity (Baisch et al., 2019). We therefore argue that it is critical to establish systems which permit regulators to account for uncertainties while managing risk, as we propose here.

6. CONCLUSIONS

We implemented a fully Bayesian approach for analysing uncertainties, such as velocity model and source location uncertainties in local earthquake magnitudes and evaluate their influence on decision-making for induced seismicity. We conclude that these uncertainties are important, as they can make a difference of up to one or two magnitude unit, and hence directly affect operational decisions by potentially moving an earthquake two zones in a traffic light system (TLS) leading to radically different operational outcomes.

To build a site-specific probabilistic TLS that accounts for uncertainties, the following three steps are necessary: (1) run one fully non-linear hypocenter-velocity tomography for the site and calculate M_L posterior distributions for each earthquake. (2) calculate threshold probability curves, choose a desired confidence level α, and determine the M_L zones A and B below the desired confidence level. (3) attribute zone A and B to "green/amber" or "amber/red" according to the desired safety system (reduce the risk of larger magnitude events (TLS^{-}) or reduce the risk of halting operations unnecessarily (TLS^{+})). From this point on, real time assignment of any new event's M_L to the correct TLS zone is trival, yet incorporates all the uncertainty in the measurements.

We applied our method to anthropogenic seismicity at a hydraulic fracturing site in the UK, and demonstrate that a red-light threshold would have been encountered earlier in a TLS^{-}, which possibly could have prevented the UK-wide shut-down. We also applied our methods to mining-related seismicity at Thoresby Colliery, UK and find they

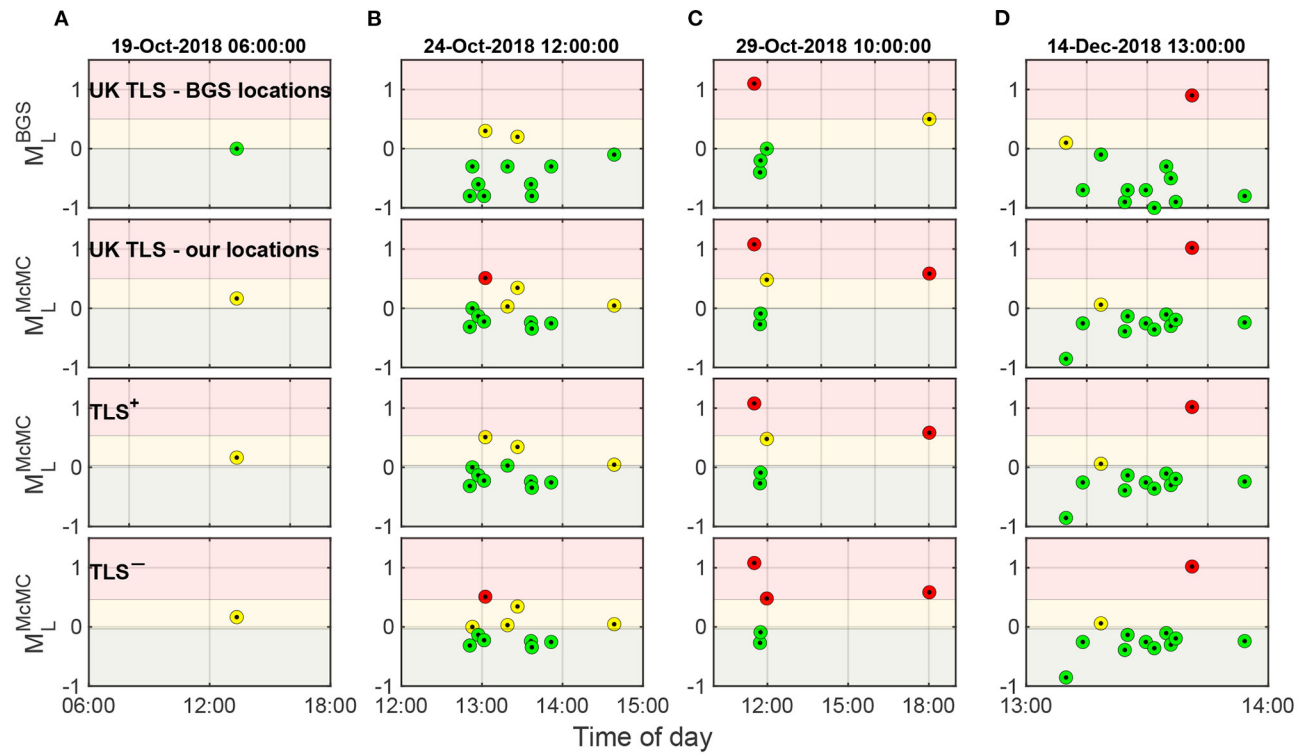

FIGURE 9 | Classification of seismic events for 4 days **(A-D)** in the UK TLS (top two rows). Row 1 shows results using the local magnitudes determined by the BGS while other rows use the maximum probability magnitude determined in this work. Row 3: Classifications for a TLS where the risk of unnecessary, costly stop of operations is reduced (TLS^{+}). Row 4: TLS where the risk of larger triggered earthquakes is potentially reduced (TLS^{-}). Both were calculated for an 80% confidence level.

apply equally well in this different setting. Hence, our approach can be applied to any site and any form of seismicity.

DATA AVAILABILITY STATEMENT

The original contributions presented in the study are included in the article/**Supplementary Materials**, further inquiries can be directed to the corresponding author/s.

AUTHOR CONTRIBUTIONS

CR processed the data, performed the analysis, prepared the figures, and wrote the paper. XZ developed the inversion code. BB provided the data of both case studies. All authors contributed to the interpretation of the results and the writing of the paper.

FUNDING

This work was supported by the Natural Environment Research Council [grant number NE/R001154/1].

ACKNOWLEDGMENTS

This work used the ARCHER UK National Supercomputing Service (http://www.archer.ac.uk) and ARC3, part of the High Performance Computing facilities at the University of Leeds, UK. The authors thank the Edinburgh Interferometry Project sponsors for supporting this research. We thank two reviewers for their comments to improve this manuscript.

SUPPLEMENTARY MATERIAL

The Supplementary Material for this article can be found online at: https://www.frontiersin.org/articles/10.3389/feart.2021.634688/full#supplementary-material

REFERENCES

Ader, T., Chendorain, M., Free, M., Saarno, T., Heikkinen, P., Malin, P. E., et al. (2020). Design and implementation of a traffic light system for deep geothermal well stimulation in Finland. *J. Seismol.* 24, 991–1014. doi: 10.1007/s10950-019-09853-y

Arabasz, W. J., Nava, S. J., McCarter, M. K., Pankow, K. L., Pechmann, J. C., Ake, J., et al. (2005). Coal-mining seismicity and ground-shaking hazard: a case study

in the Trail Mountain Area, Emery County, Utah. *Bull. Seismol. Soc. Am.* 95, 18–30. doi: 10.1785/0120040045

Baisch, S., Koch, C., and Muntendam-Bos, A. (2019). Traffic light systems: to what extent can induced seismicity be controlled? *Seismol. Res. Lett.* 90, 1145–1154. doi: 10.1785/0220180337

Bao, X., and Eaton, D. W. (2016). Fault activation by hydraulic fracturing in Western Canada. *Science* 354, 1406–1409. doi: 10.1126/science.aag2583

Bardainne, T., Dubos-Sallée, N., Sénéchal, G., Gaillot, P., and Perroud, H. (2008). Analysis of the induced seismicity of the Lacq gas field (Southwestern France) and model of deformation. *Geophys. J. Int.* 172, 1151–1162. doi: 10.1111/j.1365-246X.2007.03705.x

Bishop, I., Styles, P., and Allen, M. (1993). Mining-induced seismicity in the Nottinghamshire Coalfield. *Q. J. Eng. Geol. Hydrogeol.* 26, 253–279. doi: 10.1144/GSL.QJEGH.1993.026.004.03

Bommer, J. J., Oates, S., Cepeda, J. M., Lindholm, C., Bird, J., Torres, R., et al. (2006). Control of hazard due to seismicity induced by a hot fractured rock geothermal project. *Eng. Geol.* 83, 287–306. doi: 10.1016/j.enggeo.2005.11.002

Butcher, A., Luckett, R., Verdon, J. P., Kendall, J.-M., Baptie, B., and Wookey, J. (2017). Local magnitude discrepancies for near-event receivers: implications for the UK traffic-light scheme. *Bull. Seismol. Soc. Am.* 107, 532–541. doi: 10.1785/0120160225

Clarke, H., Eisner, L., Styles, P., and Turner, P. (2014). Felt seismicity associated with shale gas hydraulic fracturing: the first documented example in Europe. *Geophys. Res. Lett.* 41, 8308–8314. doi: 10.1002/2014GL062047

Clarke, H., Verdon, J. P., Kettlety, T., Baird, A. F., and Kendall, J. (2019). Real-time imaging, forecasting, and management of human-induced seismicity at Preston New Road, Lancashire, England. *Seismol. Res. Lett.* 90, 1902–1915. doi: 10.1785/0220190110

Davies, R., Foulger, G., Bindley, A., and Styles, P. (2013). Induced seismicity and hydraulic fracturing for the recovery of hydrocarbons. *Mar. Petrol. Geol.* 45, 171–185. doi: 10.1016/j.marpetgeo.2013.03.016

Deichmann, N., and Giardini, D. (2009). Earthquakes induced by the stimulation of an enhanced geothermal system below Basel (Switzerland). *Seismol. Res. Lett.* 80, 784–798. doi: 10.1785/gssrl.80.5.784

Department of Energy and Climate Change (2013). *Onshore Oil and Gas Exploration in the UK: Regulation and Best Practice*. Technical report.

Ellsworth, W. L. (2013). Injection-induced earthquakes. *Science* 341:1225942. doi: 10.1126/science.1225942

Elsworth, D., Spiers, C. J., and Niemeijer, A. R. (2016). Understanding induced seismicity. *Science* 354, 1380–1381. doi: 10.1126/science.aal2584

Foulger, G. R., Wilson, M. P., Gluyas, J. G., Julian, B. R., and Davies, R. J. (2018). Global review of human-induced earthquakes. *Earth Sci. Rev.* 178, 438–514. doi: 10.1016/j.earscirev.2017.07.008

Fritschen, R. (2010). Mining-induced seismicity in the Saarland, Germany. *Pure Appl. Geophys.* 167, 77–89. doi: 10.1007/s00024-009-0002-7

Garcia-Aristizabal, A., Danesi, S., Braun, T., Anselmi, M., Zaccarelli, L., Famiani, D., et al. (2020). Epistemic uncertainties in local earthquake locations and implications for managing induced seismicity. *Bull. Seismol. Soc. Am.* 110, 2423–2440. doi: 10.1785/0120200100

Gesret, A., Noble, M., Desassis, N., and Romary, T. (2011). "Microseismic monitoring: consequences of velocity model uncertainties on location uncertainties," in *Third EAGE Passive Seismic Workshop-Actively Passive 2011*. Athens.

Green, P. J. (1995). Reversible jump Markov chain Monte Carlo computation and Bayesian model determination. *Biometrika* 82, 711–732.

Grigoli, F., Cesca, S., Priolo, E., Rinaldi, A. P., Clinton, J. F., Stabile, T. A., et al. (2017). Current challenges in monitoring, discrimination, and management of induced seismicity related to underground industrial activities: a European perspective. *Rev. Geophys.* 55, 310–340. doi: 10.1002/2016RG000542

Gutenberg, B. (2013). *Seismicity of the Earth and Associated Phenomena*. Princeton: Read Books Ltd.

Gutenberg, B., and Richter, C. F. (1942). Earthquake magnitude, intensity, energy, and acceleration. *Bull. Seismol. Soc. Am.* 32, 163–191.

Häring, M. O., Schanz, U., Ladner, F., and Dyer, B. C. (2008). Characterisation of the Basel 1 enhanced geothermal system. *Geothermics* 37, 469–495. doi: 10.1016/j.geothermics.2008.06.002

Hauser, J., Dyer, K. M., Pasyanos, M. E., Bungum, H., Faleide, J. I., Clark, S. A., et al. (2011). A probabilistic seismic model for the European Arctic. *J. Geophys. Res.* 116, B01303. doi: 10.1029/2010JB007889

He, M., Li, Q., and Li, X. (2020). Injection-induced seismic risk management using machine learning methodology – A perspective study. *Front. Earth Sci.* 8:227. doi: 10.3389/feart.2020.00227

Healy, J. H., Rubey, W. W., Griggs, D. T., and Raleigh, C. B. (1968). The Denver earthquakeS. *Science* 161, 1301–1310. doi: 10.1126/science.161.3848.1301

Husen, S., and Hardebeck, J. (2010). Earthquake location accuracy. *CORSSA*.

Jaynes, E. T. (2003). *Probability Theory: The Logic of Science*. Cambridge: Cambridge University Press.

Kendall, J.-M., Butcher, A., Stork, A. L., Verdon, J. P., Luckett, R., and Baptie, B. (2019). How big is a small earthquake? Challenges in determining microseismic magnitudes. *First Break* 37, 51–56. doi: 10.3997/1365-2397.n0015

Keranen, K. M., and Weingarten, M. (2018). Induced Seismicity. *Annu. Rev. Earth Planet. Sci.* 46, 149–174. doi: 10.1146/annurev-earth-082517-010054

Klein, F. W. (2002). *User's Guide to HYPOINVERSE-2000, a Fortran Program to Solve for Earthquake Locations and Magnitudes*. Technical report, US Geological Survey.

Lei, X., Wang, Z., and Su, J. (2019). The december 2018 ML 5.7 and january 2019 ML 5.3 earthquakes in South Sichuan Basin induced by shale gas hydraulic fracturing. *Seismol. Res. Lett.* 90, 1099–1110. doi: 10.1785/0220190029

Luckett, R., Ottemöller, L., Butcher, A., and Baptie, B. (2018). Extending local magnitude ML to short distances. *Geophys. J. Int.* 216, 1145–1156. doi: 10.1093/gji/ggy484

Majer, E., Nelson, J., Robertson-Tait, A., Savy, J., and Wong, I. (2012). *Protocol for Addressing Induced Seismicity Associated With Enhanced Geothermal Systems*. US Department of Energy, Energy Efficiency and Renewable Energy, 52.

McGarr, A., Simpson, D., and Seeber, L. (2002). "40 - Case Histories of Induced and Triggered Seismicity," in *International Handbook of Earthquake and Engineering Seismology, Part A*, volume 81 of *International Geophysics*, eds W. H. Lee, H. Kanamori P. C. Jennings and C. Kisslinger (Academic Press), 647–661.

Mignan, A., Broccardo, M., Wiemer, S., and Giardini, D. (2017). Induced seismicity closed-form traffic light system for actuarial decision-making during deep fluid injections. *Sci. Rep.* 7:13607. doi: 10.1038/s41598-017-13585-9

Myers, S. C., Johannesson, G., and Hanley, W. (2007). A Bayesian hierarchical method for multiple-event seismic location. *Geophys. J. Int.* 171, 1049–1063. doi: 10.1111/j.1365-246X.2007.03555.x

Ottemöller, L., and Sargeant, S. (2013). A local magnitude scale ML for the United Kingdom. *Bull. Seismol. Soc. Am.* 103, 2884–2893. doi: 10.1785/0120130085

Poliannikov, O. V., Prange, M., Malcolm, A., and Djikpesse, H. (2013). A unified Bayesian framework for relative microseismic location. *Geophys. J. Int.* 194, 557–571. doi: 10.1093/gji/ggt119

Rawlinson, N., and Sambridge, M. (2004). Multiple reflection and transmission phases in complex layered media using a multistage fast marching method. *Geophysics* 69, 1338–1350. doi: 10.1190/1.1801950

Schultz, R., Beroza, G., Ellsworth, W., and Baker, J. (2020). Risk-informed recommendations for managing hydraulic fracturing–induced seismicity via traffic light protocols. *Bull. Seismol. Soc. Am.* 110, 2411–2422. doi: 10.1785/0120200016

Van Thienen-Visser, K., and Breunese, J. (2015). Induced seismicity of the Groningen gas field: history and recent developments. *Leading Edge* 34, 664–671. doi: 10.1190/tle34060664.1

Zhang, X., Curtis, A., Galetti, E., and de Ridder, S. (2018). 3D Monte Carlo surface wave tomography. *Geophys. J. Int.* 215, 1644–1658. doi: 10.1093/gji/ggy362

Zhang, X., Roy, C., Curtis, A., Nowacki, A., and Baptie, B. (2020). Imaging the subsurface using induced seismicity and ambient noise: 3D Tomographic Monte Carlo joint inversion of earthquake body wave travel times and surface wave dispersion. *Geophys. J. Int.* 222, 1639–1655. doi: 10.1093/gji/ggaa230

Conflict of Interest: The authors declare that the research was conducted in the absence of any commercial or financial relationships that could be construed as a potential conflict of interest.

The handling editor declared a shared affiliation with one of the authors AC at time of review.

frontiers in Earth Science

ORIGINAL RESEARCH
published: 14 June 2021
doi: 10.3389/feart.2021.663385

Reservoir-Triggered Earthquakes Around the Atatürk Dam (Southeastern Turkey)

Pınar Büyükakpınar[1,2], Simone Cesca[2], Sebastian Hainzl[2], Mohammadreza Jamalreyhani[2,3], Sebastian Heimann[2] and Torsten Dahm[2,4]*

[1] Kandilli Observatory and Earthquake Research Institute, Regional Earthquake-Tsunami Monitoring Center, Boğaziçi University, Istanbul, Turkey, [2] GFZ German Research Centre for Geosciences, Potsdam, Germany, [3] Institute of Geophysics, University of Tehran, Tehran, Iran, [4] Institute of Geosciences, University of Potsdam, Potsdam, Germany

Reservoir-triggered seismicity has been observed near dams during construction, impoundment, and cyclic filling in many parts of the earth. In Turkey, the number of dams has increased substantially over the last decade, with Atatürk Dam being the largest dam in Turkey with a total water capacity of 48.7 billion m^3. After the construction of the dam, the monitoring network has improved. Considering earthquakes above the long-term completeness magnitude of M_C = 3.5, the local seismicity rate has substantially increased after the filling of the reservoir. Recently, two damaging earthquakes of M_W 5.5 and M_W 5.1 occurred in the town of Samsat near the Atatürk Reservoir in 2017 and 2018, respectively. In this study, we analyze the spatio-temporal evolution of seismicity and its source properties in relation to the temporal water-level variations and the stresses resulting from surface loading and pore-pressure diffusion. We find that water-level and seismicity rate are anti-correlated, which is explained by the stabilization effect of the gravitational induced stress imposed by water loading on the local faults. On the other hand, we find that the overall effective stress in the seismogenic zone increased over decades due to pore-pressure diffusion, explaining the enhanced background seismicity during recent years. Additionally, we observe a progressive decrease of the Gutenberg-Richter b-value. Our results indicate that the stressing rate finally focused on the region where the two damaging earthquakes occurred in 2017 and 2018.

Keywords: reservoir-triggered seismicity, earthquake source parameters, stress-change, seismic hazard, Atatürk Dam

OPEN ACCESS

Edited by:
Antonio Pio Rinaldi, Swiss Seismological Service, ETH Zurich, Switzerland

Reviewed by:
Stella Pytharouli, University of Strathclyde, United Kingdom
Luisa Valoroso, Istituto Nazionale di Geofisica e Vulcanologia (INGV), Italy

****Correspondence:***
Pınar Büyükakpınar
pinarbuyukakpinar@gmail.com

Specialty section:
This article was submitted to Geohazards and Georisks, a section of the journal Frontiers in Earth Science

Received: *02 February 2021*
Accepted: *22 April 2021*
Published: *14 June 2021*

Citation:
Büyükakpınar P, Cesca S, Hainzl S, Jamalreyhani M, Heimann S and Dahm T (2021) Reservoir-Triggered Earthquakes Around the Atatürk Dam (Southeastern Turkey). Front. Earth Sci. 9:663385. doi: 10.3389/feart.2021.663385

INTRODUCTION

Discriminating induced or triggered seismicity related to industrial activities from natural seismicity has been a highly debated subject. Since the beginning of the last century, many earthquakes associated with anthropogenic activities have been reported, and the number of cases has been increasing due to the expanding man-made operations, such as gas and oil production, wastewater injection, mining, geothermal operations, and water impoundment (Dahm et al., 2010; Grigoli et al., 2017; Rinaldi et al., 2020). The most recent, outstanding cases debating potential induced or triggered seismicity, attracting societal interest, include the 2011 M_w 5.7 and 2016 M_w 5.8 Oklahoma earthquake sequences (Ellsworth, 2013; Keranen et al., 2013, 2014;

Walsh and Zoback, 2015; Manga et al., 2016; Yeck et al., 2016, 2017), the 2012 M_w 6.1 and 5.9 Emilia, Italy, earthquakes (Cesca et al., 2013a; Dahm et al., 2015; Juanes et al., 2016), the 2017 M_w 5.5 Pohang, South Korea, earthquake (Grigoli et al., 2018; Kim et al., 2018), the 2011 M_w 5.1 Lorca, Spain, earthquake (González et al., 2012; Martínez-Díaz et al., 2012), the 2013 M_w 4.3 Castor, Spain, earthquake sequence (Cesca et al., 2014; Gaite et al., 2016; Villaseñor et al., 2020), and the 2012 M_L 3.6 Huizinge earthquake at the Groningen gas field (Richter et al., 2020). Many more reported cases caused by human-related activities have been compiled in different studies (McGarr et al., 2002; Davies et al., 2013; Ellsworth, 2013; Foulger et al., 2018).

In recent years, some attempts have been made to differentiate induced and triggered seismicity (McGarr and Simpson, 1997; McGarr et al., 2002; Dahm et al., 2013, 2015; Shapiro et al., 2013). In the case of induced earthquakes, the nucleation, growth, and rupture process are determined by human-related stress perturbations (Dahm et al., 2013). In the case of triggered seismicity, the background stress field plays a more important role, and human activities are only responsible for the earthquake nucleation, while the rupture evolution is controlled by the background stresses (Dahm et al., 2013). This latter case may include large earthquakes, which could be triggered by small perturbations near their nucleation point, but then grow considerably, with the final size and magnitude not being controlled by the original anthropogenic stress changes but depending on fault dimensions and strain (Dahm et al., 2013; Grigoli et al., 2017). In our study, we use the term reservoir triggered seismicity (RTS) for the earthquakes that occurred close to the Atatürk Dam, as this region is located between tectonically active faults, and the background tectonic stresses presumably play a role in the size and magnitude of observed seismicity (**Figure 1**).

An influence of water reservoir loading on earthquake activity was first proposed by Carder (1945) at Lake Mead, United States. Many case studies of RTS have been reported since that time; most known RTS cases ($M_w > 6$) were observed at Xinfengjiang Dam–China, 1962 M_w 6.2, Kariba Zambia–Zimbabwe, 1963 M_w 6.2, Koyna Dam–India, 1967 M_w 6.3, and Zipingpu Reservoir–Wenchuan, 2008 M_w 7.9 (Gupta and Rastogi, 1976; Gupta, 1992, 2002; Ge et al., 2009). Wilson et al. (2017) have recently constructed a database with 186 reported cases of RTS (The Human-Induced Earthquake Database HiQuake)[1]. In Turkey, although one of the richest countries in geothermal, mining, and water resources potentials, only a few case studies of induced/triggered earthquakes have been reported in the literature so far.

Around 860 active dam sites are currently existing in Turkey, and the number is expected to increase (The General Directorate of State Hydraulic Works of Turkey; DSI)[2]. Most of these dams are located in southeast Turkey since the Southeastern Anatolia Project (GAP) was launched in 1977. Today, the Atatürk Dam is the fifth largest dam on Earth in terms of water storage capacity (48.7 billion m^3) and among the largest dam sites in terms of electricity production (DSI)[3]. It is also the largest clay-cored rock-fill dam in Turkey, with 169 m height. The construction of the Atatürk Dam was initiated in 1983, the water impoundment started in 1990, and the dam became operational in 1992 (Tosun et al., 2007; Tosun, 2012). The annual variation of the water level in the Atatürk Dam is in the range of 30 m, between 513 m and 542 m above sea level (DSI)[3]. **Table 1** summarizes the characteristics of the Atatürk Dam and its reservoir. After the water impoundment in the reservoir, field and laboratory experiments showed damages along the crest (Çetin et al., 2000) attributed to the rising amount of water. Consequently, the rock-fill part of the dam started to slake by May 1992; the upper part of the dam was then reconstructed to its original height (549 m), and the dam was maintained operational by keeping a 7 m freeboard (Çetin et al., 2000).

The Atatürk Reservoir (AR) is located on the Euphrates River between the Adıyaman-Samsat region and the Şanlıurfa province, in southeast Turkey. This region is tectonically influenced by the relative motion of the African, Arabian, and Eurasian Plates resulting in the movement of the Anatolian Plate to the west (McKenzie, 1972; Şengör and Yılmaz, 1981; Şengör et al., 1985; Reilinger et al., 2006) as shown in **Figure 1**. AR is situated between two fault systems: the Bozova Fault (BF), which is an NW-SE right-lateral strike-slip structure with 60 km length passing through the southwest of AR (Şahbaz and Seyitoğlu, 2018), and the East Anatolian Fault (EAF), in a distance of about 60 km in the northeast of AR, which is a ∼580 km left-lateral strike-slip active fault striking NE-SW direction and one of the most prominent structural elements in the region (Arpat and Şaroğlu, 1972; Duman and Emre, 2013). A recent destructive earthquake (M_w 6.8) occurred on January 24, 2020, along the EAF, within approximately 100 km distance from AR, and caused serious damages not only in the epicentral area but also in the neighboring regions (Jamalreyhani et al., 2020). **Figure 1** also shows the existence of local faults dominated by the regional tectonics in the study area. The Samsat Fault (SF) and Kalecik Fault (KF) showing parallel alignment to the BF and crossing the AR in the NW-SE direction with a right-lateral strike-slip mechanism. On the other hand, The Lice Fault (LF) indicates a left-lateral strike-slip mechanism in the NE-SW direction with respect to the BF, SF, and KF (Perinçek et al., 1987; Kartal and Kadirioğlu, 2019; Irmak et al., 2020).

Considering the historical seismicity (B.C. 1800–A.D. 1905), no strong ($M \geq 6.0$) and damaging earthquakes were reported near AR (Soysal et al., 1981). Historical earthquakes occurred mainly in the EAF to the north of the dam in 1866, 1893, 1905 (**Figure 1**). The fault zone was remarkably inactive during the 20th century (Ambraseys, 1989; Ambraseys and Jackson, 1998), facing earthquakes with magnitude up to M_w 6.6–6.8, until the most recent destructive M_w 6.8 Elazığ-Sivrice earthquake on January 24, 2020. On the other hand, some historical earthquakes occurred south of the dam, e.g., in 718, 1003, 1037 (**Figure 1**; data from the historical earthquake catalog of Turkey and its surroundings; AFAD)[4].

[1]https://inducedearthquakes.org; last accessed September 2020.

[2]https://www.dsi.gov.tr/Sayfa/Detay/754; last accessed April 2021.

[3]http://www.ataturkbaraji.com; last accessed April 2021.

[4]https://deprem.afad.gov.tr/tarihseldepremler; last accessed June 2020.

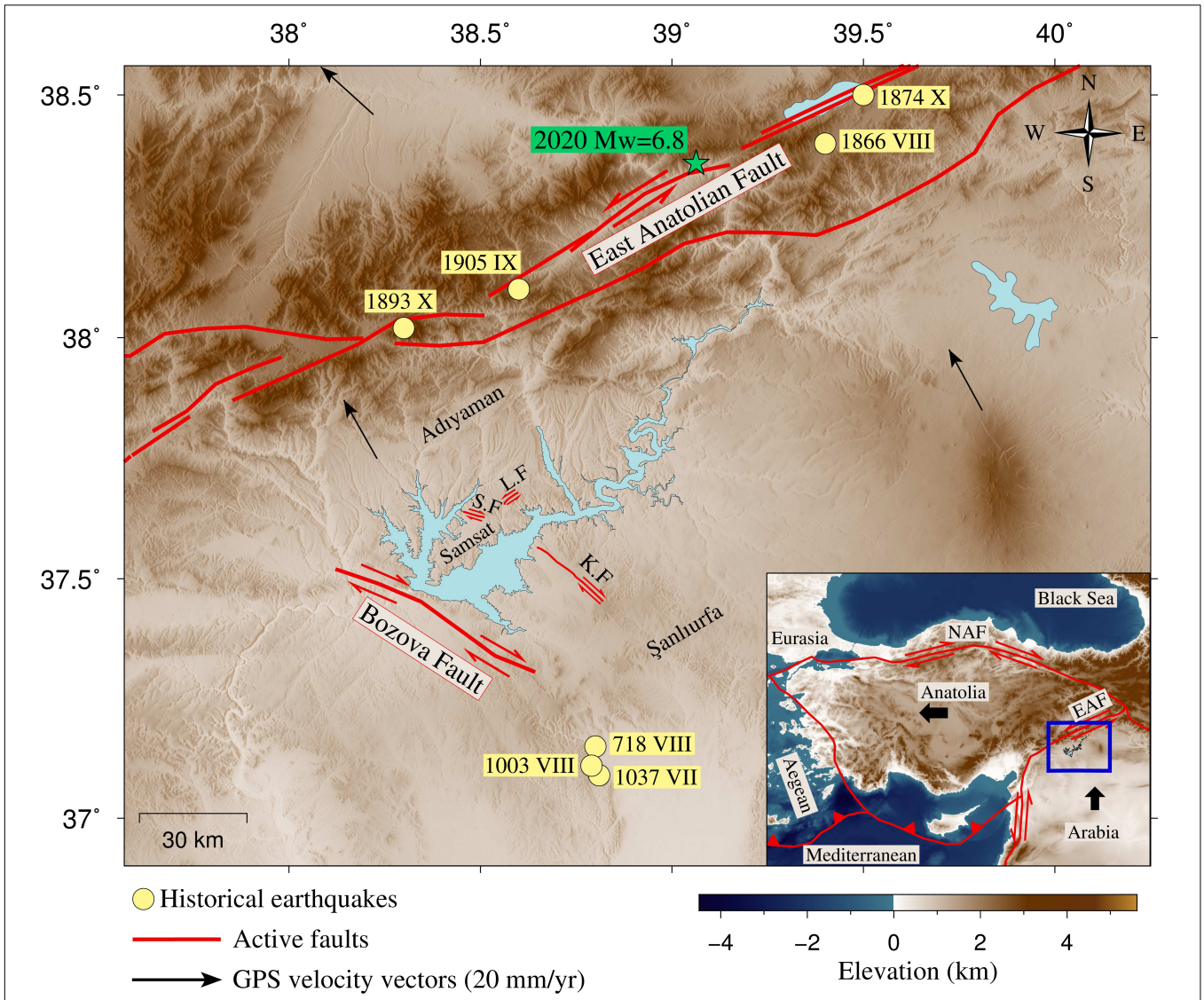

FIGURE 1 | Map of the Atatürk Dam and its vicinity. Thick red lines indicate active faults in the region obtained from the European Database of Seismogenic Faults (EDSF; Basili et al., 2013), and thin red lines illustrate the local faults; SF: Samsat Fault, KF: Kalecik Fault: LF: Lice Fault (General Directorate of Mineral Research and Exploration of Turkey; Perinçek et al., 1987; MTA, 2020). Yellow circles show historical earthquakes (Soysal et al., 1981; Ambraseys, 1989; Ambraseys and Jackson, 1998; the improved historical earthquake catalog of Turkey and its surroundings (https://deprem.afad.gov.tr/tarihseldepremler; AFAD, 2020; last accessed June 2020). The green star shows the location of the recent 2020 Elazığ-Sivrice earthquake caused by the reactivation of EAF, which had been silent for more than one century. Black arrows show GPS velocity vectors in the area (McClusky et al., 2000). The inset panel shows tectonic plates and boundaries surrounding Turkey, where red lines indicate main plate boundaries (Bird, 2003), and black arrows show the relative motion of Arabian and Anatolian Plates roughly. The blue rectangle shows the study area, which is enlarged on the map.

On March 2, 2017, and April 24, 2018, two moderate earthquakes (M_w 5.5 and M_w 5.1, respectively) struck Samsat town near AR (**Figure 1**). These earthquakes were responsible for dozens of injuries and significant damages to buildings. The occurrence of the 2017 earthquake, which is the largest event in this region, and its potential anthropogenic source triggered the interest of seismologists. Reservoir-triggered seismicity around AR was first hypothesized by Eyidoğan et al. (2010) after the occurrence of the M_L 5.2 earthquake on September 3, 2008, which was the largest earthquake prior to the 2017–2018 earthquakes. They pointed out that small-magnitude earthquakes started to occur in the vicinity of the dam soon after the water level reached its first maximum in 1994. Furthermore, they depicted a clear anti-correlation between water-level change and seismicity in the region and suggested that the September 3, 2008 earthquake (M_w 5.0) might have been triggered upon a drastic decrease in the water level, accompanying the low rainfall in the summer of 2008. On the other hand, Kartal and Kadirioğlu, 2019 listed several earthquakes from the catalog of DSI local network mostly after the dam construction and claimed that the seismicity in

the region occurs independently of changes in the water loading. Thus, it has remained a matter of debate whether or not the local seismicity near the AR is correlated with water level changes and its related effective stress changes.

In this study, we use new satellite altimetry open access data that has not been analyzed in previous studies (Database for Hydrological Time Series of Inland Waters, DAHITI; Schwatke et al., 2015). This database provides nowadays reliable and accurate water level data (average uncertainty <0.01 m) for AR over the long period 2002–2020, allowing us to compare water level and seismicity rate for 18 years in the region. Furthermore, we use sophisticated methods to obtain reliable earthquake characteristics (e.g., moment tensor solutions, focal depth estimations, and Gutenberg-Richter b-values) and decluster the earthquake catalog to remove aftershocks that might distort the signatures of RTS. Finally, we calculate the time-dependent Coulomb-stress changes at seismogenic depth resulting from water loading and pore-pressure diffusion based on the observed water-level evolution and extended reservoir geometry. Based on this analysis, the comparison of stress and seismicity pattern indicates a causal relationship between the reservoir and local seismicity.

SEISMIC NETWORKS AND SEISMICITY DISTRIBUTION

Local seismicity around the AR is monitored by permanent networks of the Disaster and Emergency Management Authority (AFAD) (1990) and Kandilli Observatory and Earthquake Research Institute, Boğaziçi University (KOERI) (1971). The distribution of active broadband seismic stations around the dam is marked in **Figure 2** for various periods. The network has been densified with time particularly after the March 2, 2017 M_w 5.5 earthquake when additional AFAD stations were installed. To get a complete earthquake catalog for our analysis, we combine the seismic catalogs from AFAD and KOERI networks between 37.3°–37.8°E and 38.1°–39.0°N (**Figure 2**). Both catalogs are compiled with the SeisAn - earthquake analysis software (Havskov and Ottemöller, 1999). Hypocenters and magnitudes are updated according to the travel time residuals (RMS) and the number of stations used in the location. The magnitude of completeness (M_C), being ∼3.5 in the beginning, decreased with the densification of the network to an ultimate value of about 1.95 in 2017 (**Figure 3** and **Supplementary Figure 1**). Taking into account only the largest events with $M \geq 3.5$, which are homogeneously detected over the whole period, the earthquake rate has significantly increased in the AR region between 1990 and 2020 (**Figure 3B**) as previously pointed out in the study of Eyidoğan et al. (2010).

The spatial pattern of the seismicity around the AR is demonstrated in **Figures 2A–D**. The lack of recorded seismic activity before the start of the dam impoundment in 1990 is shown in **Figure 2A**. After the dam operation begins and the reservoir is filled, the seismicity rate increases, especially in the vicinity of the AR (**Figures 2B,C**). The densification of the seismic stations after the March 2, 2017 M_w 5.5 has led to a significant improvement in the detection of weak events, contributing to the observed increase in detected events (**Figure 2D**). Most earthquakes are shallow, predominantly occurring at less than 11 km depth. Such shallow seismicity around the dam hints that the water filling and leakage with the consequent induced changes in pore-pressure and effective stress can have affected the local seismicity.

TABLE 1 | The characteristics of Atatürk Dam and its reservoir (The General Directorate of State Hydraulic Works of Turkey; DSI; http://www.ataturkbaraji.com; last accessed April 2021; asl* = above sea level).

Dam type	Rock-fill
Filling of water	1990
Opening date	1992
Dam height	169 m
Dam length	1.819 m
Reservoir capacity	$48.7 * 10^9 m^3$
Surface area	817 km^2
Minimum water level	513 m asl*
Maximum water level	542 m asl*

STATISTICAL ANALYSIS OF THE EARTHQUAKE CATALOG

Frequency-Magnitude Distribution

The Gutenberg-Richter (GR) relation states that the number of events (N) above a certain magnitude (M) follows the simple relation log(N) = a – bM. While the a-value, which defines the earthquake production rate above M = 0, varies largely between different tectonic regions, the b-value is usually found to be rather universal and scatters around 1.

Figure 3D shows the frequency-magnitude distributions of the earthquakes together with GR-fits for three successive periods with progressively decreasing M_C, from M_C = 2.75 in the period 2004–2012, M_C = 2.45 for 2012–2017, to M_C = 1.95 for t > 2017. At the same time, the b-value of GR distribution is estimated as 1.8, 1.4, and 0.9 for the periods of 2004–2012, 2012–2017, and 2017–2021, respectively (see also **Supplementary Figure 1**). Thus the b-value is found to systematically decrease with increasing time after the impoundment of the dam, which might be a result of increased stresses in the crust as previously hypothesized (Schorlemmer et al., 2005; Scholz, 2015).

Anti-Correlation Between Water-Level and Declustered Seismicity

For a detailed analysis of the spatial and temporal characteristics of the earthquake activity with the reservoir, aftershocks which are triggered by preceding earthquakes should be removed from the catalog. The remaining declustered earthquakes are the so-called background events, which are related to tectonic stressing or transient aseismic forcing such as reservoir-induced stress changes. To separate aftershocks and background events, we use an established scheme based on nearest-neighbor

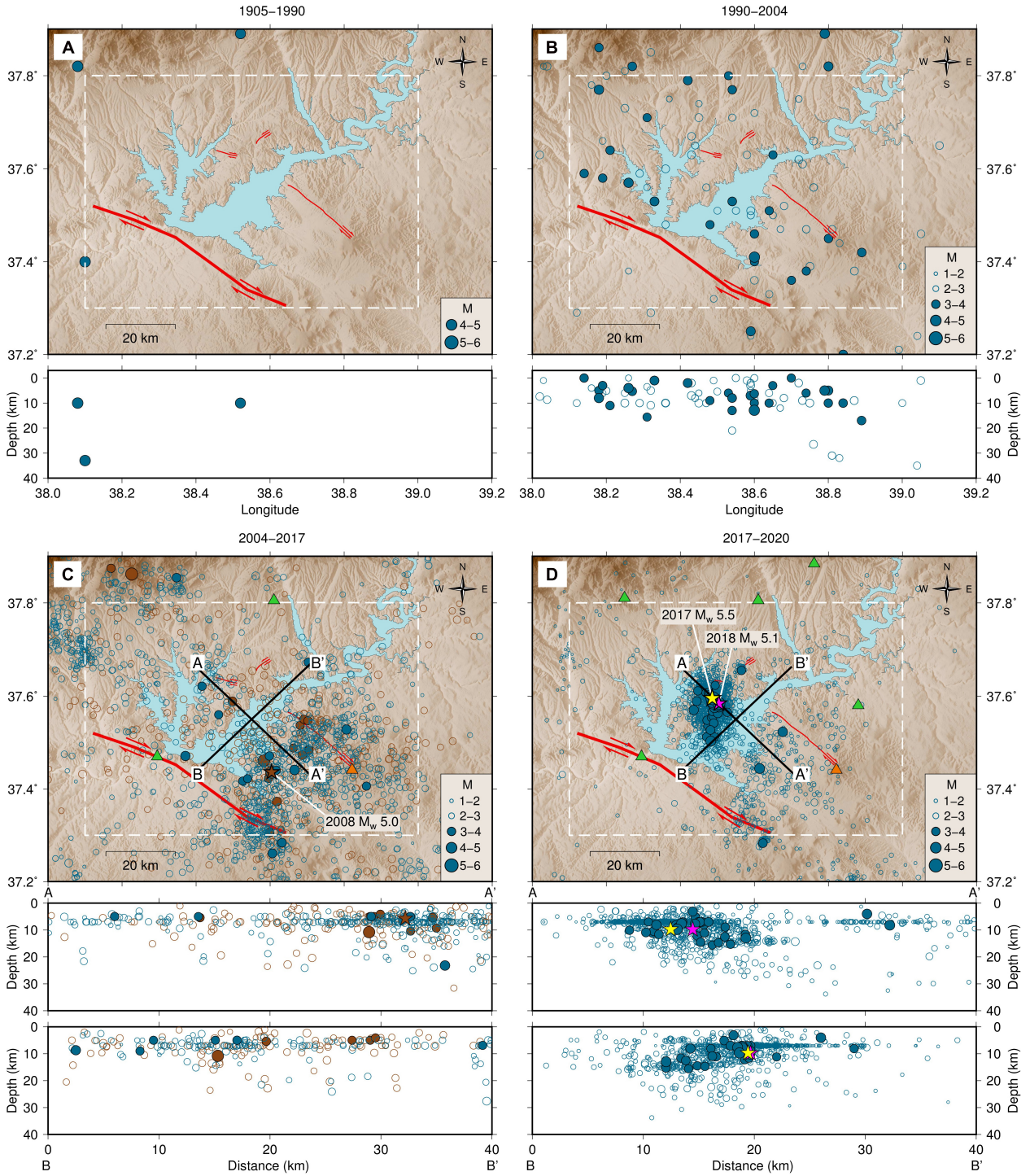

FIGURE 2 | (A–D) Long term (1905–2020) spatio-temporal evolution of recorded earthquakes with their magnitudes and depth cross-sections based on a joint KOERI-AFAD catalog near Atatürk Reservoir. The spatial earthquake distribution of historical and instrumental seismic activity around AR for **(A)** the period 1905–1990 before the water filling, **(B)** 1990–2004 after the impoundment of the dam – depth versus longitude in panels **(A–C)** 2004–2017 and two orthogonal cross-sections crossing the dam **(AA′,BB′)**. The brown dots here show the events during 2004–2008 to highlight the background seismicity, the M_w 5.0 2008 earthquake, and its aftershocks **(D)** 2017–2020, same cross sections as in panel **(C)**. The existing broadband seismic stations during the corresponding periods are marked by the green (AFAD stations) and orange (KOERI stations) triangles. Yellow and pink stars refer to the hypocenters of March 2, 2017, M_w 5.5 and April 24, 2018, M_w 5.1 earthquakes, respectively. The white dashed rectangle marks the region where the seismic catalogs are combined (37.3°-37.8°E, 38.1°-39.0°N). The red lines represent the Bozova, Samsat, Kalecik, and Lice Faults (see **Figure 1** to detail).

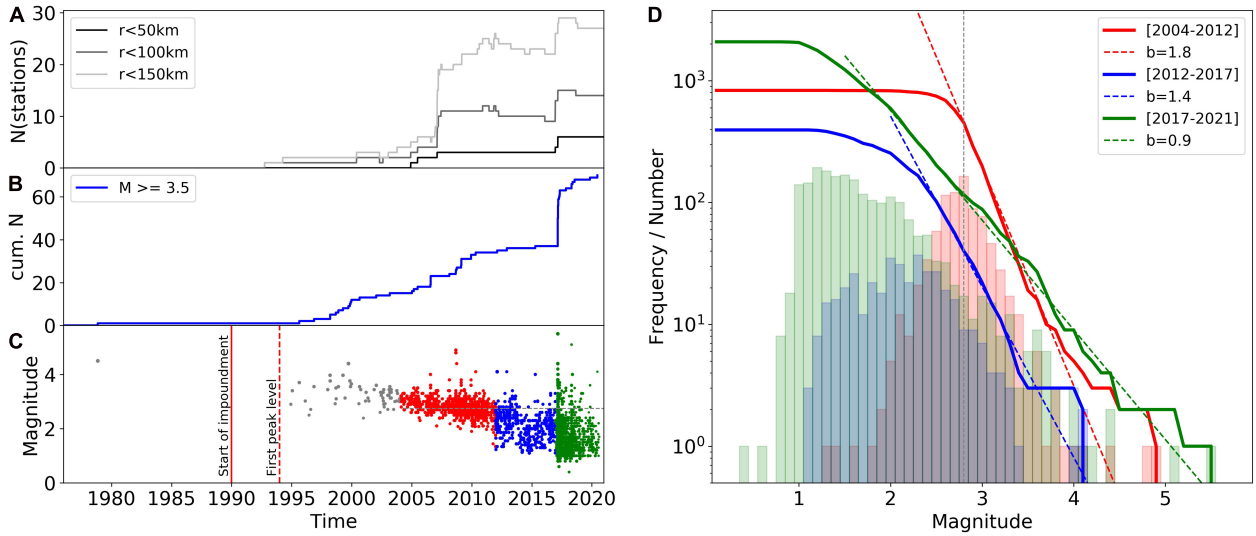

FIGURE 3 | Frequency-magnitude distribution of the observed earthquakes: **(A)** Number of seismic stations with a distance less than 50, 100, or 150 km from the 2017 M_w 5.5 epicenter as a function of time; **(B)** cumulative number of M ≥ 3.5 events and **(C)** magnitudes of all recorded events versus time, where colors refer to the different periods analyzed separately in panel **(D)** and the horizontal dashed line indicates the completeness magnitude M_C = 2.75; **(D)** histograms and cumulative distributions with GR-fits (dashed lines, the corresponding b-values are provided in the legend). Additional plots of the frequency-magnitude distributions and the b-value calculation are presented in the **Supplementary Figure 1**.

distances (Baiesi and Paczuski, 2004, 2005; Zaliapin et al., 2008; Zaliapin and Ben-Zion, 2013). This is a purely statistical method that does not rely on any particular aftershock-triggering mechanism, such as static/dynamic coseismic stress changes or afterslip. The method is described in more detail in Appendix A.

After declustering, we compare the temporal evolution of earthquake activity of the complete part of the catalog (M ≥ 2.8 for t > 2004) with the water level variations. **Figure 4** shows the monthly seismicity rate in comparison to the reversed water-level variations. A significant anti-correlation between earthquake rate and water-level is observed in the period between 2004 and 2014 with a correlation coefficient of $r = -0.48$. Afterward, the anti-correlation becomes weak, particularly because of the significantly reduced activity of M ≥ 2.8 background events (see also **Supplementary Figure 2**).

ANALYSIS OF SOURCE PROPERTIES

Construction of a Local Velocity Model

Firstly, we estimate a local 1D velocity model for our further analysis of focal depths and source mechanisms. For that purpose, we use PyVelest[5], based on the travel time inversion VELEST program (Kissling et al., 1994). We carefully select 470 well-located earthquakes in the region with root mean squared (RMS) misfit of the solution ≤0.5 s and azimuthal gap ≤180°, respectively. The recent model of Acarel et al. (2019) is used as the initial model since it is the closest model to the reservoir area. By perturbing velocities in the ±0.3 km/s range, randomly 500 synthetic velocity models are generated and inverted for the study region. Consequently, a well-defined velocity model from the mean of inverted models is constructed. The final velocity model has a good agreement with the reference model, with velocity changes not exceeding 0.2 km/s for each corresponding layer. Details of the selected events, ray coverage and final 1D velocity model are presented in the **Supplementary Figures 3–5** and **Table 1**.

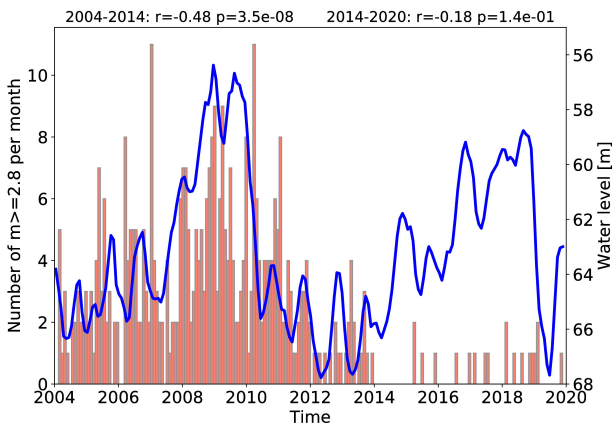

FIGURE 4 | Time evolution of the water level and the earthquake activity (declustered, M ≥ 2.8). Here the y-scale is reversed with values referring to the changes relative to the start of the impoundment. A similar plot with a normal y-scale is provided in **Supplementary Figure 2**. The corresponding correlation coefficients (r) for the periods 2004–2014 and 2014–2020 are provided in the title line together with the corresponding *p*-value (significance for $p < 0.05$).

[5]https://github.com/saeedsltm/PyVelest; last accessed September 2020.

Moment Tensor Inversion

The inversion and further decomposition of regional moment tensor solutions can be used to discuss cases of natural or anthropogenic seismicity (Cesca et al., 2013b). Here, moment tensor inversion has been performed using a probabilistic inversion method, provided by the software Grond[6] (Heimann et al., 2017, 2018). This method has been successfully applied in different studies (e.g., Dahm et al., 2018; Jamalreyhani et al., 2019, 2021; Cesca et al., 2020; Dost et al., 2020; Kühn et al., 2020; López-Comino et al., 2021) and described in some of them (e.g., Dahm et al., 2018; Dost et al., 2020; Kühn et al., 2020).

We obtain full moment tensor solutions for the two largest events, namely the M_w 5.5 2017 and M_w 5.1 2018 earthquakes, using 3-components waveform inversion in the time domain and the frequency band of 0.02–0.05 Hz. A prior data quality assessment is applied to all stations to prevent systematic errors in the moment tensor solutions due to sensor misorientations (Büyükakpınar et al., 2021). An example of waveform fits and MT solution is illustrated in **Figure 5**. Additionally, the waveform fits and MT solution are shown for the M_w 5.1 2018 earthquake in the **Supplementary Figures 6**, **7**. The full moment tensor decomposition (ISO-CLVD-DC) components show a relatively large CLVD component, 17 and 41% for 2017 and 2018 earthquakes, respectively. Furthermore, moment tensors for 66 weaker events down to M 2.8 were calculated, applying a simplified double couple representation and frequency band of 0.06–0.11 Hz. This is possible due to the presence of the densified networks in the area after 2017. All obtained source parameters are listed in **Supplementary Table 2**. **Figure 6** shows the result of all focal mechanisms. Most of the solutions are characterized by strike-slip mechanisms with relatively shallow centroid depths (<6 km and uncertainty <1 km, see **Supplementary Table 2**).

For the largest earthquake, the 2017 M_w 5.5 event, we study the distribution of the direct aftershocks to determine the rupture plane. The aftershocks are found to extend in the NW direction in agreement with the nodal plane with a strike of 313.5° (**Figure 7**). Only minor activity is found in the strike direction of the second nodal plane with a strike of 46.5°, which is interpreted as the auxiliary plane. Both the focal mechanism strike and the trend of aftershocks are in general agreement with the strike direction of the Bozova, Samsat, and Kalecik faults (see **Figure 6**). Thus we conclude that the rupture mechanism of the largest event is best described by strike = 313.5°, dip = 64.3°, and rake = 173.1°. These values are used to estimate stresses on receiver faults in the following chapter.

Focal Depths of the M_w 5.5 2017 and M_w 5.1 2018 Events

Depth values of seismic catalogs may have large uncertainties and often suffer from trade-offs between origin time and depth. A better depth constraint is substantial to discriminate induced seismicity from natural ones. We adopt here a method for an accurate source depth estimation based on the delay between direct P phases and surface reflected (pP and sP) phases at teleseismic distances. Since the waveforms of these moderate events at large distances are weak, we investigate these delays at the location of seismic arrays, where waveforms of many stations can be shifted and stacked to improve the signal-to-noise (SNR) ratio. We rely on the Abedeto algorithm[7], which has been previously used in similar studies (Negi et al., 2017; Braun et al., 2018; Gaebler et al., 2019). The qualitative comparison of observed and synthetic beams for different source depths (**Figure 8**), which are built assuming source and receiver specific crustal models and a global model for the propagation of the seismic waves in between, allows to estimate accurate focal depths. Here, the global crustal velocity model Crust 2.0 (Bassin et al., 2000) and the estimated earthquake source models are used to calculate the focal depths (see **Figure 6** and **Supplementary Table 2**). In this way, we estimate the focal depths of 11 and 5 km for the 2017 and 2018 earthquakes, respectively. We find similar results for different arrays (see **Supplementary Figures 8**, **9**). The obtained focal depths are compatible with the hypocentral depths given in the seismic catalogs.

RESERVOIR-INDUCED STRESS CHANGES

We calculate the reservoir-related variations of the Coulomb-Failure Stress (CFS) relative to the initial stress state at the beginning of the water impoundment. For that purpose, we assume a uniform and isotropic half-space and represent the Atatürk Reservoir by 246-point sources covering the reservoir surface (see **Supplementary Figure 10**). In particular, we calculate the stress induced by the water load using Boussinesq-Cerruti solutions (see, e.g., Deng et al., 2010), and pressure changes related to pore-pressure diffusion by convolution of the observed reservoir water level (extended to include the filling phase, see **Supplementary Figure 10A**) with the Green's function (Gahalaut and Hassoup, 2012; Hainzl et al., 2015). Details of the stress calculation are provided in Appendix B. The main model parameter, which influences the stress evolution, is the hydraulic diffusivity (D), while the other parameters such as friction coefficient and Skempton coefficient only have a minor impact. We use a friction coefficient of $\mu = 0.8$ and calculate CFS for the obtained rupture mechanism of the 2017 M_w 5.5 mainshock, namely strike = 313.5°, dip = 64.3°, and rake = 173.1° (see the previous section). This mechanism is assumed to be representative of the wider region due to the strong similarities of estimated focal mechanisms and the correspondence to the strike of the main regional fault.

At first, we calculate the induced Cauchy stress resulting from the water load alone, which is independent of the choice of the diffusivity (D). In particular, we determine the induced stresses for the estimated mainshock mechanism in the case of the reservoir with a 60 m water column ignoring any fluid diffusion. The result is shown in **Figure 9** indicating that the whole region

[6]https://pyrocko.org/grond

[7]https://github.com/HerrMuellerluedenscheid/ArrayBeamDepthTool; last accessed September 2020.

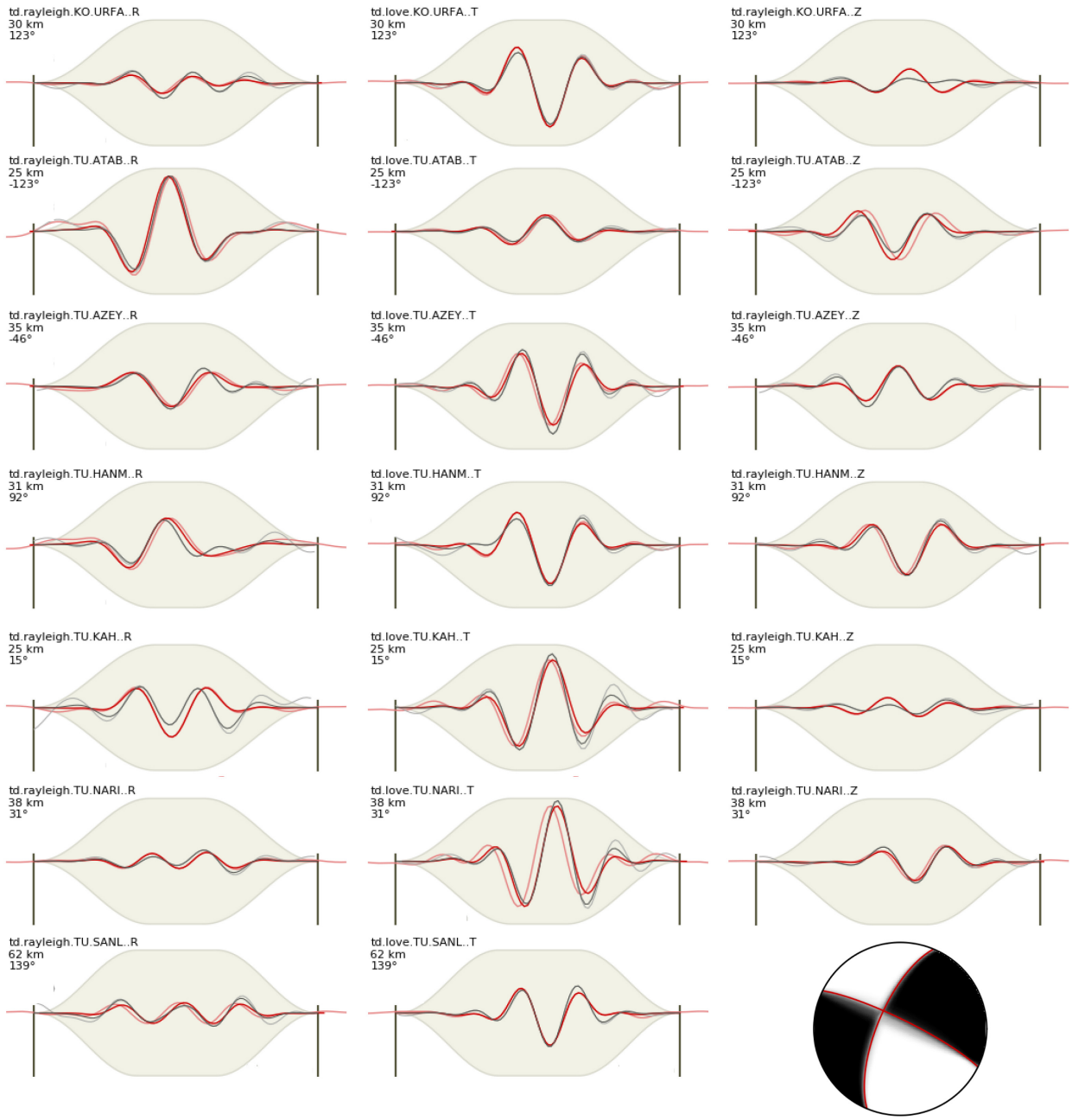

FIGURE 5 | Waveform fits in the time domain for the 2017-08-31 (UTC) 16:11:09 M 3.1 earthquake. Red and gray waveforms represent synthetic and observed records, respectively. The fuzzy MT shows the solution with its uncertainties (see also **Supplementary Figures 6**, **7**).

is unloaded at all depth layers due to water load. This means that all faults with the mainshock mechanism are firstly stabilized by the reservoir impoundment. As a counterpart, the pore-pressure diffusion leads to an increase of stress with time, but with some delay depending on the distance to the reservoir and the value of diffusivity (D). The stabilization effect of the water loading can explain the observed anti-correlation between water-level and seismicity rate. A sudden increase of the water-level leads to an immediate reduction of the CFS-value on the faults with the predominant mechanism because the related increase of the pore-pressure diffusion is delayed. This can also explain the decreased seismicity rate at peaks of the water levels.

While the stabilization effect is found to dominate in the short-term, pore-pressure diffusion leads to an increase of the effective stress with time. This is demonstrated in **Figure 10A**, where the total Coulomb stress is calculated for three different values of the hydraulic diffusivity (D = 0.05, 0.1, and 1.0 m^2/s) at 5 km depth in the three locations marked in **Figure 9**.

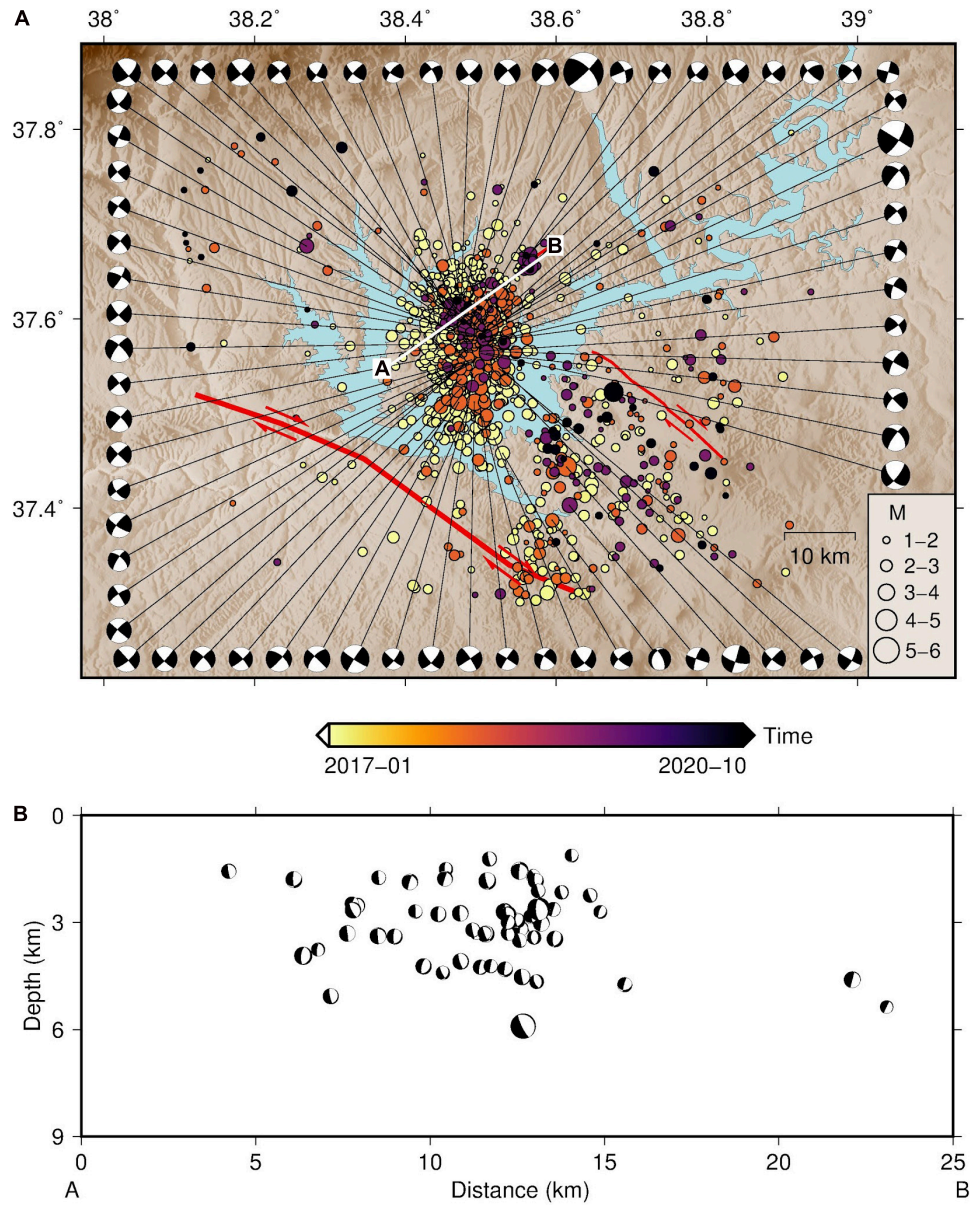

FIGURE 6 | (A) Focal mechanism solutions for 68 events that occurred between 2017 and 2020. The recorded epicenters are color-coded in time. The red lines show the faults with their slip direction. **(B)** The cross-section of the (A-B) profile in the study area showing the centroid depths mostly less than 6 km.

All curves firstly show negative values, but later a crossover to positive values is observed, after which induced seismicity might be expected. The time of this crossover is strongly dependent on the assumed D-value and the distance to the reservoir. For the location beneath the reservoir (blue cross in **Figure 9** and blue lines in **Figure 10**), it already occurs between 1993 and 2000 for D-values in the range between 0.05 and 1 m^2/s. At the farthest distance (green cross) and smallest D-value (dashed line), it occurs only in 2016. Overall, the general increase due to the pore-pressure diffusion is modulated by the instantaneous stress changes induced by changes in the water level.

The simplest seismicity model, which builds on CFS-values, assumes that the number of earthquakes is proportional to the stress change, if it is positive, while no triggering is expected for negative changes. Furthermore, considering stress shadowing (Kaiser effect), the model only assumes triggering if the absolute stress exceeds all precursory values. Thus the seismicity rate R(t) is proportional to the stressing rate, R(t)∼d/dt CFS(t), if CFS(t) > max (CFS (time < t)), otherwise R(t) = 0.

The cumulative number of events becomes simply N(t) ∼ max (CFS (time ≤ t)).

Based on this model, we calculate the expected number of events in the three locations marked in **Figure 9**. In **Figure 10B**,

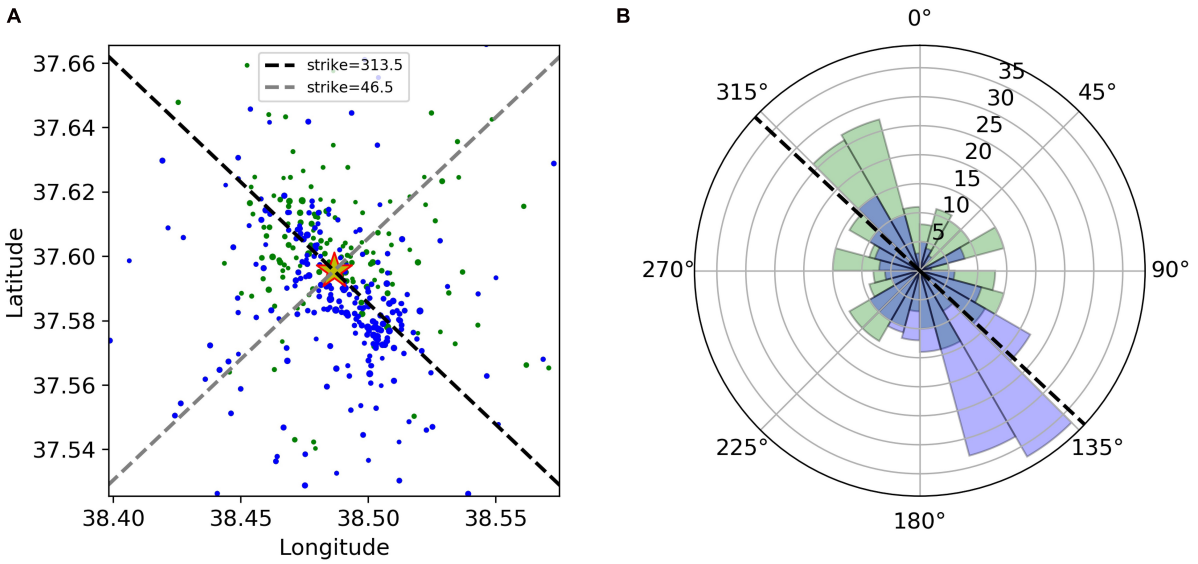

FIGURE 7 | Aftershocks of March 2, 2017, M_w 5.5 earthquake: **(A)** Spatial distribution of the first ten-day aftershocks, which were directly triggered by the mainshock according to the declustering method (green points), and all aftershocks occurred within the first day (blue points). The epicenter of the mainshock is marked by the star. **(B)** Rose diagram of the directions of the same events relative to the mainshock location, where the preferred strike value of the mainshock focal mechanism is marked as a dashed black line.

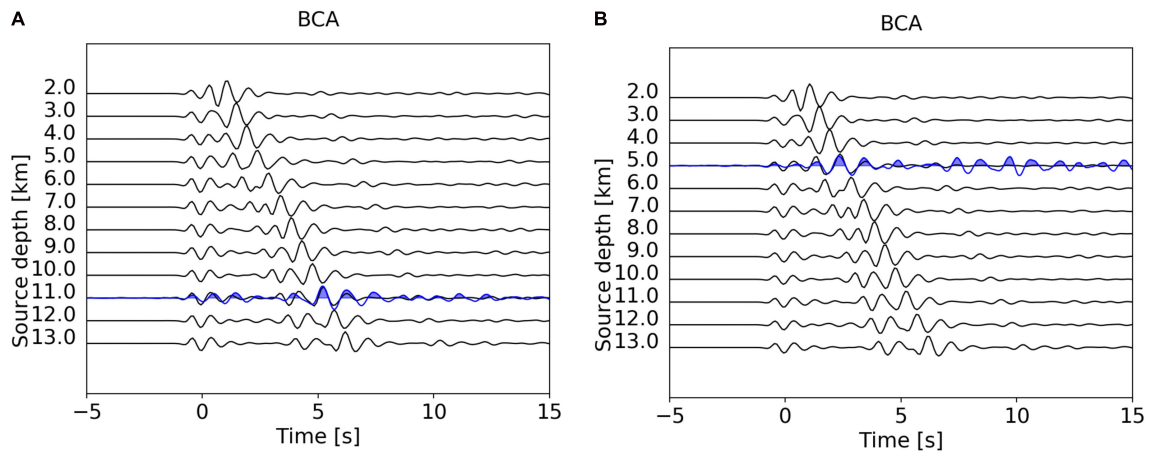

FIGURE 8 | (A,B) Modeled teleseismic depth phases for the BCA array for different assumed source depth and fixed source mechanism (black lines). For the modeling of the source side crust, we use the velocity model (see **Supplementary Figure 5** and **Table 1**) which we have obtained using PyVelest. Stacked array beams (blue lines) are seen consistent with synthetics for a depth of 11 and 5 km in the case of the M_w 5.5 2017 earthquake **(A)** and the M_w 5.1 2018 earthquake **(B)**, respectively.

the result is shown for the cumulative number of earthquakes N(t) in the case of three different D-values (0.05, 0.1, and 1 m^2/s), where we arbitrarily set the proportionality factor to 1. We cannot compare this model prediction pointwise with observations due to the limited number of recorded events. Thus, the shape of the resulting curves is compared to the evolution of the cumulative number of the homogeneously recorded $M \geq 2.8$ background events in the whole region after 2004 (gray line). Despite some variations depending on the location and chosen D-value, the shapes have a similar tendency, with a steep increase in the first period and a flattening in the later period.

For the case of D = 0.1 m^2/s and a depth of 5 km, we also calculate the CFS-values on a spatial grid at different time points. **Figure 11** (left column) shows the total CFS-stress in our study area at the beginning of 2010, 2015, and 2020, respectively. Southwest of the dam, including the Bozova fault, the total CFS values remain negative for the whole period, and no earthquakes with the mainshock mechanism are expected; only a few events are observed in this region. On the other hand, the highest stresses of about 0.7 bar occur just beneath the centers of the two arms of the lake, while the absolute value is slightly smaller (approximately 0.4 bar) in the Samsat region, where the two

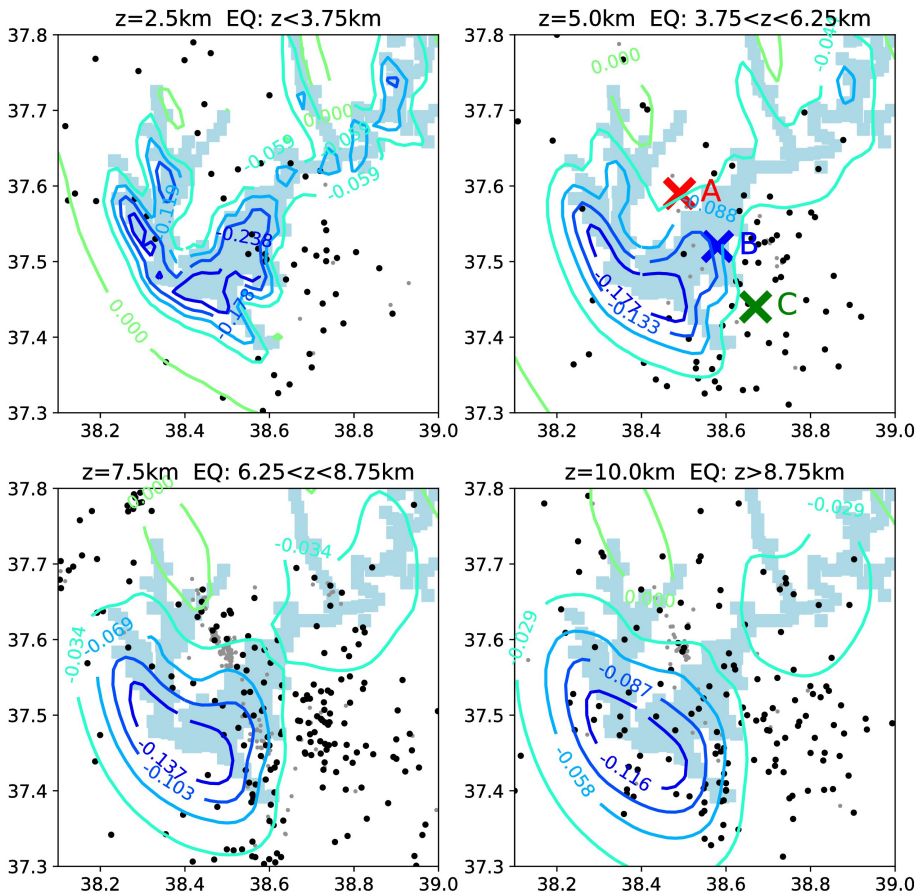

FIGURE 9 | Stress changes due to reservoir loading (60 m water column) ignoring fluid diffusion and calculated for receiver faults with the orientation of the 2017 M_w 5.5 mainshock mechanism (strike = 313.5°, dip = 64.3°, rake = 173.1°). Contour lines refer to stress values in units of MPa. Points refer to M ≥ 2.8 earthquakes (black = background, gray = aftershocks) in the depth range indicated in each title line. The colored crosses mark the three locations for which **Figure 10** shows the total stress history, including pore pressure changes.

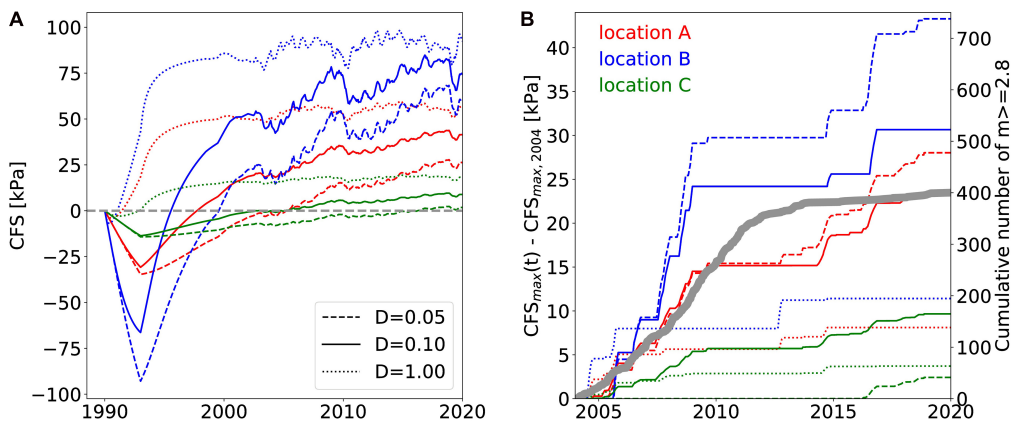

FIGURE 10 | (A) Time evolution of the total Coulomb stress calculated at the three locations indicated in **Figure 9** at 5 km depth, assuming the mainshock mechanism as a receiver. The colors of the lines refer to the location, while the line style refers to different diffusivity values (see legend); **(B)** Temporal increase of the maximum CFS value relative to the year 2004 (for the same cases). Note that the number of triggered events should be proportional to these curves at the given location according to the simple CFS-model. For comparison, the cumulative events of the recorded M ≥ 2.8 background events in the whole area are shown by the bold gray line (with a scale on the right).

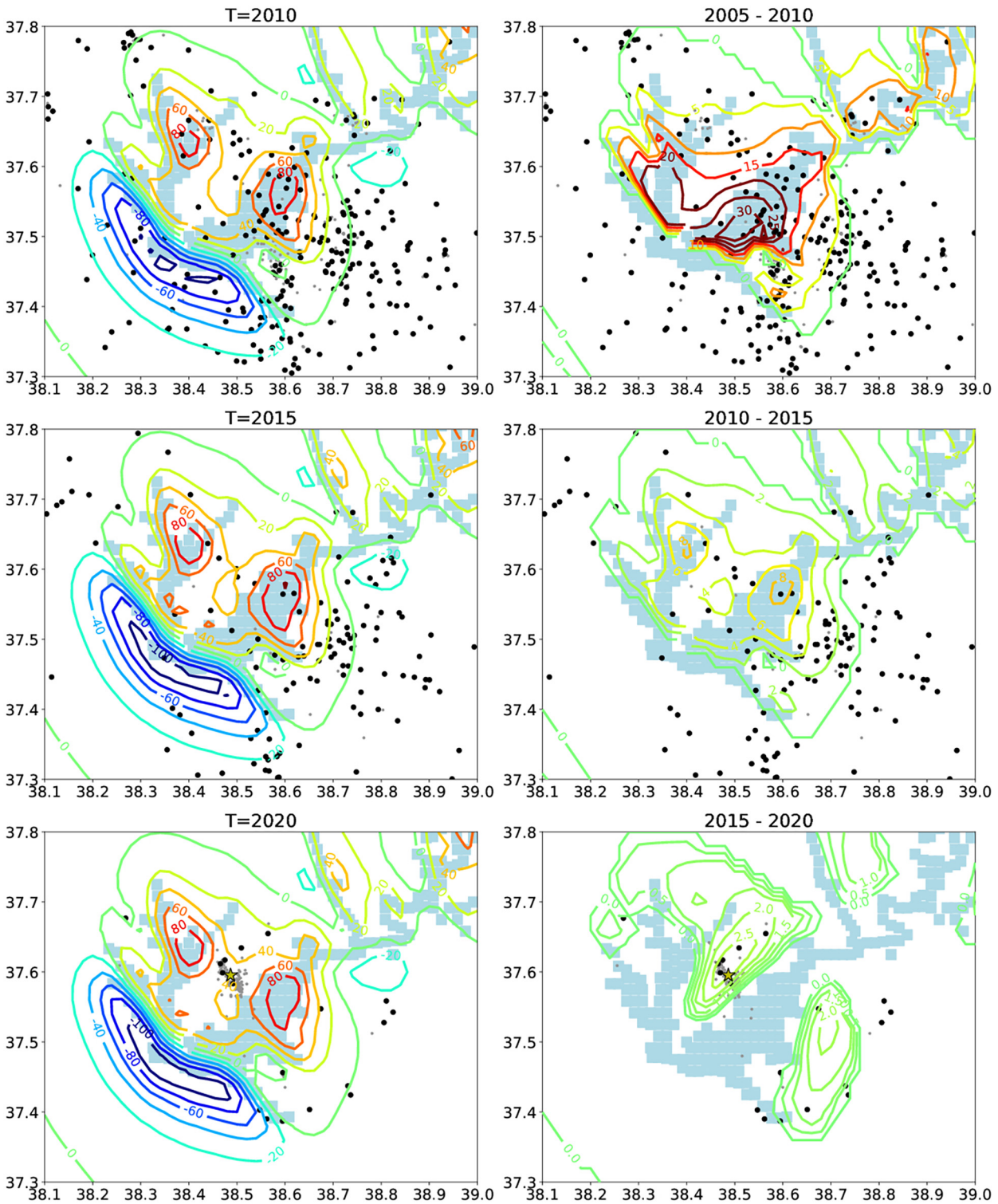

FIGURE 11 | Left column: contour lines of the total CFS-stress [kPa] at the year 2010 **(top)**, 2015 **(middle)**, and 2020 **(bottom)**, calculated for the mainshock mechanism at a depth of 5 km and D = 0.1 m^2/s. **Right column**: increase of the maximum CFS value in the period 2005–2010 **(top)**, 2010–2015 **(middle)**, and 2015–2020 **(bottom)**, which is proportional to the number of triggered earthquakes according to the simple CFS-model. For comparison, the epicenters of earthquakes (M ≥ 2.8, black = declustered, gray = aftershocks) recorded in the corresponding time intervals are plotted. In the bottom row, the star refers to the 2017 M_W 5.5 mainshock.

largest earthquakes occurred in 2017 and 2018. The earthquake probability depends not on the absolute value, but the stress increases according to the simple CFS-model, which is shown in the right column of **Figure 11**. The contour lines show that this increase just focused on the Samsat region in the period of the mainshocks.

DISCUSSION

Based on the combined catalog from regional networks in this study, the seismicity rate increases in the AR region between 1990 and 2020. However, it should be noted that the seismic network was sparse before the impoundment and only improved with time. On the other hand, the estimated magnitude of completeness (M_C) decreased from 3.5 in the beginning to approximately 1.95 after 2017 because of the seismic network's densification in the reservoir area. Nevertheless, considering only the complete part of the catalog ($M \geq 3.5$) indicates a significant activation of seismicity after the reservoir filling. Besides the changes in the seismicity rate, the shape of the magnitude distribution also changed with time. The estimated b-value successively decreased from a high value of 1.8 in the period of 2004–2012, to 1.4 in 2012–2017, and finally to 0.9 in 2017–2021, respectively. According to field and lab experiments, this significant b-value decrease may be explained by an increase in stress in the AR region (Schorlemmer et al., 2005; Scholz, 2015).

Our moment tensor solutions for 68 earthquakes, including the largest earthquakes and aftershocks down to M 2.8, indicate a clear dominance of strike-slip mechanisms that are in agreement with the results of previous studies (e.g., Eyidoğan et al., 2010; Kartal and Kadirioğlu, 2019; Irmak et al., 2020). The estimated mechanisms are consistent with the regional stress field (**Figures 1**, **6**). The spatial distribution of early aftershocks suggests that the NW-SE fault orientation is the causative fault plane, which is in general agreement with the strike of the faults in the region (e.g., the Bozova and Samsat faults). In particular, the Samsat fault is most probably responsible for the 2017 and 2018 earthquake sources, as previously indicated by Irmak et al. (2020). Furthermore, the MT solutions in this study reveal shallow centroid depths mostly below 6 km. Shallow source depths are also estimated in the study of Irmak et al. (2020). Our full moment tensor results also show relatively large CLVD components, 17 and 41% for 2017 and 2018 earthquakes, respectively. Shallow source depths and the percentage of non-double components also support the triggering mechanism in the study area.

The focal depths of the largest 2017 and 2018 events (11 and 5 km, respectively) are independently confirmed using an accurate array beam technique. Shallow focal depths (<10 km) are also revealed in the study of Irmak et al. (2020). Shallow hypocenters are often found for seismicity induced or triggered by reservoir loading in other regions (Simpson et al., 1988; Lizurek et al., 2019; Ruiz-Barajas et al., 2019) and they can be linked to the significant damage in the vicinity of the AR in 2017 and 2018. As previously indicated in the study of Irmak et al. (2020) most of the epicenters are located close to the Samsat town and mapped along the Samsat fault, which has been known but not considered as an active fault in Turkey's current faults map (Emre et al., 2018).

Induced gravitational stress due to surface loading/unloading can favor or inhibit normal faulting and thrust faulting (Simpson, 1986) but is expected to have only a small direct influence on vertical strike-slip faults. However, dipping fault planes increase the impact of the water loading also for strike-slip events. The dip of the 2017 M_w 5.5 Samsat earthquake is estimated to be 64.3°. Furthermore, pore pressure transients in response to water loading favor the occurrence of any faulting type with some delay depending on distance and hydraulic diffusivity.

The joint interpretation of the temporal evolution of water level and seismicity rate is crucial to identifying seismicity simulated by water reservoir operations and understanding its spatio-temporal evolution. Water level and seismicity rate have been analyzed here through a declustering method, resolving a clear anti-correlation between water level and seismicity by using recent additional datasets. This pattern was firstly observed by Eyidoğan et al. (2010), by comparing earthquakes between 1992 and 2009 with the water level information obtained by DSI. However, Kartal and Kadirioğlu (2019) found no evidence of any correlation between water load and earthquake activity pointing to induced/triggered seismicity; this might result from the fact that they analyzed and correlated seismicity and water level only for short periods, such as three months sequences in the intervals of August-October, 2008 and February–April, 2017. Analyzing too short periods does not allow to resolve correlations whenever the triggering mechanism requires a considerable temporal delay. Our study reveals a correlation between reservoir impoundment and triggered seismicity, which is attempted to discriminate from the induced seismicity here, in a more extended data period. We can particularly explain this anti-correlation by the immediate stabilization effect of the surface water load on the dominant rupture mechanism of regional crustal faults.

On the other hand, we show that pore-pressure diffusion increased the effective stress with time, leading to positive total stresses and fault destabilization, explaining the observed seismicity in the proximity of the Samsat fault where the estimated total stress is high, and the two largest events occurred in 2017 and 2018. Interestingly, the Bozova fault in the SW of the reservoir area remains so far in the stress shadow, which agrees with the low seismic activity observed in this region.

CONCLUSION

Two recent, damaging earthquakes, with magnitude M_w 5.5 and M_w 5.1, struck in close vicinity to the Atatürk Reservoir in 2017 and 2018, raising the question of whether they have been induced or triggered by water loading operations. In this study, we analyzed the spatio-temporal evolution of seismicity and earthquake source characteristics in relation to the stresses induced by the Atatürk Reservoir, one of the largest dam reservoirs on Earth.

The local seismicity rate has substantially increased after constructing the dam and its impoundment, which began in 1990. Despite the overall seismicity increase, our analysis confirms a clear anti-correlation among seismicity rate and water level on shorter time scales, which was so far debated (Eyidoğan et al., 2010; Kartal and Kadirioğlu, 2019). Our stress calculations show that the anti-correlation can be explained by the stabilization effect of the water load, while the overall seismicity activation is attributed to pore pressure diffusion. We also observe a significant b-value decrease with time after the impoundment operations with a reduction from 1.8 in 2004 to 0.9 in 2020, suggesting a progressive increase of the effective stresses due to increased pore pressure. Furthermore, moment tensor solutions show that the NW-SE oriented strike-slip mechanism, which is compatible with the general trend of the existing tectonic regime, is dominant in the dam area.

Our analysis provides strong indications that the observed seismicity is partly triggered by the impounding of the Atatürk Reservoir based on the data consisting of seismicity, source mechanisms, and long-term water level information (2002–2020) which is not previously taken into account in other studies.

This work shows how combining accurate seismicity analysis, stress estimations, and statistical approaches helps to better discriminate and understand reservoir-triggered seismicity. Our results provide a solid base to assess the seismic hazard near the Atatürk Dam in Turkey.

DATA AVAILABILITY STATEMENT

All seismic and satellite altimetry data used in this study are free and open access to users via the International Federation of Digital Seismograph Networks (FDSN) client code (KO; https://doi.org/10.7914/SN/KO) in the databases of the Boğaziçi University Kandilli Observatory and Earthquake Research Institute (KOERI; http://eida.koeri.boun.edu.tr; last accessed September 2020), the Disaster and Emergency Management Authority (AFAD; https://tdvms.afad.gov.tr; last accessed September 2020), and the Database for Hydrological Time Series of Inland Waters (DAHITI; https://dahiti.dgfi.tum.de/en/; last accessed September 2020). Active faults in the region were taken from the European Database of Seismogenic Faults (EDSF; http://diss.rm.ingv.it/share-edsf; last accessed September 2020). Some of the maps were prepared using the Pyrocko toolbox (https://pyrocko.org) and GMT software (http://gmt.soest.hawaii.edu). The topography data were obtained from https://topex.ucsd.edu/WWW_html/srtm15_plus.html (last accessed May 2020). Bathymetry data were taken from https://www.gebco.net/data_and_products/gridded_bathymetry_data (last accessed May 2020).

AUTHOR CONTRIBUTIONS

All the authors contributed to the work and discussed the results presented in this manuscript. All the authors performed the investigation and research.

FUNDING

This study was supported by the International Training Course "Seismology and Seismic Hazard Assessment" which has been funded by the GeoForschungsZentrum Potsdam (GFZ) and the German Federal Foreign Office through the German Humanitarian Assistance program, grant S08-60 321.50 ALL 03/19.

ACKNOWLEDGMENTS

We would like to thank Haluk Eyidoğan for his inspiration in this study. We are very grateful to Mustafa Aktar and Mohammad Mohseni Aref for constructive discussion and comments on this work. We also thank Claus Milkereit and Dorina Kroll. We also thank the editor AR and the reviewers SP and LV for their valuable comments and suggestions that helped us to improve the article.

SUPPLEMENTARY MATERIAL

The Supplementary Material for this article can be found online at: https://www.frontiersin.org/articles/10.3389/feart.2021.663385/full#supplementary-material

REFERENCES

Acarel, D., Cambaz, M. D., Turhan, F., Mutlu, A. K., and Polat, R. (2019). Seismotectonics of Malatya Fault, Eastern Turkey. *Open Geosci.* 11, 1098–1111. doi: 10.1515/geo-2019-0085

Ambraseys, N. N. (1989). Temporary seismic quiescence: SE Turkey. *Geophys. J. Int.* 96, 311–331. doi: 10.1111/j.1365-246X.1989.tb04453.x

Ambraseys, N. N., and Jackson, J. A. (1998). Faulting associated with historical and recent earthquakes in the Eastern Mediterranean region. *Geophys. J. Int.* 133, 390–406. doi: 10.1046/j.1365-246X.1998.00508.x

Arpat, E., and Şaroğlu, F. (1972). The east anatolian fault system: thoughts on its development. *Bull. Miner. Res. Explor. Inst. Turkey* 78, 33–39.

Baiesi, M., and Paczuski, M. (2004). Scale-free networks of earthquakes and aftershocks. *Phys. Revi. E* 69:066106. doi: 10.1103/PhysRevE.69.066106

Baiesi, M., and Paczuski, M. (2005). Complex networks of earthquakes and aftershocks. *Nonlinear Process. Geophy.* 12, 1–11. doi: 10.5194/npg-12-1-2005

Basili, R., Kastelic, V., Demircioglu, M. B., Garcia Moreno, D., Nemser, E. S., Petricca, P., et al. (2013). *The European Database of Seismogenic Faults (EDSF) Compiled in the Framework of the Project SHARE*. Available online at: http://diss.rm.ingv.it/share-edsf/ (accessed September 2020). doi: 10.6092/INGV.IT-SHARE-EDSF

Bassin, C., Laske, G., and Masters, G. (2000). The current limits of resolution for surface wave tomography in North America. *EOS Trans. AGU* 81:F897.

Bird, P. (2003). An updated digital model of plate boundaries. *Geochem. Geophys. Geosyst.* 4:1027. doi: 10.1029/2001GC000252

Braun, T., Caciagli, M., Carapezza, M. L., Famiani, D., Gattuso, A., Lisi, A., et al. (2018). The seismic sequence of 30th May–9th June 2016 in the geothermal

site of Torre Alfina (central Italy) and related variations in soil gas emissions. *J. Volcanol. Geothermal Res.* 359, 21–36. doi: 10.1016/j.jvolgeores.2018.06.005

Büyükakpınar, P., Aktar, M., Petersen, G. M., and Köseoğlu, A. (2021). Orientations of broadband stations of the KOERI seismic network (Turkey) from two independent methods: P- and rayleigh-wave polarization. *Seismol. Res. Lett.* 92, 1512–1521. doi: 10.1785/0220200362

Carder, D. S. (1945). Seismic investigations in the Boulder Dam area, 1940-1944, and the influence of reservoir loading on local earthquake activity. *Bull. Seismol. Soc. Am.* 35, 175–192.

Cesca, S., Braun, T., Maccaferri, F., Passarelli, L., Rivalta, E., and Dahm, T. (2013a). Source modelling of the M5–6 Emilia-Romagna, Italy, earthquakes (2012 May 20–29). *Geophys. J. Int.* 193, 1658–1672. doi: 10.1093/gji/ggt069

Cesca, S., Grigoli, F., Heimann, S., González, Á, Buforn, E., Maghsoudi, S., et al. (2014). The 2013 September–October seismic sequence offshore Spain: a case of seismicity triggered by gas injection? *Geophys. J. Int.* 198, 941–953. doi: 10.1093/gji/ggu172

Cesca, S., Letort, J., Razafindrakoto, H. N. T., Heimann, S., Rivalta, E., Isken, M. P., et al. (2020). Drainage of a deep magma reservoir near Mayotte inferred from seismicity and deformation. *Nat. Geosci.* 13, 87–93. doi: 10.1038/s41561-019-0505-5

Cesca, S., Rohr, A., and Dahm, T. (2013b). Discrimination of induced seismicity by full moment tensor inversion and decomposition. *J. Seismol.* 17, 147–163. doi: 10.1007/s10950-012-9305-8

Çetin, H., Laman, M., and Ertunç, A. (2000). Settlement and slaking problems in the world's fourth largest rock-fill dam, the Ataturk Dam in Turkey. *Eng. Geol.* 56, 225–242. doi: 10.1016/S0013-7952(99)00049-6

Dahm, T., Becker, D., Bischoff, M., Cesca, S., Dost, B., Fritschen, R., et al. (2013). Recommendation for the discrimination of human-related and natural seismicity. *J. Seismol.* 17, 197–202. doi: 10.1007/s10950-012-9295-6

Dahm, T., Cesca, S., Hainzl, S., Braun, T., and Krüger, F. (2015). Discrimination between induced, triggered, and natural earthquakes close to hydrocarbon reservoirs: a probabilistic approach based on the modeling of depletion-induced stress changes and seismological source parameters. *J. Geophys. Res. Solid Earth* 120, 2491–2509. doi: 10.1002/2014JB011778

Dahm, T., Hainzl, S., Becker, D., Bisschoff, M., Cesca, S., Dost, B., et al. (2010). "How to discriminate induced, triggered, and natural seismicity," in *Proceedings of the Workshop Induced seismicity: November 15 - 17, 2010*, (Walferdange: Centre Européen de Géodynamique et de Séismologie), 69–76.

Dahm, T., Heimann, S., Funke, S., Wendt, S., Rappsilber, I., Bindi, D., et al. (2018). Seismicity in the block mountains between Halle and Leipzig, Central Germany: centroid moment tensors, ground motion simulation, and felt intensities of two M ≈3 earthquakes in 2015 and 2017. *J. Seismol.* 22, 985–1003. doi: 10.1007/s10950-018-9746-9

Davies, R., Foulger, G., Bindley, A., and Styles, P. (2013). Induced seismicity and hydraulic fracturing for the recovery of hydrocarbons. *Mar. Pet. Geol.* 45, 171–185. doi: 10.1016/j.marpetgeo.2013.03.016

Deng, K., Zhou, S., Wang, R., Robinson, R., Zhao, C., and Cheng, W. (2010). Evidence that the 2008 Mw 7.9 Wenchuan earthquake could not have been induced by the Zipingpu reservoir. *Bull. Seismol. Soc. Am.* 100, 2805–2814. doi: 10.1785/0120090222

Disaster and Emergency Management Authority (AFAD). (1990). *Turkish National Seismic Network [Data set]. Department of Earthquake, Disaster and Emergency Management Authority*. Available online at: https://doi.org/10.7914/SN/TU (accessed September 2020).

Dost, B., Stiphout, A., van Kühn, D., Kortekaas, M., Ruigrok, E., and Heimann, S. (2020). Probabilistic moment tensor inversion for hydrocarbon-induced seismicity in the groningen gas field, the netherlands, Part 2: application. *Bull. Seismol. Soc. Am.* 110, 2112–2123. doi: 10.1785/0120200076

Duman, T. Y., and Emre, Ö. (2013). The east anatolian fault: geometry, segmentation and jog characteristics. *Geol. Soc. Lond. Special Publ.* 372, 495–529. doi: 10.1144/SP372.14

Ellsworth, W. L. (2013). Injection-induced earthquakes. *Science* 341, 1225942. doi: 10.1126/science.1225942

Emre, Ö, Duman, T. Y., Özalp, S., Şaroğlu, F., Olgun, Ş, Elmacı, H., et al. (2018). Active fault database of Turkey. *Bull. Earthq. Eng.* 16, 3229–3275. doi: 10.1007/s10518-016-0041-2

Eyidoğan, H., Geçgel, V., and Pabuçcu, Z. (2010). "Correlation between water level decrease in Atatürk Dam, Turkey and Mw5.0 earthquake on September 3, 2008," in *Proceedings ESC 2010, 6-10 September 2010*, Montpellier, 61.

Foulger, G. R., Wilson, M. P., Gluyas, J. G., Julian, B. R., and Davies, R. J. (2018). Global review of human-induced earthquakes. *Earth Sci. Rev.* 178, 438–514. doi: 10.1016/j.earscirev.2017.07.008

Gaebler, P., Ceranna, L., Nooshiri, N., Barth, A., Cesca, S., Frei, M., et al. (2019). A multi-technology analysis of the 2017 North Korean nuclear test. *Solid Earth* 10, 59–78. doi: 10.5194/se-10-59-2019

Gahalaut, K., and Hassoup, A. (2012). Role of fluids in the earthquake occurrence around Aswan reservoir, Egypt. *J. Geophys. Res.* 117, 2303. doi: 10.1029/2011JB008796

Gaite, B., Ugalde, A., Villaseñor, A., and Blanch, E. (2016). Improving the location of induced earthquakes associated with an underground gas storage in the Gulf of Valencia (Spain). *Phys. Earth Planet. Interiors* 254, 46–59. doi: 10.1016/j.pepi.2016.03.006

Ge, S., Liu, M., Lu, N., Godt, J. W., and Luo, G. (2009). Did the zipingpu reservoir trigger the 2008 wenchuan earthquake? *Geophys. Res. Lett.* 36:L20315. doi: 10.1029/2009GL040349

González, P. J., Tiampo, K. F., Palano, M., Cannavó, F., and Fernández, J. (2012). The 2011 Lorca earthquake slip distribution controlled by groundwater crustal unloading. *Nat. Geosci.* 5, 821–825. doi: 10.1038/ngeo1610

Grigoli, F., Cesca, S., Priolo, E., Rinaldi, A. P., Clinton, J. F., Stabile, T. A., et al. (2017). Current challenges in monitoring, discrimination, and management of induced seismicity related to underground industrial activities: a European perspective. *Rev. Geophys.* 55, 310–340. doi: 10.1002/2016RG000542

Grigoli, F., Cesca, S., Rinaldi, A. P., Manconi, A., López-Comino, J. A., Clinton, J. F., et al. (2018). The November 2017 Mw 5.5 Pohang earthquake: a possible case of induced seismicity in South Korea. *Science* 360, 1003–1006. doi: 10.1126/science.aat2010

Gupta, H. K. (1992). *Reservoir-Induced Earthquakes*. Amsterdam: Elsevier, 364.

Gupta, H. K. (2002). A review of recent studies of triggered earthquakes by artificial water reservoirs with special emphasis on earthquakes in Koyna, India. *Earth Sci. Rev.* 58, 279–310. doi: 10.1016/S0012-8252(02)00063-6

Gupta, H. K., and Rastogi, B. K. (1976). *Dams and Earthquakes*. Amsterdam: Elsevier, 229.

Hainzl, S., Aggarwal, S. K., Khan, P. K., and Rastogi, B. K. (2015). Monsoon-induced earthquake activity in Talala, Gujarat, India. *Geophys. J. Int.* 200, 627–637. doi: 10.1093/gji/ggu421

Havskov, J., and Ottemöller, L. (1999). SeisAn earthquake analysis software. *Seismol. Res. Lett.* 70, 532–534. doi: 10.1785/gssrl.70.5.532

Heimann, S., Isken, M., Kühn, D., Sudhaus, H., Steinberg, A., Daout, S., et al. (2018). *Grond—A Probabilistic Earthquake Source Inversion Framework. V. 1.0*. Potsdam: GFZ Data Services, doi: 10.5880/GFZ.2.1.2018.003

Heimann, S., Kriegerowski, M., Isken, M., Cesca, S., Daout, S., Grigoli, F., et al. (2017). *Pyrocko—An open-source seismology toolbox and library. V. 0.3*. Potsdam: GFZ Data Services, doi: 10.5880/GFZ.2.1.2017.001

Irmak, T. S., Bulut, I., and Doğan, B. (2020). Regional seismicity in Adıyaman – Samsat (SE Turkey). *Boll. Geofisica Teorica ed. J.* 61, 451–468.

Jamalreyhani, M., Büyükakpınar, P., Cesca, S., Dahm, T., Sudhaus, H., Rezapour, M., et al. (2020). Seismicity related to the eastern sector of anatolian escape tectonic: the example of the 24 January 2020 Mw 6.77 Elazığ-Sivrice earthquake. *Solid Earth Discussions* 1–22. doi: 10.5194/se-2020-55

Jamalreyhani, M., Pousse-Beltran, L., Büyükakpınar, P., Cesca, S., Nissen, E., Ghods, A., et al. (2021). *The 2019-2020 Khalili (Iran) Earthquake Sequence—Anthropogenic Seismicity in the Zagros Simply Folded Belt? [Preprint]. Earth and Space Science Open Archive*. Available online at: http://www.essoar.org/doi/10.1002/essoar.10506454.1 (accessed April 2021).

Jamalreyhani, M., Rezapour, M., Cesca, S., Heimann, S., Vasyura-Bathke, H., Sudhaus, H., et al. (2019). *The 2017 November 12 Mw 7.3 Sarpol-Zahab (Iran-Iraq border region) Earthquake: Source Model, Aftershock Sequence and Earthquakes Triggering, EGU General Assembly 2020, Online, 4–8 May 2020, EGU2020-759*. Available online at: https://doi.org/10.5194/egusphere-egu2020-759 (accessed September 2020).

Juanes, R., Jha, B., Hager, B. H., Shaw, J. H., Plesch, A., Astiz, L., et al. (2016). Were the May 2012 emilia-romagna earthquakes induced? a coupled flow-geomechanics modeling assessment. *Geophys. Res. Lett.* 43, 6891–6897. doi: 10.1002/2016GL069284

Kandilli Observatory and Earthquake Research Institute, Boğaziçi University (KOERI) (1971). *Bogazici University Kandilli Observatory and Earthquake Research Institute [Data set]*. Istanbul: International Federation of Digital Seismograph Networks, doi: 10.7914/SN/KO

Kartal, R. F., and Kadirioğlu, F. T. (2019). Impact of regional tectonic and water stress on the seismicity in Ataturk Dam Basin: Southeast of Turkey. *J. Seismol.* 23, 699–714. doi: 10.1007/s10950-019-09830-5

Keranen, K. M., Savage, H. M., Abers, G. A., and Cochran, E. S. (2013). Potentially induced earthquakes in Oklahoma, USA: Links between wastewater injection and the 2011 Mw 5.7 earthquake sequence. *Geology* 41, 699–702. doi: 10.1130/G34045.1

Keranen, K. M., Weingarten, M., Abers, G. A., Bekins, B. A., and Ge, S. (2014). Sharp increase in central Oklahoma seismicity since 2008 induced by massive wastewater injection. *Science* 345, 448–451. doi: 10.1126/science.1255802

Kim, K.-H., Ree, J.-H., Kim, Y., Kim, S., Kang, S. Y., and Seo, W. (2018). Assessing whether the 2017 Mw 5.4 Pohang earthquake in South Korea was an induced event. *Science* 360, 1007–1009. doi: 10.1126/science.aat6081

Kissling, E., Ellsworth, W. L., Eberhart-Phillips, D., and Kradolfer, U. (1994). Initial reference models in local earthquake tomography. *J. Geophys. Res. Solid Earth* 99, 19635–19646. doi: 10.1029/93JB03138

Kühn, D., Heimann, S., Isken, M. P., Ruigrok, E., and Dost, B. (2020). Probabilistic moment tensor inversion for hydrocarbon-induced seismicity in the groningen gas field, the Netherlands, Part 1: testing. *Bull. Seismol. Soc. Am.* 110, 2095–2111. doi: 10.1785/0120200099

Lizurek, G., Wiszniowski, J., Giang, N. V., Van, D. Q., Dung, L. V., Tung, V. D., et al. (2019). Background seismicity and seismic monitoring in the Lai Chau reservoir area. *J. Seismol.* 23, 1373–1390. doi: 10.1007/s10950-019-09875-6

López-Comino, J. Á, Braun, T., Dahm, T., Cesca, S., and Danesi, S. (2021). On the source parameters and genesis of the 2017, Mw 4 montesano earthquake in the outer border of the Val d'Agri Oilfield (Italy). *Front. Earth Sci.* 8:617794. doi: 10.3389/feart.2020.617794

Manga, M., Wang, C.-Y., and Shirzaei, M. (2016). Increased stream discharge after the 3 September 2016 Mw 5.8 Pawnee, Oklahoma earthquake. *Geophys. Res. Lett.* 43, 11588–11594. doi: 10.1002/2016GL071268

Martínez-Díaz, J. J., Bejar-Pizarro, M., Álvarez-Gómez, J. A., Mancilla, F., de, L., Stich, D., et al. (2012). Tectonic and seismic implications of an intersegment rupture: the damaging May 11th 2011 Mw 5.2 Lorca, Spain, earthquake. *Tectonophysics* 546–547, 28–37. doi: 10.1016/j.tecto.2012.04.010

McClusky, S., Balassanian, S., Barka, A., Demir, C., Ergintav, S., Georgiev, I., et al. (2000). Global positioning system constraints on plate kinematics and dynamics in the eastern mediterranean and caucasus. *J. Geophys. Res. Solid Earth* 105, 5695–5719. doi: 10.1029/1999JB900351

McGarr, A., and Simpson, D. (1997). "Keynote lecture: a broad look at induced and triggered seismicity, "Rockbursts and seismicity in mines"," in *Proceeding of 4th international symposium on rockbursts and seismicity in mines, Poland, 11–14 August 1997*, eds S. J. Gibowicz and S. Lasocki (Rotterdam: A.A. Balkema), 385–396.

McGarr, A., Simpson, D., and Seeber, L. (2002). 40—Case histories of induced and triggered seismicity. *Int. Geophys.* 81A, 647–661.

McKenzie, D. (1972). Active tectonics of the mediterranean region. *Geophys. J. Int.* 30, 109–185. doi: 10.1111/j.1365-246X.1972.tb02351.x

MTA (2020). *General Directorate of Mineral Research and Exploration. 1:100 000 scaled Geological Maps of Turkey, sheet M40-M41, Geological Research Department*. Ankara: MTA.

Negi, S. S., Paul, A., Cesca, S., Kamal Kriegerowski, M., Mahesh, P., and Gupta, S. (2017). Crustal velocity structure and earthquake processes of Garhwal-Kumaun Himalaya: Constraints from regional waveform inversion and array beam modeling. *Tectonophysics* 712–713, 45–63.

Perinçek, D., Günay, Y., and Kozlu, H. (1987). "New observations on strike-slip faults in east and southeast Anatolia", in *Proceedings 7th Biannual Petroleum Congress of Turkey, UCTEA Chamber of Petroleum Engineers, Turkish Association of Petroleum Geologists*, Ankara, 89–103.

Reilinger, R., McClusky, S., Vernant, P., Lawrence, S., Ergintav, S., Cakmak, R., et al. (2006). GPS constraints on continental deformation in the Africa-Arabia-Eurasia continental collision zone and implications for the dynamics of plate interactions. *J. Geophys. Res.* 111:B05411. doi: 10.1029/2005JB004051

Richter, G., Hainzl, S., Dahm, T., and Zöller, G. (2020). Stress-based, statistical modeling of the induced seismicity at the Groningen gas field, The Netherlands. *Environ. Earth Sci.* 79, 252. doi: 10.1007/s12665-020-08941-4

Rinaldi, A. P., Improta, L., Hainzl, S., Catalli, F., Urpi, L., and Wiemer, S. (2020). Combined approach of poroelastic and earthquake nucleation applied to the reservoir-induced seismic activity in the Val d'Agri area, Italy. *J. Rock Mechan. Geotech. Eng.* 12, 802–810. doi: 10.1016/j.jrmge.2020.04.003

Roeloffs, E. A. (1988). Fault stability changes induced beneath a reservoir with cyclic variations in water level. *J. Geophys. Res. Solid Earth* 93, 2107–2124. doi: 10.1029/JB093iB03p02107

Ruiz-Barajas, S., Santoyo, M. A., Benito Oterino, M. B., Alvarado, G. E., and Climent, A. (2019). Stress transfer patterns and local seismicity related to reservoir water-level variations. A case study in central Costa Rica. *Sci. Rep.* 9:5600. doi: 10.1038/s41598-019-41890-y

Şahbaz, N., and Seyitoğlu, G. (2018). The neotectonics of NE Gaziantep: the Bozova and Halfeti strike-slip faults and their relationships with blind thrusts, Turkey. *Bull. Miner. Res. Explor.* 156, 17–40.

Scholz, C. H. (2015). On the stress dependence of the earthquake b value. *Geophys. Res. Lett.* 42, 1399–1402. doi: 10.1002/2014GL062863

Schorlemmer, D., Wiemer, S., and Wyss, M. (2005). Variations in earthquake-size distribution across different stress regimes. *Nature* 437, 539–542. doi: 10.1038/nature04094

Schwatke, C., Dettmering, D., Bosch, W., and Seitz, F. (2015). DAHITI – an innovative approach for estimating water level time series over inland waters using multi-mission satellite altimetry. *Hydrol. Earth Syst. Sci.* 19, 4345–4364. doi: 10.5194/hess-19-4345-2015

Şengör, A. M. C., Görür, N., and Şaroğlu, F. (1985). "Strike-slip faulting and related basin formation in zones of tectonic escape: Turkey as a case study," in *Strike-slip Deformation, Basin Formation and Sedimentation*, Vol. 37, eds K. T. Biddle and N. Christie- Blick (Society of Economic Mineralogist and Paleontologists Special), 227–264. doi: 10.2110/pec.85.37.0211

Şengör, A. M. C., and Yılmaz, Y. (1981). Tethyan evolution of Turkey a plate tectonic approach. *Tectonophysics* 75, 181–241.

Shapiro, S. A., Krüger, O. S., and Dinske, C. (2013). Probability of inducing given-magnitude earthquakes by perturbing finite volumes of rocks. *J. Geophys. Res.* 118, 3557–3575. doi: 10.1002/jgrb.50264

Simpson, D. W. (1986). Triggered Earthquakes. *Annu. Rev. Earth Planet. Sci.* 14, 21–42. doi: 10.1146/annurev.ea.14.050186.000321

Simpson, D. W., Leith, W. S., and Scholz, C. H. (1988). Two types of reservoir-induced seismicity. *Bull. Seismol. Soc. Am.* 78, 2025–2040.

Soysal, H., Sipahioğlu, S., Kolçak, D., and Altınok, Y. (1981). *Earthquake Catalog for Turkey and surrounding area (2100 B.C.–1900 A.D.). The Scientific and Technological Research Council of Turkey, Report Nr: TBAG-341*. Ankara: The Scientific and Technical Research Council of Turkey (TUBİTAK), 86.

Tosun, H. (2012). "Re-analysis of ataturk dam under ground shaking by finite element models," in *Proceedings of the CDA Annual Conference*, Saskatoon, SK.

Tosun, H., Zorluer, İ, Orhan, A., Seyrek, E., Türköz, M., and Savaş, H. (2007). Seismic hazard and total risk analyses for large dams in Euphrates Basin in Turkey. *Eng. Geol.* 89, 155–170.

Villaseñor, A., Herrmann, R. B., Gaite, B., and Ugalde, A. (2020). Fault reactivation by gas injection at an underground gas storage off the east coast of Spain. *Solid Earth* 11, 63–74. doi: 10.5194/se-11-63-2020

Walsh, F. R., and Zoback, M. D. (2015). Oklahoma's recent earthquakes and saltwater disposal. *Sci. Adv.* 1:e1500195. doi: 10.1126/sciadv.1500195

Wilson, M. P., Foulger, G. R., Gluyas, J. G., Davies, R. J., and Julian, B. R. (2017). HiQuake: the human-induced earthquake database. *Seismol. Res. Lett.* 88, 1560–1565. doi: 10.1785/0220170112

Yeck, W. L., Hayes, G. P., McNamara, D. E., Rubinstein, J. L., Barnhart, W. D., Earle, P. S., et al. (2017). Oklahoma experiences largest earthquake during

ongoing regional wastewater injection hazard mitigation efforts. *Geophys. Res. Lett.* 44, 711–717. doi: 10.1002/2016GL071685

Yeck, W. L., Weingarten, M., Benz, H. M., McNamara, D. E., Bergman, E. A., Herrmann, R. B., et al. (2016). Far-field pressurization likely caused one of the largest injection induced earthquakes by reactivating a large preexisting basement fault structure. *Geophys. Res. Lett.* 43, 10198–10207. doi: 10.1002/2016GL070861

Zaliapin, I., and Ben-Zion, Y. (2013). Earthquake clusters in southern California I: identification and stability. *J. Geophys. Res. Solid Earth* 118, 2847–2864. doi: 10.1002/jgrb.50179

Zaliapin, I., Gabrielov, A., Keilis-Borok, V., and Wong, H. (2008). Clustering analysis of seismicity and aftershock identification. *Phys. Rev. Lett.* 101, 018501. doi: 10.1103/PhysRevLett.101.018501

Conflict of Interest: The authors declare that the research was conducted in the absence of any commercial or financial relationships that could be construed as a potential conflict of interest.

The handling editor declared a past co-authorship with one of the authors, SHa and TD.

APPENDIX A: DECLUSTERING

The method quantifies the correlation between an event i and a preceding event j by its magnitude-weighted space-time distance $n_{ij} = (t_i - t_j) \, |\vec{x_i} - \vec{x_j}|^d 10^{-bM_j}$ with $t, \vec{x}, M$ being the time, location, and magnitude of the events. b is the Gutenberg-Richter b-value, and d is the fractal dimension of the hypocenter distribution, which would be 2 for a planar distribution and 3 for a homogeneous three-dimensional distribution. The distance can be written as $n_{ij} = \left(T_{ij} R_{ij}\right)$ with rescaled time $T_{ij} = \left(t_j - t_i\right) 10^{-0.5bM_i}$ and rescaled distance $R_{ij} = |\vec{x_j} - \vec{x_i}|^d 10^{-0.5bM_i}$. Among all events j preceding i, the identification of the (most likely) trigger of i results from selecting that event with the lowest n_{ij}-value. To distinguish between triggered and background activity, a threshold value of n_c is set, and only events with $n_{ij} \leq n_c$ are considered as plausible mainshock-aftershock pairs. By means of epidemic-type aftershock sequence (ETAS) simulations, the applied detection method has been previously demonstrated to be robust with respect to (1) changes of the involved parameters of the method, (2) catalog incompleteness, and (3) location errors (Zaliapin and Ben-Zion, 2013). Here we used standard parameters $d = 2.3$, $b = 1$, and a threshold value of $n_c = 10^{-3.5}$.

APPENDIX B: RESERVOIR-INDUCED STRESS CHANGES

To calculate the reservoir-related stress variations, we follow the calculations of Gahalaut and Hassoup (2012), assuming a uniform and isotropic half-space. The total pressure changes p related to a reservoir is the sum of p_c and p_d, which are the change in pore pressure due to the instant compression caused by the reservoir load, and the change in pore pressure due to the diffusion of reservoir water load, respectively (Roeloffs, 1988). The instant effect p_c can be calculated by $-B\left(\sigma_{11} + \sigma_{22} + \sigma_{33}\right)/3$, where B is the Skempton coefficient. Additionally, we consider for a given receiver mechanism (strike, dip, rake), the induced shear stress τ and compressional normal stress σ_n related to the loading and finally calculate the corresponding Coulomb Failure Stress $CFS = \tau - \mu\left(\sigma_n - p\right)$ with friction coefficient μ. For that, we calculate the loading induced stress tensor σ_{ij} using 3-D Boussinesq-Cerruti solutions for a point force acting on the surface of an infinite half-space (see, e.g., Deng et al., 2010). The pressure change related to diffusion is calculated by the convolution of the observed reservoir water level L with the Green's function G (Gahalaut and Hassoup, 2012; Hainzl et al., 2015):

$$\Delta p_d\left(x, y, z, t\right) = D \int_0^t \int_{-\infty}^{\infty} \int_{-\infty}^{\infty} L\left(\bar{x}, \bar{y}, \bar{t}\right) G\left(x - \bar{x}, y - \bar{y}, z, t - \bar{t}\right) d\bar{t} d\bar{x} d\bar{y} \quad (1)$$

with $G\left(x - \bar{x}, y - \bar{y}, z, t - \bar{t}\right) = \frac{z}{8\pi^{1.5}\left[D\left(t - \bar{t}\right)\right]^{2.5}} exp\left(-\frac{(x-\bar{x})^2 + (y-\bar{y})^2 + z^2}{4D\left(t-\bar{t}\right)}\right)$

where x,y and $\bar{x}, \bar{y}$ refer to horizontal coordinates of the observation and source points, respectively, and z is the depth of the observation. For our calculations, we use the values $B = 0.5$, $\mu = 0.8$.

frontiers in Earth Science

ORIGINAL RESEARCH
published: 02 July 2021
doi: 10.3389/feart.2021.673124

Can Hydrocarbon Extraction From the Crust Enhance or Inhibit Seismicity in Tectonically Active Regions? A Statistical Study in Italy

Alexander Garcia[1]*, *Licia Faenza*[2], *Andrea Morelli*[1] and *Ilaria Antoncecchi*[3,4]

[1]Istituto Nazionale di Geofisica e Vulcanologia, Sezione di Bologna, Italy, [2]Istituto Nazionale di Geofisica e Vulcanologia, Osservatorio Nazionale Terremoti, Bologna, Italy, [3]Ministero dello Sviluppo Economico, Direzione Generale per le Infrastrutture e la Sicurezza dei Sistemi Energetici e Geominerari (DGISSEG), Rome, Italy, [4]Ricerca sul Sistema Energetico S.p.A (RSE), Milano, Italy

A number of oil- and gas-producing leases have been operating in Italy in the last decades, many of which are located in the surroundings of tectonically active regions. Identifying human-induced seismicity in areas with high levels of natural seismicity is a difficult task for which virtually any result can be a source of controversy. We implemented a large-scale analysis aiming at tracking significant departures of background seismicity from a stationary behavior around active oil and gas development leases in Italy. We analyzed seismicity rates before and after hydrocarbon peak production in six oil-producing and 43 gas-producing leases, and evaluate the significance of possible seismicity rate changes. In a considerable number of cases seismicity rate results stationary. None of the observed cases of seismicity rate increase after the peak production is statistically significant (at a *s.l.* = 0.05). Conversely, considering cases of seismicity rate decrease after peak production, our results suggest that the seismicity rate reduction is statistically significant (*s.l.* = 0.05) around one oil-producing lease (Val d'Agri, Basilicata) and around a cluster of gas-producing leases in Sicily. Our results put in evidence correlated changes between the rates of shallow seismicity and hydrocarbon production in these areas, which are then identified as hotspots requiring more detailed research; assessing actual causal relationships between these processes will require further physically-based modelling. If a physical causative link between these processes exists, then the observed seismicity rate reduction could either be due to increased seismicity during the progressive increase in production before reaching its maximum, or to an actual seismicity rate reduction after that peak. Considering that there is evidence of seismicity occurring before the start of hydrocarbon production, which contrasts with the evident reduction of events observed after the peak production, we think it likely that the seismicity inhibition is a plausible hypothesis. Using a simple model we also calculate Coulomb stress changes in planes optimally oriented for failure, and we show that under some conditions the inhibition of seismicity is feasible in at least one of these cases. We conclude that more efforts to study the mechanisms and the possible consequences of anthropogenically-driven seismicity inhibition are required.

Keywords: regional seismicity, hydrocarbon production, correlation analysis, seismicity rate changes, Italy, anthropogenic hazards

OPEN ACCESS

Edited by:
Rebecca M. Harrington, Ruhr University Bochum, Germany

Reviewed by:
Agnes Helmstetter, Université Grenoble Alpes, France
Piero Poli, Université Grenoble Alpes, France

***Correspondence:**
Alexander Garcia
alexander.garcia@ingv.it

Specialty section:
This article was submitted to Solid Earth Geophysics, a section of the journal Frontiers in Earth Science

Received: *26 February 2021*
Accepted: *07 June 2021*
Published: *02 July 2021*

Citation:
Garcia A, Faenza L, Morelli A and Antoncecchi I (2021) Can Hydrocarbon Extraction From the Crust Enhance or Inhibit Seismicity in Tectonically Active Regions? A Statistical Study in Italy. Front. Earth Sci. 9:673124. doi: 10.3389/feart.2021.673124

1 INTRODUCTION

The complex geological setting that characterizes the Italian peninsula is the result of different geodynamical processes closely acting in time and space; consequently, today the crust in this zone is characterized by a complex stress field with tightly spaced compressional and extensional regions (Amato and Montone, 1997). The most predominant geomorphologic features in this region are the Southern Alps and the Apennines mountain chains, which are characterized by thrust-and-fold belts originated from the interaction between the European and the Adriatic-African tectonics plates (see e.g., Calamita et al., 1994; Cello and Mazzoli, 1998; D'Agostino et al., 2001; Bertello et al., 2010; Handy et al., 2010; Cazzini et al., 2015; van Hinsbergen et al., 2020). Such an active and complex tectonic setting makes of Italy a seismically active region where on average, every year, more than 2,000 seismic events with magnitude ≥2.0 are located by the Italian national seismic network (see e.g., the Bollettino Sismico Italiano, Pagliuca et al., 2020). Moreover, Italian seismic sequences are generally very complex, often characterised by the occurrence of either foreshocks, multiple mainshocks, or strong aftershocks; this feature of the seismicity in this region has a strongly influence on the seismic hazard (Guidoboni and Valensise, 2015).

In recent years, the interest in the possible influence of anthropogenic activities on seismicity has significantly grown mainly because of a generalized public concern, which has stimulated the development of independent scientific research to support objective policy making (e.g., Ellsworth, 2013; Dahm et al., 2015; van der Voort and Vanclay, 2015; Garcia–Aristizabal et al., 2020). The Italian territory is the scenario of a wide number of underground industrial activities such as oil and gas extraction, geothermal energy production, and gas storage, many of which have been suspected to have direct or indirect causal links with some seismic events located nearby; however, to date there are no unambiguously documented reports of damaging seismic events associated with anthropogenic activities in the country (see e.g., Braun et al., 2018). Probably, the only clear cases of seismicity linked to underground geo-resource development in Italy are the low-magnitude seismicity occurrences recorded in connection

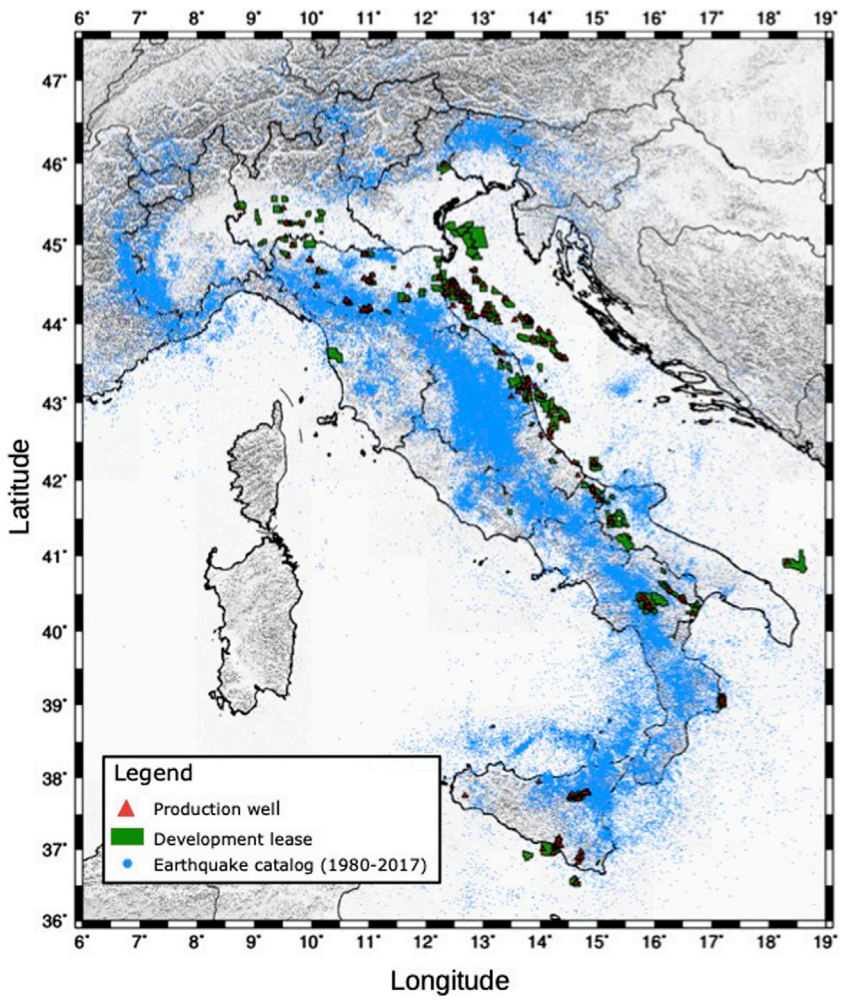

FIGURE 1 | Map showing the spatial distribution of the oil and gas production leases in Italy, as well as the epicenters of the earthquakes from the HORUS catalog used in this study.

with wastewater reinjection at the Costa Molina 2 well in the High Val d'Agri, southern Italy (Valoroso et al., 2009; Improta et al., 2015), and the seismicity recorded near geothermal power plants in Tuscany (Evans et al., 2012).

Among all the anthropic activities having the potential to stimulate earthquakes to occur, the effects of fluid injection or extraction from the crust are probably the processes arising more concern, in particular the activities related with oil and gas production. In Italy, hydrocarbons are found in several oil and gas provinces, most of which are located in the Po plain, the northern Adriatic sea, the southern Apennines, and in Sicily (e.g., Bertello et al., 2010); as a consequence, these are the areas hosting most of the development leases in the country (**Figure 1**). According to data published by the Italian Ministry of Economic Development (MISE), as of 2019 there were 193 development leases in the country, 127 of which are onshore and the other 66 offshore (UNMIG, 2020).

Discriminating natural from induced seismicity in seismically active regions is a particularly complex task. Early attempts to discriminate induced from natural seismicity were performed, for fluid injection operations, by Davis and Frohlich (1993), and for fluid withdrawal by Davis and Nyffenegger (1995); however, these approaches were mainly based on qualitative assessments.

More quantitative, physically-based and/or stochastic methods for discriminating natural from induced seismicity have recently been proposed in literature (a review can be found, e.g., in Grigoli et al., 2017). For example, Dahm et al. (2015) propose a quantitative probabilistic approach to discriminate induced, triggered, and natural earthquakes, calculating the probability that events have been anthropically triggered/induced from the modeling of Coulomb stress changes and a rate-and-state dependent seismicity model.

Schoenball et al. (2015) analyzed inter-event times, spatial distribution, and frequency-size distributions for natural and induced earthquakes around a geothermal field. Determining the distribution of nearest neighbor distances in a combined space-time-magnitude metric, they identify clear differences between both kinds of seismicity. For example, it is suggested that compared to natural earthquakes, induced earthquakes feature a larger population of background seismicity and nearest neighbors at large magnitude rescaled times and small magnitude rescaled distances. They argue that unlike tectonic processes, stress changes caused by anthropic underground operations occur on much smaller time scales and appear strong enough to drive small faults through several seismic cycles. As a result, it is likely to record seismicity close to previous hypocenters after short time periods.

Zhang et al. (2016) compared moment tensors of both natural and induced events in the Western Canadian Sedimentary Basin. These authors calculated full moment tensors and stress drop values for eight induced earthquakes (magnitudes between 3.2 and 4.4), as well as for a nearby M5.3 event considered as a natural earthquake. This study suggests that, first, it may be possible to discriminate between induced and natural seismicity considering region-specific attributes, as for example the focal depths (which they suggest as the most robust parameter since the induced events in their study area are significantly shallower than most of the intra-plate earthquakes in the Canadian Shield). Moreover, they found a non-negligible (>25%), non double couple component for most of the induced events studied.

Zaliapin and Ben–Zion (2016) analyzed statistical features of background and clustered subsets of earthquakes in California and in South Africa. These authors suggest that, compared to regular tectonic activity, induced seismicity in the analyzed data sets exhibit remarkable features as i) a higher rate of background events, ii) faster temporal offspring decay, iii) higher rate of repeating events (i.e., earthquakes located in the rupture area of some previous earthquakes, but that occur at times far exceeding the typical duration of an aftershock series), iv) larger proportion of small clusters, and v) larger spatial separation between parent and offspring.

Discriminating human-induced from natural seismicity is therefore a difficult problem for which virtually any solution can be a source of controversy. For this reason, the evaluation of possible interactions between seismicity and hydrocarbon production, if possible, should rely on multidisciplinary analyses such as e.g., detailed physically-based modelling complemented by sophisticated stochastic methods able to provide probabilistic assessments and to take uncertainties into account. It is worth noting however that the ways in which these interactions may occur are complex and their identification in a context characterized by high levels of naturally-occurring seismicity is not straightforward. Moreover, given the relatively high number of development leases active in Italy, performing such analyses at the national scale may be considered an intractable problem.

These reasons pushed us to explore the possibility to implement large-scale screening methods aiming at tracking measurable phenomena, such as e.g., changes in seismicity rates, that plausibly could occur if notable interactions between underground human operations and nearby seismicity sources are actually occurring in a given area. Spatial and temporal correlation between human activity and event rates is usually considered a key parameter to suspect possible relationships between seismicity and underground anthropic activity (e.g., Shapiro et al., 2007, 2010; Cesca et al., 2014; Leptokaropoulos et al., 2017; Garcia-Aristizabal, 2018; Molina et al., 2020); for example, significant changes in seismicity rates with respect to background seismicity, as well as the spatial and temporal correlation of gas injection operations and seismicity were analyzed by Cesca et al. (2014) to suggest a possible case of triggered/induced seismicity near an offshore platform used for gas storage in Spain (the Castor project).

However, underground human-induced perturbations (as e.g., pore pressure variations due to fluid injections) can produce changes at large distances and/or with large temporal delays, potentially causing earthquakes to occur several kilometers away as well as months/years after the industrial operations have stopped or reached the maximum peak (e.g., Mulargia and Bizzarri, 2014); likewise, natural seismicity may also occur within few kilometers from industrial sites. Therefore, in seismically active regions (such as in Italy), spatio-temporal correlations between industrial activity and significant changes in seismicity rates with respect to background activity by

themselves usually do not provide irrefutable proofs of causal relationships between hydrocarbon production and seismic activity. Despite this, we argue that studying such correlations has a remarkable added value since it gives us the possibility of performing large-scale, systematic analyses of a huge amount of seismic and production data and, under the working hypotheses considered, to identify hotspot areas where it could be possible to perform, in a later stage, more detailed research to verify possible causal relationships.

The industrial data publicly available for this study consists of a time series of hydrocarbon production volumes; for this reason, our analyses are particularly focused on studying the possible effects on seismicity of stress perturbations caused by fluid withdrawal processes. The working hypothesis in this work therefore starts from assuming that fluid withdrawal from the crust may induce deformations in the surroundings of the host rock (especially in depleting reservoirs); the magnitude of such deformations will depend on multiple factors such as, for example, the litology, the structural geology, the volume and rate of fluid removed, the geomechanical features of the reservoir, and its behavior during the fluid withdrawal process, among others. The deformations may in turn alter the local stress field and, as a consequence, stimulate or inhibit seismicity in the surroundings.

We assume that in absence of other stress perturbation sources, the regional release of background seismicity is predominantly influenced by the regional tectonic stress field; in such a context, it can be expected that a steady stress field should tend to generate background seismicity with stationary rates; however, if other natural (e.g., hydrogeology: see Hainzl et al., 2006; Pintori et al., 2021) or man-made (e.g., pressurized fluid injections: see Shapiro et al., 2007; Garcia-Aristizabal, 2018) processes are able to perturb the local stress field, then it is possible that the rate at which seismicity is released in that specific area can be altered. In such a case, slight deviations from stationarity could possibly be measured.

In this work we are interested in identifying significant departures of background seismicity from a stationary behavior around productive oil and gas development leases in Italy. We are particularly interested in exploring cases in which the long-term hydrocarbon production may have left a measurable footprint on the release of background seismicity (as e.g., by processes related to reservoir depletion), and to test whether possible changes in the rate at which background seismicity is released in such areas are correlated with the main changes in the hydrocarbon production patterns.

The article is structured as follows: first we present the seismic and the hydrocarbon production data available for this study. Second, we present the methodological approach used in order to identify zones with possible anomalies in seismicity rates concomitant with significant changes in oil and gas production. Finally, we present the results and discuss the importance and limitations of these findings.

2 DATA

For this study we use a national-wide seismic catalog containing earthquake locations and magnitudes, as well as the most detailed public oil and gas production data from development leases in Italy. All the used data are freely accessible from public sources (**Section 7** for details).

2.1 Seismicity

We use the seismic data collected in the publicly-available HORUS catalog (Homogenized instrumental seismic catalog, Lolli et al., 2020a, b). This is an extended instrumental seismic catalog reporting earthquake locations and magnitudes since 1960 and is continuously updated as new data is processed. An outstanding feature of this catalog is the effort made to harmonize the event magnitudes in terms of an equivalent homogeneous moment magnitude, M_w.

We use the data in the time interval 1980–2017, which includes 368,258 earthquakes (**Figure 1**). This time interval is selected because it covers the same time window of available hydrocarbon production data; moreover, the eighties are probably the period when the national seismic network started to grow more consistently, improving as a consequence the quality of the earthquake locations and reducing the completeness magnitude (M_c). However, this process does not evolve uniformly throughout the whole country, since the spatial and temporal distribution of new seismic stations is not spatially homogeneous. For example, **Figure 2** shows the temporal evolution of the Italian National Seismic Network; the stations belong to different networks deployed for seismic monitoring in Italy (e.g., the Italian Seismic Network and the Euro-Mediterranean Network, both maintained by INGV; the Italian Strong Motion Network, managed by the National Civil Protection; the networks operated by other national institutes and universities such as the Istituto Nazionale di Oceanografia e di Geofisica Sperimentale, the University of Basilicata, the University of Genoa, the University of Trieste, the University of Bari, and other organisations in the border areas).

The completeness magnitude (M_c) of this catalog therefore changes in time and in space, as a consequence of different factors as e.g., changes in the number and distribution of seismic stations available for locating events, as well as the quality of the instrumentation and of the site facilities. Therefore, identifying a single completeness magnitude (in both time and space) for the full catalog results in a very high M_c value; adopting such a choice would force us to discard an important amount of seismic data, and for this reason, the M_c is rather determined locally for each site, as discussed in the **Section 3**.

2.2 Oil and Gas Production Data

We collected the most detailed public information about hydrocarbon production in Italy (available from the Italian Ministry of Economic Development, MISE, **Section 7** for details). Out of 109 active development permits (**Figure 1**), we got production data from 102 leases in which a total of 588 production wells are present. The available data set includes the annual oil and gas production since 1980 (volumes in thousands of cubic meters of oil or standard cubic meters of gas); the data is aggregated by development lease, that is, summing up the production/year from all the wells producing within the lease.

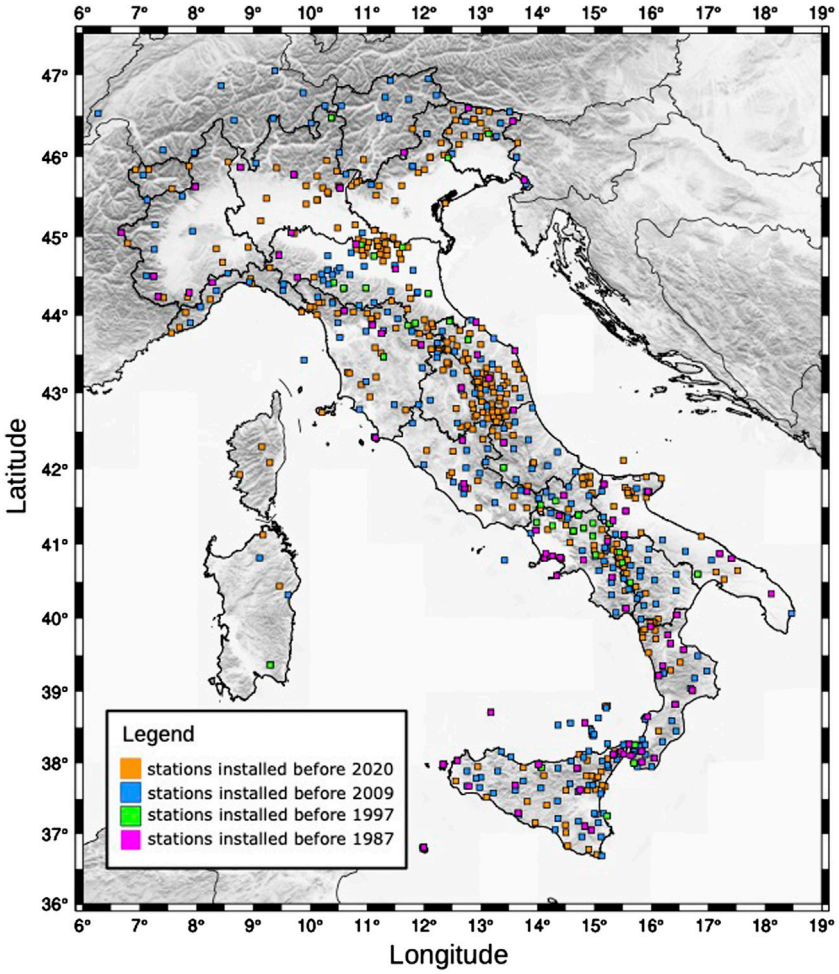

FIGURE 2 | Temporal evolution of the deployment of monitoring seismic stations in Italy, maintained by various Italian and international institutes and universities (see the text for details). Substantial increases in the number of stations concurred with the occurrence of different seismic sequences.

For development leases in which production started before 1980, the total oil and gas production preceding 1980 is also available.

It is worth noting that besides the hydrocarbon production, a number of sites where underground waste water injection is performed are also present in Italy; nevertheless, the fluid injection-related data are not publicly available and for this reason these activities were not considered in this study.

As **Figure 1** shows, the active development leases are mostly distributed along the Adriatic coast (onshore and offshore), as well as along the Po Valley (in the North), the central/southern Apennines and Sicily. In this study we consider the hydrocarbon production from 1980 up to 2017 (**Figure 3**). From the 102 development leases for which production data is available, 85 exclusively produce gas, one exclusively produces oil, and 16 produce both oil and gas. The development leases with the highest annual oil production in the study period are found in the Val d'Agri (Basilicata region), Villafortuna-Trecate (Piemonte region, western Po Valley), B.C 8. LF (offshore, southern Adriatic sea), and C.C 6. EO (Sicily, southern Italy) leases (**Figure 3A**); on the other hand, those with the highest annual gas productions in the same period are the A.C 7. AS (offshore, central Adriatic sea), D. C 1. AG (Calabria region), A.C 2. AS and A.C. 27. EA (offshore, northern Adriatic sea, **Figure 3B**).

3 METHODS

We perform a large-scale screening of the behavior of background seismicity (i.e., the events considered independent, as described in **Section 3.3**) in areas around oil and gas production sites in Italy. Our goal is to attempt i) to identify correlated changes between seismicity rates and hydrocarbon production, and ii) to test the significance of these seismicity rate changes.

First, a pre-processing step is performed in order to identify the areas around the target leases where a reasonable amount of both seismic and production data is available. Afterwards, we proceed with the proper data analyses, namely i) identification of independent background seismicity in the lease area, ii) selection of background events located within a distance δx from the

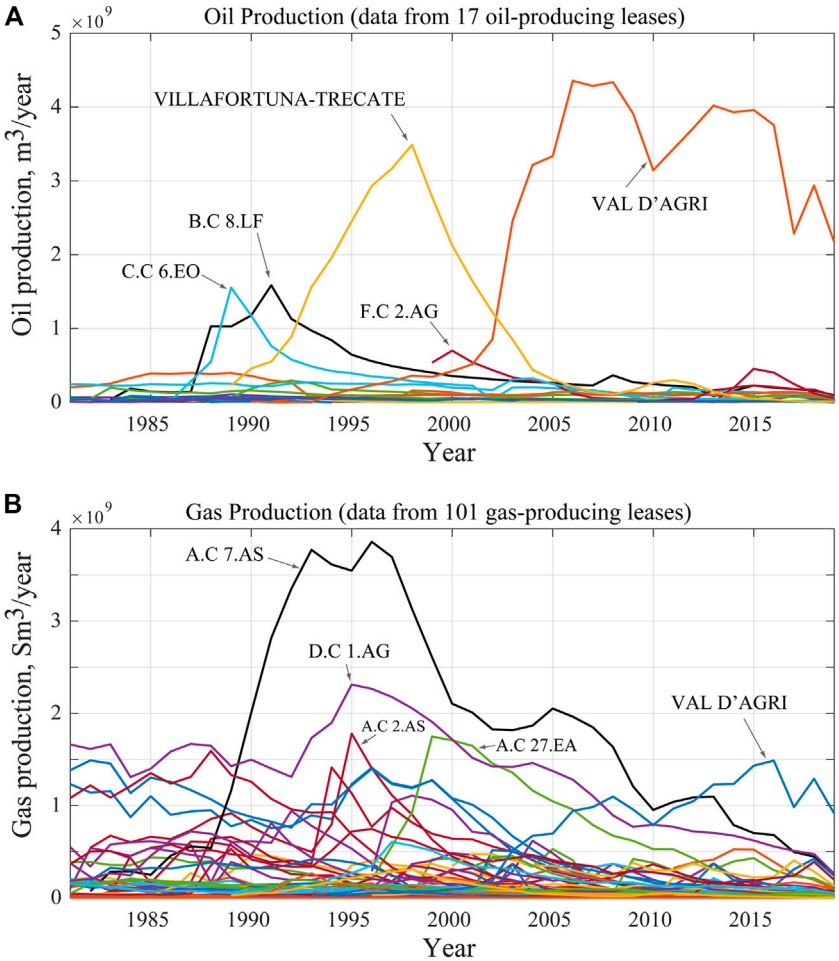

FIGURE 3 | Annual oil and gas produced between 1980 and 2017 in Italy from 102 development leases in Italy: **(A)** Oil is produced from 17 leases (one of which exclusively produces oil); **(B)** Gas is produced from 101 leases (85 of which exclusively produce gas). Data available from the Italian Ministry of Economic Development (MISE).

production wells, and iii) test the significance of possible seismicity rate changes correlated with changes in hydrocarbon production. These steps are explained in the following paragraphs.

3.1 Identifying Development Leases for the Analyses

If the withdrawal of fluids from the crust affects the stress field and the seismicity release in a given zone, then a possible way to identify potential traces of such effects is to look for changes in background seismicity rates before and after important changes in the rate at which fluids are extracted. Observing the time series of production data (**Figure 3**), it can be seen that in most of the sites, the oil production (**Figure 3A**) and the gas production (**Figure 3B**) have some outstanding features: after the production starts, it follows different paths up to a point in which it reaches maximum production. The time at which oil or gas production reaches its maximum is hereinafter called the maximum production time, t_m. Afterwards, for times $t > t_m$, the production tends to decrease (probably related to field depletion processes).

Looking in detail at the development of the time series of production data, the main change points in oil and gas production data of potential interest for the analyses in this article are the start of production and the time at which production reaches its maximum. We consider the peak of maximum hydrocarbon production as the reference point for exploring possible changes in seismicity rates (before and after the peak). Changes before and after the production start cannot be analyzed because in most of the sites the time at which production initiates precede the start of the seismic data catalog.

An essential requirement to study changes in seismicity rates consists of taking a sufficiently long time window of seismic data in the time periods preceding and following the change point in production data considered for comparing seismicity rates. In general, the longer the time window, the more representative will our data set likely be. Taking into account the time window of

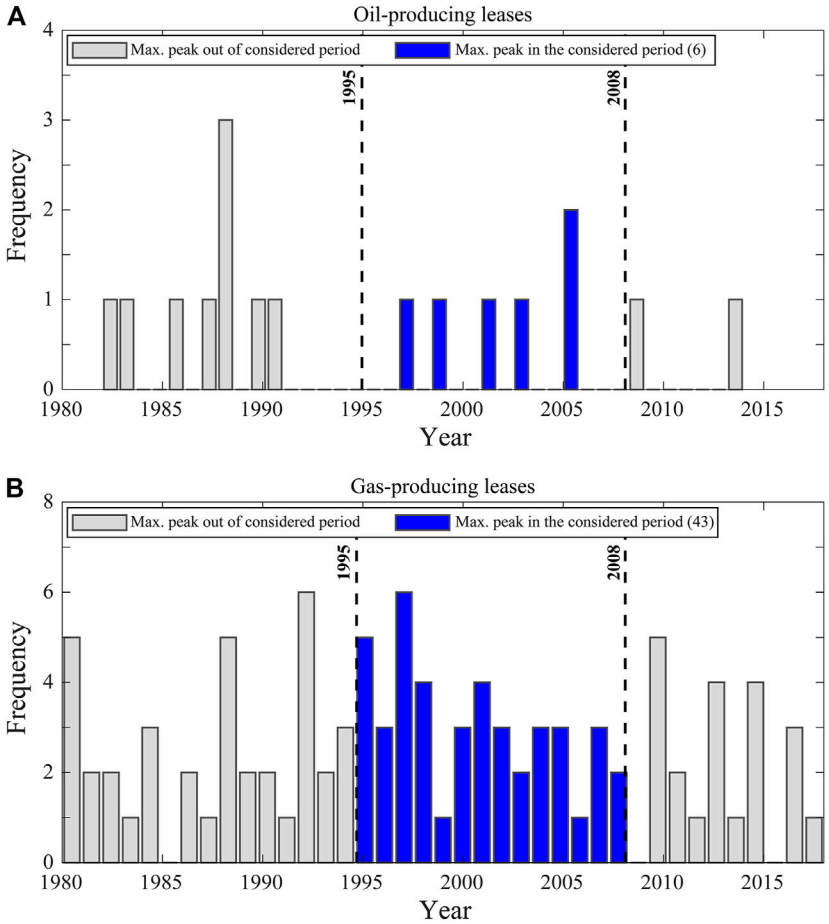

FIGURE 4 | Year at which the maximum production is reached in the available data at each development lease (t_m). Histograms shows the number of **(A)** oil- and **(B)** gas-producing leases in which t_m is reached in the respective year; the blue bars identify the period selected for the analyses (1995–2008) according to the described criteria.

data available for this study (1980–2017), as well as the average seismicity rates observed around the active development leases, we consider as a requirement for including a given development lease in this analysis the availability of a complete set of seismic data for at least 10 years before and 10 years after the t_m associated with the peak production in the respective development lease.

Figure 4 shows histograms summarizing the t_m at which maximum oil (**Figure 4A**) and gas (**Figure 4B**) production are reached in all the development leases for which data are available. Adopting the minimum 10-years time window before and after t_m, and also considering the temporal completeness identified for the seismicity around the leases (**Section 3.2** for details), the sites that can be reliably analyzed in this work reduce to those for which the peak production in the available time series is reached between 1995 and 2008 (i.e., $1995 \leq t_m \leq 2008$). In this way, six oil-producing leases and 43 gas-producing comply with these conditions and are selected for further analyses.

The time series of oil and gas production data from the selected development leases are shown, respectively, in **Figures 5A,B**. Taking the peak oil/gas production as a reference, the data follow different patterns that can be better observed normalizing the production by the maximum production reached in each lease and realigning the time series with respect to t_m (**Figures 5C,D**). For the sake of simplicity, we identify three main patterns (**Figure 5E**): pattern I (the most frequent), is when the production rate steadily increases with time up to reach its maximum; afterwards the production progressively reduces with time. Patterns II and III instead refer to cases where production increases up to remain at relatively high levels for a while, before significantly decreasing again. In some cases the peak production is reached at the end (pattern II), and in other cases it is reached at the beginning (pattern III) of the high-production period.

3.2 Seismic Data Selection

We first calculate the epicentral distance between each earthquake in the catalog and the nearest production well in a lease. This information is used to select the whole seismicity located around each lease, paying particular attention to include all possible clusters of events in time and space observed in the surroundings (i.e., to avoid including incomplete data of seismic sequences, for example). This generally means including

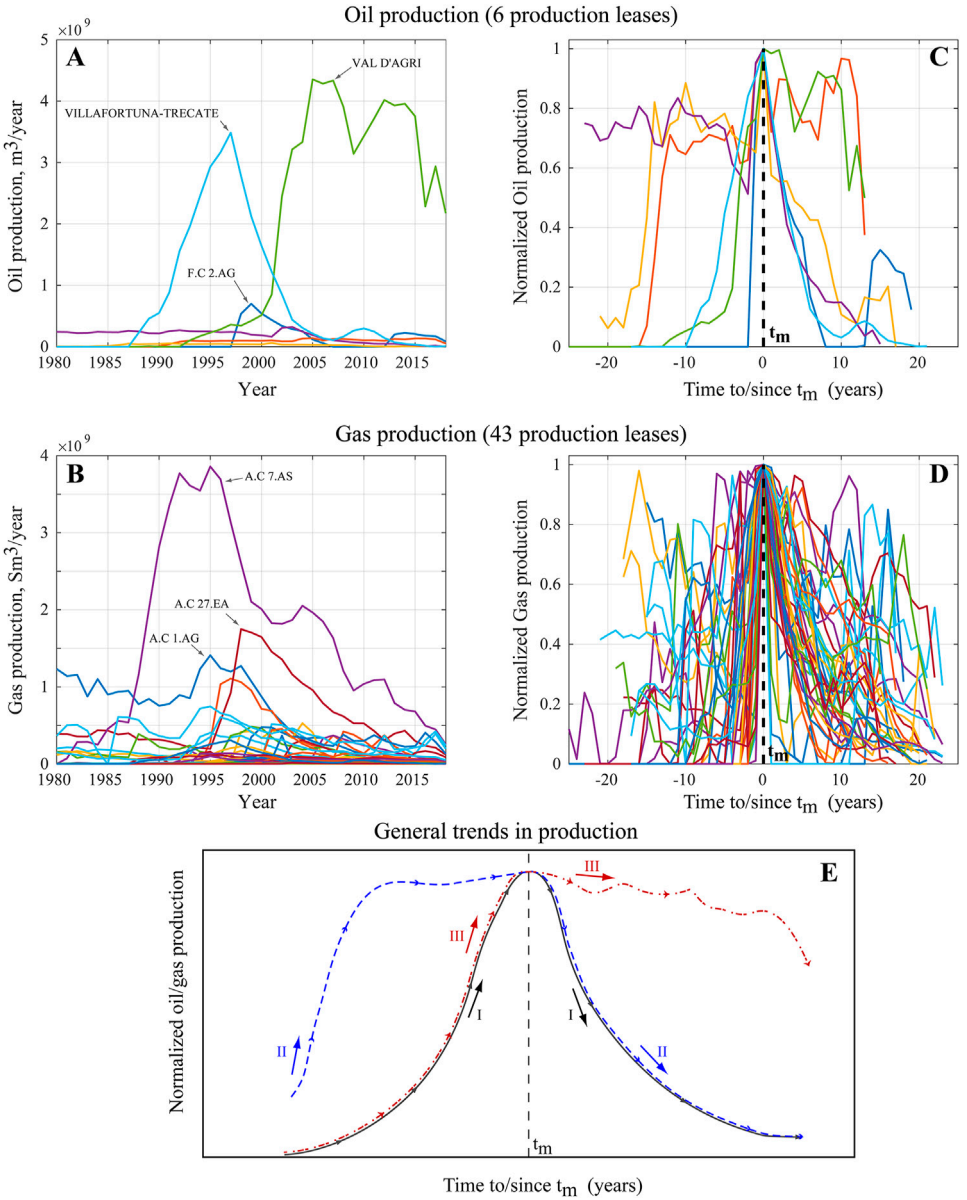

FIGURE 5 | Annual production of identified sites in which it is possible to perform the proposed analyses. Annual production of **(A)** oil and **(B)** gas in the selected development leases. Production data normalized by the maximum value reached in each time series and realigned respect to peak time, t_m are shown in plots **(C)** (oil) and **(D)** (gas). **(E)** Main temporal trends observed in production data.

seismicity located within a few hundred kilometers around each lease (**Figure 6A**). Moreover, since it is generally observed that events induced by man-made, underground operations tend to be shallower than most natural, tectonically driven events, and that induced events often occur at depths comparable to the depth of wells (see e.g., Zhang et al., 2016; Foulger et al., 2018), then for this analysis we only consider the events with depth shallower than 15 km.

Finally, for each resulting (local) catalog we calculate the completeness magnitude (M_c) using, comparatively, three methods [the Maximum Curvature, the Goodness of Fit (Wiemer and Wyss, 2000), and the Modified Goodness of Fit (Leptokaropoulos et al., 2013)], that are available as open tools in the EPOS (European Plate Observing System) platform for anthropogenic hazards (IS-EPOS, 2016; Orlecka-Sikora et al., 2020). In this way, for each lease we obtain a seismic catalog covering a given time interval and is complete above a given minimum magnitude M_c (**Figures 6A,B**).

3.3 Declustering the Seismic Catalog

Since our main target is the identification of depletion-induced effects on seismicity, to perform the analyses proposed in this work we suggest to use a seismic catalog composed as much as possible by independent events, that is, events not likely triggered

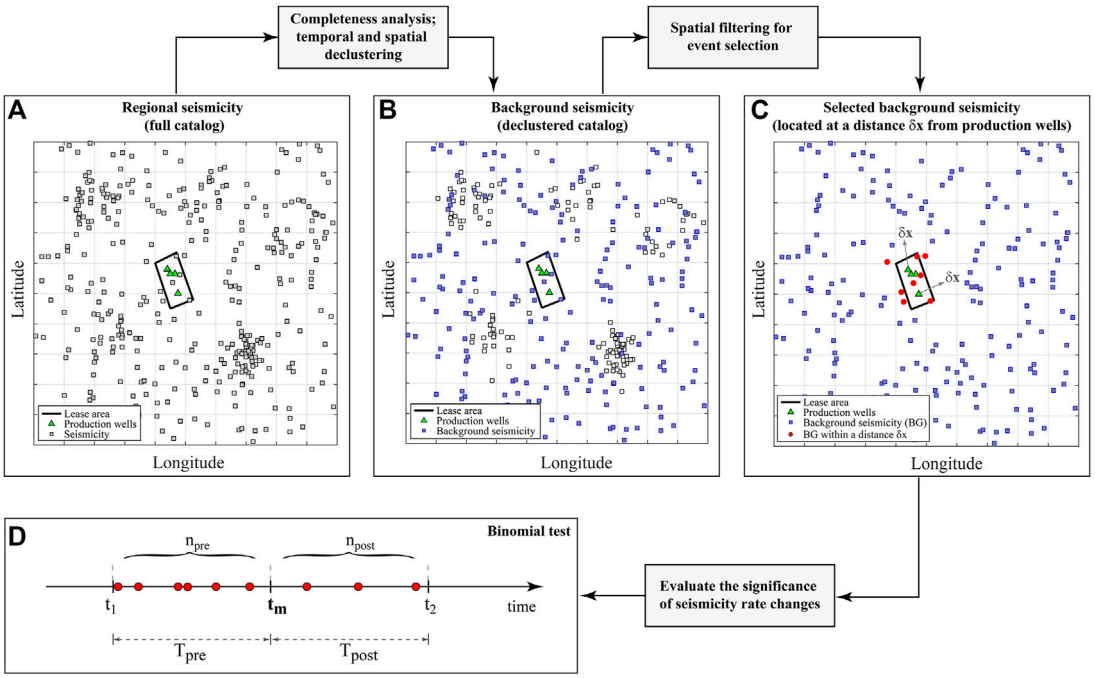

FIGURE 6 | Summary of the processing for selecting seismic data around a given production lease for the correlation analysis: **(A)** Regional seismicity around the lease, for which the M_c is evaluated; **(B)** Identification of background seismicity from the regional catalog (considering events above M_c) using declustering techniques; **(C)** Spatial filtering by selecting events located within a distance δx from production wells; **(D)** binomial test for evaluating the significance of seismicity rate changes.

by earthquake interaction processes (as e.g., aftershocks). That set of independent events is hereinafter referred to as background seismicity (see e.g., **Figure 6B**).

The seismic declustering is a crucial issue in statistical seismology. In general, the term "background" (or "independent") events refers to events that are typically related to regional tectonic activity. Triggered events occur in space-time clusters, and are associated with the occurrence of previous events (e.g., stimulated by stress perturbations from previous-earthquakes); they are often referred to as "dependent events." The distinction within a catalog between the contribution of independent and dependent earthquakes is very complex, and each method inherently contains subjectivity (Zhuang et al., 2002). This characteristic implies that applying different declustering models to the same catalog may generate catalogs of independent events that may differ. Moreover, uncertainties on the data (as e.g., earthquake locations and magnitudes) may challenge the proper performance of declustering algorithms.

In seismology, several techniques have been developed to address the problem of declustering; van Stiphout et al. (2012) provides an overview of this issue, describing the pros and cons of the most popular algorithms. In this work we use the Nearest-Neighbour (NN) Clustering Analysis technique, developed by Zaliapin and Ben-Zion (2013). An outstanding advantage of the NN algorithm is its simplicity because the link between the background events with those triggered is a metric that only concerns a distance measure in time, space and magnitude between any pair of events. The technique consists of calculating, for each earthquake ith in the catalog, the distance to any other jth earthquake subsequently occurred as:

$$\eta_{ij} = t_{ij} r_{ij}^{d_f} 10^{-bm_i} \quad (1)$$

selecting, for each earthquake i, the smallest η_{ij}. In **Equation 1**, the $t_{ij} = t_j - t_i$ is the difference between the two occurrence times expressed in years (with $t_{ij} > 0$); r_{ij} is the distance between the two hypocenters in km; d_f is the fractal dimension of the distribution of hypocenters, which in this work was set to 1.2 following the values suggested by Kagan (1991) and used for declustering seismicity in Italy by Stallone and Marzocchi (2019); b is the Gutenberg-Richter b-value, which is calculated for the seismicity around each lease using the method described in Marzocchi and Sandri (2003); and m_i is the magnitude of the i earthquake.

Within a complete seismic catalog, the distribution of these 3-dimensional distances always shows a bi-modal pattern: the first group of earthquakes is characterized by unusually small distances and represents earthquakes that are "clustered," whereas the second group identifies the events interpreted as "background earthquakes," since in the considered parameter space they exhibit greater distances from each other.

3.4 Evaluating the Significance of Seismicity Rate Changes

Once the background seismicity around a given lease is obtained, we select a set of seismic events for studying possible changes in seismicity rate correlated with changes in hydrocarbon

production. With this aim, we set a maximum distance from the producing wells, δx, to define the volume enclosing the events to be included in the analysis (**Figure 6C**). Defining δx is critical since it reflects the spatial extent where the potential deformations and stress perturbations are supposed to alter the natural occurrence of seismicity. In principle it should be carefully evaluated case by case accounting for different local factors such as, e.g., the size and depth of the reservoir, the volume of fluids withdrawn from the crust, etc. If δx is small, there is a risk of including a small, non representative sample of events; on the other hand, if δx is very large, the significance of possible local changes in seismicity rates can be hidden by a large sample of regional (and presumably stationary) background seismicity.

In tectonic earthquake interaction studies, the size of the area at which earthquake triggering is mostly expected to occur is usually mapped by static stress perturbations; if L is the mainshock source length (as derived from scaling relations, such as for example Wells and Coppersmith, 1994), a characteristic distance in the range 1–3 L is often suggested as a plausible distance within which triggered aftershock are expected to occur (e.g., Parsons and Velasco, 2009; Tahir et al., 2012). Some authors have suggested similar scaling properties for determining characteristic distances for seismicity induced by reservoir impoundments (Grasso et al., 2019) and gas reservoirs (Grasso et al., 2021); in such cases, the characteristic distance is determined as a function of the size of the reservoir. We do not have information about the dimensions of the oil and gas reservoirs from where hydrocarbons are produced in the analyzed cases; therefore, heuristically we select events located at distances within $\delta x = 5$ and 10 km from the production wells, which seems a reasonable and conservative choice for this study.

We look for significant seismicity rate changes before and after t_m using the binomial test proposed by Leptokaropoulos et al. (2017). Let $T_{pre} = [t_1, t_m]$ be the time interval identified before the maximum production peak (with $t_m - t_1 \geq 10$ years, as defined before), and $T_{post} = [t_m, t_2]$ the time interval identified after the maximum production peak (with $t_2 - t_m \geq 10$ years as well, see **Figure 6D** for reference). Let n_{pre} be the number of events that occurred in the period T_{pre}, and n_{post} the number of events that occurred in the period T_{post}. The total number of events in both periods is therefore $N = n_{pre} + n_{post}$ (**Figure 6D**). If the seismicity rate exhibit changes that are correlated with changes in the production trend before and after the time at which the maximum production is reached (t_m), that is, if the seismicity rate during T_{pre} is significantly different from the seismicity rate during T_{post}, then the actual division of the total number of events N in both periods into n_{pre} and n_{post} should be significantly different from the division which could be attained at random. Therefore, if we hypothesize stationary seismicity, the proposed null hypothesis, H_0, states that:

H_0 : n_{post} can be obtained at random from N under probability P, where P is related to the time partitions as follows:

$$P = \frac{T_{post}}{T_{pre} + T_{post}} \tag{2}$$

This hypothesis is tested by means of the binomial test (e.g., Wonnacott and Wonnacott, 1977). If N events occur randomly in the interval $[t_1, t_2]$, this test provides i) the probability p_1 that the number of events in the interval $[t_m, t_2]$ is less than or equal to n_{post},

$$p_1 = Pr\left\{n \leq n_{\text{post}} \middle| N, P\right\} = \sum_{n=0}^{n_{\text{post}}} \binom{N}{n} P^n (1-P)^{N-n} \tag{3}$$

or ii) the probability p_2 that the number of events in the interval $[t_m, t_2]$ is greater than or equal to n_{post},

$$p_2 = Pr\left\{n \geq n_{\text{post}} \middle| N, P\right\} = 1 - \sum_{n=0}^{n_{\text{post}}-1} \binom{N}{n} P^n (1-P)^{N-n} \tag{4}$$

The binomial test assumes that each event is independent, with equal probability of occurrence in the interval $[t_1, t_2]$; the null hypothesis (H_0) is evaluated at a given significance level (e.g., $s.l. = 0.05$), so that if p_1 (or p_2) $< s.l.$, we conclude that there is evidence, with a given significance $s.l.$, that rate in the interval $[t_m, t_2]$ decreased (or increased) with respect to the rate in the interval $[t_1, t_m]$.

4 RESULTS

One of the main issues faced to perform the data analysis was to concentrate our efforts in areas where both seismic and production data were sufficiently representative to avoid, as much as possible, data-driven biases in our results. For this reason, and given the time span covered by the seismic and production data available for this study, we avoided analyzing any region in which the minimum data requirements defined in the **Methods** section were not accomplished. In particular, the minimum length of the time window of seismic data before and after t_{m}, the time at which the maximum production is reached, becomes one of the main constraints, forcing us to not considering about 56% of the leases for which production data are actually available (that is, 57 out of the 102 leases). In such cases, the peak production occurred too close to the end or the beginning of the seismic catalog, which prevents an accurate estimation of the pre– and post– t_{m} seismicity rate. On the remaining 45 leases (39 produce gas only, two produce oil only, and four produce both gas and oil), we applied the analyses described in **Section 3**. The spatial distribution of the analyzed leases cover different areas of the country, including the western Po plain, the northern and central Adriatic sea, southern Apennines and Sicily.

The completeness magnitudes and b values determined for the regional seismicity around each lease are summarized in **Table 1** (for the oil-producing leases) and **Table 2** (for the gas-producing leases). It is worth noting that, in general, the completeness magnitudes tend to be relatively high due to our interest in having seismic data sets as long as possible in time; in fact, the M_{c} has been selected for the seismicity around each lease so that completeness is ensured, at least, since 1985. The seismic catalogs, composed of nearby regional events with magnitudes above the

TABLE 1 | Oil-producing leases analyzed in this study. For each lease we present the estimated completeness magnitude, the b value, as well as the p values (p_1 and p_2) of the binomial test performed considering the seismicity located within a distance δx = 5 and δx = 10 km (the symbol — indicates cases in which both the seismicity rate in both the pre- and the post- t_m time windows are zero).

Oil leases		Completeness		b value	δx = 5 km		δx = 10 km	
n	Lease name	M_c	Since...		p_1 (Lesser)	p_2 (Greater)	p_1 (Lesser)	p_2 (Greater)
1	F.C 2.AG	2.8	1985	0.68	—	—	4.2×10^{-1}	
2	GIAURONE	2.1	1985	0.76	—	—	6.1×10^{-1}	
3	MASSERIA VERTICCHIO	2.2	1985	1.07	4.8×10^{-1}		3.3×10^{-1}	
4	RAGUSA	1.7	1985	0.91		4.3×10^{-1}		4.3×10^{-1}
5	**VAL D'AGRI**	2.4	1985	1.08	**1.6×10^{-5}**		**3.3×10^{-8}**	
6	VILLAFORTUNA-TRECATE	1.9	1985	0.70	—	—	—	—

Bold values represent the cases in which the obtained p value is considered significant (respect to the s.l. taken as reference).

M_c specifically determined for each study area, are then declustered using the NN clustering analysis technique (**Section 3.3**) to obtain a sample of background seismicity composed of independent events at regional scale.

It is worth noting that the declustering step deserves some specific considerations. We argue that in the context of this work, declustering is an important step given our particular interest in detecting seismicity rate changes induced by eventual stress changes caused by depleting reservoirs located in areas where regional stresses are assumed to generate stationary background seismicity. Therefore, the proposed approach can hardly be applied to cases where induced seismicity tends to be strongly clusterized in time and space, as for example cases of seismicity induced by pressurized fluid injections. Moreover, uncertainties related to the effects of declustering could overshadow the reliability of the seismicity rate variations identified with the proposed approach; to mitigate this risk, we also discuss the results that can be obtained by analyzing the full complete catalog (that is, considering events above M_c without declustering); such results, along with the data sets (both the full and the declustered catalogs) are available in the **Supplementary Material**.

After declustering, we identify background events located within δx = 5 and δx = 10 km from the production wells in a given lease, and select the events before and after the respective t_m. In this way we calculate the number of events before (n_{pre}) and after (n_{post}) the peak production time, t_m, as well as the respective time window lengths T_{pre} and T_{post} (see e.g., **Figure 6D** for reference). The same procedure is performed using the full complete catalog (**Supplementary Material**) to compare the results obtained with and without the declustering processing.

Using these data, we first calculate the seismicity rate (in terms of average number of events/year) observed before and after t_m for events located within a distance δx from the producing wells. Comparing the seismicity rates before and after the peak production, it is possible to highlight the areas with seismicity rate variations. For example, **Figure 7A** and **Figure 8A** show the location and estimate of seismicity rate variations around, respectively, the six oil-producing and 43 gas-producing leases analyzed in this study when considering seismicity within δx = 5 km from production wells; colors indicate the behavior of the seismicity rate (i.e., increase, decrease, unchanged) before and after t_m. Regarding the oil-producing leases, the seismicity rate around three sites results null and unchanged before and after t_m (green squares in **Figure 7A**; names can be seen in **Table 1**), in 2 cases (Masseria Verticchio and Val d'Agri) the seismicity rate before the peak production results higher than the seismicity rate in the time window after t_m (blue squares in **Figure 7A**), whereas in one case (Ragusa) we observe the opposite situation (that is, the seismicity rate before is lower than the seismicity rate after t_m, red squares in **Figure 7A**). Regarding the gas-producing leases, we observe that in 20 sites the seismicity rate does not change (18 of which have zero events before and after t_m). These sites are represented as green squares in **Figure 8A**. In the remaining 23 leases (names can be seen in **Table 2**), a seismicity rate variation has been detected: nine sites exhibit an increase (red squares in **Figure 8A**), whereas 14 sites exhibit a decrease in the rate (blue squares in **Figure 8A**). When considering δx = 10 km, one oil-producing and 10 gas-producing leases do not exhibit seismicity rate changes, in 4 and 22 leases (oil and gas, respectively) the seismicity rate before t_m results higher than the seismicity rate after the peak production, whereas the opposite behavior is observed in one oil- and 11 gas-producing leases.

We then evaluate the significance of these seismicity rate variations using the binomial test described in **Section 3.4**. For the areas exhibiting a reduction in seismicity rate after t_m, we calculate p_1 (**Eq. 3**) to evaluate the significance of the observed seismicity rate reduction in the time interval $T_{post} = [t_m, t_2]$ with respect to the rate observed in the interval $T_{pre} = [t_1, t_m]$. Likewise, for the areas exhibiting an increase in seismicity rate after t_m we calculate p_2 (**Eq. 4**) to evaluate the significance of the observed increase in the time interval T_{post} with respect to the rate observed in the interval T_{pre}. The results of these calculations, considering seismicity located within both δx = 5 and δx = 10 km from production wells, are presented in **Table 1** for the oil-producing and in **Table 2** for the gas- producing leases.

The resulting probability values (p_1 and p_2) provide an indication about how likely it is to observe the number of events n_{post} under the null hypothesis (which basically reflects what would be expected in case of stationary seismicity in the whole interval $[t_1, t_2]$, see **Figure 6D** for reference). Therefore, the lower the p value, the more unlikely is to observe n_{post} under such hypothesis (and therefore the more evidence in favor of a significant seismicity rate change). Considering for example a significance level *s.l.* = 0.05 we find that, on the one hand, none of the cases in which an increase in seismicity rate was observed after t_m is statistically significant (considering seismicity located within

TABLE 2 | Gas-producing leases analyzed in this study. For each lease we present the estimated completeness magnitude, the b value, as well as the p values (p_1 and p_2) of the binomial test performed considering the seismicity located within a distance δx = 5 and δx = 10 km (the symbol ++ indicate cases with equal seismicity rates in both the pre- and the post-t_m time windows, whereas the symbol—indicates cases in which both rates are zero).

Gas leases		Completeness		b value	δx = 5 km		δx = 10 km	
n	Lease name	M_c	Since...	—	p_1 (Lesser)	p_2 (Greater)	p_1 (Lesser)	p_2 (Greater)
1	A.C 1.AG	2.2	1985	1.05		7.0×10^{-1}		7.0×10^{-1}
2	A.C 13.AS	2.1	1985	1.00	6.1×10^{-1}		4.6×10^{-1}	
3	A.C 17.AG	2.1	1985	0.92	5.8×10^{-1}		1.9×10^{-1}	
4	A.C 18.AG	2.2	1985	0.99	—	—	6.7×10^{-1}	
5	A.C 21.AG	2.2	1985	0.91	—	—	6.4×10^{-1}	
6	A.C 25.EA	2.2	1985	1.03	—	—	—	—
7	A.C 27.EA	2.2	1985	1.11		3.7×10^{-1}	++	++
8	A.C 28.EA	2.2	1985	0.89	5.2×10^{-1}			4.8×10^{-1}
9	A.C 34.AG	1.9	1985	0.76	—	—	—	—
10	A.C. 6.AS	1.9	1985	0.78	—	—	3.9×10^{-1}	
11	A.C 7.AS	2.2	1985	0.97	—	—		4.9×10^{-1}
12	A.C 8.ME	1.9	1985	0.85	—	—	1.8×10^{-1}	
13	B.C 13.AS	2.0	1985	0.87		5.2×10^{-1}		5.2×10^{-1}
14	B.C 14.AS	2.2	1985	0.97	3.3×10^{-1}		1.9×10^{-1}	
15	B.C 17.TO	2.3	1985	0.93	—	—	—	—
16	B.C 22.AG	2.2	1985	0.87	—	—	—	—
17	B.C 5.AS	2.0	1985	0.70	—	—	—	—
18	BRONTE - S.NICOLA	2.8	1985	1.05		6.3×10^{-1}	6.5×10^{-2}	
19	Case SCHILLACI	2.9	1985	1.04	4.8×10^{-1}		1.6×10^{-1}	
20	CERVIA MARE	1.9	1985	0.94		4.9×10^{-1}		6.5×10^{-1}
21	D.C 4.AG	2.6	1985	0.99		4.4×10^{-1}		3.0×10^{-1}
22	F.C 2.AG	2.8	1985	0.68	—	—	5.2×10^{-1}	
23	**FIUMETTO**	2.7	1985	1.01	**2.1×10^{-2}**		**1.2×10^{-2}**	
24	FORNOVO DI TARO	2.2	1985	0.98	—	—	4.4×10^{-1}	
25	MASSERIA VERTICCHIO	2.2	1985	1.07	++	++	++	++
26	MISANO ADRIATICO	2.1	1985	1.26	6.1×10^{-1}		8.2×10^{-2}	
27	MONTE MORRONE	1.5	1985	0.88	3.6×10^{-1}			3.1×10^{-1}
28	MONTE URANO	2.0	1985	0.72	4.3×10^{-1}		2.5×10^{-1}	
29	MONTEARDONE	2.1	1985	0.93	++	++		4.3×10^{-1}
30	MONTIGNANO	1.8	1985	0.84	5.9×10^{-1}		1.5×10^{-1}	
31	POLICORO	2.2	1985	0.94	—	—	3.3×10^{-1}	
32	QUARTO	2.2	1985	0.90	—	—	—	—
33	RAGUSA	1.7	1985	0.91		4.3×10^{-1}		4.3×10^{-1}
34	RAPAGNANO	1.8	1985	0.63		7.3×10^{-2}		6.2×10^{-2}
35	RECOLETA	1.5	1985	0.71	—	—	4.8×10^{-1}	
36	RECOVATO	1.6	1985	0.63		3.3×10^{-1}	5.9×10^{-1}	
37	**ROCCA CAVALLO**	2.7	1985	0.98	**1.6×10^{-2}**		**4.5×10^{-3}**	
38	S. ANDREA	1.8	1985	0.73	4.6×10^{-1}			9.5×10^{-2}
39	SAN MARCO	1.9	1985	0.91	3.5×10^{-1}		8.2×10^{-2}	
40	SORESINA	2.1	1985	0.83	—	—	—	—
41	TERTIVERI	2.4	1985	1.07	1.1×10^{-1}		1.1×10^{-1}	
42	TORRENTE CIGNO	2.2	1985	1.08	—	—	5.5×10^{-1}	
43	VILLAFORTUNA-TRECATE	1.9	1985	0.70	—	—	—	—

Bold values represent the cases in which the obtained p value is considered significant (respect to the s.l. taken as reference).

both 5 and 10 km from production wells). On the other hand, regarding the cases exhibiting a seismicity rate decrease after t_m, our results suggest that the observed seismicity rate change is statistically significant for one oil-producing lease (the Val d'Agri) and two gas-producing leases (Fiumetto and Rocca Cavallo). The location of all the analyzed leases, classified by the calculated p values considering as reference a *s.l.* = 0.05, are shown in **Figure 7B** for the oil-producing and **Figure 8B** for the gas-producing leases. The Val d'Agri lease is located in the Basilicata region, in the Southern Appenines, whereas Fiumetto and Rocca Cavallo leases are located in Sicily, near Etna Volcano.

The leases for which the seismicity rate change is considered statistically significant are identified using events within both δx = 5 and δx = 10 km (see **Tables 1** and **2**). It is worth to note that in most of the cases the rate change (i.e., increase or decrease) is coherent for seismicity selected considering both δx values. However, in a few cases of data selected around some gas-producing leases (5 sites out of 43, namely A.C 28. EA, Bronte-S. Nicola, Monte Morrone, Recovato, and S. Andrea), there is a change in the observed trend of seismicity rate variation (for example, a decrease observed for the seismicity located within 5 km contrasts with an increase observed when selecting events

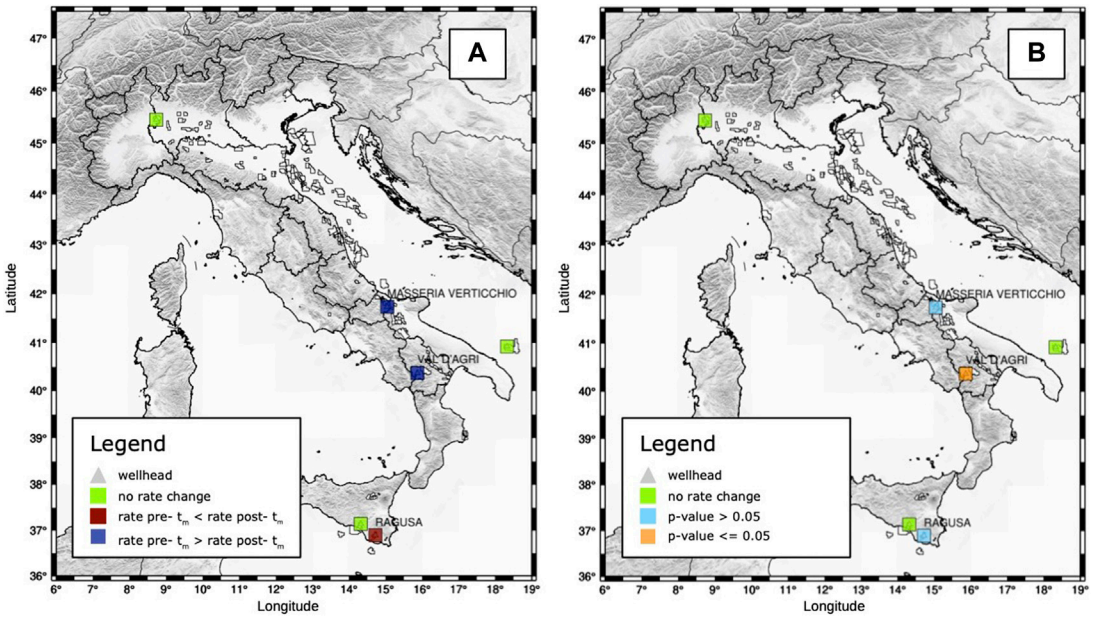

FIGURE 7 | Map of the pre– and post– t_m seismicity rate changes **(A)** and p values **(B)** for the six oil-producing leases analyzed in this work considering the seismicity located within δx = 5 km from producing wells.

within a 10 km distance); discrepancies in such areas are due to instabilities mainly caused by either low seismic activity (such as, e.g., in the Po plain or offshore in the Adriatic sea) or sites close to seismically active sources (such as, e.g., very active tectonic or volcanic areas). It is worth noting however that in all these cases, as well as for cases in which no events are identified within the first 5 km, the observed rate changes are in any case not statistically significant.

In order to compare these results with the results that would be obtained if we do not use the background events only, the same analyses were performed using the full, complete catalog (i.e., considering events above M_c). It is worth noting that using the full catalog may somehow violate the methodological assumption considered for the statistical test (that is, assuming that in the absence of external stress perturbations, seismicity is expected to be stationary). Nevertheless, in this case such comparison is useful to demonstrate that the significant seismicity rate changes found in this work are not artificially created by the declustering procedure. These results are reported in **Supplementary Tables S1** and **S2** and in **Supplementary Figures S1** and **S2** in the **Supplementary Material**. When using the full catalog, we still find evidence of significant seismicity rate changes in the same three leases described in the previous paragraph (i.e., Val d'Agri, Fiumetto, and Rocca Cavallo). Nevertheless, it is worth observing that using the full catalog a few additional zones show some evidence of significant rate changes, especially when considering seismicity located at distances within 10 km from production wells; we consider however that such results are unreliable (for example, in the same area the rate may change e.g., from rate increase to rate decrease– when considering events at different distances, see for instance Tables S1 and S2 in the **Supplementary Material**); such unstable results are most probably due to the presence of clusters of aftershock events randomly located around some leases.

5 DISCUSSION

In this work we monitor significant departures of background seismicity from a stationary behavior around active oil and gas development leases in Italy. We collected oil and gas production data from 102 leases in the period 1980–2017, and we used the seismic data from the HORUS catalog (Lolli et al., 2020b). After a close and conservative inspection of the available data, it has been possible to implement the proposed analyses in six oil-producing and 43 gas-producing leases in the country (including about 44% of the leases from which production data was available). We identify statistically significant seismicity rate changes (considering a *s.l.* = 0.05) concomitant with outstanding changes in hydrocarbon production (i.e., before and after peak production) in one oil-producing lease, Val d'Agri (**Figure 7B**), and two gas-producing leases, Fiumetto and Rocca Cavallo (**Figure 8B**). In all these cases, the seismicity rate after the peak production results significantly lower with respect to the seismicity rate observed before it.

It is worth to remind that spatial and temporal correlations between background seismicity rates and industrial activity, as the one highlighted in these areas, do not constitute an absolute proof to establish a causal relationship between hydrocarbon production and seismic activity. Therefore, we stress that the main value of this finding is to highlight these areas as hotspot zones deserving further detailed analyses to verify (or discard) possible causal relationships. If the oil or gas production in the

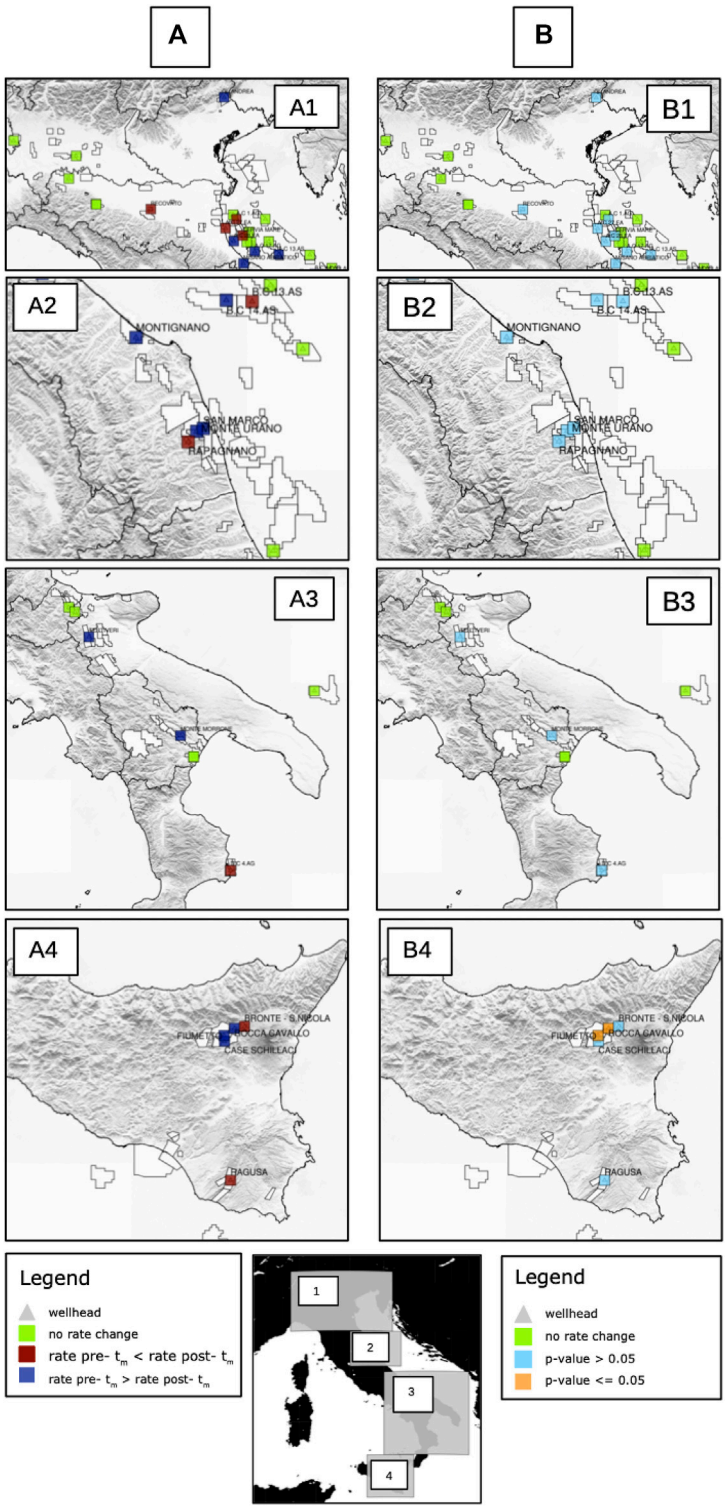

FIGURE 8 | Map of the pre– and post–t_m seismicity rate changes **(A)** and p values **(B)** for the 43 gas-producing leases analyzed in this work considering the seismicity located with-in δx = 5 km from producing wells.

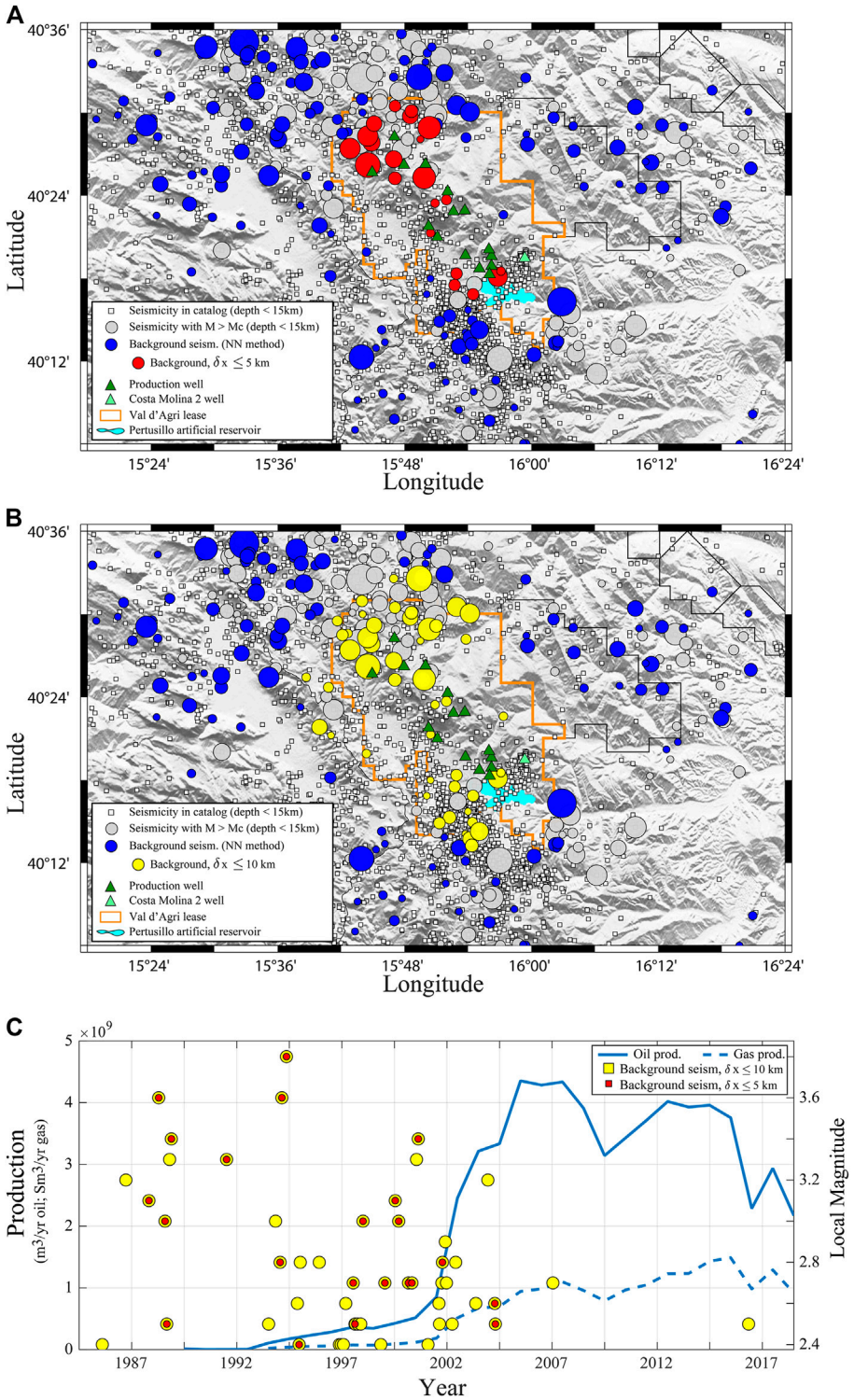

FIGURE 9 | Seismic and production data used in the analysis for the Val d'Agri lease. Panels **(A,B)** show the event locations: squares represent the full catalog, and circles represent events above M_c; earthquakes identified as background seismicity are presented as colored circles, highlighting in particular the events located at distances δx = 5 (panel **(A)**, red circles) and 10 km (panel **(B)**, yellow circles) from the production wells. **(C)** Time series of production data and plot of the temporal occurrence and magnitude of seismic events

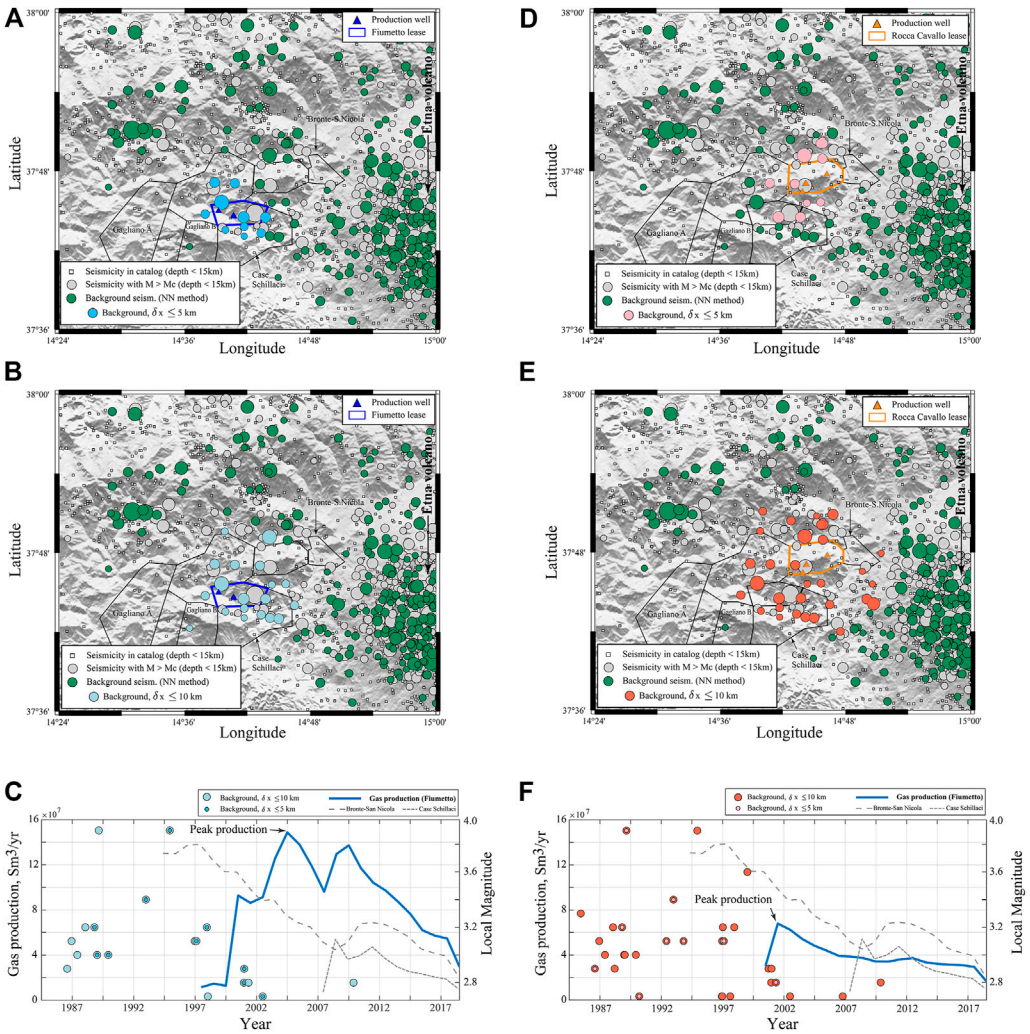

FIGURE 10 | Seismic and production data used in the analysis for Fiumetto **(A,B,C)** and Rocca Cavallo **(D,E,F)** leases. For the event locations: squares represent the full catalog, whereas the circles show all the events above M_c; colored circles show events identified as background seismicity. Top: map showing background seismicity, highlighting all the events located at distances δx = 5 from the production wells. Middle: the same as the top, but highlighting events at δx = 10 km. Bottom: Time series of production data and plot of the temporal occurrence and magnitude of seismic events. Production data and location of the nearby Bronte-S. Nicola and Case Schillaci leases are also shown for reference.

Val d'Agri, Fiumetto and Rocca Cavallo leases played a role to alter shallow earthquake occurrences in these areas, then more sophisticated, physically-based studies are required to understand if the observed changes in seismicity rates are actually an observable consequence of physical mechanisms able to generate such changes. However, such analyses require access to detailed, geological, structural and geomechanical information.

Val d'Agri, located in the Basilicata region, is a particularly interesting case (**Figure 9**). This area hosts the largest onshore oil and gas field in Europe, where possibly-induced seismicity has been detected in connection with wastewater reinjection at the Costa Molina 2 well (e.g., Stabile et al., 2014b; Improta et al., 2015; Buttinelli et al., 2016; Improta et al., 2017). Moreover, some authors reported clustered seismicity located to the south of the nearby Pertusillo artificial water reservoir, whose origin has been suggested to be induced by rapid water level changes of the Pertusillo impoundment (Valoroso et al., 2009, 2011; Stabile et al., 2014a).

Figure 9 shows the location of the Val d'Agri lease, the production wells, as well as the regional seismicity in the area (gray squares), the events with magnitude above M_c (all circles), the background seismicity identified using the NN clustering analysis technique (colored circles), and the selected background seismicity located within a distance δx = 5 km (**Figure 9A**, red circles) and δx = 10 km (**Figure 9B**, yellow circles) from production wells. Only a few selected events are located in the southern part of the lease, close to the cluster of seismicity located south of the Pertusillo lake. **Figure 9C** shows the time series of annual oil and gas production from the Val d'Agri, and the plot of event times and magnitudes of selected seismicity. What we

actually observe is a clear reduction in the number of shallow ($z \leq 15$ km) background seismic events just after the oil production in Val d'Agri reached its maximum in 2005.

A similar significant change in the seismicity rate has been detected in the surroundings of Fiumetto and Rocca Cavallo leases, which are located in Sicily, near Etna Volcano (**Figure 10**). These two leases are located in an area where other five gas-producing leases operate (namely Bronte-S. Nicola, Case Schillaci, Gagliano A, Gagliano B, and Samperi), forming a "cluster" of production leases distributed in a relatively small area (about 400 km^2, see e.g., **Figure 10A**). The results of the correlation analysis for Bronte-S. Nicola and Case Schillaci are also reported in **Table 2** and **Figure 8**, whereas the last three leases were not included in this study because they did not meet the data requirements defined in **Section 3.1**. For completeness, we also reproduced the study using the full catalog of events (that is, without removing the most likely aftershock sequences identified using a declustering approach). Such a test allowed us to demonstrate that the observed reduction in seismicity rate after hydrocarbon peak production in the three production leases outlined in this study is not artificially introduced by the declustering procedure.

Figure 10 shows the geographical location and gas production for Fiumetto and Rocca Cavallo leases, and the background seismicity identified for this zone. We also plotted the location of all the other leases in the area, as well as the gas production of the other two cases included in this study (Bronte-S.Nicola and Case Schillaci). It is worth noting that Gagliano has been producing gas for much more longer time with respect to the other four, but it was not possible to include it in the analysis since the peak production precedes the time interval considered in this study. In these plots we highlight all the background events located within 5 and 10 km from the production wells in Fiumetto (**Figures 10A,B**) and Rocca Cavallo (**Figures 10D,E**) leases.

In this context, a correlation analysis between seismicity and hydrocarbon production for this area is particularly complex, probably requiring an integrated analysis considering all the leases together. Analyzing the results obtained considering each lease independently, similar to what is observed in Val d'Agri, we observe a decrease in the rate of shallow seismicity after the peak gas production in both Fiumetto and Rocca Cavallo (**Figures 10C,F**). A similar behavior is observed in the Case Schillaci site as well, but the p value in this case is not statistically significant at the *s.l.* adopted (neither considering $\delta x = 5$ km nor $\delta x = 10$ km). Finally, and as mentioned before, the results for Bronte-S. Nicola are contrasting when considering different δx values, as a probable effect of intense, shallow seismicity related to activity at the nearby Etna volcano. It is worth noting that the higher peaks in gas production in this area (in the time interval considered in this study) are reached in Fiumetto, Rocca Cavallo and Bronte-S. Nicola between ~1997 and ~2005, a period in which the reduction in the number of events starts to be evident in the zone. However, it should be kept in mind that this area is a particularly complex case due to different factors, such as the closeness of different active leases and the proximity of a seismically active volcano, therefore any further analysis probably requires taking into account the whole cluster of leases together (considering also the influence in this particular area of possible stress perturbations caused by activity at the nearby Etna volcano).

In the areas highlighted by low p values in this study we observe that the seismicity after t_m occurs at a lower rate with respect to the seismicity occurring before the peak production. In the case of a link with fluid withdrawal, such observation could result from either an increase in seismicity rate associated with the phase preceding t_m, when the fluid withdrawal rate had an increasing trend (see e.g., **Figure 5E** for reference), or because seismicity is somehow inhibited as the fluid withdrawal process goes on (which results particularly evident after t_m). An analysis of the seismicity rate before and after the start of fluid withdrawal operations would be useful to understand which of the two scenarios dominates; however, the seismic data for times preceding the start of operations is too scarce for reliable and systematic analyses. Looking however at the seismicity and production data in **Figures 9**, **10**, it is interesting to note that background seismic events are anyhow present before the start of production in the highlighted cases, and this observation contrasts with the apparent seismicity rate drop observed after the peak production. Moreover, some authors have reported evidences of reservoir depletion processes in the Val d'Agri field; for instance, Improta et al. (2017) reported lacking seismicity correlated with low Vp/Vs zones and interpreted these zones as possible depleted sectors of the Val d'Agri production reservoir. They conclude that these observations agree with increased frictional resistance on preexisting faults within the hydrocarbon reservoir caused by the increase of the effective normal stress resulting from pore pressure depletion induced by significant fluid withdrawal (Improta et al., 2017). These observations lead us to think that the change in rate would primarily be due to a decrease in the number of earthquakes after the peak.

In an attempt to better understand if deformative phenomena associated with fluid withdrawal from the crust may explain an apparent inhibition of shallow seismicity, we analyzed a hypothetical case of deformation related to reservoir depletion and calculate the Coulomb stress changes on fault planes optimally oriented for failure (see e.g., Lin and Stein, 2004; Toda et al., 2005). In practice, we assume the contraction of a sub-horizontal dike in an elastic halfspace. For this theoretical exercise we use approximate geomechanical properties of the Val d'Agri zone taken from literature. The modeled dike has an area that roughly covers the area outlined by the production wells active in the Val d'Agri lease (that we assume as an approximate proxy of the actual areal distribution of the reservoir), and is located at a depth of ~4 km below surface (information about the depth of the reservoir in Val d'Agri can be found in e.g., Stabile et al., 2014b; Improta et al., 2017).

In agreement with the regional stress field inferred for this region, we assume an extensional tectonic environment (characteristic of normal faulting regimes) with $S_V > S_{H_{\max}} > S_{H_{\min}}$, and where the minimum horizontal stress is oriented in the direction NNE-SSW (Cucci et al., 2004; Montone et al., 2012; Improta et al., 2017). The results of the Coulomb

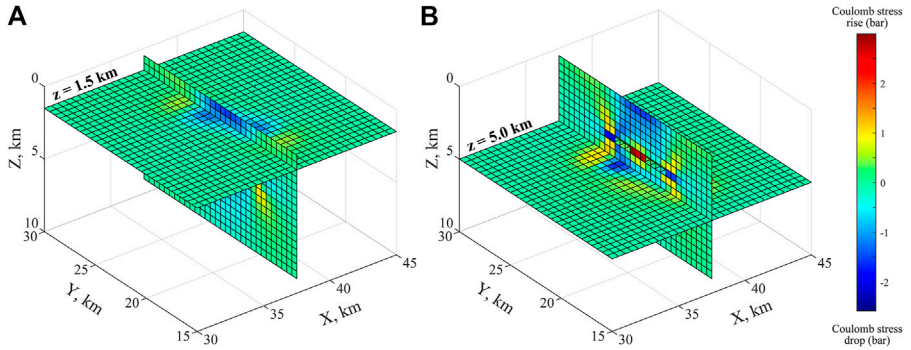

FIGURE 11 | Coulomb stress change (bar) calculated on fault panes optimally oriented for failure, considering as the source of deformation the contraction of a sub-horizontal dike located at ~4 km depth. Both plots show a vertical cross section in the NS direction, crossed by horizontal layers located at **(A)** 1.5 km and **(B)** 5.0 km below the surface. (Stress field generated with Coulomb3, Lin and Stein, 2004; Toda et al., 2005) using the following parameter values: i) Poisson ratio 0.25; ii) Young's modulus = 8.0×10^5 bar; iii) friction coefficient = 0.7; iv) regional stress tensor: $S_V > S_{H_{max}} > S_{H_{min}}$, with values scaled as: $S_V = 50 \times S_{H_{min}}$; $S_{H_{max}} = 10 \times S_{H_{min}}$ (oriented in the direction NNW-SSE); and $S_{H_{min}}$ oriented in direction NNE-SSW.

stress change resolved on optimally oriented planes for this setting is shown in **Figure 11**; cold (blue) colors in **Figure 11** indicate zones with negative Coulomb stress, outlining areas in which the modeled deformation would tend to inhibit seismicity. Such results depict a simple example in which fluid withdrawal operations are allowed to induce a contraction (compaction) of the reservoir; in such a case, the resulting deformation would tend to inhibit seismicity at least in the shallow crust around the area of a depleting reservoir. Therefore, under some circumstances it seems feasible to observe a reduction in seismicity rates following the period of largest hydrocarbon production. Nevertheless, more accurate analyses using detailed geomechanical information and based on the results of a more adequate poroelastic model (as done e.g., by Segall, 1989; Segall et al., 1994) would be required for better capturing the nature of such processes.

6 CONCLUSION

In areas characterized by high levels of natural seismicity, the identification of human-induced seismicity is a difficult task for which, virtually, any result can be a source of controversy. In Italy, a relatively high number of oil- and gas-producing leases have been operating in the last decades, many of which are located in the surroundings of seismically active regions (e.g., Sicily, and the central and southern Apennines). Besides hydrocarbon production, underground waste water injection is also performed in different areas of the country, but these activities were not considered in this study because injection-related data are not publicly available.

Therefore, our analyses are focused on areas where fluids (oil and gas) are withdrawn from the crust. Performing detailed, physically-based analyses at the national scale to identity cases of anthropogenic seismicity in Italy may be considered an intractable problem. Consequently, we implemented a large-scale screening procedure aiming at tracking measurable phenomena, such as, e.g., changes in seismicity rates, that plausibly could occur if notable interactions between fluid withdrawal from the crust and nearby seismicity sources are actually occurring in a given area. We stress however that spatial-temporal correlations between proxies of industrial activity and significant changes in seismicity rates do not provide an absolute proof of causal relationships between hydrocarbon production and seismic activity; rather, studying such correlations gives us the possibility of performing large-scale, systematic analyses of a huge amount of seismic and production data, and to identify in this way hotspot areas where to focus more detailed research to verify, in a later stage, possible causal relationships.

In this context, we analyzed seismicity rates before and after peak production in six oil-producing and 43 gas-producing leases, and evaluate the significance of potential seismicity rate changes. Such cases are about the 44% of the development leases active in Italy (the other 56% were not analyzed due to data limitation constraints). The main findings resulting from this study can be summarized as follows:

- When considering the background seismicity located within 5 km from the production wells, about 50% of the oil-producing and 46% of the gas-producing leases analyzed in this study do not show any change in seismicity rate before and after the time at which the peak production is reached; in most of these cases the seismicity rate is zero (basically due to the short distance considered). The percentage of oil- and gas-producing leases with no observed change in the seismicity rate reduces respectively to about 17 and 23% when considering seismicity located within 10 km from production wells.
- None of the observed cases of seismicity rate increase after the hydrocarbon peak production is statistically significant (at a *s.l.* = 0.05); such cases include about 17% of the oil- and 21–25% of the gas-producing leases analyzed in this study (depending on δx). This result is obtained selecting background seismicity within both 5 and 10 km from production wells.
- Regarding the cases exhibiting a seismicity rate decrease after the hydrocarbon peak production, our results suggest

that the observed seismicity rate change is statistically significant (*s.l.* = 0.05) for one oil-producing lease (the Val d'Agri, in Basilicata) and two gas-producing leases (Fiumetto and Rocca Cavallo, in Sicily). These three leases, which basically correspond with two geographical areas since the later two are adjacent to each other (and to other active leases as Bronte S. Nicola, Case Schillaci, and Gagliano, all clusterized in a relatively small area) can be identified as hotspots deserving future research to study whether there may exist a causal relationship between the hydrocarbon production and the observed reduction in seismicity rate following the peak production.

In conclusion, our analyses highlight areas near some oil- and gas-producing leases in Italy where the seismicity rate reduces after peak production is reached (as compared to the seismicity rate preceding it). We emphasize however that our results just put in evidence a correlated change between the rates of shallow seismicity and hydrocarbon production in these areas, and that assessing actual causal relationships between these two processes will require further detailed, physically-based research. Despite this, we argue that should a physical link exist between these processes, the observed seismicity rate reduction could either be due to increased seismicity during the progressive increase in production rate before t_m, or to actual seismicity rate reduction after t_m. This second scenario would put in evidence possible processes of seismicity inhibition. Considering that the occurrence of seismicity before the start of hydrocarbon production in the hotspot areas contrasts with the reduction of events observed after the peak production, we suspect that the seismicity inhibition is a plausible hypothesis in these cases. With a simple theoretical exercise based on modelling Coulomb stress changes we showed that, at least under some simplified conditions, inhibition of seismicity is actually possible; nevertheless, more accurate models (e.g., using poroelastic theory) are required for better understanding the nature of such processes.

Our observations draw attention to an interesting research problem: the characteristics and implications of increased seismicity caused by anthropogenic activities (e.g., pressurized fluid injection) have so far had a prominent role in research on induced seismicity; the implications, instead, of anthropic processes potentially capable of inhibiting seismicity—in particular, on seismic hazard in seismically active regions—have received less attention, or have been neglected. We consider that more efforts to study the mechanisms and the possible consequences of anthropogenically-driven seismicity inhibition, as well as to document possible cases of such phenomenon, are required.

DATA AVAILABILITY STATEMENT

The seismic data set analyzed in this study can be accessed through the HORUS (HOmogenized instRUmental Seismic catalog) website: http://horus.bo.ingv.it/ (Lolli et al., 2020a, b). The hydrocarbon production data are publicly available in the website of the Direzione Generale per le Infrastrutture e la Sicurezza dei Sistemi Energetici e Geominerari (DGISSEG), Ufficio Nazionale Minerario per gli Idrocarburi e le Georisorse (UNMIG)", from the Italian Ministry of Economic Development (MISE): https://unmig.mise.gov.it/index.php/it/dati. The ViDEPI project-Visibilità dei dati afferenti all'attività di esplorazione petrolifera in Italia (Visibility of data related to mineral exploration activities in Italy, in Italian), is available at https://www.videpi.com/ (all sites, last accessed: February 2021).

AUTHOR CONTRIBUTIONS

AG and LF conceived the experiment, implemented the methods used to analyze the data, and interpreted the achieved results. LF performed the spatial and temporal declustering of the seismic catalog. AG performed the correlation analyses and the Coulomb stress calculations. AM contributed in the discussion of results and in writing. IA collected the industrial data and created the database of hydrocarbon production used in the study. AG and LF wrote the bulk of the text, with inputs from all the co-authors. All the authors have read and approved the manuscript.

FUNDING

This study was performed with the support of Clypea, the Innovation Network for Future Energy financed by the Italian Ministry of Economic Development, Direzione Generale per le Infrastrutture e la Sicurezza dei Sistemi Energetici e Geominerari (MISE—DGISSEG).

ACKNOWLEDGMENTS

The authors thank the invaluable support from the "Direzione Generale per le Infrastrutture e la Sicurezza dei Sistemi Energetici e Geominerari (DGISSEG), Ufficio Nazionale Minerario per gli Idrocarburi e le Georisorse (UNMIG)," from the Italian Ministry of Economic Development (MISE), as well as their Innovation Network for Future Energy (Clypea). Maps were plotted using Generic Mapping Tools (GMTs) (Wessel et al., 2019, https://www.generic-mapping-tools.org/, last accessed January 2021). The authors thank also Anna Nardi, Antonio Rossi and Patrizia Battelli for sharing data on the history of the Italian seismic monitoring network. Any use of trade, firm, or product names is for descriptive purposes only. The results and conclusions of this work do not necessarily represent the position of MISE - DGISSEG.

SUPPLEMENTARY MATERIAL

The Supplementary Material for this article can be found online at: https://www.frontiersin.org/articles/10.3389/feart.2021.673124/full#supplementary-material

REFERENCES

Amato, A., and Montone, P. (1997). Present-day Stress Field and Active Tectonics in Southern Peninsular Italy. *Geophys. J. Int.* 130, 519–534. doi:10.1111/j.1365-246X.1997.tb05666.x

Bertello, F., Fantoni, R., Franciosi, R., Gatti, V., Ghielmi, M., and Pugliese, A. (2010). From Thrust-and-fold belt to Foreland: Hydrocarbon Occurrences in italy. *Pet. Geology Conf. Ser.* 7, 113–126. doi:10.1144/0070113

Braun, T., Cesca, S., Kühn, D., Martirosian-Janssen, A., and Dahm, T. (2018). Anthropogenic Seismicity in italy and its Relation to Tectonics: State of the Art and Perspectives. *Anthropocene* 21, 80–94. doi:10.1016/j.ancene.2018.02.001

Buttinelli, M., Improta, L., Bagh, S., and Chiarabba, C. (2016). Inversion of Inherited Thrusts by Wastewater Injection Induced Seismicity at the Val d'Agri Oilfield (Italy). *Sci. Rep.* 6, 37165. doi:10.1038/srep37165

Calamita, F., Cello, G., Deiana, G., and Paltrinieri, W. (1994). Structural Styles, Chronology Rates of Deformation, and Time-Space Relationships in the Umbria-Marche Thrust System (central Apennines, Italy). *Tectonics* 13, 873–881. doi:10.1029/94TC00276

Cazzini, F., Zotto, O. D., Fantoni, R., Ghielmi, M., Ronchi, P., and Scotti, P. (2015). Oil and Gas in the Adriatic Foreland, italy. *J. Pet. Geology* 38, 255–279. doi:10.1111/jpg.12610

Cello, G., and Mazzoli, S. (1998). Apennine Tectonics in Southern Italy: A Review. *J. Geodynamics* 27, 191–211. doi:10.1016/S0264-3707(97)00072-0

Cesca, S., Grigoli, F., Heimann, S., González, Á., Buforn, E., Maghsoudi, S., et al. (2014). The 2013 September-October Seismic Sequence Offshore Spain: a Case of Seismicity Triggered by Gas Injection? *Geophys. J. Int.* 198, 941–953. doi:10.1093/gji/ggu172

Cucci, L., Pondrelli, S., Frepoli, A., Mariucci, M. T., and Moro, M. (2004). Local Pattern of Stress Field and Seismogenic Sources in the Pergola-Melandro basin and the Agri valley (Southern Italy). *Geophys. J. Int.* 156, 575–583. doi:10.1111/j.1365-246X.2004.02161.x

D'Agostino, N., Giuliani, R., Mattone, M., and Bonci, L. (2001). Active Crustal Extension in the central Apennines (Italy) Inferred from GPS Measurements in the Interval 1994-1999. *Geophys. Res. Lett.* 28, 2121–2124. doi:10.1029/2000GL012462

Dahm, T., Cesca, S., Hainzl, S., Braun, T., and Krüger, F. (2015). Discrimination between Induced, Triggered, and Natural Earthquakes Close to Hydrocarbon Reservoirs: A Probabilistic Approach Based on the Modeling of Depletion-Induced Stress Changes and Seismological Source Parameters. *J. Geophys. Res. Solid Earth* 120, 2491–2509. doi:10.1002/2014JB011778

Davis, S. D., and Frohlich, C. (1993). Did (Or Will) Fluid Injection Cause Earthquakes? - Criteria for a Rational Assessment. *Seismological Res. Lett.* 64, 207–224. doi:10.1785/gssrl.64.3-4.207

Davis, S. D., and Nyffenegger, P. A. (1995). The 9 April 1993 Earthquake in South-central texas: Was it Induced by Fluid Withdrawal? *Bull. Seismological Soc. America* 85, 1888–1895.

Ellsworth, W. L. (2013). Injection-induced Earthquakes. *Science* 341, 1225942. doi:10.1126/science.1225942

Evans, K. F., Zappone, A., Kraft, T., Deichmann, N., and Moia, F. (2012). A Survey of the Induced Seismic Responses to Fluid Injection in Geothermal and CO2 Reservoirs in Europe. *Geothermics* 41, 30–54. doi:10.1016/j.geothermics.2011.08.002

Foulger, G. R., Wilson, M. P., Gluyas, J. G., Julian, B. R., and Davies, R. J. (2018). Global Review of Human-Induced Earthquakes. *Earth-Science Rev.* 178, 438–514. doi:10.1016/j.earscirev.2017.07.008

Garcia-Aristizabal, A., Danesi, S., Braun, T., Anselmi, M., Zaccarelli, L., Famiani, D., et al. (2020). Epistemic Uncertainties in Local Earthquake Locations and Implications for Managing Induced Seismicity. *Bull. Seismological Soc. America* 110, 2423–2440. doi:10.1785/0120200100

Garcia-Aristizabal, A. (2018). Modelling Fluid-Induced Seismicity Rates Associated with Fluid Injections: Examples Related to Fracture Stimulations in Geothermal Areas. *Geophys. J. Int.* 215, 471–493. doi:10.1093/gji/ggy284

Grasso, J.-R., Amorese, D., and Karimov, A. (2019). Anthropogenic Seismicity as Aftershocks for Geo-Resource Production? Implications for Mmax Estimates (Reservoir Impoundment Cases). *Geophys. J. Int.* 219, 958–967. doi:10.1093/gji/ggz337

Grasso, J.-R., Amorese, D., and Karimov, A. (2021). Did Wastewater Disposal Drive the Longest Seismic Swarm Triggered by Fluid Manipulations? Lacq, France, 1969-2016. *Bull. Seismological Soc. America*. doi:10.1785/0120200359

Grigoli, F., Cesca, S., Priolo, E., Rinaldi, A. P., Clinton, J. F., Stabile, T. A., et al. (2017). Current Challenges in Monitoring, Discrimination, and Management of Induced Seismicity Related to Underground Industrial Activities: A European Perspective. *Rev. Geophys.* 55, 310–340. doi:10.1002/2016RG000542

Guidoboni, E., and Valensise, G. (2015). On the Complexity of Earthquake Sequences: a Historical Seismology Perspective Based on the L'Aquila Seismicity (Abruzzo, Central Italy), 1315-1915. *Earthquakes and Structures* 8, 153–184. doi:10.12989/eas.2015.8.1.153

Hainzl, S., Kraft, T., Wassermann, J., Igel, H., and Schmedes, E. (2006). Evidence for Rainfall-Triggered Earthquake Activity. *Geophys. Res. Lett.* 33. doi:10.1029/2006GL027642

Handy, M. R., M. Schmid, S. S., Bousquet, R., Kissling, E., and Bernoulli, D. (2010). Reconciling Plate-Tectonic Reconstructions of Alpine Tethys with the Geological-Geophysical Record of Spreading and Subduction in the Alps. *Earth-Science Rev.* 102, 121–158. doi:10.1016/j.earscirev.2010.06.002

Improta, L., Bagh, S., De Gori, P., Valoroso, L., Pastori, M., Piccinini, D., et al. (2017). Reservoir Structure and Wastewater-Induced Seismicity at the Val d'Agri Oilfield (Italy) Shown by Three-DimensionalVpandVp/VsLocal Earthquake Tomography. *J. Geophys. Res. Solid Earth* 122, 9050–9082. doi:10.1002/2017JB014725

Improta, L., Valoroso, L., Piccinini, D., and Chiarabba, C. (2015). A Detailed Analysis of Wastewater-Induced Seismicity in the Val d'Agri Oil Field (Italy). *Geophys. Res. Lett.* 42, 2682–2690. doi:10.1002/2015GL063369

IS-EPOS (2016). Completeness Magnitude Estimation [web Application/source Code] – https://tcs.ah-epos.eu/

Kagan, Y. Y. (1991). Fractal Dimension of Brittle Fracture. *J. Nonlinear Sci.* 1, 1–16. doi:10.1007/BF01209146

Leptokaropoulos, K. M., Karakostas, V. G., Papadimitriou, E. E., Adamaki, A. K., Tan, O., and Inan, S. (2013). A Homogeneous Earthquake Catalog for Western turkey and Magnitude of Completeness Determination. *Bull. Seismological Soc. America* 103, 2739–2751. doi:10.1785/0120120174

Leptokaropoulos, K., Staszek, M., Lasocki, S., Martínez-Garzón, P., and Kwiatek, G. (2017). Evolution of Seismicity in Relation to Fluid Injection in the North-Western Part of the Geysers Geothermal Field. *Geophys. J. Int.* 212, 1157–1166. doi:10.1093/gji/ggx481

Lin, J., and Stein, R. S. (2004). Stress Triggering in Thrust and Subduction Earthquakes and Stress Interaction between the Southern san andreas and Nearby Thrust and Strike-Slip Faults. *J. Geophys. Res.* 109. doi:10.1029/2003JB002607

Lolli, B., Randazzo, D., Vannucci, G., and Gasperini, P. (2020b). Horus - Homogenized Instrumental Seismic Catalog – http://horus.bo.ingv.it/ doi:10.13127/HORUS

Lolli, B., Randazzo, D., Vannucci, G., and Gasperini, P. (2020a). The Homogenized Instrumental Seismic Catalog (HORUS) of Italy from 1960 to Present. *Seismological Res. Lett.* 91, 3208–3222. doi:10.1785/0220200148

Marzocchi, W., and Sandri, L. (2003). A Review and New Insights on the Estimation of the B-Valueand its Uncertainty. *Ann. Geophys.* 46 (6), 1271–1282. doi:10.4401/ag-3472

Molina, I., Velásquez, J. S., Rubinstein, J. L., Garcia-Aristizabal, A., and Dionicio, V. (2020). Seismicity Induced by Massive Wastewater Injection Near Puerto Gaitán, Colombia. *Geophys. J. Int.* 223, 777–791. doi:10.1093/gji/ggaa326

Montone, P., Mariucci, M. T., and Pierdominici, S. (2012). The Italian Present-Day Stress Map. *Geophys. J. Int.* 189, 705–716. doi:10.1111/j.1365-246X.2012.05391.x

Mulargia, F., and Bizzarri, A. (2014). Anthropogenic Triggering of Large Earthquakes. *Sci. Rep.* 4, 6100–6107. doi:10.1038/srep06100

Orlecka-Sikora, B., Lasocki, S., Kocot, J., Szepieniec, T., Grasso, J. R., Garcia-Aristizabal, A., et al. (2020). An Open Data Infrastructure for the Study of Anthropogenic Hazards Linked to Georesource Exploitation. *Sci. Data* 7, 89. doi:10.1038/s41597-020-0429-3

Pagliuca, N. M., Battelli, P., Berardi, M., Modica, G., Castellano, C., Melorio, C., et al. (2020). Bollettino Sismico Italiano (BSI), III Quadrimestre 2019. *Istituto Nazionale di Geofisica e Vulcanologia (INGV)*. doi:10.13127/BSI/201903

Parsons, T., and Velasco, A. A. (2009). On Near-Source Earthquake Triggering. *J. Geophys. Res.* 114 (B10), B10307, 1–14. doi:10.1029/2008JB006277

Pintori, F., Serpelloni, E., Longuevergne, L., Garcia, A., Faenza, L., D'Alberto, L., et al. (2021). Mechanical Response of Shallow Crust to Groundwater Storage Variations: Inferences from Deformation and Seismic Observations in the Eastern Southern Alps, italy. *J. Geophys. Res. Solid Earth* 126, e2020JB020586. doi:10.1029/2020JB020586

Schoenball, M., Davatzes, N. C., and Glen, J. M. G. (2015). Differentiating Induced and Natural Seismicity Using Space-Time-Magnitude Statistics Applied to the Coso Geothermal Field. *Geophys. Res. Lett.* 42, 6221–6228. doi:10.1002/2015GL064772

Segall, P. (1989). Earthquakes Triggered by Fluid Extraction. *Geol.* 17, 942–946. doi:10.1130/0091-7613(1989)017<0942:ETBFE>2.3.CO;2

Segall, P., Grasso, J.-R., and Mossop, A. (1994). Poroelastic Stressing and Induced Seismicity Near the Lacq Gas Field, Southwestern france. *J. Geophys. Res.* 99, 15423–15438. doi:10.1029/94JB00989

Shapiro, S. A., Dinske, C., and Kummerow, J. (2007). Probability of a Given-Magnitude Earthquake Induced by a Fluid Injection. *Geophys. Res. Lett.* 34, 1–5. doi:10.1029/2007GL031615

Shapiro, S. A., Dinske, C., Langenbruch, C., and Wenzel, F. (2010). Seismogenic index and Magnitude Probability of Earthquakes Induced during Reservoir Fluid Stimulations. *The Leading Edge* 29, 304–309. doi:10.1190/1.3353727

Stabile, T. A., Giocoli, A., Lapenna, V., Perrone, A., Piscitelli, S., and Telesca, L. (2014a). Evidence of Low-Magnitude Continued Reservoir-Induced Seismicity Associated with the Pertusillo Artificial Lake (Southern Italy). *Bull. Seismological Soc. America* 104, 1820–1828. doi:10.1785/0120130333

Stabile, T. A., Giocoli, A., Perrone, A., Piscitelli, S., and Lapenna, V. (2014b). Fluid Injection Induced Seismicity Reveals a Ne Dipping Fault in the southeastern Sector of the High Agri valley (Southern italy). *Geophys. Res. Lett.* 41, 5847–5854. doi:10.1002/2014GL060948

Stallone, A., and Marzocchi, W. (2019). Empirical Evaluation of the Magnitude-independence assumption. *Geophys. J. Int.* 216, 820–839. doi:10.1093/gji/ggy459

Tahir, M., Grasso, J.-R., and Amorèse, D. (2012). The Largest Aftershock: How strong, How Far Away, How Delayed? *Geophys. Res. Lett.* 39, 1–5. doi:10.1029/2011GL050604

Toda, S., Stein, R. S., Richards-Dinger, K., and Bozkurt, S. B. (2005). Forecasting the Evolution of Seismicity in Southern california: Animations Built on Earthquake Stress Transfer. *J. Geophys. Res.* 110, 1–17. doi:10.1029/2004JB003415

UNMIG (2020). *Unmig databook 2020. ministero dello sviluppo economico, direzione generale per le infrastrutture e la sicurezza dei sistemi energetici e geominerari, ufficio nazionale minerario per gli idrocarburi e le georisorse*. link: https://unmig.mise.gov.it/images/stat/databook-2020.pdf (last accessed November, 2020).

Valoroso, L., Improta, L., Chiaraluce, L., Di Stefano, R., Ferranti, L., Govoni, A., et al. (2009). Active Faults and Induced Seismicity in the Val d'Agri Area (Southern Apennines, Italy). *Geophys. J. Int.* 178, 488–502. doi:10.1111/j.1365-246X.2009.04166.x

Valoroso, L., Improta, L., De Gori, P., and Chiarabba, C. (2011). Upper Crustal Structure, Seismicity and Pore Pressure Variations in an Extensional Seismic belt through 3-D and 4-D VPand VP/VSmodels: The Example of the Val d'Agri Area (Southern Italy). *J. Geophys. Res.* 116, 1–21. doi:10.1029/2010JB007661

van der Voort, N., and Vanclay, F. (2015). Social Impacts of Earthquakes Caused by Gas Extraction in the Province of Groningen, the netherlands. *Environ. Impact Assess. Rev.* 50, 1–15. doi:10.1016/j.eiar.2014.08.008

van Hinsbergen, D. J. J., Torsvik, T. H., Schmid, S. M., Maţenco, L. C., Maffione, M., Vissers, R. L. M., et al. (2020). Orogenic Architecture of the Mediterranean Region and Kinematic Reconstruction of its Tectonic Evolution since the Triassic. *Gondwana Res.* 81, 79–229. doi:10.1016/j.gr.2019.07.009

van Stiphout, T., Zhuang, J., and Marsan, D. (2012). Seismicity Declustering, Community Online Resource for Statistical Seismicity Analysis, available at http://www.corssa.orgdoi:10.5078/corssa-52382934

Wells, D. L., and Coppersmith, K. J. (1994). New Empirical Relationships Among Magnitude, Rupture Length, Rupture Width, Rupture Area, and Surface Displacement. *Bull. Seismological Soc. America* 84, 974–1002.

Wessel, P., Luis, J. F., Uieda, L., Scharroo, R., Wobbe, F., Smith, W. H. F., et al. (2019). The Generic Mapping Tools Version 6. *Geochem. Geophys. Geosyst.* 20, 5556–5564. doi:10.1029/2019GC008515

Wiemer, S., and Wyss, M. (2000). Minimum Magnitude of Completeness in Earthquake Catalogs: Examples from alaska, the Western united states, and japan. *Bull. Seismological Soc. America* 90, 859–869. doi:10.1785/0119990114

Wonnacott, T., and Wonnacott, R. J. (1977). *Introductory Statistics*. 3rd Edn. New York, NY: John Wiley & Sons, Inc.

Zaliapin, I., and Ben-Zion, Y. (2016). Discriminating Characteristics of Tectonic and Human-Induced Seismicity. *Bull. Seismological Soc. America* 106, 846–859. doi:10.1785/0120150211

Zaliapin, I., and Ben-Zion, Y. (2013). Earthquake Clusters in Southern california I: Identification and Stability. *J. Geophys. Res. Solid Earth* 118, 2847–2864. doi:10.1002/jgrb.50179

Zhang, H., Eaton, D. W., Li, G., Liu, Y., and Harrington, R. M. (2016). Discriminating Induced Seismicity from Natural Earthquakes Using Moment Tensors and Source Spectra. *J. Geophys. Res. Solid Earth* 121, 972–993. doi:10.1002/2015JB012603

Zhuang, J., Ogata, Y., and Vere-Jones, D. (2002). Stochastic Declustering of Space-Time Earthquake Occurrences. *J. Am. Stat. Assoc.* 97, 369–380. doi:10.1198/016214502760046925

Conflict of Interest: The authors declare that the research was conducted in the absence of any commercial or financial relationships that could be construed as a potential conflict of interest.

frontiers in Earth Science

ORIGINAL RESEARCH
published: 14 July 2021
doi: 10.3389/feart.2021.671207

How to Assess the Moment Tensor Inversion Resolution for Mining Induced Seismicity: A Case Study for the Rudna Mine, Poland

Alicja Caputa[1]*, *Łukasz Rudziński*[1] and *Simone Cesca*[2]

[1]Institute of Geophysics, Polish Academy of Sciences, Warszawa, Poland, [2]GFZ German Research Centre for Geosciences, Potsdam, Germany

Underground exploitation of georesources can be highly correlated with induced seismic activity. In order to reduce the risk and improve the mining operations safety, the mining activity is monitored by a dedicated seismic network. Moment tensor inversion is a powerful method to investigate the rupture process of earthquakes in mines, providing information on the geometry of the earthquake source and the moment release. Different approaches have been proposed to estimate the source mechanisms, with some advantages and limitations. One of the simplest and most used methods rely on the fit of the polarity and amplitude of first P wave onsets. More advanced techniques fit the full waveforms and their spectra. Here, we test and compare moment tensor and focal mechanism estimations for both inversion techniques. In order to assess the inversion resolution, we built realistic synthetic data, accounting for real seismic noise conditions and network geometry for the Rudna copper mine, SW Poland. The Rudna mine pertains to the Legnica-Glógow Copper District, where thousands of mining induced earthquakes are detected yearly, representing a serious hazard for miners and mining infrastructures. We simulate a range of different processes and locations, considering pure double couple, deviatoric and full moment tensors with different magnitudes and located in different mining panels. Results show that the P-wave first onset inversion is very sensitive to the geometry of the seismic network, which is limited by the existing underground infrastructure. On the other hand, the quality of the moment tensor solutions for the full waveform inversion is mainly determined by the strength of mining tremor and the signal-to-noize ratio. We discuss the performance of both inversion techniques and provide recommendations toward a reliable moment tensor analysis in mines.

Keywords: mining seismicity, moment tensor, synthetic tests, seismic monitoring, underground mining

OPEN ACCESS

Edited by:
Rebecca M. Harrington,
Ruhr University Bochum, Germany

Reviewed by:
Jan Sileny,
Institute of Geophysics (ASCR), Czechia
Ruijia Wang,
University of New Mexico, United States

***Correspondence:**
Alicja Caputa
acaputa@igf.edu.pl

Specialty section:
This article was submitted to Geohazards and Georisks, a section of the journal Frontiers in Earth Science

Received: *23 February 2021*
Accepted: *02 July 2021*
Published: *14 July 2021*

Citation:
Caputa A, Rudziński Ł and Cesca S (2021) How to Assess the Moment Tensor Inversion Resolution for Mining Induced Seismicity: A Case Study for the Rudna Mine, Poland. Front. Earth Sci. 9:671207. doi: 10.3389/feart.2021.671207

INTRODUCTION

Seismicity induced by mining is considered to accounts for ~37% of all human-induced earthquakes (Wilson et al., 2017). Mining operations were responsible for some of the strongest and most destructive anthropogenic earthquakes, such as the M 5.2 earthquake at the Klerksdorp mining district, South Africa (Fernandez and Van der Heever, 1984), the M 5.4 event occurred at the Ernst Thaelmann Potash Mine, Germany (McGarr et al., 2002), or the tragic collapses occurred at the

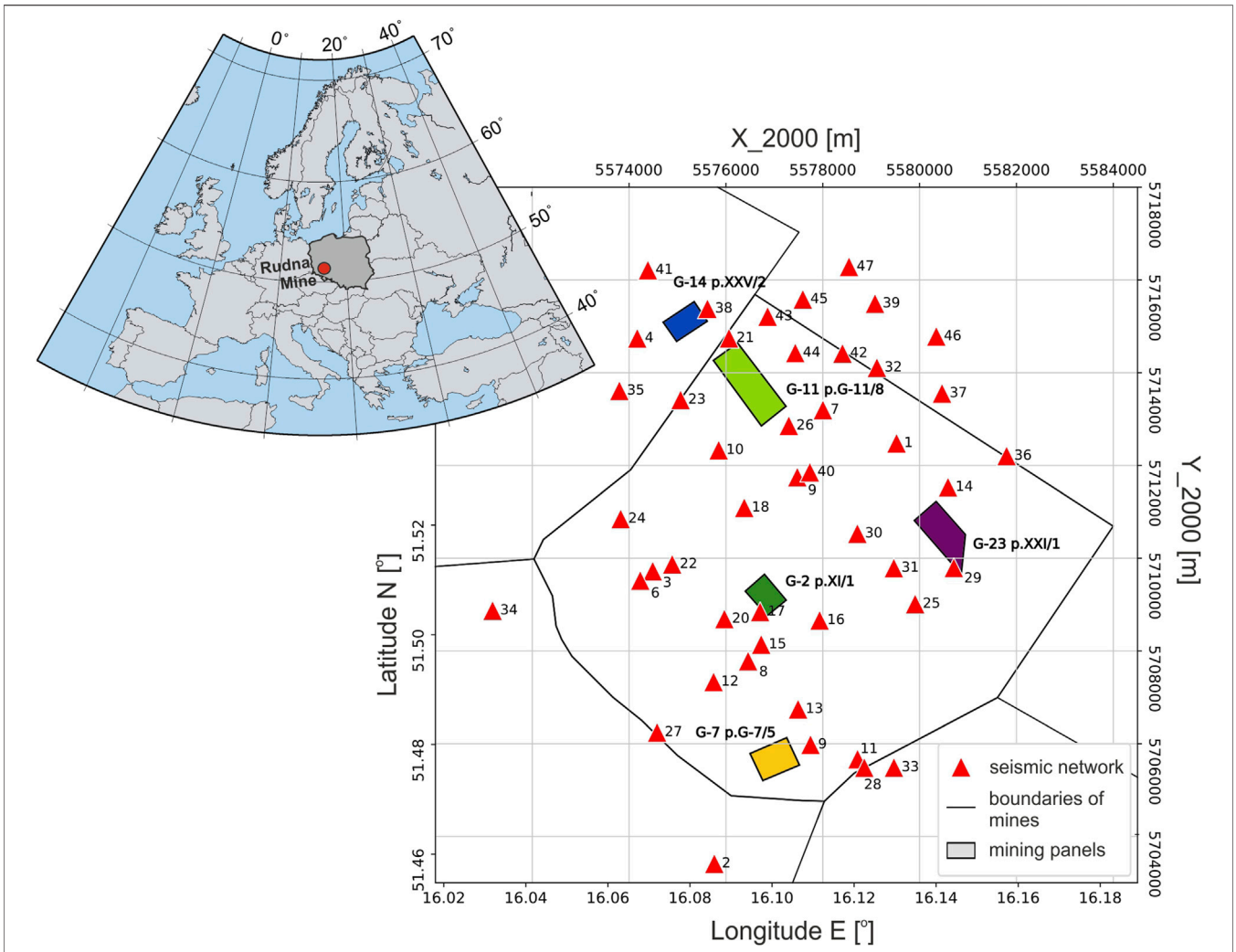

FIGURE 1 | Map of Rudna mine seismic monitoring system and location of analyzed mining panels. Five panels are selected for comparison, and plotted with different colors, as referenced in the result section. Short period seismometers of the in-mine monitoring are marked by triangles and numbered. The upper left inset shows the location of the mine (red circle).

Crandall Canyon Mine, Utah (Dreger et al., 2008) and Rudna Copper Mine, Poland (Lasocki et al., 2017).

Seismic activity in mining regions are monitored with a broad variety of seismic networks, including installations within mining tunnels and underground facilities. Even though, sensors are located relatively close to the seismic sources, the network geometry is strongly dependent on the underground infrastructures. An underground network is also operated at the Rudna Copper Mine, southern Poland (**Figure 1**). The mine is part of the Legnica–Głogów Copper District (LGCD) together with Polkowice-Sieroszowice and Lubin Mines. In LGCD area rich copper deposits are located approximately 1 km below the surface. Since the very beginning of mining operations (early 70s of the XX century), the LGCD area has been affected by high seismicity rate, associated with rockbursts hazard. More than 2,000 events with magnitude between 0.8 and 4.5 are observed in the region every year (Lasocki, 2005; Rudziński and Dineva, 2017). Detailed monitoring and seismic source analysis provide valuable information for the evaluation of risk and related hazard. The in-mine monitoring is mainly used for events localization and energy/magnitude estimation. Seismological studies further use these data to infer source mechanisms of largest mining tremors, to characterize the fault plane geometry, the rupture process and the stresses acting inside the rock mass (Lizurek and Wiejacz, 2011; Rudziński et al., 2016; Caputa and Rudziński, 2019). Unfortunately, the limited network geometry and signal clipping can limit the performance of such analysis (Caputa et al., 2015).

The purpose of this work is to precisely test full waveform and P-wave first onset inversions in the conditions of a real underground seismic monitoring system. Tests were set in order to determine the limitations and/or strengths of both methods in non-routine seismic analysis of mining induced

seismicity. In this study we focus on the influence of the network geometry toward the estimation of source mechanisms. Our work is based on synthetic tests of various non double couple (non-DC) and double couple (DC) sources located in mining panels with active exploitation placed in different parts of Rudna mine.

METHODOLOGY AND DATA

Methodology

First studies concerning source mechanism induced in mines have shown that mining events are similar to natural earthquakes (e.g., McGarr, 1971; Spottiswoode and McGarr, 1975; Potgieter and Roering, 1984). However, further analysis concluded that, while tectonic earthquakes are typically occurring as shear failures, mining-induced events can be the result of a variety of rupture processes. Hasegawa et al. (1989) proposed different types of failures, which can occur in underground mines. Besides shear faulting, described by DC source models, other process such as roof collapse, outburst and pillar burst are considered, and their model discussed. These processes are modeled including non-DC source components. Consequently, a robust identification of non-DC source terms is of great importance toward the safety of mining operations, as these processes are often accompanied or followed by tunnel damages. Mining seismicity source investigations have been performed at several underground mines, and for different geological conditions (e.g., Spottiswoode and McGarr, 1975; McGarr, 1992; Vavryčuk, 2001; Trifu, 2002; Šílený and Milev, 2006; Lizurek and Wiejacz, 2011; Stec and Drzewiecki, 2012; Vavryčuk and Kühn, 2012). Since non-DC components are often found in mines, mining seismicity source mechanisms are usually described by a full moment tensor (MT) which is the representation of nine equivalent force couples under a point source approximation (Aki and Richards, 2002). The MT is a symmetric tensor, with six independent components. The MT can be decomposed into an isotropic (ISO) and a deviatoric part. The deviatoric terms is often further decomposed into a DC and a compensated linear vector dipole (CLVD). While the isotropic term provides a measure of the volume change, e.g., in the case of a collapse, the deviatoric term and its decomposition can be used to describe other source models, including those proposed by Hasegawa et al. (1989), with high CLVDs. Such non-DC mechanisms have been observed in different mines, including South African gold mines (McGarr 1992; Šílený and Milev 2008), in coal mines in US (Arabasz and Pechmann, 2001; Bowers and Walter, 2002; Dreger et al., 2008), in China (Li et al., 2007; Ma et al., 2019, 2018b) and also in Polish underground coal and copper mines (Stec and Drzewiecki, 2012; Dubiński, 2013; Rudziński et al., 2016; Caputa and Rudziński, 2019; Rudziński et al., 2019).

The MT is obtained by solving an inverse problem, in which six independent MT components are obtained by fitting a range of seismic observations. Several approaches have been proposed, based on the fit of body waves polarities and/or amplitudes (Fitch et al., 1980; Bergman and Solomon, 1985; Wiejacz, 1991; Trifu et al., 2000; Vavryčuk, 2001; Hardebeck and Shearer, 2003; Zhu and Ben-Zion, 2013) surface waves (Kanamori and Given, 1981; Hong and Kanamori, 1995; Bukchin et al., 2010) or full waveform in the time and/or frequency domain (Dreger, 2003; Fletcher and McGarr, 2005; Šílený and Milev, 2006; Fichtner et al., 2008; Vavryčuk and Kühn, 2012; Cesca et al., 2013)

At the Rudna mine, the MT inversion has been done so far based on the amplitude and polarization of the P-wave first onset (Gibowicz and Kijko, 1994; Kwiatek et al., 2016), thus using only a short duration, initial part of the seismic signal. This enables to use also close stations for the MT inversion. At the same time clipped records from closest seismometers are useless in full waveform inversion approaches (Rudziński et al., 2016; Rudziński et al., 2017). In this work, we compare the performance of a method based on P wave arrivals, similar to the one in use at the Rudna mine, and a full waveform approach.

The first P-wave arrivals inversion approach relies on the method developed by Fitch et al. (1980) described by Wiejacz (1991) and implemented in the FOCI MT software (Kwiatek et al., 2016). The input information for this method is the integral of the first pulse (half-period) of the P wave, the area below the P wave onset. The misfit between observed and theoretical P wave first motion amplitudes is represented as a normalized root-mean-square (RMS) fitting error,. The moment tensor is calculated using a minimum of 6 observations (i.e. first P-wave arrivals). The method allows for the determination of a simple shear model (i.e. DC constraint), as well as a full MT solution. It has been suggested that the resolution of time domain P-wave first arrivals can be strongly affected by a poor azimuthal coverage and velocity model accuracy (Cesca and Grigoli, 2015; Lizurek, 2017; Ma et al., 2018a).

The second approach used in our study is a full waveform inversion (FW). In general, a FW consists in determining the focal mechanism based on the fitting of real waveforms with full synthetic signals generated on the basis of the Green's functions. An important limitation of the full waveform inversion in the time domain is its sensitivity to errors and inaccuracies of the adopted velocity model. These limitations can especially affect low-energy earthquakes, where the wavelengths are shorter than the size of the heterogeneities of the geological medium (Cesca et al., 2006). Induced seismicity is mostly characterized by low magnitudes and high frequency signals, what may result in a reduction of solutions quality. The inversion approach used in this work is based on the KIWI Tools software (http://kinherd.org; Heimann, 2011). Kiwi performs a point source inversion in two steps, first in the frequency domain, fitting full waveform amplitude spectra, and then in the time domain, fitting the corresponding full waveforms (Cesca et al., 2010; Cesca et al., 2013). The frequency domain approach has shown to be less dependent on the velocity model and network geometry (Cesca et al., 2006; Domingues et al., 2013; Sen et al., 2013). We further perform additional inversions, assuming perturbed velocity models, to test the stability of the FW results. At Rudna mine, seismograms clipping at stations closest to the hypocenter can reduce the amount of available data, a general problem for in-mine networks.

In-Mine Monitoring System

The underground Rudna's monitoring system (**Figure 1**) consists of 47 short period, vertical Willmore MkIII sensors and works as

TABLE 1 | Schematic table of dataset content.

Mining Pannel	Model of non-DC Mechanism	Magnitude	Model of DC Mechanism	Magnitude
G-2 p.XI/1 G-7 p.G-7/5 G-11 p.G-11/8 G-14 p.XXV/2 G-23 p.XXI/1	10% of ISO/CLVD	(1.0 – 2.0)	DC 1 (190/45/89)	(1.0 – 1.5)
		(2.0 – 3.0)		(1.5 – 2.0)
		(3.0 – 4.0)		(2.0 – 2.5)
	20% of ISO/CLVD	(1.0 – 2.0)		(2.5 – 3.0)
		(2.0 – 3.0)		(3.0 – 4.0)
		(3.0 – 4.0)		
	30% of ISO/CLVD	(1.0 – 2.0)	DC 2 (105/30/-90)	(1.0 – 1.5)
		(2.0 – 3.0)		(1.5 – 2.0)
		(3.0 – 4.0)		(2.0 – 2.5)
	40% of ISO/CLVD	(1.0 – 2.0)		(2.5 – 3.0)
		(2.0 – 3.0)		(3.0 – 4.0)
		(3.0 – 4.0)		
	50% of ISO/CLVD	(1.0 – 2.0)	DC3 (87/70/90)	(1.0 – 1.5)
		(2.0 – 3.0)		(1.5 – 2.0)
		(3.0 – 4.0)		(2.0 – 2.5)
	60% of ISO/CLVD	(1.0 – 2.0)		(2.5 – 3.0)
		(2.0 – 3.0)		(3.0 – 4.0)
		(3.0 – 4.0)		
	70% of ISO/CLVD	(1.0 – 2.0)		
		(2.0 – 3.0)		
		(3.0 – 4.0)		
	80% of ISO/CLVD	(1.0 – 2.0)		
		(2.0 – 3.0)		
		(3.0 – 4.0)		
	90% of ISO/CLVD	(1.0 – 2.0)		
		(2.0 – 3.0)		
		(3.0 – 4.0)		
	100% of ISO/CLVD	(1.0 – 2.0)		
		(2.0 – 3.0)		
		(3.0 – 4.0)		
SUM OF EVENTS:	ISO **150** / CLVD **150**			**75**

a seismic network with dynamic range around 66 dB (Koziarz and Szłapka, 2010). The sensors are located mainly at the deposit level, with an average depth of 800 m below the ground. Four sensors are also located in the middle of the shafts. However, these are typically not useful due to the very high noise level; thus, we do not consider them in this work. The network monitors more than 100 panels under exploitation and already mined out, with substantial differences in terms of azimuthal coverage (**Figure 1**).

Synthetic Data

To support our investigation, we developed a testing framework, which can be used to assess the performance of selected techniques (López-Comino et al., 2017); this is achieved by computing a broad synthetic dataset, which includes both a catalog of synthetic earthquakes and the corresponding synthetic waveforms. We consider both DC and non-DC source models, and choose locations within five selected mining panels with various azimuthal coverage (**Figure 1**). We also consider synthetic earthquakes with different magnitudes, ranging between M_w 1.0 and 4.0. The resulting catalog of 375 earthquakes pretends to simulating realistic mining earthquakes and contains two groups of events (**Table 1**): the first group consists of pure shear sources with three different fault plane configurations DC1: 190/45/89, DC2: 105/30/-90, DC3: 87/70/90. The DC sources have been chosen as the most common planes configurations on the basis of previous studies (Caputa, 2014). The second group is composed by non-DC sources, including isotropic and CLVD terms. Non-DC sources were also prepared based on earlier experience at the Rudna mine: a few real mining events with stable, mixed solutions (with both ISO and CLVD components) had been chosen as reference. To proof the performance of different inversion techniques to resolve ISO and CLVD components of different amount, we modified the scalar moment of ISO and CLVD components, forcing them to contribute with specific shares (e.g., 10, 40, 70, and 100% in **Figure 6**) to the full moment tensor. Note that, since some reference solutions include substantial CLVD or ISO components, the source models to discuss the resolution of isotropic sources may include also large CLVD terms (especially when the ISO percentage is low), and vice versa.

The synthetic catalog is accompanied by the corresponding synthetic seismograms, produced by each source in the catalog at each sensor in the network. For the synthetic seismograms computation, we assumed a local velocity model, which describes the shallow crustal structure and geological condition inside the mine (**Figure 9B**). Finally, to better simulate real recordings, all synthetic seismograms were contaminated by a white noise, with station dependent amplitudes, estimated upon the typical noise level registered at each station used in our

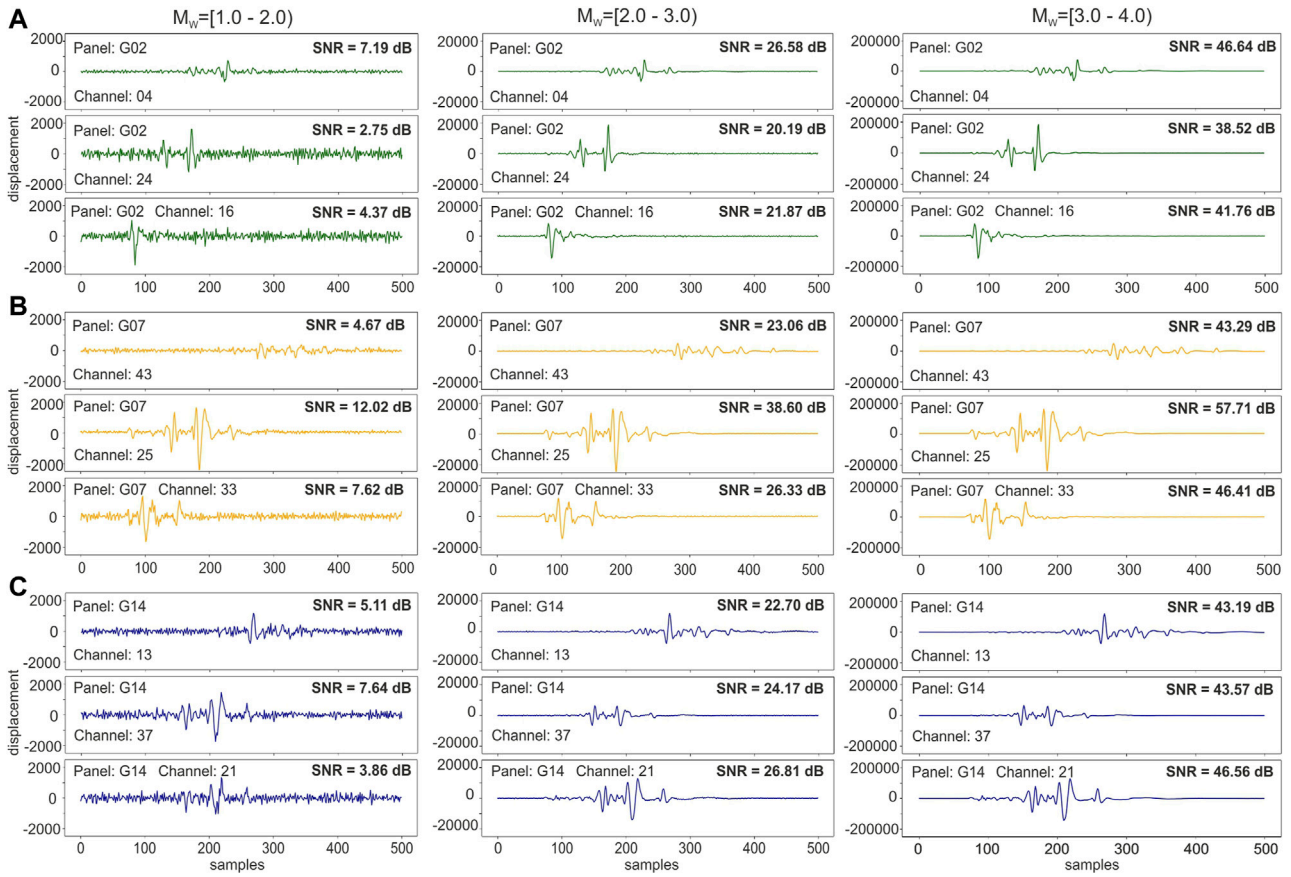

FIGURE 2 | An example of noise contamination for selected waveforms of different magnitude and registration location. **(A)** – synthetic waveforms generated for panel G02; **(B)** – synthetic waveforms generated for panel G07; **(C)** – synthetic waveforms generated for panel G14.

analysis (**Figure 2**). All waveforms were prepared with sampling rate complies with sampling rate of the monitoring system (i.e. 100 sps).

The final database includes seismic catalog and corresponding seismograms for 375 source models (**Table 1**): 75 pure shear sources (3 different mechanisms, with five different locations and 5 different magnitudes), 150 isotropic earthquakes (a reference DC mechanism plus an isotropic component, with 10 different isotropic percentage from 10 to 100%, with five different locations and 3 different magnitudes), 150 CLVD events (a reference DC mechanism – same as ISO source - plus a CLVD component, with 10 different CLVD percentage from 10 to 100%, with five different locations and 3 different magnitudes).

RESULTS

Results are here discussed separately for different families of earthquakes (i.e. DC vs. non-DC source models). Results are obtained independently using the two chosen techniques, one based on P-wave first arrival signals (P) and one on full waveforms (FW). For the P-wave inversion approach, all seismograms were manually picked and the inversion was done event by event. The results for the second, full waveform approach, were obtained automatically.

Resolution of Magnitude

First of all we discuss the moment magnitude distribution within all tested locations and both groups of model sources, DC and non-DC. In average DC magnitude estimation results are close to reference values. In group of P solutions the mean overestimation of M_w is only 0.02, while for FW solutions M_w is underestimated in average by 0.01 (**Figures 3A,B**). P solutions present a higher variability of magnitude errors. Largest magnitude differences are found for the weakest earthquakes (M_w 1.1), for which we find an average overestimate of 0.22; this value does not exceed 0.06 for larger magnitudes. The M_w obtained with the FW inversion are even better resolved and closer to catalog values. On average the differences varies from 0.02 (for M_w 2.7) to 0.08 (for M_w 3.5). Additionally, we do not observe any significant correlation of the magnitude error with the source location within selected mining panels.

For the group of non-DC sources, P magnitudes are in average overestimated by 0.32, while those of the FW inversion are underestimated by 0.19 (**Figure 3**). Magnitude errors of P solutions for the CLVD and ISO groups of sources are most remarkable for sources located at those panels, such as G-7 and

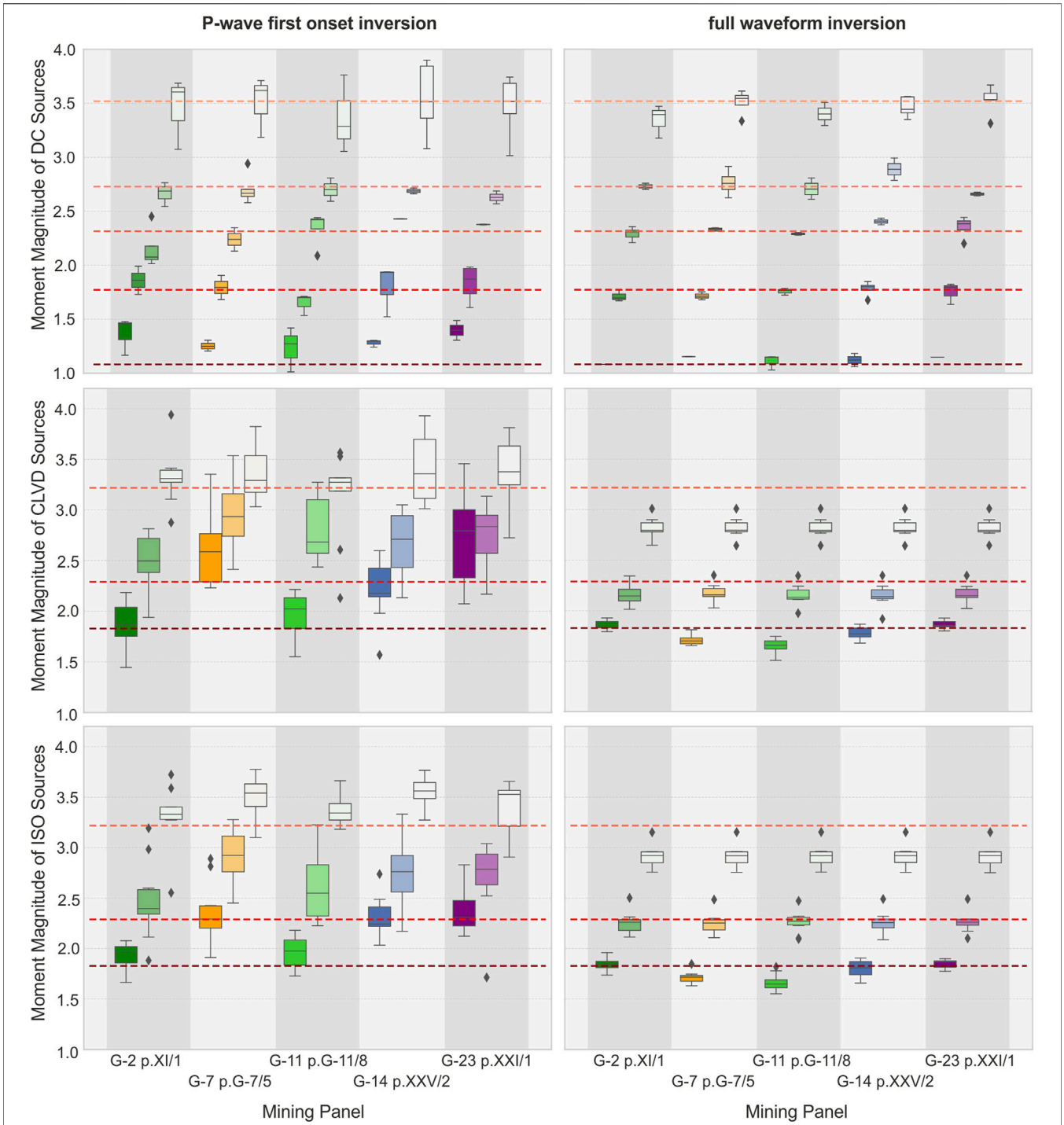

FIGURE 3 | Magnitude distribution in relation to panels with reference magnitude levels (red dashed lines); Separate boxes are ploted on the basis of DC, CLVD and ISO sources prepared for selected magnitudes but different share of MT components. The median values of M_w are marked on boxplots as black lines in boxes, the bottom and top edges of each box indicate the 25th and 75th percentiles, the whiskers represent extreme data and diamonds represent outliers. Color of boxes indicate the magnitudes, low magnitudes are marked with darker colors and high M_w is representing by pale/whitish colors; **(A)**, **(C)**, **(E)** - the first P-wave inversion; **(B)**, **(D)**, **(F)** – the full waveform inversion.

G-23, with the poorest station coverage (**Figure 7C**). Here, the average M_w overestimation can be as large as 0.56 in G-23, for CLVD sources, and 0.48 in G-7, for isotropic sources (**Figure 3E**). The overestimation of moment magnitude for both type of non-DC sources, is significantly lower in panels G-2 and G-11, in the central part of Rudna mine.

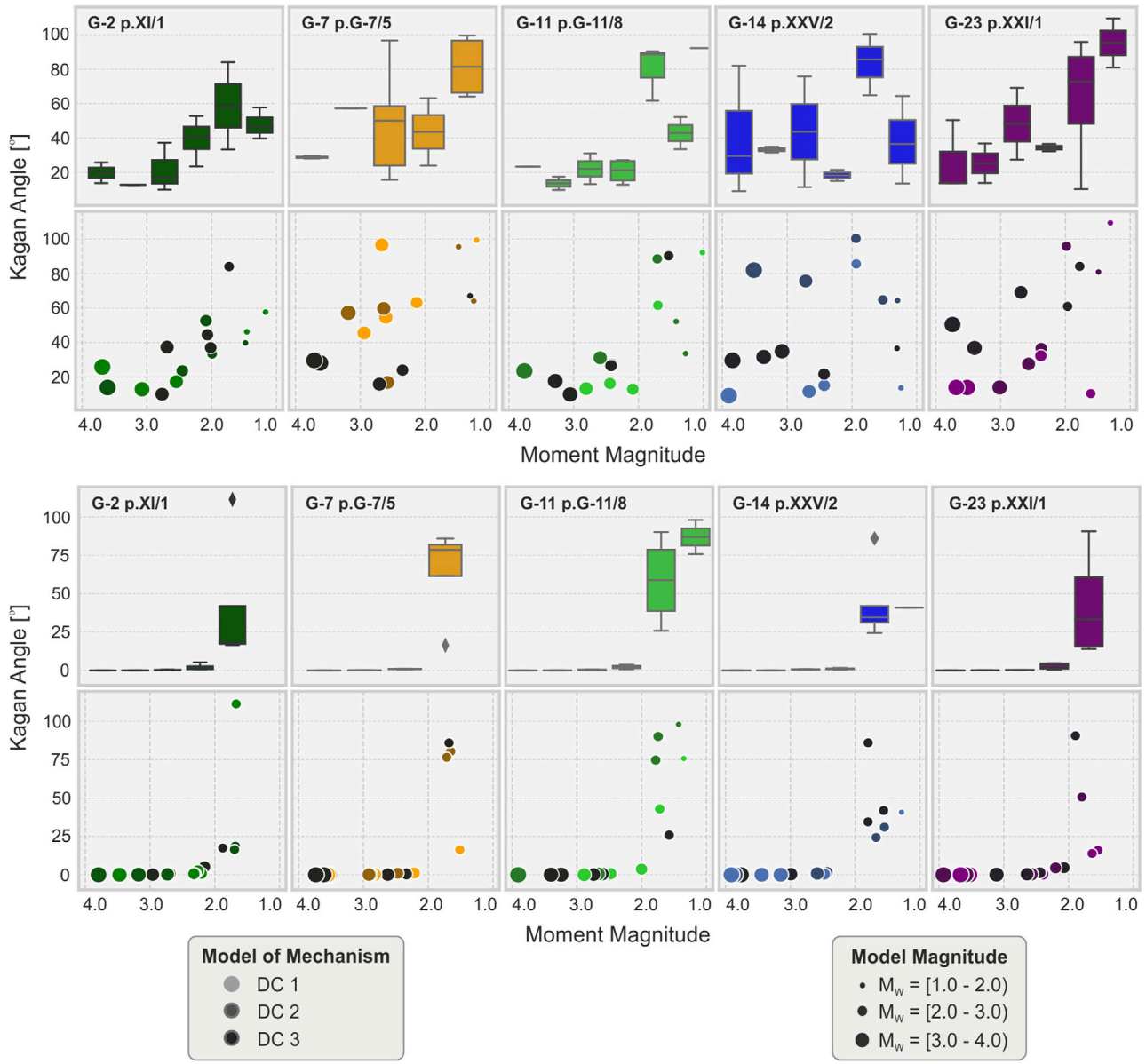

FIGURE 4 | Kagan angle vs. magnitude for the P-wave inversion **(A)** and the full waveform inversion **(B)**. Circle colors and size reflect different panels and magnitude, respectively, as in the bottom legends. Box plots present distribution of Kagan angle in different magnitude ranges which refer to the axis of lower scatter plots. The median values ok κ are marked on boxplots as black lines in boxes, the bottom and top edges of each box indicate the 25th and 75th percentiles and the whiskers represent extreme data.

In the case of the FW inversion, a correlation among the magnitude discrepancy and the source location is not evident. On the other hand, for both group of sources, ISO and CLVD, the amount of the magnitude discrepancy appears to be proportional to the magnitude of the considered event, i.e. underestimations of 0.33, 0.11, and 0.07 are found for reference magnitudes of M_w 3.2, 2.3, and 1.8, respectively.

Resolution of Focal Mechanism Orientation

We first report the inversion results for pure DC source models. A simple and effective way to quantify the difference among the true and estimated focal mechanisms is by means of the Kagan angle (Kagan, 2005, 2007), here denoted as κ, which describes the rotation angle among the two focal mechanisms. P results (**Figures 4A**, **5A**) are characterized by a high variability of Kagan angles, for different source models and magnitudes (**Figure 5A**). The mean κ value in each magnitude range exceeds 9°. Worst results are found for magnitudes below 2.0 at all analyzed source locations. Nevertheless, the largest discrepancies are found for panels G-7, G-14, and G-23, located close to the edge of the mine and with a larger azimuthal gap, where κ reaches values of ~95°–100°. For magnitudes larger than 2.0, average Kagan angles at panels G-7, G-

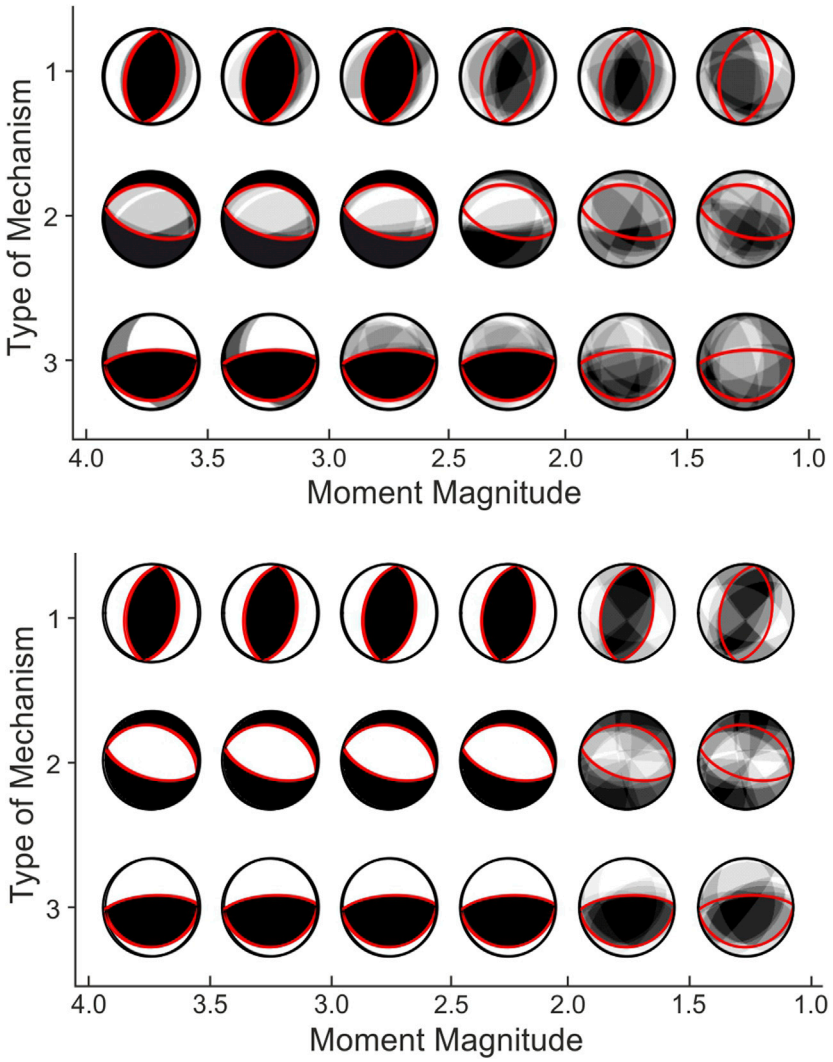

FIGURE 5 | Comparison of true (red line) and resolved (black) focal spheres for double-couple earthquake using first P-wave **(A)** and full waveform **(B)** inversion. In this graphical representation, the resolved focal spheres for different panels are plotted semi-transparent and overlapped.

14, and G-23 are 45°, 34°, and 34°, respectively. Conversely, for panel located well within the seismic network (i.e. those marked in green tonalities in **Figure 1**), mean values (m) of κ are much lower (i.e. m = 23° for G-2 and m = 20° for G-11). Different results for different panels are also characterizing the Kagan angle distributions: the standard deviations (σ) for outer panels G-7, G-14, and G-23 for events with M 2.0 is in the range 29–43°, compared to 13–14° for inner panels G-2 and G-11.

FW inversion results are considerably more stable (**Figures 4B**, **5B**). The mismatch between original and resolved focal mechanism (**Figure 5B**) is significant only for weakest events with M < 2.0. The mean Kagan angle for these small events is highest in panel G-11 (m = 73°) and G-7 (m = 65°) and lower at panels G-2, G14, and G-23 (m ~ 41–43°). For the magnitude range M 2.0–4.0, the κ standard deviation is less than 1° for almost all sources of the catalog. Only the smallest events with M close to 2.0 in panels G-2 and G-23 are characterized by larger σ.

Non-Double Couple Source Models

In this paragraph we discuss inversion results for non-DC models, i.e. those including either ISO or CLVD sources. Firstly, it is worth to notice that for small quakes (M < 2) the solutions are very unstable for both tested methods. That is clearly visible on Hudson plots (Hudson et al., 1989) for CLVD (**Figure 6A**) and ISO (**Figure 6B**) sources.

Further variations in our dataset are observed when we consider the particular MT parts for events with M > 2. For both methods, the CLVD term is underestimated (**Figure 7**): in case of P technique in average by 14%, while for the FW by 6%. In general variation between the modeled CLVD part and obtained value, is in the range from 0 to 95%. Again, we depict a dependency on the source location for the P-wave inversion approach, where the difference in the CLVD percentage are higher (15–22°) at outer panels, and lower (7–10°) at inner ones (G-2 and G-11). Differences between tested locations and inversion approaches can be noted more clearly in terms of high CLVD contribution (CLVD >70% in

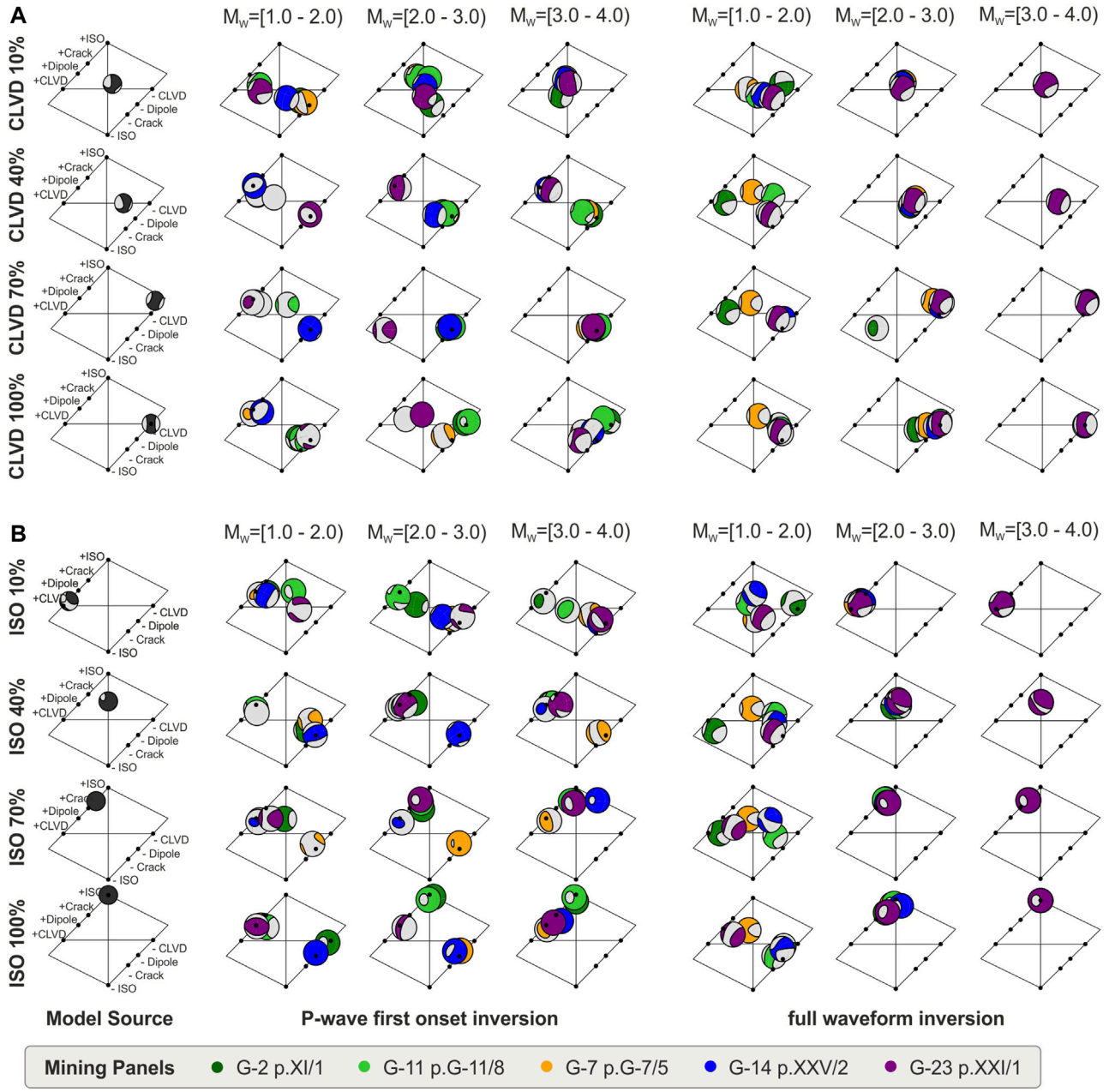

FIGURE 6 | Hudson's plots of non-DC sources. Full MT solutions of chosen CLVD sources **(A)** and ISO sources **(B)** are presented in three different magnitude ranges in comparison to modeled sources (first, left column); colors of plotted beachballs refers to the mining panels.

full MT decomposition) (**Figure 7**). In this group of data obtained CLVD values are on average 24% lower than assumed model, in comparison with 9% for the full waveform inversion results. Variations in full MT depending on the tested location should be also highlighted in this group where CLVD value is underestimated by 27–35° for outer panels and only 9–11° at inner locations. Concerning the full waveform inversion, we do not depict an influence of the network geometry on our solutions.

Similar differences affect the MT inversion for sources including an isotropic component. As in the previous case, the estimation of the isotropic component can be severely biased. For both techniques, the difference between reference and estimated ISO components can vary between 0% to more than 90% (**Figure 8**). The mean difference between the reference isotropic percentage and obtained values is 25% for the P-wave and 16% for the full waveform inversion solutions. Disproportions are again more significant for highly isotropic sources (>70% of ISO component in full MT). In this group of sources, mean underestimation of isotropic component equals 33 and 5% for P and FW solutions, respectively. Similarly as CLVD,

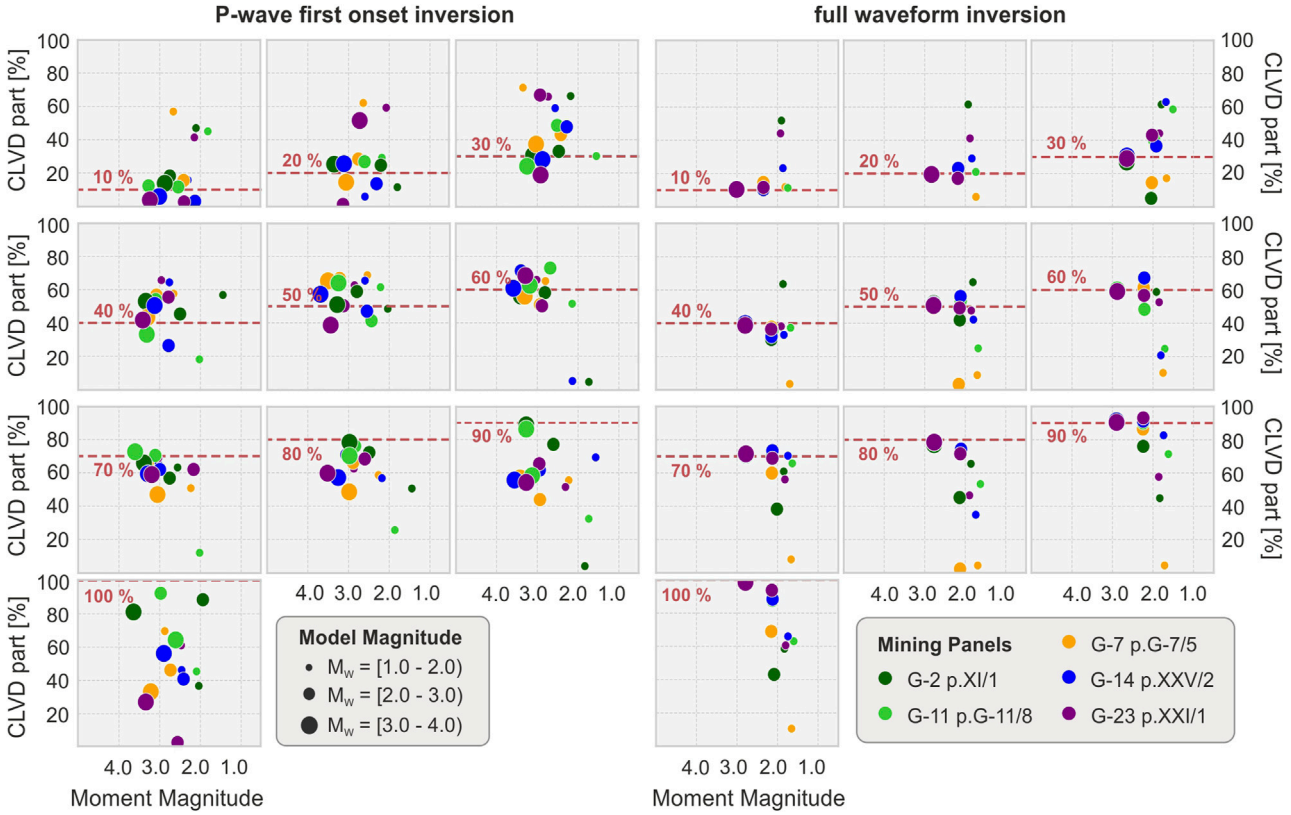

FIGURE 7 | CLVD contribution in MT decomposition in terms of moment magnitude and reference CLVD level (dashed red lines).

P solutions have a better resolution of the ISO component for sources in the central panels (ISO differences of 6–11%), than in outer panels (in average 26–33% underestimate) Again, FW solutions are more robust, and their ISO resolution decreases with magnitude, being poorly resolved below M2 (**Figures 6B**, **8**).

Figure 9 shows the differences in misfit values between reference and synthetic seismograms calculated during both inversion procedure. They are shown in the form of Kernel Density Estimation plot (KDE), which is a standard nonparametric probability density estimation. KDE is calculated by weighting the distances over all data points (Rosenblatt, 1956; Parzen, 1962). Obtained values are presented with respect to three magnitude groups. The misfits for the P-wave first motion inversion (**Figure 9A**) is largest for outer panels (G-7, G-14, and G-23) and weakest earthquakes (below M2.0). Misfit plots for the FW inversion (**Figure 9C**) show a higher resolution and a lower dependency on the source location. The factor mostly influencing the FW inversion is the magnitude of the events, i.e. the signal-to-noize ratio.

Shallow Underground Structure Mismodeling

Using simplified or non accurate velocity model can strongly affect the full waveform inversion, first by producing a misalignment of synthetics and observed waveforms. This section aims at assessing the influence of the shallow crustal structure mismodeling toward the stability and accuracy of MT results. We repeated the same scheme of FW inversions as it had been conducted for "basic" research but using two disturbed velocity models. To the analysis of new models influence we used the same dataset presented in the *Synthetic Data* thus there have been all 375 synthetic sources taken into account. These models were prepared, perturbing the starting velocity model: the first one (velocity mismodeled model, VMM) was obtained by randomly introduced changes in P and S velocities by 10% (**Figure 9E**), the second one (depth mismodeled model, DMM) was created by random changes in the thickness of geological layers by 10% (**Figure 9F**).

As it is to be expected, MT solutions obtained using both perturbed models show higher misfits, compared to the unperturbed model. The quality of MT solutions remain however stable, as illustrated for the case of the magnitude in **Figures 9D,G**. Observed resolution of magnitudes presents similar patterns as for the unperturbed model (*Resolution of Magnitude*) and there are no significant differences between the two tested perturbed models. Magnitudes of DC sources are underestimated by ~0.1 for both perturbed models. Magnitudes of non-DC sources deviates by ~0.2–0.3, respect to the unperturbed case. Again, larger differences are found for larger events. Similarly as for the reference model we do not observe any spatial dependence of the magnitude resolution.

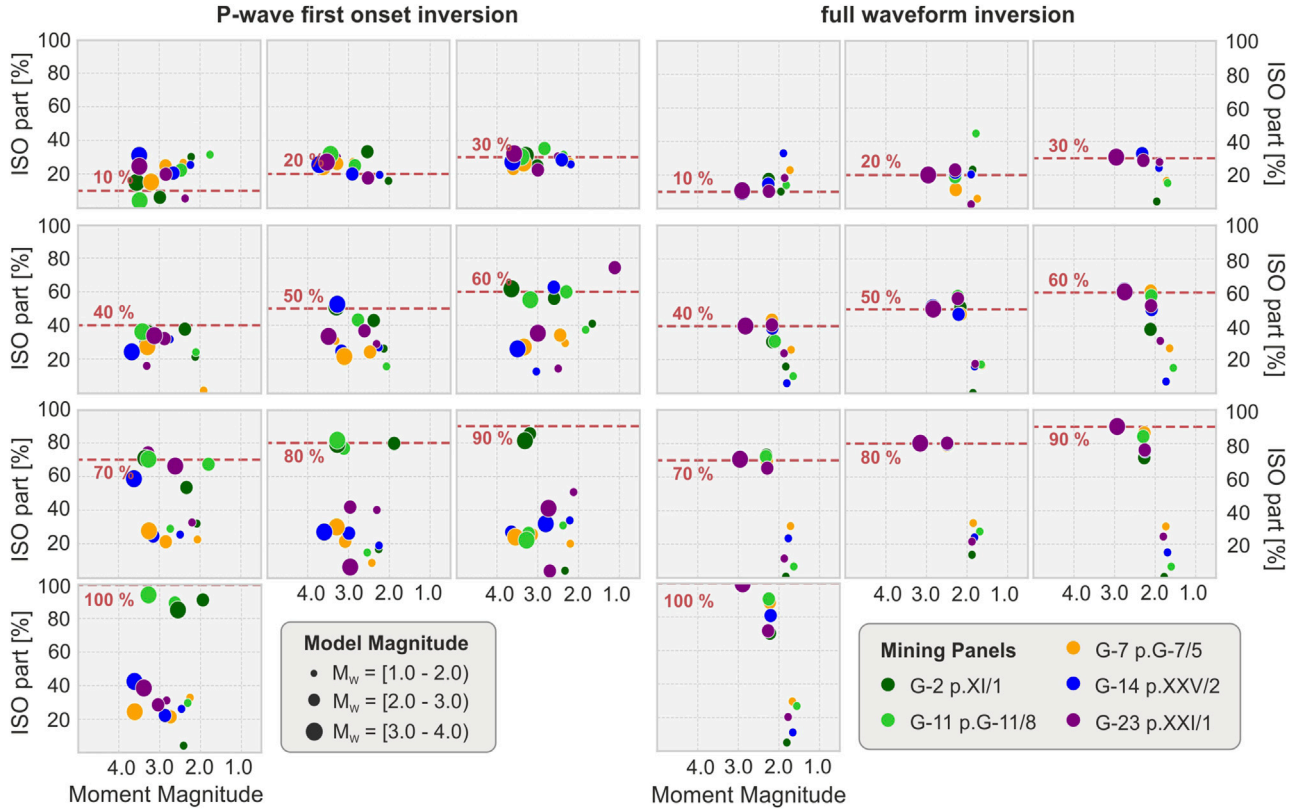

FIGURE 8 | ISO contribution in MT decomposition in terms of moment magnitude and reference ISO level (dashed red lines).

The resolved geometry of the nodal planes are also comparable for both perturned models. Higher Kagan angle are found for the weakest (M < 2) events, where the mean κ for both tested schemes is ~57°, compared to ~19° for events with M > 3.

The quality of the MT decomposition and resolution of non-DC terms are comparable to those assuming the reference model, described in *Non-Double Couple Source Models*. Largest errors in the resolved CLVD components are found for the group of solutions with CLVD >70% with a full MT decomposition. For these sources, the CLVD component may be misestimated by ~40–50%, compared to ~20% for the group of source models with CLVD below 70%. Similar results are found for the isotropic components, with major differences found for sources including a large isotropic component. Again, we observe no differences in the quality of MT solutions obtained for different source locations and with a different azimuthal coverage.

DISCUSSION

Seismological observations in mines are limited by the tunnels extent and their geometry. Thus, the only possibility to improve the seismological analysis, such as MT inversion, is to use novel, advanced techniques, which can provide robust results, even with sub-optimal network configurations. The first tests to perform should aim at assessing the performance of available methods and approaches; assessing source parameter uncertainties is also crucial to quantify the potential limitations of a full MT inference toward hazard assessment. On the base of an accurate testing and assessment, relying on a solid synthetic framework, one can provide recommendations, which would help stakeholders to deal with the data processing. In this work, we aim at establishing the resolution of the source mechanism estimations for typical in-mine seismic network. Hence, we used the real network geometry and built synthetic recordings for a range of source models, with different size and mechanism types.

The first parameter which we resolve is the moment magnitude. For both tested inversion techniques (i.e. P and FW approaches), as well as for all considered source types, a minimum magnitude of M2.0 appears as a threshold to obtain reliable results at Rudna. This implies that the analysis of weaker events, with a lower signal-to-noize ratio, is in general not possible with these techniques and the current network configuration. Earthquakes with magnitude above M2.0 may be ~150 per year at the Rudna mine, in comparison to a higher rate of smaller events. Thus, the current magnitude threshold will strongly reduce the number of events for which we can infer a robust moment tensor. The quality of P and FW inversion is comparable toward the magnitude estimation. Interestingly, the P approach tends consistently to overestimate the reference magnitude, while the FW solutions

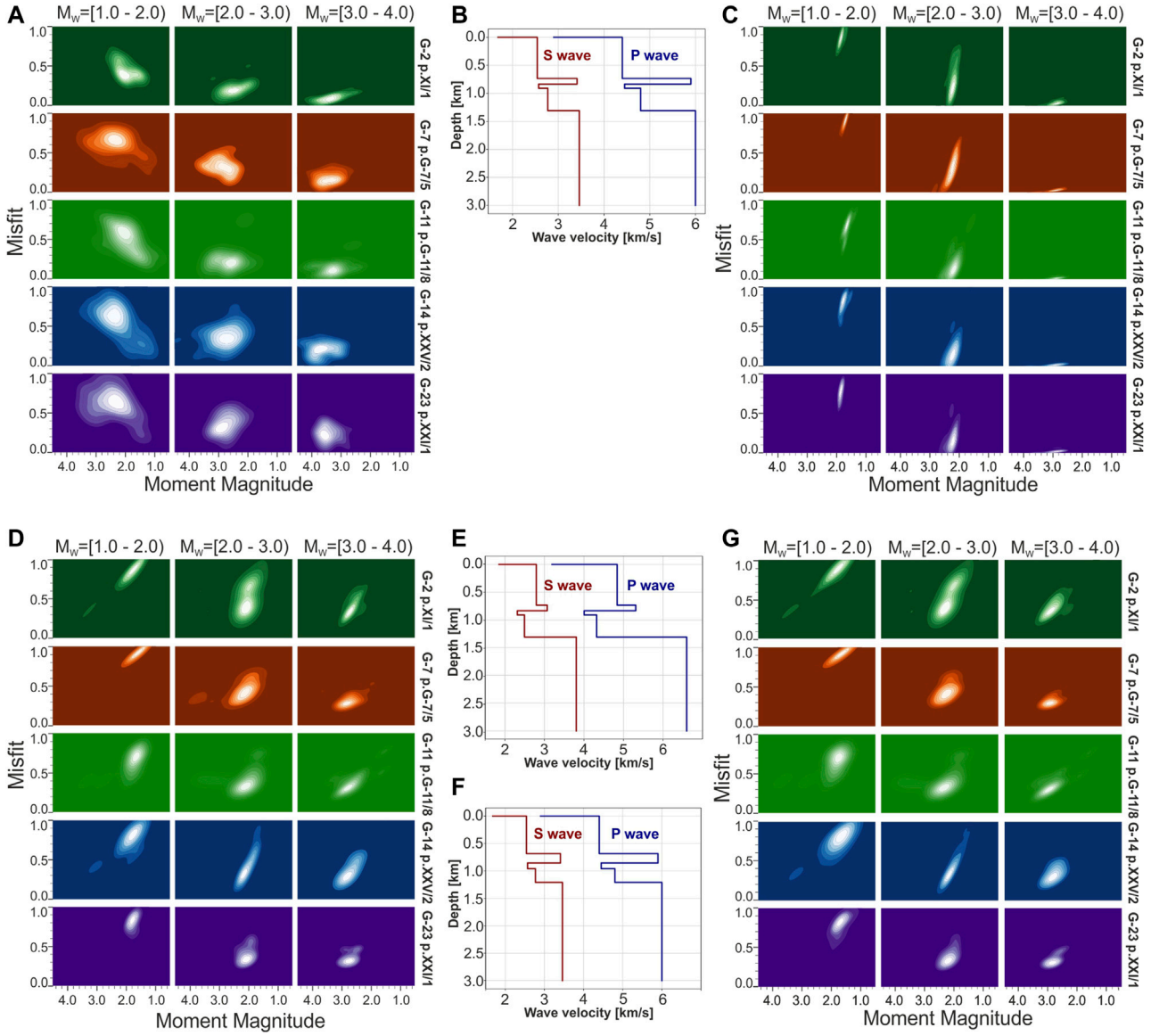

FIGURE 9 | Probability density estimation (Kernel Density Estimation - KDE) plot of normalized fitting errors with velocity models used for analysis. KDE obtained for selected mining panels (marked by colors) and for three different magnitude ranges (titled by the model magnitudes above the columns), magnitudes calculated by MT inversion are presented on x-axis in a range from 0.5 to 4.5 and the misfit is presented in the range from 0 to 1.0 on y-axis of each plot; **(A)** – Misfit obtained for the first P-wave inversion; **(C)** – Misfit values obtained for the full waveform inversion with original velocity model **(B)**; **(D)** - Misfit values obtained for the full waveform inversion with velocity model of disturbed velocities by 10% **(E)**; **(G)** - Misfit values obtained for the full waveform inversion with velocity model of disturbed layers depth **(F)**.

slightly underestimate these; this observation is presumably controlled by a poor source resolution, in the case of P solutions, and by the data noise contamination, in the case of FW solutions. We observed a consistent magnitude underestimation with a FW inversion, with larger deviations for larger events. This issue was observed both using the reference velocity model, as well as for perturbed models. We argue that this result may be due to the intrinsic MT resolution limitations, when modeling very shallow sources using low frequency waveforms (e.g., Cesca and Heimann 2018). In these conditions, certain components of the moment tensor are poorly resolved, what can also affect also the resolution of the scalar moment and moment magnitude. For events with M > 2.0 the quality of the results depends on the chosen inversion technique. P solutions, and most of all those obtained for non-DC solutions, suggest that this approach is very sensitive to the source coverage, and solutions quality may strongly vary depending on the source location. Specifically, estimated moment tensors and magnitudes present important variability for source located close to the Rudna mine borders, where the azimuthal coverage becomes

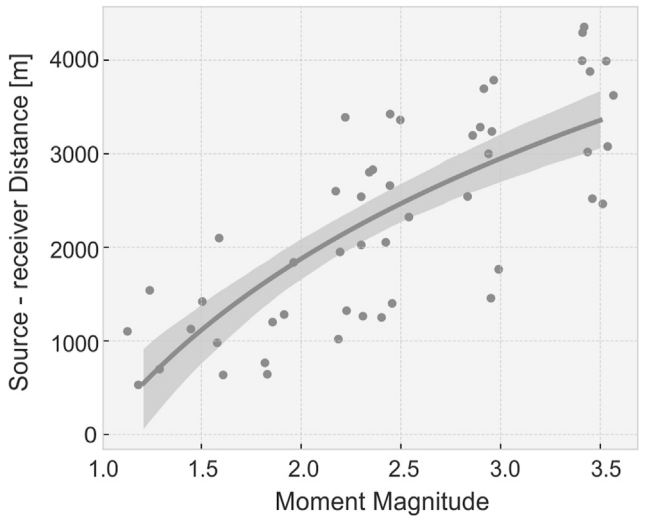

FIGURE 10 | Plot of seismogram clipping as a function of magnitude and source – receiver distance based on real records of Rudna in-mine monitoring system. Gray circles reflect to the farthest clipped seismograms observed for particular moment magnitude for selected mining events. Gray line present linear regression model fit and shadow area represents 95% confidence interval for that regression. Data on y axis (source – receiver distance) is plotted in log scale.

more poor and the number of sensor at local distances is smaller, extending the observation by Cesca and Grigoli (2015) and Ma et al. (2018b), that the time domain inversion methods can be affected by network geometry, to the P approach. At the Rudna mine, this issue was also raised by Lizurek (2017).

Seismic noise is partially affecting the P approach, namely reducing the accuracy of P onsets picks and the overall quality of the inversion results. Since the network geometry inside the mine is limited by the excavation area, this cannot be easily improved. In the current conditions, the events located in panels close to the Rudna mine borders are still monitored by numerous stations, but epicentral distances are considerable longer that the average network size, and the azimuthal coverage is poor. Unfortunately, with the propagation of the exploitation close to the mines boundaries, the seismic activity in this parts of the mine is increasing. Hence, one can just recommend the full waveform inversion as an alternative tool to the currently implemented approach.

Our results confirm the stability of FW solutions in difficult conditions of in-mine monitoring. There are evidences that mainly the seismic noise contamination represent a significant source for parameter uncertainties. The mismodeling of the velocity model, which is a common problem in mining seismology, can also affect the results. However, our tests did not show significant differences between results obtained using affected models. It can be a sign that the method is stable. Nevertheless, since we consider only two disturbed models, we cannot provide any kind of relation which describes behavior of FW solutions with respect to different "geological" conditions. Moreover, the FW inversion can be further affected by signals clipping, which can limit the applicability of this approach. The low dynamic range and the relatively strong ground motions produced by mining tremors can affect the stations located closest to the seismic source, spoiling the full waveform signals. **Figure 10** presents an overview of the estimated influence of the event size on seismic records distortion, as a function of source-receiver distance. Clipped recordings are challenging to be used to reconstruct the true ground motions for the full waveforms, and these records need to be reconstructed with advanced methods or simply excluded by the full waveform inversion procedure. Unfortunately, seismograms clipping is commonly observed for high energy events at the Rudna underground seismic network (Rudziński, 2013; Rudziński et al., 2017) (**Figure 10**). Here, signal clipping typically affect S onsets and the seismogram coda, so that P phases are generally well recorded and can be used for modeling approaches.

In conclusion, given the previous considerations, an hybrid approach, combining the fit of P phases at closest distances and full waveforms at larger distances can provide the optimal setup for the future monitoring of mining seismicity, able to combine the potential of both approaches and preserving their most valuable features.

CONCLUSION

The robust inversion of source mechanism in mines remains a challenging task, and available techniques should be tested for the specific mining network to assess the quality of their solution. In this work we built a realistic synthetic catalog and a synthetic dataset to test the robustness of different moment tensor approaches to resolve the source parameters of mining induced seismicity. Such implementation is ideal to quantify the resolution power of different inversion techniques.

We find out that both approaches, namely the inversion based on the fit of P phase amplitude and polarity, and based on the full waveforms and their spectra, have specific advantages, but also strong limitations. In the case of undisturbed signals, the full waveform inversion approach is to be preferred, and it is able, for the typical noise condition of the Rudna mine, to accurately resolve DC and non-DC sources down to a magnitude M2.0. The P wave inversion technique, in contrast, is not sensitive to late clipping of the seismograms, if the P wave pulses are well preserved, but it is in general much less stable, and the solution quality is strongly affected by the source coverage, potentially affecting magnitude estimation, fault plane orientation and non-DC components. In these conditions, the quality of the moment tensor solution drastically decreases when seismicity occurs at the edges of the seismic network, as often observed with the extension of mining activity.

Toward a robust assessment of mining seismicity source parameters, we recommend an hybrid inversion approach, where P onsets are fitted at station at close epicentral distances, whenever full waveform signals are corrupted, and full waveforms are fitted at larger distances. The definition of a maximal distance, where the seismic recordings can be clipped and not be usable, can be easily defined at Rudna on the base of an early rough magnitude estimate, so that an automated inversion, taking care of the proper parametrization of the fitting procedure, can be implemented. Such hybrid approach, able to

simultaneously take advantage of the potential of both approaches and to overcome their limitations, provides the optimal configuration for monitoring mining seismicity at the Rudna mine and potentially at other mines.

DATA AVAILABILITY STATEMENT

The raw data supporting the conclusions of this article will be made available by the authors, without undue reservation except the exact in-mine monitoring system details, which are owned by KGHM Polska Miedź.

AUTHOR CONTRIBUTIONS

ŁR contributed to conception of the study. The design of the analysis was given mainly by SC and AC. AC and SC prepared the database of synthetic waveforms and the catalog of synthetic events. AC performed inversion of prepared data and all analysis contained in the manuscript text. AC wrote the first draft of the manuscript. ŁR and SC wrote sections of the manuscript. All authors contributed to manuscript revision, read, and approved the submitted version.

FUNDING

Work of AC and ŁR was supported by a subsidy from the Polish Ministry of Education and Science for the Institute of Geophysics, Polish Academy of Sciences. The work was also partially supported within Polish National Science Center project: PRELUDIUM 13 No. 2017/25/N/ST10/01759 (AC). SC received funding by the European Union RFCD project PostMinQuake, grant 899192.

ACKNOWLEDGMENTS

Authors wish also thank to KGHM Polska Miedź S.A. for the technical information concerning underground monitoring system in the Rudna mine.

REFERENCES

Aki, K., and Richards, P. G. (2002). *Quantitative Seismology*. Sausalito: University Science Books.

Arabasz, W. J., and Pechmann, J. C. (2001). Seismic Characterization of Coal-Mining Seismicity in Utah for CTBT Monitoring, Technical Report UCRL-CR-143772. Livermore, CA: Lawrence Livermore National Laboratory. LLNL Research Agreement No. B344836, 1–120. Available at: www/seis.utah.edu/Reports/llnl2001.

Bergman, E. A., and Solomon, S. C. (1985). Earthquake Source Mechanisms from Body-Waveform Inversion and Intraplate Tectonics in the Northern Indian Ocean. *Phys. Earth Planet. Interiors* 40 (1), 1–23. doi:10.1016/0031-9201(85)90002-0

Bowers, D., and Walter, W. R. (2002). Discriminating between Large Mine Collapses and Explosions Using Teleseismic P Waves. *Pure Appl. Geophys.* 159 (4), 803–830. doi:10.1007/s00024-002-8660-8

Bukchin, B., Clévédé, E., and Mostinskiy, A. (2010). Uncertainty of Moment Tensor Determination from Surface Wave Analysis for Shallow Earthquakes. *J. Seismol* 14 (3), 601–614. doi:10.1007/s10950-009-9185-8

Caputa, A. (2014). *Mechanizm Wstrząsów Po Strzelaniach W Kopalni Miedzi Rudna KGHM S.A.* MSc thesis. Katowice, Poland: University of Silesia.

Caputa, A., and Rudziński, Ł. (2019). Source Analysis of Post-Blasting Events Recorded in Deep Copper Mine, Poland. *Pure Appl. Geophys.* 176 (8), 3451–3466. doi:10.1007/s00024-019-02171-x

Caputa, A., Talaga, A., and Rudziński, Ł. (2015). Analysis of post-blasting Source Mechanisms of Mining-Induced Seismic Events in Rudna Copper Mine, Poland. *Contemp. Trends Geosci.* 4 (1), 26–38. doi:10.1515/ctg-2015-0003

Cesca, S., Buforn, E., and Dahm, T. (2006). Amplitude Spectra Moment Tensor Inversion of Shallow Earthquakes in Spain. *Geophys. J. Int.* 166 (2), 839–854. doi:10.1111/j.1365-246X.2006.03073.x

Cesca, S., and Grigoli, F. (2015). Full Waveform Seismological Advances for Microseismic Monitoring. *Adv. Geophys.* 56, 169–228. doi:10.1016/bs.agph.2014.12.002

Cesca, S., and Heimann, S. (2018). "Challenges in Regional Moment Tensor Resolution and Interpretation," in *Moment Tensor Solutions*. Editor S. D'Amico (Springer, Cham: Springer Natural Hazards). doi:10.1007/978-3-319-77359-9_7

Cesca, S., Heimann, S., Stammler, K., and Dahm, T. (2010). Automated Procedure for point and Kinematic Source Inversion at Regional Distances. *J. Geophys. Res.* 115, 1–24. doi:10.1029/2009JB006450

Cesca, S., Rohr, A., and Dahm, T. (2013). Discrimination of Induced Seismicity by Full Moment Tensor Inversion and Decomposition. *J. Seismol* 17 (1), 147–163. doi:10.1007/s10950-012-9305-8

Domingues, A., Custódio, S., and Cesca, S. (2013). Waveform Inversion of Small-To-Moderate Earthquakes Located Offshore Southwest Iberia. *Geophys. J. Int.* 192 (1), 248–259. doi:10.1093/gji/ggs010

Dreger, D. S. (2003). "85.11 TDMT_INV: Time Domain Seismic Moment Tensor INVersion," in *International Handbook of Earthquake and Engineering Seismology*. Editors W.H.K. Lee, H. Kanamori, P.C. Jennings, and C. Kisslinger (London: Academic Press), 81, 1627. doi:10.1016/S0074-6142(03)80290-5

Dreger, D. S., Ford, S. R., and Walter, W. R. (2008). Source Analysis of the Crandall Canyon, Utah, Mine Collapse. *Science* 321, 217. doi:10.1126/science.1157392

Dubiński, J. (2013). "The Mechanisms and Consequences of strong Mining Tremors that Occur in Polish Hard Coal and Copper Mines," in *Rock Mechanics for Resources, Energy and Enviroment* Editors Kwaśniewski and Łydżba (Wroclaw, Poland), 31–38.

Fernandez, L. M., and Van der Heever, P. K. (1984). "Ground Movement and Damage Accompanying a Large Seismic Events in the Klerksdorp District," in Proceedings 1st International Congress on Rockbursts and Seismicity in Mines, Johannesburg, 213–224. doi:10.1016/b978-0-12-812234-1.00007-8

Fichtner, A., Kennett, B. L. N., Igel, H., and Bunge, H.-P. (2008). Theoretical Background for continental- and Global-Scale Full-Waveform Inversion in the Time-Frequency Domain. *Geophys. J. Int.* 175 (2), 665–685. doi:10.1111/j.1365-246X.2008.03923.x

Fitch, T. J., McCowan, D. W., and Shields, M. W. (1980). Estimation of the Seismic Moment Tensor from Teleseismic Body Wave Data with Applications to Intraplate and Mantle Earthquakes. *J. Geophys. Res.* 85 (B7), 3817–3828. doi:10.1029/JB085iB07p03817

Fletcher, J. B., and McGarr, A. (2005). Moment Tensor Inversion of Ground Motion from Mining-Induced Earthquakes, Trail Mountain, Utah. *Bull. Seismological Soc. America* 95 (1), 48–57. doi:10.1785/0120040047

Gibowicz, S. J., and Kijko, A. (1994). *An Introduction to Mining Seismology*. San Diego: Academic Press

Hardebeck, J. L., and Shearer, P. M. (2003). Using S/P Amplitude Ratios to Constrain the Focal Mechanisms of Small Earthquakes. *Bull. Seismological Soc. America* 93 (6), 2434–2444. doi:10.1785/0120020236

Hasegawa, H. S., Wetmiller, R. J., and Gendzwill, D. J. (1989). Induced Seismicity in Mines in Canada-An Overview. *Pure Appl. Geophys.* 129 (3–4), 423–453. doi:10.1007/BF0087451810.1007/978-3-0348-9270-4_10

Heimann, S. (2011). *A Robust Method to Estimate Kinematic Earthquake Source Parameters*. PhD Thesis. Hamburg, Germany: Universit at Hamburg.

HongKie, T., and Kanamori, H. (1995). Moment-tensor Inversions for Local Earthquakes Using Surface Waves Recorded at TERRAscope. *Bull. Seismological Soc. America* 85 (4), 1021–1038.

Hudson, J. A., Pearce, R. G., and Rogers, R. M. (1989). Source Type Plot for Inversion of the Moment Tensor. *J. Geophys. Res.* 94 (B1), 765–774. doi:10.1029/jb094ib01p00765

Kagan, Y. Y. (2005). Double-couple Earthquake Focal Mechanism: Random Rotation and Display. *Geophys. J. Int.* 163 (3), 1065–1072. doi:10.1111/j.1365-246X.2005.02781.x

Kagan, Y. Y. (2007). Simplified Algorithms for Calculating Double-Couple Rotation. *Geophys. J. Int.* 171 (1), 411–418. doi:10.1111/j.1365-246X.2007.03538.x

Kanamori, H., and Given, J. W. (1981). Use of Long-Period Surface Waves for Rapid Determination of Earthquake-Source Parameters. *Phys. Earth Planet. Interiors* 27 (I), 8–31. doi:10.1016/0031-9201(81)90083-2

Koziarz, E., and Szłapka, M. (2010). Kierunki Dalszego Rozwoju Informatycznego Systemu Do Bezpośredniej Lokalizacji Zjawisk Dynamicznych W O/ZG "Rudna" KGHM "Polska Miedź" SA. *Wiadomości Górnicze* 3, 159–174.

Kwiatek, G., Martínez-Garzón, P., and Bohnhoff, M. (2016). HybridMT: A MATLAB/Shell Environment Package for Seismic Moment Tensor Inversion and Refinement. *Seismological Res. Lett.* 87 (4), 964–976. doi:10.1785/0220150251

Lasocki, S., Orlecka-Sikora, B., Mutke, G., Pytel, W., and Rudziński, Ł. (2017). "A Catastrophic Event in Rudna Copper-Ore Mine in Poland on 29 November, 2016: what , How and Why," in Proc. 9th International Symposium on Rockbursts and Seismicity in Mines. Editor J. A. Vallejos (Santiago, Chile: Editec S.A), 316–324.

Lasocki, S. (2005). "Probabilistic Analysis of Seismic hazard Posed by Mining Induced Events. Controlling Seismic Risk," in Proc. 6th International Symposium on Rockburst and Seismicity in Mines 9-11 March 2005. Editors Y. Potvin and M. Hudyma (Nedlands, Australia: Australian Centre for Geomechanics), 151–156.

Li, T., Cai, M. F., and Cai, M. (2007). A Review of Mining-Induced Seismicity in China. *Int. J. Rock Mech. Mining Sci.* 44 (8), 1149–1171. doi:10.1016/j.ijrmms.2007.06.002

Lizurek, G. (2017). Full Moment Tensor Inversion as a Practical Tool in Case of Discrimination of Tectonic and Anthropogenic Seismicity in Poland. *Pure Appl. Geophys.* 174 (1), 197–212. doi:10.1007/s00024-016-1378-9

Lizurek, G., and Wiejacz, P. (2011). "Moment Tensor Solution and Physical Parameters of Selected Recent Seismic Events at Rudna Copper Mine," in *GeoPlanet: Earth and Planetary Sciences*. Editors A.F. Idziak and R. Dubiel, 3, 11–19. doi:10.1007/978-3-642-19097-1_2

López-Comino, J. A., Cesca, S., Kriegerowski, M., Heimann, S., Dahm, T., Mirek, J., et al. (2017). Monitoring Performance Using Synthetic Data for Induced Microseismicity by Hydrofracking at the Wysin Site (Poland). *Geophys. J. Int.* 210 (1), 42–55. doi:10.1093/gji/ggx148

Ma, J., Dineva, S., Cesca, S., and Heimann, S. (2018a). Moment Tensor Inversion with Three-Dimensional Sensor Configuration of Mining Induced Seismicity (Kiruna Mine, Sweden). *Geophys. J. Int.* 213 (3), 2147–2160. doi:10.1093/gji/ggy115

Ma, J., Dong, L., Zhao, G., and Li, X. (2018b). Discrimination of Seismic Sources in an Underground Mine Using Full Waveform Inversion. *Int. J. Rock Mech. Mining Sci.* 106, 213–222. doi:10.1016/j.ijrmms.2018.04.032

Ma, J., Dong, L., Zhao, G., and Li, X. (2019). Focal Mechanism of Mining-Induced Seismicity in Fault Zones: A Case Study of Yongshaba Mine in China. *Rock Mech. Rock Eng.* 52 (9), 3341–3352. doi:10.1007/s00603-019-01761-4

McGarr, A. (1992). Moment Tensors of Ten Witwatersrand Mine Tremors. *Pageoph* 139 (3–4), 781–800. doi:10.1007/BF00879963

McGarr, A., Simpson, D., and Seeber, L. (2002). "40 Case Histories of Induced and Triggered Seismicity," in *International Handbook of Earthquake and Engineering Seismology*. Editors W.HH Lee Kanamori, P.C Jennings, and C Kisslinger, 81, 647–661. doi:10.1016/S0074-6142(02)80243-1

McGarr, A. (1971). Violent Deformation of Rock Near Deep-Level, Tabular Excavations-Seismic Events by arthur Mcgarr. *Bull. Seismological Soc. America* 61 (5), 1453–1466.

Parzen, E. (1962). On Estimation of a Probability Density Function and Mode. *Ann. Math. Statist.* 33 (3), 1065–1076. doi:10.1214/aoms/1177704472

Potgieter, G. J., Roering, C., Gay, N. C., and Wainwright, A. H. (1984). "The Influence of Geology on the Mechanisms of Mining-Associated Seismicity in the Klerksdorp Gold-Field," in *Rockbursts and Seismicity in Mines* (Johannesburg: S. Afr. Inst. Min. Metal), 45–50.

Rosenblatt, M. (1956). Remarks on Some Nonparametric Estimates of a Density Function. *Ann. Math. Statist.* 27 (3), 832–837. doi:10.1214/aoms/1177728190

Rudziński, L., Cesca, S., and Lizurek, G. (2016). Complex Rupture Process of the 19 March 2013, Rudna Mine (Poland) Induced Seismic Event and Collapse in the Light of Local and Regional Moment Tensor Inversion. *Seismological Res. Lett.* 87 (2A), 274–284. doi:10.1785/0220150150

Rudziński, Ł., and Dineva, S. (2017). "Towards Energy Magnitude for Mining Induced Seismicity," in *Proc. 9h International Symposium on Rockbursts and Seismicity in Mines*. Editor J.A. Vallejos (Santiago, Chile: Editec S.A), 182–188.

Rudziński, Ł., Mirek, J., and Lizurek, G. (2017). Identification of Seismic Doublets Occurred on Rudna Mine, Poland. *Acta Geophysica* 65 (2), 287–298. doi:10.1007/s11600-017-0034-9

Rudziński, Ł., Mirek, K., and Mirek, J. (2019). Rapid Ground Deformation Corresponding to a Mining-Induced Seismic Event Followed by a Massive Collapse. *Nat. Hazards* 96 (1), 461–471. doi:10.1007/s11069-018-3552-0

Rudziński, Ł. (2013). Rozwiązanie Mechanizmu Zjawiska Sejsmicznego Poprzez Inwersję Sejsmogramów. *Przegląd Górniczy* 69 (5), 49–55.

Sen, A. T., Cesca, S., Bischoff, M., Meier, T., and Dahm, T. (2013). Automated Full Moment Tensor Inversion of Coal Mining-Induced Seismicity. *Geophys. J. Int.* 195 (2), 1267–1281. doi:10.1093/gji/ggt300

Šílený, J., and Milev, A. (2006). Seismic Moment Tensor Resolution on a Local Scale: Simulated Rockburst and Mine-Induced Seismic Events in the Kopanang Gold Mine, South Africa. *Pure Appl. Geophys.* 163 (8), 1495–1513. doi:10.1007/s00024-006-0089-z

Šílený, J., and Milev, A. (2008). Source Mechanism of Mining Induced Seismic Events - Resolution of Double Couple and Non Double Couple Models. *Tectonophysics* 456 (1–2), 3–15. doi:10.1016/j.tecto.2006.09.021

Spottiswoode, S. M., and McGarr, A. (1975). Source Parameters of Tremors in a Deep-Level Gold Mine. *Bull. Seismological Soc. America* 65 (1), 93–112. doi:10.1016/0148-9062(76)91997-5

Stec, K., and Drzewiecki, J. (2012). Mine Tremor Focal Mechanism: An Essential Element for Recognising the Process of Mine Working Destruction. *Acta Geophys.* 60 (2), 449–471. doi:10.2478/s11600-011-0036-y

Trifu, C.-I., Angus, D., and Shumila, V. (2000). A Fast Evaluation of the Seismic Moment Tensor for Induced Seismicity. *Bull. Seismological Soc. America* 90 (6), 1521–1527. doi:10.1785/0120000034

Trifu, C. I. (2002). *The Mechanism of Induced Seismicity*. Springer Basel AG. doi:10.1017/978-3-0348-8179-1

Vavryčuk, V. (2001). Inversion for Parametes of Tensile Earthquake. *J. Geophys. Res.* 106 (B8), 16339–16355. doi:10.1029/2001JB000372

Vavryčuk, V., and Kühn, D. (2012). Moment Tensor Inversion of Waveforms: A Two-step Time-Frequency Approach. *Geophys. J. Int.* 190 (3), 1761–1776. doi:10.1111/j.1365-246X.2012.05592.x

Wiejacz, P. (1991). *Badania Mechanizmów Wstrząsów Górniczych Przy Wykorzystaniu Tensora Momentu Sejsmicznego*. Warszawa: Wyd. Instytutu Geofizyki PAN.

Wilson, M. P., Foulger, G. R., Gluyas, J. G., Davies, R. J., and Julian, B. R. (2017). HiQuake: The Human-Induced Earthquake Database. *Seismological Res. Lett.* 88 (6), 1560–1565. doi:10.1785/0220170112

Zhu, L., and Ben-Zion, Y. (2013). Parametrization of General Seismic Potency and Moment Tensors for Source Inversion of Seismic Waveform Data. *Geophys. J. Int.* 194, 839–843. doi:10.1093/gji/ggt137

Conflict of Interest: The authors declare that the research was conducted in the absence of any commercial or financial relationships that could be construed as a potential conflict of interest.

frontiers in Earth Science

ORIGINAL RESEARCH
published: 14 September 2021
doi: 10.3389/feart.2021.685841

Time-dependent Seismic Footprint of Thermal Loading for Geothermal Activities in Fractured Carbonate Reservoirs

B. B. T. Wassing, T. Candela, S. Osinga, E. Peters, L. Buijze, P. A. Fokker and J. D. Van Wees*

TNO Applied Geoscience, Utrecht, Netherlands

This paper describes and deploys a workflow to assess the evolution of seismicity associated to injection of cold fluids close to a fault. We employ a coupled numerical thermo-hydro-mechanical simulator to simulate the evolution of pressures, temperatures and stress on the fault. Adopting rate-and-state seismicity theory we assess induced seismicity rates from stressing rates at the fault. Seismicity rates are then used to derive the time-dependent frequency-magnitude distribution of seismic events. We model the seismic response of a fault in a highly fractured and a sparsely fractured carbonate reservoir. Injection of fluids into the reservoir causes cooling of the reservoir, thermal compaction and thermal stresses. The evolution of seismicity during injection is non-stationary: we observe an ongoing increase of the fault area that is critically stressed as the cooling front propagates from the injection well into the reservoir. During later stages, models show the development of an aseismic area surrounded by an expanding ring of high seismicity rates at the edge of the cooling zone. This ring can be related to the "passage" of the cooling front. We show the seismic response of the fault, in terms of the timing of elevated seismicity and seismic moment release, depends on the fracture density, as it affects the temperature decrease in the rock volume and thermo-elastic stress change on the fault. The dense fracture network results in a steeper thermal front which promotes stress arching, and leads to locally and temporarily high Coulomb stressing and seismicity rates. We derive frequency-magnitude distributions and seismic moment release for a low-stress subsurface and a tectonically active area with initially critically stressed faults. The evolution of seismicity in the low-stress environment depends on the dimensions of the fault area that is perturbed by the stress changes. The probability of larger earthquakes and the associated seismic risk are thus reduced in low-stress environments. For both stress environments, the total seismic moment release is largest for the densely spaced fracture network. Also, it occurs at an earlier stage of the injection period: the release is more gradually spread in time and space for the widely spaced fracture network.

Keywords: injection-induced seismicity, geothermal operations, seismic hazard, long-term thermal loading, fractured carbonates

OPEN ACCESS

Edited by:
Antonio Pio Rinaldi,
Swiss Seismological Service, ETH Zurich, Switzerland

Reviewed by:
Zahid Rafi,
Pakistan Meteorological Department, Pakistan
Alessandro Verdecchia,
Ruhr University Bochum, Germany

****Correspondence:***
B. B. T. Wassing
brecht.wassing@tno.nl

Specialty section:
This article was submitted to Geohazards and Georisks, a section of the journal Frontiers in Earth Science

Received: *25 March 2021*
Accepted: *24 August 2021*
Published: *14 September 2021*

Citation:
Wassing BBT, Candela T, Osinga S, Peters E, Buijze L, Fokker PA and Van Wees J D (2021) Time-dependent Seismic Footprint of Thermal Loading for Geothermal Activities in Fractured Carbonate Reservoirs. Front. Earth Sci. 9:685841. doi: 10.3389/feart.2021.685841

1 INTRODUCTION

The role of geothermal energy production in the global energy supply is expected to grow (IEA, 2020), as the energy transition requires a shift from fossil-fuel based to renewable and sustainable energy sources. Geothermal energy can be produced from high-enthalpy geothermal fields, but also low-enthalpy sedimentary formations such as found in intraplate regions like e.g. the Netherlands. In the last 2 decades, over 20 low enthalpy geothermal doublet production systems have been successfully developed in the Netherlands (e.g. Van Wees et al., 2020). The majority of these doublets target porous sandstone reservoirs of Permian to Cretaceous age (Buijze et al., 2019). However, the increased demand for sustainable heat and electricity calls for a broadening of the geological targets for geothermal energy. Therefore, exploration efforts now also target the potential of the Lower Carboniferous Dinantian play in the Netherlands (e.g. Bouroullec et al., 2019; Ter Heege et al., 2020). These Dinantian carbonates typically show heterogeneous porosity and permeability due to the presence of karstification and fractures, as well as relatively high rock competence. The deeper reservoirs among them, which are mainly located in the northern part of the Netherlands, show high *in-situ* reservoir temperatures up to 190°C (e.g. Lipsey et al., 2016). Consequently, the expected difference between the re-injection temperature and ambient rock temperature is large. The shallower reservoirs in the southeastern part of the Netherlands lie in the Ruhr Valley Graben, a tectonically active region. The full set of reservoir characteristics–tectonic setting, depth, *in-situ* temperatures, rock competence, poro-perm distribution and the presence or absence of fractures–will affect flow, heat transport and geomechanical response and thereby the seismicity potential of these geothermal plays. Generally speaking, the induced seismicity potential of the Dinantian fractured carbonates is considered to be higher than for the "conventional" sandstone reservoirs (Buijze et al., 2019). Induced earthquakes of magnitudes large enough to be felt at the surface can pose a problem for geothermal doublet operations.

In the southeast of the Netherlands, two geothermal doublets have been operated in carbonate reservoirs of the Dinantian. In contrast to the geothermal doublets producing from porous sandstone reservoirs, where no induced seismicity has been reported to date, some small seismic events have been recorded in the Dinantian reservoirs (Baisch and Vörös, 2018; Vörös and Baisch, 2019). This led to the cessation of the geothermal doublet operations. Recent research points towards a causal relation between operations in the Dinantian carbonates and seismic events (Baisch and Vörös, 2018; Vörös and Baisch, 2019). However, unambiguous conclusions on the relation between subsurface operations and causal mechanisms of induced events were hampered by lack of available data from the subsurface, as well as significant uncertainties in seismic event depth (State Supervision of Mines, 2019). This calls for an improved understanding of the driving mechanisms of induced seismicity in these carbonate reservoirs.

Simulation models capable to assess the potential of fault reactivation and seismicity are crucial to understand the interplay between the operational factors and the evolution of pressures, temperatures and associated changes in the stress fields near geothermal systems (i.e. Wassing et al., 2014; Candela et al., 2018; Van Wees et al., 2020; Wassing et al., 2021). Such models take into account pressure and temperature changes prompted by the production of warm water and re-injection of cooled water which cause changes in stresses in the geothermal reservoir. These may lead to fault reactivation and induced seismicity. Effects of temperature changes on the short term are expected to be limited to the near-well area. However, most geothermal doublets will operate over long periods, up to lifetimes of 50 years. Extensive cooling of the reservoir rocks and the associated stress changes may play a significant role in fault reactivation. Moreover, thermo-elastic stresses may dominate over poro-elastic stress changes and pressure changes, since injection pressures in the carbonate reservoirs are relatively low and thermal stresses can be significant in particular in stiff rocks (e.g. Jacquey et al., 2015). The potential for pressure- or thermally induced seismicity depends on reservoir characteristics, operational conditions and flow rates during geothermal production. Gan and Elsworth (2014) investigated the propagation of fluid pressures and thermal stresses in a prototypical geothermal doublet in a fractured reservoir, and demonstrated that the likelihood for late-stage thermally-induced seismicity depends on the shape of the thermal front.

In the present paper, we focus on seismicity induced by geothermal operations in fractured carbonate reservoirs, such as the Dinantian carbonates in the Netherlands. Using a numerical 3D coupled thermo-hydro-mechanical model (following and extending the method of Gan and Elsworth, 2014), in combination with Dieterich's rate-and-state-theory (Dieterich, 1994; Segall and Lu, 2015), we investigate and discuss the nucleation of seismicity and the spatial and temporal pattern of seismicity–the "seismic footprint."

2 METHODOLOGY FOR ASSESSING SEISMIC FOOTPRINT DURING GEOTHERMAL OPERATIONS

2.1 Model Geometry

We employ the coupled numerical thermo-hydro-mechanical simulator of FLAC3D-TOUGHREACT (Taron and Elsworth, 2010; Gan and Elsworth, 2014; Wassing et al., 2021). The simulator accounts for the two-way coupling between the thermal, hydraulic and mechanical processes, and provides the spatial and temporal evolution of pore pressures, temperatures and stresses in the model domain. For the present analysis, we do not use the chemical options available in the TOUGHREACT part of the coupled code.

We use a simplified model geometry and modelled pressure, temperature and stress changes due to fluid injection into a single well close to a fault plane. For computational efficiency, we model a quarter of a symmetrical reservoir with a single vertical injection well. Our workflow can easily be extended to model the geometry and configuration of a typical geothermal doublet. Model dimensions are 2,500 × 2500 × 2,100 m. The stress evolution can be computed at any location in the reservoir, over- and

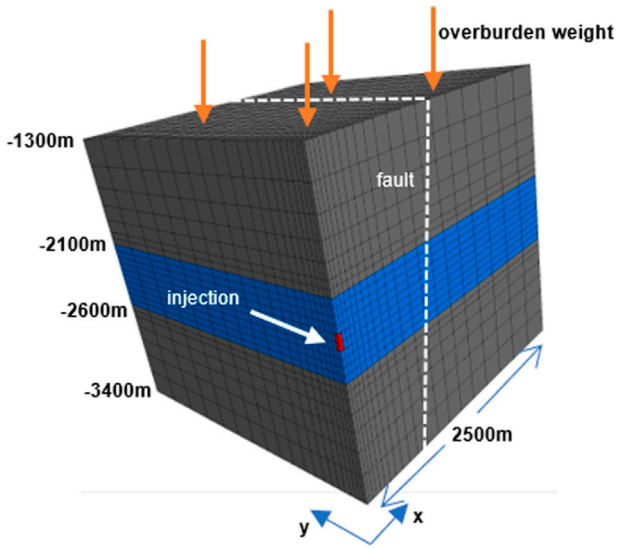

FIGURE 1 | Geometry of the model in FLAC3D-TOUGHREACT. Blue color indicates the carbonate reservoir. Red interval depicts injection interval, dashed white line shows position of fault plane, which intersects reservoir and surrounding rocks.

TABLE 1 | Model parameters and model ranges for FLAC3D-TOUGHREACT. Values between square brackets indicate a stochastic range of input parameters (uniform distribution).

Model parameter	FLAC3D-TOUGHREACT
Bulk density (kg/m^3)	2260
Young's modulus (GPa)[a]	50
Poisson's ratio (–)[a]	0.25
Biot coefficient (–)	1.0
Friction threshold criticality (–)	0.4 [0.3–0.5]
Bulk fracture permeability (m^2)	1.e–13
Matrix permeability (m^2)	1.e–17
Volume fraction fractures (–)	0.02
Porosity of the fractures (–)	0.2
Matrix porosity (–)	0.03
Rock thermal conductivity (W/m°C)[b]/[c]	2.4
Rock heat capacity (J/kg°C)[c]	880
Linear thermal expansion coefficient (°C^{-1})[c]	8.0e–6
Fracture distance (m)	2 and 200
Fault dip (°)	70 [60–80]
Vertical total stress gradient (MPa/km)	22.6
Horizontal total stress gradient (MPa/km)	16.0
Pore pressure gradient (MPa/km)	10.0
Initial temperature (°C)	90

[a]*Based on.*
[b]*Based on Chen et al., 2013.*
[c]*Based on Roberson, 1988.*

underburden. The fault plane itself is not explicitly modelled. We are therefore flexible in choosing the location and orientation of the fault, as there is no need for model remeshing. We define a fault without offset, striking N-S and dipping 70° towards the injection well at a distance of approximately 300 m from the injection well (see **Figure 1**). Pressures in the fault and stress conditions at the location of the fault plane are derived from 3D interpolation of fracture pressure and stress at the center of the mesh elements.

TABLE 2 | Parameters and ranges for modelling rate-and-state seismicity and frequency-magnitudes distributions. Values between square brackets indicate a stochastic range of input parameters (uniform distribution).

Model parameter	Seismicity (dieterich)
A (–)	0.001
r_0 (N/yr)	1
$\dot{\tau}_0$ (MPa/yr)	0.0002
M_{min} (–)	0
M_{max} (–)	4
b-value (–)	1 [0.8–1.2]
Δσ (MPa)	5.0 [0.1–10.0]
f_{crit} (–)	0.4 [0.3–0.5]

2.2 Model Parameterization, Initial Conditions and Boundary Conditions

We model the seismic response of a fault in a fractured carbonate reservoir. The top of the reservoir is located at a depth of −2,100 m. Initial reservoir temperature is 90°C. Depth, *in-situ* temperature, hydrological and thermal parameters of the reservoir are representative of the Dinantian carbonate reservoirs as reported in Ter Heege et al., 2020. The carbonate reservoir itself is relatively thick, 500 m; the fluid is assumed to be injected in an open hole section of 100 m at the center of the reservoir at a depth between −2,300 m and −2,400 m. Fracture sets in the reservoir are modelled as orthogonal with equal spacing and permeability, using the double porosity-permeability approach in TOUGHREACT (Pruess et al., 2012). We distinguish two end-members for the fracture spacing: a small fracture spacing of 2 m and a large fracture spacing of 200 m.

We assume elastic isotropic material behaviour for the reservoir and burden. Elastic properties are uniform throughout the model (see **Table 1**).

Initial stress gradients are chosen to be representative of the *in-situ* stress field in the Netherlands, i.e., an extensional tectonic setting, with little anisotropy in the horizontal stresses ($S_v > S_{Hmax} = S_{hmin}$, respectively −22.6, −16.0, and −16.0 MPa/km). In our model, the minimum horizontal stress is oriented perpendicular to the strike of the fault (parallel to the model x-axis), and maximum horizontal stress is oriented parallel to the fault strike (y-axis). In all modelled cases we assume a hydrostatic pressure gradient. As a result, the initial slip tendency of the fault, defined as the ratio of shear (τ_s) over effective stress (σ'_n) is non-critical with a value $|\tau_s/\sigma'_n| \approx 0.3$ at the start of injection. We use the convention that compressive stress is negative.

Cold fluid is injected into the quarter of the injection well at a temperature of 25°C, at a constant rate of 50 kg/s over an open hole section of 100 m. We only model flow and heat transfer in the reservoir section; no flow or thermal conduction into the seal and base rock is modelled. As boundary conditions for flow and heat transport, we impose constant pressure and temperature at the far field vertical boundaries, 2,500 m from the injection well.

We assume no displacements in the horizontal direction at the vertical boundaries. For the horizontal boundary at the top and bottom we impose a constant stress, to simulate the weight of the overburden and initial stress equilibrium at depth. The stress response associated to the change of pressure and temperature is computed for the entire model, including the under- and overburden rocks.

Mechanical, thermal and hydrological model parameters and initial conditions and assumptions for the TOUGHREACT-FLAC3D simulations are summarized in **Table 1**.

2.3 Coulomb Stress at Fault and Seismicity

As a first step we compute effective normal and shear stresses from the stress tensor at the location of the fault plane. From these we derive the Coulomb stress changes on the fault. Coulomb stress change on a fault is an important proxy for seismicity potential. It is defined by the change of the vertical distance of the effective normal and shear stress to the Mohr-Coulomb failure line in a Mohr diagram. The Coulomb stress changes then result from two contributions. The first is the increase in pore pressures in the fault itself, due to diffusion of pressures through the fracture network (fracture pressure P_1) into the fault (so-called "direct pore pressure effect"). The second is the combination of poroelastic and thermoelastic stress changes, caused by the deformation of the rocks due to pressure changes in the fractures (P_1) and matrix (P_2), respectively temperature changes in the matrix rocks (T_2). The Coulomb stress changes are written as:

$$\Delta\tau_{cs} = \Delta\tau_s - \mu\Delta\sigma_n + \mu\Delta P_1 \tag{1}$$

where the symbol Δ denotes a change, τ_s is shear stress, σ_n is total normal stress on the fault, μ is friction coefficient of the fault and P_1 is the pore pressure change in the fault. A positive Coulomb stress change indicates that the stress on that fault segment follows a destabilizing path; conversely a negative Coulomb stress change indicates a stabilizing path. The first two components on the right-hand side in **Eq. 1** denote the contribution of poro- and thermoelastic stressing; the last component μP_1 gives the contribution of the "direct pore pressure effect" in the fault.

From the evolution of Coulomb stress changes over time we derive Coulomb stressing rates. In turn, the stressing rates are used as input to the rate-and-state seismicity theory originally proposed by Dieterich (1994) to derive seismicity rate (see also Segall and Lu, 2015; Heimisson and Segall, 2018; Candela et al., 2019). Seismicity rates are calculated as:

$$\frac{dR}{dt} = \frac{R}{t_a(t)}\left(\frac{\dot{\tau}_{cs}}{\dot{\tau}_0} - R\right) \tag{2}$$

where the Coulomb stressing rate is defined as:

$$\dot{\tau}_{cs} = \dot{\tau}_s - [\mu(t) - \gamma]\dot{\sigma}_n' \tag{3}$$

with $\dot{\tau}_s$ is the shear stress rate, $\dot{\sigma}_n'$ is the effective normal stress rate, $\mu(t)$ is the coefficient of fault friction, in which the functional dependence on t denotes that it depends on the temporal evolution of shear stress over normal stress. For γ, a constitutive parameter, we use zero in this study. R is the relative seismicity rate, i.e. the seismicity rate divided by background (tectonic) seismicity rate r_0, $\dot{\tau}_0$ is the tectonic stressing rate, and $t_a(t)$ is a characteristic time decay which corresponds to the time scale of decay of the aftershock rate following a main shock back to the background rate. $t_a(t)$ depends on background stressing rate, fault parameter A (which quantifies the direct effect of rate and state friction behavior of the fault) and the temporal evolution of normal effective stress σ_n':

$$t_a = A\frac{\sigma_n'}{\dot{\tau}_0} \tag{4}$$

In our model workflow, the Dieterich parameters A, r_0, $\dot{\tau}_0$ are kept constant for all the simulations.

We refer to Segall and Lu (2015) for a more in-depth discussion of the theory and the parameters involved.

Fault material behaviour is assumed to be fully elastic (i.e. no explicit slip and associated stress redistribution is modelled). To prevent the increase of shear stress and normal effective stress far beyond a realistic failure envelope for shear and tensile strength, we apply corrections for effective normal stress $\sigma_n^{'}$ and for ratio of shear stress to normal effective stress ($\tau_s/\sigma_n^{'}$):

- if $\sigma_n' > -1e{-}5$ MPa $\rightarrow \sigma_n' = -1.e{-}5$ MPa
- if $|\ \tau_s/\sigma'_n\ | > 1 \rightarrow |\ \tau_s/\sigma'_n\ | = 1$

Based on the spatial and temporal evolution of Coulomb stresses and relative seismicity rates we estimate the time-dependent frequency-magnitude distribution of the simulated seismicity at the fault plane near the injector well.

Here we can distinguish two end members: 1) injection in a so-called "low-stress" environment (Segall and Lu, 2015; Maurer and Segall, 2018) and 2) injection in a tectonically active "high-stress" environment. In a high-stress environment, once an event nucleates, it can potentially propagate over the entire fault plane. In a low-stress environment nucleation and propagation of seismic events is assumed to be restricted by the size of the fault segment that is critically stressed (i.e. there will be no run-away rupture outside this perturbed fault segment). In our approach, we use a critical value of shear-over effective normal stress to distinguish between critically and non-critically stressed fault area. In the low-stress environment seismic slip can only nucleate and propagate inside the critically-perturbed area of the fault, i.e. where $|\ \tau_s/\sigma_n'\ | \geq f_{crit}$.

The estimation of the frequency-magnitude distribution of seismic events is thus dependent on the stress environment.

For the high-stress environment, we assume a time-dependent truncated Gutenberg-Richter as representative of the frequency-magnitude distribution:

$$N(M \geq m) = a_{GR}\frac{10^{-b(m-M_{min})} - 10^{-b(M_{max}-M_{min})}}{1 - 10^{-b(M_{max}-M_{min})}} \tag{5}$$

where:

$a_{GR} = \int R.r_0$ is the seismicity rate integrated over the predefined fault plane. $N(M \geq m)$ is the expectation value for the number of events with a magnitude (M) larger than or equal

to m. The M_{max} can be chosen representative of the size of the predefined fault plane, or can be defined based on the regional tectonic M_{max}. The b-value is chosen constant equal to unity.

For the low-stress environment, again we assume a time-dependent truncated Gutenberg-Richter as representative of the frequency-magnitude distribution where $a_{GR} = \int R.r_0$is the seismicity rate integrated over the perturbed area. The b-value can be either a constant or a stochastic a-priori parameter. However, in this case the M_{max} is constrained by the dimensions of the critically-perturbed area, which depend on the evolution of shear and effective normal stress on the fault and the value of f_{crit}. We can choose f_{crit} as a constant or stochastic parameter. We approximate the critically-perturbed area by a rectangle with dimensions which evolve during the injection period. The smallest dimension corresponds to the R_{max} of the maximum magnitude event M_{max} at a specific moment in time. Assuming an a-priori stress drop $\Delta\sigma$ (either constant or stochastic parameter), and a disk-shaped rupture (aspect ratio of 1), M_{max} then equals:

$$M_{max} = \frac{2}{3}\log_{10}\left(\Delta\sigma\frac{16}{7}R_{max}^3\right) - 6.03 \quad (6)$$

Our workflow for the assessment of the seismic response of the fault, in terms of the frequency-magnitude evolution then involves the following steps:

- Compute spatial-temporal distribution of the pressure, temperature and stress changes in the reservoir;
- Define a fault geometry (dip, strike, location) in the model;
- Resolve shear, normal stresses and compute Coulomb stress rates on the fault;
- Calculate area-integrated seismicity rate (a_{GR}) from Dieterich's rate-and-state seismicity theory;
- *For high-stress environment:* define a stress drop, minimum and maximum magnitude and b-value, and based on a_{GR}, calculate the time-dependent truncated Gutenberg-Richter frequency-magnitude distribution. Note here that the M_{max} is derived a-priori from the size of the predefined fault plane.
- *For low-stress environment:* calculate the time-dependent critically-perturbed area and derive R_{max}. Define a stress drop, minimum and maximum magnitudes and b-value; and based on a_{GR}, calculate the time-dependent truncated Gutenberg-Richter frequency-magnitude distribution. Note here that the M_{max} is derived from the R_{max}.

3 MODELLING RESULTS: EFFECT OF THERMAL FRONT ON SEISMIC FOOTPRINT IN DENSELY AND SPARSELY FRACTURED CARBONATE RESERVOIR

For the two cases of fracture spacing defined above, we investigate the evolution of pressure, temperature, fault stress (rate) and seismicity in space and time. As described in Gan and Elsworth (2014), for the end-member of a high flowrate and large fracture spacing, the thermal drawdown in the reservoir is expected to be gradual in time and space, without the presence of a distinct thermal front. For the end-member of low flowrates and small fracture spacing, the thermal drawdown propagates through the reservoir as a distinct front similar as in a porous medium. In our models we keep the injection rates constant, and vary the fracture distance between 2 m (case 1) and 200 m (case 2). All other model parameters for the two models are kept equal.

Figure 2 shows the evolution of pressures and temperatures for the orthogonal fracture network with 200 m spacing within the first 100 days of injection. Pressures reach a steady state within a few days after the start of the injection, and even in the matrix, pressures approach steady state conditions within the first 100 days of the injection period (**Figure 2A**). The response in terms of temperature changes is much slower: though temperature changes are observed in the fractures during the first 100 days, the effect on the rock matrix is negligible (**Figure 2B**).

Figure 3 presents the long-term evolution of temperatures in the fractures and rock matrix for both the 2 m fracture distance and the 200 m fracture distance. In case of the 2 m fracture distance, the delay in cooling between rock matrix and fractures is very limited, resulting in almost equal mean equilibrium temperatures for fractures and matrix. Consequently, the temperature gradients observed in the rock matrix follow gradients in the fractures, and the temperature propagates through the rock matrix as a sharp front: over a distance of less than 100 m temperature differences of more than 60°C can exist. In case of the 200 m fracture distance, cooling of the rock matrix is more delayed, resulting in a clear temperature difference between fractures and rock matrix, largest in the first years of injection and gradually declining further away.

In **Figure 4A**—f, we present the short- and long-term evolution of pressure, temperature and Coulomb stress change on the fault plane. The stress path on the fault varies and depends on the location of monitoring, due to the 3D geometry of the pressure and temperature front and fault. We choose a monitoring position which is located at the center of the fault (see **Figure 1** at $y = 0$), just below mid-height of the reservoir (at depth = −2,375 m). Stress changes at the early stages of injection result from a combination of direct pore pressure, poro- and thermoelastic effects, whilst fault stress changes at later stages are mainly due to propagation of the temperature front.

Figure 4A shows the evolution of pressure and temperature during the first days of injection, for 200 m fracture spacing. **Figure 4B** presents the associated contributions of pressure, total normal stress and shear stress to the Coulomb stress, and the resulting Coulomb stress change on the fault plane. We use the convention that compressive stress is negative; a positive normal stress change ("unclamping" of the fault) results in an increase of Coulomb stress on the fault. We observe a small, but rapid Coulomb stress loading immediately after the start of the injection operations. This can be explained by the quick diffusion of pressures (P_1) in the high permeability fractures, which almost immediately affects the pressures in the fault plane. It is followed by a temporary decrease of Coulomb stresses during the first days, when pressures in the matrix (P_2) gradually increase

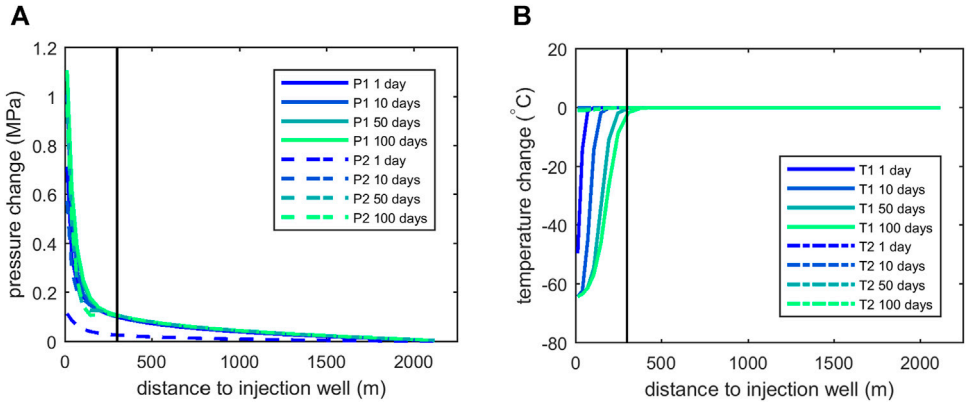

FIGURE 2 | (A) Short-term pressure evolution during first 100 days after onset injection; 200 m fracture spacing, **(B)** short-term temperature evolution during first 100 days after onset injection; 200 m fracture spacing. Solid lines (T_1, P_1) indicate values in the fractures, dashed lines (T_2, P_2) in the matrix. The black vertical line represents the horizontal position of the fault, measured at mid-height reservoir level.

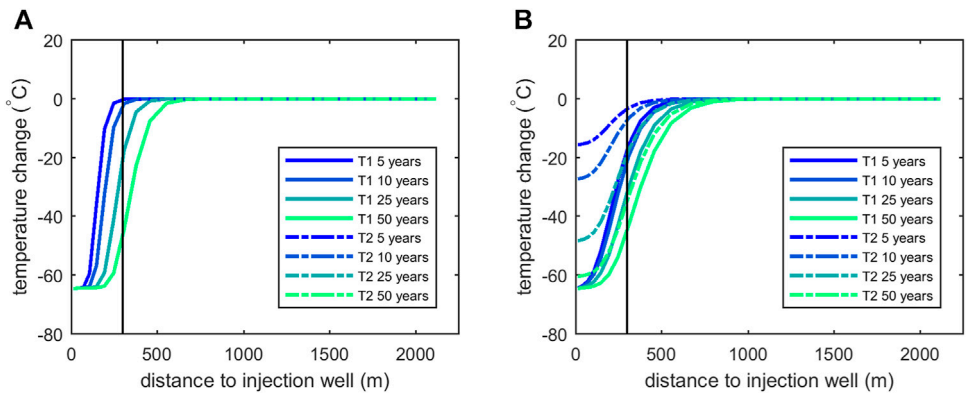

FIGURE 3 | Long-term temperature evolution in the fractures and rock matrix, **(A)** for fracture distance of 2 m, **(B)** for fracture distance of 200 m. Solid lines (T_1) indicate fracture temperature change, dashed lines (T_2) indicate matrix temperature change. The black vertical line represents the horizontal position of the fault, measured at mid-height reservoir level.

and volumetric changes result in a (stabilizing) poroelastic loading of the fault. Thermo-elastic effects are linked to the temperatures (T_2) and thermal strains in the matrix rocks. The role of thermo-elastic stress during the early stages of injection is negligible, as temperature changes in the matrix are still very small. We observe a similar short-term response in our model for the 2 m fracture spacing (not plotted here).

For the long-term temperature effects are dominant. In **Figures 4C,E** we plot the temperatures and pressures for the 2 m, respectively 200 m fracture spacing. Temperatures in the matrix rocks decrease by −30 to −45°C, whereas pressure changes in both the fractures and the matrix are negligible after the first 100 days.

In both types of reservoirs, cooling and thermal contraction of the matrix rocks leads to a continuous lowering of total normal stresses at the fault which results in "unclamping" of the fault and a positive contribution to the Coulomb stress change (black lines in **Figures 4D,F** and **Eq. 1**). The vertical dashed line in **Figure 4D** shows the level at which effective normal stress at the fault becomes tensile. For the 2 m case we observe tensile stresses at the central monitoring point after 31 years of injection. From that time onwards normal effective stresses are kept constant, as we do not allow opening of the fault. For the 200 m fracture spacing, the normal stress at the fault does not become tensile at this particular location.

As temperatures in the rock matrix decline, fault shear stress in the densely fractured reservoir gradually increases during the first 25 years of injection (**Figure 4D**). Thereafter shear stresses decline again. The net result are positive Coulomb stress changes, which destabilize this fault location during the first 31 years of injection. The combination of constant normal stress and simultaneous decrease of shear stress during the last 19 years of the injection period results in a net decrease of Coulomb stress (**Figure 4D**). For the 200 m fracture spacing the shear stress increases during the first 45 years of injection (**Figure 4F**), whereafter shear stress remains unchanged. In this

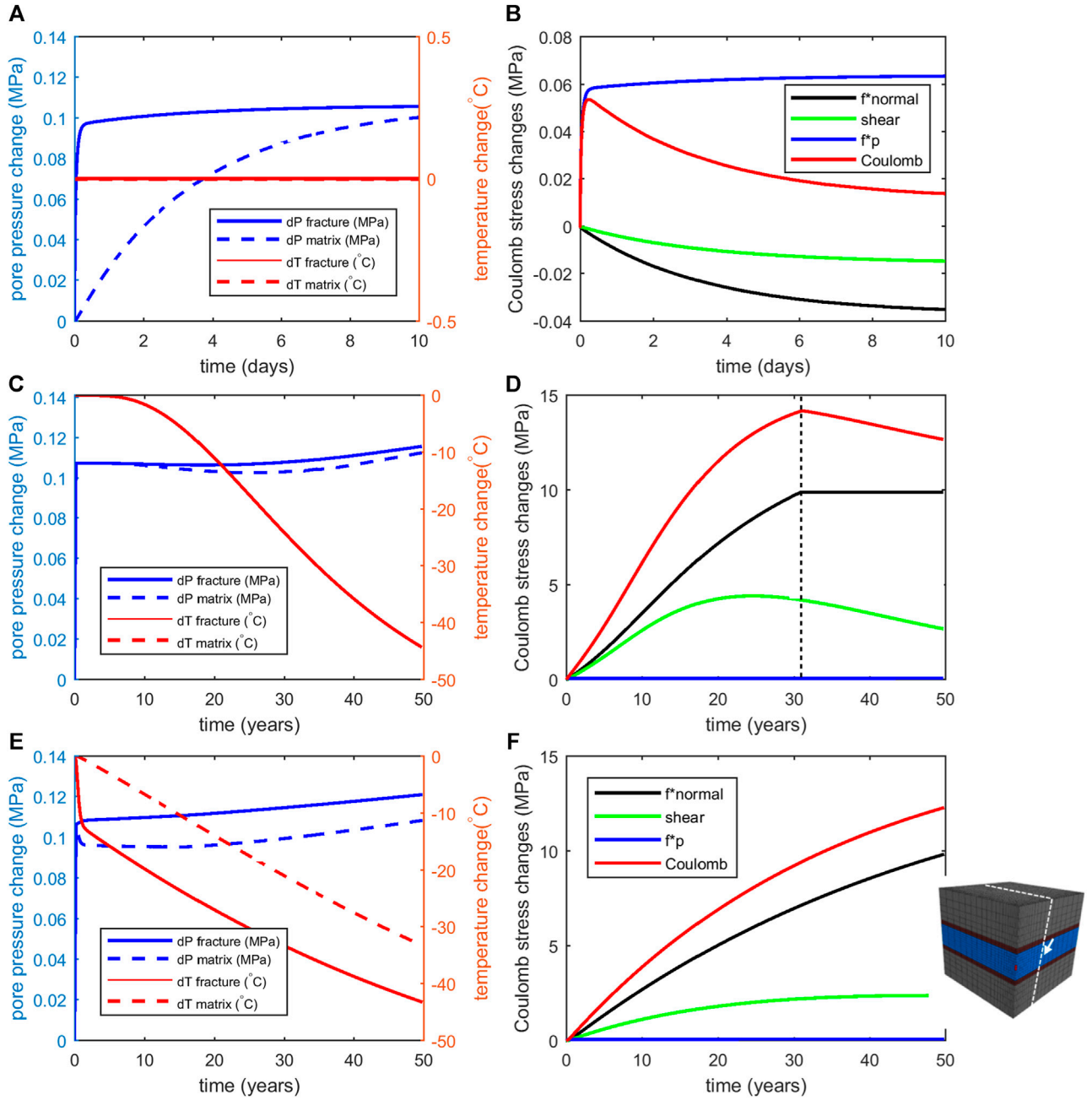

FIGURE 4 | Pressure and temperature changes on the fault (central, mid-height location) at 300 m distance from the injection well. **(A)** pressure and temperature change during first 10 days–fracture distance 200 m, **(B)** contribution of direct pressure effect (blue), total normal stress changes (black), shear stress (green) to Coulomb stress change on the fault (red), fracture distance 200 m, during first 10 days, **(C)** pressure and temperature change during total period of 50 years–fracture distance 2 m, **(D)** contribution of direct pressure effect (blue), total normal stress changes (black), shear stress (green) to Coulomb stress change on the fault (red), fracture distance 2 m, during total period of 50 years. Dashed black line indicates moment normal stresses become tensile. Shear stress declines after 25 years due to the effects of stress arching, **(E)** pressure and temperature change during total period of 50 years–fracture distance 200 m, **(F)** contribution of direct pressure effect (blue), total normal stress changes (black), shear stress (green) to Coulomb stress change on the fault (red), fracture distance 200 m, during total period of 50 years.

case Coulomb stress continues to grow up to 50 years (**Figure 4F**). In both cases the effect of direct pressure on the long-term Coulomb stress changes is negligible.

Figure 5A shows changes in both normal and shear stress with time at a fault position just below mid-height reservoir (at $y = 0$). The stress paths in **Figure 5A** can be related to the propagation of the temperature front, which causes arching of stresses within and around the cooling rocks. Thermal compaction of the reservoir causes a decrease of the horizontal stress in the reservoir, both within and around the cooled rock mass. In

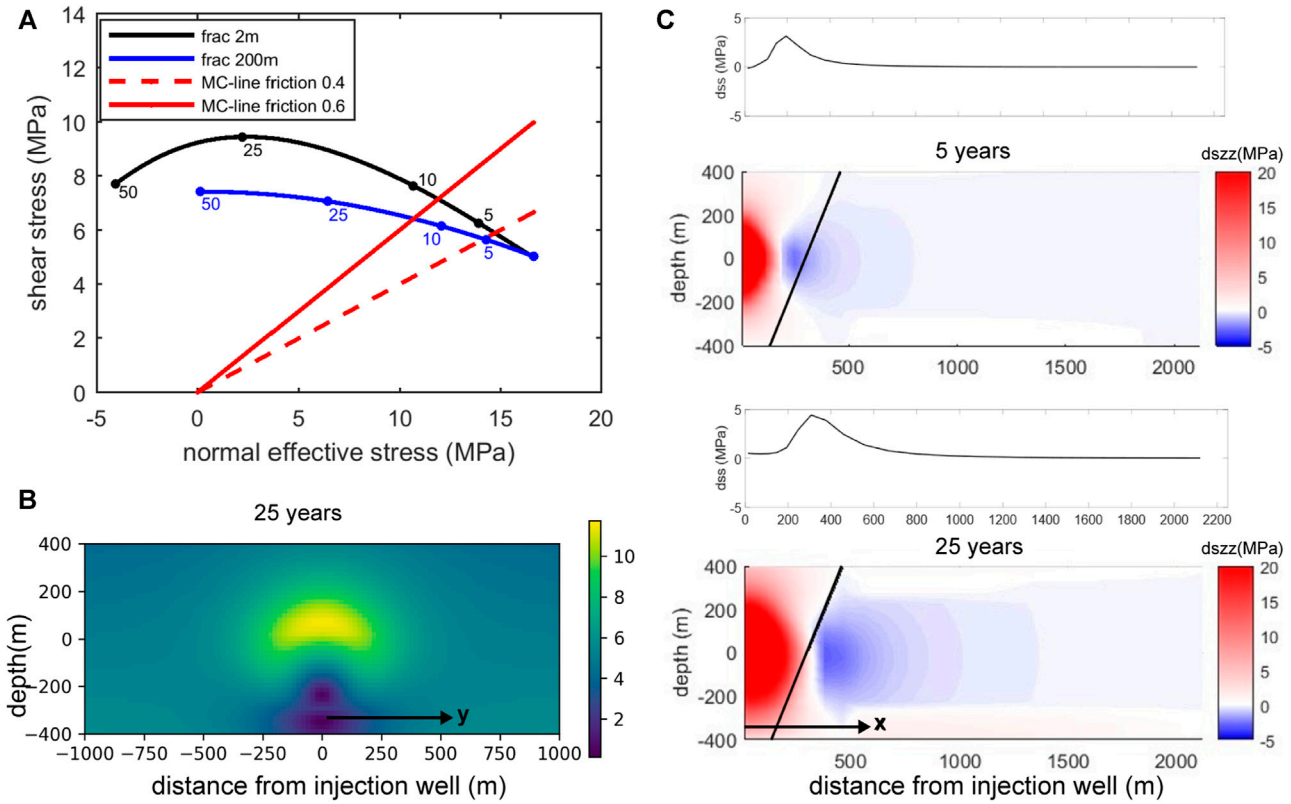

FIGURE 5 | (A) Stress path at the fault, just below mid-height reservoir at location y = 0, for both small and large fracture spacing. The four circles on the stress paths indicate stress conditions at 5, 10, 25, and 50 years after onset of injection. **(B)** Shear stress at the fault plane. Vertical axis: Mid-height reservoir at 0 m, units in depth (m) along dip. Location of projected injection well at y = 0. **(C)** Arching of total vertical stress around the cooling rock volume, for 2 m fracture spacing. Contour plots represent a vertical cross section (x-direction) through the injection well, perpendicular to the fault plane. Contour plots show change in total vertical stress (dszz) after 5 and 25 years of injection. Mid-height reservoir at 0 m, units in depth (m) along dip. Location of projected injection well at x = 0. Note compressive stress = negative; hence positive value for dszz means total vertical stress decreases. Black solid line shows position of the fault. Small graphs above contour plots show change in shear stress dss, which affects stress path gradients in **(A)**.

addition, it causes a decrease of vertical stress within the cooled rock and an increase of vertical stress in the reservoir section just around the cooled area. In **Figure 5C** we show the change in total vertical stress, for the 2 m fracture spacing. Stress arching affects the shear stress on the fault (see **Figure 5C**–small graphs). The contribution of shear stress to fault loading varies with position on the fault. **Figure 5B** shows that after 25 years of injection shear stress on the upper fault segment (above the level of the injection interval), caused by volumetric compaction, add to the shear stress already present from the tectonic loading. The increments in induced shear stresses on the lower fault segment however counteract the *in-situ* tectonic shear stresses. Effects of stress arching are most pronounced for the 2 m fracture spacing, where a sharp temperature front evolves.

Coulomb stress change is less for the 200 m spaced network than for the 2 m spaced network, mainly because the temperature decrease in the bulk rock mass (the matrix) and the related thermo-elastic stress changes are smaller and more gradual. Rates of Coulomb stress changes during this first period are higher for the 2 m spacing (**Figure 4D**) than for the 200 m spaced fracture network (**Figure 4F**). This is confirmed by the direction of the stress path for the two cases, as shown in **Figure 5A**.

From Coulomb stress change vs time shown in **Figure 4**, Coulomb stress rates are derived, which are converted to seismicity rates through the Dieterich model (**Eq. 2**). **Figure 6** presents the temporal evolution of relative seismicity rates on the fault (i.e. relative to the tectonic background rates) on a section along-dip at position $y = 0$. Values are shown for one particular realization (input model values are shown in the caption of **Figure 6**). Variations in stressing and seismicity rates are relatively large for the 2 m fracture distance (**Figure 6A**), with high seismicity rates at mid-height of the reservoir during the first 25 years of injection (shear stresses increasing, see also **Figures 4D**, **5A**). During late-stage injection seismicity rates at the central part of the reservoir decrease as shear stresses are reducing, and ultimately vanish once tensile normal stresses evolve. Deeper sections of the fault show significant seismic activity at late-stage injection. Note that distance of the fault plane to the injection interval varies with depth due to fault dip orientation. Fault dip orientation also affects the sign of the change in shear stress (as shown in **Figure 5B**) and thus the seismicity potential with depth.

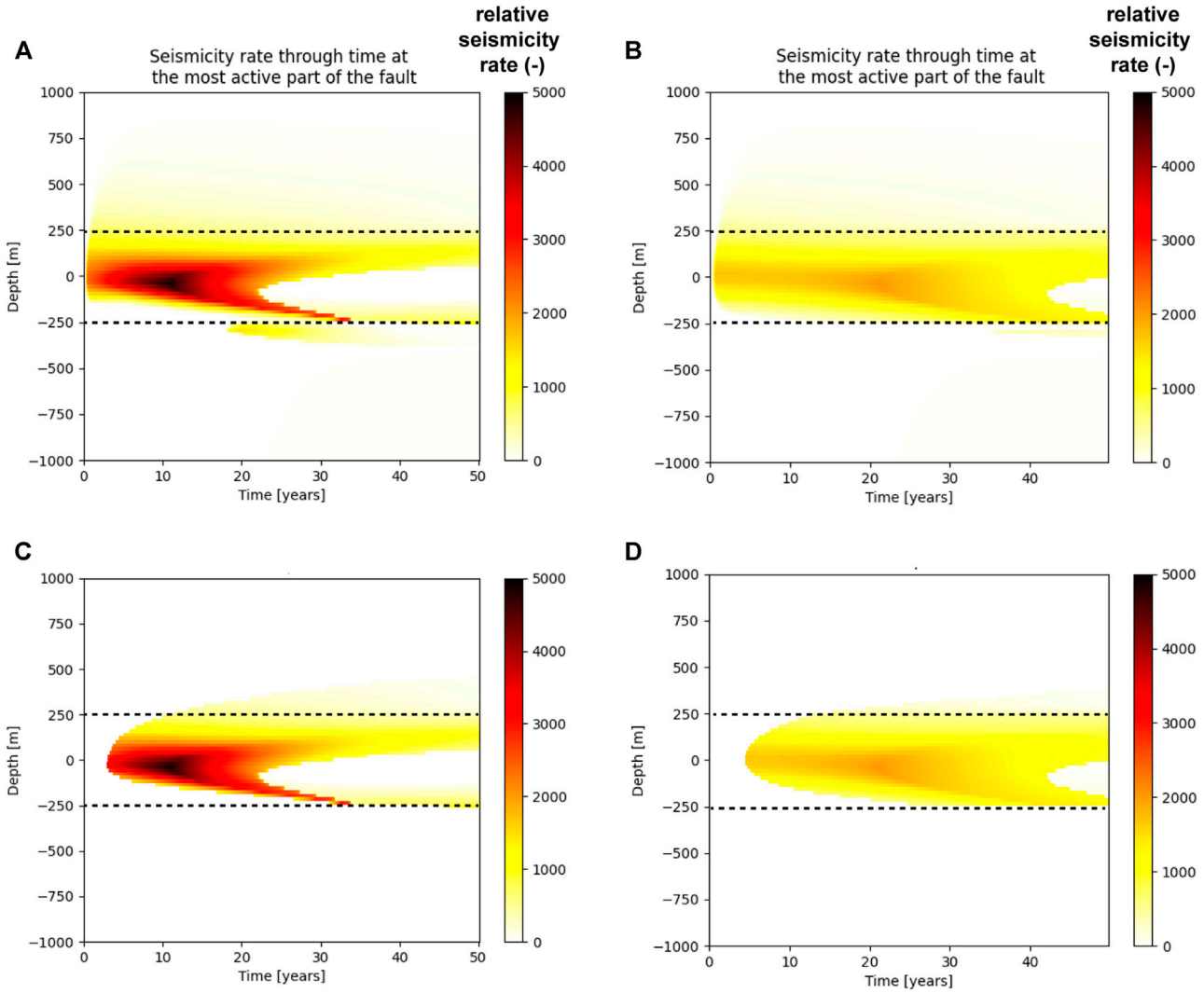

FIGURE 6 | Relative seismicity rates versus time after onset of injection for **(A)** 2 m fracture spacing uncorrected for the size of the perturbed area and **(B)** 200 m fracture spacing uncorrected for the size of the perturbed area, **(C)** 2 m fracture spacing, spatial distribution is corrected for the size of the perturbed area and **(D)** 200 m fracture spacing, spatial distribution is corrected for the size of the perturbed area. Dashed lines indicate top and bottom of reservoir layer. Mid-height reservoir at 0 m, units in depth (m) along dip. Location of projected injection well at y = 0. Relative seismicity rates (*R*) are shown for one particular realization, with $f_{crit} = 0.4$, $M_{min} = -1$, $A = 0.001$ and $\dot{\tau}_0 = 0.0002$ and $b = 1$.

The reservoir with 200 m fracture distance (**Figure 6B**), characterized by a slower cooling of the reservoir rocks and an absence of a sharp cooling font, shows seismicity rates that are much more constant in time, with the exception of the rapid rise in seismicity rates observed almost immediately after the start of injection. Here relative seismicity rates peak between 20 and 25 years after the onset of injection. **Figures 6C,D** show relative seismicity rates for the same realization, but now corrected for the size of the critically perturbed area. In both cases, during the first stages of injection no seismicity is expected, as the fault is not yet critically stressed (no perturbed fault area present yet).

Figure 7 shows the evolution of the critically stressed area and the cumulative number of seismic events. We observe that for the 200 m fracture distance, the onset of seismicity is later than for the 2 m fracture distance, due to the slower development of fault criticality. The total critically-perturbed fault area and number of events that nucleate on the entire fault plane is highest for the 2 m fracture distance.

Figure 8 presents relative seismicity rates at selected times. During the later stages of injection, the spatial pattern of Coulomb stressing rates and relative seismicity rates for the cases with 2 and 200 m fracture spacing is distinctly different. In case of the 2 m fracture distance we observe a clear ring or "halo" of elevated Coulomb stressing and seismicity rates, which is related to higher rates of cooling at the passage of the thermal front (see **Figure 8A**). Inside, a seismically quiet area arises, where cooling rates after the "passage" of the thermal front have effectively come to an end. Moreover, effective normal stresses

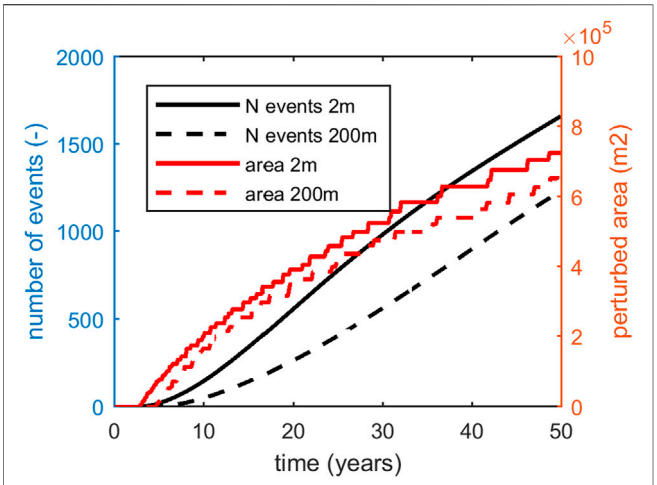

FIGURE 7 | Temporal evolution of perturbed area and total number of seismic events for the 2 and 200 m fracture spacing, in a low stress environment.

within this ring can be tensile. This aseismic area appears at a much later stage for the 200 m fracture distance. The general distribution of seismicity rates for the widely spaced fracture network is more homogeneous.

Finally, the extent of the perturbed fault area and the seismicity rates are used to derive the temporal evolution of seismicity (as described in **Section 2.3**). **Figure 9A** shows an example of the time-dependent truncated Gutenberg-Richter frequency-magnitude distribution of seismic events for the densely fractured carbonate reservoir. The frequency-magnitude distribution shows an increase of the probability of higher magnitudes in time. Note that here we show the outcome for a single realization. The frequency magnitude distribution is created using input parameters and assumptions summarized in **Table 2**. **Figure 9B** shows the evolution of cumulative seismic moment release over time in a low stress environment, for both the densely fractured and less damaged carbonate. Cumulative seismic moment release for the 2 m fracture spacing is significantly larger than for the case with 200 m spacing. Rates of seismic moment release for the 200 m fracture spacing during later stages of injection "catch up" with rates of seismic moment release for the 2 m fracture spacing. This is due to the fact that after the passage of the thermal front, a large part of the fault in the densely fractured carbonate reservoir is aseismic. **Figure 9C** presents estimates of cumulative seismic moment release for the 2 m fractures spacing in a low stress environment, taking into account parameter uncertainty for fault dip, stress drop, threshold f_{crit} and b-value (parameter ranges used are summarized in **Table 2**). Estimates for the total amount of seismic moment that is released vary between ~7 10^{13} Nm (P_{10}) and 8.7 10^{14} Nm (P_{90}). However we emphasize that the amount of seismic moment release on the fault is directly dependent on the choice of M_{min}. In the current analysis we choose a constant value of M_{min} = 0 in combination with a background seismicity rate of r_0 = 1 event per year, which means 1 tectonic event occurs per year with a magnitude of at least M = 0.

In practice, M_{min} and r_0 cannot be chosen independently and should be based on the characteristics of the seismic monitoring network (completeness) and the observed natural seismicity rates.

4 DISCUSSION

In current state-of-the-art, fault stability and seismicity potential is mostly assessed based on analysis of Coulomb stress changes and reactivated fault area. In our workflow, we adopt rate-and-state seismicity theory to assess changes in seismicity rates based on Coulomb stressing rates (Segall and Lu, 2015; Maurer and Segall, 2018) in our numerical scheme. We compare the seismic response of a fault during constant-rate injection in a highly fractured and a sparsely fractured carbonate reservoir. Our study indicates that even though the thermal loading is generally slow, stressing rates can still cause elevated seismicity rates during the approach and "passage" of the thermal front through the fault plane. Our models show that stressing rates and seismicity rates in densely fractured carbonates are highest, which can be explained by the propagation of a steep thermal front related to stronger and more localized cooling of the reservoir. This steep thermal front and localized strong cooling promotes arching of stresses and locally and temporarily high Coulomb stressing and seismicity rates. The occurrence of steep thermal fronts are not necessarily limited to densely fractured carbonates. Steep temperature gradients can also occur in more homogeneous porous sandstone reservoirs, specifically under low injection rates.

The effects of varying thermal loading rates in time and space on fault stability and seismic risk need to be further understood to enable long-term seismic risk assessment of injection operations. We note that we compare the "seismic footprint" in the densely fractured and less damaged carbonates under the assumption that the rate-and-state parameters for the fault in both types of reservoirs are similar. In reality, rate-and-state parameters for faults in different types of carbonate reservoirs may differ.

Another point of attention is the change of nucleation length (the minimum length of critically stressed fault required for seismic rupture to occur) during progressive cooling of the reservoir. As shown, the simultaneous increase of pressures and thermal contraction of the rocks during injection may lead to very low effective normal stresses on the fault plane. The nucleation length tends to increase with lowering normal effective stress. Also, in the current study stress drop was assumed constant, but in reality the stress drop will decrease as the normal stress decreases as they are linked through frictional weakening. This would lead to smaller events or even aseismic behavior. It needs to be further analyzed in what way low normal stresses influence the role of aseismic fault slip during progressive cooling of the rocks.

The dimensions of the fault segment that becomes critically stressed during operations form an important factor for the magnitude of seismic events in a low stress environment. At present, our method is based on the assumption that the rupture area of the seismic events is circular. More insight is needed on what aspect ratios of fault rupture can realistically occur in

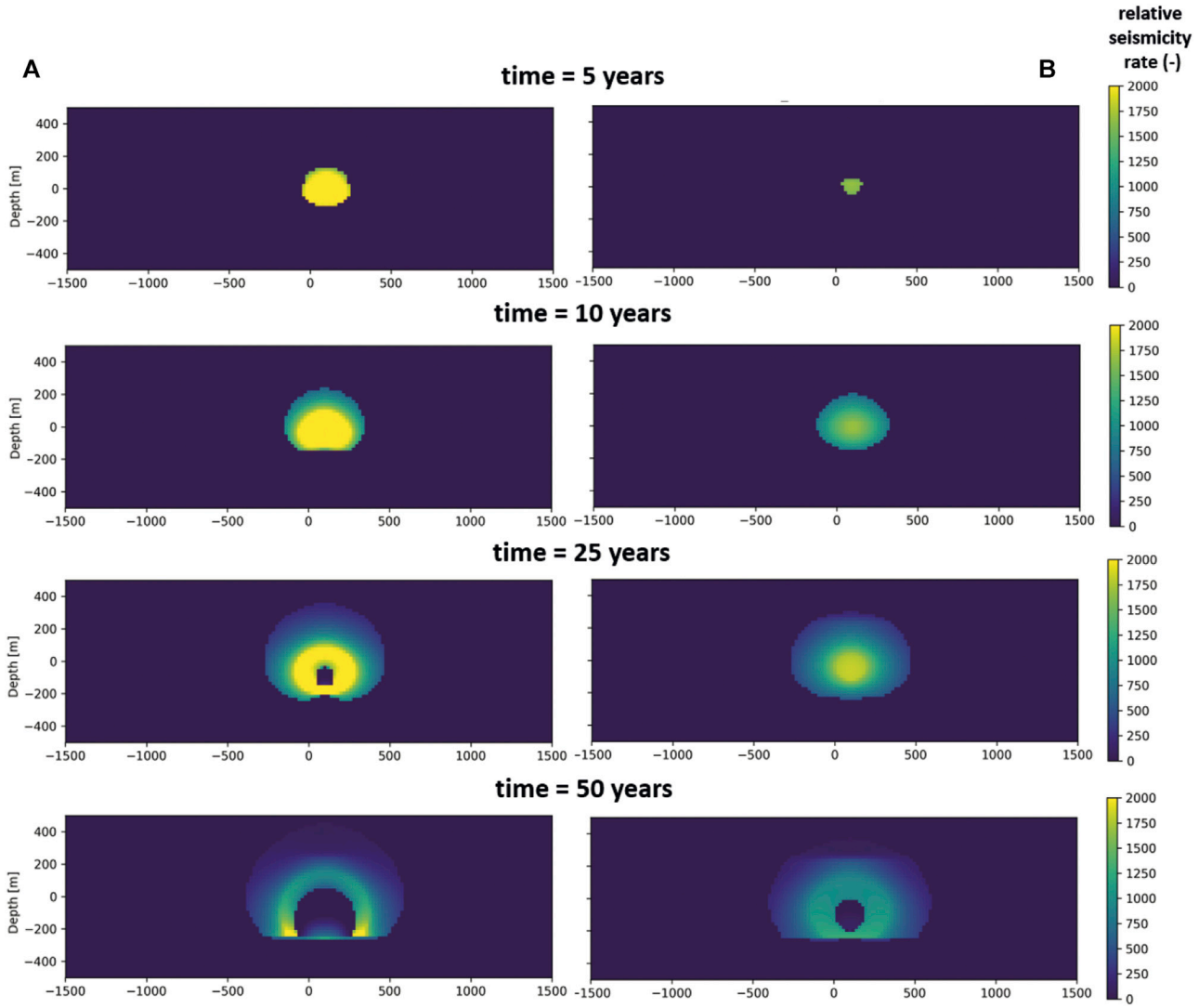

FIGURE 8 | Comparison of relative seismicity rates (*R*) at the fault plane in a low stress environment. Location of projected injection well at y = 0. Left **(A)** 2 m fracture spacing, right **(B)** 200 m fracture spacing. Mid-height reservoir at 0 m, units in depth (m) along dip.

elongated reservoirs that are potential targets for geothermal energy production, and what is the effect of reservoir confinement on frequency-magnitude distributions and seismic risks.

In our approach we aim to analyze the loading of a fault by the pressure and temperature changes in the surrounding medium. In our simplified model, we do not account for the presence of damage zones around faults with locally high fracture density, nor the effects of fault barriers and sealing faults. Anisotropies caused by the presence of high permeability flow paths in damage zones or low permeability fault cores impeding fault-perpendicular flow will affect the pressure and temperature fields, fault loading and seismicity (Wassing et al., 2021).

The workflow has been demonstrated for a synthetic injection case in a fractured carbonate reservoir. Seismicity is dependent on a large number of input parameters, most of which are poorly constrained before the start of the operations. As shown in **Figure 9**, parameter uncertainty has a large effect on the estimates of seismic moment release. As a result, at this stage the workflow can only be used for a relative "ranking" of reservoirs of different characteristics. Input data for models are generally poorly constrained, therefore models need to be calibrated and validated based on data from seismic monitoring networks. Parameter ranges and uncertainties need to be constrained based on information from (seismicity) monitoring: details on the specifics of the network used for seismic monitoring (e.g. level of completeness defining M_{min}), mapped total fault area and fault density, stress drops, seismicity rates and magnitudes recorded during the injection operations. In addition to monitoring during operations, the understanding of changes in seismicity rates and seismicity potential of the faults requires monitoring of background seismicity rates well in

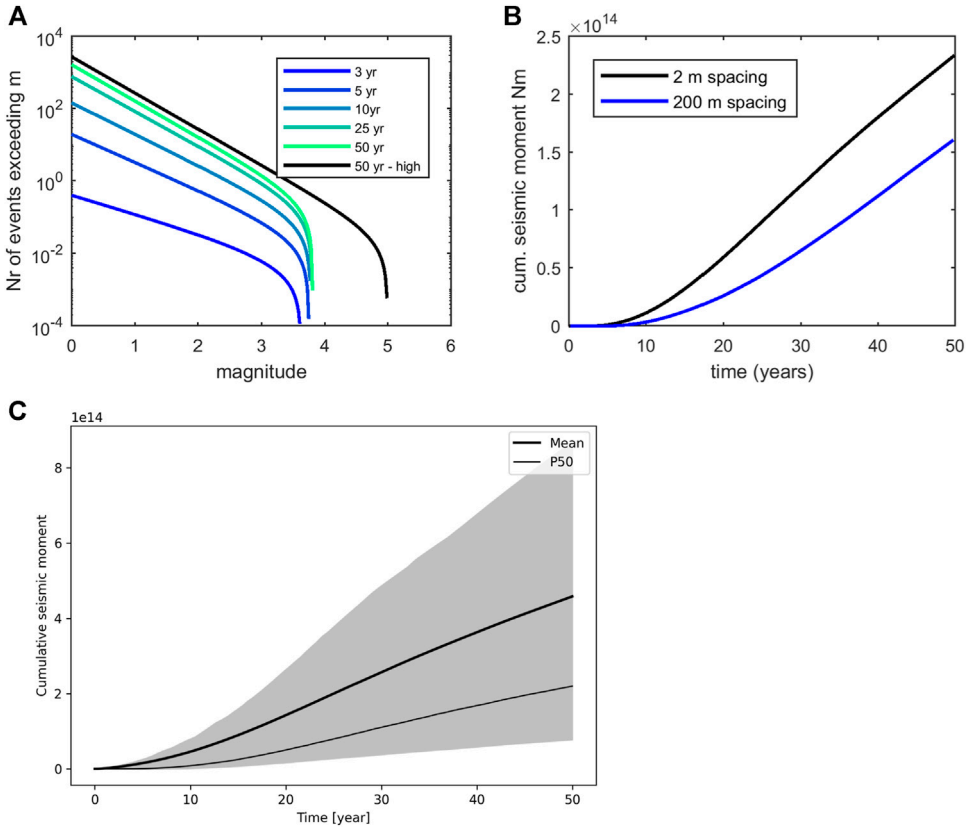

FIGURE 9 | (A) Temporal evolution of truncated Gutenberg-Richter frequency-magnitude distribution of seismic events for 2 m fracture distance (single realization). Vertical axis shows number of events $N(M \geq m)$, i.e. the expectation value for the number of events with a magnitude (M) larger than or equal to m. Blue to green colors represents FMD in low-stress environment at different times after onset of injection, see legend. Black line presents FMD after 50 years of injection for the high-stress environment. Input parameters for low-stress environment: M_{min} = 0, b-value = 1, $\Delta\sigma$ = 5.0 MPa. Input [M_{min}, M_{max}] = [0, 5.0] for high-stress environment. Dieterich seismicity parameters for this realization: A = 0.001, $\dot{\tau}_0$= 0.002 MPa/yr, and r_0 = 1; f_{crit} = 0.4. **(B)** Comparison of cumulative seismic moment release for both fracture distances in a low stress environment (single realization). Input parameters for this realization equal to values mentioned under **Figure 9A**. **(C)** Distribution of cumulative seismic moment release on the fault in densely fractured reservoir in a low stress environment, taking into account uncertainties in parameters. Shaded area shows cumulative seismic moment release between P10 and P90. Parameters fault dip (60°–80°), f_{crit} (0.3–0.5), $\Delta\sigma$ (0.1–10 MPa) and b-value (0.8–1.2). Values for other input parameters equal to values mentioned under **Figure 9A**.

advance of the injection operations. A closed loop of seismic monitoring (near-)real-time data-assimilation and model updating is considered crucial for a robust estimation and update of seismic risks during injection operations.

5 CONCLUSION

We built a workflow to assess the evolution of seismicity associated to injection of cold fluids in a single injector close to a fault. We employ the coupled numerical thermo-hydro-mechanical simulator of FLAC3D-TOUGHREACT to simulate the spatial and temporal evolution of pore pressures and temperatures in a fractured carbonate reservoir and the associated Coulomb stress changes on the fault. Adopting rate-and-state seismicity theory we assess induced seismicity rates from Coulomb stressing rates at the fault. Seismicity rates are then used to assess the evolution of seismicity in terms of the time-dependent frequency-magnitude distribution of seismic events. We compare the seismic response of a fault in a highly fractured and a sparsely fractured carbonate reservoir. We analyze the effect of tectonic regime and compare the seismic response in a low-stress and high-stress environment. From the above analysis, we draw the following conclusions:

- The seismic response of the fault, in terms of the timing of the peaks of elevated seismicity and total seismic moment release, depends on the fracture density, because this density affects the heat exchange rate between cold fluid in the fractures and the intermediate matrix and hence the temperature decrease in the bulk rock volume and thermo-elastic stress change.
- A dense fracture network results in a steeper thermal front which promotes stress arching, which leads to locally and temporarily high Coulomb stressing rates. The total seismic moment release is consequently largest for the densely spaced fracture network. Also, it occurs at an earlier stage of the injection period: the release is more

gradually spread in time and space for the widely spaced fracture network.

- Frequency-magnitude distributions and seismic moment release have been derived both for a low-stress subsurface and a tectonically active area with initially critically stressed faults. The evolution of seismicity in the low-stress environment depends on the dimensions of the fault area that is perturbed by the induced stress changes. The probability of larger, "felt", earthquakes and the associated seismic risk are thus reduced in low-stress environments.
- Injection of cold fluids into a competent rock like carbonate causes cooling of the reservoir and significant thermal stresses. Pore pressures reach steady-state conditions relatively quickly, but the evolution of seismicity during injection over the long-term is non-stationary: we observe an ongoing increase of the fault area that is critically stressed as the cooling front continues to propagate from the injection well into the reservoir. During later stages, models show the development of an aseismic area surrounded by an expanding ring of high Coulomb stressing and seismicity rates at the edge of the cooling zone. This ring can be related to the "passage" of the cooling front.
- Input data are generally poorly constrained, therefore models need to be calibrated and validated based on data from seismic monitoring networks. A closed loop of seismic monitoring (near-)real-time data-assimilation and model updating is considered crucial for a robust estimation and update of seismic risks during injection operations.

DATA AVAILABILITY STATEMENT

The original contributions presented in the study are included in the article/Supplementary Material, further inquiries can be directed to the corresponding author.

AUTHOR CONTRIBUTIONS

BW, TC, and SO contributed to conception and design of the study. BW, TC, EP, and SO performed the modelling and interpretation of results, BW, TC, LB, PF, and JW wrote sections of the manuscript. All authors contributed to manuscript revision, read, and approved the submitted version.

FUNDING

This project has been subsidized through the ERANET Cofund GEOTHERMICA (Project no. 731117), from the European Commission, Topsector Energy subsidy from the Ministry of Economic Affairs of the Netherlands, Federal Ministry for Economic Affairs and Energy of Germany and EUDP. The workflow was partially developed using funding from the European Union's Horizon 2020 research and innovation programme under grant agreement number 764531, project SECURe.

REFERENCES

Baisch, S., and Vörös, R. (2018). *Earthquakes Near the Californie Geothermal Site: August 2015 – November 2018. Prepared for Californie Lipzig Gielen Geothermie BVReport No. CLGG005*. Q-con GmbH.

Bouroullec, R., Nelskamp, S., Kloppenburg, A., Abdul Fattah, R., Foeken, J., Ten Veen, J., et al. (2019). Burial and Structural Analysis of the Dinantian Carbonates in the Dutch Subsurface. Report by SCAN. scan_dinantian_burial_and_structuration_report.pdf .

Buijze, L., van Bijsterveldt, L., Cremer, H., Paap, B., Veldkamp, H., Wassing, B. B., et al. (2019). Review of Induced Seismicity in Geothermal Systems Worldwide and Implications for Geothermal Systems in the Netherlands. *Neth. J. Geosciences* 98. doi:10.1017/njg.2019.6

Candela, T., Van Der Veer, E. F., and Fokker, P. A. (2018). On the importance of thermo-elastic stressing in injection-induced earthquakes. *Rock Mech. Rock Eng.* 51 (12), 3925–3936.

Candela, T., Osinga, S., Ampuero, J. P., Wassing, B., Pluymaekers, M., Fokker, P. A., et al. (2019). Depletion-Induced Seismicity at the Groningen Gas Field: Coulomb Rate-and-State Models Including Differential Compaction Effect. *J. Geophys. Res. Solid Earth* 124 (7), 7081–7104. doi:10.1029/2018JB016670.2019

Chen, J., Donald, J., and Huang, H., (2013). Determination of thermal Conductivity of Carbonate Cores. SPE 165460. doi:10.2118/165460-ms

Dieterich, J. (1994). A Constitutive Law for Rate of Earthquake Production and its Application to Earthquake Clustering. *J. Geophys. Res.* 99, 2601–2618. doi:10.1029/93jb02581

Gan, Q., and Elsworth, D. (2014). Thermal Drawdown and Late-stage Seismic-slip Fault Reactivation in Enhanced Geothermal Reservoirs. *J. Geophys. Res. Solid Earth* 119, 8936–8949. doi:10.1002/2014jb011323

Heimisson, E. R., and Segall, P. (2018). Constitutive Law for Earthquake Production Based on Rate-and-State Friction: Dieterich 1994 Revisited. *J. Geophys. Res. Solid Earth* 123, 4141–4156. doi:10.1029/2018JB015656

IEA (2020). *Geothermal*. Paris: IEA. available at: https://www.iea.org/reports/geothermal.

Jacquey, A. B., Cacace, M., Blöcher, G., and Scheck-Wenderoth, M. (2015). Numerical Investigation of Thermoelastic Effects on Fault Slip Tendency during Injection and Production of Geothermal Fluids. *Energ. Proced.* 76, 311–320. doi:10.1016/j.egypro.2015.07.868

Lipsey, L., Pluymaekers, M., Goldberg, T., Van Oversteeg, K., Ghazaryan, L., Cloetingh, S., et al. (2016). Numerical Modelling of thermal Convection in the Luttelgeest Carbonate Platform, the Netherlands. *Geothermics* 64, 135–151. doi:10.1016/j.geothermics.2016.05.002

Maurer, J., and Segall, P. (2018). Magnitudes of Induced Earthquakes in Low-Stress Environments. *Bull. Seismological Soc. America* 108 (3A), 1087–1106. doi:10.1785/0120170295

Pruess, K., Oldenburg, C., and Moridid, G. (2012). *TOUGH2 User's Guide*. Version 2.

Robertson, E. C. (1988). *Thermal Properties of Rocks*. Reston, VA: USGS Open-File Report, 88–441.

Rubin, A. M., and Ampuero, J.-P. (2007). Aftershock Asymmetry on a Bimaterial Interface. *J. Geophys. Res.* 112, BO5307. doi:10.1029/2006JB004337

Segall, P., and Lu, S. (2015). Injection-induced Seismicity: Poroelastic and Earthquake Nucleation Effects. *J. Geophys. Res. Solid Earth* 120, 5082–5103. doi:10.1002/2015jb012060

State Supervision of Mines (2019). *Analyse onderbouwing CLG aardwarmte en seismiciteit*. The Hague: Technical Report , Staatstoezicht op de Mijnen (State Supervision of Mines).

Taron, J., and Elsworth, D. (2010). Coupled Mechanical and Chemical Processes in Engineered Geothermal Reservoirs with Dynamic Permeability. *Int. J. Rock Mech. Mining Sci.* 47, 1339–1348. doi:10.1016/j.ijrmms.2010.08.021

Ter Heege, J., van BijsterveldtWassing, L. B., Osinga, S., Paap, B., and Kraaijpoel, D. (2020). *Induced Seismicicity Potential for Geothermal Projects Targeting Dinantian Carbonates in the Netherlands*. Utrecht: Final report by SCAN.

Van Wees, J-D., Kahrobaei, S., Osinga, S., Wassing, B., Buijze, L., Candela, T., et al. (2019a). *3D Models for Stress Changes and Seismic hazard Assessment in Geothermal Doublet Systems in the Netherlands*. Reykjavik, Iceland: World Geothermal Congress 2020. April 26-May 2, 2020; submitted.

Van Wees, J. D., Veldkamp, H., Brunner, L., Vrijlandt, M., De Jong, S., Heijnen, N., et al. (2020). Accelerating Geothermal Development with a Play-Based Portfolio Approach. *Neth. J. Geosciences* 99. doi:10.1017/njg.2020.4

Vöros, R., and Baisch, S. (2019). *Seismic hazard Assessment for the CLG-Geothermal System – Study Update March 2019*, Report No. CLG006. Q-con GmbH.

Wassing, B. B. T., Van Wees, J. D., and Fokker, P. A. (2014). Coupled continuum modeling of fracture reactivation and induced seismicity during enhanced geothermal operations. *Geothermics* 52, 153–164.

Wassing, B. B. T., Gan, Q., Candela, T., and Fokker, P. A. (2021). Effects of Fault Transmissivity on the Potential of Fault Reactivation and Induced Seismicity: Implications for Understanding Induced Seismicity at Pohang EGS. *Geothermics* 91, 101976. doi:10.1016/j.geothermics.2020.101976

Conflict of Interest: The authors declare that the research was conducted in the absence of any commercial or financial relationships that could be construed as a potential conflict of interest.

frontiers in Earth Science

ORIGINAL RESEARCH
published: 11 November 2021
doi: 10.3389/feart.2021.685300

Practical Issues in Monitoring a Hydrocarbon Cultivation Activity in Italy: The Pilot Project at the Cavone Oil Field

Lucia Zaccarelli[1], Mario Anselmi[2], Maurizio Vassallo[3], Irene Munafò[3], Licia Faenza[1,2], Laura Sandri[1], Alexander Garcia[1], Marco Polcari[2], Giuseppe Pezzo[2], Enrico Serpelloni[1,2], Letizia Anderlini[1], Maddalena Errico[1], Irene Molinari[1], Giampaolo Zerbinato[1] and Andrea Morelli[1]*

[1]*Istituto Nazionale di Geofisica e Vulcanologia, Sezione di Bologna, Bologna, Italy,* [2]*Istituto Nazionale di Geofisica e Vulcanologia, Osservatorio Nazionale Terremoti, Roma, Italy,* [3]*Istituto Nazionale di Geofisica e Vulcanologia, Sezione Roma 1, Roma, Italy*

OPEN ACCESS

Edited by:
Rebecca M. Harrington, Ruhr University Bochum, Germany

Reviewed by:
Birendra Jha, University of Southern California, United States
Maria Mesimeri, ETH Zurich, Switzerland

***Correspondence:**
Lucia Zaccarelli
lucia.zaccarelli@ingv.it

Specialty section:
This article was submitted to Solid Earth Geophysics, a section of the journal Frontiers in Earth Science

Received: *24 March 2021*
Accepted: *21 October 2021*
Published: *11 November 2021*

Citation:
Zaccarelli L, Anselmi M, Vassallo M, Munafò I, Faenza L, Sandri L, Garcia A, Polcari M, Pezzo G, Serpelloni E, Anderlini L, Errico M, Molinari I, Zerbinato G and Morelli A (2021) Practical Issues in Monitoring a Hydrocarbon Cultivation Activity in Italy: The Pilot Project at the Cavone Oil Field. Front. Earth Sci. 9:685300. doi: 10.3389/feart.2021.685300

In this paper we describe the results of an experimental implementation of the recent guidelines issued by the Italian regulatory body for monitoring hydrocarbon production activities. In particular, we report about the pilot study on seismic, deformation, and pore pressure monitoring of the Mirandola hydrocarbon cultivation facility in Northern Italy. This site hosts the Cavone oil field that was speculated of possibly influencing the 2012 M_L 5.8 Mirandola earthquake source. According to the guidelines, the monitoring center should analyse geophysical measurements related to seismicity, crustal deformation and pore pressure in quasi real-time (within 24–48 h). A traffic light system would then be used to regulate underground operations in case of detecting significant earthquakes (i.e., events with size and location included in critical ranges). For these 2-year period of guidelines experimentation, we analysed all different kinds of available data, and we tested the existence of possible relationship between their temporal trends. Despite the short time window and the scarce quantity of data collected, we performed the required analysis and extracted as much meaningful and statistically reliable information from the data. We discuss here the most important observations drawn from the monitoring results, and highlight the lessons learned by describing practical issues and limitations that we have encountered in carrying out the tasks as defined in the guidelines. Our main goal is to contribute to the discussion about how to better monitor the geophysical impact of this kind of anthropogenic activity. We point out the importance of a wider seismic network but, mostly, of borehole sensors to improve microseismic detection capabilities. Moreover, the lack of an assessment of background seismicity in an unperturbed situation -due to long life extraction activities- makes it difficult to get a proper picture of natural background seismic activity, which would be instead an essential reference information for a tectonically-active regions, such as Northern Italy.

Keywords: Italian guidelines for monitoring industrial activities, induced seismicity, pore pressure monitoring, deformation monitoring, seismic monitoring

1 INTRODUCTION

On May 20, 2012 a M_L 5.9 earthquake struck the Po plain in northern Italy, and 9 days after, a M_L 5.8 seismic event occurred at a distance of about 16 km. These two mainshocks triggered a strong aftershock sequence (the Emilia seismic sequence) that lasted several months (Malagnini et al., 2012; Govoni et al., 2014). Due to the epicentral proximity of a few kilometres of the second major seismic event to the Mirandola-Cavone hydrocarbon cultivation field (see also **Figure 1**), a scientific commission (named ICHESE) was charged with investigating a possible relationship between anthropic and seismic activities. In fact, at that time, injection of production water was already underway in this oil field. The conclusions of the ICHESE commission suggested that "it is highly unlikely that the activities of hydrocarbon exploitation at Mirandola have produced sufficient stress change to induce a seismic event in the source area of the 2012 mainshocks"; still, they stated that "the current state of knowledge and all the processed and interpreted information does not allow the ruling out of the possibility that the actions involved in hydrocarbon exploitation in the Mirandola field may have contributed to trigger the Emilia seismic activity". Since then, an extensive debate has started both inside the scientific community and among the governmental authorities. Among activities carried on within a joint initiative among industrial operator and regulator authorities (Cavone Laboratory, www.labcavone.it), Juanes et al. (2016) indicated—by means of coupled geomechanic and fluidodynamic modelling of the pressure changes caused by extraction and injection operation at the M_L 5.8 fault—that the industrial activity did not appear able to provoke significant stress change on the earthquake source. Other scientists have tested the low probability that human activity could have triggered the second mainshock of the sequence (Cesca et al., 2013; Pezzo et al., 2018). At the same time the governmental authorities have instituted a working group of experts that could list the guidelines for monitoring seismicity, deformation and pore pressure changes in exploitation areas (Dialuce et al., 2014). The new guidelines highlighted a double action. On the one hand, they have indicated the need to identify an external institution not directly or indirectly involved in hydrocarbon cultivation, gas storage, or geothermal activity, taking on industrial activity monitoring. The second action concerns industries and the need to update and improve their monitoring networks. The INGV has been charged with monitoring three areas of industrial activity (the Minerbio gas storage and the oil fields of Cavone and Val d'Agri: Braun et al., 2020; Carannante et al., 2020) during a 2-year experimental phase. Many other authors reported about the monitoring of industrial activity around the world (Mordret et al., 2014; Priolo et al., 2015, describe analysis of data from very dense *ad-hoc* networks), some of them reporting about clear episodes of induced seismicity (Maury et al., 1992; Keranen et al., 2013; van Thienen-Visser and Breunese, 2015, respectively for the Groningen gas field in the Nederlands, the Wilzetta oil field in Oklahoma, United States, and the Lacq gas field in France, among the others), some others developing models for computing stress changes due to well operations on the nearby faults (Zhao and Jha, 2019). This paper describes the work done in the first attempt of guidelines' application at the Cavone oil field during 2018 and 2019. The first year of guidelines' experimental phase has been devoted to the meetings between the different party representatives and to set the basis of the monitoring work in practice: writing the agreement, defining the terms for data exchange, deciding the monitoring network improvement. At that time, in fact, the seismic stations operating around the Cavone oil center were four 3-component velocimeters, working in triggering mode with DCF synchronisation. Moreover, no GPS stations were installed in the area. In light of this conditions, the first action towards reliably monitoring the Cavone oil field was establishing an appropriate seismic and GPS network. Thus the operator decided to upgrade the existing seismic network to get continuous recordings synchronised via GPS, and to install a GPS station on December 18, 2018. These two improvements do not fully satisfy the seismic and geodetic monitoring network requirements, as detailed in the guidelines. Still, they represented the first step in that direction, following the gradual improvement and the enhancement of the available instrumentation principles, as defined in the same document (Dialuce et al., 2014).

In presenting the 2-year pilot application of the Italian guidelines to the Cavone case, we structure the paper describing the oil field firstly, and then separately outlining the monitoring networks and the specific analysis on microseismicity, ground deformation, and pore pressure data. Finally, we will devote a section to further discussion regarding the tasks assumed by a research institution in monitoring a hydrocarbon deposit. We will highlight strengths and achievements and possible improvements that could be applied both to the general guidelines and their specific implementation, as in the Cavone area of analysis. We aim to contribute to the general discussion on the monitoring of underground energy technologies, drawing from our experience.

2 THE CAVONE OIL FIELD

The NE-verging Apennines belt developed during Neogene and Quaternary in the framework of the collision between the European continental margin and the Adria microplate. The fold-and-thrust system is buried by thick Quaternary sediments of the Po plain (Malinverno and Ryan, 1986; Doglioni et al., 1999). The Mirandola anticline belongs to the Ferrara arc (Scrocca et al., 2007; Carminati et al., 2010; Govoni et al., 2014) and is located in the Apennines foreland. In the Mirandola area correspondence, the Apennines belt front has a roughly E-W trending (Pieri, 1983; Burrato et al., 2003; **Figure 1**). The Cavone oil field is set in correspondence of a "structural high" of the Mirandola anticline. Tectonic structures in this area are dominated by deep-seated reverse faults or blind thrusts (Ciaccio and Chiarabba, 2002). This structural style is evident in the Cavone oilfield area: in this segment the Mirandola thrust

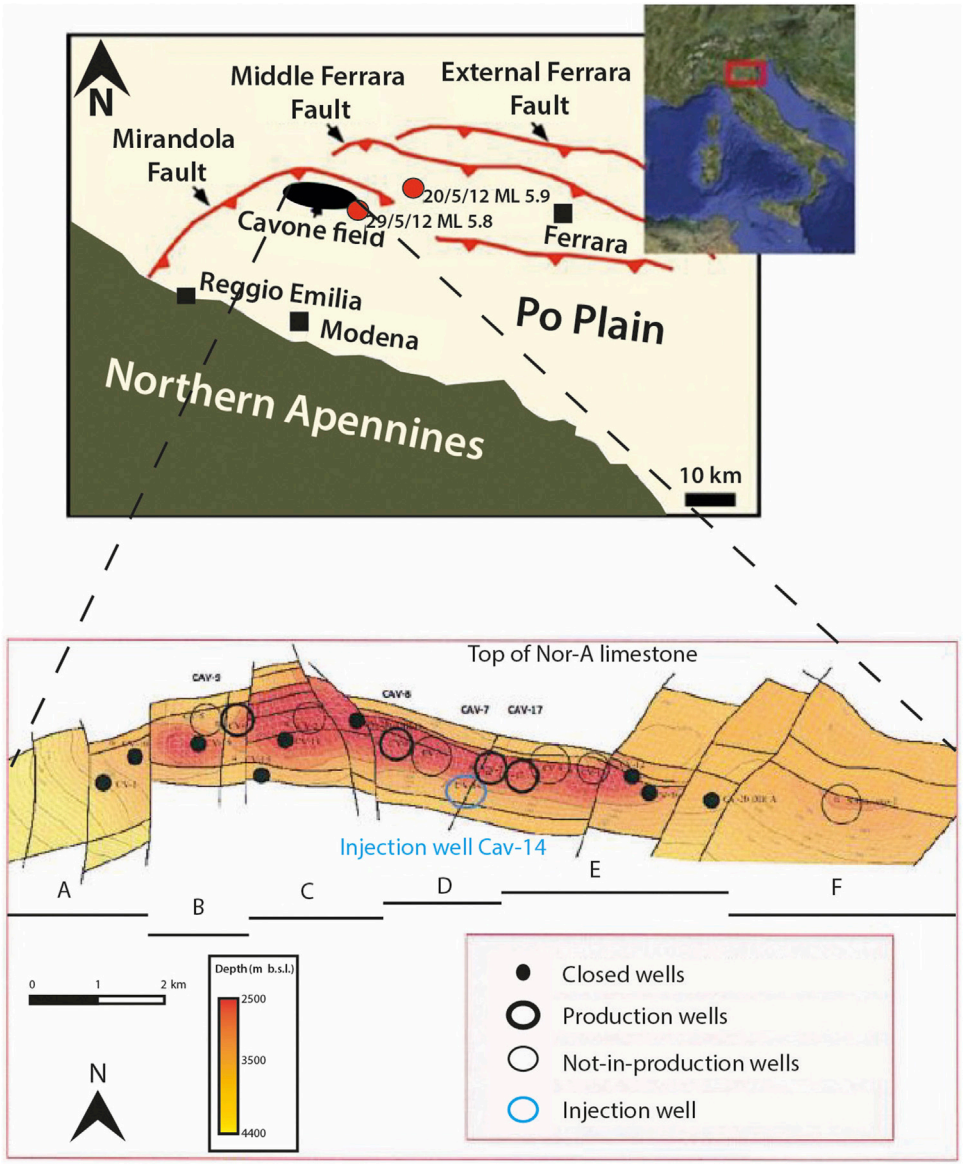

FIGURE 1 | Top panel: regional map showing location of the Cavone oil field (the inset highlights the area of interest along the Italian peninsula), epicentral locations of the two 2012 Emilia mainshocks (red circles), and principal thrust faults from Pieri (1983). Bottom panel (Società Padana Energia personal communication, 2019): letters (A–F) indicate the different blocks of the oil field, identified by both the tear faults (have an almost N-S strike) and the topography of the Top of Noriglio-A (Nor-A) formation.

(that hosted the 29 May M_L 5.8 s main-shock of the 2012 Emilia sequence) has a roughly WE strike, is south dipping, and superimposed by a north-vergent fault-propagation fold (Suppe and Medwedeff, 1990; Carminati and Vadacca, 2010). The main structural lineaments are sketched in the map included in the top panel of the **Figure 1**. The Cavone oil field is placed 25 km north of Modena (Northern Italy), in the exploitation permit named "Mirandola". Its area is about 15 km^2, and the productive reservoir datum is 2,900 m at depth, mainly hosted inside a carbonatic sequence. The discovering of the oil field happened in 1973 after a deep exploration of the Ferrara arc's more internal front and the positive feedback obtained by the *Cavone1* well. The oil field is segmented by a set of N-S tear faults that divided the anticline, perpendicularly to its strike, in different domains (defined blocks A,B,C,D,E, and F on **Figure 1**). The fluid extracted from the reservoir is a mixture of oil, methane gas, and water. Two nonproductive wells (*Cavone5* e *Cavone14*) were dedicated to re-injection of the produced waters, even though in practice only the *Cavone14* (placed at the boundary between D and E block) is used at this scope since January 1993. The injection is performed at a depth range from 3,302 to 3,367 m, deeper than the "water-oil contact" (3,130 m deep) starting level in the Noriglio-B limestone formation, beneath the Noriglio-A limestone formation (ICHESE, 2014).

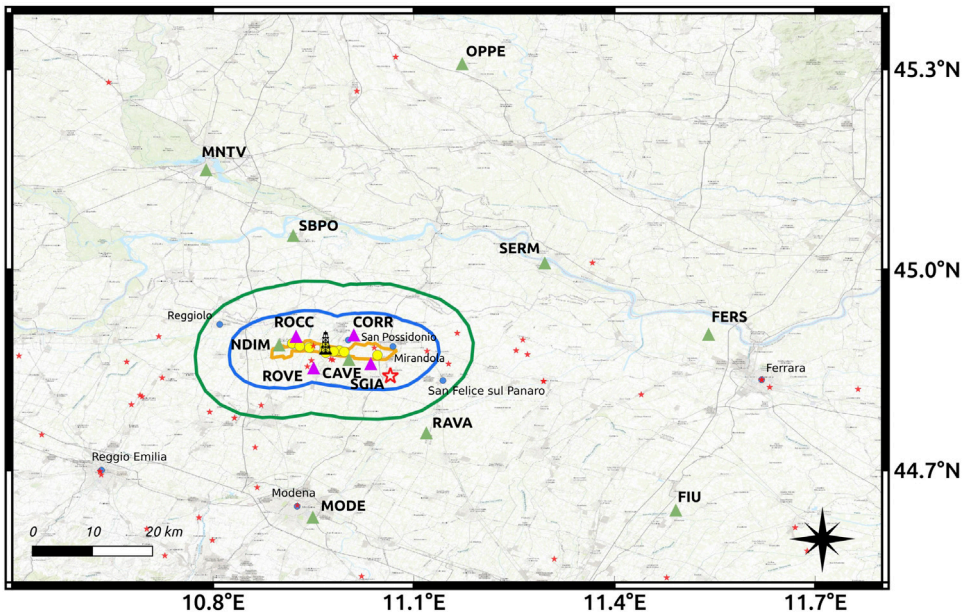

FIGURE 2 | Map of the Cavone oil field with local VO seismic stations (purple triangles) and Italian Seismic Network IV station (green triangles) locations. The yellow circles indicate the approximate positions of the extraction wells, while the injection one is sketched in black. The orange line delineates the reservoir projection on the surface. The blue and green lines are contouring the domains of interest ID and ED respectively (see text for more details). The red stars show the locations of the historical earthquakes with $M_W \geq 4.5$, occurred in the area, with the bigger one highlighting that on the 29 May, 2012, as from Rovida et al. (2020).

3 SEISMIC MONITORING

The guidelines define two volumes of interest around the reservoir where the monitoring efforts have to be addressed: an Internal Domain (ID) where it is plausible that induced seismicity may occur, and an Extended Domain (ED), surrounding the ID, useful for better contextualisation of the observed seismicity. In the case of hydrocarbon cultivation with re-injection of the produced water inside the reservoir (the Cavone case) the ID is the volume that includes the mineralised zone, reaches the surface, and extends for further 5 km from the border and bottom of the reservoir; while the ED is the volume range that extends from the ID for further 5 km in all directions (Dialuce et al., 2014; see **Figure 2**).

The Cavone seismic network in the current configuration has been installed in November, 1990, it consists of four stations, whose name and coordinates are listed in **Supplementary Table S1** and mapped in **Figure 2** (purple triangles). All stations are equipped with 3-component Lennartz Le-3D/1s sensors, and were firstly coupled with Lennartz MARS88 (Lennartz Electronic GmbH), they were working in triggering mode and synchronised through DCF-77 radio signal until December 18, 2018. Subsequently, the MARS88 have been substituted with Dymas24 by Sara Electronic Instruments S.r.l., which allows a continuous acquisition and a GPS synchronisation, thus reaching the current standard level for a seismic network. To ensure a unique data flux the local network have been registered at the International Federation of the Digital Seismic Networks as VO, with station names CORR, ROCC, ROVE e SGIA that have been registered at the International Registry of Seismograph Stations.

The sampling frequency is now (since the network improvement of December 2018) 200 Hz, that allows a signal band of 1–80 Hz. In the guidelines' experimental period, the local seismic network has been enhanced with the 10 stations of the Italian Seismic Network (network code IV) in a radius of 50 km from San Possidonio (the village with a central location with respect to the reservoir elongation), shown as green triangles in the map of **Figure 2** and listed in **Supplementary Table S2**. INGV manages these latter stations, and all technical information are reported in the network webpage (INGV Seismological Data Centre, 2006). The integrated seismic network includes thus 14 stations, six of them are located close to each other inside the reservoir projection at the surface, one (RAVA) is just outside all detection domains, while the other seven are quite far away.

3.1 Seismic Network Performance Evaluation

Before starting the monitoring phase, we evaluate the seismic network's theoretical performance in terms of detection threshold, i.e., the minimum magnitude event that has a 90% probability of being identified and accurately localized using the data acquired by the network stations (Ringdal, 1975). For estimating the network detection threshold we followed a mixed indirect approach based on the comparison of the real noise level recorded at the seismic stations with the theoretical spectra associated to the rupture models for small earthquakes (McNamara et al., 2004; Marzorati and Bindi, 2006; Vassallo et al., 2012).

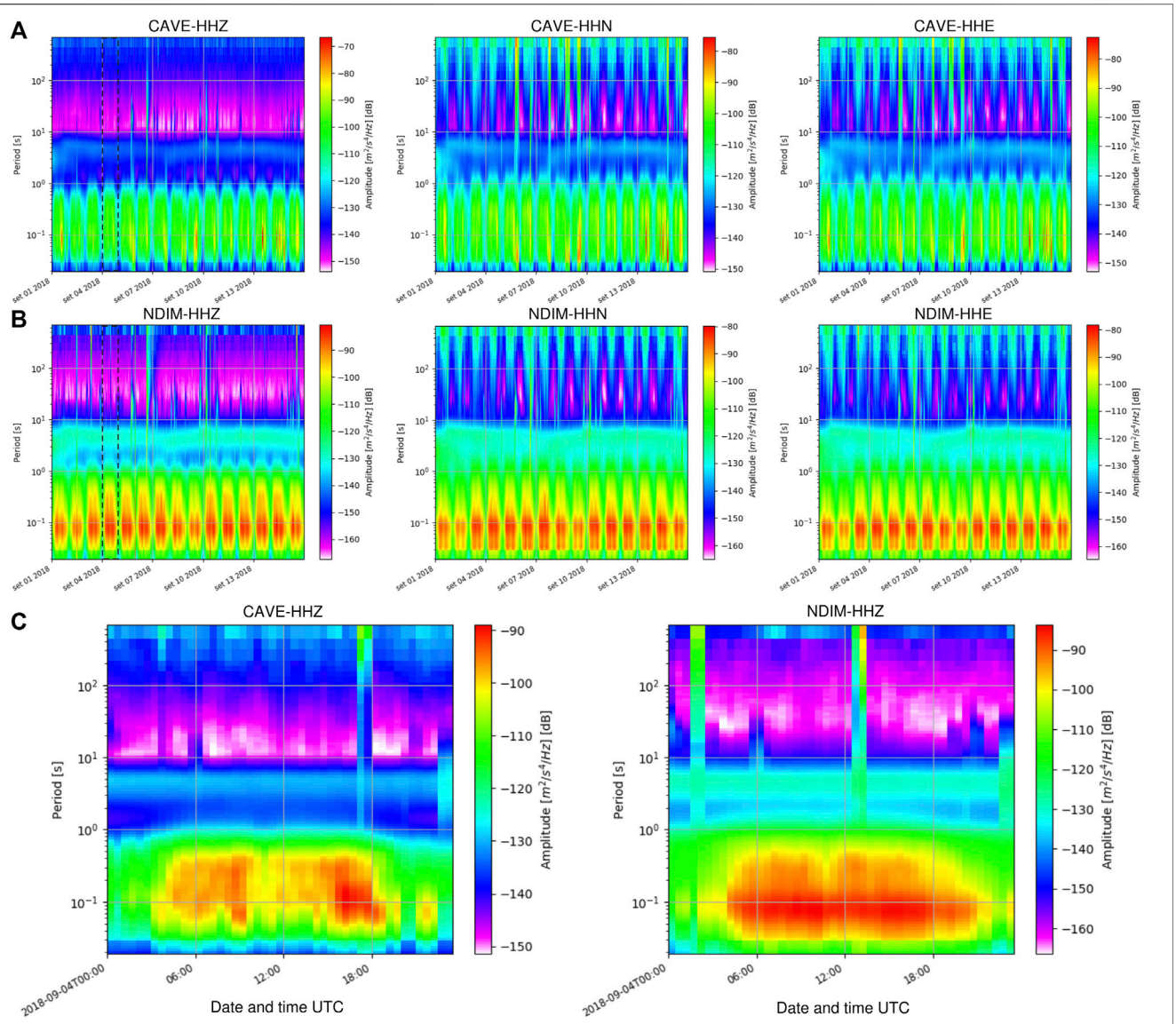

FIGURE 3 | Spectrograms for the three components of CAVE **(A)** and NDIM **(B)** stations using the data acquired from 1 to 15 September, 2018. In **(C)** is a zoom on the day of 4 September for both stations vertical components, to emphasise the daytime increase in seismic noise levels at periods less than 1 s. The selected day is indicated by the dashed vertical lines in the HHZ spectrograms of panels **(A)** and **(B)**. The color scale represents the PSD value in dB with respect to 1 m/s and is optimised for each sub-figure.

The Cavone oil field area's noise level, has been evaluated on the basis of 15 days of seismic signal acquired between 1 and 15 September, 2018 at NDIM and CAVE stations. These two IV stations (INGV Seismological Data Centre, 2006), are the closest to the Cavone oil field (a few kilometres away from the reservoir, **Figure 2**), and are equipped with broad band velocimeters. Unlike the monitoring stations of the local VO network, they were continuously recording at that time. We extended the results of the noise analysis produced for NDIM and CAVE to the local VO seismic stations for the above mentioned reasons, and only afterwards, with the continuous data from the VO stations, we could verify that the seismic noise recordings of all these stations are very similar (see **Supplementary Figures S1, S2** for comparison). We analysed the three components continuous recordings for characterising their noise levels in terms of Power Spectral Density (PSD, Peterson, 1993). We computed the PSD on all 1-h segments, sliding half an hour, composing the continuous recording of each station component, thus enhancing the noise sources' spectral characteristics (Peterson, 1993). **Figure 3** shows the spectrograms obtained starting from the PSDs calculated for the two stations. Seismic noise shows a clear day-night variation with noise levels that increase during the day and decrease at night. This characteristic appears clearly at low periods (less than 1 s, see panel c in **Figure 3**) for both stations at all components. **Figure 4** shows the temporal variations of the seismic noise calculated in three different period ranges:

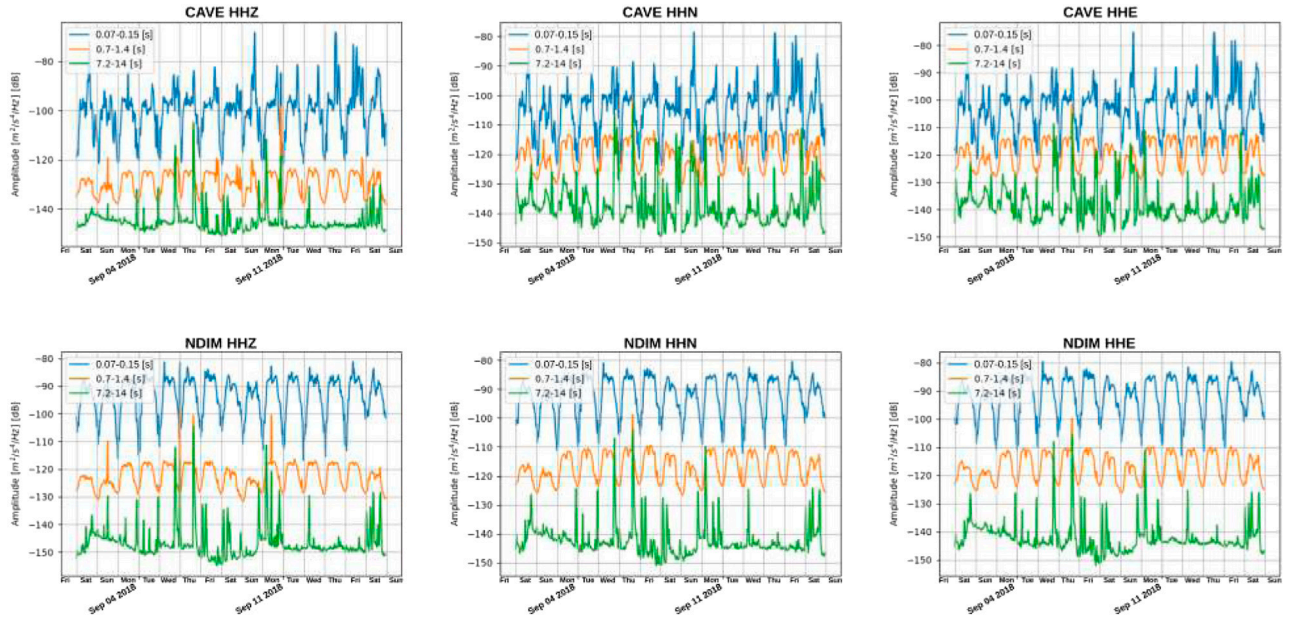

FIGURE 4 | Time variability of the noise levels (PSD in dB) averaged in three different period bands (0.07 ÷ 0.15 s; 0.7 ÷ 1.4 s; 7.2 ÷ 14 s) for the three components of CAVE and NDIM stations using the data recorded between 1 and 15 September, 2018. In each sub-plot, the corresponding days of the week are shown on the abscissa axis in order to emphasise the diurnal variations of the noise level and the variations during the weekends.

0.07 ÷ 0.15 s; 0.7 ÷ 1.4 s; 7.2 ÷ 14 s. The seismic noise recorded at CAVE at low period (0.07÷0.15 s) decreases by about 20–25 dB during night compared to the daytime levels. Similar variations are also observed for the NDIM station where a decrease in noise levels by about 25–30 dB is observed during the nights for all components. Also in the intermediate period band (0.7÷1.4 s) there is an important but more contained day-night variation compared to the previous band. In effect, in the latter band, the noise level decreases by about 10–15 dB at night for both CAVE and NDIM stations. Finally, at high periods, between 7.2÷14 s, there are no important variations attributable to the day-night transition. Furthermore, the spectrograms and the PSD temporal variations (**Figures 3**, **4**) highlight a decrease of noise level in the two period bands 0.07 ÷ 0.15 s and 0.7÷1.4 s during the weekends (days 1, 2, 8, 9, and 15 of September, 2018). Both the observed day-night variations and the noise decrease during the weekends suggest that anthropogenic noise is among the main source of low period/high frequency noise (periods less than 1.4 s, frequencies higher than 0.7 Hz) recorded at these stations. Through a statistical analysis carried out on all the PSD curves computed for the different hours, we determined the PSD curves relating to the 90-th percentile for each component. These curves were considered as reference levels of towing to the stations to derive the entire network's detection thresholds. For the local VO network (CORR, ROC, ROVE, SGIA), we adopted the 90-th percentile curves of the CAVE station as representative. This station was chosen as a reference since, similarly to the Cavone oil field stations, it is positioned further away from anthropogenic noise sources compared to NDIM (which is located in the urban area of the municipality of Novi di Modena, Modena province).

We used the Brune source model in a homogeneous medium to represent the P and S amplitude spectra of the recorded velocity associated to an earthquake of fixed seismic moment and recorded at a fixed hypocentral distance. The Brune spectrum is computed after defining the seismic source and propagation medium parameters such as stress-drop, density, P and S waves velocities, anelastic attenuation. For the investigated area, we used: stress-drop $\Delta\sigma$ = 1.0 MPa, attenuation t^* = 0.08 s (reduced time) (Carannante et al., 2020), Vp = 4,400 m/s, Vs = 2,500 m/s, density ρ = 2.4 g/cm^3 (Malagnini et al., 2012; Milana et al., 2014). We also need to set the average depth of the seismic events recorded in this area, from the seismicity analysis results reported in the following **Section 3.2**, we fixed this value to 6 km. In this way, for a single station the P and S waves' theoretical amplitude depends on the hypocentral distance, i.e., on the earthquake location. To investigate the areal dependence of the source signal, we defined a regular grid with cell size of 1 × 1 km^2, then we moved the epicentral location along each node of the grid, by setting its depth at 6 km. For each node, we then computed the smallest amplitude associated with a seismic event recorded by at least five stations with a signal-to-noise ratio higher than 5, and from that amplitude value we could then retrieve the seismic moment that could generate it, i.e., the M_w associated to the smallest detectable event. The 90-th percentile curves in 1–30 Hz band for vertical and horizontals components are used for computing the signal-to-noise ratio and for determining the detection threshold map for P and S waves. The thresholds that were chosen for the signal-to-noise ratio and

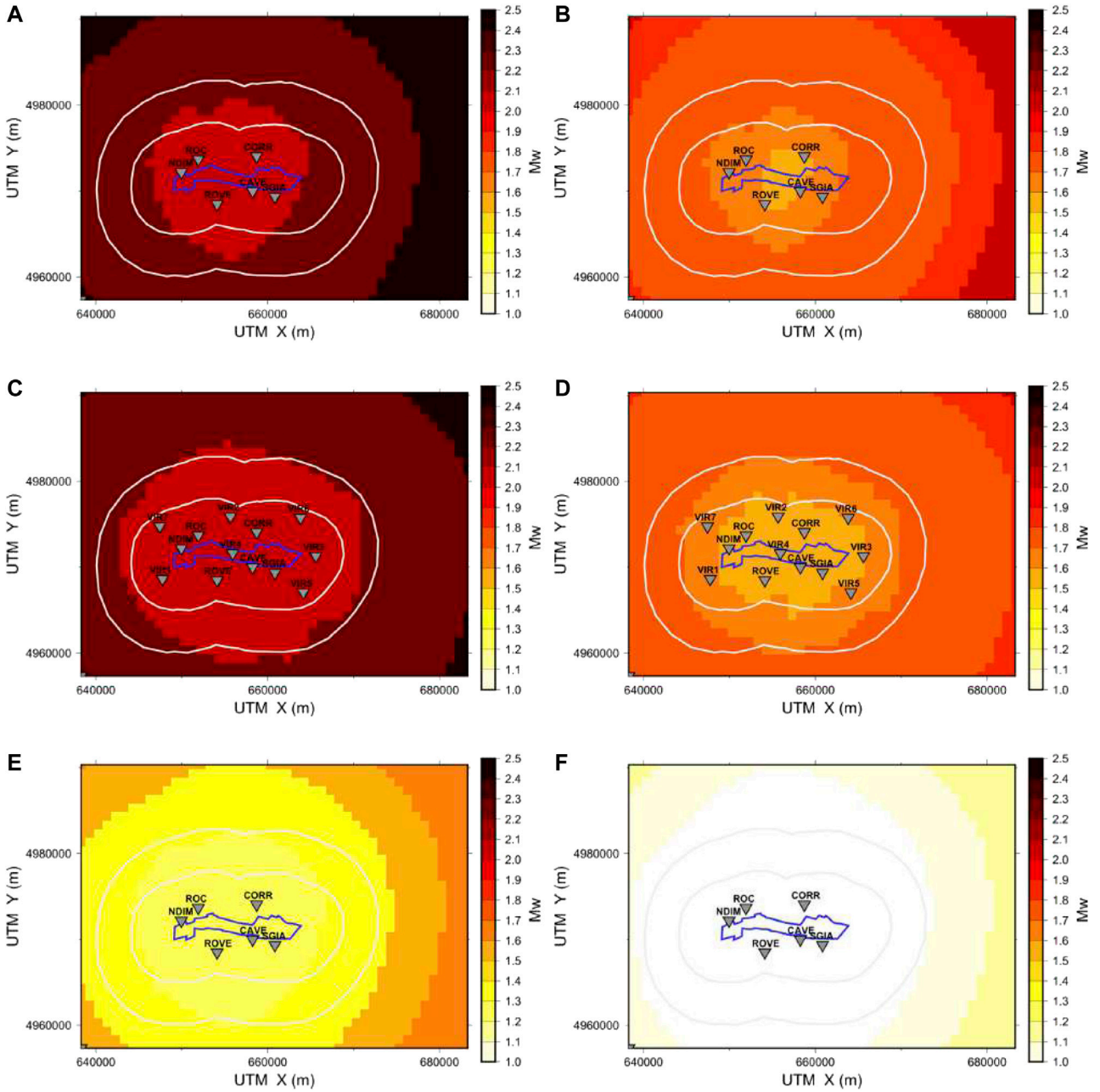

FIGURE 5 | Detection threshold maps for the Cavone oil field area for P and S waves (left and right columns respectively). Panels **(A)** and **(B)** report the results for the actual network composed by four VO and two IV stations. The detection thresholds in **(C)** and **(D)** are computed for the improved network composed by the six actual stations and seven virtual stations (VIR). The maps in **(E)** and **(F)** show the detection thresholds obtained assuming the actual six seismic stations as placed in boreholes at a depth of about 120 m, and considering a reduction in PSD levels (in 1–30 Hz range) equal to 25 dB for each station and component.

for the number of stations ensure an accurate estimation of both location and magnitude (Vassallo et al., 2012). **Figures 5A,B** show the detection thresholds maps determined for the Cavone oil field for P and S waves. The smallest magnitudes detectable at all points inside both ID and ED are 2.1 for P waves and 1.6 for S waves. However, the maps show significant spatial variations of about 0.2–0.3 units in M_W which are mainly attributable to the network geometry since for threshold evaluation we used noise levels equals for all the involved stations except for NDIM. Beyond the scientific interest in testing the seismic network's possible performance, the guidelines (Dialuce et al., 2014) require minimum requisite in terms of seismic network performance. In particular, the seismic network should "in the internal detection domain, detect and locate earthquakes starting from local

TABLE 1 | List of the 49 earthquakes analysed in during 2018–2019. The date is expressed in year-month-day, then we report location estimates (longitude, latitude and depths in km), M_W, PGA in g percentages and PGV in cm/s. The last column report the domain where the hypocenter location falls (ID, ED, or none of the two).

N	Date	Longitude	Latitude	Depth	M_W	PGA	PGV	Domain
	yyyy-mo-dd hh:mi	°E	°N	km		%g	cm/s	
1	2018-03-03 20:12	11.1507	44.8317	7.82	2.2	0.020	0.006	ED
2	2018-03-04 14:37	11.0108	44.887	5.68	2.3	0.020	0.010	ID
3	2018-03-07 15:10	11.1457	44.8448	6.86	2.3	0.102	0.020	ED
4	2018-05-27 03:31	10.9633	44.8867	5.11	2.0	0.010	0.003	ID
5	2018-08-03 21:14	10.9485	44.8915	5.44	2.0	0.082	0.007	ID
6	2018-08-05 04:07	10.9523	44.8928	4.11	2.0	0.010	0.002	ID
7	2018-08-27 04:08	10.9972	44.8845	5.93	2.0	0.031	0.006	ID
8	2018-09-12 13:29	10.974	44.8902	4.7	2.6	0.153	0.040	ID
9	2018-09-15 20:00	10.9847	44.8918	5.54	2.1	0.102	0.010	ID
10	2018-10-23 14:11	11.0147	44.8825	4.46	2.1	0.306	0.100	ID
11	2018-11-24 02:04	10.9242	44.8932	5.47	2.0	0.091	0.010	ID
12	2018-11-25 23:32	11.0232	44.8327	10.35	2.2	0.051	0.050	ED
13	2018-12-11 19:24	11.0733	44.8943	6.98	2.3	0.041	0.040	ID
14	2019-01-10 23:53	10.9607	44.9827	0.27	1.3	0.008	0.001	ID
15	2019-01-17 01:03	10.9275	44.8865	6.89	1.7	0.008	0.001	ID
16	2019-01-19 10:16	11.0187	44,9605	1.79	1,3	0.005	0.001	ED
17	2019-03-03 15:21	11.0512	44.878	5.39	2.0	0.076	0.013	ID
18	2019-03-03 16:08	11.0398	44.856	5.3	2.1	0.010	0.001	ID
19	2019-03-07 02:30	11.0327	44.8617	5.94	1.8	0.036	0.005	ID
20	2019-03-13 14:22	11.2145	44.8447	18.21	2.8	0.086	0.020	none
21	2019-03-23 03:53	10.977	44.8807	5.88	1.4	0.006	0.001	ID
22	2019-03-27 16:36	10.594	44.8362	20.25	2.3	0.011	0.003	none
23	2019-05-04 23:01	11.238	44.8582	17.1	2.4	0.011	0.003	none
24	2019-05-12 15:24	11.1037	44.8957	10.75	1.9	0.014	0.002	ED
25	2019-05-28 20:07	11.0153	44.8805	5.73	1.8	0.046	0.006	ID
26	2019-06-16 10:49	10.9988	44.8593	7.11	1.8	0.019	0.003	ID
27	2019-06-18 00:57	11.0137	44.8582	7.65	1.8	0.016	0.002	ID
28	2019-06-18 22:26	11.0202	44.8763	5.68	1.7	0.046	0.005	ID
29	2019-06-30 17:49	11.0242	44.8768	5.42	2.3	0.235	0.049	ID
30	2019-06-30 22:59	11.0233	44.8752	5.26	2.1	0.133	0.024	ID
31	2019-07-13 04:18	10.9245	44.8928	5.41	1.8	0.210	0.017	ID
32	2019-07-15 05:48	10.8757	44.8688	9.12	2.3	0.051	0.010	ED
33	2019-07-18 00:13	10.6917	44.8217	11.11	2.3	0.007	0.001	none
34	2019-07-20 21:08	10.9245	44.8898	5.43	1.9	0.042	0.004	ID
35	2019-07-27 11:11	10.9398	44.8895	6.31	2.2	0.092	0.015	ID
36	2019-07-27 11:12	10.9437	44.895	6.45	2.2	0.109	0.017	ID
37	2019-07-31 22:49	11.0233	44.8197	8.63	2.0	0.014	0.002	ED
38	2019-08-18 20:23	10.9723	44.8917	5.58	1.6	0.014	0.002	ID
39	2019-08-26 04:02	10.8762	44.8667	8.98	1.9	0.032	0.005	ED
40	2019-09-03 00:48	11.0017	44.873	5.81	1.6	0.012	0.001	ID
41	2019-09-03 02:49	11.0177	44.871	6.13	2.0	0.016	0.002	ID
42	2019-09-18 19:59	10.9062	44.8888	8.77	1.8	0.013	0.002	ED
43	2019-09-18 20:00	10.9042	44.8892	8.91	1.6	0.014	0.001	ED
44	2019-10-01 21:29	11.03	44.8767	5.39	1.7	0.018	0.003	ID
45	2019-10-04 13:23	11.3345	44.8995	11.21	2.8	0.017	0.005	none
46	2019-10-31 08:22	11.041	44.965	13.89	3.0	0.03	0.012	none
47	2019-11-25 00:03	10.9127	44.8883	5.6	1.5	0.019	0.002	ID
48	2019-12-03 08:42	10.9218	44.9023	6.91	1.6	0.03	0.003	ID
49	2019-12-18 18:07	11.2583	44.8502	11.36	2.5	0.020	0.005	none

magnitude M_L between 0 and 1 ($0 \leq M_L \leq 1$)". The detection thresholds obtained from the proposed analysis show minimum magnitudes in the ID greater than those required by the guidelines, considering the $M_L - M_W$ relationship for small earthquakes (Munafò et al., 2016). This may be due either to the high seismic noise present in the Cavone oil field area at high frequency (>0.7 Hz), either to the small number of stations composing the seismic monitoring network. To understand which of these two factors plays a major role, we carried out two tests using virtual seismic stations on the surface and in the borehole to obtain helpful information on improving the network detection threshold. In the first test we simulated a significant increase in the station's number operating in the area. We virtually expanded the local seismic network up to 13 stations by adding seven of them on the surface to better cover the Cavone ID. At each of these seven virtual stations we have associated the

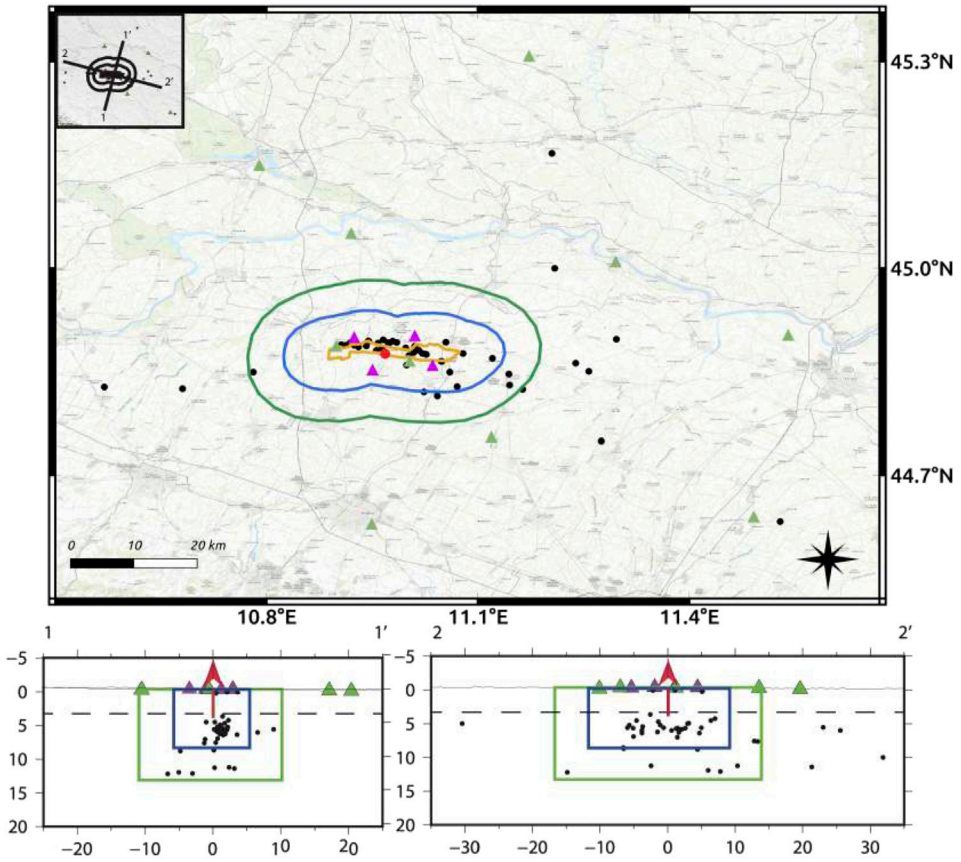

FIGURE 6 | Map of the seismicity (black dots) recorded and localised during 2018–2019 monitoring period. The local seismic station (VO network) and Italian Seismic Network station (IV network) locations are also showed as purple and green triangles respectively. The red dot in the map corresponds to the red arrow in the sections below and indicates the position of the *Cavone14* injection well. The blue and green contour lines sketch the two internal and extended domains of interest. The yellow polygon shows the reservoir projection at the surface, whose depth is approximately on the dashed line in the two vertical sections, while the solid line marks the topography profile.

noise level recorded at CAVE, which, among the stations of the network, has levels of 90 percentiles (in the band 1–30 Hz) slightly lower (5–10 dB) than the remaining stations. We then computed the detection threshold obtaining the results of **Figures 5C,D** for P and S phases, respectively. Despite the significant increase in seismic stations (the number has more than doubled inside the ID), the improvement in terms of detection threshold is rather limited. The benefits of an enhanced network consist almost exclusively in an extension of the lower detection threshold area. Increasing the number of stations decreases the detection threshold by only about 0.1 in the ID and in large part of the ED. The detection threshold values however remain very far from what is required by the guidelines. We carried out a second test for exploring the effect in terms of detection thresholds linked to a decrease in the noise level recorded at the existing station locations, as if the sensors were installed in boreholes. The installation of seismic sensors in borehole is a solution that has been taken into consideration by several authors to reduce the high levels of noise recorded in the Po alluvial basin area (Margheriti et al., 2000; Cocco et al., 2001). Pesaresi et al. (2014) compared the background noise of the Ferrara borehole station (sited in Casaglia, about 40 km east from the centre of the VO network) with the free field station installed on top of the borehole. At Casaglia the borehole seismic sensor was installed at a depth of 135 m, below the quaternary basement observed at 130 m depth. The noise values recorded by the free field station of Casaglia exceed Peterson (1993)'s NHNM thresholds, similarly (in terms of PSD values and in spectral shapes) to those observed at CAVE and NDIM. The seismic noise recorded in Casaglia borehole decreases significantly compared to that on the surface by a factor of about 20–25 dB [re 1 (m/s)2/Hz] at about 1 Hz up to a factor of about 35–40 dB [re 1 (m/s)2/Hz] at frequency of 30 Hz. Similarly to the Casaglia, the measurement sites of the Cavone network are also located at the top of soft layers composed by alluvial sediments of about 100–200 m thick as can be seen from studies for subsurface of the Po plain reconstructions using geological and geophysical information available from the literature and from public datasets (Maesano et al., 2015; Martelli et al., 2017). More precise information on sediment depth for the Cavone oil field area can be extracted from the analysis performed on downhole and sediment cores extracted from the well performed in the Mirandola town, located within

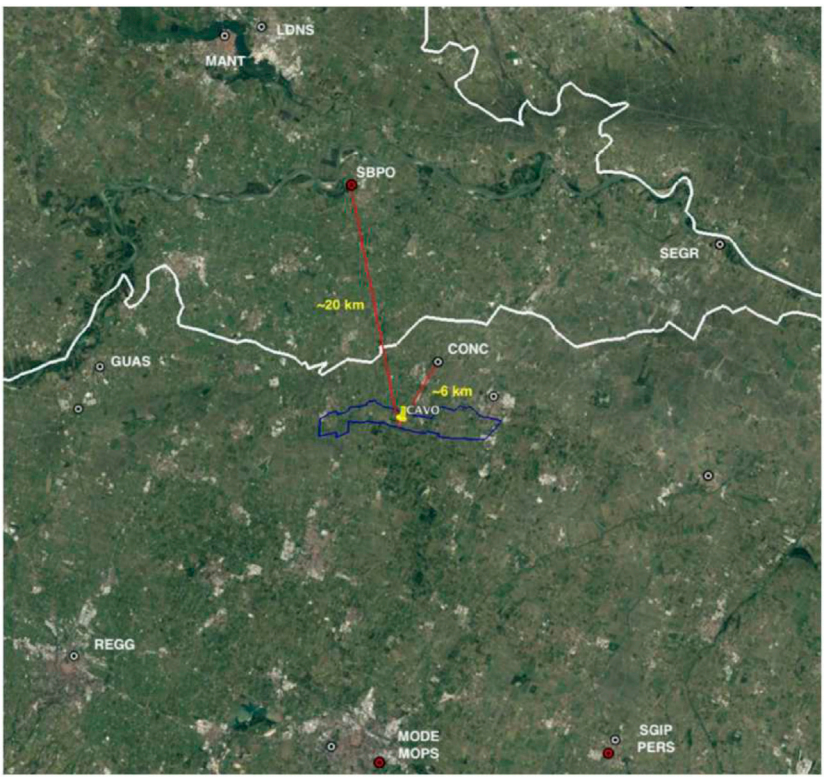

FIGURE 7 | Location of the Cavone GNSS station (CAVO) and distance from the nearest active GNSS stations, with the OWC extension projected on the surface shown in blue. Red circles: active RING stations, white circles with names: other active GNSS stations; white circles with no names: other inactive GNSS stations.

the ID. In this well, the thickness of sediments is 118 m (Garofalo et al., 2016; Minarelli et al., 2016). We assumed to install the Cavone sensors at a depth of about 120 m, below the soft layer of alluvial sediments. Then, we recomputed the detection thresholds for the Cavone network, assuming for the borehole sensors an average reduction in PSD levels at the different stations equal to 25 dB (with respect to the noise levels of the corresponding free field stations) in the frequency range between 1 and 30 Hz. The results obtained are shown in **Figures 5E,F**. In this case, by considering the same six stations currently operating in the ID, we observe a marked decrease in the detection thresholds that reaches values of M_w equal to 1.1 and 1.2 for the P waves in the ID and ED, respectively; and values lower than M_w 1 both in ID and ED for S waves.

3.2 Cavone Seismicity

During the 2018–2019 period of guidelines' experimentation we detected, located and analysed 49 events (listed in **Table 1**). In the first year the seismic network was operating in triggering mode, therefore this list of events does not constitute a homogeneous catalog (and in fact events falling far away from the reservoir are detected only in 2019, as specified in the following). We could not work in real-time because in the second year we just started setting up the entire monitoring structure (hardware and software), hence the data were transferred by the operator every 3 months and we reported our analysis during the sporadic operational committee meetings. Nevertheless, even without a real-time response to the event detection, we could profit from this experimentation period for setting the basis for hydrocarbon cultivation seismic monitoring, understanding the local background seismicity and the real performances of the integrated seismic networks. After picking the P and S phases we localised each event using the Hypoellipse software by Lahr (1989) and a 1-D model built ad-hoc for the Cavone oil field by the operator and provided to us in the framework of the experimental monitoring (Società Padana Energia, personal communication, 2018; and **Supplementary Table S3**). We preliminarily performed a comparison for testing the performance of this local velocity model ("Cavone-model") with respect to the one built by (Govoni et al., 2014) for the 2012 Emilia sequence. We located thousand of earthquakes occurred during the seismic sequence in 2012 in the ID area. The location errors computed with the two different velocity models are reported in the **Supplementary Figure S3**, and show lower values for the Cavone-model, thus supporting its use in locating the 2018–2019 events. Some of the IV stations demonstrated to be too far away for being sensitive to this kind of low energetic seismicity in a noisy (both in high frequencies due to the human activity, and in the low frequencies due to the superficial soft sediments) alluvial plain: FERS, MNTV, and OPPE stations do not detect any of the events, while FIU only one. Still, the six remaining stations were very

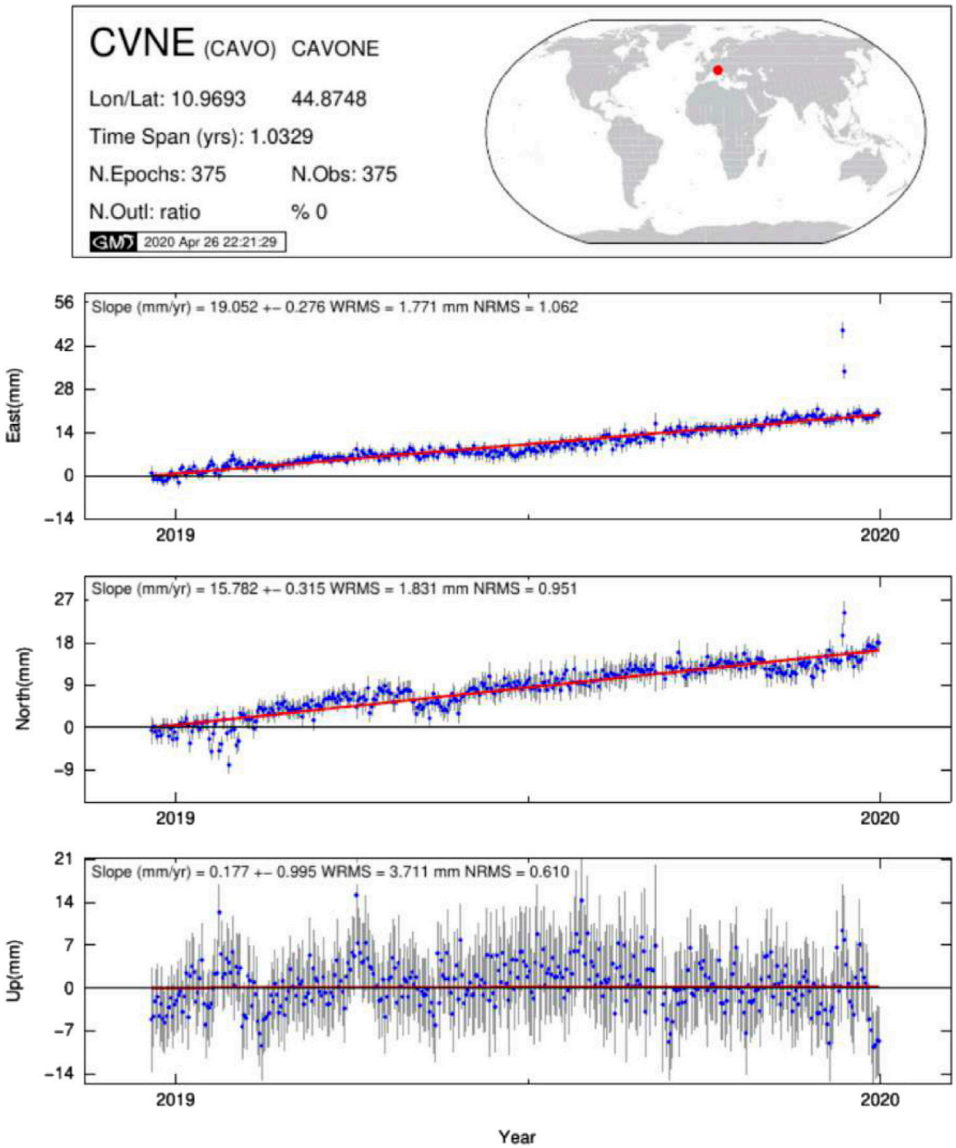

FIGURE 8 | Displacement time series of the CAVO station in the IGS14 global reference frame. The gray lines indicate the error bars (1σ) and the red line represents the estimated linear trend.

helpful in locating this seismicity especially by adding useful picks to those events occurred inside the network, allowing minor RMS, and errors on the locations (see **Supplementary Table S4**). Although we are aware about the variability of the location procedure, which depends on the input parameters and on the personal choices of the analyst (for time picks definition), and of the epistemic uncertainty (Garcia-Aristizabal et al., 2020), we operate as these locations were reliable enough. This is a first approximation: we leave for a future monitoring period to determine the probabilistic locations able to take into accounts all different sources of uncertainties. More than half out of these 49 events (32, i.e., 65% of the total), fall inside the ID, 10 are located in the ED, and seven are out of both domains (see **Figure 6**). We observe that the epicenters mainly follow the E-W elongated reservoir projection on the surface, but this may be also an effect of the seismic network configuration with six stations installed well inside the ID or even along the borders of the same reservoir projection (**Figure 2**). The locations of course suffer by variable error measurements that are reported in the **Supplementary Table S4**, depending mainly on the number of available picks. Then we computed the moment magnitude M_W for all events. In case of small earthquakes ($M_W < 3$, i.e., our case) the M_W estimate does not yet rely on a routine procedure due to technical difficulties and the only viable option for the quantification of accurate M_W is the spectral correction.

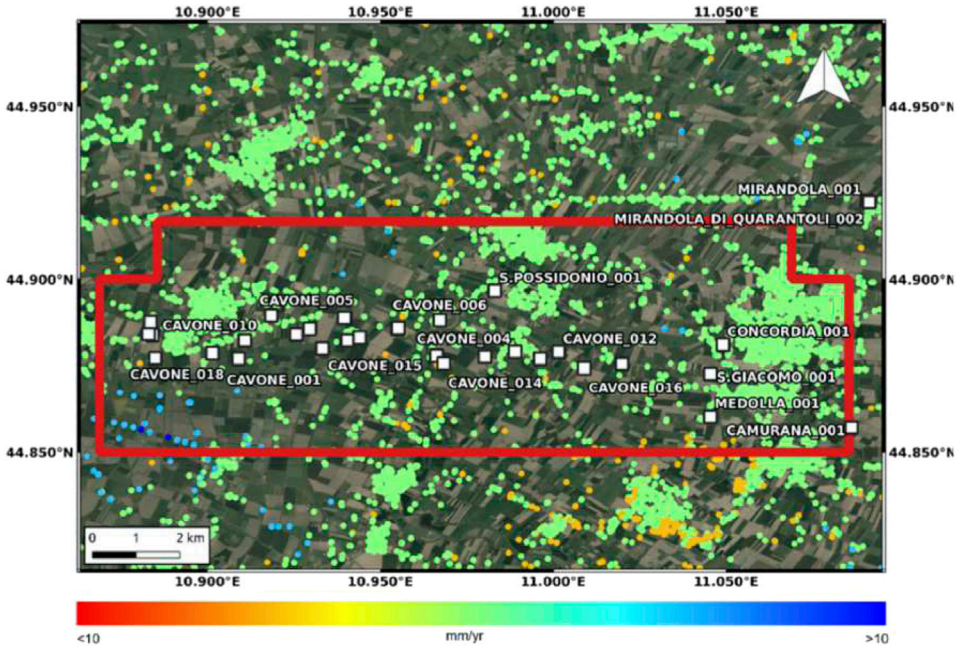

FIGURE 9 | Sentinel-1 InSAR Line-of-Sight (LoS) velocity map. The red polygon represents the Mirandola concession area as it was in 2018–2019. The white squares indicate the oil wells.

Therefore, we followed the technique defined by Munafò et al. (2016): we maximized the signal-to-noise-ratio (SNR) through a procedure based on the analysis of peak values of bandpass-filtered time histories by relying on a tool called Random Vibration Theory (RVT, Cartwright and Longuet-Higgins, 1956). We then computed the seismic moments after spectral correction for the regional attenuation parameters (Malagnini and Munafò, 2017), and calculating the RMS values of the low frequency spectral plateaus on the Fourier amplitudes; on the peak amplitudes we use previous results to compute all moments by spectral ratio. By looping through all events, we obtain averages and standard deviations for the seismic moments of all earthquakes in the data set. Our approach provides the utmost accuracy, the measurement errors on our M_W estimates are of the order of 0.05, therefore, in a conservative way, we truncated their values at the first decimal digit.

Peak Ground Velocity and Acceleration (PGV and PGA respectively) have been computed as the maximum values observed in the recordings (velocity) and their derivatives (acceleration) at any stations and all horizontal components. All these estimates are listed in **Table 1**. Even though the catalog is undoubtedly too short for statistical analysis, we estimated the completeness magnitude that is required by the guidelines to be less than one in the ID, just to get a rough idea of what we could expect from our data. A plot of the number of events versus magnitude is reported as **Supplementary Figure S4**, the completeness magnitude results $Mc = 2$, in agreement with the theoretical estimates reported in **Section 3.1**.

4 CRUSTAL DEFORMATION MONITORING

Hydrocarbon production activity involving underground extraction, injection or storage of fluids can induce ground displacements, even of considerable entity of the order of centimeter per year (e.g., Vasco et al., 2000; Teatini et al., 2011; Qu et al., 2015; Deng et al., 2020). An appropriate geodetic monitoring system aims to provide information on both the temporal and spatial evolution of ground deformation (Dialuce et al., 2014), highlighting any variations in space and time with respect to a condition not perturbed by the hydrocarbon production activity. For this purpose in the guidelines the deformation monitoring is recommended to be performed using satellite geodetic techniques, acquiring mainly Global Navigation Satellite System (GNSS), and Interferometric Synthetic Aperture Radar (InSAR) measurements of the superficial projection of the survey domains (internal and extended). The two geodetic techniques are complementary (Montuori et al., 2018) since GNSS data allows to obtain a daily (or sub-daily) evolution of the three-components (E, N, Vertical) position of a GNSS station with millimeter precision, while InSAR measurements can provide spatially-dense information of ground displacement along the satellite line of sight (LOS) direction with a temporal sampling spanning from few days to almost a month, depending on the specific satellite sensor used/available.

A time series of ground displacement obtained from a GNSS station contains signals of different nature, deriving from processes acting on different spatial and temporal scales. The linear term (or displacement velocity), for example, describes the

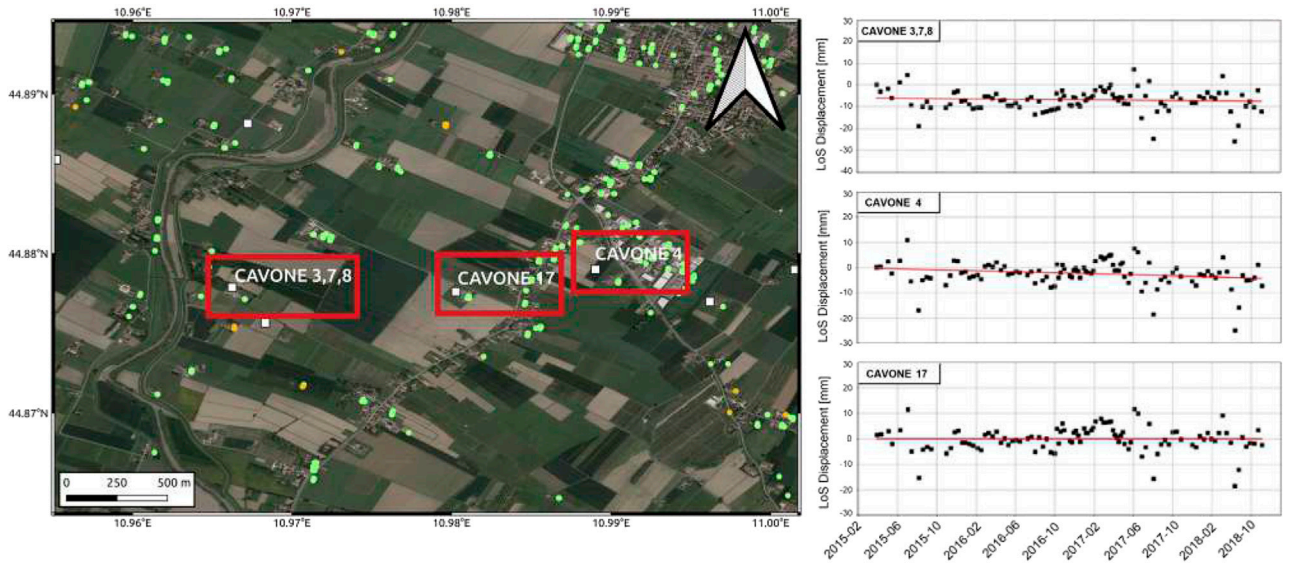

FIGURE 10 | Focus on some wells of the Cavone oil field: InSAR time series extracted from point targets in proximity of the wells shown on top.

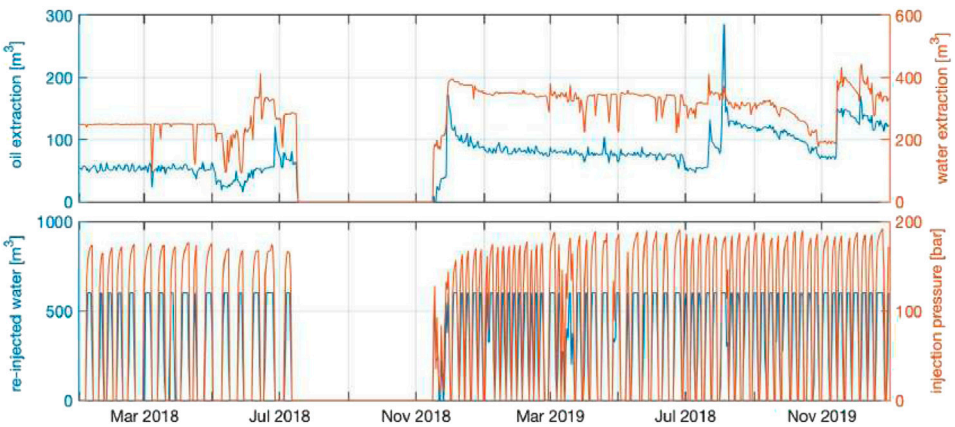

FIGURE 11 | (A) Time series of oil and water produced form the Cavone field (m^3/day). **(B)** volume (in m^3/day) and pressure (bar) of produced water re-injected through the *Cavone14* well.

rate at which the station moves in the planar components (east and north) and in the vertical component in a given reference system mainly due to tectonic and geodynamic processes, although the vertical rate is much more sensitive to local, non-tectonic processes, than the horizontal ones (e.g., Devoti et al., 2011; Serpelloni et al., 2013). The accuracy and precision of this measurement depends on the quality of the data recorded by the station, the length of the time series analyzed and the presence and amplitude of other seasonal and non-seasonal signals. Seasonal signals, primarily of annual and semi-annual period, mainly come from loading processes acting at continental and regional scales (e.g., surface hydrology, atmospheric loading). Subsurface hydrology, also, may be responsible for non-seasonal or multi-annual ground displacements (e.g., Silverii et al., 2016; Serpelloni et al., 2018). The same deformation signals are recorded also by InSAR measurements whose temporal sampling allows to extract displacement and related rates along the satellite LOS direction. In order to obtain a more complete 3D picture of the spatial and temporal evolution of ground displacements, it is recommended to integrate the two geodetic measurements when long enough records allow to compare them in terms of velocities and displacement time series.

4.1 GNSS Monitoring

The GNSS monitoring infrastructure of the Cavone hydrocarbon concession consists of one GNSS station (CAVO) installed on December 18, 2018, which is equipped by a geodetic-class receiver, for which only Global Positioning System (GPS)

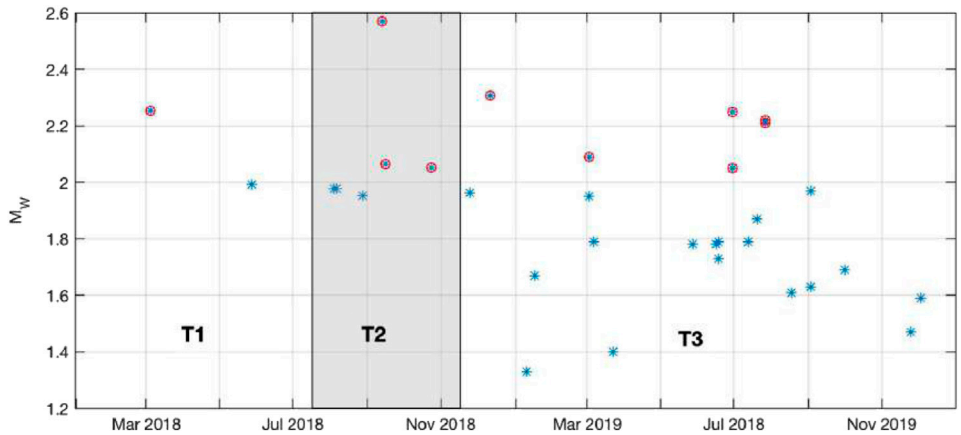

FIGURE 12 | Temporal occurrence of the 32 events recorded and located within the internal monitoring domain versus magnitudes M_W. The red circles indicate the 10 events for which M_W overcomes the completeness magnitude. The shadowed area indicates the industrial activity shutdown period, and the time periods T1, T2, and T3, defined for testing the seismic rate variations are indicated at the bottom.

observations are available, and a choke-ring type antenna, with an adequate monumentation suitable for geophysical purposes (as indicated in the guidelines), the latter being co-located with a radar corner reflector. It is the only station located above the oil field (**Figure 7**) and in around 20 km away there are two active GNSS stations, both located to the north, that are: CONC (Concordia sul Secchia) managed by a private company and part of the NetGeo network, and SBPO (San Benedetto Po), part of the INGV RING network. Given the extension of the field (about 15 km) mainly along the EW direction, the current geodetic network requires significant improvements in order to allow the proper monitoring of crustal deformation signals associated with the hydrocarbon cultivation activities at Cavone. Following the indications of the guidelines, in fact, "the local GPS network of permanent precision stations must be installed, appropriately distributed according to the extension and characteristics of the area to be monitored [. . .] it is required that the stations have inter-distances of less than 10–15 km" (Dialuce et al., 2014). Therefore it would be necessary to install at least three additional monitoring sites, two at the east and west edges and one to the south, allowing to accurately measure the local deformation signals both along the NS direction and along the direction of extension of the reservoir.

During this experimental phase, the available daily raw GPS data, in Receiver INdependent EXchange (RINEX) format of the CAVO station are available form 18 December, 2018 to 31 December, 2019. We have performed a pre-processing step to evaluate the raw observables' quality by using the TEQC software. The indices considered in this analysis are MP1, i.e., root mean square residual given by multipaths on L1 phase, due to reflections of the radio signal sent by the satellites which affect the correct calculation of the satellite-receiver distance, and MP2, the same as MP1 but for the L2 phase. **Supplementary Figure S5** shows the daily MP1 and MP2 values obtained for the CAVO station, and, considering as a reference the IGS network of the International GNSS Service, for which 50% of IGS stations have RMS values for MP1 and MP2 less than 0.4 and 0.6 m respectively, the results indicate that the station records high-quality data.

Subsequently, daily RINEX data have been processed with scientific geodetic software with the aim of estimating the positions of this station in the same, global, international reference frame used for standard INGV processing of the Euro-Mediterranean GNSS stations (e.g., Devoti et al., 2017). We have followed a procedure based on three steps, as described in Serpelloni et al. (2006), Serpelloni et al.(2013), Serpelloni et al.(2018), which consists of: 1) phase analysis, i.e., the observations recorded by the GPS stations of a sub-network that includes CAVO plus other active permanent GPS stations belonging to the EUREF and IGS network (later used to combine the solutions of this sub-network with those of the other sub-networks elaborated at INGV and to align the solutions to a global international reference frame) producing weakly constrained network solutions (positions, orbits, etc. . .); 2) combination of the daily solutions of the sub-network with the solutions of other subnets processed at INGV and simultaneous alignment of the solutions to the IGS14 reference frame that is the GPS realization of the ITRF2014 reference system (Altamimi et al., 2016); 3) analysis of the time series for the estimation of displacement rates, seasonal signals and uncertainties. For the first two steps, we have used the GAMIT/GLOBK software (version 10.70) obtaining the three-dimensional daily positions and uncertainties for all the stations considered.

The position time series have been analysed in the third step for estimating the linear term of displacement rate in the three components, east, north ,and vertical, by using the analyze_tseri module of the QOCA software. Due to the short time-span available, we do not estimate the seasonal terms. It is worth to note that the scientific literature agrees in defining in 2.5 years the minimum length of a GPS time series for a velocity estimate not influenced by seasonal signals (Blewitt and Lavallée, 2002), and since GNSS time series can be influenced by several other

transient signals of tectonic and non-tectonic nature (e.g., Serpelloni et al., 2018), even longer time series may be required (e.g., Masson et al., 2019). **Figure 8** shows the displacement time series (with respect to the coordinates calculated at first epoch) of the CAVO station in the east, north and vertical directions, in the IGS14 reference frame. Although the time interval (~ 1 year) does not allow an evaluation of the seasonal components and an accurate estimate of the displacement rate in the three directions, the data continuity and the low level of noise (NRMS values < 1 in **Figure 8**) are indicative of a high quality GPS station suitable for the monitoring purpose. In any case, longer time series will be necessary in order to estimate the seasonal (annual and semi-annual period) signal associated with hydrological loading and detect any possible deviation from the linear and/or seasonal model associated with anthropogenic processes.

4.2 InSar Data Analysis

The guidelines for hydrocarbon cultivation activity's monitoring in the remote sensing domain recommend the use of Synthetic Aperture Radar Interferometry (InSAR) data in a time window of at least 10 years. In this first attempt, we exploit SAR acquisitions from Sentinel-1 mission of the European Space Agency (ESA) since they are free and easily accessible. Moreover, they offer an unprecedented revisit time of 6 days which is an essential condition for the future performing of a quasi-real-time InSAR-based monitoring service. However, the first satellite, i.e., Sentinel-1 A, was launched in 2014 thus reducing the temporal window available for the analysis. In particular, the SAR dataset exploited here consists of 103 images acquired along descending orbit from March 2015 to July 2018. The geometry of view is characterised by incidence and azimuth angle of about 39° and 14°. InSAR analysis was performed by Interferometric Point Target Analysis (IPTA, Werner et al., 2003). We first multi-looked the data by 24 looks along range and six looks along azimuth obtaining a pixel spacing of about 90 m, the same size of the Digital Elevation Model (DEM) of the SRTM mission exploited for removing the topographic contribution in the phase signal. We estimated the interferometric pairs by setting the perpendicular and temporal baseline thresholds to 200 m e 90 days, respectively, obtaining a well connected network of 757 interferograms. We then filtered (Goldstein and Werner, 1998) and unwrapped (Costantini, 1998) all the interferograms and retrieved the InSAR time series by Singular Value Decomposition (SVD) analysis. The results of InSAR analysis in terms of ground velocity are shown in **Figure 9**. In the Mirandola hydrocarbon cultivation area (the red polygon in the figure), there are no significant deformation patterns associated with the Cavone oil field. Some subsidence phenomena are observed SW the concession area with values peaking at about 2.5 mm/yr. They are probably due to local water pumping activity not connected with the Cavone industrial activity. Such outcome is also shown by InSAR time series extracted from point targets in the proximity of some wells of Cavone field highlighted in **Figure 10**, top panel. Indeed, quite scattered behaviours are observed along the time series, likely due to seasonal effects or tropospheric artefacts (**Figure 10**). However, the linear trend along the analysed time window is very close to zero further confirming the absence of any ground deformation phenomena associated with the extraction activity. In conclusion, for the analysed time interval spanning from 2015 to 2018, ground deformations induced by the activity of the Cavone field, detectable within the limit of accuracy of the technique (Casu et al., 2006) are not taking place.

5 PORE PRESSURE MONITORING

One of the main interests in seismically monitoring underground industrial activities is understanding whether stress perturbations caused by such activities influence the local seismicity. Nevertheless, discriminating natural from induced seismicity in seismically active regions is a particularly complex task. Early attempts to discriminate induced from natural seismicity were performed, for fluid injection operations, by Davis and Frohlich (1993), and for fluid withdrawal by Davis and Nyffenegger (1995); however, these approaches were mainly based on qualitative assessments. More quantitative approaches, based on physical and/or stochastic features of recorded seismicity also have been proposed in literature (a review can be found, e.g., in Dahm et al., 2015; Schoenball et al., 2015; Grigoli et al., 2017; Garcia et al., 2021). In principle, evaluating possible interactions between seismicity and hydrocarbon production should rely on multidisciplinary analyses such as detailed physically-based modelling and stochastic methods. These latter may provide probabilistic assessments and take uncertainties into account (Segall, 1989; Segall et al., 1994; Gishig and Wiemer, 2013; Dahm et al., 2015; Schoenball et al., 2015; Grigoli et al., 2017; Garcia-Aristizabal, 2018, among others). Even though, the ways in which the interactions may occur are complex, and their identification in a context characterised by naturally-occurring seismicity is not straightforward (Garcia et al., 2021). These reasons stimulate the implementation of alternative statistical methods to track measurable phenomena, as changes in seismicity rates. That rate variations could occur if notable interactions between underground human operations and nearby seismicity sources arise in a given area. In fact, spatial and temporal correlation between human activity and event rates are usually considered key parameters to suspect possible relationships between seismicity and underground anthropic activity (e.g., Shapiro et al., 2007; Cesca et al., 2014; Leptokaropoulos et al., 2017; McClure et al., 2017; Garcia-Aristizabal, 2018; Schultz and Telesca, 2018; Skoumal et al., 2018; Molina et al., 2020).

Among the duties prescribed by the Italian guidelines for geophysical monitoring of underground operations, analyses of the temporal evolution of seismicity, deformation and pore pressure are expected aiming at spotting any possible causal relationships between the industrial activity and the natural observations (Dialuce et al., 2014). With this scope. The daily measurements of the well head pressure were transmitted directly by the operator together with the information on daily volumes of the extracted oil, extracted water, and injected water. Analysing the deformation time series we were unable to discriminate any

significant temporal variation (mainly due to the short time span of the data, see **section 4**). Moreover, considering the limited duration of the experimentation and the relatively low level of seismic activity observed in this area, statistical analyses of possible seismicity rate changes are particularly challenging because of the low number of recorded events. The production in the oil center are carried out at a reasonably constant rate, in particular for the 2018–2019 testing period, apart from a shutdown of the entire plant due to routine maintenance from 16 July to 16 November, 2018. This feature can be seen in **Figure 11**, where the daily oil and water volumes produced from this field (**Figure 11A**) and the daily volume and pressure of re-injected water into the *Cavone14* well (**Figure 11B**) present a roughly constant trend, interrupted by the industrial activity stop mentioned before. **Figure 12** shows the temporal occurrence of 32 events recorded and located within the internal monitoring domain, plotted against the M_W magnitudes (12a), with the shadowed area indicating the shutdown period for reference. Considering the completeness magnitude determined for the M_W in this data set ($Mc = 2.0$), only 10 events above Mc are identified (red circled asterisks in **Figure 12**). Such a low number of seismic events in the complete catalog makes the statistical analysis application a particularly challenging task that may produce not informative results. For this reason, in this work we only set up a possible analysis procedure to check for possible significant changes in seismicity rates correlated with changes in the industrial activity (i.e., before and after the shutdown period occurred during 4 months in 2018). To perform this task we implement the binomial test (e.g., Wonnacott and Wonnacott, 1977) proposed by Leptokaropoulos et al. (2017), because it is suitable also for few samples. For completeness we show the details of its application on our data in the **Supplementary Section 1**.

6 DISCUSSION

The seismic monitoring operated during these 2 years period in the Cavone oil field allowed us to detect and locate 49 events mainly clustered along the reservoir projection on the surface. Nevertheless, the location distribution may be biased by the geometry of the seismic stations (see discussion in **Sections 3.1,3.2** and the maps of **Figures 2**, **6**). Even though this seismic catalog is not statistically highly populated, we attempted to estimate the completeness magnitude, finding a value of $M_W = 2$ compatible with the theoretical estimates based on the typical seismic noise recorded at two seismic stations centrally located within the network. This completeness magnitude value would not be in agreement with the guidelines' requirements, which prescribe the detection and location of events with magnitude less than 1. Possible reasons for such a high value could be ascribed primarily to the high seismic noise of this area due to the resonance of the Po plain sediments, and only secondarily to the seismic network configuration since there are no stations in the ED. From our simulations, in fact, we could show how the main factor in decreasing the detection threshold seems to be the removal of the sedimentary basin resonances by installing borehole stations (as from results in **Figure 5**). While an even large increase in seismic station number on the surface would not change much the detection threshold, helping only in extending the detection area. This result is not so surprising if we think that the Po plain sedimentary layer may deepen some km from the surface (8.5 km at most, Pieri, 1983). This unfavourable geological condition coupled with a multitude of anthropogenic noise sources (the Po plain is the area with the highest concentration of inhabitants and economic activities in Italy) cause very high seismic noise levels observed thorough the plain (Margheriti et al., 2000; Cocco et al., 2001; Pesaresi et al., 2014; Laurenzano et al., 2017). And the presence of seismic noise generates a low number of detected events and a high completeness magnitude. Anyway, we would need a much longer monitoring period for collecting many more events, necessary to find a stable and reliable value of completeness magnitude. This information would also help in determining the magnitude threshold for passing the color code in the traffic light system (e.g., Bommer et al., 2006) tuned for this specific oil field. The deformation monitoring (mainly from InSAR analysis) did not highilght any significant trend on the surface displacements that may be related to the Cavone industrial activity. We highlight that 1 year of data is too few for a correct GPS analysis. Furthermore, the only GNSS station installed in the area is not enough to thoroughly monitor the possible deformations due to the industrial activities. Even though the Cavone reservoir is surrounded by carbonatic rocks, we strongly recommend as a best practice for this type of study, to implement a monitoring network capable of recording the entire deformation field due to the hydrocarbon production activity, which usually generates the maximum of the vertical displacements at the center of the reservoir, and the maximum of the horizontal ones at the edges. For these reasons in this case we suggest the installation of three more stations (with the same technical characteristics as the one already installed) to the east, west, and south of the reservoir allowing to identify the main surface deformation patterns along the three displacement components.

7 CONCLUSION

In this paper we report the main outcomes of a 2-year pilot application of the Italian guidelines for monitoring seismicity, ground deformation, and pore pressure in the Cavone hydrocarbon cultivation field, in Northern Italy. We acknowledge that this experiment has been limited in scope by the too-short time period and by the weakness of the geophysical instrument network. In fact, in the monitoring domain only four seismic stations run by the industrial operator, integrated with three stations from INGV's national network (all located in the highly anthropised and noisy Po plain sedimentary basin) and 1 GNSS receiver station are available for the analysis. In spite of these limitations, helpful considerations may be drawn. The first evident conclusion is that a more extended observation period is needed for a better assessment. In fact the Cavone oil field lies in a seismic territory, but we could not ascertain the background

microseismic activity for lack of a detailed survey preceding the oil extraction. Beside, we notice that, given the high natural seismic noise of the environment (Po plain sediments), the magnitude of detection is relatively high compared to the standpoint of the national-scale seismic network, despite the presence of local VO stations in the area. This fact lead us to stress the importance of a seismic monitoring network installed and maintained both before and during extraction and production water re-injection activities. Also, it should consist of borehole installations to reduce the seismic resonance of the plain soft sediments and, consequently, improve the detection capability. All these strategies will extend the magnitude threshold to (much) less energetic seismic events, reaching a crucial point also highlighted by the guidelines. We note also that the operational application of a traffic light system (e.g., Bommer et al., 2006) would require detection of lower-magnitude seismic events. Ground deformation monitoring would also require more than one GNSS station in the area, and a longer observation time. With these limitations, no significant crustal deformation was observed. The seismic events we detected and located are too few for being meaningful on possible significant contribution from the produced water injection on the crustal stress field. However an explicit fluid-geo-mechanical study (outside the scope of the test application of the national guidelines, and of this paper) would be necessary to quantify this effect. Studies of perturbations of the crustal stress field may be particularly important in tectonically active regions, where critically stressed faults are present. A study of this type in the region has been performed by Juanes et al. (2016), who modeled geomechanics and coupled flows for resolving stresses inside and outside the reservoir, assessing the impact of both pressure and effective stress changes on the Mirandola fault. Their results indicate very small stress changes in the region near the May 29, 2012 hypocenter, which drive the authors to conclude that the very minor -if any- effects of production and injection calculated at the hypocenter area may indicate that the combined effects of fluid production and injection from the Cavone oil field were not a driver for the seismicity observed in 2012. To perform a similar modelling, but applied to the microseismicity recorded during this experimental period, a more detailed set of fault planes in and around the reservoir would be required. Therefore a complete 3D maps of the local fault system would be desirable for better understanding the nature of the seismic occurrences.

DATA AVAILABILITY STATEMENT

The data analyzed in this study is subject to the following licenses/restrictions: The Cavone seismic and GNSS network are subject to the third party restrictions: Data are available from the authors with the permission of Società Padana Energia S. p.a. Requests to access these datasets should be directed to MassimoCapelletti@gasplus.it.

AUTHOR CONTRIBUTIONS

LZ summarised the results in the present paper, co-ordinated the research and monitoring activities, and managed the agreement with the San Possidonio municipality. MA provided the geological information and has performed the P and S phase pickings for the seismic events, and has located them. MV analysed the seismic network detection capability. IMu evaluated the moment magnitude for all seismic events. LF computed the PGA and PGV values. LS estimated the completeness magnitude for the seismic event catalog. AG statistically tested the relationship between seismic rate and industrial activity in time. MP and GP analysed the InSAR data. ES and LA analysed the GPS data. ME produced the maps of the Cavone oil field. IMo and GZ computed and produced the maps for the PPSD at the local VO stations. AM supervised the Cavone experimental application of the guidelines for monitoring industrial activities. All authors participated in writing this article.

FUNDING

This research was financed by the "Convenzione tra il comune di San Possidonio e l'Istituto Nazionale di Geofisica e Vulcanologia -I.N.G.V.- per l'attuazione del monitoraggio nella concessione di coltivazione idrocarburi "Mirandola" finalizzata alla messa in opera di attività di monitoraggio di sperimentazione degli indirizzi e linee guida per i monitoraggi ILG ed assunzione funzioni di Struttura Preposta al Monitoraggio di cui all'art. 6 del Protocollo Operativo".

ACKNOWLEDGMENTS

We thank the MiSE and Società Padana Energia S.p.a. staff, in particular M. Capelletti and C. Triunfo for the fruitful collaboration. We profit by the discussion with L. Martelli, D. Susanni, and M. Mileti, and more generally all participants to the operational committee meetings. We thank Leica-Geosystem and Topcon Positioning Italy for providing GPS data of the SmartNet and NetGeo GNSS networks, respectively, and the European Space Agency for providing Sentinel-1 SAR data. We greatly thank two reviewers that helped us in deeply improving the article.

SUPPLEMENTARY MATERIAL

The Supplementary Material for this article can be found online at: https://www.frontiersin.org/articles/10.3389/feart.2021.685300/full#supplementary-material

REFERENCES

Altamimi, Z., Rebischung, P., Métivier, L., and Collilieux, X. (2016). ITRF2014: A New Release of the International Terrestrial Reference Frame Modeling Nonlinear Station Motions. *J. Geophys. Res. Solid Earth* 121, 6109–6131. doi:10.1002/2016jb013098

Blewitt, G., and Lavallée, D. (2002). Effect of Annual Signals on Geodetic Velocity. *J. Geophys. Res.* 107, B7. doi:10.1029/2001jb000570

Bommer, J. J., Oates, S., Cepeda, J. M., Lindholm, C., Bird, J., Torres, R., et al. (2006). Control of hazard Due to Seismicity Induced by a Hot Fractured Rock Geothermal Project. *Eng. Geol.* 83, 287–306. doi:10.1016/j.enggeo.2005.11.002

Braun, T., Danesi, S., and Morelli, A. (2020). Application of Monitoring Guidelines to Induced Seismicity in italy. *J. Seismol.* 24, 1015–1028. doi:10.1007/s10950-019-09901-7

Carannante, S., D'Alema, E., Augliera, P., and Franceschina, G. (2020). Improvement of Microseismic Monitoring at the Gas Storage Concession "Minerbio Stoccaggio" (Bologna, Northern Italy). *J. Seismol.* 24, 967–977. doi:10.1007/s10950-019-09879-2

Carminati, E., Scrocca, D., and Doglioni, C. (2010). Compaction-induced Stress Variations with Depth in an Active Anticline: Northern Apennines, Italy. *J. Geophys. Res.* 115, 17p. doi:10.1029/2009JB006395

Carminati, E., and Vadacca, L. (2010). Two- and Three-Dimensional Numerical Simulations of the Stress Field at the Thrust Front of the Northern Apennines, Italy. *J. Geophys. Res.* 115, 21p. doi:10.1029/2010JB007870

Cartwright, D. E., and Longuet-Higgins, M. S. (1956). The Statistical Distribution of the Maxima of a Random Function. *Proc. Math. Phys. Sci.* 237, 212–232.

Casu, F., Manzo, M., and Lanari, R. (2006). A Quantitative Assessment of the Sbas Algorithm Performance for Surface Deformation Retrieval from Dinsar Data. *Remote Sensing Environ.* 102, 195–210. doi:10.1016/j.rse.2006.01.023

Cesca, S., Braun, T., Maccaferri, F., Passarelli, L., Rivalta, E., and Dahm, T. (2013). Source Modelling of the M5-6 Emilia-Romagna, Italy, Earthquakes (2012 May 20-29). *Geophys. J. Int.* 193, 1658–1672. doi:10.1093/gji/ggt069

Cesca, S., Grigoli, F., Heimann, S., González, Á., Buforn, E., Maghsoudi, S., et al. (2014). The 2013 September-October Seismic Sequence Offshore Spain: a Case of Seismicity Triggered by Gas Injection? *Geophys. J. Int.* 198, 941–953. doi:10.1093/gji/ggu172

Ciaccio, M. G., and Chiarabba, C. (2002). Tomographic Models and Seismotectonics of the Reggio Emilia Region, Italy. *Tectonophysics* 344, 261–276. doi:10.1016/S0040-1951(01)00275-X

Cocco, M., Ardizzoni, F., Azzara, R. M., Dall'Olio, L., Delladio, A., Di Bona, M., et al. (2001). Broadband Waveforms and Site Effects at a Borehole Seismometer in the Po Alluvial basin (Italy). *Ann. Geophys.* 44, 137–154. doi:10.4401/ag-3611

Costantini, M. (1998). A Novel Phase Unwrapping Method Based on Network Programming. *IEEE Trans. Geosci. Remote Sensing* 36, 813–821. doi:10.1109/36.673674

Dahm, T., Cesca, S., Hainzl, S., Braun, T., and Krüger, F. (2015). Discrimination between Induced, Triggered, and Natural Earthquakes Close to Hydrocarbon Reservoirs: A Probabilistic Approach Based on the Modeling of Depletion-Induced Stress Changes and Seismological Source Parameters. *J. Geophys. Res. Solid Earth* 120, 2491–2509. doi:10.1002/2014jb011778

Davis, S. D., and Frohlich, C. (1993). Did (Or Will) Fluid Injection Cause Earthquakes? - Criteria for a Rational Assessment. *Seismol. Res. Lett.* 64, 207–224. doi:10.1785/gssrl.64.3-4.207

Davis, S. D., and Nyffenegger, P. A. (1995). The 9 April 1993 Earthquake in South-central Texas: Was it Induced by Fluid Withdrawal? *Bull. Seismol. Soc. Am.* 85, 1888–1895.

Deng, F., Dixon, T. H., and Xie, S. (2020). Surface Deformation and Induced Seismicity Due to Fluid Injection and Oil and Gas Extraction in Western Texas. *J. Geophys. Res. Solid Earth* 125, e2019JB018962. doi:10.1029/2019JB018962

Devoti, R., D'Agostino, N., Serpelloni, E., Pietrantonio, G., Riguzzi, F., Avallone, A., et al. (2017). A Combined Velocity Field of the Mediterranean Region. *Ann. Geophys.* 60, 0215. doi:10.4401/ag-7059

Devoti, R., Esposito, A., Pietrantonio, G., Pisani, A. R., and Riguzzi, F. (2011). Evidence of Large Scale Deformation Patterns from GPS Data in the Italian Subduction Boundary. *Earth Planet. Sci. Lett.* 311, 230–241. doi:10.1016/j.epsl.2011.09.034

Dialuce, G., Chiarabba, C., Bucci, D. D., Doglioni, C., Gasparini, P., Lanari, R., et al. (2014). Indirizzi e linee guida per il monitoraggio della sismicità, delle deformazioni del suolo e delle pressioni di poro nell'ambito delle attività antropiche. Available at: https://unmig.mise.gov.it/images/docs/151_238.pdf (Last Accessed November 04, 2021).

Doglioni, C., Harabaglia, P., Merlini, S., Mongelli, F., Peccerillo, A., and Piromallo, C. (1999). Orogens and Slabs vs. Their Direction of Subduction. *Earth Sci. Rev.* 45, 167–208. doi:10.1016/s0012-8252(98)00045-2

Enrico Serpelloni, E., Marco Anzidei, M., Paolo Baldi, P., Giuseppe Casula, G., and Alessandro Galvani, A. (2012). GPS Measurement of Active Strains across the Apennines. *Ann. Geophys.* 49, 319–329. doi:10.4401/ag-5756

Garcia, A., Faenza, L., Morelli, A., and Antoncecchi, I. (2021). Can Hydrocarbon Extraction From the Crust Enhance or Inhibit Seismicity in Tectonically Active Regions? A Statistical Study in Italy. *Front. Earth Sci.* 9:673124. doi:10.3389/feart.2021.673124

Garcia-Aristizabal, A., Danesi, S., Braun, T., Anselmi, M., Zaccarelli, L., Famiani, D., et al. (2020). Epistemic Uncertainties in Local Earthquake Locations and Implications for Managing Induced Seismicity. *Bull. Seismol. Soc. Am.* 110, 2423–2440. doi:10.1785/0120200100

Garcia-Aristizabal, A. (2018). Modelling Fluid-Induced Seismicity Rates Associated with Fluid Injections: Examples Related to Fracture Stimulations in Geothermal Areas. *Geophys. J. Int.* 215, 471–493. doi:10.1093/gji/ggy284

Garofalo, F., Foti, S., Hollender, F., Bard, P. Y., Cornou, C., Cox, B. R., et al. (2016). InterPACIFIC Project: Comparison of Invasive and Non-invasive Methods for Seismic Site Characterization. Part II: Inter-comparison between Surface-Wave and Borehole Methods. *Soil Dyn. Earthquake Eng.* 82, 241–254. doi:10.1016/j.soildyn.2015.12.009

Gishig, V., and Wiemer, S. (2013). A Stochastic Model for Induced Seismicity Based on Nonlinear Pressure Diffusion and Irreversible Permeability Enhancement. *Geophys. J. Int.* 194, 1229–1249. doi:10.1093/gji/ggt164

Goldstein, R. M., and Werner, C. L. (1998). Radar Interferogram Filtering for Geophysical Applications. *Geophys. Res. Lett.* 25, 4035–4038. doi:10.1029/1998GL900033

Govoni, A., Marchetti, A., De Gori, P., Di Bona, M., Lucente, F. P., Improta, L., et al. (2014). The 2012 Emilia Seismic Sequence (Northern Italy): Imaging the Thrust Fault System by Accurate Aftershock Location. *Tectonophysics* 622, 44–55. doi:10.1016/j.tecto.2014.02.013

Grigoli, F., Cesca, S., Priolo, E., Rinaldi, A. P., Clinton, J. F., Stabile, T. A., et al. (2017). Current Challenges in Monitoring, Discrimination, and Management of Induced Seismicity Related to Underground Industrial Activities: A European Perspective. *Rev. Geophys.* 55, 310–340. doi:10.1002/2016RG000542

ICHESE (2014). Report on the Hydrocarbon Exploration and Seismicity in Emilia Region. Paper Presented at International Commission on Hydrocarbon Exploration and Seismicity in the Emilia Region. Available at: http://mappegis.regione.emilia-romagna.it/gstatico/documenti/ICHESE/ICHESE_Report.pdf.

INGV Seismological Data Centre (2006). Rete Sismica Nazionale. Italy: Istituto Nazionale di Geofisica e Vulcanologia (INGV). doi:10.13127/SD/X0FXNH7QFY

Juanes, R., Jha, B., Hager, B. H., Shaw, J. H., Plesch, A., Astiz, L., et al. (2016). Were the May 2012 Emilia-Romagna Earthquakes Induced? a Coupled Flow-Geomechanics Modeling Assessment. *Geophys. Res. Lett.* 43, 6891–6897. doi:10.1002/2016gl069284

Keranen, K. M., Savage, H. M., Abers, G. A., and Cochran, E. S. (2013). Potentially Induced Earthquakes in oklahoma, usa: Links between Wastewater Injection and the 2011 Mw 5.7 Earthquake Sequence. *Geology* 41, 699–702. doi:10.1130/g34045.1

Lahr, J. C. (1989). *Hypoellipse/version 2.0: A Computer Program for Determining Local Earthquake Hydrocentral Parameters, Magnitude, and First Motion Pattern: Open-File Report*. Menlo Park, California: U.S. Geological Survey, 89–116. doi:10.3133/ofr89116

Laurenzano, G., Priolo, E., Mucciarelli, M., Martelli, L., and Romanelli, M. (2017). Site Response Estimation at Mirandola by Virtual Reference Station. *Bull. Earthquake Eng.* 15, 2393–2409. doi:10.1007/s10518-016-0037-y

Leptokaropoulos, K., Staszek, M., Lasocki, S., Martínez-Garzón, P., and Kwiatek, G. (2017). Evolution of Seismicity in Relation to Fluid Injection in the North-Western Part of the Geysers Geothermal Field. *Geophys. J. Int.* 212, 1157–1166. doi:10.1093/gji/ggx481

Luca Minarelli, L., Sara Amoroso, S., Gabriele Tarabusi, G., Marco Stefani, M., and Gabriele Pulelli, G. (2016). Down-hole Geophysical Characterization of

Middle-Upper Quaternary Sequences in the Apennine Foredeep, Mirabello, Italy. *Ann. Geophys.* 59, S0543. doi:10.4401/ag-7114

Maesano, F. E., D'Ambrogi, C., Burrato, P., and Toscani, G. (2015). Slip-rates of Blind Thrusts in Slow Deforming Areas: Examples from the Po Plain (Italy). *Tectonophysics* 643, 8–25. doi:10.1016/j.tecto.2014.12.007

Malagnini, L., Herrmann, R. B., Munafò, I., Buttinelli, M., Anselmi, M., Akinci, A., et al. (2012). The 2012 Ferrara Seismic Sequence: Regional Crustal Structure, Earthquake Sources, and Seismic hazard. *Geophys. Res. Lett.* 39, a–n. doi:10.1029/2012GL053214

Malagnini, L., and Munafò, I. (2017). Mws of Seismic Sources under Thick Sediments. *Bull. Seismol. Soc. Am.* 107, 1413–1420. doi:10.1785/0120160243

Malinverno, A., and Ryan, W. B. F. (1986). Extension in the Tyrrhenian Sea and Shortening in the Apennines as Result of Arc Migration Driven by Sinking of the Lithosphere. *Tectonics* 5, 227–245. doi:10.1029/TC005i002p00227

Margheriti, L., Azzara, R. M., Cocco, M., Delladio, A., and Nardi, A. (2000). Analysis of Borehole Broadband Recordings: Test Site in the Po Basin, Northern Italy. *Bull. Seismol. Soc. Am.* 90, 1454–1463. doi:10.1785/01199900616

Martelli, L., Calabrese, L., Ercolessi, G., Molinari, F. C., Severi, P., Bonini, M., et al. (2017). "The New Seismotectonic Map of the Emilia-Romagna Region and Surrounding Areas," in Atti Del. 36° Convegno Nazionale GNTS, Trieste, Italy, November 14–16, 2017, 47–53.

Marzorati, S., and Bindi, D. (2006). Ambient Noise Levels in north central italy. *Geochem. Geophys. Geosyst.* 7, Q09010. doi:10.1029/2006GC001256

Masson, C., Mazzotti, S., Vernant, P., and Doerflinger, E. (2019). Extracting Small Deformation beyond Individual Station Precision from Dense Global Navigation Satellite System (GNSS) Networks in France and Western Europe. *Solid Earth* 10, 1905–1920. doi:10.5194/se-10-1905-2019

Maury, V. M. R., Grassob, J.-R., and Wittlinger, G. (1992). Monitoring of Subsidence and Induced Seismicity in the Lacq Gas Field (france): the Consequences on Gas Production and Field Operation. *Eng. Geol.* 32, 123–135. doi:10.1016/0013-7952(92)90041-v

McClure, M., Gibson, R., Chiu, K. K., and Ranganath, R. (2017). Identifying Potentially Induced Seismicity and Assessing Statistical Significance in oklahoma and california. *J. Geophys. Res.* 122, 2153–2172. doi:10.1002/2016jb013711

McNamara, D. P. B. R., Buland, R. P., Benz, H., and Leith, W. (2004). Earthquake Detection and Location Capabilities of the Advanced National Seismic System. American Geophysical Union, Fall Meeting, San Francisco, CA, December 13–17, 2004. abstract id. S21A-0264. Bibcode: 2004AGUFM.S21A0264M.

Milana, G., Bordoni, P., Cara, F., Di Giulio, G., Hailemikael, S., and Rovelli, A. (2014). 1D Velocity Structure of the Po River plain (Northern Italy) Assessed by Combining strong Motion and Ambient Noise Data. *Bull. Earthquake Eng.* 12, 2195–2209. doi:10.1007/s10518-013-9483-y

Molina, I., Velásquez, J. S., Rubinstein, J. L., Garcia-Aristizabal, A., and Dionicio, V. (2020). Seismicity Induced by Massive Wastewater Injection Near Puerto Gaitán, Colombia. *Geophys. J. Int.* 223, 777–791. doi:10.1093/gji/ggaa326

Montuori, A., Anderlini, L., Palano, M., Albano, M., Pezzo, G., Antoncecchi, I., et al. (2018). Application and Analysis of Geodetic Protocols for Monitoring Subsidence Phenomena along On-Shore Hydrocarbon Reservoirs. *Int. J. Appl. Earth Obs. Geoinf.* 69, 13–26. doi:10.1016/j.jag.2018.02.011

Mordret, A., Shapiro, N. M., and Singh, S. (2014). Seismic Noise-Based Time-Lapse Monitoring of the Valhall Overburden. *Geophys. Res. Lett.* 41, 4945–4952. doi:10.1002/2014gl060602

Munafò, I., Malagnini, L., and Chiaraluce, L. (2016). On the Relationship betweenMwandMLfor Small Earthquakes. *Bull. Seismol. Soc. Am.* 106, 2402–2408. doi:10.1785/0120160130

P. Burrato, P., F. Ciucci, F., and G. Valensise, G. (2003). An Inventory of River Anomalies in the Po Plain, Northern Italy: Evidence for Active Blind Thrust Faulting. *Ann. Geophys.* 46, 865–882. doi:10.4401/ag-3459

Pesaresi, D., Romanelli, M., Barnaba, C., Bragato, P. L., and Durì, G. (2014). OGS Improvements in 2012 in Running the North-eastern Italy Seismic Network: the Ferrara VBB Borehole Seismic Station. *Adv. Geosci.* 36, 61–67. doi:10.5194/adgeo-36-61-2014

Peterson, J. (1993). Observation and Modeling of Seismic Background Noise. *U.S. Geol. Surv. Open-file Rept* 93, 94.

Pezzo, G., De Gori, P., Lucente, F. P., and Chiarabba, C. (2018). Pore Pressure Pulse Drove the 2012 Emilia (Italy) Series of Earthquakes. *Geophys. Res. Lett.* 45, 682–690. doi:10.1002/2017GL076110

Pieri, M. (1983). "Three Seismic Profiles through the Po Plain," in *Seismic Expression of Structural Styles. A Picture and Work Atlas*. Editor A. W. Bally (Tulsa: American Association of Petroleum Geologists).

Priolo, E., Romanelli, M., Plasencia Linares, M. P., Garbin, M., Peruzza, L., Romano, M. A., et al. (2015). Seismic Monitoring of an Underground Natural Gas Storage Facility: the Collalto Seismic Network. *Seismol. Res. Lett.* 86, 109–123. doi:10.1785/0220140087

Qu, F., Lu, Z., Zhang, Q., Bawden, G. W., Kim, J.-W., Zhao, C., et al. (2015). Mapping Ground Deformation over Houston-Galveston, Texas Using Multi-Temporal InSAR. *Remote Sensing Environ.* 169, 290–306. doi:10.1016/j.rse.2015.08.027

Ringdal, F. (1975). On the Estimation of Seismic Detection Thresholds. *Bull. Seismol. Soc. Am.* 65, 1631–1642. doi:10.1785/bssa0650061631

Rovida, A., Locati, M., Camassi, R., Lolli, B., and Gasperini, P. (2020). The Italian Earthquake Catalogue Cpti15. *Bull. Earthquake Eng.* 18, 2953–2984. doi:10.1007/s10518-020-00818-y

Schoenball, M., Davatzes, N. C., and Glen, J. M. G. (2015). Differentiating Induced and Natural Seismicity Using Space-Time-Magnitude Statistics Applied to the Coso Geothermal Field. *Geophys. Res. Lett.* 42, 6221–6228. doi:10.1002/2015gl064772

Schultz, R., and Telesca, L. (2018). The Cross-Correlation and Reshuffling Tests in Discerning Induced Seismicity. *Pure Appl. Geophys.* 175, 3395–3401. doi:10.1007/s00024-018-1890-1

Scrocca, D., Carminati, E., Doglioni, C., and Marcantoni, D. (2007). "Slab Retreat and Active Shortening along the central-northern Apennines," in *Thrust Belts and Foreland Basins*. Editors O. Lacombe, F. Roure, J. Lavé, and J. Vergés (Berlin, Heidelberg: Springer Berlin Heidelberg), 471–487. doi:10.1007/978-3-540-69426-7_25

Segall, P. (1989). Earthquakes Triggered by Fluid Extraction. *Geol* 17, 942–946. doi:10.1130/0091-7613(1989)017<0942:etbfe>2.3.co;2

Segall, P., Grasso, J.-R., and Mossop, A. (1994). Poroelastic Stressing and Induced Seismicity Near the Lacq Gas Field, Southwestern france. *J. Geophys. Res.* 99, 15423–15438. doi:10.1029/94jb00989

Serpelloni, E., Faccenna, C., Spada, G., Dong, D., and Williams, S. D. P. (2013). Vertical GPS Ground Motion Rates in the Euro-Mediterranean Region: New Evidence of Velocity Gradients at Different Spatial Scales along the Nubia-Eurasia Plate Boundary. *J. Geophys. Res. Solid Earth* 118, 6003–6024. doi:10.1002/2013JB010102

Serpelloni, E., Pintori, F., Gualandi, A., Scoccimarro, E., Cavaliere, A., Anderlini, L., et al. (2018). Hydrologically Induced Karst Deformation: Insights from GPS Measurements in the Adria-Eurasia Plate Boundary Zone. *J. Geophys. Res. Solid Earth* 123, 4413–4430. doi:10.1002/2017JB015252

Shapiro, S. A., Dinske, C., and Kummerow, J. (2007). Probability of a Given-Magnitude Earthquake Induced by a Fluid Injection. *Geophys. Res. Lett.* 34, L22314. doi:10.1029/2007GL031615

Silverii, F., D'Agostino, N., Métois, M., Fiorillo, F., and Ventafridda, G. (2016). Transient Deformation of Karst Aquifers Due to Seasonal and Multiyear Groundwater Variations Observed by GPS in Southern Apennines (Italy). *J. Geophys. Res. Solid Earth* 121, 8315–8337. doi:10.1002/2016JB013361

Skoumal, R. J., Ries, R., Brudzinski, M. R., Barbour, A. J., and Currie, B. S. (2018). Earthquake Induced by Hydraulic Fracturing Are Pervasive in oklahoma. *J. Geophys. Res.* 123, 10,918–10,935. doi:10.1029/2018jb016790

Suppe, J., and Medwedeff, D. A. (1990). Geometry and Kinematics of Fault-Propagation Folding. *Eclogae Geologicae Helvatiae* 83, 409–454.

Teatini, P., Castelletto, N., Ferronato, M., Gambolati, G., Janna, C., Cairo, E., et al. (2011). Geomechanical Response to Seasonal Gas Storage in Depleted Reservoirs: A Case Study in the Po River basin, Italy. *J. Geophys. Res.* 116, F02002. doi:10.1029/2010JF001793

van Thienen-Visser, K., and Breunese, J. N. (2015). Induced Seismicity of the Groningen Gas Field: History and Recent Developments. *Leading Edge* 34, 602–728. doi:10.1190/tle34060664.1

Vasco, D. W., Karasaki, K., and Doughty, C. (2000). Using Surface Deformation to Image Reservoir Dynamics. *Geophysics* 65, 132–147. doi:10.1190/1.1444704

Vassallo, M., Festa, G., and Bobbio, A. (2012). Seismic Ambient Noise Analysis in Southern Italy. *Bull. Seismol. Soc. Am.* 102, 574–586. doi:10.1785/0120110018

Werner, C., Wegmuller, U., Strozzi, T., and Wiesmann, A. (2003). "Interferometric point Target Analysis for Deformation Mapping," in IEEE International Geoscience and Remote Sensing Symposium, Toulouse, France, July 21–25, 2003 (Piscataway, NJ, USA: IEEE), 4362–4364.

Wonnacott, T., and Wonnacott, R. J. (1977). *Introductory Statistics*. New York: Wiley.

Zhao, X., and Jha, B. (2019). Role of Well Operations and Multiphase Geomechanics in Controlling Fault Stability during CO 2 Storage and Enhanced Oil Recovery. *J. Geophys. Res. Solid Earth* 124, 6359–6375. doi:10.1029/2019jb017298

Conflict of Interest: The authors declare that the research was conducted in the absence of any commercial or financial relationships that could be construed as a potential conflict of interest.

Publisher's Note: All claims expressed in this article are solely those of the authors and do not necessarily represent those of their affiliated organizations, or those of the publisher, the editors and the reviewers. Any product that may be evaluated in this article, or claim that may be made by its manufacturer, is not guaranteed or endorsed by the publisher.

Advantages of publishing in Frontiers

OPEN ACCESS
Articles are free to read for greatest visibility and readership

FAST PUBLICATION
Around 90 days from submission to decision

HIGH QUALITY PEER-REVIEW
Rigorous, collaborative, and constructive peer-review

TRANSPARENT PEER-REVIEW
Editors and reviewers acknowledged by name on published articles

Frontiers
Avenue du Tribunal-Fédéral 34
1005 Lausanne | Switzerland

Visit us: www.frontiersin.org
Contact us: frontiersin.org/about/contact

REPRODUCIBILITY OF RESEARCH
Support open data and methods to enhance research reproducibility

DIGITAL PUBLISHING
Articles designed for optimal readership across devices

FOLLOW US
@frontiersin

IMPACT METRICS
Advanced article metrics track visibility across digital media

EXTENSIVE PROMOTION
Marketing and promotion of impactful research

LOOP RESEARCH NETWORK
Our network increases your article's readership